

Optoelectronic Physics and Engineering of Atomically  
Thin Photovoltaics

Thesis by  
Joeson Wong

In Partial Fulfillment of the Requirements for the  
Degree of  
Doctor of Philosophy

Caltech

CALIFORNIA INSTITUTE OF TECHNOLOGY  
Pasadena, California

2022  
Defended November 22, 2021

© 2022

Joeson Wong  
ORCID: 0000-0002-6304-7602

All rights reserved

## ACKNOWLEDGEMENTS

It's amazing that six years has passed by so quickly. I have gained many new experiences and perspectives—some I would have never thought would be part of a PhD program. Certain lessons were definitely more painful than others, but assuredly, those are lessons I will never forget. None of those lessons, however, would have been possible without the amazing people I have had a chance to interact with and learn from throughout my time at Caltech, so it is my pleasure to acknowledge their contributions to this PhD journey.

I would first and foremost like to acknowledge my PhD advisor and scientific mentor for the past six years, Harry Atwater. Harry has an infectious enthusiasm and curious nature for scientific problems which I have absorbed, in part, through osmosis. The energy he brings towards science is akin to the quote from Michigan football coach Jim Harbaugh, "Attack each day with enthusiasm unknown to mankind". I am reminded of those words whenever we engage in a scientific discussion. I have also gained a deep respect for Harry's "superman" ability to juggle and excel at both his social and academic responsibilities, something that I hope to echo in my life as well. Harry also has a deep affinity to solving issues in today's society, which is reflected by both the diversity of his research group and in his research directions. There are many other things I could say about Harry, but perhaps the most important thing I can say is just 'thank you'. Thank you for taking a chance on this boy from Michigan and teaching me so much these past six years, I am forever indebted to having you as my scientific mentor.

Two other special mentors I must acknowledge are Deep Jariwala and Artur Davoyan, both postdocs in the group that soon became professors of their own. Both of them contributed substantially to the works discussed in Chapters 3, 4, and 5. Deep has taught me so much regarding experimental procedures and the scientific process, and always had a seemingly limitless knowledge of 2D materials literature and other current events. His intentional but playful attitude towards experimental research is something I have tried to emulate throughout my PhD. I am also grateful to have learned early on from Deep that collaborating with others is often the most efficient way to get things done. Artur also deserves a special acknowledgement. I remember my first impression of him was that he was extremely harsh and intimidating with his probing questions! Over the years however, I have developed a deep respect and friendship with Artur, and I regard him as one of the most intelligent and

outside-the-box thinkers I know of. His visionary perspective on solving impactful problems is contagious. The long nights we would have doing or chatting about science together and the advice he has given me throughout my PhD are some of the most valuable.

I would also like to thank my thesis committee members, Professor Joseph Falson, Professor Stevan Nadj-Perge, and Professor Tony Heinz as well as my candidacy committee members, Professor Marco Bernardi, Professor Stevan Nadj-Perge, and Professor David Hsieh, for their helpful suggestions and feedback throughout my PhD. I specifically want to thank Professor Falson for his career advice in a life in academia, I hope I can put it to good use. I would also like to specifically thank Professor Nadj-Perge and his group for interactions early on that enabled making higher quality heterostructures of 2D materials. Finally, I would like to thank Professor Heinz for seemingly knowing everything there is about the optical properties of layered materials and laying the foundation for studying these materials. I would also like to thank the National Science Foundation for supporting me for the first few years of my PhD, which enabled me to carve out a unique independent research direction. For the last few years, I have been supported by the Photonics at Thermodynamics Limit EFRC grant, which has also been a deeply scientifically enriching experience.

I have also had the chance to interact with many other folks throughout the years, both in and out of the Atwater group. In particular, I would like to thank those who have joined me as major contributors to the variety of projects as it pertains to this thesis. Stefan “Brochenko” Omelchenko contributed significantly to the initial ideas and examining the analysis I did in Chapter 2, and I am grateful to have someone to bounce my wild ideas off of as I went through that project. I have always thought that Stefan personified the word “chill”, and I very much appreciated that. Cora Went has been a partner-in-crime throughout most of my years as a PhD student and doubles as an amazing travel buddy. She has contributed significantly to many of my projects, including the measurements of TMDC band tails in Chapter 2, ongoing work with strong coupling and absorbers as it pertains to Chapter 3, and for continuing the carrier selective contacts and stroboSCAT work discussed in the Outlook. I hope we can get more soup dumplings together in the future. Bolin Liao and the late Ahmed Zewail contributed significantly to the USEM measurements of the band bending junction work in Chapter 5. Seeing movies of electrons and holes moving around in a semiconductor is something I used to only dream of. In a similar vein, I would

like to thank the Advanced Light Source beamline scientists: Eli Rotenberg, Aaron Bostwick, and Chris Jozwiak. They taught me both the instrumental procedures and the principles of ARPES, which was used for the work in Chapter 5, and I certainly felt like a kid in a candy store the first time I saw bandstructure in real time. Hannah Weaver, Dipti Jasrasaria, Professor Eran Rabani, and Professor Naomi Ginsberg have also been essential to the stroboSCAT work. I am particularly grateful to Hannah, who has been persistently working on this project with me for many years. Chace (Chullhee) Cho and his advisor Professor SungWoo Nam also deserve a special acknowledgement for their contributions to Chapter 6. I am grateful that SungWoo decided to do a sabbatical in Harry's group in 2018, where Chace subsequently joined me as an officemate. I have learned tremendously about mechanical strain and its effects on materials as I collaborated with you both. The nights with Korean BBQ (Honey Pig!) and soju definitely fueled a variety of late-night endeavors as well. Last but certainly not least, I would like to thank Souvik Biswas for his contributions to our work on monolayer black phosphorus. Souvik has a relentless effort towards research, and I have yet to see a single person work harder than he has throughout my PhD. He shares very much the same attitude I have towards science, and I am deeply appreciative of our scientific discussions and our occasional (Ed Sheeran) jam sessions while doing some late-night lab work.

I would also be remiss to not acknowledge other co-authors, including Michelle Sherrott, William Whitney, Giulia Tagliabue, Ognjen Ilic, Zakaria Al Balushi, Hamidreza Akbari, Takashi Taniguchi, Kenji Watanabe, Albert Davydov, Amir Taqieddin, Narayana Aluru, Alberto Crepaldi, Andrey Krayev, Kiyoung Jo, George Rossman, Arky Yang, Tony Low, Aditya Mohite, and Michael Enright. Thank you all for either being a part of my projects or allowing me to be a part of and learn from yours.

I have also been given the opportunity to mentor a few undergraduate researchers throughout my time at Caltech, which have deeply impacted my views on mentorship. Kevin Tat was a SURF student in 2016 and contributed to the devices fabricated in Chapter 4, for which he is a co-author on. I'm thankful he was patient with me as I was teaching him things I had only recently learned. Sara Anjum was a SURF with me throughout the summer of 2018 and subsequently became a graduate student in the group the following year. She contributed to our knowledge on 2D materials transfer and I wish her the best of luck throughout the remainder of her PhD. Tyler Colenbrander was a SURF student with me throughout the summer of 2020 in the

middle of the COVID-19 pandemic. He made several important contributions to the analysis on monolayer absorbers in Chapter 3 and allowed me to “experiment” with different methods of teaching and mentorship. Thank you all for reminding me the thrilling feeling of being a teacher.

I would also like to give an acknowledgement and word of encouragement to the newly formed “2D-PV” team: Susana Torres-Londono, Rachel Tham, and Miles Johnson. Particularly with Susana, who joined Caltech early in part to work with me. I feel honored, humbled, and utterly responsible for all of you—so don’t be a stranger, even after I depart. Best of luck with your PhD journey, and always remember that it’s a marathon. Don’t forget to enjoy the running too.

Harry’s group is a special place, especially being both large and diverse which contrasts with a small school like Caltech. I first have to thank several of my forebearers from when I first joined the group, you all set in place the joyful culture of the A-team. Cris Flowers and Dagny Fleischman subtly coerced me into being the next ebeam guru in my first year, and I have learned a tremendous amount from working with them and the ebeam system. Will Whitney and Michelle Sherrott were my first officemates in 244 Watson and quickly helped me “grow up” as a graduate student, sharing with me lessons they learned throughout their PhD. Kelly Mauser was always a joy to spend time with and my go-to conference buddy. Benjamin “Benji” Vest was the founding member of the Bourbon and Burgers night (aka B&B&B) and I greatly appreciated his spirit to increase group social activities and his knowledge of optics. Thank you for showing me around Paris, too. Phil Jahelka has an amazing knowledge of semiconductors and anything related to chemistry, despite not being a chemist by training. I appreciated deeply his insights and the fun gatherings we had at his home. Mike Kelzenberg was a source of infinite wisdom on electronics and instrumentation, as well as random historical anecdotes of the group, and I appreciate his ‘wizardry’ greatly. Rebecca Glaudell was always thoughtful in terms of keeping the lab organized and running smoothly, and I thank her immensely for her duties as my go-to safety officer whenever I was unsure of safety procedures. The ‘Taiwanese Squad’, consisting of Sophia (Wen-Hui) Cheng, Pin Chieh Wu, Yu-Jung Lu (aka Yuri the Beautiful), and Yi-Rung Lin were always fun to be around late at night, and I enjoyed our food outings together. Giulia Tagliabue was always very warm and I’m grateful for some of the tips and tricks she showed me in the lab, as well as those in the climbing gym. I would also like to thank those that made my experience in Harry’s group particularly warm when I first joined the group,

including my interactions with Laura Kim, Jeremy Brouillet, Sisir Yalamanchilli, Carissa Eisler, Sunita Darbe, and John Lloyd.

There are also many of my contemporaries that I would like to acknowledge as well. Alex Welch and Magel Su became the next generation of ebeam gurus, and I'm especially thankful for Alex for taking a nice picture when the ebeam was spouting water—no one would have believed us otherwise. I've appreciated my many coffee hours with many members of the group, including (but not limited to): Hamid (Hamidreza) Akbari, Souvik Biswas, Komron Shayegan, and Parker Wray. I especially want to thank Parker for his advice on my personal life on many occasions. Megan Phelan was always a source of encouragement and thoughtfulness, and I'm thankful for our friendship and occasional wine nights together. Samuel Loke always had a multitude of board games to play at his place and is one of the most thoughtful activity hosts I know of. Finally, I want to thank Cora Went and Souvik Biswas once again, not just for their contributions throughout my thesis, but for taking the baton in many occasions.

I would also like to acknowledge and thank the administrative staff that has made Caltech such a wonderful and truly unique place, including: Kam Flower, Jonathan Gross, Angie Riley, Lyann Lau, Liz Hormigoso, Tiffany Kimoto, Jennifer Blankenship, Carrie Hofmann, and Christy Jenstad. I especially want to thank Jonathan Gross and Christy Jenstad. They were one of the first people I met when I was visiting Caltech and their warmth was something that instantly drew me here.

Outside of Harry's group, I've had the fortune to have some amazing friends. I have a special gratitude to Peishi Cheng, who has been my roommate and close friend for over four years and always has something good cooking in the kitchen. I've enjoyed many of our foodventures together (including the one and only Tsujita) and appreciate your thoughtfulness on many of the personal aspects of my life. I would also like to give a special thank you to Jash Bunker, who has also been one of my closest friends throughout my PhD. I have enjoyed so many of our times together while exploring Los Angeles and I am grateful that I met someone with so many mutual interests. I hope I can visit you soon in Germany! A special thank you needs to be given to Joanne Wai, who has made me grow tremendously as an individual. I hope you're surviving the Utah weather! The 'Yangji' squad also deserves a special shoutout, consisting of Jash, Michelle, Kai, Pai, Claire, Nori, Shiori, and Sam. Somehow we ended up being an amalgamation of folks from the Asian diaspora, and I am glad to have both connected culturally with my roots and made some

great friends along the way. Our game nights together were so much fun. I would also like to thank many of the other friends that I have shared special moments with throughout these last several years: Ali Naqvi, Jessica Chen, Tom Liu, Vanna Quon, Vivienne Do, Qui Nguyen, Tara Kwan, Irene Hong, Daniel Pan, Lynn Yi, Erika Ye, Brynn Holbrook, Steven Wood, Aya Mimura, Thom Bohdanowicz, Austin Liu, Bryce Edwards, Anthony Ardizzi, Megan Schill, Elise Tookmanian, Rebecca Gallivan, Eowyn Lucas, Amylynn Chen, Wei-Lin Tan, Siobhan McArdle, Katherine Rinaldi, Oscar and Hannah Zamora, Jane Siu, Louis Tsui, Jordan Goldstein, and Mohammad Islam. I'm sorry if I missed anyone specifically, but if you ever put a smile on my face, I am thankful for you, too.

I would also like to express my deepest gratitude for the scientific mentors I had during undergrad that made this PhD journey even remotely possible: Jeremy Feldblyum, Adam Matzger, Vidya Ganapati, Eli Yablonovitch, Alan Teran, Jamie Philips, Aaron Rosenberg, Katja Nowack, John Kirtley, and Kam Moler. Jeremy Feldblyum deserves a special acknowledgement, as his mentorship in my first ever research experience was likely what made me continue pursuing research opportunities throughout undergrad and eventually a PhD.

Much of this thesis would also not be possible without the support and encouragement of my family. Dad, thank you for always supporting me in this academic path and your general cheerfulness in the face of adversity. Your passion for esoteric topics, while hardly scientific, is likely how I developed an interest in topics as esoteric as the ones in science. Mom, thank you for encouraging me to seek academic opportunities when I was younger and supporting me with all of your food and advice the last few years. I'm grateful that being at Caltech has allowed me to reconnect with you. I would also like to acknowledge my sister and my cousins, specifically: Mickey, Rose, Roby, Wayman, and Jerry. Our game nights during the COVID-19 pandemic was nostalgic of our younger years together.

## ABSTRACT

Materials that are atomically thin behave substantially different than those of their bulk counterparts. However, when most materials become thinner, their surface-to-volume ratio increases and the number of unpassivated dangling bonds at the surface approaches the number of internal crystalline bonds, which prevents examining the intrinsic properties of most ultrathin materials. The recent discovery of layered materials, whose crystal structures have naturally passivated basal planes, has enabled the possibility to examine materials' thicknesses that approach a single atomic layer. In this thesis, we examine and explore the consequence of this new regime of thickness for active layers in photovoltaic applications. Specifically, we focus on the three aspects that define photovoltaic operation and explore their differences in these ultrathin materials: optical absorption of photons, subsequent carrier generation and transport, and finally, free energy extraction of collected carriers. We first discuss the implications of band-edge abruptness on the maximum efficiency of a solar cell. Then, we show that optical absorption in these ultrathin materials is dominated by cavity wave optics, and design structures that enable near-unity absorption in both ultrathin ( $\sim 10$  nm) and atomically-thin ( $\sim 7$  Å) active layers. Using these optical design rules, we design heterostructures with record incident photon to electron conversion efficiency ( $>50\%$ ). Next, we examine new methods of creating electrical junctions by using *thickness* to vary the amount of band bending in a material. We spatiotemporally image these 'band-bending junctions' for the first time. Finally, we argue that photoluminescence can be used as a direct readout of the open circuit voltage potential, and motivate examination of monolayer materials which have substantially higher radiative efficiency. We therefore examine the strain tuning of photoluminescence properties of both monolayer TMDC and heterobilayer TMDC systems. This work illustrates that van der Waals materials are an ideal system for examining the novel optoelectronic physics of atomically thin photovoltaics.

## PUBLISHED CONTENT AND CONTRIBUTIONS

\* indicates equal contribution

[1] Chullhee Cho\*, **Joeson Wong\***, Amir Taqieddin, Souvik Biswas, Narayana R. Aluru, SungWoo Nam, and Harry A. Atwater. Highly strain-tunable interlayer excitons in  $\text{mos}_2/\text{wse}_2$  heterobilayers. *Nano Letters*, 4 2021. doi:[10.1021/acs.nanolett.1c00724](https://doi.org/10.1021/acs.nanolett.1c00724).  
*J.W. generated the ideas, participated in fabrication and optical measurements of the samples, analyzed the data, and assisted with writing the manuscript.*

[2] Deep Jariwala, Artur R. Davoyan, Giulia Tagliabue, Michelle C. Sherrott, **Joeson Wong**, and Harry A. Atwater. Near-unity absorption in van der waals semiconductors for ultrathin optoelectronics. *Nano Letters*, 16(9):5482–5487, 2016. doi:[10.1021/acs.nanolett.6b01914](https://doi.org/10.1021/acs.nanolett.6b01914).  
*J.W. contributed to the fabrication and measurement of the samples.*

[3] Deep Jariwala, Artur R. Davoyan, **Joeson Wong**, and Harry A. Atwater. Van der waals materials for atomically-thin photovoltaics: Promise and outlook. *ACS Photonics*, 11 2017. doi:[10.1021/acsphotonics.7b01103](https://doi.org/10.1021/acsphotonics.7b01103).  
*J.W. performed the modified detailed balance calculations and contributed to the writing and presentation of the manuscript.*

[4] **Joeson Wong**, Tyler Colenbrander, Cora Went, Susana Torres-Londono, Rachel Tham, and Harry A. Atwater. Perfect absorption in monolayer  $\text{ws}_2$ . *In Preparation*, 2022.  
*J.W. generated the ideas, fabricated the samples, created and automated the optical set-up, performed all the measurements, data analysis, and calculations, and wrote the manuscript.*

[5] **Joeson Wong\***, Deep Jariwala\*, Giulia Tagliabue, Kevin Tat, Artur R. Davoyan, Michelle C. Sherrott, and Harry A. Atwater. High photovoltaic quantum efficiency in ultrathin van der waals heterostructures. *ACS Nano*, 11(7):7230–7240, 2017. doi:[10.1021/acsnano.7b03148](https://doi.org/10.1021/acsnano.7b03148).  
*J.W. generated the ideas, fabricated and measured the devices, analyzed the data, performed the calculations, and wrote the manuscript.*

[6] **Joeson Wong\***, Stefan T. Omelchenko\*, and Harry A. Atwater. Impact of semiconductor band tails and band filling on photovoltaic efficiency limits. *ACS Energy Letters*, 6(1):52–57, 12 2020. doi:[10.1021/acsenergylett.0c02362](https://doi.org/10.1021/acsenergylett.0c02362).  
*J.W. generated the ideas, performed all the derivations, calculations, analysis, and wrote the manuscript.*

[7] **Joeson Wong**, Artur Davoyan, Bolin Liao, Andrey Krayev, Kiyoung Jo, Eli Rotenberg, Aaron Bostwick, Chris M. Jozwiak, Deep Jariwala, Ahmed H. Ze-

wail, and Harry A. Atwater. Spatiotemporal imaging of thickness-induced band-bending junctions. *Nano Letters*, 6 2021. doi:[10.1021/acs.nanolett.1c01481](https://doi.org/10.1021/acs.nanolett.1c01481).

*J.W. generated the ideas, fabricated the samples, performed the ARPES measurements, assisted in the KPFM and SUEM measurements, analyzed the data, performed the calculations, and wrote the manuscript.*

[8] **Joeson Wong**, Stefan T. Omelchenko, and Harry A. Atwater. Fundamental photovoltaic efficiency limits due to semiconductor band tails. In *2021 IEEE 48th Photovoltaic Specialists Conference (PVSC)*, pages 1315–1317, 2021. doi:[10.1109/PVSC43889.2021.9518548](https://doi.org/10.1109/PVSC43889.2021.9518548).

*J.W. generated the ideas, performed all the derivations, calculations, analysis, and wrote the manuscript.*

## TABLE OF CONTENTS

Acknowledgements . . . . .	iii
Abstract . . . . .	ix
Published Content and Contributions . . . . .	x
Table of Contents . . . . .	xi
List of Illustrations . . . . .	xv
List of Tables . . . . .	xix
Chapter I: Introduction . . . . .	1
1.1 Physics and Engineering of Conventional Photovoltaics . . . . .	1
1.2 Entering Flatland: van der Waals Materials . . . . .	14
1.3 What's Different in Atomically-thin Photovoltaics? . . . . .	16
1.4 Scope of the Thesis . . . . .	19
 <b>I Absorption Defines the Limits</b>	<b>21</b>
Chapter II: Impact of the Semiconductor Band-Edge on Photovoltaic Efficiency Limits . . . . .	22
2.1 Introduction . . . . .	22
2.2 Photovoltaic Efficiency Limit for Semiconductors with Band Tails . .	24
2.3 Generalized Voltage Loss for Semiconductors with Nonabrupt Band Edges . . . . .	26
2.4 Outlook on Examining Semiconductor Band Tails . . . . .	31
2.5 Importance of the Direct-Indirect Gap Splitting on the Efficiency Potential of Ultrathin TMDC Photovoltaics . . . . .	33
2.6 Appendix . . . . .	39
Chapter III: Optical Design of Cavity Coupling to Excitonic TMDCs . . . . .	58
3.1 Linear Dielectric Function of TMDCs . . . . .	58
3.2 Multilayer Near Unity Absorption . . . . .	62
3.3 Monolayer Near Unity Absorption . . . . .	66
3.4 Monolayer Near Unity Absorption at Room Temperature . . . . .	68
3.5 Experimental Demonstration of Near Unity Absorption in Monolayer WS <sub>2</sub> at Room Temperature . . . . .	70
3.6 Efficiency Limits of Excitonic Multijunctions . . . . .	75
 <b>II Traversing through Flatland</b>	<b>80</b>
Chapter IV: High photovoltaic quantum efficiency in ultrathin van der Waals heterostructures . . . . .	81
4.1 Introduction . . . . .	81
4.2 Van der Waals Heterostructure Device Fabrication . . . . .	83

4.3 Spatial Photocurrent Map and IV Measurements . . . . .	86
4.4 Spectral Response Measurements . . . . .	86
4.5 Electromagnetic Simulations and Error Estimation . . . . .	87
4.6 Prototypical Optoelectronic Device Characterization . . . . .	88
4.7 Absorption in van der Waals heterostructures . . . . .	90
4.8 Carrier collection efficiency in van der Waals semiconductor junctions	93
4.9 High Photovoltaic Quantum Efficiency Outlook . . . . .	100
4.10 Appendix . . . . .	102
<b>Chapter V: Spatiotemporal Imaging of Thickness-Induced Band Bending</b>	
Junctions . . . . .	106
5.1 Introduction . . . . .	106
5.2 Correlation between Electronic Properties and Thickness in Ultrathin Semiconductors . . . . .	107
5.3 Spatiotemporal Imaging of Charge Carrier Separation due to Thickness	111
5.4 Conclusions and Outlook . . . . .	119
5.5 Appendix . . . . .	120
<b>III The Luminescence is the Voltage</b>	<b>123</b>
<b>Chapter VI: Highly strain tunable interlayer excitons in MoS<sub>2</sub>/WSe<sub>2</sub> Heterobilayers</b>	
6.1 Introduction . . . . .	124
6.2 Local Strain Engineering of Intra- vs. Inter-layer excitons . . . . .	125
6.3 Tuning Interlayer Coupling through Strain Engineering . . . . .	132
6.4 <i>ab initio</i> strain calculations of TMDC heterobilayers . . . . .	135
6.5 Conclusion and Outlook . . . . .	139
6.6 Appendix . . . . .	140
<b>IV What's next for Flatland?</b>	<b>142</b>
<b>Chapter VII: Conclusions and Outlook</b>	
7.1 Outlook from Semiconductor Band Tails Work . . . . .	144
7.2 Outlook on Unity Absorbance and Cavity Coupling to Excitonic Absorbers . . . . .	146
7.3 Outlook on Achieving High-Efficiency, TMDC-based Photovoltaic Devices . . . . .	149
Bibliography . . . . .	152
<b>Appendices</b>	<b>176</b>
<b>Appendix A: Microscopic Physics of Excitonic Systems</b>	
A.1 Formation and Dissociation of Excitons . . . . .	177
<b>Appendix B: Macroscopic Optical Properties of Layered Structures</b>	
B.1 Boundary conditions on Electromagnetic Fields . . . . .	184
B.2 Optical Waves in Homogenous Media . . . . .	188

B.3 Transfer Matrix Method for Layered Media . . . . .	192
B.4 Lorentz Oscillator Model . . . . .	198
B.5 Reflection, Transmission, and Absorption of a 2D exciton . . . . .	200
Appendix C: Thermodynamics Considerations of Photovoltaic Systems . . . . .	205
C.1 Derivation of Blackbody Radiation . . . . .	205
C.2 The Chemical Potential of a Photon . . . . .	210
C.3 The Validity of a Thermalized Population as the Major Contribution to Photoluminescence Under Steady State Excitation . . . . .	214
C.4 The Validity of A Single Quasi-Fermi Level to Describe Carriers Occupying Multiple Energy Levels . . . . .	216
Appendix D: Computer Code . . . . .	220

## LIST OF ILLUSTRATIONS

<i>Number</i>	<i>Page</i>
1.1 Typical Solar Cell IV Curves . . . . .	3
1.2 NREL Efficiency Chart . . . . .	4
1.3 $J_{sc}$ vs. $V_{oc}$ . . . . .	5
1.4 Detailed Balance Efficiency Limit . . . . .	14
1.5 van der Waals Heterostructures . . . . .	15
1.6 van der Waals Photovoltaics Schematic . . . . .	16
1.7 Dimensionality Effects on Exciton Screening . . . . .	17
2.1 Accounting for band filling in modified reciprocity relations . . . . .	23
2.2 Effects of band tailing on photovoltaic limiting efficiencies . . . . .	25
2.3 Dependence of photovoltaic figures of merit on the Urbach parameter	26
2.4 Effects of thickness on photovoltaic figures of merit . . . . .	27
2.5 Analysis of a Gaussian band tail distribution . . . . .	28
2.6 Effects of band tail states on photoluminescence . . . . .	29
2.7 Generalized voltage losses parametrized as a two-bandgap absorber .	30
2.8 Voltage loss due to a nonabrupt band-edge . . . . .	32
2.9 Unique Bandstructure and Absorption Edge of Bulk TMDCs . . . . .	34
2.10 Absorption Toy Model for Bulk TMDCs . . . . .	36
2.11 Photovoltaic Figures of Merit of $WS_2$ for Varying $C_{AE}$ and $ERE_0$ .	38
2.12 Photovoltaic Figures of Merit of $MoSe_2$ for Varying $C_{AE}$ and $ERE_0$ .	39
2.13 The importance of including band filling effects . . . . .	44
2.14 Effects of band tails and band filling on ideality factor and current-voltage relationships . . . . .	47
2.15 Analysis of a two-bandgap toy model . . . . .	50
2.16 Effects of a sub-unity collection efficiency below the bandgap . . . .	54
2.17 Different band edges that map onto a two-bandgap model . . . . .	57
3.1 First measurements of the bulk $MoS_2$ dielectric function . . . . .	59
3.2 Room temperature dielectric function of monolayer TMDCs . . . . .	60
3.3 Bandstructure as a function of thickness . . . . .	61
3.4 Designing ultrathin absorbing cavities . . . . .	62
3.5 Near Unity Absorption in ultrathin TMDCs . . . . .	64
3.6 Angle dependence of absorption in ultrathin TMDC/Ag structures .	66

3.7	Metallic Optical Cavity for Monolayer Perfect Absorption . . . . .	70
3.8	Dielectric-Metal Optical Cavity for Monolayer Perfect Absorption . .	71
3.9	Relationship between Absorption and Excitonic Linewidth . . . . .	72
3.10	Geometric tolerance of monolayer perfect absorption optical cavities	73
3.11	Experimental Demonstration of Near-Unity Absorption in WS <sub>2</sub> at Room Temperature . . . . .	74
3.12	Schematic of Reflectance Measurement Set-up . . . . .	76
3.13	Limiting Efficiency of Excitonic Multijunctions . . . . .	77
3.14	Optimal Absorption Spectra of Excitonic Multijunctions . . . . .	79
4.1	Achieving High External Quantum Efficiency in van der Waals heterostructures . . . . .	82
4.2	High Photovoltaic Quantum Efficiency Sample Images . . . . .	85
4.3	Optoelectronic Performance Characteristics . . . . .	89
4.4	Power dependent device characteristics . . . . .	91
4.5	Absorbance in van der Waals heterostructures . . . . .	92
4.6	Charge transport and collection in vertical PN and Schottky junction geometries . . . . .	96
4.7	Few-layer graphene as a transparent top contact . . . . .	97
4.8	Absorbance and EQE of thick and thin PN heterojunctions . . . . .	99
4.9	Thickness dependence on charge collection efficiency . . . . .	100
4.10	Estimated 1 Sun AM 1.5G Performance . . . . .	103
5.1	Thickness-dependent surface potentials due to vertical band bending .	108
5.2	Experimental observation of thickness-dependent surface doping in MoS <sub>2</sub> /Au	109
5.3	Contact potential difference of other MoS <sub>2</sub> flakes on Au . . . . .	110
5.4	Photoemission spectroscopy of another MoS <sub>2</sub> flake on Au . . . . .	112
5.5	Scanning Ultrafast Electron Microscopy Imaging of a Band Bending Junction	113
5.6	Scanning ultrafast electron microscopy of bulk MoS <sub>2</sub> on Au . . . .	114
5.7	Scanning ultrafast electron microscopy of monolayer MoS <sub>2</sub> on Au .	115
5.8	Schematic depiction of carrier transport at a band bending junction .	116
5.9	Simulated carrier dynamics for various material parameters . . . . .	117
5.10	Hole dominated charge transport . . . . .	118
5.11	Simulation of Carrier Dynamics at a Bend Bending Junction . . . . .	119
6.1	Fabrication of wrinkled MoS <sub>2</sub> /WSe <sub>2</sub> heterobilayer . . . . .	126
6.2	Sample fabrication and characterization of wrinkled heterostructures	127
6.3	Optical characterization of flat heterobilayers of MoS <sub>2</sub> /WSe <sub>2</sub> on PDMS	128

6.4	Photoluminescent mapping of the fabricated wrinkled MoS <sub>2</sub> /WSe <sub>2</sub> heterobilayer . . . . .	129
6.5	Photoluminescence of strained heterobilayers . . . . .	130
6.6	Optical characterization of different wrinkled MoS <sub>2</sub> /WSe <sub>2</sub> heterobilayer samples . . . . .	131
6.7	Photoluminescence (PL) measurement on wrinkled heterobilayers of MoS <sub>2</sub> /WSe <sub>2</sub> via vertical scanning (XZ-PL scanning) accounting for the finite depth of focus . . . . .	132
6.8	Raman spectroscopy and deformation potentials of strained heterobilayers . . . . .	133
6.9	Raman mapping of strained heterobilayers . . . . .	135
6.10	Wrinkle geometry-driven strain analysis . . . . .	135
6.11	Density functional theory calculation of strained MoS <sub>2</sub> /WSe <sub>2</sub> heterobilayers . . . . .	136
6.12	Weighted band structures obtained using DFT calculations . . . . .	137
6.13	Band hybridization as a function of strain with different interlayer distances . . . . .	138
6.14	Effects of strain, interlayer spacing, and different stacking configurations on the electronic band structure of MoS <sub>2</sub> /WSe <sub>2</sub> heterobilayer system obtained using DFT calculations . . . . .	139
7.1	I-V performance of a carrier selective contact device . . . . .	150
7.2	X-ray photoemission spectroscopy of TiO <sub>x</sub> and NiO <sub>x</sub> . . . . .	151
A.1	Exciton Wavefunction under an Electric Field . . . . .	179
A.2	Exciton Dissociation Efficiency under an Electric Field . . . . .	180
A.3	Exciton Binding Energy under an Electric Field . . . . .	180
A.4	Exciton Binding Energy vs. Screening Length . . . . .	181
A.5	Wavefunctions of the excitons in the 2D Keldysh potential, for $n = 1, 2, 3, 4$ for each row, i.e. $s, p, d, f$ -like wavefunctions. Wavefunctions are similar to the hydrogenic model. . . . .	183
B.1	A schematic of a Gaussian pillbox (dotted box) with height $h$ and area $A$ sandwiched between two materials with dielectric constant $\epsilon_1$ and $\epsilon_2$ . . . . .	185
B.2	A schematic of a Gaussian loop (dotted rectangle) with height $h$ and length $l$ drawn between two materials with dielectric constant $\epsilon_1$ and $\epsilon_2$ . . . . .	187

B.3 Schematic of a one-dimensional stack consisting of $N$ layers. The arrows represent the reflected and transmitted electromagnetic waves in each layer. . . . .	192
C.1 Schematic depiction of the relative timescales relevant to electron-electron scattering (equilibration), electron-phonon coupling (thermalization), and electron-hole recombination. Adapted from Y. Takeda et al., 2014 . . . . .	215

## LIST OF TABLES

<i>Number</i>		<i>Page</i>
2.1	Parameter values for ultrathin $WS_2$ modified detailed balance calculations . . . . .	37
2.2	Tabulated values of Urbach Energies (Experiment) and $\Delta V_{oc}$ loss (Calculated) . . . . .	54
3.1	Room temperature values for the excitonic sheet conductor model of various TMDCs. . . . .	69

## Chapter 1

### INTRODUCTION

*“You don’t have to be great to get started, but you have to get started to be great.”*

— Les Brown

#### 1.1 Physics and Engineering of Conventional Photovoltaics

Photovoltaic devices are systems that convert incident radiation (typically sunlight, in which case is referred to as a solar cell) into electrical energy. In many ways, photovoltaic systems are essentially light-powered batteries where load matching is necessary to maximize the output power of the solar cell. In this section, we first introduce the internal physics that is common to the operation of every solar cell. Next, we introduce and describe the typical current-voltage behavior of solar cells in the form of the modified diode equation. We then connect the three main factors that make up the solar cell power conversion efficiency to internal physical processes and discuss how they are conventionally engineered. Finally, we describe the efficiency limits of a solar cell by invoking detailed balance arguments, which motivates and further elucidates the behavior of a conventional solar cell.

#### Current Voltage Characteristics of a Typical Solar Cell

The current-voltage ( $I - V$ ) characteristics of solar cells can be typically represented with an equivalent circuit model:

$$I(V) = I_0 \left( \exp\left(\frac{q(V - IR_s)}{n_{id}k_bT}\right) - 1 \right) + \frac{V - IR_s}{R_{sh}} - I_L \quad (1.1)$$

where  $q$  is the fundamental unit of charge ( $= 1.6 \times 10^{-19}$  C),  $k_bT$  is the thermal energy ( $= 25.8$  meV at room temperature),  $I_0$  is the recombination current prefactor,  $n_{id}$  is the diode ideality factor,  $R_s$  is the equivalent internal series resistance of the solar cell,  $R_{sh}$  is the equivalent internal shunt resistance,  $I_L$  is the photogenerated current, and  $I, V$  is the output current, voltage of the solar cell, respectively. Because the current-voltage curves are strongly asymmetric with voltage (as opposed to the symmetric case of an ideal resistor), the current-voltage relation is *rectifying* and therefore reminiscent of a diode, where current flows nearly entirely in one direction.

The power  $P$  generated from the solar cell can be found by the usual expression

$$P(V) = I(V)V \quad (1.2)$$

where we note that the expressions for the power is dependent on the voltage across the solar cell. Note that [Equation 1.2](#) has powers that are negative, since the current itself is negative, i.e., the power is *generated* from the solar cell, as opposed to the current through a resistor where the power is *dissipated*. The maximum power point of the solar cell is denoted by  $P_{mpp} = I_{mpp}V_{mpp}$ , which specifies a specific load condition to maximize the energy harvested from a solar cell. For a given load  $R_L$ , the output current is given by:

$$-I(V) = \frac{V}{R_L} \quad (1.3)$$

where the current  $I(V)$  from the solar cell is now dissipated in the resistive load, so the negative sign in front of the current accounts for this factor. The specific current and voltage for a given load resistance can be solved graphically, as shown in [Figure 1.1](#). Thus, it is clear that the load that maximizes the energy harvested is given simply by

$$R_{ch} = \left| \frac{V_{mpp}}{I_{mpp}} \right| \quad (1.4)$$

Therefore, once the current-voltage relations of a solar cell is carefully characterized, we can maximize its output power by matching the load resistance to its characteristic resistance. To note, the maximum power point can also be written as

$$P_{mpp} = I_{mpp}V_{mpp} = I_{sc}V_{oc}FF \quad (1.5)$$

which separates the power generation of the solar cell into three distinct but inter-related terms. Here,  $I_{sc}$  refers to the short circuit current, which describes the photogenerated current of the solar cell under short-circuit conditions (i.e., when the external load is  $R_L = 0$ ),  $V_{oc}$  is the open-circuit voltage, which describes the photovoltage when the solar cell is under open-circuit conditions (i.e., when the external load is  $R_L = \infty$ ), and  $FF$  is the fill factor, which describes the square-ness of the  $I - V$  curve and can be seen as being equal to

$$FF = \frac{I_{mpp}V_{mpp}}{I_{sc}V_{oc}} \quad (1.6)$$

Thus, the power conversion efficiency  $\eta$  can be calculated as

$$\eta = \frac{P_{mpp}}{P_{sun}} = \frac{I_{sc}V_{oc}FF}{P_{sun}} \quad (1.7)$$

where  $P_{\text{sun}}$  is the incident power from the sun. The above terms are typically normalized to the area of the solar cell so that the terms are not *a priori* dependent on cell size. Therefore, currents are typically referred to as current densities (e.g.  $J_{sc}$  is the short-circuit current *density*, in units of  $\text{mA}/\text{cm}^2$ ), resistances are typically quoted as *sheet* resistances ( $r_s$  and  $r_{sh}$ , in units of  $\Omega\text{-cm}^2$ ), and incident power  $P_{\text{sun}}$  is typically quoted in units of power *density* (e.g.  $\text{W}/\text{m}^2$ ).

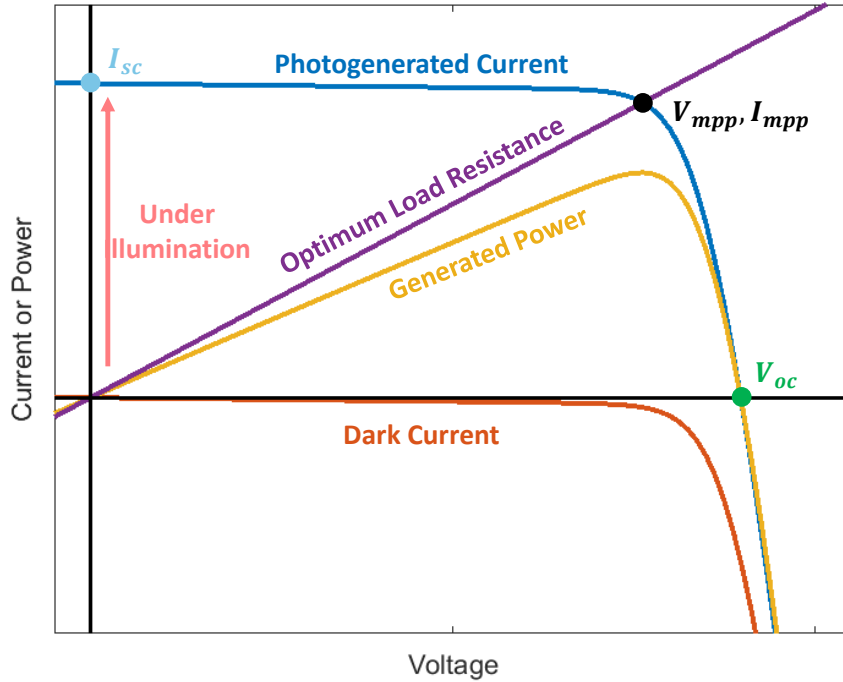


**Figure 1.1: Typical Solar Cell IV Curves.** Typical current-voltage curves of a solar cell under illumination (blue) and in the dark (orange), along with its power-voltage curve (yellow) curve. Here, we plot the generated current and power as a positive quantity. The purple curve corresponds to the current-voltage curve of a resistive load  $R_L$ . In this case, the load resistance is matched to the characteristic resistance,  $R_L = R_{ch} = |V_{mpp}/I_{mpp}|$ , which maximizes the energy harvesting of the solar cell, i.e., it operates at its max power point. The short-circuit current  $I_{sc}$  and open-circuit voltage  $V_{oc}$  points are also labelled.

### Engineering for Maximum Efficiency

Since solar cells are made to generate electrical power, the power conversion efficiency  $\eta$  becomes an important figure of merit to describing the technological

potential of a solar cell technology as well as a method to reducing the overall capital cost of commercializing solar cell modules. Since 1976, NREL has kept track of the maximum efficiencies achieved in different solar cell technologies, reproduced in [Figure 1.2](#). Here, we briefly discuss the typical engineering considerations in maximizing the efficiency potential of a solar cell material, which involves simultaneously optimizing the  $J_{sc}$ ,  $V_{oc}$ , and  $FF$  of the solar cell.

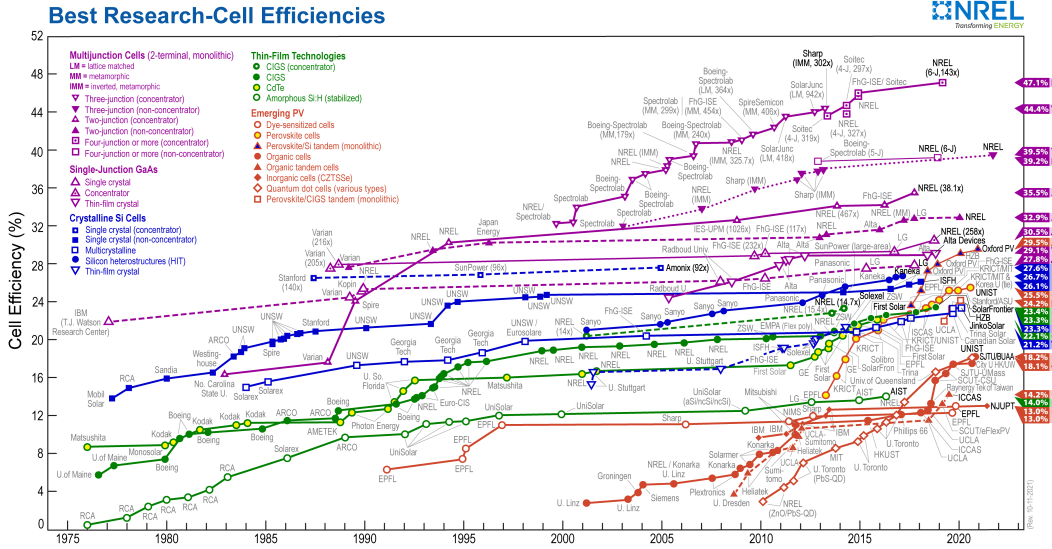


**Figure 1.2: NREL Efficiency Chart.** Maximum power conversion efficiencies achieved in different photovoltaic technology, plotted as a function of the year the record was achieved.

### $J_{sc}$

The short circuit current density  $J_{sc}$  describes the photogenerated current when the solar cell is shorted as illustrated in [Figure 1.3a](#). Thus, to maximize  $J_{sc}$ , we must optimize both the optical absorption (generation of electron-hole pairs) and subsequent collection of the electron-hole pairs. To see this more explicitly, the short circuit current density can be written a

$$J_{sc} = q \int_0^{\infty} EQE(E)S_{sun}(E)dE \quad (1.8)$$

where  $E$  is the energy of the incident photon,  $S_{sun}(E)$  is the incident spectral solar flux (in units of photons/m<sup>2</sup>/sec), and  $EQE(E)$  is the *external quantum efficiency*, which defines the number of incident photons that are converted to collected electrons. Therefore, the maximum  $EQE$  is unity, and given the typical solar fluence

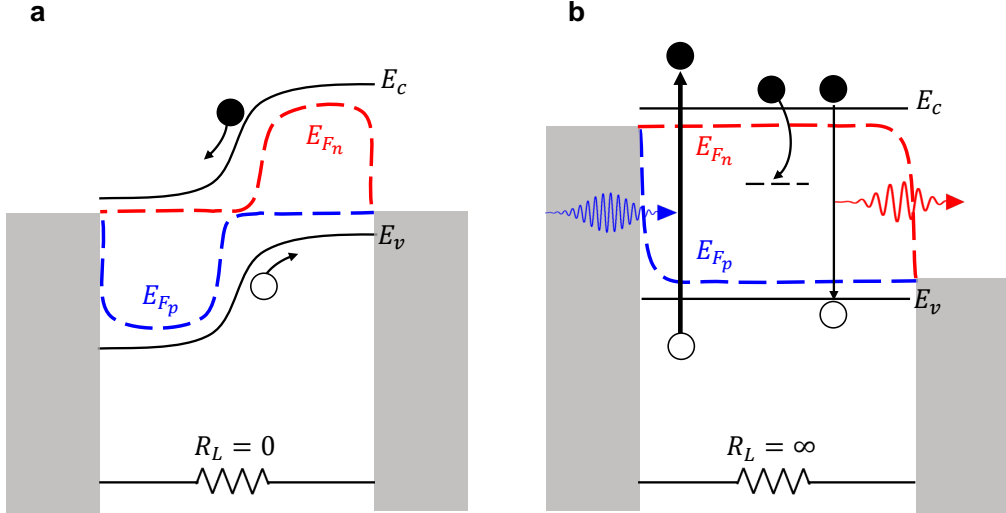


Figure 1.3:  $J_{sc}$  vs.  $V_{oc}$ . Schematic depiction of the solar cell under short-circuit **a** and open-circuit **b** conditions.

$S_{sun}(E)$  (specified as AM 1.5G), the maximum short circuit current density achievable is  $\sim 70$  mA/cm<sup>2</sup>.

The  $EQE$  is a product of two terms:

$$EQE(E) = a(E)IQE(E) \quad (1.9)$$

where  $a(E)$  describes the probability of a photon to be absorbed at photon energy  $E$ , and  $IQE(E)$  describes the *internal quantum efficiency*, or the probability of the generated electron-hole pair to be collected. Therefore,  $IQE$  is purely a description of the electronic geometry, and is wavelength-independent *a priori*. However, different photon energies may result in different amounts of generation and recombination in different places, and therefore there is a subtle photon energy dependence<sup>1</sup>.

To maximize absorbance, it is necessary to engineer the optical configuration and/or thickness of the active layer. Absorption in the ray-optics regime (i.e.,  $L \gg \lambda$ ) is typically described by the Beer-Lambert law:

$$a(E) = (1 - R(E))(1 - \exp(-\alpha(E)L)) \quad (1.10)$$

---

<sup>1</sup>For example, in a typical solar cell, bluer photons are absorbed closer to the surface due to the increased absorption coefficient at higher energies, and therefore the generated electron-hole pairs with that energy are less likely to be collected due to their distance from the junction of the solar cell and finite surface recombination velocity.

where  $R(E)$  describes the reflectance of the semiconductor, primarily dictated by the air-semiconductor interface,  $\alpha(E)$  is the absorption coefficient, a relatively intrinsic property of a semiconductor, and  $L$  is the thickness of the semiconductor or its equivalent absorption path length. Therefore, absorption is maximized by (1) minimizing reflectance, e.g., with the use of an anti-reflection coating, (2) maximizing absorption coefficient, e.g., with the use of a direct bandgap semiconductor, and (3) increasing the thickness of the semiconductor.

On the other hand, maximizing the carrier collection efficiency requires both the breaking the symmetry of electron and hole transport (e.g., with an electric field, or more generally, through the asymmetries in the electrical conductivity of the respective charge carrier) and maximizing the diffusion length  $L_D$  of the respective carriers. In contrast to absorbance, carrier collection efficiency typically *decreases* with an increase in the active layer thickness, because carriers are only collected within a diffusion length  $L_D$  of the electrical junction of the solar cell. Therefore, our main constraint for the thickness of the solar cell active layer is  $L \lesssim L_D$ . A further increase in the absorption path length can therefore be achieved with light trapping geometries, e.g., with the addition of surface texturing and a back reflector,  $L_{eff} = 4n_r^2 L$ , [213] where  $n_r$  is the refractive index of the semiconductor.

### $V_{oc}$

We next turn our attention to the physics of the open circuit voltage  $V_{oc}$ , which is schematically depicted in Figure 1.3b. To understand the physics of the open-circuit voltage, it is necessary to recall that it is an *electrochemical* quantity, and therefore related to the electrochemical potentials of the charge carriers:

$$qV = E_{f, left} - E_{f, right} = E_{f_n, left} - E_{f_p, right} \quad (1.11)$$

where  $E_f$  refers to the Fermi level, specifically of the metal contacts (one on the left and the other on the right), and  $E_{f_n, p}$  corresponds to the *quasi-Fermi* levels that describe the local carrier concentration  $n = \int g_n(E) f(E, E_{f, n}) dE$ , where

$$f(E, E_{f_n}) = \frac{1}{\exp\left(\frac{E-E_{f_n}}{k_b T}\right) + 1} \quad (1.12)$$

is the Fermi occupation factor and  $g_n(E)$  is the density of states for the electrons. A similar expression holds for holes. Here, quasi-Fermi levels are necessary to describe the carrier population *out of equilibrium*<sup>2</sup>, e.g., under photoexcitation

<sup>2</sup>To see a more detailed derivation for when a single quasi-Fermi level is an accurate picture, see section C.4.

(i.e.,  $n = n_0 + \Delta G$ , where  $n_0$  is the equilibrium carrier population and  $\Delta G$  is the photogenerated carrier population). If the quasi-Fermi levels are sufficiently far from the band-edges of the semiconductor (e.g.,  $(E_c - E_{f_n})/k_b T \gtrsim 3$ , which is almost always true for solar cells under 1 sun illumination), it is possible to approximate the above expression for carriers as

$$n = N_c \exp\left(-\frac{E_c - E_{f_n}}{k_b T}\right) \quad (1.13)$$

where  $N_c$  is the effective density of the states for the conduction band,  $E_c$  is the conduction band energy, and similarly for holes, we have  $p = N_v \exp\left(-\frac{E_{f_p} - E_v}{k_b T}\right)$ . Thus,

$$np = N_c N_v \exp\left(-\frac{E_g}{k_b T}\right) \exp\left(\frac{\Delta\mu}{k_b T}\right) = n_i^2 \exp\left(\frac{\Delta\mu}{k_b T}\right) \quad (1.14)$$

where  $\Delta\mu = E_{f_n} - E_{f_p}$  is the quasi-Fermi level splitting (or the *internal* voltage) and  $n_i$  is the intrinsic carrier population (which is a property of the semiconductor). Since a small but finite gradient of the quasi-Fermi levels are necessary to drive current flow

$$J_i = \frac{\sigma_i}{q} \nabla E_{f_i} \quad (1.15)$$

where  $i = n, p$  refers to the electron and hole current densities, then we generally have  $qV < \Delta\mu$  as a constraint. At open circuit, this condition still holds, since only the total current  $J = J_n + J_p$  must be zero. Therefore, we generally have  $qV_{oc} < \Delta\mu$ . To summarize the above analysis, we have connected the external voltage  $V$  to the electrochemical potentials of the electron and hole. The external open circuit voltage  $V_{oc}$  will be limited by the internal quasi-Fermi level splitting  $\Delta\mu$ , which is related to the steady state populations of the electrons and holes. Therefore, to maximize the open circuit voltage  $V_{oc}$ , we must maximize generation and minimize carrier recombination.

Another way of understanding the open circuit voltage is from the diode model of the solar cell [Equation 1.1](#), where we shall set  $R_s = 0$  and  $R_{sh} = \infty$  for simplicity.<sup>3</sup>. Therefore, we have

$$V_{oc} = \frac{n_{id} k_b T}{q} \ln\left(\frac{J_{sc}}{J_0} + 1\right) \quad (1.16)$$

where we have normalized the current densities to their areas  $J = I/A$  and denoted the photogenerated current  $J_L$  as  $J_{sc}$ , which is the same in this scenario. It is clear

---

<sup>3</sup>More generally, since open circuit implies  $I = 0$ , series resistance  $R_s$  has no direct effect on the open circuit voltage. However,  $R_{sh}$  can have a dramatic effect on the open circuit voltage. The physical causes and implications of a finite  $R_{sh}$  and  $R_s$  will be discussed in the fill factor section below.

then that the open circuit voltage  $V_{oc}$  is increased with generation (in the form of  $J_{sc}$ ) and decreasing with increased recombination current density  $J_0$ . The rate of change is partially modulated by  $n_{id}$ , which depends on the dominant form of carrier recombination.

There are three main forms of recombination that dominate traditional photovoltaic materials, which are (1) Shockley-Reed-Hall (trap-assisted) recombination, (2) Radiative recombination, (3) Auger-Meitner recombination. Trap-assisted recombination stems from trap states (typically due to defects in the crystal structure) which allows electrons to relax prematurely in a non-radiative way from the conduction band to the valence band. Typically, the non-radiative relaxation (in the form of phonon emission) stems from a small but continuous set of states near the band-edge, in the form of a semiconductor band tail. This continuity of states comes from the breaking of the crystalline symmetry due to the random positioning of defects, and the eventual trap-assisted recombination can be parametrized as

$$R^{SRH} = \frac{np - n_i^2}{\tau_n^{SRH}(p + p_1) + \tau_p^{SRH}(n + n_1)} \quad (1.17)$$

where  $R^{SRH}$  is the Shockley-Reed-Hall (SRH) recombination rate (in units of  $1/\text{cm}^3/\text{s}$ ),  $n$  and  $p$  are the electron and hole populations,  $n_1$  and  $p_1$  are the density of available trap states for the electrons and holes, and  $\tau_i^{SRH}$  is the Shockley-Reed-Hall recombination lifetime. For doped semiconductors (e.g.,  $n = N_D \gg p, n_1, p_1$ ), we have

$$R_{\text{n-type}}^{SRH} \approx \frac{p}{\tau_p^{SRH}} \quad (1.18)$$

so that the minority carrier dominates the SRH recombination. Furthermore, SRH recombination is typically a single-carrier process.

Radiative recombination is a fundamental process where the recombination of an electron and hole results in an emitted photon. The rate is simply given as

$$R^{Rad} = k_r(np - n_i^2) \quad (1.19)$$

where  $k_r$  is radiative recombination rate coefficient.  $k_r$  is substantially larger in materials that have a direct bandgap (e.g. GaAs) compared to those with an indirect bandgap (e.g. Si). Note that radiative recombination is generally a two-carrier process.

Finally, Auger-Meitner recombination refers to the energy transfer of an electron-hole interaction that is transferred directly to another electron or hole. Since the

energetically “hot” electron or hole is then subsequently thermalized to the band-edge, this process is also typically non-radiative. Its parametrization is given by

$$R^{Aug-Meit} = (C_n n + C_p p)(np - n_i^2) \quad (1.20)$$

where  $C_n$  and  $C_p$  are the Auger-Meitner coefficients for the electrons and holes. Here, it is clear that Auger-Meitner is a three-carrier process.

Since these three recombination modalities are common to many traditional semiconductors, it is common to use an “ABC” recombination model:

$$R = R^{SRH} + R^{Rad} + R^{Aug-Meit} \approx Ax + Bx^2 + Cx^3 \quad (1.21)$$

where  $x$  is the minority carrier type (either  $n$  or  $p$ ). This model captures the effects of the different types of recombination in a straightforward manner. If there are larger asymmetries between the electron and hole or the solar cell is operated under high injection, it may be necessary to use the full expressions of each recombination model. Furthermore, since  $n \sim \exp(\Delta\mu/(2k_bT))$ , it is clear that the ideality factor  $n_{id}$  approaches 2 for SRH-dominated recombination, approaches 1 for Radiative-dominated recombination, and approaches 1/2 for Auger-Meitner-dominated recombination.

Of additional interest is the recombination due to the *surface* of a material, which is usually due to the breaking of crystalline symmetry at the interface and therefore results in surface states. Some of these states can be passivated with appropriate termination of chemical bonds, but nonetheless, the interface can typically be characterized by a surface recombination velocity  $S_x$ , where  $x = n, p$ . In general, this additional surface recombination acts as a boundary condition on the current density:

$$\mathbf{J}_x \cdot \hat{n} = \pm qS_x(x - x_0) \quad (1.22)$$

where  $\hat{n}$  is the normal vector of the interface, and  $x_0$  corresponds to the carrier concentration in the dark. Here, the negative sign is associated with electrons  $n$  and the positive sign is associated with holes  $p$ . We note that generally the effective lifetime  $\tau_{eff}$  due to both bulk and surface recombination is given as:

$$\frac{1}{\tau_{eff}} = \frac{1}{\tau_b} + \frac{1}{\tau_s} \quad (1.23)$$

where  $\tau_b$  is the bulk lifetime and  $\tau_s$  is the surface recombination lifetime. This can be approximated as

$$\tau_s = \frac{L}{2S} + \frac{1}{D} \left( \frac{L}{\pi} \right)^2 \quad (1.24)$$

for when there are two surfaces with approximately equal surface recombination velocities (i.e.,  $S = S_1 \approx S_2$  [179]). Here,  $L$  is the thickness of the solar cell and  $D$  is the diffusion coefficient.

## FF

We finally discuss the mechanisms that affect the fill factor of a solar cell, which describes the “squareness” of the  $I - V$  curve. From inspection of [Equation 1.1](#), the largest effects are due to the finite series resistance  $R_s$  and shunt resistance  $R_{sh}$  in a solar cell.

In the case of series resistance, this may come from the resistance in the bulk of the active layer or at the contacts. Since the resistance is given as  $R = \rho L/A$ , where  $\rho$  is the resistivity,  $L$  is the thickness of the semiconductor,  $A$  is the cross-sectional area, it can be modified either geometrically or through carrier doping. The resistivity is related to the conductivity as

$$\sigma = \frac{1}{\rho} = e(n\mu_n + p\mu_p) \quad (1.25)$$

and is therefore a measure of both the local carrier concentration and the mobility of charge carriers. Large bandgap materials typically have a lower conductivity due to their reduced intrinsic carrier concentration, dopant states that are further from the band-edge, and a reduction in the overall solar-generated carriers. The effect of series resistance can be first observed as a change in the slope of the  $J - V$  curves near  $V_{oc}$ , and for large series resistances, will also impact  $J_{sc}$ .

Another practical concern is the shunt resistance, which is a measure of other effective electrical circuits that are in parallel to the dominant electrical junction. For example, in an ideal solar cell, there is a single electrical path for all the carriers to follow. However, due to spatial heterogeneity and defects, it may be possible for certain carriers to follow a different electrical path, resulting in an effective shunt resistance. As an example, if the two sides of the solar cell contacts were connected, the shunt resistance  $R_{sh} \rightarrow 0$ , and therefore diode behavior would no longer be observed. In other words, shunt resistance is often a measure of carrier selectivity, i.e., as the transport of electrons and holes become more symmetric, the diode behavior transitions to resistive behavior, and therefore the carrier selectivity is lost. Thus, the effects of shunt resistance are first observed in the slope of the short circuit current  $J_{sc}$  and then for large shunt resistances at  $V_{oc}$ .

It is important to note that both descriptions of the series and shunt resistances are perturbative to the diode model of a solar cell. It is important to note that for a given solar cell, the electrical characteristics may be drastically different due to the nature of the electrical interfaces and the specific geometry of the solar cell. Therefore, it is necessary to observe diode-like rectifying behavior before ascribing series and shunt resistances, which may be meaningless in certain situations. Thus, carrier selectivity and the aforementioned symmetry breaking of electron and hole transport is fundamental to the operation of a solar cell.

### Single Junction Detailed Balance Efficiency Limit

To further elucidate the mechanisms intrinsic to solar cell operation as well as to ascribe practical efficiencies achievable, it is useful to consider the thermodynamic efficiency limit of a solar cell. Consider a hypothetical scenario where the solar cell can be considered as a zero-dimensional object, where local gradients internal to the solar cell are ignored. Then, the solar cell becomes a steady state flux balance expression where

$$J_{gen} - J_{recomb} - J_{collected} = 0 \quad (1.26)$$

where electron-hole pairs are generated at a rate  $J_{gen}$ , collected electrically at a rate  $J_{collected}$ , and recombines internally as  $J_{recomb}$ . Note that the generation of carriers is directly related to the absorbance of the solar cell, i.e.,

$$J_{gen} = q \int_0^{\infty} a(E) S_{sun}(E) dE \quad (1.27)$$

where  $a(E)$  is the absorbance of the solar cell and  $S_{sun}(E)$  describes the solar flux. Further,  $J_{collected} = J = J_{gen} - J_{recomb}$  is the current density that we observe in our electrical circuit. Then, what is the form of  $J_{recomb}$ ? Clearly there are various recombination mechanisms that are possible, as described in [section 1.1](#). However, which mechanism is thermodynamically necessary?

Let us consider an alternative situation where the solar cell is instead in the dark, without solar radiation. In this case, we must have  $J_{collected} = J = 0$ , since we are in thermodynamic equilibrium. Thus, we have

$$J_{gen,dark} = J_{recomb,dark} \quad (1.28)$$

In this case, without solar flux, the only generation of electron-hole pairs is from the

ambient blackbody radiation:

$$S_{bb}(E)dE = \frac{2\pi}{h^3 c^2} \frac{E^2}{\exp\left(\frac{E}{k_b T_c}\right) - 1} dE \quad (1.29)$$

where  $T_c$  is the temperature of the solar cell (e.g. 300 K). Therefore, in the dark, we have

$$J_{gen,dark} = J_{recomb,dark} = q \int_0^\infty a(E)S_{bb}(E)dE \quad (1.30)$$

In other words, since the solar cell has a finite radiative absorption, it must have some finite radiative recombination. To understand the differences under illumination, we note that the derivation for the law of mass action should still hold, i.e.,  $np = n_i^2 \exp(\Delta\mu/k_b T)$ . Furthermore, even under illumination, if we examine open-circuit conditions, we must still have  $J = 0$ . Thus, since the generation is increased by a factor of  $\exp(\Delta\mu/k_b T)$ , so must the recombination rate, i.e.,

$$J_{recomb} = J_{recomb,dark} \exp\left(\frac{\Delta\mu}{k_b T}\right) = q \exp\left(\frac{\Delta\mu}{k_b T}\right) \int_0^\infty a(E)S_{bb}(E)dE \quad (1.31)$$

Finally, we note that the ambient blackbody flux contributes a negligible flux even under solar illumination:

$$J_{gen} = q \int_0^\infty a(E)S_{sun}(E)dE + q \int_0^\infty a(E)S_{bb}(E)dE \quad (1.32)$$

Thus, the  $J - V$  characteristics of a solar cell that is only limited by radiative recombination (which is necessary, due to finite absorption) is given by

$$J(V) = J_{sc} - J_0 \left( \exp\left(\frac{qV}{k_b T}\right) - 1 \right) \quad (1.33)$$

where  $J_{sc} = q \int_0^\infty a(E)S_{sun}(E)dE$  and  $J_0 = q \int_0^\infty a(E)S_{bb}(E)dE$ . We have used the fact that in this hypothetical zero-dimensional solar cell, the internal and external voltages are the same, i.e.,  $qV = \Delta\mu$ . Finally, note that the form of the  $J_{sc}$  implicitly assumes the carrier collection efficiency (*IQE*) is unity. The final assumption in the detailed balance efficiency limit is an explicit functional form for the absorbance, which is characterized by a step-function:

$$a(E) = \begin{cases} 0 & \text{if } E < E_g \\ 1 & \text{if } E \geq E_g \end{cases} \quad (1.34)$$

Since we now have an explicit form for every parameter in the  $J(V)$  expression, we can calculate the maximum power conversion efficiency by optimizing  $P(V) =$

$VJ(V)$  for every bandgap  $E_g$ . The solar spectrum typically used as a reference is referred to as the Air Mass 1.5 Global (abbreviated as AM 1.5G) spectrum, i.e.,  $S_{sun}(E) = S_{AM1.5G}(E)$ , as shown in Figure 1.4a. This spectrum is approximately equal to that of a blackbody spectrum with a blackbody temperature  $T_s \approx 5760$  K. The dips in the spectrum in the infrared part of the spectrum is mostly due to absorption of carbon dioxide and water vapor, whereas in the UV there is some minor absorption from ozone. The calculation of the maximum power conversion efficiency is shown in Figure 1.4b, where we find the maximum efficiency to be approximately 33.7%. The incident power density of the sun can be calculated as

$$P_{sun} = \int_0^{\infty} ES_{sun}(E) dE \quad (1.35)$$

Upon inspection, it is of a curious nature to understand where all the energy went. Surely the *limiting* efficiency must be larger! However, the surprisingly low efficiency is limited primarily by carrier thermalization and the subsequent recombination of those carriers. In general, the two main loss mechanisms in a conventional single-junction solar cell is due to the imperfect absorption of photons below the bandgap of a solar cell:

$$\eta_{abs,loss} = \frac{\int_0^{E_g} ES_{sun}(E) dE}{\int_0^{\infty} ES_{sun}(E) dE} \quad (1.36)$$

and for photons above the band-edge, it is due to carrier thermalization to the band-edge of the semiconductor:

$$\eta_{therm,loss} = \frac{\int_{E_g}^{\infty} ES_{sun}(E) dE - E_g \int_{E_g}^{\infty} S(E) dE}{\int_0^{\infty} ES_{sun}(E) dE} \quad (1.37)$$

The relative contribution of these loss mechanisms is shown in Figure 1.4b. While near-unity absorbance across the solar spectrum has been demonstrated [217], the problem of carrier thermalization to the band-edge is a fundamental challenge to high efficiency. Attempts to mediate the loss due to carrier thermalization has been successfully demonstrated with multijunction solar cells, where solar cells with multiple different bandgaps are optically connected in series, as shown in Figure 1.2. The maximum solar cell efficiency experimentally demonstrated with six junctions under solar concentration is 47.1% (by NREL), while the experimentally demonstrated efficiency maximum of a single junction under 1 sun illumination is 29.1% (demonstrated by Alta Devices). More discussion on the physics of carrier thermalization and whether it is appropriate in most semiconductors is described in

section C.3. However, it is clear from experimental demonstrations that these losses are difficult to avoid, and the exploration of new materials physics is necessary to achieve higher power conversion efficiencies.

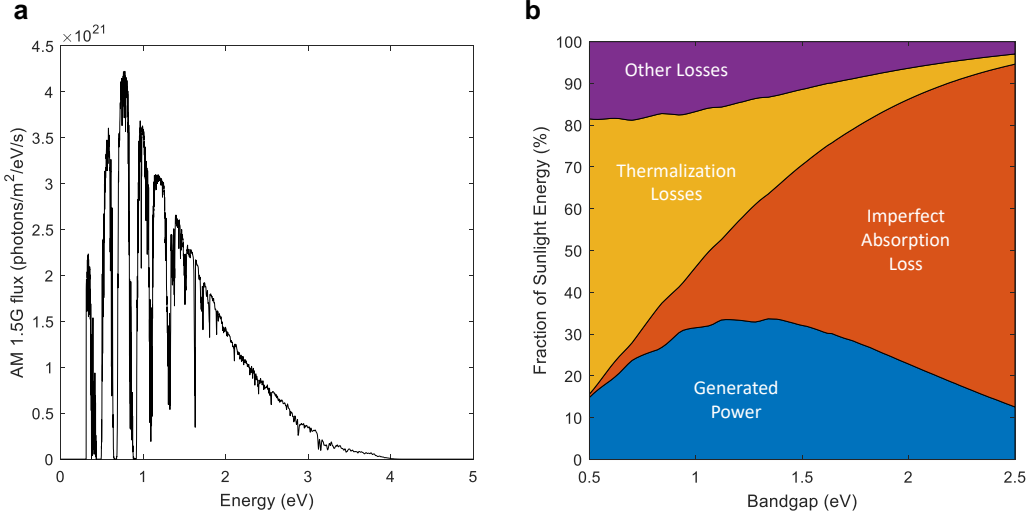


**Figure 1.4: Detailed Balance Efficiency Limit** **a** The AM 1.5G solar flux  $S_{AM1.5G}(E)dE$ , which is typically used as an approximation for the incident solar spectrum. **b** The detailed balance efficiency limit of a solar cell (highlighted in blue) under AM 1.5G illumination. Also listed are different efficiency loss mechanisms.

## 1.2 Entering Flatland: van der Waals Materials

Van der Waals (vdW) materials are materials whose out-of-plane forces are characterized by van der Waals interactions, making their bonding strength highly anisotropic between the in-plane vs. the out-of-plane directions. These materials were first thoroughly characterized in the 1960s and 1970s [52], where a number of their electrical and optical properties were examined for both bulk and ultrathin layers. Because of their weak out-of-plane interactions, their crystals can be cleaved with the application of an adhesive surface, such as with Scotch tape. The field of van der Waals (“2D”) materials rapidly grew in 2004, when Novoselov and Geim cleaved few-layer graphene and examined its field-effect properties [140]. Since then, hundreds of other 2D materials have been discovered<sup>4</sup> with a variety of entirely new properties found and various technological applications that have been

<sup>4</sup>Many of these materials were actually examined already in the 1960s, as noted in the earlier citation, but most had not been cleaved down to a single monolayer, stacked together (to form vdW heterostructures), and implemented into device geometries.

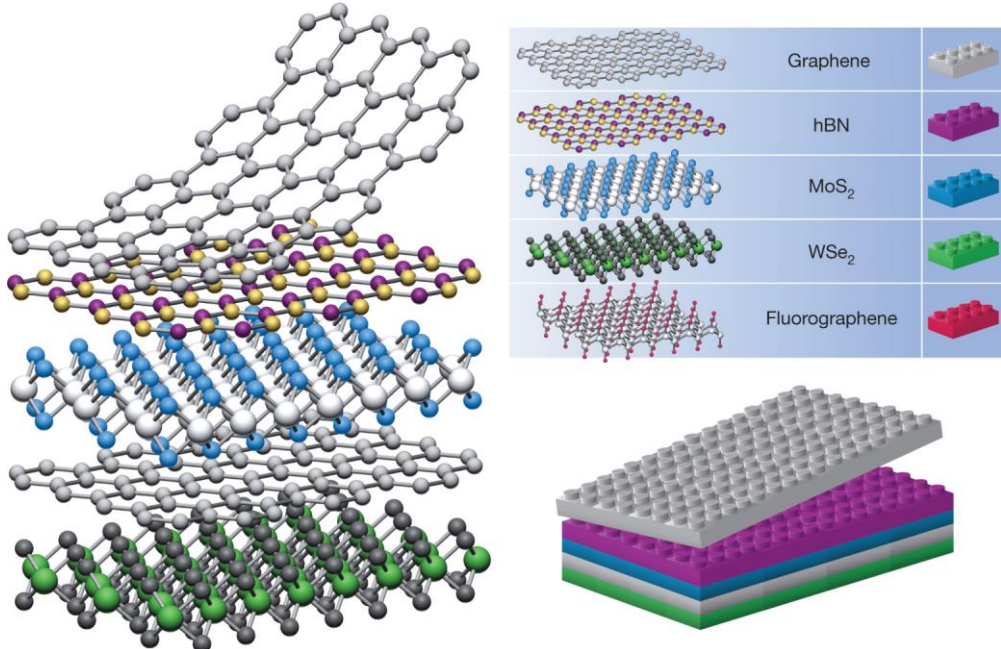


**Figure 1.5: van der Waals Heterostructures.** Schematic depiction of heterostructuring different van der Waals materials together, showing that different combinations of materials can be combined to form entirely new materials. This arbitrary heterostructuring stems from the van der Waals interactions along the basal plane, adapted from [56].

proposed. Furthermore, these different layered materials can be stacked together in various configurations, forming a van der Waals heterostructure (Figure 1.5).

Of considerable interest is the family of transition metal dichalcogenides (TMDCs), whose crystal structure in the 2H form results in semiconducting materials. The most air stable forms of these materials have an elemental composition of  $\text{MX}_2$ , where  $\text{M} = \text{Mo, W}$  and  $\text{X} = \text{S, Se}$ . While these materials were initially studied in the 1960s [52], the Heinz [117] and Wang [178] groups discovered that these materials became direct bandgap in their monolayer form, which drastically increased their light-matter coupling and the possibility to use them for light-emitting applications. Following this discovery, these materials were subsequently proposed to be used as active layers for photovoltaic applications in 2013 [14], where their strong light-matter coupling and atomically-thin layers could result in device structures with record high specific powers. However, several fundamental science questions arose, particularly on the physical mechanism of the photovoltaic behavior and how to engineer these materials. Experimental demonstrations soon followed after the initial proposal where these materials were used as active layers in photovoltaic devices

[11, 28, 54, 101, 155, 166]. However, besides the initial demonstration, very little work had been done on optimizing and understanding the photovoltaic behavior in these materials.

### 1.3 What's Different in Atomically-thin Photovoltaics?

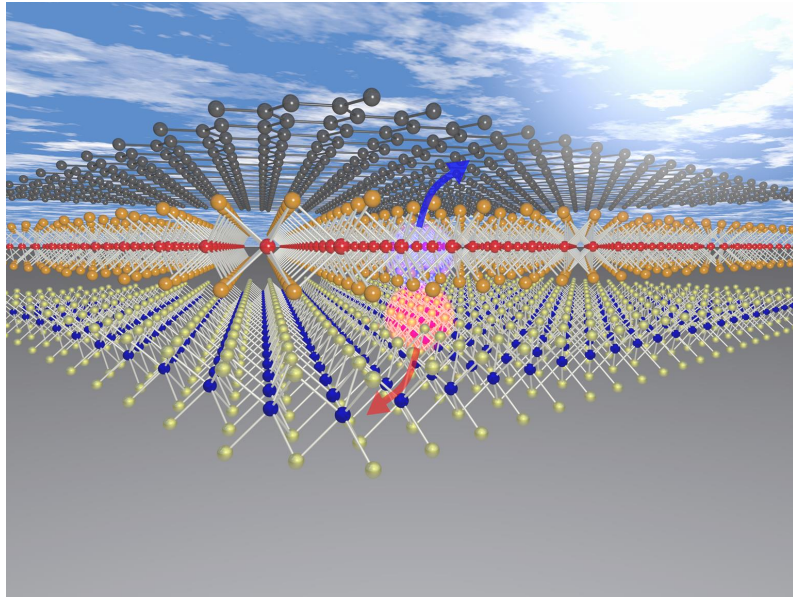


**Figure 1.6: van der Waals Photovoltaics Schematic.** Schematic depiction of a photovoltaic device formed purely from van der Waals materials.

The central theme of this thesis is to consider the use of these materials as atomically-thin active layers in photovoltaic devices. In doing so, we must study and understand the absorption, transport, and recombination properties of these materials. Due to the nature of these materials, we expect a variety of different physics and engineering design rules to emerge, as opposed to those discussed in [section 1.1](#). Specifically, we can delineate two main attributes that causes substantial differences when compared to conventional materials used for photovoltaics (e.g. Si or GaAs): (1) the vastly different thicknesses of the active layers and (2) the van der Waals interactions in the out-of-plane direction. We briefly describe implications of these two properties below.

#### Effects of Thickness

Arguably the largest difference between using van der Waals materials as active layers compared to that of conventional materials is their thickness. The typical thickness of GaAs solar cells are usually a few microns thick, whereas Si solar

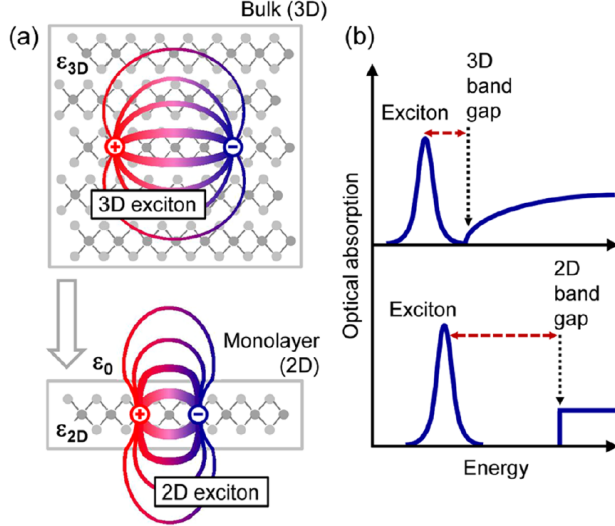


**Figure 1.7: Dimensionality Effects on Exciton Screening.** Schematic depiction of excitons in bulk (3D) materials vs. monolayer (2D) materials. Due to the lack of electrons in the out-of-plane direction, the electric field lines between electrons and holes have substantially less screening, increasing the electron-hole interactions and therefore the binding energy of excitons. Figure from [29].

cells are of order  $\sim 100 \mu\text{m}$  or more. In contrast, the van der Waals materials of interest studied in this thesis are routinely  $L \ll \lambda$ , i.e., their thicknesses are deeply subwavelength, perhaps only a few nm. This suggests that different optical physics must be considered (specifically, wave optics), and that novel light trapping schemes must be employed to achieve near-unity absorption in these ultrathin materials.

Further, this regime of thickness requires many different electronic considerations as well. For example, these materials routinely have thicknesses that are either comparable or even thinner than their electronic screening length. While this effect has been utilized to create 2D devices with large gate tunability, this property also has implications for the transport of carriers and types of electrical junctions formed. For example, in an atomically thin pn junction, the two sides of the junction are completely depleted. Thus, carrier separation in those types of junctions are expected to be extremely efficient. Furthermore, the large surface to volume ratio in these materials suggests that interfacial recombination, e.g. parametrized as a surface recombination velocity, will likely be dominant or comparable to the “bulk” recombination rates.

In addition, there are a variety of differences due to the presence of quantum mechanical effects. Of particular note is the electric screening of photogenerated electrons

and holes, which can form bound states referred to as *excitons*<sup>5</sup>. The large binding energies comes from the fact that the Bohr radius of the exciton is comparable to the thickness of the material, which results in less electrostatic screening [29] (Figure 1.7). Since excitons are electrically neutral, these excitons must be dissociated to generate free carriers and therefore electrical current. Therefore, unlike traditional solar cells where free carriers are directly generated from photoexcitation, we generate excitons that must be dissociated first. Indeed, since monolayer TMDCs have exciton binding energies that are routinely a few hundred meV, these excitonic quasiparticles dominate the optoelectronic physics at this thickness regime. It is also important to note that for a given 2D material, there are typically many different types of excitons, each with their own binding energy. For example, while the A exciton in bulk TMDCs have binding energies of approximately 50 meV, the indirect optical transitions in the bulk have minimal excitonic contribution.

### Effects of van der Waals interactions

The van der Waals interactions in these layered materials uniquely enable the creation of atomically-thin flakes. A simple estimate of the relative in-plane to out-of-plane bond strength can be made from the relative dimensions of exfoliated flakes. For flakes that are a few nm in thickness, the typical flake dimensions are roughly a few microns to a few 10s of microns in thickness. Therefore, the relative dimensional anisotropy is  $\sim 1000$ , and we can estimate the bonding strength between the in-plane covalent bonds and the out-of-plane van der Waals interactions to be of the same order of magnitude, assuming linear scaling. Interestingly, the transport anisotropy in these materials are roughly of the same order of magnitude, with the mobilities in TMDCs to be roughly 1000 times lower in the out-of-plane direction compared to the in-plane direction [121]. There are also large differences between the in-plane and out-of-plane dielectric constants, notably the absence of strong excitonic resonances in the out-of-plane dielectric function [197].

Despite these differences between the vertical and in-plane directions, there are several distinguishing features of the van der Waals interaction. First, it enables the formation of high quality van der Waals heterostructures, which do not suffer from the same lattice matching problem that is typical in traditional semiconductors (such as III-V semiconductors). This enables a larger variety of different materials to be heterostructured, and allows for “designer” materials (Figure 1.5). Furthermore, as

---

<sup>5</sup>A primer on the microscopic formation and dissociation of excitons is described in section A.1.

was noted in the original works of Novoselov and Geim [140], the presence of these van der Waals interactions in the out-of-plane direction results in atomically thin materials that are almost completely absent of dangling bonds. This is due to the inherent nature of the crystal structure, which is substantially different than non-layered materials. Thus, we are able to create materials with nearly zero intrinsic surface states, which enables the study of truly “two-dimensional” materials.

#### 1.4 Scope of the Thesis

As discussed earlier in [section 1.1](#), the three pillars of understanding the properties and power conversion efficiency of photovoltaic devices stems from a holistic understanding of the *absorption* of photons and subsequent generation of electron-hole pairs, *transport* and collection of those generated electron-hole pairs, and eventual *recombination* of those electron-hole pairs. In this thesis, we explore, understand, and engineer these three pillars in atomically-thin materials in our quest to use them as photovoltaic-active layers.

In [Part I](#) of this thesis, we discuss the interplay between optical absorption and the thermodynamic efficiency limits of atomically-thin materials. [Chapter 2](#) focuses directly on how the optical absorption limits the fundamental efficiency achievable in photovoltaic materials. This analysis is of general validity to all optoelectronic materials and is derived from optoelectronic reciprocity relations. We then use these relations to analyze the effects of semiconductor band tails on the fundamental photovoltaic efficiency limits. Afterward, we focus our attention to atomically-thin materials, which have unique bandstructures and defect states. This analysis lays the foundation for choosing appropriate materials when optimizing a photovoltaic device. [Chapter 3](#) then focuses on engineering the optical properties of ultrathin transition metal dichalcogenide materials, which have strongly excitonic properties. These excitonic properties result in immense light-matter coupling, enabling nearly perfect absorption in both ultrathin ( $\sim 10$  nm) and atomically-thin ( $\sim 7$  Å) with the use of simple optical cavities. Finally, we discuss conceptually the possibilities of an excitonic multijunction solar cell assuming near-unity absorbance can be achieved.

In [Part II](#) of this thesis, we discuss the transport of both free carriers and excitons in atomically-thin materials. [Chapter 4](#) focuses on *vertical* heterostructures of atomically-thin materials that utilizes the optical design of Chapter 3 and the electronic optimization of heterojunctions and metal contacts. This initial optimization results in unprecedented photovoltaic quantum efficiencies of ( $>50\%$ ), which is a

record for van der Waals materials. We then turn our attention to new methods of separating electrons and holes in ultrathin materials, in the form of a “band-bending junction”, which utilizes the finite band-bending in materials whose thicknesses are thinner than their electrostatic screening length. [Chapter 5](#) focuses on the conceptual physics and experimental demonstration of these band-bending junctions by utilizing various surface-sensitive probes and numerical calculations.

In [Part III](#) of this thesis, we discuss the intimate relationship between photoluminescence, recombination dynamics, and the internal photovoltage of a semiconductor and therefore motivate examining the photoluminescence properties of atomically-thin semiconductors. Specifically, we examine the photoluminescence properties in monolayer and heterobilayer systems and examine how they can be modified, which modifies their recombination dynamics. [Chapter 6](#) therefore focuses on how strain can be utilized to engineer the photoluminescence properties of  $\text{MoS}_2/\text{WSe}_2$  heterobilayers, which have quasiparticles referred to as *interlayer* excitons.

Finally, in [Part IV](#) of this thesis, we give an outlook and perspective on the work shown here, and discuss some of the remaining grand challenges and research opportunities for the field of van der Waals materials as well as that specific to using them for photovoltaic applications.

## **Part I**

### **Absorption Defines the Limits**

## Chapter 2

## IMPACT OF THE SEMICONDUCTOR BAND-EDGE ON PHOTOVOLTAIC EFFICIENCY LIMITS

*“If I have seen farther it is by standing on the shoulders of giants.”*

— Sir Isaac Newton

### 2.1 Introduction

Since the seminal work of Shockley and Queisser, assessing the detailed balance between absorbed and emitted radiative fluxes from a photovoltaic absorber has been the standard method for evaluating solar cell efficiency limits [17, 163, 175]. The principle of detailed balance is one dictated by reciprocity and steady state, so that photons can be absorbed and emitted with equal probability. This basic principle has also been extended to evaluate the effects of multiple junctions [5, 120], hot carriers [167, 210], nanostructured geometries [4, 212], multiexciton generation [68, 91], sub-unity radiative efficiency [125], and many other solar cell configurations and nonidealities to estimate limiting efficiencies via modifications to the detailed balance model.

Another important modification to the Shockley-Queisser model is to examine the assumption of an abrupt, step-like onset of the densities of electronic states and absorption coefficient. Specifically, it has long been recognized from spectroscopic measurements of semiconductors that band edges are often not abrupt and that the density of states and absorption functions can be characterized by a band tail. This was first recognized by Urbach [188], who found the absorption coefficient for a variety of materials below their bandgaps to be characterized by an exponential tail:

$$\alpha(E < E_g) = \alpha_0 \exp\left(\frac{E - E_g}{\gamma}\right) \quad (2.1)$$

where  $\alpha_0$  is the absorption coefficient value at the energy of the bandgap,  $E_g$  is the bandgap of the material, and  $\gamma$  is referred to as the Urbach parameter, which describes the rate at which the absorption coefficient goes to zero. The magnitude of the Urbach parameter can be influenced by impurities and disorder and is typically attributed to fluctuations in the electrostatic potential within a semiconductor. Urbach tails

have been observed in a wide range of absorber materials including amorphous, organic, perovskite, and II-VI, III-V and group IV semiconductors [35, 39, 83, 84, 96, 133, 180]. While the Urbach exponential tail is the most prominent functional form observed for band tail states, other forms such as Gaussian band tails have been reported, and different functional forms have been attributed to the underlying physics of those systems [87]. In most cases, the band tail can be characterized by an exponential with an argument raised to some power.

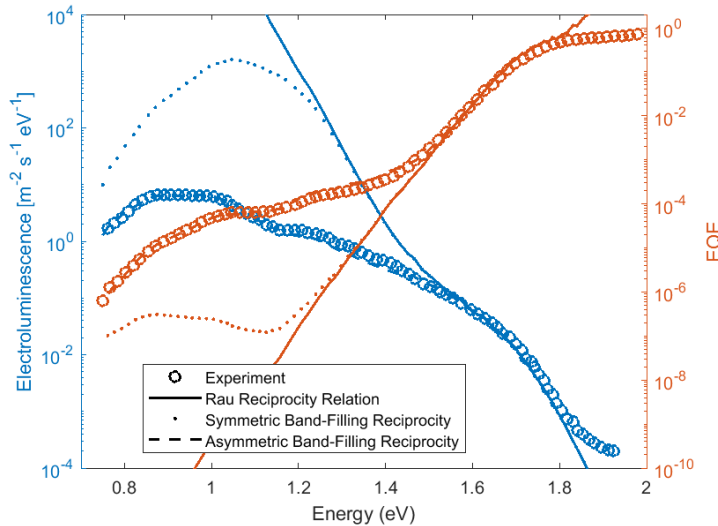


**Figure 2.1: Accounting for band filling in modified reciprocity relations.** Experimentally measured a-Si:H EQE and EL from [163] (open circles). Solid lines correspond to the Rau reciprocity relation, whereas the dashed line is a fit that includes band filling effects with asymmetric effective masses in the parabolic approximation ( $m_h/m_e = 1.818$ ,  $\Delta\mu = 1.164$  V, and  $E_g = 2.439$  eV). The dotted line includes band filling with the same fitted parameters except  $m_h/m_e = 1$ , i.e., assumes symmetric effective masses. All spectra are normalized by  $\exp(\Delta\mu/k_b T)$  and the various reciprocity relations overlay for  $E > E_{g,Abs}$ .

Recent detailed balance analyses have also suggested how this important effect, i.e., a departure from a step-like absorbance spectra can also degrade the limiting efficiency of solar cells [17, 32, 60, 82, 133, 161]. However, a key element missing from previous analyses of photovoltaic efficiency is the effect of band filling for semiconductors with nonabrupt band edges, wherein the electron-hole quasi-Fermi level splitting can thereby modify the absorption spectrum, and therefore the radiative emission spectrum as well. This voltage-dependent absorption effect was first recognized by Parrott [145] as being necessary to make the detailed balance formulation self-consistent. Perhaps the most intuitive description of why this is

necessary is found by examining the generalized Planck's law [209]:

$$S_{PL}(E) = a(E)S_{bb}(E, \delta\mu) \quad (2.2)$$

where

$$S_{bb}(E, \Delta\mu) = \frac{2\pi}{h^3 c^2} \frac{E^2}{\exp\left(\frac{E-\Delta\mu}{k_b T}\right) - 1} \quad (2.3)$$

and  $S_{PL}(E)$  describes the luminescence flux,  $a(E)$  is the absorbance,  $E$  is the photon energy,  $\Delta\mu$  is the quasi-Fermi level splitting,  $h$  is Planck's constant, and  $c$  is the speed of light. A clear singularity occurs at  $E = \Delta\mu$ , which is typically ignored in detailed balance calculations because for a step-like absorbance function, we have  $E \geq E_g > \Delta\mu$ . As a result, the  $-1$  in the denominator is neglected and Boltzmann statistics are assumed. Clearly, the situation must change if we consider energies  $E < E_g$ , as is the case when band tails affect the luminescence spectrum. In this case, the absorptivity must be modified such that  $a(E = \Delta\mu) = 0$ , and in general the absorption coefficient is occupation dependent:

$$\alpha(E, \Delta\mu) = \alpha_{0K}(E)(f_v - f_c) \quad (2.4)$$

where  $\alpha_{0K}(E)$  is the absorption coefficient without band-filling and  $(f_v - f_c)$  is the band-filling factor [16, 87, 209]. This contribution of band-filling has also been recognized in experiments as being necessary to accurately fit photoluminescence spectra under high level injection [58, 136]. We suggest that this contribution is also important for systems with large band tails, and as an example, we have used this modified reciprocity relation to fit the electroluminescence spectrum of a-Si:H which the Rau reciprocity relation [160, 163] was previously unable to fit completely (see Figure 2.1).

## 2.2 Photovoltaic Efficiency Limit for Semiconductors with Band Tails

By using the generalized Planck's law (Equation 2.2) and accounting for band filling (Equation 2.4), we can calculate the detailed balance limit for photovoltaic efficiency with band tails in the radiative limit (See section 2.6 and section 2.6). In Figure 2.2, we consider the case of a band tail parameterized as an exponential Urbach tail and analyze the effects of varying the Urbach parameter. While the spectral response of this modified absorbance appears to be similar to the step function response originally used by Shockley and Queisser (black dashed line), the maximum achievable efficiency drops rapidly from the Shockley-Queisser limit for Urbach parameters larger than the thermal energy,  $k_b T$ . These effects are relatively

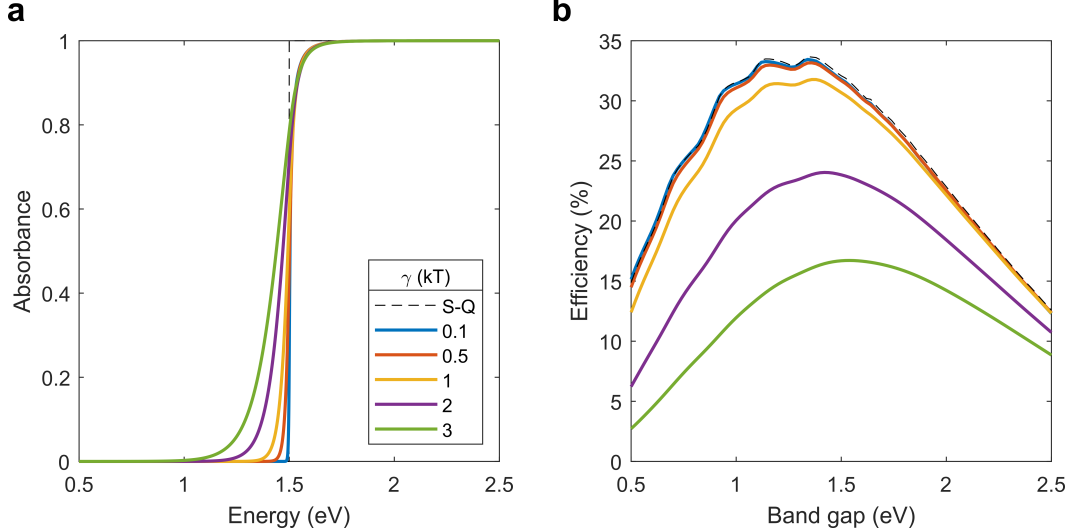


**Figure 2.2: Effects of band tailing on photovoltaic limiting efficiencies.** **a** The spectral absorbance of a photovoltaic cell with a bandgap of  $E_g = 1.5$  eV and a thickness  $\alpha_0 L = 1$  plotted for various Urbach parameters ( $\gamma$ ) in units of  $k_b T$ . The dashed line represents the step function absorbance typically used in the Shockley-Queisser (S-Q) limit. **b** The detailed balance efficiencies as a function of the bandgap energy. Different colored lines correspond to different Urbach parameters, with the coloring scheme equal to the legend shown in **a**.

insensitive to the choice of bandgap and thickness (see [Figure 2.3](#) and [Figure 2.4](#)), and [Figure 2.3](#) suggests the efficiency drop is primarily due to a voltage loss mechanism.

To analyze the cause of the voltage loss, we examine the luminescence spectrum by using [\(Equation 2.2\)](#) and plot these spectra for various Urbach parameters ([Figure 2.6a](#)). In addition, we plot the distribution of bandgaps  $P(E_g) = \partial_E a|_{E=E_g}$  proposed by Rau et al. [\[163\]](#) recently, which generalizes the definition of the photovoltaic bandgap for arbitrary absorbance spectra. While the luminescence spectrum is narrow and overlaps significantly with the absorption edge for  $\gamma < k_b T$ , this is not the case for  $\gamma > k_b T$ . In this limit, the luminescence spectrum is significantly broadened and shifts away from the absorption band-edge and suggests the definition of a second bandgap, defined by the luminescence spectra. This idea is schematically depicted in [Figure 2.6b](#), where the absorption bandgap is defined as before, i.e.,  $P(E_{g,Abs}) = \max(P_{E_g})$ , while the second bandgap,  $E_{g,PL}$ , is defined by the luminescence spectra  $S_{PL}$ . We note that this analysis is modified significantly with the inclusion of band-filling effects, which we describe in [section 2.6](#) and [section 2.6](#) of the Appendix (see also [Figure 2.13](#) and [Figure 2.14](#)). We also observe the effects of broadening followed by luminescence spectral shifts in band tails parameterized

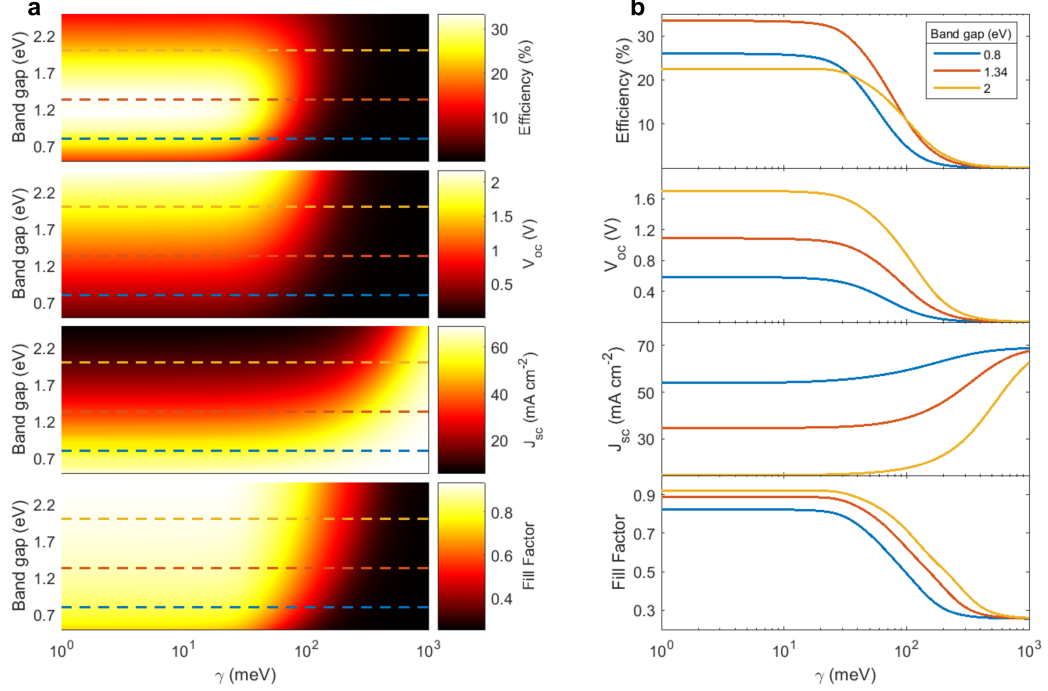


**Figure 2.3: Dependence of photovoltaic figures of merit on the Urbach parameter.** **a** The detailed balance limited value of conversion efficiency, open circuit voltage, short circuit current, and fill factor for different bandgaps and Urbach parameters assuming a thickness of  $\alpha_0 L = 1$ . **b** Linecuts of **a** at specific bandgap values.

by a Gaussian band tail (Figure 2.5), where the onset of efficiency loss occurs at approximately  $\gamma = 2k_b T$  instead.

### 2.3 Generalized Voltage Loss for Semiconductors with Nonabrupt Band Edges

The similarity between the effects of broadening followed by luminescence shifting for increasing band tail energies suggests a general picture for the voltage loss mechanism, for any band tail functional form. A general trend is the observation of a Stokes shift, i.e., the shift between the absorbance and luminescence spectra, that occurs precisely at the onset of efficiency loss. However, it is unclear whether the voltage loss is just directly proportional to the observed Stokes shift  $\Delta E_g$ .

To develop an understanding of this loss mechanism, we consider a simpler absorbance spectrum as a two bandgap model, represented by the sum of two step function absorbances:

$$a(E) = a_1 \theta(E - E_{g,1}) \theta(E_{g,2} - E) + a_2 \theta(E - E_{g,2}) \quad (2.5)$$

Here,  $a_{1,2}$  is the sub-gap and above-gap absorbances respectively, while  $\theta(E -$

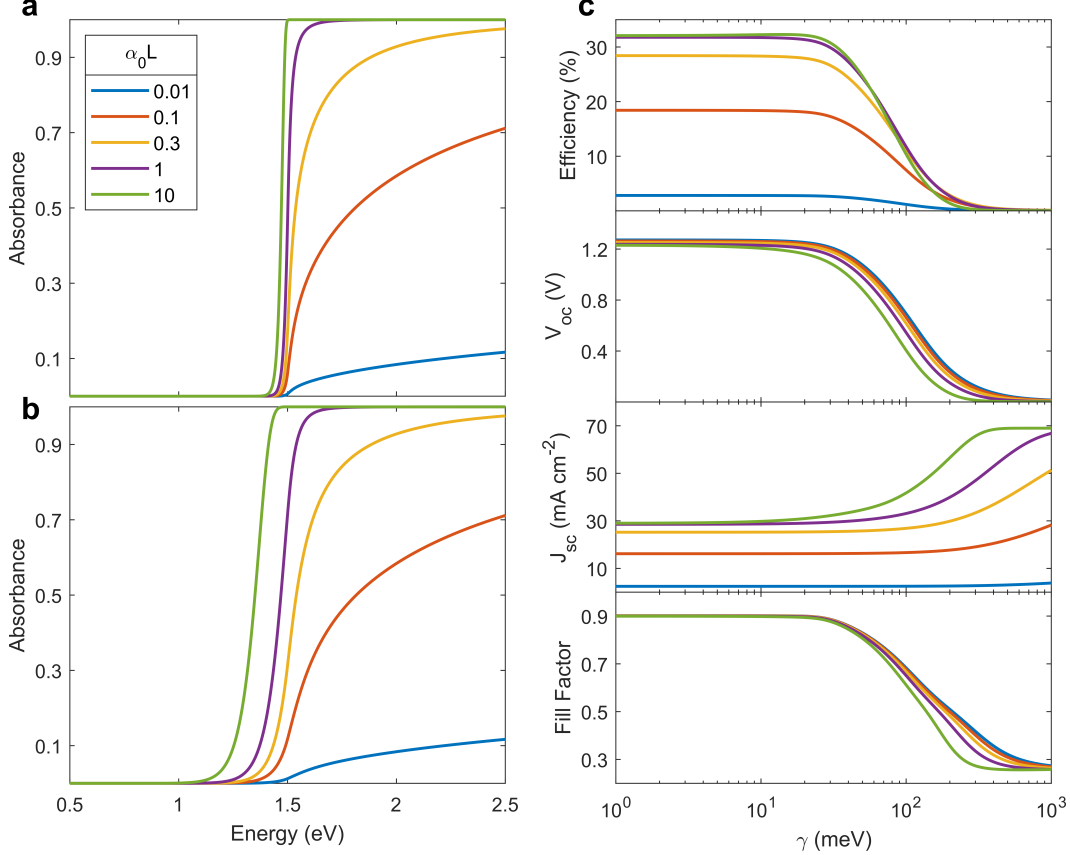


**Figure 2.4: Effects of thickness on photovoltaic figures of merit.** **a** Absorbance of a photovoltaic cell plotted with different normalized thicknesses ( $\alpha_0 L$ ) for  $\gamma = 0.5k_bT$  and **b**  $\gamma = 2k_bT$  assuming a bandgap  $E_g = 1.5$  eV. **c** Conversion efficiency, open circuit voltage, short circuit current, and fill factor calculated for different normalized thicknesses assuming a bandgap  $E_g = 1.5$  eV. The different colored lines correspond to the same legend shown in **a**.

$E_g$ ) is the Heaviside step function, typically considered in the SQ analysis. The photovoltaic bandgap, i.e., that defined by absorption, is given by  $E_{g,2}$ , while  $E_{g,1}$  defines the luminescence bandgap. The SQ limit is recovered in the limit that  $E_{g,1} \rightarrow E_{g,2}$  or  $a_1 \rightarrow 0$ . By varying  $a_1$  and  $E_{g,1}$  and fixing  $E_{g,2}$  to 1.34 eV and  $a_2 = 1$ , we can analyze the effects of this simple model as we deviate from the SQ limit (see [section 2.6](#) and [Figure 2.15](#) for more details). Interestingly, we find qualitatively similar effects of voltage and efficiency loss in this absorbance model compared to the full effects of the Urbach band tail, albeit parametrized by  $a_1$  and  $E_{g,1}$  instead of the Urbach parameter  $\gamma$ . However, we also find that the quantitative bandgap-voltage relation can be significantly affected by the actual functional form used to more accurately model the band tail state distribution, as illustrated in

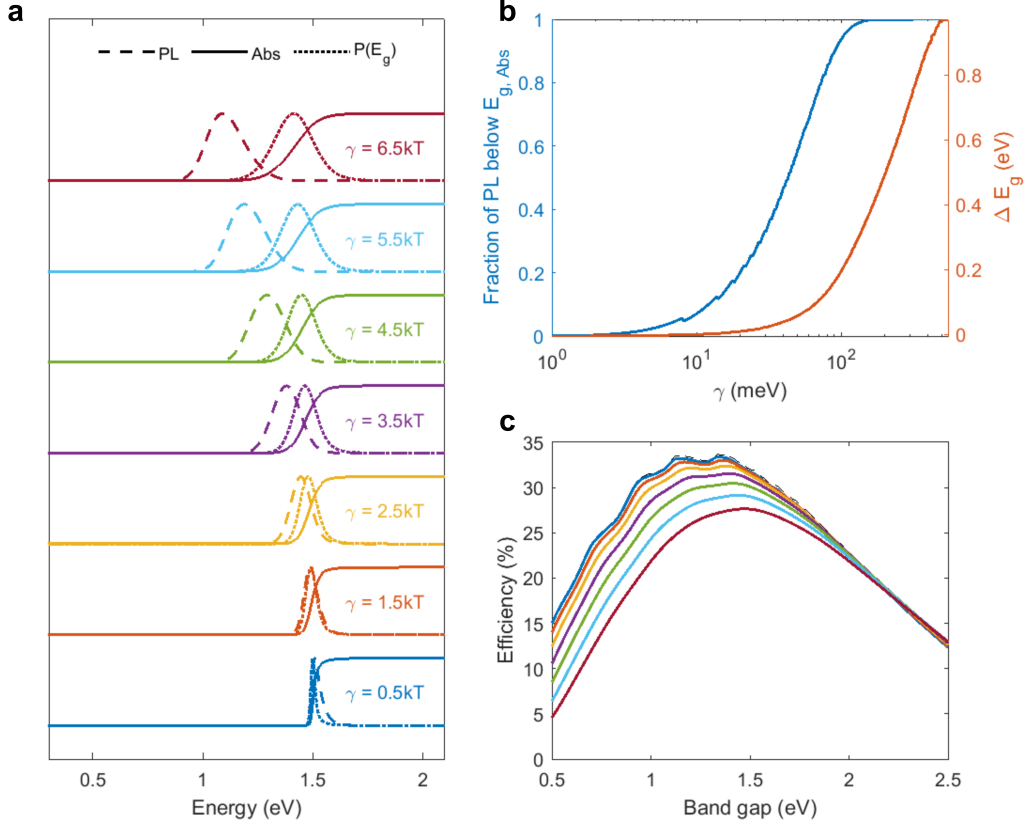


**Figure 2.5: Analysis of a Gaussian band tail distribution.** **a** Calculated absorbance (solid line), photoluminescence (dashed line) and distribution of bandgaps (dotted line) for an increasing Gaussian tail ( $\gamma$ ). Here, the Gaussian tail distribution is calculated by taking  $\theta = 2$  in Eqn. 14. **b** Fraction of integrated photoluminescence below the band gap (solid blue line) and Stokes shift  $\Delta E_g$  (solid orange line) for a Gaussian tail distribution. **c** Calculated detailed balance efficiency for different bandgaps plotted for increasing Gaussian tail widths. The different colored lines correspond to the same values of the Gaussian tail displayed in **a**.

**Figure 2.7.**

Non-abrupt band-edge absorbances can be mapped onto the two bandgap model and therefore there is a general relation that explains the voltage loss mechanism for any absorbance spectrum given by

$$\Delta V_{oc,rad} = \frac{k_b T}{q} \ln \left[ \frac{\bar{a}_{SG}}{\bar{a}_{AG}} \exp \left( \frac{\Delta E_g}{k_b T} \right) + 1 - \frac{\bar{a}_{SG}}{\bar{a}_{AG}} \right] \quad (2.6)$$

where  $\bar{a}_{SG}$  is the weighted sub-gap absorbance,  $\bar{a}_{AG}$  is the weighted above-gap absorbance, and  $\Delta E_g = E_{g,Abs} - E_{g,PL}$  describes the observed Stokes shift between the absorption and luminescence (see definitions in section 2.6 of the Appendix).

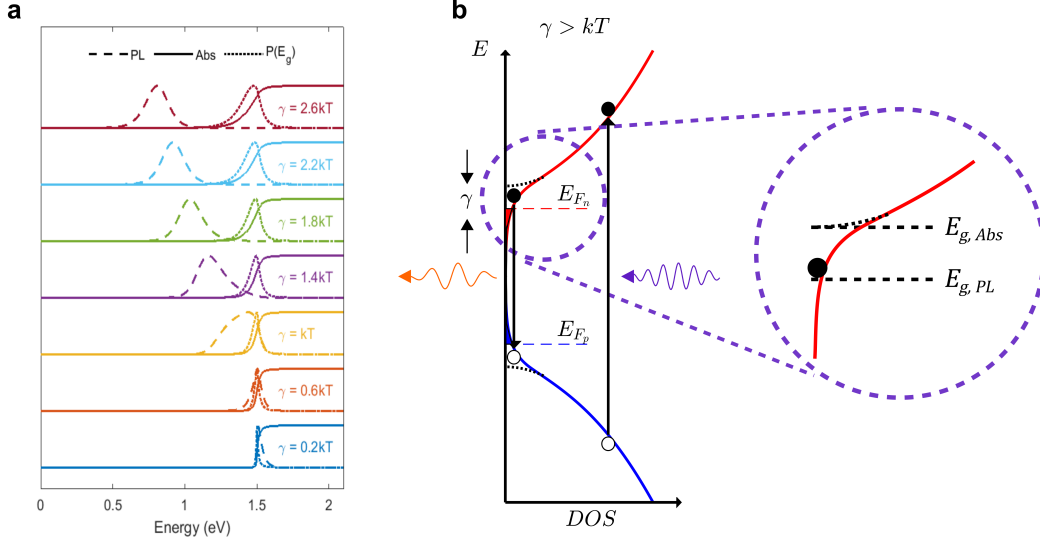


**Figure 2.6: Effects of band tail states on photoluminescence.** **a** The normalized spectral photoluminescence (dashed line) of a photovoltaic cell operating at the radiative limit under 1 sun AM 1.5G illumination for increasing Urbach parameter ( $\gamma$ ) with an offset included for clarity. The corresponding absorbance (solid line) and effective distribution of bandgaps (dotted line) is also plotted, where they are normalized to their peak value. **b** Schematic depiction of the density of states profile along with carrier excitation and recombination;  $\gamma$  describes the effective width of the band tail. For small band tailing ( $\gamma < k_b T$ ), the effect of band tailing is to simply broaden the luminescence peak. For systems with large band tailing ( $\gamma > k_b T$ ), the luminescence shifts to energies below the nominal absorption band edge.

Here,  $\Delta V_{oc,rad}$  is a voltage loss due purely to the non-abruptness of the absorption spectrum, for a semiconductor with assumed unity radiative efficiency. More generally, although non-radiative losses parametrized by a non-unity external radiative efficiency have not been accounted for (see some discussion of radiative efficiency effects in [section 2.6](#)), band edge non-abruptness by itself can contribute significantly to voltage loss. Indeed, [Equation 2.6](#) results in no net voltage loss as  $\Delta E_g \rightarrow 0$ , and suggests that a finite Stokes shift should be directly correlated to a voltage loss. The magnitude of the voltage loss is scaled by the ratio  $\bar{a}_{SG}/\bar{a}_{AG}$ , and clearly as the ratio approaches 0 or 1, [Equation 2.6](#) recovers the appropriate losses of 0 and  $\Delta E_g/q$ , respectively.

To observe whether this two bandgap model can quantitatively describe the more complex band edge functional forms seen in experiments, we choose appropriate definitions for  $\bar{a}_{SG}$ ,  $\bar{a}_{AG}$ , and  $E_{g,PL}$  and use Rau's definition for  $E_{g,Abs}$  (see more details in [section 2.6](#), [section 2.6](#), and with [Figure 2.17](#)). We consider both power

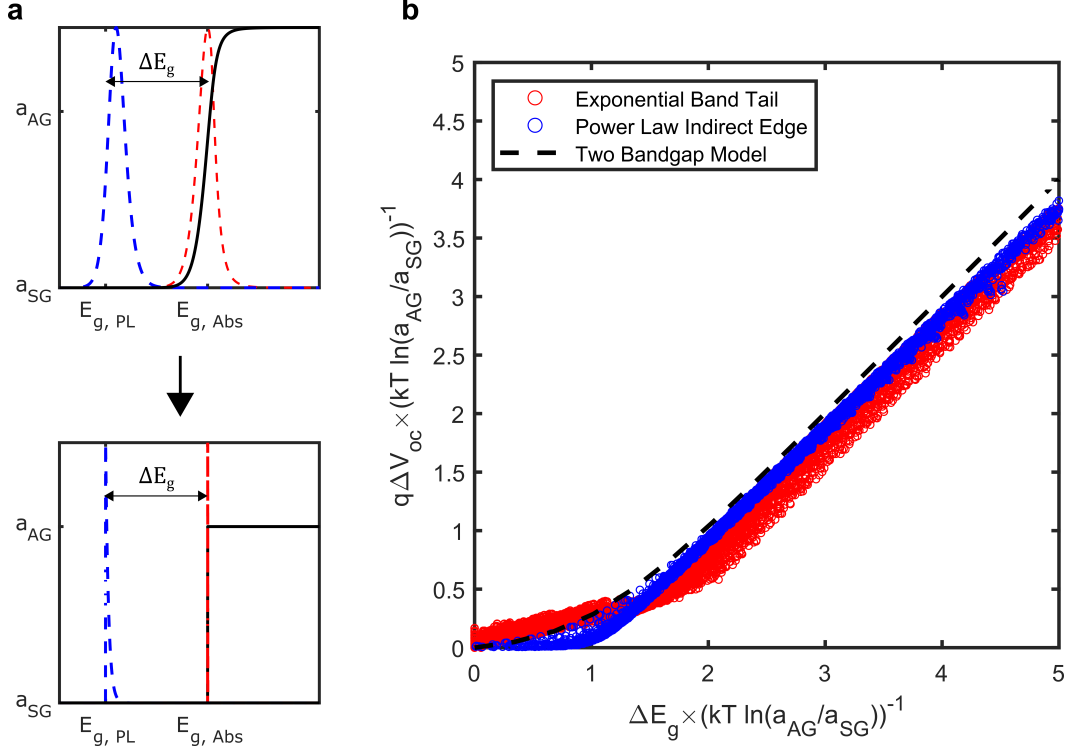


Figure 2.7: Generalized voltage losses parametrized as a two-bandgap absorber: **a** Schematic depiction representing a general absorbance and luminescence spectrum as a simpler two-bandgap step function absorbance. Black solid lines are the absorption spectrum, whereas the red dashed line corresponds to the bandgap distribution  $P(E_g)$ . Blue dashed lines correspond to the luminescence spectrum  $S_{PL}$ . Typically,  $\bar{a}_{SG} \ll 1$ , which is not visible on a linear scale but still contributes to the luminescence spectra due to carrier thermalization. **b** Calculated voltage loss  $\Delta V_{oc} = V_{oc,SQ}(E_{g,Abs}) - V_{oc,rad}$  versus observed bandgap shift  $\Delta E_g = E_{g,Abs} - E_{g,PL}$ , normalized to the energy scale  $k_b T \ln(\bar{a}_{AG}/\bar{a}_{SG})$ . Every plotted point corresponds to a different absorption spectrum, with  $V_{oc,rad}$  calculated using the complete absorption spectra and the full reciprocity relations. The dashed line represents the two bandgap model, i.e., [Equation 2.6](#), where we have chosen  $\bar{a}_{SG}/\bar{a}_{AG} = 0.1$ .

law band-edges, as a parametrization of indirect band-edges, as well as exponential band tails. We find reasonable qualitative agreement but quantitative disagreement between the calculations utilizing the full absorbance spectra and that given by [Equation 2.6](#) ([Figure 2.7b](#)), suggesting that the two-bandgap model is a reasonable first-order representation of the voltage loss mechanism, but importantly, consideration of the actual band tail functional form yields more accurate results. Furthermore, we find that the dimensionless parameter  $\xi = \Delta E_g / (k_b T \ln(\bar{a}_{AG}/\bar{a}_{SG}))$  describes the physical regime of voltage loss. Generally, for  $\xi < 1$ , voltage loss is minimal since the emission spectrum can be considered as simply a broadening of

a single photovoltaic bandgap. In this regime, the efficiency penalty is negligible and generally the detailed balance efficiency limit for  $E_{g,Abs}$  can be achieved given sufficient absorption above the photovoltaic bandgap. However, for  $\xi > 1$ , it is appropriate to define a second bandgap given by the emission spectrum (Figure 2.7a), resulting in a substantial voltage and efficiency penalty due to additional thermalization losses. Thus, the tuning of the band tail parameter  $\gamma$  merely sweeps through different values of  $\xi$ , and we find that  $\xi > 1$  is equivalent to  $\gamma > k_b T$  in the case of an Urbach tail (section 2.6). The discrepancy in Equation 2.6 for large  $\xi$  can be attributed to neglecting higher order terms (section 2.6).

The correlation between the magnitude of the bandgap shift ( $\Delta E_g$ ) and open circuit voltage has already been recognized in the organic photovoltaics literature, where the presence of low energy charge transfer states generally results in cells with a lower voltage and efficiency [9, 112, 133, 156, 159]. Here, we have developed a unified picture with an arbitrarily-shaped band tail and by explicitly including band-filling effects, for both large and small band tails, the voltage loss mechanism can be qualitatively captured with a simple two bandgap model. In addition, by extracting the weighted absorbance ratios, a  $\bar{a}_{AG}/\bar{a}_{SG}$ , we can estimate the voltage losses in the radiative limit using Equation 2.6. We therefore suggest that any radiative transition below the photovoltaic absorption edge  $E_{g,Abs}$ , measurable in luminescence measurements, should result in an efficiency penalty. This efficiency penalty can be viewed as either stemming from a voltage penalty, due to carrier thermalization within the band tails, or equivalently interpreted as being due to incomplete absorption at the lower energy transition.

## 2.4 Outlook on Examining Semiconductor Band Tails

To emphasize the implications of these results for various photovoltaic technologies, we have calculated the predicted voltage losses due to a nonabrupt band-edge for several different material systems and plotted experimentally-measured values for these in Figure 2.8 (See Table 2.2 for references and individual datapoints) [39, 82, 133]. Since Urbach parameters are much more commonly reported than both high sensitivity EQE and EL spectra, we have used the observed Urbach parameters to calculate the voltage loss directly rather than through Equation 2.6. As expected, we find that semiconductors with large band tails ( $\gamma > k_b T$ ) or equivalently, large Stokes shifts ( $\Delta E_g \gg k_b T$ ) have a substantially modified maximum achievable  $V_{oc}$ , which should be assessed when examining their efficiency potential (e.g., CIGS, a-Si, kesterites, and OPVs). It should be noted that a more accurate calculation can

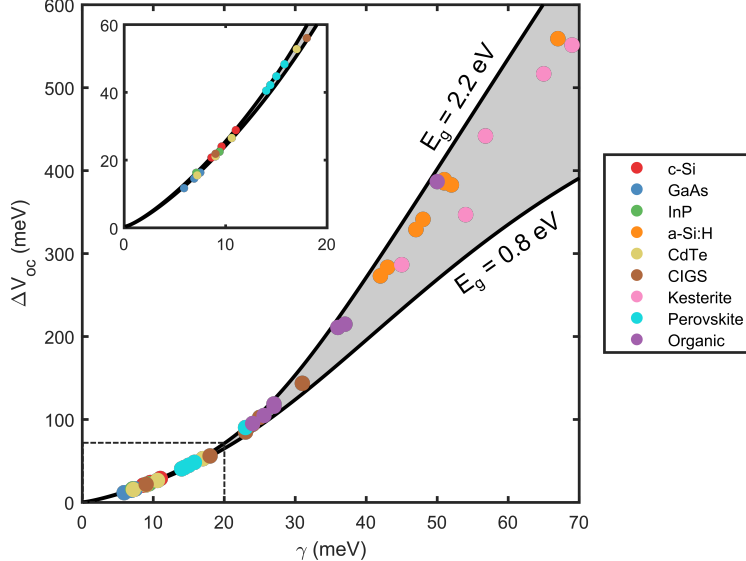


**Figure 2.8: Voltage loss due to a nonabrupt band-edge.** Expected open circuit voltage loss as a function of the observed Urbach parameter  $\gamma$ , plotted for different materials. The top and bottom black solid lines represent the calculated voltage loss assuming a bandgap of 2.2 and 0.8 eV, respectively. The gray area in between represents the voltage loss expected for bandgap values in between 0.8 and 2.2 eV, which correspond to most of the materials considered for photovoltaics. The colored data points indicate the expected voltage loss for an experimentally-measured Urbach parameter. The dashed line corresponds to the region of the inset, where the voltage loss is minimal and approximately the same irrespective of bandgap.

be made by using the directly measured EQE and EL spectra for a given device.

The analysis presented here should be applicable to any system with nonabrupt band-edges that obeys the optoelectronic reciprocity relations and should be employed to evaluate the radiative limits on the open circuit voltage. We demonstrated here that the voltage dependence of the absorbance or EQE, specifically via band filling, must be included to self-consistently apply the generalized Planck's law for semiconductors. We also suggest that in order to accurately estimate efficiency limits, the abruptness of the band-edge should be experimentally characterized by measuring both the absorption and luminescence spectra of photovoltaic materials, and in a completed photovoltaic device, photocurrent and electroluminescence spectra should be used to assess the effects of transport on the reciprocity relations. The magnitude of the voltage loss can then be estimated directly from the spectroscopic measurements by applying reciprocity relations. Additional experimental details and nonidealities for a given photovoltaic material or device may modify the maximum efficiency potential even further, such as reduction in the external radiative

efficiency or the finite mobility of charge carriers. However, our analysis suggests the important role that band edge abruptness and band filling can play in defining the limit on open circuit voltage and efficiency potential of emerging and established photovoltaic materials.

## 2.5 Importance of the Direct-Indirect Gap Splitting on the Efficiency Potential of Ultrathin TMDC Photovoltaics

Based on the analysis from above, it is clear that the abruptness of the band-edge can have drastic effects on the efficiency potential of a solar cell material. Furthermore, any weakly absorbing state can *effectively* have a similar impact on the efficiency limit of a solar cell. Thus, we now turn our attention to apply the above analysis to ultrathin ( $\sim 10$  nm) but electronically bulk TMDCs, for which we are interested in using as active layers. This material system effectively behaves as a system that has two band-edges, because of the weakly absorbing indirect edge (typically around 1.3 eV for all the TMDCs) and the strongly absorbing direct-edge (A exciton, which is between 1.55 to 2.0 eV). The bandstructure that gives rise to this unique absorption edge is shown schematically in [Figure 2.9a](#) and the corresponding experimental photocurrent spectra (which is proportional to absorbance) is shown in [Figure 2.9b](#). It is clear that while the majority of the photocurrent (and generally, absorbance), occurs at and above the A exciton, the indirect-edge results in a second, low-energy, band-edge, which will have deleterious effects on the open-circuit voltage potential and limiting efficiency.

To analyze this further, it is useful to develop a simple model that contains the essential features of the absorption profile and analyze the effects it may have on the limiting efficiency of an ultrathin TMDC. One of the simplest models for the absorption-edge of an exciton is given by the Elliott expression:

$$\alpha_{exc}(E) = \alpha_{0,exc} \left( \frac{E}{E_b} \right) \left[ \frac{\theta(\Delta)}{1 - \exp(-2\pi/\sqrt{\Delta})} + \sum_n \frac{4\pi}{n^3} \delta \left( \Delta + \frac{1}{n^2} \right) \right] \quad (2.7)$$

where  $\Delta = (E - E_{g,dir})/E_b$  is dimensionless and represents the photon energy relative to the exciton binding energy. Here,  $E_{g,dir}$  is the quasiparticle bandgap of the direct band-edge,  $E_b$  is the exciton binding energy,  $\delta(x)$  is the Dirac-delta function,  $\theta(x)$  is the Heaviside step function, and  $\alpha_{0,exc}$  represents the effective oscillator strength. We further assume a Gaussian broadening given as

$$\alpha_{exc,gauss}(E) = \alpha_{exc}(E) * N(\sigma_E) \quad (2.8)$$

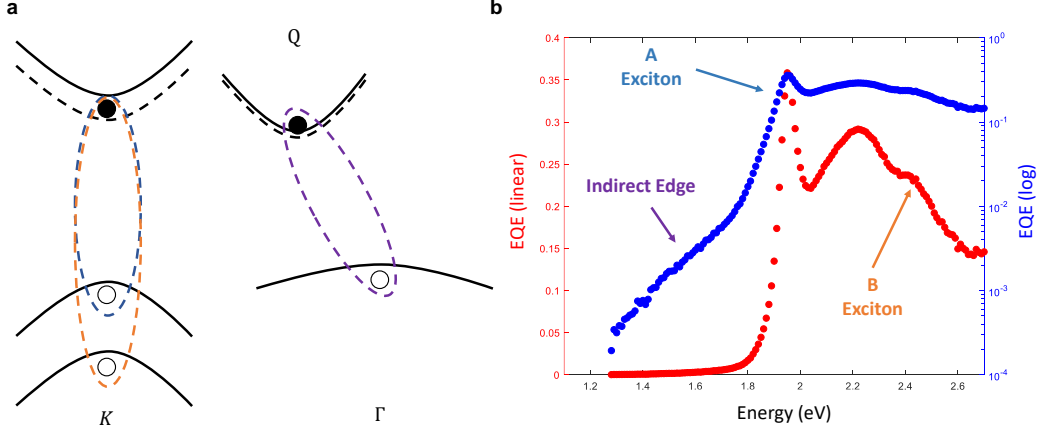


Figure 2.9: **Unique Bandstructure and Absorption Edge of Bulk TMDCs.** **a** Schematic bandstructure for bulk TMDC layers, with the associated excitonic transitions overlaid as dashed ovals. The first direct-edge exciton, i.e., the *A* exciton, occurs at the  $K$  point (blue oval), while the indirect-edge exciton occurs between the  $\Gamma$  and  $Q$  points (purple oval). **b** External quantum efficiency (EQE) spectra of a 20 nm Au/16 nm WS<sub>2</sub>/Ag sample, measured using Fourier transform photocurrent spectroscopy. Appropriate excitons and edges are also labelled. Left axis is a linear scale, and right axis is a log scale.

where  $N(\sigma_E)$  represents a normalized Gaussian with width  $\sigma_E$ , and ‘\*’ operator represents the convolution operation. Another essential feature is the indirect-edge exciton, which is typically represented by a power-law near the indirect-edge. Both linear and parabolic expressions are commonly observed. We shall use

$$\alpha_{ind}(E) = \alpha_{0,ind} \left( \frac{E - E_{g,ind}}{k_b T} \right)^2 \quad (2.9)$$

where we could consider convoluting the indirect absorption edge with some band tailing form (e.g., see [Equation 2.28](#)), but as we shall soon see, those effects are substantially smaller than the effects of the absorption into the indirect edge. The effects of the power law exponent are also weak. The total absorption coefficient of the bulk TMDC layer is then just given as the sum as the individual components:

$$\alpha_{TMDC} = \alpha_{exc,gauss}(E) + \alpha_{ind}(E) \quad (2.10)$$

Finally, we are interested in relating the absorption *coefficient* to the overall absorbance. In general, for ultrathin materials, wave optics is the appropriate formalism that relates the two quantities (e.g. see [Appendix B](#)). However, the specific optical structures surrounding the ultrathin TMDC layer critically describes this connection.

Instead, for sake of simplicity, we consider a non-dispersive relationship inspired by the work of [220] that parametrizes the effects of absorption enhancement as

$$a = \frac{\alpha L}{\alpha L + 1/C_{AE}} \quad (2.11)$$

where  $C_{AE}$  can be interpreted as the enhancement factor relative to a single pass absorption. This expression is derived strictly in the limit that the single pass absorption  $\alpha L$  is infinitesimal. Another possible expression is motivated by [162], which is given as

$$a = 1 - \exp(-\alpha L C_{AE}) \quad (2.12)$$

where  $\alpha$  in both these situations is the absorption coefficient, and  $L$  is the thickness of the active layer. Both expressions reproduce fairly similar results, the main difference being the rate at which  $a$  rises to unity as  $C_{AE}$  is large. For small  $\alpha L$ , note that both expressions are equivalent (i.e.,  $a \approx C_{AE} \alpha L$  from a first order expansion). Given the faster rise in absorbance and the natural form of the exponential in wave-like expressions, we use Equation 2.12 as our relationship between  $\alpha$  and  $a$ . However, similar results are obtained in both situations. In the ray-optics limit, the maximum absorption enhancement is  $C_{AE,\text{ray-optics}} = 4n_r^2$ , where  $n_r$  is the real part of the refractive index of the active layer. For TMDCs, the ray-optics limit on the enhancement factor can be nearly 100, but nanophotonic structures can offer values that are even higher.

Once the absorbance is specified, we can calculate the luminescence spectral flux by the reciprocity relations (Equation 2.20), which may be compared to photoluminescence spectra (see Figure 2.10a). Here, it is clear that the presence of the indirect edge results in a substantial Stokes shift between absorption and emission, although this is partially modulated by the amount of absorption enhancement  $C_{AE}$  Figure 2.10b. We further consider that, in general, the radiative efficiency is sub-unity. Therefore, we can parametrize its effects on the dark current as:

$$J_{dark} = \frac{J_{rad}}{ERE} = \frac{\int S_{PL}(E, \Delta\mu) dE}{ERE} \quad (2.13)$$

where the external radiative efficiency  $ERE$  is given as:

$$ERE = \frac{J_{rad}}{J_{rad} + J_{nrad,0}} = \frac{\frac{J_{rad}}{J_{rad,0}}}{\frac{J_{rad}}{J_{rad,0}} + \frac{1}{ERE_0} - 1} \quad (2.14)$$

where we have used the fact that  $J_{rad,0}/ERE_0 = J_{rad,0} + J_{nrad,0}$ . In the weakly absorbing limit (i.e.,  $\alpha L \ll 1$ ), we have  $J_{rad}/J_{rad,0} = C_{AE}$ , so that

$$ERE = \frac{C_{AE}ERE_0}{C_{AE}ERE_0 + (1 - ERE_0)} \quad (2.15)$$

In other words, we are taking into account the *Purcell factor* effect on the radiative efficiency for a finite increase in the absorption enhancement (which, in the limit of infinitesimal absorption, is equivalent to an enhancement in the radiative efficiency, i.e., is a Purcell factor).

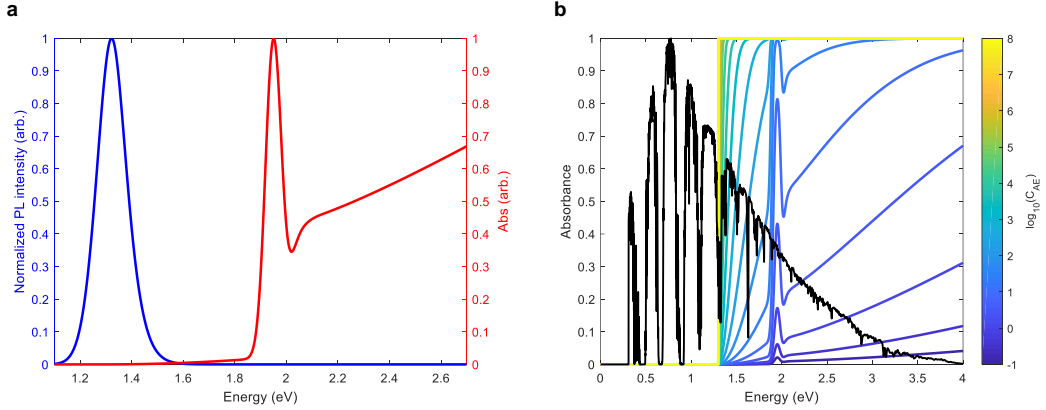


**Figure 2.10: Absorption Toy Model for Bulk TMDCs.** **a** Representative absorbance spectra from the toy model developed above, where the indirect edge is clearly visualized below the exciton and results in substantial luminescence. The first direct-edge exciton is also modelled. We ignore the higher order excitons, which do not substantially change the results shown here. **b** The calculated absorbance curves as a function of different absorption enhancement factors  $C_{AE}$ . Different colors of the curve correspond to different amounts of  $C_{AE}$ , given by the color bar on the right (plotted in a log scale). The AM 1.5G solar flux spectra is also plotted in black (normalized, units of photons/m<sup>2</sup>/s/eV).

We can now examine the effects of the specific absorption spectra on the efficiency limits of an ultrathin layer of WS<sub>2</sub> using the modified detailed balance calculations (section 2.6). The effects of the different initial radiative efficiencies ( $ERE_0$ ) and absorption enhancement factors  $C_{AE}$  is shown in Figure 2.11. We first note that, somewhat surprisingly, the current densities for reasonable absorption enhancement factors are far below their detailed balance value. At the ray-optics trapping limit of TMDCs, we would only achieve  $\sim$ 60% of the detailed balance  $J_{sc}$ . This fact stems from the small thicknesses ( $L = 10$  nm) considered in this analysis as well as the equally small absorption coefficient at the indirect edge  $\alpha_{0,ind} = 2 \times 10^3$ . The low indirect-edge absorption coefficient was estimated from experimental data (Figure 2.9), and the 10 nm regime of thickness is a common regime of thickness considered in device structures. To first order, this dramatic reduction in the  $J_{sc}$  scales with the power conversion efficiency, so that the practical efficiency limit for ultrathin WS<sub>2</sub> structures is closer to  $\sim$ 20%. Therefore, the absorption into the

*indirect* edge is a critical limiting factor in the efficiency potential of electronically bulk TMDCs, a fact that has not been recognized in the TMDC photovoltaics literature. To achieve >95% of the efficiency potential in electronically bulk WS<sub>2</sub>, absorption enhancement factors  $C_{AE}$  would need to be at least 1500.

It is clear that with an indirect edge at 1.3 eV, the detailed balance efficiency potential of ~33% can only be reached when there is complete absorption above the band-edge. Also of importance is the limiting open-circuit voltage potential ([Figure 2.11b](#)). We see that for different values of  $ERE_0$ , the open circuit voltage drops by  $k_b T / q \ln(ERE_1 / ERE_2)$ , i.e., 60 mV per decade. It is useful to note two other regimes in the open-circuit plot. As the absorption enhancement factor  $C_{AE}$  increases, the  $V_{oc}$  increases due to the Purcell factor and the overall increase in  $ERE$ . However, at very large  $C_{AE}$ , the optical absorption spectra gradually shifts from a system that has its main absorption edge at  $E_{g,dir}$  to one that has its main absorption edge at  $E_{g,ind}$  (see [Figure 2.10b](#)). This resultant shift in the *effective* band-edge results in a reduction in  $V_{oc}$ . At intermediate values of  $C_{AE}$ , there is a competition between both effects. The resultant Stokes shift  $\Delta E_g$  is reduced as  $C_{AE}$  increases, and therefore the overall efficiency potential increases with  $C_{AE}$  ([Figure 2.11c](#)), since the system transitions from two band-edges to a single abrupt band-edge (c.f. [section 2.6](#)).

Table 2.1: Parameter values for ultrathin WS<sub>2</sub> modified detailed balance calculations

Parameter	Value
$E_{g,dir}$ (eV)	2.05
$E_b$ (meV)	100
$\sigma_E$ (meV)	30
$\alpha_{0,exc}$ (1/m)	$6.14 \times 10^4$
$\alpha_{0,ind}$ (1/m)	$2 \times 10^3$
$E_{g,ind}$ (eV)	1.3
$L$ (nm)	10

It is important now to summarize some of our main observations from this analysis. It is rather clear that there is a substantial efficiency impact due to the large energetic difference between the direct and indirect edge of WS<sub>2</sub>. The magnitude of this effect is partially due to the magnitude of the indirect edge absorption  $\alpha_{0,ind}$  (c.f. [Equation 2.6](#)), but only scales logarithmically with those values. Thus, one

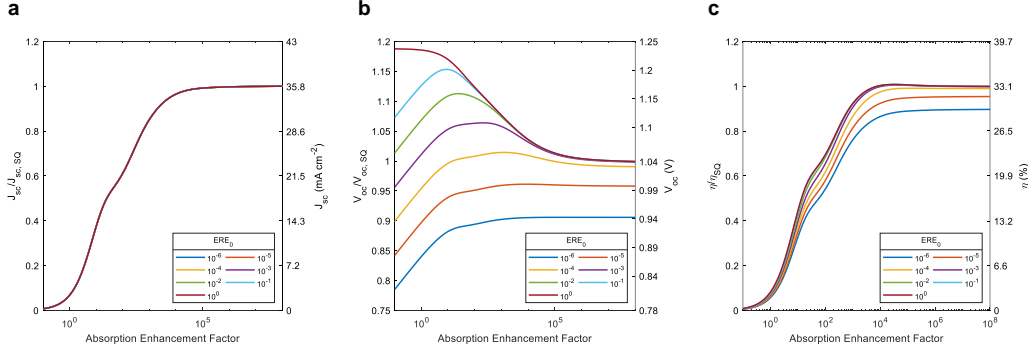


**Figure 2.11: Photovoltaic Figures of Merit of  $WS_2$  for Varying  $C_{AE}$  and  $ERE_0$ .** Calculated photovoltaic figures of merit from detailed balance calculations using the materials parameters in Table 2.1, where we plot the **a** short-circuit current density  $J_{sc}$  **b** open-circuit voltage  $V_{oc}$ , and the **c** power conversion efficiency  $\eta$ . All of the figures of merit are normalized to the equivalent detailed balance value for a step function absorbance at  $E_{g,ind}$ .

consequence of this analysis is to compare these results if the direct band-edge was substantially closer to the indirect edge, e.g. if  $E_{g,dir} = 1.55$  eV. This is shown in Figure 2.12, and this situation is akin to that of using  $MoSe_2$  as an active layer. While at first glance these figures look qualitatively quite similar, it soon becomes readily apparent that the efficiency potential is substantially higher for moderate  $C_{AE}$ , with >95% of the maximum efficiency achieved when  $C_{AE} \approx 25$ . These values of absorption enhancement is readily attainable in a variety of optical structures, and is far below the ray-optics limit. This result can be traced back to the abruptness of the band-edge and the two-bandgap model derived earlier. In this case, the Stokes shift between the direct and indirect edge is minimized, and maximum efficiency is achieved in a much more tolerable geometry.

In conclusion, we have found that electronically bulk TMDCs suffer from the existence of both a direct and indirect band-edge. We find that the presence of the additional band-edge to have deleterious effects on the maximum solar photovoltaic efficiency potential. This penalty is minimized when the direct to indirect band-edge energy splitting is minimized, and therefore, materials like  $WSe_2$ ,  $MoSe_2$ , or  $MoTe_2$  should be the main materials considered for achieving maximum solar photovoltaic efficiency in ultrathin active layers. These results could be refined by carefully measuring the experimental parameters of the various absorption coefficients, such as the parameters depicted in Table 2.1. However, we suspect that those values will not substantially change the conclusions presented here.

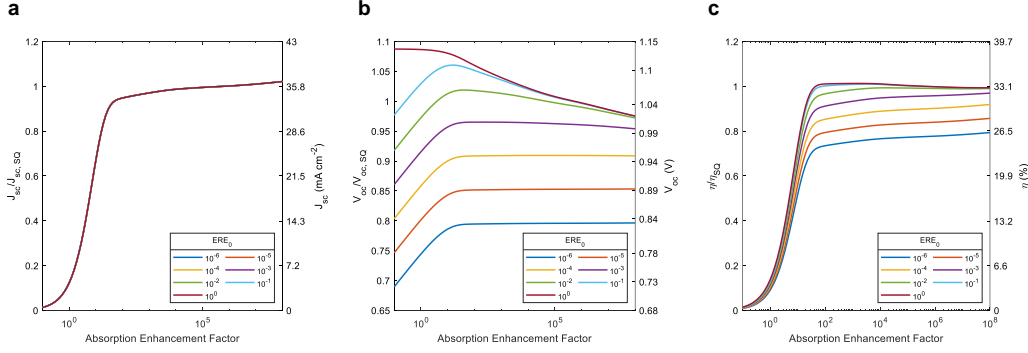


**Figure 2.12: Photovoltaic Figures of Merit of MoSe<sub>2</sub> for Varying  $C_{AE}$  and  $ERE_0$ .** Calculated photovoltaic figures of merit from detailed balance calculations using the materials parameters in [Table 2.1](#), except  $E_{g,dir} = 1.55$  eV. We plot the **a** short-circuit current density  $J_{sc}$  **b** open-circuit voltage  $V_{oc}$ , and the **c** power conversion efficiency  $\eta$ . All of the figures of merit are normalized to the equivalent detailed balance value for a step function absorbance at  $E_{g,ind}$ .

## 2.6 Appendix

### Optoelectronic Reciprocity Relations

The connection between absorption and emission has been known for quite some time. Kirchhoff in 1860 [90] is often cited as being the first to recognize the relation between the two processes, noting that the absorption and emission probability of a photon must be equal, i.e.  $a(E) = e(E)$ , through arguments of thermal equilibrium. A surface with  $e(E) = 1$  for all energies is known as a perfect black body. However, the precise spectral dependence of a perfect black body emitter was not derived until Planck did so in 1906 [153]. He theorized a cavity with perfectly absorbing walls filled with a gas of photons with a small hole that would leak out a spectral flux characteristic of a black body:

$$I_{bb}(E) = E \times S_{bb}(E) = \frac{2\pi}{h^3 c^2} \frac{E^3}{\exp\left(\frac{E}{k_b T}\right) - 1} \quad (2.16)$$

which relates the temperature of a black body to its spectral characteristics, often referred to as thermal radiation. Here,  $S_{bb}(E)$  is the energy-resolved photon flux per unit area per unit time of black-body radiation and  $I_b$  refers to the spectrally resolved intensity of the radiation. The above expression can be generalized to non-black bodies by combining it with Kirchhoff's law:

$$I(E) = a(E)I_{bb}(E) \quad (2.17)$$

To form a general law for thermal radiation with surfaces characterized by an absorptivity. In an analogous manner, van Roosbroeck and Shockley [191] generalized Planck's law to semiconductors and related the absorption coefficient ( $\alpha$ ) to the internal photon emission rate per unit volume:

$$R(E) = 4n_r^2(E)\alpha(E)S_{bb}(E) = \frac{8\pi n_r^2}{h^3 c^2} \frac{E^2 \alpha(E)}{\exp\left(\frac{E}{k_b T}\right) - 1} \quad (2.18)$$

which holds for systems at thermal equilibrium. It was not until Lasher and Stern [97] considered the situations of spontaneous emission were the above expressions further generalized to include non-equilibrium, steady-state conditions in terms of the quasi-Fermi level splitting  $\Delta\mu$ , which is exactly equal to the chemical potential of the photon in a spontaneous emission process:

$$R(E, \Delta\mu) = \frac{8\pi n_r^2}{h^3 c^2} \frac{E^2 \alpha(E)}{\exp\left(\frac{E - \Delta\mu}{k_b T}\right) - 1} \quad (2.19)$$

Here, we note that this expression is valid only when quasi-thermal equilibrium holds, where exactly two different quasi-Fermi levels accurately describe the energy dependence of the two separate populations of electrons and holes (e.g. after the electron-electron interactions subsequent to the excitation of carriers, the carriers will be distributed according to the Fermi-Dirac distribution), resulting in a single quasi-Fermi level splitting  $\Delta\mu$ . We assume this to be true in the case of the carriers in the band tails described here with the carriers above the respective band edges. For example, in the case of band tails caused by some ensemble of defects, an impurity band may be formed. If this impurity band is several  $k_b T$  away from the band edges, the electrons in this band would likely thermalize amongst themselves, forming a separate quasi-Fermi level. Therefore, these relations would need to be modified to include this effect. Wurfel [209] then generalized the Lasher-Stern relation to an external flux of radiative emission from a semiconductor surface:

$$S_{PL}(E) = a(E)S_{bb}(E, \Delta\mu) \quad (2.20)$$

where

$$S_{bb}(E, \Delta\mu) = \frac{2\pi}{h^3 c^2} \frac{E^2}{\exp\left(\frac{E - \Delta\mu}{k_b T}\right) - 1} \quad (2.21)$$

is the spectral flux of a photon gas with chemical potential  $\Delta\mu$  and temperature  $T$ . Here,  $E$  is the energy of the emitted photon,  $k_b$  is the Boltzmann constant,  $h$  is Planck's constant, and  $c$  is the speed of light. Wurfel's expression, with a relation

that connects the absorbance to the absorption coefficient (e.g. through the Beer-Lambert law of  $a(E) = 1 - \exp(-\alpha L)$  or more complex light-trapping geometries) suggests a complete set of self-consistent expressions that connect *external* properties (e.g. absorbance, external luminescence) of the semiconductor to its *internal* properties (e.g. bandgap, absorption coefficient, quasi-fermi level splitting, internal luminescence). External properties are therefore geometry dependent and can be carefully engineered from the internal properties using photonic design. Moreover, external properties are typically the only properties that are experimentally accessible.

We note that the above expression has an apparent divergence at  $E = \Delta\mu$ . The resolution requires including an occupation factor in the absorption coefficient:

$$\alpha(E) = \alpha_{0K}(E)(f_v - f_c) \quad (2.22)$$

where  $f_v$  and  $f_c$  are the occupation for the holes and electrons, respectively. In the case of a semiconductor with equal effective mass for the holes and electrons and described by a parabolic dispersion, the occupation factor has a simple form:

$$f_v - f_c = \tanh\left(\frac{E - \Delta\mu}{4k_b T}\right) \quad (2.23)$$

While real systems may have more complex occupation factors (typically not representable analytically due to a fairly complex band structure), we note that  $f_v - f_c$  is generally a function with limiting values from -1 to 1 with a value of zero at  $E = \Delta\mu$ , which is captured by the simple expression above. For simplicity and to capture the physics of the band filling irrespective of other materials properties, we use the simple expression above when calculating band filling effects.

It was suggested more recently by Rau [160] that the principle of optical reciprocity can be further generalized to an *optoelectronic* reciprocity by including the serial collection/injection with Donolato's theorem [46] to describe photovoltaic cells and LEDs:

$$S_{EL}(E) = EQE(E)S_{bb}(E, \Delta\mu) \quad (2.24)$$

where  $EQE(E) = a(E) \times IQE(E)$  and describes the process of absorbing a photon with probability  $a(E)$  with a subsequent collection probability of  $IQE(E)$ . Thus, the LED quantum efficiency  $Q_{LED}(E) = \eta_{inj}(E) \times e(E)$  is a detailed balance pair with the photovoltaic quantum efficiency, taking the injection and collection efficiencies to be detailed balance pairs. We note that while the above generalized

Planck's law (Wurfel's expression) holds quite generally by any system that can be characterized by two distinct quasi-Fermi levels and a thermodynamic temperature, Rau's reciprocity relation strictly holds only in systems where carrier transport under illumination is well modelled as a linear perturbation of thermal equilibrium (qualitatively, the law of superposition in the current-voltage curves needs to hold). We also note that previous examples of using optoelectronic reciprocity for photovoltaic analysis (e.g. modified detailed balance models) has often approximated the black-body flux as

$$S_{bb}(E, \Delta\mu) \approx S_{bb}(E, 0) \exp\left(\frac{\mu}{k_b T}\right) = \left( \frac{2\pi}{h^3 c^2} \frac{E^2}{\exp\left(\frac{E}{k_b T}\right) - 1} \right) \exp\left(\frac{\mu}{k_b T}\right) \quad (2.25)$$

While the above expression has no singularities and generally results in numerically accurate results for most systems of interest (e.g. idealistic systems with  $a(E \leq E_g) = 0$  will generally have  $(E - \mu)/k_b T \gg 1$ ), De Vos and Pauwels [38] noted the subtle differences this approximation has in analyzing entropy generation in the detailed balance limit. We show in this paper that accounting for band filling effects has qualitative and quantitative differences on the luminescence spectra of semiconductors with significant band tailing, which we emphasize in [Figure 2.1](#) with a-Si:H as an example. Therefore, we use the full expression above without any approximations.

### Modified Detailed Balance Limit Calculations

With the above expressions of optoelectronic reciprocity in hand, we can assemble a modified detailed balance model for solar cells that account for carrier generation, extraction, and recombination:

$$\int EQE(E, \Delta\mu) S(E) dE = \frac{\int EQE(E, \Delta\mu) S_{bb}(E, \Delta\mu) dE}{\eta_{ext}(\Delta\mu)} + \frac{J(\Delta\mu)}{q} \quad (2.26)$$

where the left-hand side describes carrier injection (e.g. from sunlight or other light source) and the right-hand side describes carrier extraction, either through radiative recombination, non-radiative recombination (parametrized by  $\eta_{ext}(\Delta\mu)$ ), or usefully as carrier collection ( $J(\Delta\mu)/q$ ). In steady state, these populations must be balanced. In our analysis in the main text, we consider the modified detailed balance expression in the radiative limit i.e.  $\eta_{ext} = 1$ ,  $\Delta\mu = qV$ ,  $EQE(E, \Delta\mu) = a(E, \Delta\mu)$  (see [section 2.6](#) for a short analysis on non-unity radiative or collection efficiency), with absorptivity described by a Beer-Lambert expression:

$$a(E) = 1 - \exp(-2\alpha L) \quad (2.27)$$

with a perfect back reflector and perfect anti-reflection coating to describe the optical configuration. To parametrize the band edge density of states, we take inspiration from Katahara and Hillhouse [87] and convolve a sub-gap exponential density of states with a parabolic density of states above the bandgap, giving

$$\alpha_{0K}(E) = \alpha_0 \sqrt{\frac{\gamma}{k_b T}} G\left(\frac{E - E_g}{\gamma}\right) \quad (2.28)$$

with

$$G(x) = \text{real} \left( \frac{1}{2\Gamma\left(1 + \frac{1}{\theta}\right)} \int_{-\infty}^{\infty} \exp(-|x'|^{\theta}) \sqrt{x - x'} dx' \right) \quad (2.29)$$

And the simplified expression above (Equation 2.23) to account for band filling. Here,  $\gamma$  is the energy width parameter (i.e. the Urbach parameter, for  $\theta = 1$ ).  $E_g$  is the bandgap,  $\Gamma$  is the Gamma function,  $\alpha_0$  scales the absorption coefficient (i.e.,  $\alpha(E = E_g) = \alpha_0 \sqrt{\pi\gamma/16k_b T}$ , and  $\theta$  describes the power of the sub-gap exponential distribution. Our expression has an extra factor of  $\sqrt{k_b T}$  compared to the Katahara model, where  $k_b T$  is the thermal energy, so that  $\alpha_0$  has the usual units of absorption coefficient. Using a simple piecewise continuous function for the absorption coefficient above and below the gap yields similar results, as long as the absorption coefficient below the gap is still modeled as an Urbach tail. Thus, for a given set of materials parameters (e.g.  $\alpha_0 L$ ,  $\gamma$ ,  $E_g$ ) and a specific voltage  $V = \Delta\mu$ , we can calculate the appropriate absorption coefficient and consequently the absorption and luminescence characteristics. The current-voltage curve of the photovoltaic cell in the detailed balance limit is then calculated using Equation 2.26. Specific figures of merit can then be extracted from the current-voltage curves.

### Band filling Contribution to Photoluminescence

In general, we are interested in the contribution of including the band filling on the luminescence spectrum of a semiconductor with significant band tails. Let us examine the case where we are weakly absorbing, which is generally true in the spectral region of a band tail. In this limit, we can take  $a \approx 2\alpha L$ , where we assume a planar system with a perfect mirror and a perfect antireflection coating as above. In this case, the external luminescence flux by reciprocity becomes

$$S_{PL}(E, \Delta\mu) = a(E, \Delta\mu) S_{bb}(E, \Delta\mu) \approx 2\alpha(E, \Delta\mu) L S_{bb}(E, \Delta\mu) \quad (2.30)$$

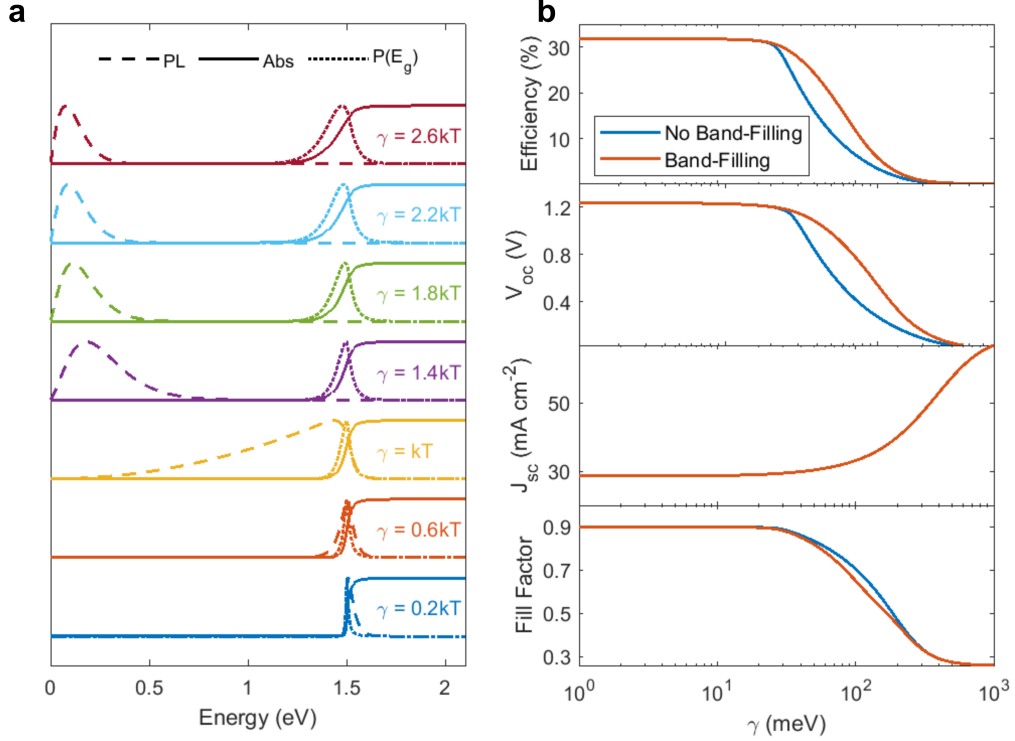


Figure 2.13: **The importance of including band filling effects.** **a** Calculated absorbance (solid line), photoluminescence (dashed line), and distribution of bandgaps (dotted line) for different Urbach parameters ( $\gamma$ ) without including band filling effects. **b** Calculated efficiency, open circuit voltage, short circuit current, and fill factor with (orange solid line) and without (blue solid line) including band filling effects.

For systems with intrinsic doping and equal effective masses, we have  $\alpha(E, \Delta\mu) = \alpha(E, 0)(f_v - f_c) = \alpha(E, 0) \tanh\left(\frac{E - \Delta\mu}{4k_b T}\right)$ . To see this, note that generally speaking,

$$f_v - f_c = \frac{1}{\exp\left(\frac{E_h - E_{f_p}}{k_b T}\right) + 1} - \frac{1}{\exp\left(\frac{E_e - E_{f_n}}{k_b T}\right) + 1} \quad (2.31)$$

And for intrinsic doping and equal effective masses,  $E_{f_p} - E_i = -\Delta\mu/2$  and  $E_{f_n} - E_i = \Delta\mu/2$  by symmetry arguments. Here,  $E_{f_{p/n}}$  is the quasi-Fermi level for the holes/electrons,  $E_i$  is the Fermi level of the intrinsic system (at mid-gap), and  $\Delta\mu = E_{f_n} - E_{f_p}$  is the quasi-Fermi level splitting. By symmetry of the electron and hole in this case, we must have  $E_e - E_i = E/2$  and  $E_h - E_i = -E/2$ , where  $E$  is the energy of the photon. Thus,

$$f_v - f_c = \frac{1}{\exp\left(-\frac{E - \Delta\mu}{2k_b T}\right) + 1} - \frac{1}{\exp\left(\frac{E - \Delta\mu}{2k_b T}\right) + 1} \quad (2.32)$$

For simplicity in analysis, let us set  $x = (E - \Delta\mu)/k_b T$ . Thus,

$$\begin{aligned}
f_v - f_c &= \frac{1}{e^{-x/4}(e^{-x/4} + e^{x/4})} - \frac{1}{e^{x/4}(e^{x/4} + e^{-x/4})} \\
&= \frac{[\exp(x/4) + \exp(-x/4)][\exp(x/4) - \exp(-x/4)]}{[\exp(x/4) + \exp(-x/4)]^2} \\
&= \frac{[\exp(x/4) - \exp(-x/4)]}{[\exp(x/4) + \exp(-x/4)]} \\
&= \frac{\sinh(x/4)}{\cosh(x/4)} \\
&= \tanh(x/4) \\
&= \tanh\left(\frac{E - \Delta\mu}{4k_b T}\right)
\end{aligned} \tag{2.33}$$

We have argued already above that  $\tanh((E - \Delta\mu)/4k_b T)$  should serve as a good approximation to  $f_v - f_c$  for most systems and should capture the main physics of band filling. It may be modified to yield more accurate results in the case of high doping or a large mismatch between the electron and hole effective masses under the parabolic bands approximation. For the purposes of this work, let us proceed with the simple expression so that the luminescence becomes

$$S_{PL}(E, \Delta\mu) = \left( \frac{4\pi L}{h^3 c^2} \alpha(E, 0) E^2 \right) \left( \frac{\tanh\left(\frac{E - \Delta\mu}{4k_b T}\right)}{\exp\left(\frac{E - \Delta\mu}{k_b T}\right) - 1} \right) \tag{2.34}$$

where the term on the left is a sole function of  $E$  and the term on the right includes both  $E$  and  $\Delta\mu$ . Note that by taking  $x = (E - \Delta\mu)/k_b T$ , we have

$$\begin{aligned}
\frac{\tanh(x/4)}{\exp(x) - 1} &= \frac{\sinh(x/4)}{\cosh(x/4)(\exp(x) - 1)} \\
&= \frac{1}{\exp(x) - 1} \frac{[\exp(x/4) - \exp(-x/4)]}{[\exp(x/4) + \exp(-x/4)]} \\
&= \frac{1}{\exp(x) - 1} \frac{[\exp(x/2) - 1]}{[\exp(x/2) + 1]} \\
&= \frac{1}{[\exp(x/2) - 1][\exp(x/2) + 1]} \frac{[\exp(x/2) - 1]}{[\exp(x/2) + 1]} \\
&= \frac{1}{(\exp(x/2) + 1)^2}
\end{aligned} \tag{2.35}$$

Let us double check that there are no singularities as  $x \rightarrow 0$ , since  $\tanh(0)/(\exp(0) - 1) = 0/0$ . To do so, we shall use L'Hôpital's rule, i.e.,

$$\lim_{x \rightarrow c} \frac{f(x)}{g(x)} = \lim_{x \rightarrow c} \frac{f'(x)}{g'(x)} \tag{2.36}$$

with  $f(x) = \tanh(x/4)$  and  $g(x) = \exp(x) - 1$ , giving  $f'(x) = \text{sech}^2(x/4)/4$  and  $g'(x) = \exp(x)$ . Thus,  $\lim_{x \rightarrow 0} \frac{\tanh(x/4)}{\exp(x)-1} = 1/4$ , so that there are no singularities and the luminescence can be rewritten as

$$S_{PL}(E, \Delta\mu) = \frac{4\pi L}{h^3 c^2} \frac{\alpha(E, 0)E^2}{(\exp\left(\frac{E-\Delta\mu}{2k_b T}\right) + 1)^2} \quad (2.37)$$

which is positive definite and is a good approximation for the luminescence with significant band tailing while explicitly including the band filling effects. Note that when  $(E - \Delta\mu)/k_b T \gg 1$ , we have

$$S_{PL}(E, \Delta\mu) \approx \frac{4\pi L}{h^3 c^2} \alpha(E, 0) E^2 \exp(-E/k_b T) \exp(\Delta\mu/k_b T) \quad (2.38)$$

which recovers the expression without band filling contribution, suitable for low injection and sharp band edges and has been the standard expression used in most detailed balance analyses of solar cells. It is clear from [Equation 2.37](#) that the luminescence spectra and radiative current will scale non-linearly with  $\Delta\mu$ . Furthermore, for  $\alpha(E, 0) \sim \exp((E - E_g)/\gamma)$ , as in the case of Urbach tails, we can take a derivative of the luminescence flux and find that the peak position will occur at

$$E_{PL}^{max} = \Delta\mu - 2k_b T \ln\left(\frac{1}{\frac{2k_b T}{E_{PL}^{max}} + \frac{k_b T}{\gamma}} - 1\right) \quad (2.39)$$

For  $\gamma > k_b T$ . A simpler but approximate solution can be found by taking  $E_{PL}^{max} \gg k_b T$ , and neglecting that term, so that

$$E_{PL}^{max} \approx \Delta\mu + 2k_b T \ln\left(\frac{k_b T}{\gamma - k_b T}\right) \quad (2.40)$$

which shows that the luminescence peak depends directly on  $\Delta\mu$ , for  $\gamma > k_b T$ .

### Effects of band tails on J-V characteristics

While [Equation 2.37](#) suggests a rather complex dependence of the band filling characteristics on current, we find that the  $J - V$  characteristics can be well fitted to a modified diode expression in most cases:

$$J_{rad}(V) \sim J_0(\gamma, E_g) \exp\left(\frac{qV}{n_{eff}(\gamma, E_g)k_b T}\right) \quad (2.41)$$

In other words, the effect of band filling and band tails is to modify the recombination current prefactor  $J_0$  and effective ideality factor  $n_{eff}$ , which manifest in the voltage loss as described in the main text and in [section 2.6](#). Of particular interest is  $n_{eff}$ ,

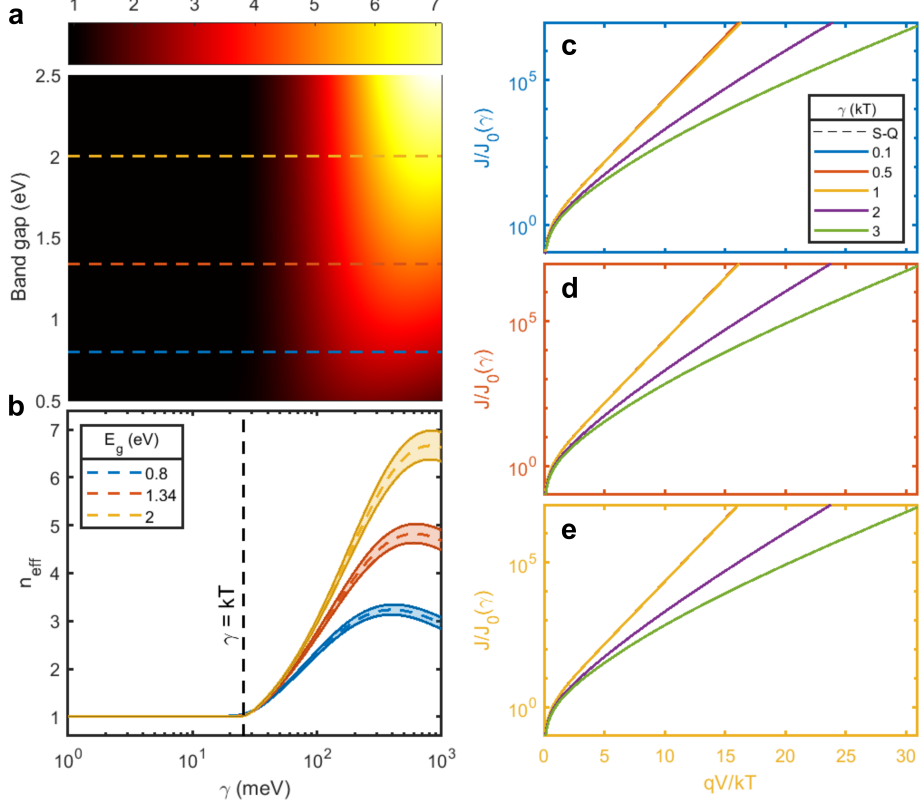


**Figure 2.14: Effects of band tails and band filling on ideality factor and current-voltage relationships.** **a** Fitted  $n_{eff}$  for varying Urbach parameter ( $\gamma$ ) and bandgap  $E_g$ . Fits were performed for the range  $3k_bT < qV < E_g - 3k_bT$ . Linecuts of **a** occur at  $E_g = 0.8$  (blue), 1.34 (orange), and 2.0 eV (yellow). **b** Corresponding linecuts of **a** plotted for varying Urbach parameter ( $\gamma$ ). Note the transition that occurs at  $\gamma = k_bT$  to larger effective ideality factors, corresponding to the onset of band tailing and band filling effects. Dashed lines represent the fit, while solid lines represent the 95% confidence interval.  $J - V$  characteristics for different bandgaps of 0.8 eV **c**, 1.34 eV **d**, and 2.0 eV **e**. The different lines in a given plot represent different Urbach parameters. The legend in **c** is the same for **d** and **e**. All plots have voltages normalized to  $k_bT/q$  and current densities normalized to their radiative dark current  $J_0$ , which is a function of  $\gamma$ . Thicknesses were assumed to be  $\alpha_0 L = 1$ . Note that for Urbach parameters typically observed in experiment (i.e.,  $\gamma \sim 3k_bT$ ),  $n_{eff}$  is generally less than 3. For larger Urbach parameters, a modified ideality factor no longer describes the voltage scaling appropriately, since  $E_{g,PL} \rightarrow k_bT$ .

which should be measurable in electroluminescence measurements, because non-radiative dark current occurs in parallel to the radiative dark current. Thus, we would expect the  $n_{eff}$  estimated here in Figure 2.14 to be accurate even in systems far away from the radiative limit, as long as we measure the radiative current flux through voltage-dependent electroluminescence. We note that the calculated  $n_{eff}$  for a-Si

(assuming  $E_g \sim 1.7$  eV and  $\gamma \sim 50$  meV) is around 1.7, which is quite similar to the value measured by Rau et al [163]. To get an approximate analytic expression for  $n_{eff}$ , we use Equation 2.37 and assume that  $E^2$  varies slowly compared to the exponentials in the integrand and that we are in the weakly absorbing limit. Thus,  $J_{rad}(V) \sim \int dE \exp\left(\frac{E-E_g}{\gamma}\right) \left(\exp\left(\frac{E-V}{2k_bT}\right) + 1\right)^{-2}$  and with some rewriting, we find that  $J_{rad}(V) \sim \int dx \exp\left(\frac{k_bTx + V - E_g}{\gamma}\right) \left(\exp(x/2) + 1\right)^{-2} \sim \exp(V/\gamma)$ . That is, we expect

$$n_{eff} \approx \frac{\gamma}{k_bT} \quad (2.42)$$

which seems to hold somewhat well for small  $\gamma$  just above  $k_bT$ , as observed in Figure 2.14. Furthermore, using the diode approximation from above, we can also calculate the modified fill factor expression as

$$FF(n_{eff}, V_{oc}) \approx \frac{\frac{qV_{oc}}{n_{eff}k_bT} - \ln\left(1 + \frac{qV_{oc}}{n_{eff}k_bT}\right)}{1 + \frac{qV_{oc}}{n_{eff}k_bT}} \quad (2.43)$$

which reduces the fill factor slightly compared to the case without band tails and is an additional efficiency loss mechanism.

## Two bandgap model for band tails

To develop a simple picture for the apparent bandgap shift, voltage loss, and effects of band tailing, we use a simplistic model of the absorbance parametrized by two step functions. We will refer to this as the “two bandgap model”, whose absorbance can be seen in Figure 2.15a and is given by:

$$A(E) = a_1\theta(E - E_{g,1})\theta(E_{g,2} - E) + a_2\theta(E - E_{g,2}) \quad (2.44)$$

where  $a_2 = 1$  and  $E_{g,2} = 1.34$  eV. The above model represents a simplistic picture of a system with band tails as it deviates from the Shockley-Queisser limit. Here,  $E_{g,2}$  defines the absorption bandgap,  $E_{g,1}$  is the lower bandgap that forms as a result of band tailing, and  $a_1$  is the effective sub-gap absorption. We then calculate the typical photovoltaic figures of merit in Figure 2.15b while varying  $\Delta E_g = E_{g,2} - E_{g,1}$  and  $a_1$ . The result is qualitatively similar to what is seen with a band tail (e.g. see Figure 2.3 for comparison), where the efficiency loss is essentially all in the voltage. Moreover, there is a specific transition point where the voltage loss is linear with the bandgap separation, dependent on the value of  $a_1$ . To see this, recall that  $V_{oc} = k_bT/q \ln(J_{sc}/J_0 + 1)$ , where  $J_0 = \int A(E)S_{BB}(E)dE$  and  $A(E)$  is given in Equation 2.44. The loss due to a lower bandgap  $E_{g,1}$  is then

$$\Delta V_{oc} = \frac{k_bT}{q} \ln\left(\frac{J_{sc}}{J_2} + 1\right) - \frac{k_bT}{q} \ln\left(\frac{J_{sc}}{J_0} + 1\right) \approx -\frac{k_bT}{q} \ln\left(\frac{J_1}{J_2} + 1\right) \quad (2.45)$$

where  $J_{1,2} = \int A_{1,2}(E)S_{BB}(E)dE$ ,  $A_{1,2}(E) = a_{1,2}\theta(E-E_{g_{1,2}})$ , and we have assumed  $J_{sc} \gg J_0, J_2$ . Thus, from the perspective of the voltage loss in the detailed balance analysis,  $E_{g,1}$  does not appear as a photovoltaic bandgap until  $J_1 > J_2$ . This occurs when

$$\frac{a_1 e^{-E_{g,1}/k_b T} \left( \left( \frac{E_{g,1}}{k_b T} \right)^2 + 2 \left( \frac{E_{g,1}}{k_b T} \right) + 2 \right)}{a_2 e^{-E_{g,2}/k_b T} \left( \left( \frac{E_{g,2}}{k_b T} \right)^2 + 2 \left( \frac{E_{g,2}}{k_b T} \right) + 2 \right)} > 1 \quad (2.46)$$

Assuming  $E_{g_{1,2}} \gg k_b T$ , we can neglect the terms outside of the exponential to first order because it shows up logarithmically with  $\Delta E_g$ . Thus, the transition to a new bandgap occurs when

$$\Delta E_g > k_b T \ln \left( \frac{a_2}{a_1} \right) \quad (2.47)$$

In other words, from the perspective of the Shockley-Queisser limit and voltage loss, the Stokes shift is not apparent until [Equation 2.47](#) is satisfied. At this point, the voltage loss scales linearly with increasing  $E_{g,1}$ . To see this clearly, we plot the voltage loss with bandgap shift with energies and voltages normalized to  $k_b T \ln(a_2/a_1)$  in [Figure 2.15c](#). We see that indeed the transition occurs under the condition of [Equation 2.47](#), where thereafter  $\frac{\partial \Delta V_{oc}}{\partial \Delta E_g} \approx 1$ . This is true irrespective of the value of  $a_1$ . Moreover, while [Equation 2.47](#) is derived for two discrete bandgaps, we can generalize the concept to how sharp a continuous absorption spectrum should be to avoid a Stokes shifted voltage loss. Let us define  $a_2 = \Delta a + a_1$  and take the limit as  $\Delta a, \Delta E \rightarrow 0$ . Thus, the generalized continuous form of [Equation 2.47](#) becomes

$$\frac{k_b T}{a} \frac{\partial a}{\partial E} < 1 \quad (2.48)$$

In the case of weakly absorbing Urbach band tails,  $a \sim \alpha L \sim C \exp\left(\frac{E-E_g}{\gamma}\right)$ . Thus, [Equation 2.48](#) predicts a Stokes shift should occur when  $\gamma > k_b T$ , which is what we observe in [Figure 2.6](#).

### General Expression for Voltage Loss due to Nonabrupt Band Edges

The plots of [Figure 2.7](#) and [Figure 2.15](#) in the main text suggests a general relation between bandgap shifts and voltage loss, irrespective of the exact functional form of the band edge. To see this, note that the majority of the luminescence of the step-function absorbance is concentrated within  $k_b T$  of the band edge and its integral varies exponentially with the bandgap energy. Thus, the effective bandgap of the luminescence,  $E_{g,PL}$  must be chosen to integrate to nearly the majority of the

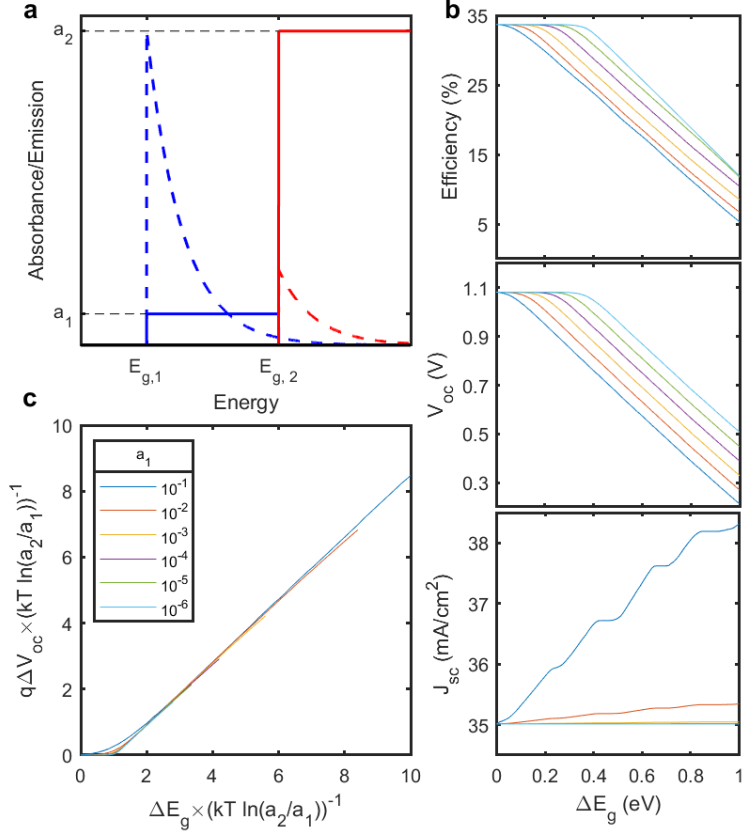


**Figure 2.15: Analysis of a two-bandgap toy.** **a** Absorbance and emission of the two-bandgap toy model, parametrized by two step-functions. Solid lines correspond to absorbance, whereas dashed lines correspond to emission. **b** Plot of the photovoltaic figures of merit ( $\eta, V_{oc}, J_{sc}$ ) for varying bandgap difference  $\Delta E_g = E_{g,2} - E_{g,1}$  and values of the lower bandgap absorbance  $a_1$ .  $a_2$  is assumed to be 1 while  $E_{g,2} = 1.34$  eV. Colors correspond to the same as the legend in **c**. **c** Voltage loss versus bandgap difference in normalized units of  $k_b T \ln(a_2/a_1)$ , showing the transition to the Stokes shift behavior for large enough band gap separation, dependent on  $a_2/a_1$ .

luminescence flux. Thus, we pragmatically define it as

$$\max(E_{g,PL}) \in \frac{\int_{E_{g,PL}}^{\infty} S_{PL}(E, \Delta\mu) dE}{\int_0^{\infty} S_{PL}(E, \Delta\mu) dE} \geq 0.90 \quad (2.49)$$

While this definition of  $E_{g,PL}$  is not unique, it parametrizes the luminescence typically assumed under step-function absorbance to a greater variety of luminescence spectra and is somewhat less sensitive to noise. We further define the above-gap

absorbance as

$$\bar{a}_{AG} = \frac{\int_{E_{g,Abs}}^{\infty} a(E, \Delta\mu) S_{BB}(E, \Delta\mu) dE}{\exp(\Delta\mu/k_b T) \int_{E_{g,Abs}}^{\infty} S_{BB}(E, 0) dE} = \frac{\int_{E_{g,Abs}}^{\infty} S_{PL}(E, \Delta\mu) dE}{\exp(\Delta\mu/k_b T) \int_{E_{g,Abs}}^{\infty} S_{BB}(E, 0) dE} \quad (2.50)$$

and below-gap absorbance as

$$\bar{a}_{SG} = \frac{\int_{E_{g,PL}}^{E_{g,Abs}} a(E, \Delta\mu) S_{BB}(E, \Delta\mu) dE}{\exp(\Delta\mu/k_b T) \int_{E_{g,PL}}^{E_{g,Abs}} S_{BB}(E, 0) dE} = \frac{\int_{E_{g,PL}}^{E_{g,Abs}} S_{PL}(E, \Delta\mu) dE}{\exp(\Delta\mu/k_b T) \int_{E_{g,PL}}^{E_{g,Abs}} S_{BB}(E, 0) dE} \quad (2.51)$$

where both values are apparently dependent on  $\Delta\mu$ . Accurate estimation of the quantity  $\frac{S_{PL}(E, \Delta\mu)}{\exp(\Delta\mu/k_b T)}$  can be achieved by taking  $E \gg \Delta\mu$  and fitting the luminescence spectra to the high energy absorption/EQE, or by fitting the full spectrum with the band filling factor. Alternatively, since [Equation 2.6](#) of the main text only requires knowledge of the ratio  $\bar{a}_{AG}/\bar{a}_{SG}$ , we can simply use the directly measured luminescence spectrum:

$$\frac{\bar{a}_{AG}}{\bar{a}_{SG}} = \frac{\int_{E_{g,Abs}}^{\infty} S_{PL}(E, \Delta\mu) dE}{\int_{E_{g,PL}}^{E_{g,Abs}} S_{PL}(E, \Delta\mu) dE} \frac{\int_{E_{g,PL}}^{E_{g,Abs}} S_{BB}(E, 0) dE}{\int_{E_{g,Abs}}^{\infty} S_{BB}(E, 0) dE} \quad (2.52)$$

And the definitions of  $E_{g,Abs}$  and  $E_{g,PL}$  to estimate the weighted absorbance ratio.

These definitions work well because the integrated number of recombination electrons is what matters in the detailed balance analysis, which is achieved by the appropriate definitions of weighted absorption and bandgaps. Therefore, the voltage loss is given by a form that is quite similar to [Equation 2.45](#):

$$\Delta V_{oc} = \frac{k_b T}{q} \ln \left( \frac{\bar{a}_{SG}}{\bar{a}_{AG}} \exp \left( \frac{E_{g,Abs} - E_{g,PL}}{k_b T} \right) \left[ \frac{\left( \frac{E_{g,PL}}{k_b T} \right)^2 + 2 \left( \frac{E_{g,PL}}{k_b T} \right) + 2}{\left( \frac{E_{g,Abs}}{k_b T} \right)^2 + 2 \left( \frac{E_{g,Abs}}{k_b T} \right) + 2} \right] + 1 - \frac{\bar{a}_{SG}}{\bar{a}_{AG}} \right) \quad (2.53)$$

Noting the logarithmic dependence on the argument and assuming  $\Delta E_g = E_{g,Abs} - E_{g,PL} \ll E_{g,Abs}$ , as well as  $E_{g,Abs}, E_{g,PL} \gg k_b T$ , we arrive at a simple expression that only depends on the observed bandgap shifts and the ratio of the above-gap and sub-gap absorbances:

$$\Delta V_{oc} \left( \frac{\bar{a}_{SG}}{\bar{a}_{AG}}, \Delta E_g \right) \approx \frac{k_b T}{q} \ln \left( \frac{\bar{a}_{SG}}{\bar{a}_{AG}} \exp \left( \frac{\Delta E_g}{k_b T} \right) + 1 - \frac{\bar{a}_{SG}}{\bar{a}_{AG}} \right) \quad (2.54)$$

Note that this expression recovers the expected values of voltage loss as  $\bar{a}_{SG}/\bar{a}_{AG} \rightarrow 0, 1$  and as  $\Delta E_g \rightarrow 0$ . Furthermore, the functional form of the sub-gap ab-

sorbance is captured by its effect of varying the value of  $\bar{a}_{SG}$ . From an experimental standpoint, another method to estimate the voltage loss is by using the modified  $J - V$  characteristics found in [section 2.6](#). It is clear then that  $J_{rad}(V) \approx J_{0,rad} \exp\left(\frac{qV}{n_{eff} k_b T}\right) = \int S_{EL}(E, V) dE$ . Furthermore, it is possible to estimate  $n_{eff}$  directly from the slope of voltage-dependent electroluminescence  $S_{EL}(E, V)$ . Integrating over  $S_{EL}(E, V)$  and dividing by  $\exp(qV/n_{eff} k_b T)$  then yields  $J_{0,rad}$ . Note that the  $V_{oc}$  loss due to an imperfect band edge can be equivalently written in the form of  $\Delta V_{oc} = \frac{k_b T}{q} \ln\left(\frac{J_{sc,SQ}}{J_{0,rad,SQ}}\right) - \frac{n_{eff} k_b T}{q} \ln\left(\frac{J_{sc}}{J_{0,rad}}\right)$  using [Equation 2.41](#), which can be expanded to yield

$$\Delta V_{oc} = \frac{k_b T}{q} \ln\left(\frac{J_{sc,SQ}}{J_{sc}}\right) + \frac{k_b T}{q} \ln\left(\frac{J_{0,rad}}{J_{0,rad,SQ}}\right) - \frac{(n_{eff} - 1) k_b T}{q} \ln\left(\frac{J_{sc}}{J_{0,rad}}\right) \quad (2.55)$$

where the first term is the voltage loss due to incomplete absorption above the bandgap. The second term is the voltage loss due to band tailing, while the third term is a voltage gain due to band filling effects (e.g. see [Figure 2.13](#)).

### Effects of Sub-Unity Radiative and Quantum Efficiencies

We have thus far only analyzed the situation assuming the reciprocity between absorption and photoluminescence, which holds quite generally but concerns primarily the internal open circuit voltage of a device i.e. the quasi Fermi level splitting. To analyze the effects of a system with sub-unity quantum efficiencies, which may be particularly relevant for localized states below the absorption gap, we assume Donolato's theorem still holds and apply [Equation 2.24](#). Therefore, by reciprocity, the injection efficiency into these localized states would be relatively low, lowering the electroluminescence recombination rate and increasing the limiting  $V_{oc}$  ([Figure 2.16](#)). This situation would be analogous to considering free carrier absorption in the absorption band tail, where  $IQE \rightarrow 0$ , and therefore the absorption of free-carriers do not lead to photovoltaic current [89]. Thus, photogenerated carriers that do not contribute to photovoltaic current, whether they are localized states or free carriers, would not result in a loss to the open circuit voltage in the radiative limit. In general, the effect of band tails on the radiative limit should be determined via photocurrent spectroscopies, which captures this effect experimentally directly.

To analyze the voltage loss effects away from the radiative limit, i.e., sub-unity radiative efficiency, we note that generally [Equation 2.41](#) holds and the discussion in [section 2.6](#) suggests that  $J(V) = J_{sc} - \frac{J_{0,rad}}{\eta_{ext}} \left( \exp\left(\frac{qV}{n_{eff} k_b T}\right) - 1 \right)$  which is quite similar to [Equation 2.26](#). Thus, it is readily apparent that the loss due to non-radiative

recombination is modified with an ideality factor  $n_{eff} \geq 1$ , so that

$$\Delta V_{oc,nr} = -\frac{n_{eff} k_b T}{q} |\ln(\eta_{ext})| \quad (2.56)$$

It should be noted that  $\eta_{ext}$  is generally a function of voltage as well and should be measured/calculated at the operating voltage. This radiative ideality factor has already been recognized by Rau et al. to be relevant in amorphous Si [163] when analyzing its non-radiative losses. In many devices, sub-unity radiative efficiencies and sub-unity quantum efficiencies are both present and are likely competing to provide the observed voltage. In contrast, concentration benefits the voltage by a similar factor  $\Delta V_{oc,conc} = \frac{n_{eff} k_b T}{q} |\ln(C)|$ , where  $C > 1$  is the concentration factor.

### Parametrization of the Band edge Functional Form

In Figure 2.7, we considered various band edge functional forms to argue that there exists a general expression that relates  $\Delta V_{oc,rad}$  to the existence of a Stokes shift, i.e.  $\Delta E_g$ . We considered two main types of band edges: exponential tails and indirect edge power laws. Exponential tails are the main form of band edges we have discussed in this article and we have thus far used the analysis described in section 2.6. For the calculations in Figure 2.17 and Figure 2.7, we vary  $\theta$ ,  $E_g$ , and  $\gamma$  to generate various functional forms for the band tail given by Equation 2.28. Furthermore, we consider only the absorption spectra that yield a luminescence bandgap above  $4k_b T$ , since we assume that  $E_g \gg k_b T$  in deriving Equation 2.6. We further consider a general power law form for a semiconductor band edge that has a weak oscillator strength (e.g. an indirect transition) with a higher energy direct transition with larger oscillator strengths:

$$\alpha(E) = \alpha_{0,ind}(E - E_{g,ind})^n \theta(E - E_{g,ind}) \theta(E_{g,dir} - E) + \alpha_{0,dir} \theta(E - E_{g,dir}) \quad (2.57)$$

where  $E_{g,ind}$  and  $E_{g,dir}$  represent the indirect and direct band edge, respectively, while  $\alpha_{0,ind}$  and  $\alpha_{0,dir}$  represent the absorption coefficients of the indirect and direct gaps, respectively.  $n$  parametrizes the different energetic scaling relations of the indirect edge, typically  $n < 3$  experimentally.

For both forms of band edges, we calculate  $V_{oc,rad}$  from the complete modified detailed balance analysis, including band filling effects and assuming  $\eta_{ext} = 1$  (Equation 2.26),  $E_{g,Abs}$  is then derived from the calculated absorption spectrum using Rau's definition, and therefore  $V_{oc,SQ}(E_{g,Abs})$  is calculated using a step-function at  $E_{g,Abs}$ .  $E_{g,PL}$ ,  $\bar{a}_{SG}$ ,  $\bar{a}_{AG}$  is then calculated from the definitions in section 2.6

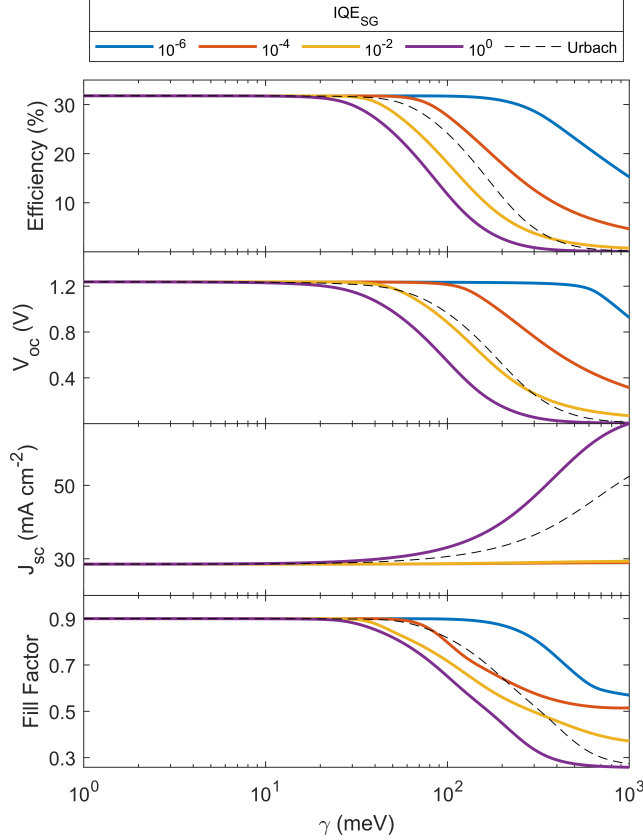


**Figure 2.16: Effects of a sub-unity collection efficiency below the bandgap.** Calculated power conversion efficiency, open circuit voltage, short circuit current density, and fill factor assuming that the collection efficiency below the bandgap ( $IQE_{SG}$ ) is less than 1 and given by a constant average value. That is, we take the external quantum efficiency to be  $EQE(E) = a(E) (IQE_{SG}\theta(E_g - E) + \theta(E - E_g))$ . The “Urbach” curve is calculated assuming the collection efficiency decays with a similar Urbach parameter to that used in the absorption calculation (i.e.  $IQE_{SG}(\gamma, E) = \exp((E - E_g)/\gamma)$ ), which may approximate the mobility-edge better than a constant.

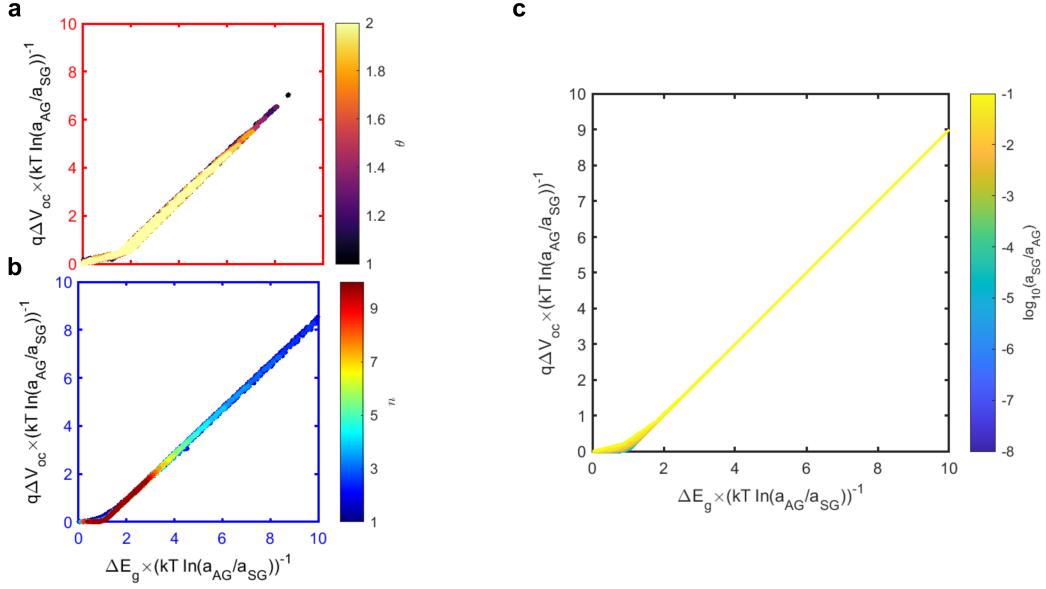
by examining the luminescence spectra,  $S_{PL}$ . The results of these different band edges map well onto a simple relation described by [Equation 2.54](#), suggesting a two bandgap model is an adequate representation of most experimentally observed band edge forms.

Table 2.2: Tabulated values of Urbach Energies (Experiment) and  $\Delta V_{oc}$  loss (Calculated) .

Material Name	Bandgap (eV)	Urbach Energy (meV)	Calculated $\Delta V_{oc}$ (mV)	References
---------------	--------------	---------------------	---------------------------------	------------

c-Si	1.12	9.6	24.0	[34]
c-Si	1.12	8.6	20.7	[34]
c-Si	1.12	11	28.9	[63]
GaAs	1.42	6.9	14.6	[181]
GaAs	1.42	7.5	16.3	[84]
GaAs	1.42	5.9	11.7	[12]
InP	1.355	9.4	22.5	[182]
InP	1.361	10.6	26.6	[182]
InP	1.34	7.1	16.3	[12]
a-Si:H	1.72	42	273.1	[33]
a-Si:H	1.64	52	382.8	[33]
a-Si:H	1.69	67	559.1	[35]
a-Si:H	1.70	43	283.5	[183]
a-Si:H	1.69	47	329.0	[184]
a-Si:H	1.7	48	341.3	[192]
a-Si:H	1.8	51	385.3	[192]
a-Si:H	1.85	51	389.1	[192]
CdTe	1.45	17	52.8	[158]
CdTe	1.5	7.2	15.5	[119]
CdTe	1.5	9	21.1	[129]
CdTe	1.5	10.6	26.5	[172]
CIGS	1.53	24	94.2	[71]
CIGS	1	18	56.0	[71]
CIGS	1.18	23	84.9	[71]
CIGS	1.2	31	143.6	[186]
CIGS	1.67	25	102.5	[124]
CIGS	1.08	9	21.9	[174]
Kesterite	1.5	69	551.4	[77]
Kesterite	1.1	54	346.9	[77]
Kesterite	1.38	45	286.6	[214]
Kesterite	1.54	65	516.7	[214]
Kesterite	1.68	56.8	441.8	[135]
Perovskite	1.57	15	44.7	[39]
Perovskite	2.23	23	90.2	[168]

Perovskite	1.57	14	40.5	[224]
Perovskite	1.57	14.4	42.2	[224]
Perovskite	1.57	15.8	48.3	[224]
Organic	1.66	37	214.9	[62]
Organic	2	50	386.8	[94]
Organic	1.31	25.6	104.8	[112]
Organic	1.47	27	115.9	[159]
Organic	1.88	36	211.0	[193]
Organic	1.71	27	118.7	[110]
Organic	1.67	24	95.2	[156]



**Figure 2.17: Different band edges that map onto a two-bandgap model.** Stokes shift  $\Delta E_g$  and radiative voltage loss  $\Delta V_{oc}$  calculated from the full detailed balance analysis with the appropriate definitions of  $E_{g,Abs}$ ,  $E_{g,PL}$ ,  $a_{AG}$ ,  $a_{SG}$ , as described in Section S6. We vary the parameters for the exponential band tail model **a** and the indirect edge power law model **b**. For the exponential band tail model we take  $\alpha_0 L = 10$ , whereas for the indirect edge model we take  $\alpha_{0,dir} L = 100$ ,  $\alpha_{0,ind} L = 0.1$ . Both forms map well onto the generalized expression **c**. The colorbar for the generalized expression in **c** is  $\log_{10} \left( \frac{a_{SG}}{a_{AG}} \right)$ , i.e., describes the ratio of the sub-gap to above-gap absorption. The different ratios plots are overlaid, showing the similarity irrespective of  $a_{SG}/a_{AG}$ , assuming it is sufficiently small.

## OPTICAL DESIGN OF CAVITY COUPLING TO EXCITONIC TMDCS

*“Nothing in life is to be feared. It is only to be understood.”*

— Marie Curie

### 3.1 Linear Dielectric Function of TMDCs

The optical properties of the bulk semiconducting transition metal dichalcogenides of interest (i.e.,  $\text{MX}_2$ , where  $\text{M} = \text{Mo, W}$  and  $\text{X} = \text{S, Se}$ ) were first examined in the 1970s [52] as shown in Figure 3.1, where a variety of sharp excitonic resonances were quickly observed [134]. The direct optical transitions of these materials were found to be excitonic, particularly when  $\mathbf{E} \perp \mathbf{c}$  and the excitonic effect becomes stronger as their thickness approaches the exciton Bohr radius. More recently, [104] extracted the dielectric properties for *monolayer* TMDCs by assuming they are made up of a superposition of Lorentzian oscillators<sup>1</sup> and fitting the reflection spectrum to the dielectric function:

$$\varepsilon(E) = 1 + \sum_{k=1}^N \frac{f_k}{E_k^2 - E^2 - iE\gamma_k} \quad (3.1)$$

where  $f_k$  and  $\gamma_k$  are the oscillator strength and the linewidth of the  $k$ th oscillator, and  $E_k$  runs over the full spectral range and is the energy of each oscillator. The linear dielectric function of each monolayer TMDC material extracted from micro-reflectance measurements is plotted in Figure 3.2, and this method of dielectric function extraction has become the standard method of extracting dielectric function in micron-sized samples (as opposed to ellipsometry, which typically requires much larger samples). The dimensionality effect on the excitonic resonances is evident between the monolayer and bulk materials due to the strength and linewidth of the excitonic transitions. It should be noted that the first two optical transitions are typically referred to as the *A* and *B* excitons, which are similar in their wavefunction nature but differ in the specific spin state (specifically, the spin-orbit splitting in the

---

<sup>1</sup>The simplest model for the electronic response from an electromagnetic field is a damped harmonic oscillator, for which the Lorentz oscillator model is the solution, as described in section B.4.

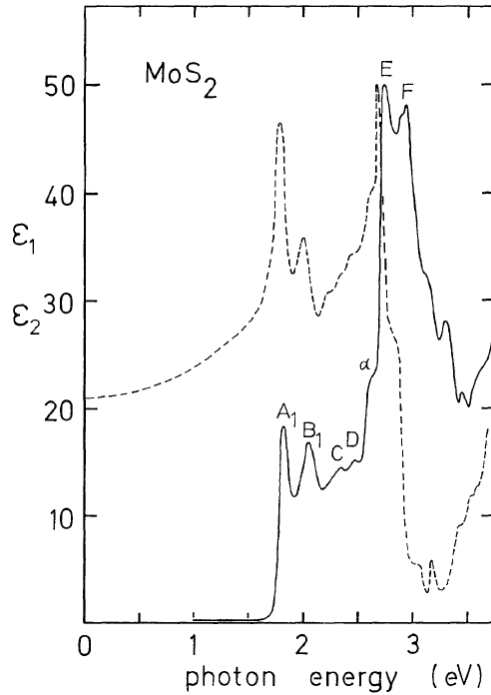
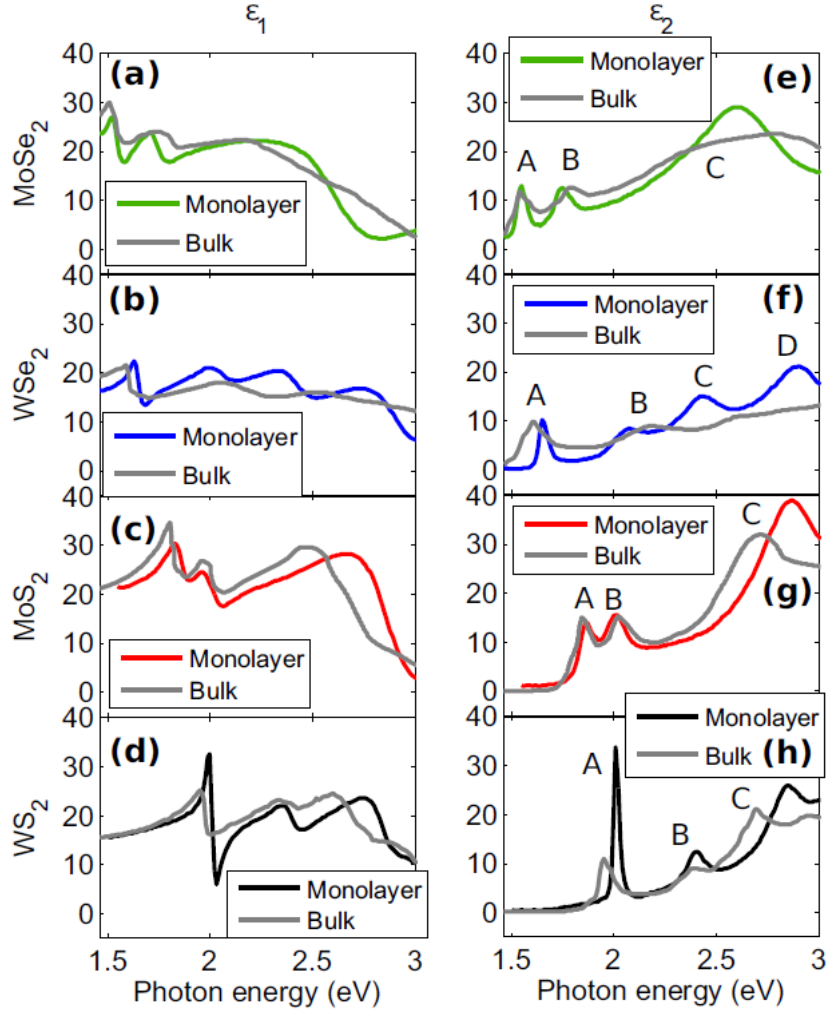


Figure 3.1: **First measurements of the bulk  $\text{MoS}_2$  dielectric function.** Dielectric function of  $\text{MoS}_2$  for  $\mathbf{E} \perp \mathbf{c}$ , adapted from [134].

valence band is the main contribution to the  $A - B$  splitting). To illustrate these different excitonic states more clearly, the bandstructure of monolayer  $\text{MoS}_2$  and its associated optical transitions are shown in Figure 3.3a. Also labelled is the  $C$  exciton, whose peculiar nature comes from the band-nesting phenomenon (i.e., parallel lines that result in a large value of the joint density of optical states) along the  $\Gamma - K$  line of the Brillouin zone. Incidentally, since the largest effects in the quantum confinement occur closer to the  $\Gamma$  and  $\Sigma_{\min}$ <sup>2</sup> points in the valence and conduction band, respectively, the  $C$  exciton is more sensitive to quantum confinement than the  $A$  and  $B$  excitons are. Specifically, the  $A$  and  $B$  excitonic wavefunctions are largely in-plane, and therefore the main effect of thickness is to modify their dielectric screening environment, and therefore the Coulomb interactions. To first order, the decrease in the attractive electron-hole interactions (which describes the magnitude of the exciton binding energy  $E_b$ ) are compensated by the decreased repulsive electron-electron interactions (which partially describes the magnitude of the quasiparticle bandgap). Thus, the actual optical transition energy of the  $A$  and  $B$  excitons are relatively insensitive to thickness, as seen in Figure 3.2. The bandstructure of

<sup>2</sup>The  $\Sigma_{\min}$  point is also often referred to as the  $Q$  or  $\Lambda$  point in the 2D materials literature.



**Figure 3.2: Room temperature dielectric function of monolayer TMDCs.** Room temperature dielectric function of **a,e** MoSe<sub>2</sub>, **b,f** WSe<sub>2</sub>, **c,g** MoS<sub>2</sub>, and **d,h** WS<sub>2</sub>, adapted from [104]

other TMDCs are quite similar in nature, with some subtleties. For example, for tungsten-based compounds, the spin-orbit splitting in the valence band is larger and the conduction band spin-orbit splitting is also of an opposite sign, so that the lowest-energy excitonic states for tungsten compounds are optically dark [199]. Other essential differences is the energetic difference between the  $\Gamma - K$  points in the valence band and the  $\Sigma_{\min} - K$  splitting in the conduction band, which partially dictates the amount of intervalley scattering in the optical transition (which can be tuned with strain, as we shall see in [Chapter 6](#)).

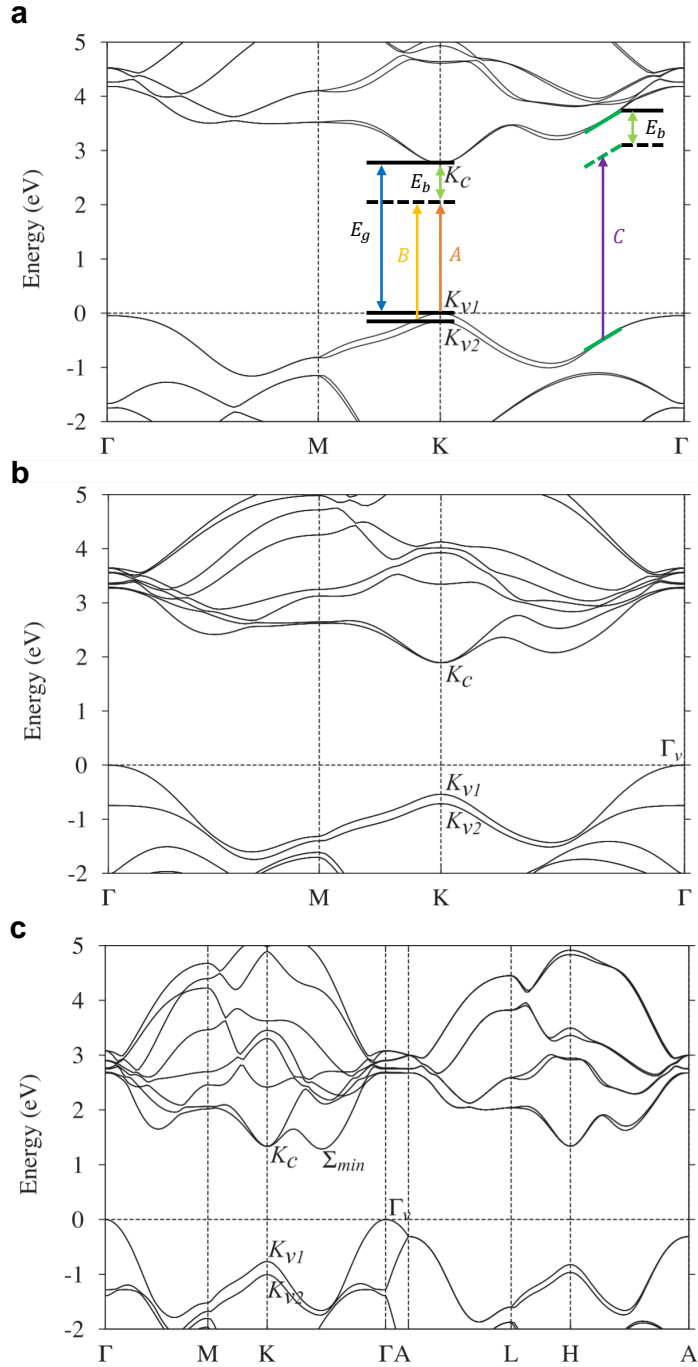
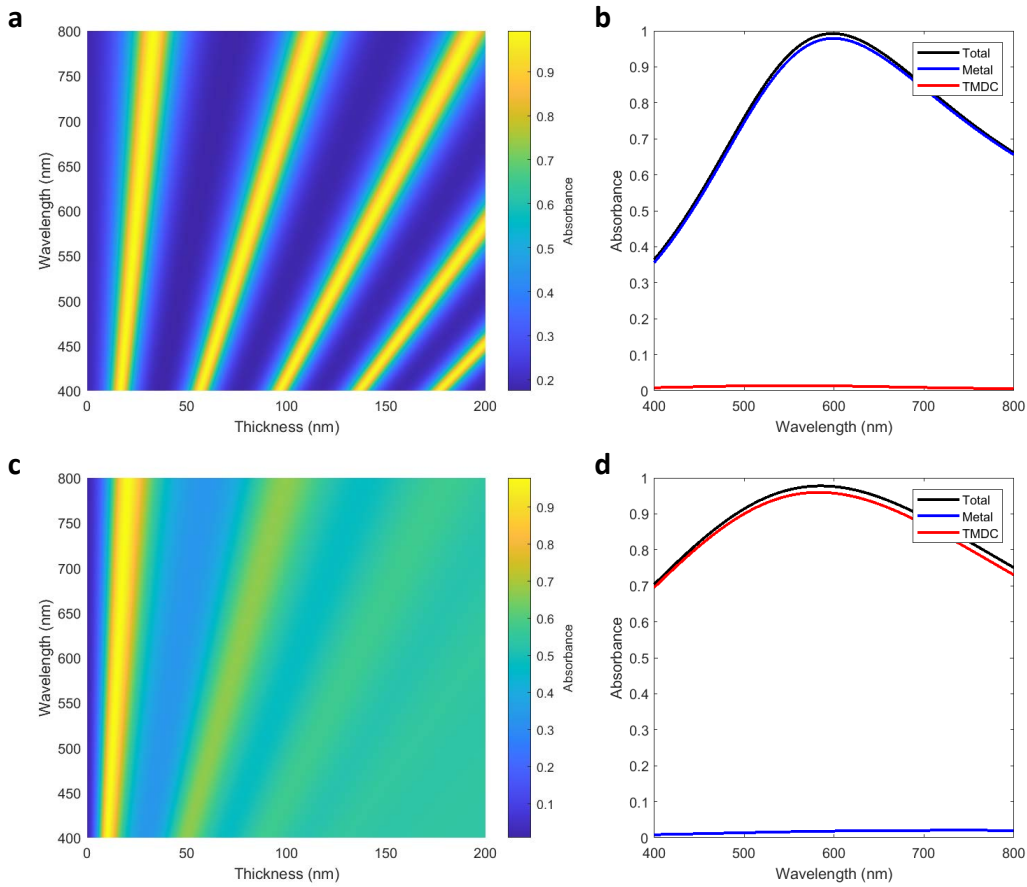


Figure 3.3: **Bandstructure as a function of thickness.** Calculated bandstructure of **a** monolayer, **b** bilayer, and **c** bulk MoS<sub>2</sub> using the quasi-particle self-consistent *GW* method, adapted from [25].

### 3.2 Multilayer Near Unity Absorption

Knowing the different dielectric functions of both the monolayer and optically ‘bulk’ layered materials, we are now able to calculate various linear optical responses of the materials, including its reflectance  $R$ , transmittance  $T$ , and absorbance  $A$ . For layered stacks that can be effectively modelled as 1D optical media, it is possible to use the transfer matrix method to completely solve for their optical properties<sup>3</sup>.



**Figure 3.4: Designing ultrathin absorbing cavities.** **a** Calculated total absorption assuming  $n_{\text{TMDC}} = 5.0 + 0.01i$  and  $n_{\text{metal}} = 10 + 10i$ , for varying thickness of the TMDC layer. **b** Absorption spectrum for  $t = 25$  nm, the absorption in the TMDC and metal layers is also shown. **c** Calculated total absorption assuming  $n_{\text{TMDC}} = 5.0 + 1.0i$  and  $n_{\text{metal}} = 0.05 + 5i$ , for varying thickness of the TMDC layer. **d** Absorption spectrum for  $t = 15$  nm, the absorption in the TMDC and metal layers is also shown.

We are now interested in designing optical structures that can achieve near-unity

<sup>3</sup>A detailed derivation and discussion of the transfer matrix method, and a primer on Maxwell’s equations and wave optics, can be found in [Appendix B](#).

absorption, which is an essential feature to operate solar photovoltaics with high efficiency. Let us suppose we have a sub-wavelength thick structure suspended in air, so that it forms an air/TMDC/air structure. This situation is a two-port structure, i.e., light can be incident/reflected from both sides. However, under typical photovoltaic operation, we would expect illumination from only one side. By decomposing the incident wave into even and odd modes, where only the even modes have a non-zero electric field intensity at the TMDC (odd modes have zero intensity at the center, by definition), we would expect a maximum absorbance of only 50% [150]. Thus, to maximize absorption, additional symmetry breaking must be done.

The simplest method to improve the maximum absorbance is to reduce a two-port structure into a single-port structure by including a back mirror, e.g. we optically consider a three-layer stack of air/TMDC/metal. For a three layer stack, the explicit expression for the reflectivity has a simple analytic expression:

$$\tilde{r} = \frac{\tilde{r}_{12} + \tilde{r}_{23}e^{2i\tilde{\beta}}}{1 + \tilde{r}_{12}\tilde{r}_{23}e^{2i\tilde{\beta}}} \quad (3.2)$$

where

$$\tilde{r}_{ab} = \frac{\tilde{n}_a - \tilde{n}_b}{\tilde{n}_a + \tilde{n}_b}, \quad \tilde{\beta} = \frac{2\pi\tilde{n}_2}{\lambda}t \quad (3.3)$$

is the interfacial reflectance and the phase accumulation due to propagation, respectively. It is important to note that in the absence of transmittance (e.g. with a metallic substrate), we simply have  $A = 1 - R - T = 1 - R = 1 - |\tilde{r}|^2$ . Thus, to achieve near-unity absorption, we must equivalently have  $\tilde{r} \rightarrow 0$ . Thus, to achieve unity absorbance, we require

$$\exp(2i\tilde{\beta}) = -\frac{\tilde{r}_{12}}{\tilde{r}_{23}} \quad (3.4)$$

There are a few scenarios where this equation can be nearly satisfied. Let us first consider the scenario with an ideal metal as the back mirror and a lowly absorbing TMDC layer (e.g.,  $\tilde{n}_2 = \tilde{n}_{\text{TMDC}} = 5.0 + 0.01i$  for the sake of illustration). In this scenario, we would expect  $\tilde{r}_{23} \rightarrow -1$  because an ideal metal can be modelled as having an index  $\tilde{n}_{\text{metal}} = \eta + i\kappa$  with  $\eta \rightarrow \infty, \kappa \rightarrow \infty$ . Similarly, since the middle layer (i.e., the TMDC) is lowly absorbing, we would expect  $\tilde{r}_{12} \rightarrow -1$ . Therefore, to satisfy Equation 3.4, one must have  $t \approx m\lambda/(4\eta_2)$ , where  $m$  is an odd integer (see Figure 3.4a). This condition is one that is akin to that of a ‘Salisbury screen’ type geometry. However, it is important to note that while the *total* absorption can be close to unity, the absorption within the semiconductor is actually closer

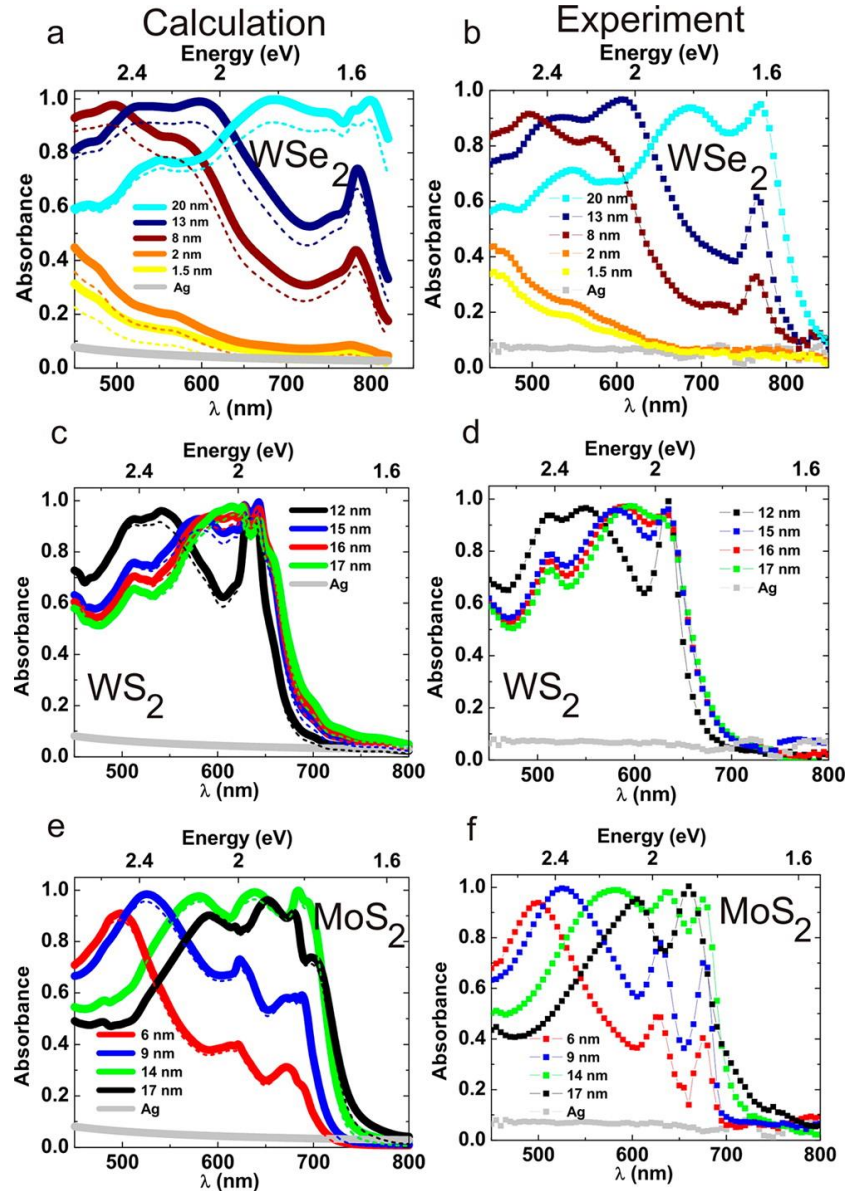


**Figure 3.5: Near Unity Absorption in ultrathin TMDCs.** Calculated and experimental absorption spectra of **a,b**  $\text{WSe}_2$ , **c,d**  $\text{WS}_2$ , and **e,f**  $\text{MoS}_2$  on silver substrates (i.e., the optical stack is air/TMDC/Ag). Calculations take into account the real, dispersive nature of the silver and TMDC. The dotted lines in the calculated data are the *active* layer absorption, i.e., the absorption within the TMDC layer. Experimental data was extracted from normalized reflectance measurements,  $A = 1 - R$ . Figure adapted from [80].

to 0 (since the loss in the TMDC is low compared to that of the metal and the

thickness is small for the first order resonance<sup>4</sup>, see [Figure 3.4b](#)). This situation is certainly not advantageous for photovoltaic operation, and for real TMDCs, the optical loss is significantly higher above its band-edge, which is the operational point of photovoltaic behavior.

A surprisingly different analysis occurs if we consider the significant loss of a TMDC layer (e.g.  $\tilde{n}_{\text{TMDC}} = 5.0 + 1.0i$ ). In this scenario,  $\tilde{r}_{12}$  is no longer on the real axis, and for a finite conductivity of a real metal (e.g.,  $n_{\text{metal}} = 0.05 + 5i$ , which is a similar value to that of silver in the visible part of the spectrum), neither is  $\tilde{r}_{23}$ . Thus, it is possible to rewrite [Equation 3.4](#) as

$$\exp\left(i\pi + i\frac{4\pi(\eta_2 + i\kappa_2)}{\lambda}t\right) = r_0 e^{-i\phi} \quad (3.5)$$

where we have defined  $r_0 e^{-i\phi} = \tilde{r}_{12}/\tilde{r}_{23}$ . Defining further  $t = t_0 - \Delta t$ , where  $t_0 = \lambda/(4\eta_2)$ , we can rewrite the expression above as

$$\exp(-\alpha_2 t) \exp\left(-i\frac{4\pi\eta_2}{\lambda}\Delta t\right) = r_0 \exp(-i\phi) \quad (3.6)$$

In other words, we require  $r_0 = \exp(-\alpha_2 t)$ , where  $\alpha_2 = 4\pi\kappa_2/\lambda$  is the absorption coefficient of the TMDC layer, and  $\phi = 4\pi\eta_2\Delta t/\lambda$ . In other words, the substantial loss in the TMDC layer as well as the finite conductivity of the metal results in non-trivial phase shifts at the interface ( $\tilde{r}_{ab}$ ), which enables designing absorbing geometries with thicknesses below  $\lambda/(4\eta_2)$  where the *loss* is a critical component of the design [\[88\]](#). Because of the significant loss in the TMDC layer and the finite but small loss in the metal, we are able to achieve nearly complete absorption in the active layer (see [Figure 3.4c,d](#)). Thus, by using these design rules of the non-trivial interfacial phase shifts and taking into account the real materials dispersions of metals (e.g. noble ones like Ag or Au) and TMDCs (e.g. WSe<sub>2</sub>, MoS<sub>2</sub>, WS<sub>2</sub>), we are able to design near-unity absorption within layers of TMDCs that are approximately 10-15 nm thick, as shown in [Figure 3.5](#).

Although the absorption peaks in our structure are dependent on path length, they are highly insensitive to the angle of incidence due to the large refractive index of the TMDC layer, as can be seen for the case of 13 nm WSe<sub>2</sub> on Ag ([Figure 3.6](#)). The peak absorption stays over 80% even at a 60° incident angle ([Figure 3.6b](#)) suggesting relatively low sensitivity to the angle of incident light. This feature of

---

<sup>4</sup>For an ideal metal where the skin depth approaches zero, it is clear that the absorbance in the metal must also approach zero. In this case, unity absorbance is not generally achieved for the first order resonance, and larger thicknesses are required.

TMDC/Ag heterostructures is highly advantageous for off-normal light collection and combined with their near-unity active layer absorbance, these structures may be of a particular interest for photovoltaic applications and solar energy harvesting.

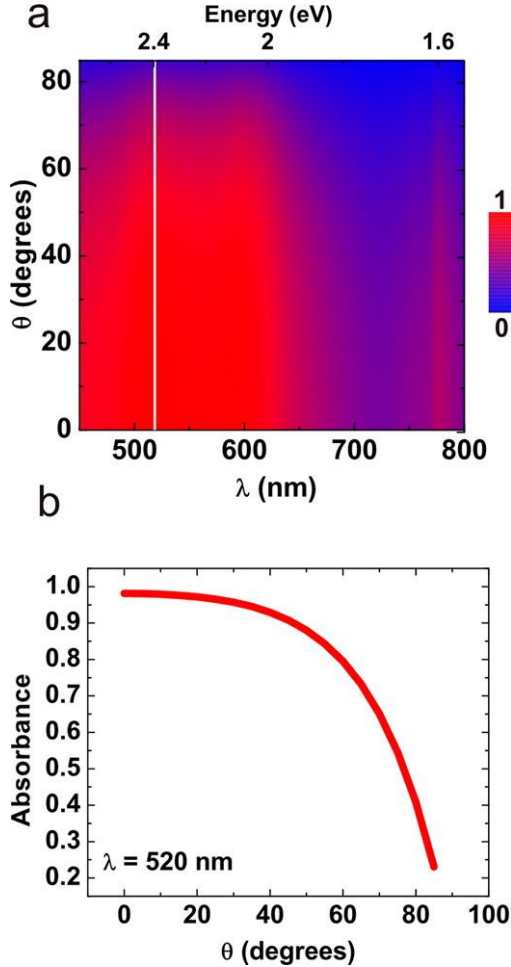


**Figure 3.6: Angle dependence of absorption in ultrathin TMDC/Ag structures.**  
**a** Contour plot of calculated absorption spectra at varying angles for 13 nm WSe<sub>2</sub> on Ag back reflector. The insensitivity of the absorption as a function of incident angle is apparent. **b** Line cut from **a** at 520 nm showing the angle dependence of peak absorption. Figure adapted from [80].

### 3.3 Monolayer Near Unity Absorption

We are now also interested in the possibility of achieving near-unity absorption in a *single monolayer* of a TMDC ( $\sim 7$  Å). It may be tempting to assume that, with a judicious choice of a substrate, it would be possible to satisfy [Equation 3.4](#) for the specific optical properties of a TMDC monolayer. However, in the limit of monolayer absorption, the phase accumulation through the monolayer must be

small, so that  $\exp(2i\tilde{\beta}) \rightarrow 1$ , i.e.,  $\tilde{r}_{12} = -\tilde{r}_{23}$ . This expression can only be satisfied if  $\tilde{n}_1 = \tilde{n}_3$ , which is the same as the TMDC being suspended in air or immersed in a material with index  $\tilde{n}_1$ . In this case, it is clear that the maximum absorbance would be only 50% by symmetry arguments, as described previously.

To yield unity absorption in an atomically thin material, it is still necessary to break the optical symmetry by, for example, removing an optical port with a back mirror. However, as shown above, a simple three layer optical stack cannot yield unity absorption in this regime of thicknesses. Thus, we shall consider the next simplest structure: a four-layer structure, where we have an ideal 2D exciton on a dielectric spacer with index  $n_2$  and thickness  $d$ , which is on top of a back mirror. This mirror will be parametrized by an interface reflection  $r_{23}$  and transmission amplitude  $t_{23} = 0$ . The analysis continues similar to the above case, except now we have a more complicated scattering matrix in this air/exciton/dielectric spacer/mirror system:

$$S = J_{1,2}^\sigma L_2 J_{2,3} \quad (3.7)$$

where

$$\begin{aligned} J_{1,2}^\sigma &= \begin{pmatrix} 1 + Z_0\sigma/2 & Z_0\sigma/2 \\ -Z_0\sigma/2 & 1 - Z_0\sigma/2 \end{pmatrix} \\ L_2 &= \begin{pmatrix} \exp(-iqd) & 0 \\ 0 & \exp(iqd) \end{pmatrix} \\ J_{2,3} &= \frac{1}{t_{23}} \begin{pmatrix} 1 & r_{23} \\ r_{23} & 1 \end{pmatrix} \end{aligned} \quad (3.8)$$

and we have implicitly taken  $n_1 = n_2 = 1$  (i.e., the exciton is suspended over air, which does not come with a loss of generality in our qualitative results, as we shall soon see), so that  $r_{12} = 0$  and  $t_{12} = 1$ . We have not specified  $r_{23}$  yet, but we will soon.  $q = 2\pi n_2 / \lambda = 2\pi / \lambda$  and  $d$  is the spacing of the exciton from the back mirror. Furthermore, we have parametrized the optical properties of the monolayer TMDC as an interfacial sheet conductor, with an infinitesimal thickness. Thus, we are implicitly assuming there is little to no phase propagation through the TMDC monolayer. The sheet conductor model<sup>5</sup> for an excitonic material is given as

$$\sigma_{2D}(\omega) = \frac{1}{Z_0} \frac{\omega}{\omega_0} \frac{i\gamma_r}{\omega - \omega_0 + i\gamma_{nr}/2} \quad (3.9)$$

---

<sup>5</sup>the Lorentzian sheet conductor model for a 2D exciton and some analysis of their optics is discussed in [section B.4](#) and [section B.5](#).

where  $Z_0$  is the impedance of free space,  $\omega_0$  is the energy of the exciton,  $\gamma_r$  is the radiative rate of the exciton (which is proportional to its oscillator strength), and  $\gamma_{nr}$  is the non-radiative rate of the exciton (which is what typically dictates its linewidth). Multiplying the matrices together and examining the reflection amplitude gives us the expression:

$$r = \frac{-\frac{Z_0\sigma}{2} [r_{23} \exp(2iqd) + 1] + r_{23} \exp(2iqd)}{\frac{Z_0\sigma}{2} [r_{23} \exp(2iqd) + 1] + 1} \quad (3.10)$$

Note that if we now consider an ideal mirror on the back, we would expect  $r_{23} = -1$ . This is because an ideal mirror would cause a null in the electric field at the surface of the mirror, and the reflected wave would be opposite in sign (or equivalently for an ideal metallic mirror,  $\eta \rightarrow \infty$  and  $\kappa \rightarrow \infty$ ). Thus, if the exciton was placed exactly at  $d = \lambda/4$ , our reflectivity expression would be modified to

$$r = \frac{1 - Z_0\sigma}{1 + Z_0\sigma} \quad (3.11)$$

where the absorbance,  $A = 1 - |r|^2$  (note that  $T = 0$  since a perfect metal forces  $t_{23} = 0$ ), is therefore maximized when  $Z_0\sigma = 1$ . In other words, *when the surface impedance of the exciton is matched with that of the free-space impedance, the absorption is unity*. This condition is most easily achieved when  $\omega = \omega_0$ , i.e., the impedance is highest at the excitonic resonance, and therefore the condition for unity absorbance is given as  $\sigma(\omega_0)Z_0 = 1 = 2\gamma_r/\gamma_{nr}$ . Thus, perfect absorption in this case requires  $2\gamma_r = \gamma_{nr}$ . Notice for a fixed  $\gamma_r$ , the mirror has now reduced the required  $\gamma_{nr}$  to achieve this critical coupling condition by a factor of two<sup>6</sup>. Moreover, the absorbance can now reach a value of 100%, and this is from removing the superfluous port with the back mirror.

### 3.4 Monolayer Near Unity Absorption at Room Temperature

The above derivation suggests a straightforward method of achieving unity absorbance, with the caveat that we can satisfy the expression  $\gamma_{nr} = 2\gamma_r$ . [Table 3.1](#) shows the extracted values for the radiative and non-radiative rates of the exciton from the monolayer dielectric function data shown in [\[104\]](#). It is clear that at typical room temperature conditions, the expression above is far from ever being satisfied.

---

<sup>6</sup>c.f. [section B.5](#) where we required  $\gamma_r = \gamma_{nr}$  to achieve 50% absorbance.

Table 3.1: Room temperature values for the excitonic sheet conductor model of various TMDCs.

	WS <sub>2</sub>	MoS <sub>2</sub>	WSe <sub>2</sub>	MoSe <sub>2</sub>
$\hbar\gamma_r$ (meV)	4.11	3.35	1.47	2.38
$\hbar\gamma_{nr}$ (meV)	38.6	76.2	53.2	72.7
$\hbar\omega_0$ (eV)	2.01	1.87	1.65	1.55

Experimentally, there are a few well known methods of tuning  $\gamma_{nr}$  in TMDCs, including via temperature, strain, charge concentration, and/or van der Waals encapsulation. In contrast,  $\gamma_r$  is typically set by the optical transition rates of the excitonic absorption, and is much less sensitive compared to  $\gamma_{nr}$ . Epstein and others demonstrated that with hBN encapsulation and cryogenic temperatures ( $\sim 100\text{K}$ ), near-unity absorption can be achieved in WS<sub>2</sub> [51]. However, for any practical application (such as a photovoltaic device), this must be achieved at room temperature.

To do so, we examine the more general analysis of an exciton in an arbitrary photonic structure<sup>7</sup>, whose excitonic absorbance approaches unity when

$$\gamma_{nr} = 2 \frac{|E(\omega_0, x_0, y_0, z_0)|^2}{|E_0|^2} \gamma_r \quad (3.12)$$

For the Salisbury screen geometry (described above) where we simply have a single mirror on one side, the electric field intensity at the surface is exactly that of the incident wave, i.e.,  $\frac{|E(\omega_0, x_0, y_0, z_0)|^2}{|E_0|^2} = 1$ . In general, to achieve the absorption at more reasonable non-radiative rates, the electric field at the exciton must be significantly enhanced.

To do so, we consider a more complex layered structure which has a metallic back mirror and a *partially transmissive/partially reflective* top mirror, which is the geometry of an optical cavity. In this situation, it is possible to build up an electric field intensity that is far above the incident electric field, due to the formation of standing waves with significant quality factors. A simple optimized geometry using a thin piece of silver as the top mirror is shown in Figure 3.7, where roughly 85% absorbance is achieved in the exciton. Note also the electric field intensity is substantially higher than in the Salisbury screen geometry, and suggests that  $F_{abs} \approx 10$ , which enables near-unity absorption at room temperature conditions.

---

<sup>7</sup>See section B.5 for derivation, where we also define  $F_{abs} = 2 \frac{|E(\omega_0, x_0, y_0, z_0)|^2}{|E_0|^2}$ .

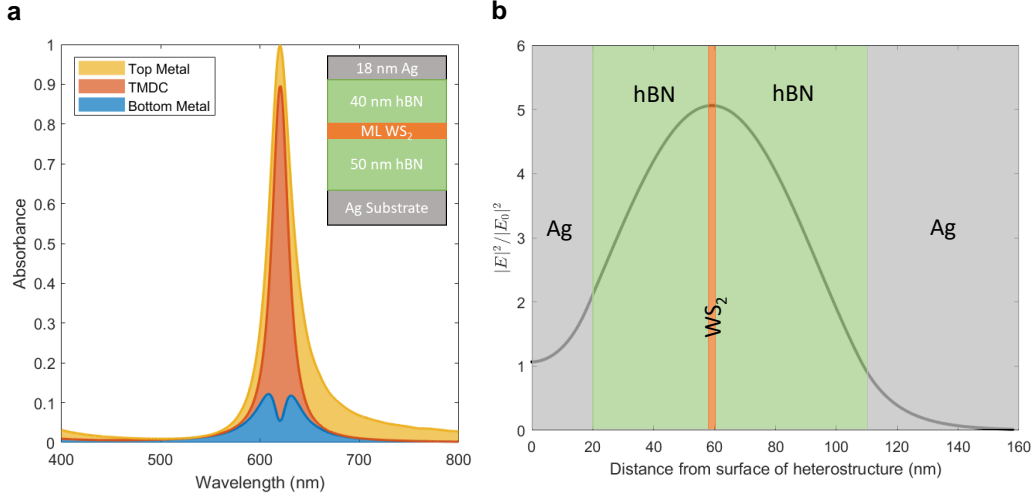


**Figure 3.7: Metallic Optical Cavity for Monolayer Perfect Absorption.** **a** Calculated absorption spectrum of monolayer WS<sub>2</sub> in an metallic optical cavity and its associated **b** electric field profile, showing the substantial increase in the electric field intensity. Roughly 85% absorbance in the exciton is achieved in this optical geometry

### 3.5 Experimental Demonstration of Near Unity Absorption in Monolayer WS<sub>2</sub> at Room Temperature

Due to experimental challenges with fabricating ultrathin low-loss metallic mirrors (such as the one considered in Figure 3.7), we consider a top mirror that is composed of lossless dielectric elements. The simplest form of a dielectric mirror is that of a distributed Bragg reflector (DBR), where alternating high and low refractive indices form a unit cell, and these unit cells are cascaded serially to increase the interference effects. As the number of unit cells increases, the reflectance can approach unity. However, as suggested by the scenario with a thin metal, the actual reflectance of the top mirror is likely small, and could be achieved in a low number of unit cells. It is also important to note that by employing materials with large index contrasts for the high and low index materials, it may be possible to use a lower number of unit cells, which could drastically lower the fabrication of these unity absorbing structures. Therefore, we examine the use of GaS ( $n_r \approx 2.7$ ) and Mica ( $n_r \approx 1.55$ ) as the materials of choice for a top dielectric mirror. These materials also happen to be layered materials, can be exfoliated and stacked like the TMDCs considered thus far. Figure 3.8 shows the results of using a top dielectric mirror composed of GaS and Mica, where >90% absorbance can be achieved in the TMDC layer. Also shown is a significant increase in the electric field intensity, as needed.

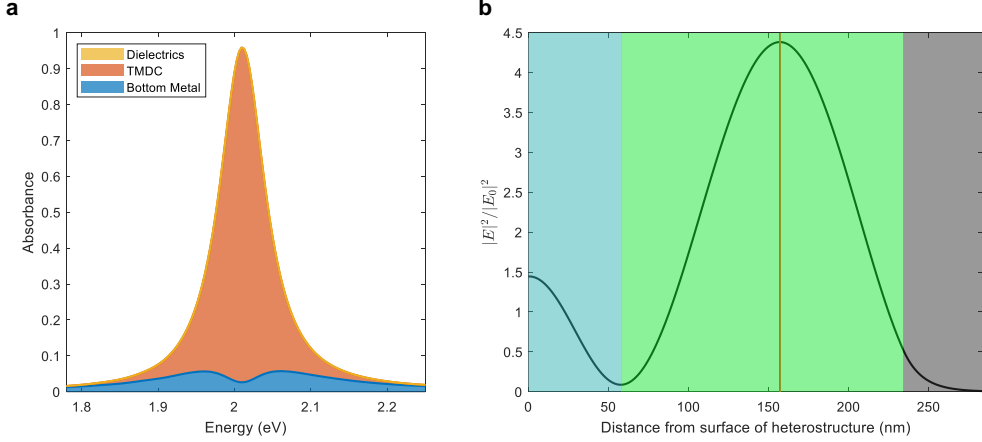


**Figure 3.8: Dielectric-Metal Optical Cavity for Monolayer Perfect Absorption.** **a** Calculated absorption spectrum of a heterostructure stack consisting of 58 nm GaS/99 nm Mica/Monolayer WS<sub>2</sub>/77 nm Mica/Ag. The parameters for WS<sub>2</sub> assumed a sheet conductor model with values from Table 3.1. The parasitic absorption in the silver is less than 5%. The refractive index of GaS and Mica was assumed to be  $n_{\text{GaS}} = 2.7$  and  $n_{\text{Mica}} = 1.55$ . **b** Electric field profile at the exciton frequency, with the different shaded regions corresponding to different materials (aqua = GaS, green = Mica, orange = WS<sub>2</sub>, and grey = silver).

The results shown in Figure 3.8 is particularly promising since both parasitic loss is minimized and the absorption efficiency is achieved with room temperature parameters. To more carefully understand the potential temperature dependence and effects of linewidth on the excitonic absorption, we calculate the peak excitonic absorption as a function of different non-radiative rates (Figure 3.9). The radiative rate is fixed to that from Table 3.1. We also perform a similar calculation assuming the Salisbury Screen geometry, as studied earlier. We note two important distinctions between the two optical geometries: (1) Unity absorbance can be achieved for much larger non-radiative rates  $\gamma_{nr}$ . For the cavity geometry, this is achieved at approximately  $\gamma_{nr} = 23$  meV, compared to roughly 8 meV for the Salisbury screen geometry. (2) The optical cavity geometry is significantly more tolerant to small perturbations of the non-radiative rate. In other words, for the cavity geometry, we can achieve >90% excitonic absorbance for any  $\gamma_{nr}$  between roughly 14 to 44 meV, while the Salisbury screen geometry achieves >90% absorbance for roughly 4 to 15 meV. We further analyze the linewidth dependence by fitting the resultant absorption spectrum to a Lorentzian with total linewidth  $\gamma_T$  as we vary  $\gamma_{nr}$ . This is useful to compare to experimental spectra, where we typically measure the total linewidth  $\gamma_T$  rather than any individual component. Here, it is even more evident that the optical cavity

geometry is significantly more tolerant to small perturbations. These linewidths are readily achievable even at room temperature (Figure 3.9).

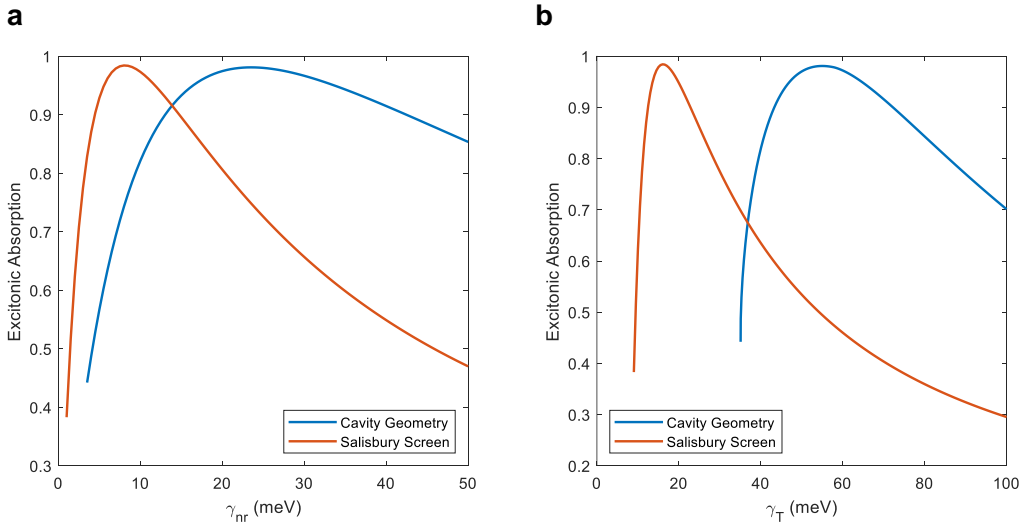


**Figure 3.9: Relationship between Absorption and Excitonic Linewidth.** **a** Calculated peak excitonic absorbance for WS<sub>2</sub> in an optical cavity geometry (Figure 3.8) and a Salisbury Screen geometry (where we remove the top mirror but keep the same thickness for the Mica). **b** Same as in **a**, except we plot the total linewidth  $\gamma_T$ , which is extracted from fitting the resultant absorption spectrum for each  $\gamma_{nr}$  to a Lorentzian with total linewidth  $\gamma_T$ . Generally, we have  $\gamma_T \approx F_{P,Abs} \gamma_r + \gamma_{nr}$ .

We next examine the effects of tuning the geometric parameters of the optical cavity on the final excitonic absorption (Figure 3.10). We analyze the effects of varying one of the parameters at a given time, assuming the others are at an optimal value (again, excitonic parameters given by Table 3.1). For every parameter, we find that we generally have a tolerance of  $\pm \sim 4$  nm to achieving  $>90\%$  absorbance. While this tolerance may seem experimentally daunting, it is possible to use a variety of methods to ensure the appropriate thickness (e.g. atomic force microscopy). We also develop a method of using reflection contrast spectroscopy itself as a method to accurately assert the thickness of a given dielectric layer, which is akin to the methods used in ellipsometry Figure 3.12.

Using the analysis described above and this optical cavity geometry, we are able to experimentally demonstrated near-unity absorbance in monolayer WS<sub>2</sub> (Figure 3.11). Instead of using a typical silver substrate, we cap the silver with a thin layer of SiO<sub>2</sub>, which dramatically reduces the rate at which silver tarnishes (usually to form silver sulfide). In this case, the SiO<sub>2</sub> can also act as a dielectric spacer. Our anal-

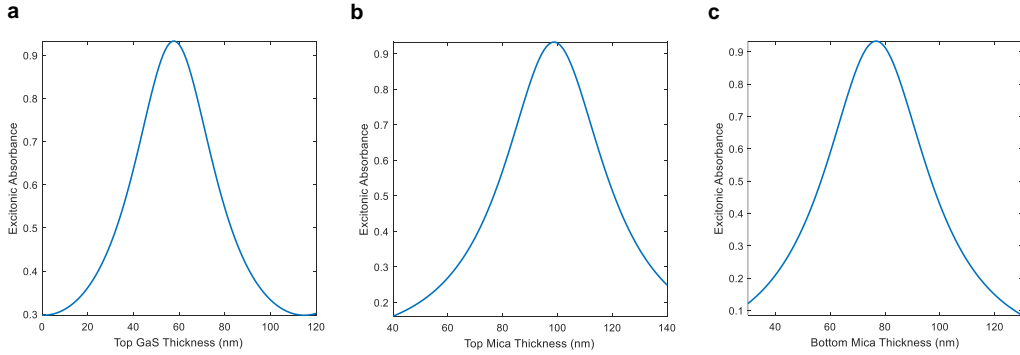


**Figure 3.10: Geometric tolerance of monolayer perfect absorption optical cavities.** Calculated peak excitonic absorbance where the other parameters are fixed but the **a** Top GaS thickness is varied **b** Top Mica thickness is varied and **c** Bottom Mica thickness is varied.

ysis where we encapsulate the  $WS_2$  on both sides with Mica is still essentially the same, except the finite  $SiO_2$  will reduce our thickness for the bottom spacer. We therefore use conventional van der Waals heterostructure fabrication techniques (specifically, PDMS exfoliation and subsequent layered stacking), to form a van der Waals heterostructure (Figure 3.11a). Here, every layer was subsequently analyzed in both reflection and PL spectroscopy as the heterostructure was assembled, and we performed one vacuum anneal once the heterostructure was formed. We note that the heterostructure formed in this way results in a variety of optical geometries that have gone through the same amount of processing and uses the same crystalline flakes. Therefore, the properties between the different heterostructures can be quantitatively compared (Figure 3.11b). We analyze the absorption and emission of the  $WS_2$  in a cavity geometry, i.e., similar to what we have discussed, and that without the top dielectric mirror. We observe not only is the emission enhanced in the cavity geometry relative to the Salisbury screen geometry, the absorption at the excitation wavelength ( $\lambda = 532$  nm) is *decreased* in the cavity geometry. Therefore, the luminescence yield has improved by more than a factor 6 due to the presence of this optical cavity. This factor of 6 is already comparing that of the Salisbury screen geometry, suggesting that the luminescence quantum yield has substantially increased. Our analytic analysis suggests that, if we were to achieve near-unity absorption, the quantum yield would be approximately 50%.

We next turn our attention to reflection spectroscopy to examine the absorbance properties in this sample (Figure 3.11c). We perform reflectance mapping mea-

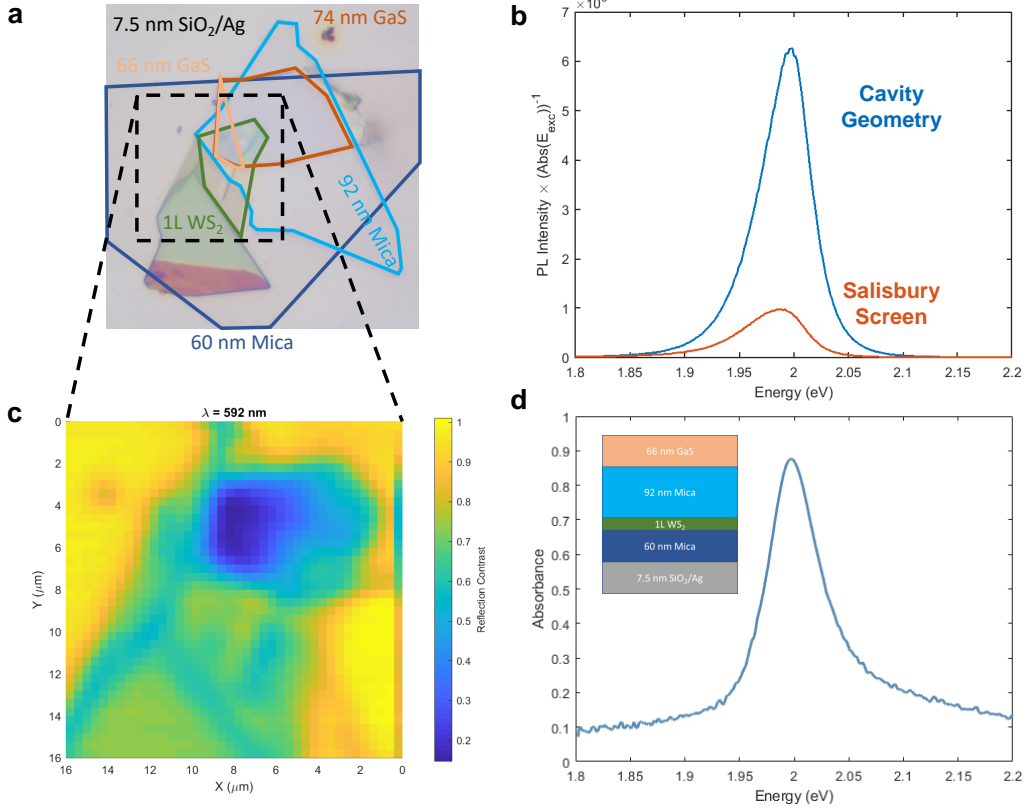


**Figure 3.11: Experimental Demonstration of Near-Unity Absorption in  $WS_2$  at Room Temperature.** **a** Optical micrograph of fabricated heterostructure, with different flakes and their corresponding thicknesses overlaid (thicknesses are measured with AFM). In this configuration, we use  $SiO_2$  as a capping layer to  $Ag$  to reduce the ambient tarnishing. **b** Measured enhancement of the photoluminescence in the optical geometry ( $66\text{ nm GaS}/92\text{ nm Mica}/1\text{L } WS_2/60\text{ nm Mica}/7.5\text{ nm } SiO_2/Ag$ ) compared to that in the Salisbury screen geometry ( $1\text{L } WS_2/60\text{ nm Mica}/7.5\text{ nm } SiO_2/Ag$ ). **c** Experimental microreflectance measurements as a function of position over the region of interest (see **a**). At each pixel, a reflection contrast spectrum  $R/R_0$  is measured. Here  $R_0$  is the reflectance on the substrate. It is clear where there is minimal reflectance, i.e., maximum absorbance. **d** Spectral response of a monolayer  $WS_2$  within an optical cavity, achieving roughly 90% absorbance experimentally.

surements, where the reflection spectrum  $R$  is taken at every spot, and therefore Figure 3.11c represents a linecut of a hyperspectral image. We find that near the excitonic frequency, there is minimal reflectance where the full heterostructure is formed. Equivalently, with appropriate normalization of the substrate reflectance and that of the sample, we find that we indeed achieve near-unity absorbance in  $WS_2$  in this dielectric-metal optical cavity Figure 3.11d. It is likely possible to achieve absorbances that are even slightly higher, since the thicknesses observed here are

slightly offset from the optimal values. However, the fact that we do observe near-unity absorbance experimentally demonstrates the tolerance of this optical cavity design to small perturbations. Moreover, given this simple optical geometry, it should be possible to directly integrate electrical contacts to these samples to create a fully functioning photovoltaic device.

### 3.6 Efficiency Limits of Excitonic Multijunctions

Having designed structures that have the possibility of achieving unity absorption, we now consider the prospect of using excitonic van der Waals materials as active layer absorbers in a multijunction solar cell and consider their efficiency potential. While the absorbance of each individual van der Waals layer is typically far below unity (typically between 5 - 20%), the wide array of different van der Waals materials along with their lattice-mismatch free hetero-structuring suggests that a ‘metamaterial’ with near-unity absorbance over the solar spectrum can be theoretically engineered. Assuming carrier selective contacts and negligible resistive losses between the subcells, theoretical efficiencies of these van der Waals multijunctions can far exceed the single-junction Shockley-Queisser limit.

To consider the maximum power efficiency potential of a van der Waals heterostructure, we consider a stack with  $N$  layers and consider the  $I - V$  characteristics of the  $i$ th layer. We assume we are in the radiative limit (i.e., the materials have an internal luminescence yield of 100%) and that the materials are spaced far enough away from one another that their luminescent coupling and individual absorbances can be described with ray optics. Further, we assume that anti-reflection coatings have been applied between the different layers of the van der Waals materials, so that there is no reflection when the light interacts with the layered material, i.e.,  $A(E) = 1 - T(E)$ . Further, we approximate the absorbance of the van der Waals materials as being dominated by a narrow absorbance peak (e.g., an excitonic absorber), which we parameterize as a Gaussian:

$$A(E) = A_{exc} \exp\left(-\frac{(E - E_{exc})^2}{2\sigma_{exc}^2}\right) \quad (3.13)$$

Let’s consider first the current density of the  $i$ th layer. Here, we enumerate  $i = 1$  as the first cell (top cell) and the  $N$ th cell as the bottom cell. The current for the top cell can be written as

$$J_{sc,i} = \int A_i(E) [S_{sun,top}(E) + S_{PL,top}(E, V_k) + S_{PL,bot}(E, V_k)] dE \quad (3.14)$$

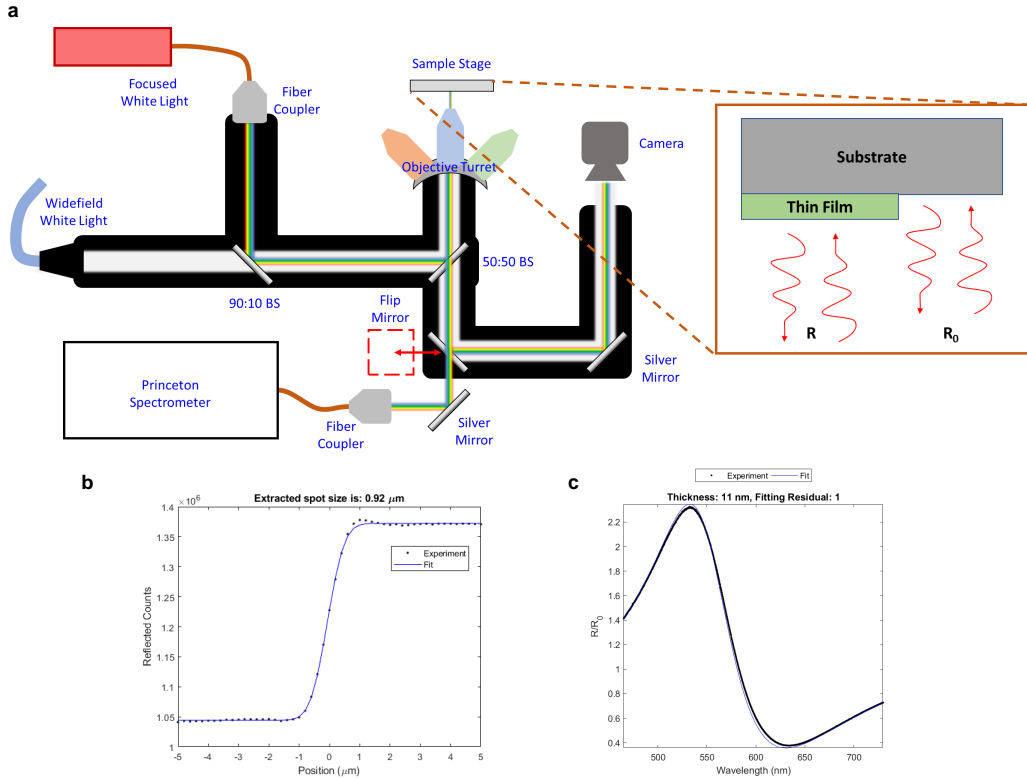


**Figure 3.12: Schematic of Reflectance Measurement Set-up. a** Schematic depiction of reflectance measurement set-up used throughout the analysis with monolayer absorbers. Here, a stabilized white light source (ThorLabs SLS201L) is fiber-coupled into an inverted microscope (Leica). A 90:10 beamsplitter is used to simultaneously image the sample and the light source. A flip mirror is used that directs the reflected light to either the camera (used for imaging) or to a spectrometer (Princeton). The observed spectra at the output of the spectrometer is a convolution of many different factors, including the light source spectral flux, reflectance of the actual sample, and the wavelength-dependent optical efficiencies of the entire set-up. To remove all these effects besides the reflectance of the sample, we measure a reference spectrum  $R_0$  nearby the sample under the same conditions as  $R$ . Therefore, the reflectance contrast spectrum  $R/R_0$  has normalized away the effects of the set-up optical efficiency and lamp spectra. **b** Achieved spatial resolution of the optical set-up described in **a**, using a ‘knife-edge’ measurement of the reflectance to quantify a spot size. The spatial resolution roughly  $1 \mu\text{m}$  and the spot diameter is roughly  $2 \mu\text{m}$ . **c** Example reflectance contrast spectra  $R/R_0$  and fitting procedure used to extract out the thickness of the dielectric layer. In this case, we examined hBN exfoliated on  $\text{SiO}_2/\text{Si}$ . We are able to achieve precise fits down to a nm or so in resolution, although this accuracy is partially dictated by the index of the material and the optical properties of the substrate.

where  $S_{\text{sun},\text{top}}(E)$  is the flux from the sunlight that is transmitted through the  $i - 1$  number of layers,  $S_{PL,\text{top}}(E, V_k)$  is the luminescent flux from the  $k = 1$  to the  $k = i - 1$  van der Waals layers, dependent on the electrical voltage  $V_{k \neq i}$ , and

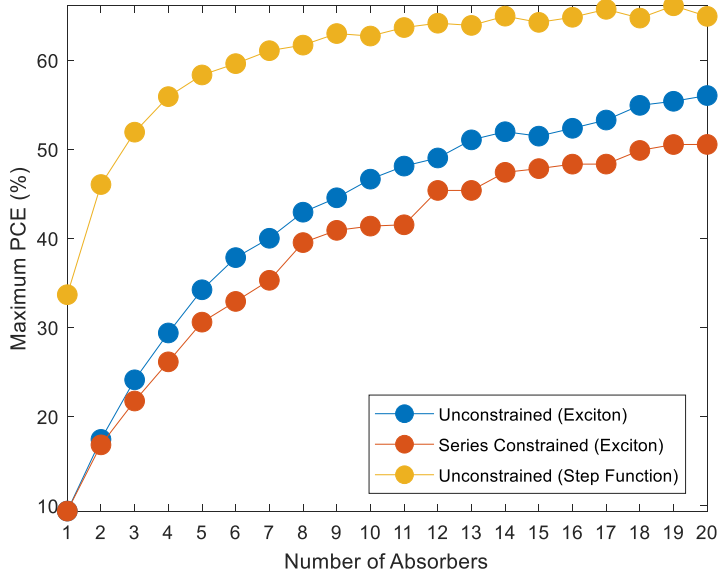


Figure 3.13: **Limiting Efficiency of Excitonic Multijunctions.** Maximum power conversion efficiency as a function of the number of excitonic absorbers. Series constrained refers to a two-terminal device where the current density between every absorber must be matched, whereas unconstrained has  $2N_{exc}$  number of terminals and each absorber can have an arbitrary current-voltage curve. Also shown is the efficiency maximum optimization for a step-function absorber response, which is what is traditionally considered. The single junction limit is 33.7% and the multijunction limit is 68%.

similarly for  $S_{PL,bot}(E, V_k)$  for  $k = i + 1$  to  $k = N$ . Explicitly, we have:

$$S_{sun,top}(E) = S_{sun}(E) \left( \prod_{j=1}^{j=i-1} T_j(E) \right) \quad (3.15)$$

$$S_{PL,top}(E, V_k) = \sum_{k=1}^{k=i-1} S_{PL,k}(E, V_k) \left( \prod_{j=k+1}^{j=i-1} T_j(E) \right) \quad (3.16)$$

$$S_{PL,bot}(E, V_k) = \sum_{k=i+1}^{k=N} S_{PL,k}(E, V_k) \left( \prod_{j=i+1}^{j=k-1} T_j(E) \right) \quad (3.17)$$

where we take  $\prod_{j=i}^{j=i-1} T_j(E) = 1$  and  $\prod_{j=i+1}^{j=i} T_j(E) = 1$  for the products, which corresponds to unity coupling for the nearest neighbor. The luminescent flux of each absorber assuming quasi-equilibrium of electrons and holes with the photon gas is given by the usual reciprocity relation:

$$S_{PL,k}(E, V_k) = (\exp(qV_k/kT) - 1) A_k(E) S_{BB}(E) \quad (3.18)$$

The net current extracted from each cell is then given by

$$J_i = J_{sc,i}(V_{k \neq i}) - J_{rad}(V_i) = J_i(V_1, V_2, \dots, V_i, \dots, V_{N-1}, V_N) \quad (3.19)$$

where we note that  $J_i$  is dependent on the voltages of the other layers due to luminescent coupling, and the radiative recombination current is given by the usual detailed balance expression:

$$J_{rad}(V_i) = (\exp(qV_i/kT) - 1) \int A_i(E) S_{BB}(E) dE \quad (3.20)$$

Therefore, the net power from each cell is given by  $P_i = J_i V_i$  and the total power for the entire multijunction is

$$P_{total} = \sum_i P_i \quad (3.21)$$

For a given set of  $N$  absorbers defined by their absorptance  $A_i(E)$ , we can calculate the power of each subcell  $P_i$  using the above expressions. The transmittance is given as  $T_j(E) = 1 - A_j(E)$  and the voltage of each subcell  $V_i$  is optimized to yield the maximum power of the multijunction solar cell. We run an optimization to yield the limiting efficiency as a function of the number of subcells in [Figure 3.13](#). We find that once we have approximately 6 or more excitonic absorbers, we can readily surpass the single-junction detailed balance limit. The absorption spectra for a given number of absorbers is shown in [Figure 3.14](#). Interestingly, we find that even under a series constraint (i.e., the  $J_{sc}$  must be matched between the different absorbers), the limiting efficiency can still be very appreciable. By examining [Figure 3.14](#), we see that this is due to the linewidth of the exciton acting as another tuning knob that can modulate the integrated absorption.

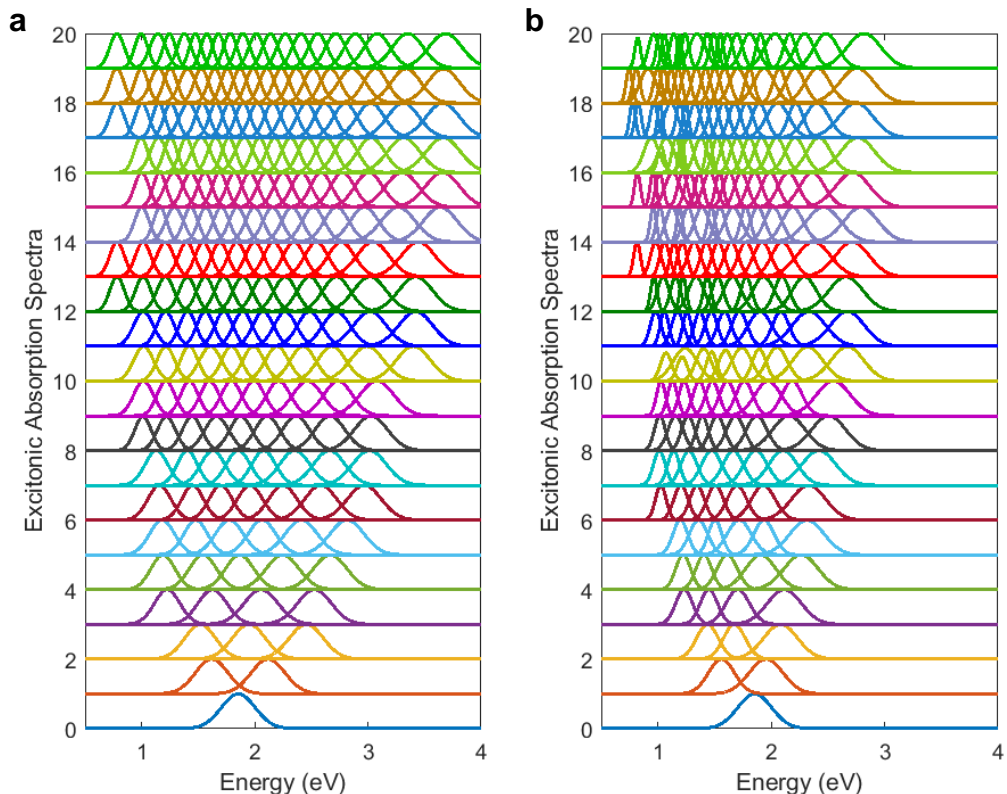


Figure 3.14: **Optimal Absorption Spectra of Excitonic Multijunctions.** Optimized absorption spectra of **a** unconstrained and **b** series-constrained excitonic multijunctions.

## **Part II**

### **Traversing through Flatland**

## Chapter 4

## HIGH PHOTOVOLTAIC QUANTUM EFFICIENCY IN ULTRATHIN VAN DER WAALS HETEROSTRUCTURES

*“You can dream, create, design, and build the most wonderful place in the world... but it requires people to make the dream reality.”*

— Walt Disney

### 4.1 Introduction

Owing to their naturally passivated basal planes and strong light-matter interactions, transition metal dichalcogenides are of considerable interest as active elements of optoelectronic devices such as light-emitting devices, photodetectors and photovoltaics. [14, 151] Ultrathin transition metal dichalcogenide (TMD) photovoltaic devices a few atomic layers in thickness have been realized using TMDs such as molybdenum disulfide ( $\text{MoS}_2$ ) and tungsten diselenide ( $\text{WSe}_2$ ). [11, 19, 54, 101, 155, 219] Complete absorption of the solar spectrum is a challenge as the thickness is reduced to the ultrathin limit, [8, 50, 73] whereas efficient carrier collection is challenging in thicker bulk TMD crystals. The active layers in conventional photovoltaics typically range from a few microns in direct gap materials (gallium arsenide) to a hundred microns thick or more in indirect gap materials (silicon). [27]

Efficient ultrathin and ultralight ( $<100 \text{ g/m}^2$ ) photovoltaics have long been sought for many applications where weight and flexibility are important design considerations, such as applications in space power systems, internet-of-things devices, as well as portable and flexible electronics. [59, 107, 202] Conventional photovoltaic materials are mechanically fragile when thinned down to the ultrathin ( $< 10 \text{ nm}$ ) regime, and interfacial reactions mean that a large fraction of the crystal consists of surface-modified regions rather than intrinsically bulk material. Surface oxides and dangling bonds in ultrathin films often result in increased nonradiative recombination losses, lowering photovoltaic efficiencies. By contrast, transition metal dichalcogenides have intrinsically high absorption and their layered crystallographic structures suggest the possibility of achieving intrinsically passive basal planes in high quality crystals.

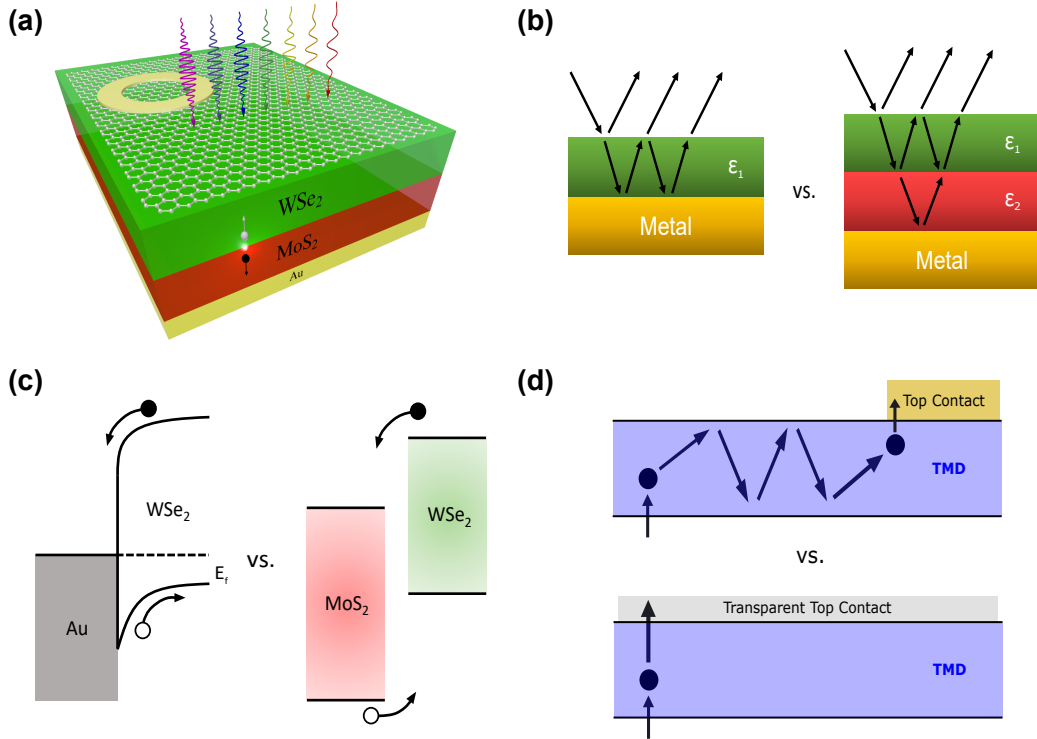


**Figure 4.1: Achieving High External Quantum Efficiency in van der Waals heterostructures.** **a** A schematic of the van der Waals device stack where nanophotonic light trapping combined with efficient exciton dissociation and carrier collection yields EQEs  $>50\%$ . **b** A schematic of comparing near-unity absorption in a single semiconducting layer on metal with a heterostructure of different semiconductors on metal. **c** A schematic of comparing a pn heterojunction with a Schottky junction for exciton dissociation and charge carrier separation in van der Waals materials. **d** A schematic of comparing vertical and lateral carrier collection schemes in van der Waals materials.

Photovoltaics that can approach the Shockley-Queisser limit, [154, 175] have two prerequisites: first, that at open circuit, every above-bandgap photon that is absorbed is extracted as an emitted photon at the band-edge of the material, i.e., it has perfect external radiative efficiency. [125] Amani et al. have recently demonstrated that superacid-treated monolayers of  $\text{MoS}_2$  and  $\text{WS}_2$  exhibit internal radiative efficiency  $> 99\%$ , [2] suggesting that the condition of very high external radiative efficiency might be satisfied in transition metal dichalcogenides. The second prerequisite is that at short circuit, the photovoltaic device must convert every incident above-bandgap photon into an extracted electron, i.e., it has external quantum efficiency (EQE) approaching unity.

To understand the path to high EQE, we can deconvolute the external quantum

efficiency into the product of two terms: the absorbance and internal quantum efficiency (IQE). High EQE devices exhibit both high absorption and internal quantum efficiency, i.e., carrier generation and collection efficiency per absorbed photon. To date, reports of van der Waals based photovoltaic devices have not considered both of these concepts and separately evaluated them as criteria for high efficiency photovoltaics.

Coupling electromagnetic simulations with absorption and EQE measurements enables quantitative characterization of few-atomic-layer thickness optoelectronic devices in van der Waals heterostructures. In this paper, we demonstrate external quantum efficiencies  $> 50\%$  (Figure 4.1a), indicating that van der Waals heterostructures have considerable potential for efficient photovoltaics. We show that high EQE results from both high optical absorption and efficient electronic charge carrier collection. We analyze the optical response using electromagnetic simulations to explain how near-unity absorption can be achieved in heterostructures (Figure 4.1b). We find that experimental absorption results for van der Waals heterostructures match well with these electromagnetic simulations. Thus, we can separate optical absorption and electronic transport to quantitatively compare their effects on charge collection efficiency for both pn heterojunctions and Schottky junctions (Figure 4.1c). In addition, we analyze the role of few-layer graphene as a transparent top contact (Figure 4.1d). Finally, we outline important considerations for designing high efficiency photovoltaic devices. By simultaneously maximizing both external radiative efficiency and external quantum efficiency in a single device, van der Waals materials based photovoltaic devices could in principle achieve efficiencies close to the Shockley-Queisser limit for their bandgaps.

## 4.2 Van der Waals Heterostructure Device Fabrication

Atomically smooth metal substrates were prepared using the template stripping technique. [122, 198] We prepared the substrates using polished silicon wafers (University Wafer) with native oxide and then cleaned the silicon substrates via sonication in acetone (10 minutes) followed by sonication in isopropyl alcohol (10 minutes). Samples were then blow dried with nitrogen gas before cleaning with oxygen plasma (5 minutes, 100 W, 300 mTorr under O<sub>2</sub> flow).

Metal was then deposited via electron beam evaporation on the polished and cleaned surface of the silicon wafer. For gold (Plasmaterials, 99.99% purity), base pressures of  $\sim 3\text{e-}7$  was achieved before depositing at 0.3 Å/s. This continued until a thickness

of  $\sim$ 20 nm was achieved. Then, the rate was slowly ramped to 1  $\text{\AA/s}$  and then held there until a total thickness of 120 nm was reached. For silver (Plasmaterials, 99.99% purity), following McPeak et al., [123] we deposited at a base pressure of  $\sim$ 3e-7 at 40  $\text{\AA/s}$  for a final thickness of 150 nm. After deposition of the metal, an adhesive handle was formed using a thermal epoxy (Epo-Tek 375, Epoxy Technology). 1 g of part A Epo-Tek 375 and 0.1 g of part B Epo-Tek 375 was mixed in a glass vial and was let to settle for  $\sim$ 30 min. Afterward, individual droplets of the mixture was added directly onto the metallic surface before placing cleaned silicon chips ( $\sim 1 \text{ cm}^2$ ) on top. The droplet of epoxy was let to settle under the weight of the silicon chip before placing on a hot plate ( $\sim$ 80  $^{\circ}\text{C}$ ) for 2 hours. Individual chips were then cleaved with a razor blade, forming the final substrate consisting of atomically smooth metal/thermal epoxy/silicon. Typical RMS surface roughness of the metal was  $< 0.3 \text{ nm}$  using this technique (examined via AFM).

The bottom-most layer of the van der Waals heterostructure (e.g.  $\text{MoS}_2$ ) was directly exfoliated onto the metallic substrates prepared using the above technique. Exfoliation was performed using bulk crystals purchased from HQ Graphene using Scotch tape. Subsequent layers were formed using a visco-elastic dry transfer technique [22] using a home-built set-up at room temperature. Dry transfer was performed using PF-20-X4 Gel Film from Gel-Pak as the transparent polymer. Van der Waals materials were directly exfoliated onto the polymer using Nitto tape and then mechanically transferred onto the  $\text{MoS}_2$ /metal substrate. Samples were examined in the optical microscope during each layer of the process and an AFM scan was performed afterwards to extract out the thicknesses of individual layers. Thicknesses were then corroborated with optical measurements and calculations.

A top electrode was patterned using standard photolithography techniques. NR-9 1000 PY was used as a negative resist. The resist was spun at 5000 RPM for 55 s before baking at 150  $^{\circ}\text{C}$  for 1 minute. A mask aligner with a pre-patterned mask was used to define the features and aligned on top of the van der Waals heterostructure. After exposure for  $\sim$ 18s under 10 mW of UV light ( $\lambda = 365 \text{ nm}$ ), the resist was post-baked at 105  $^{\circ}\text{C}$  for 1 min and cooled to room temperature. Finally, the resist was developed using RD-6 developer for 10-15 seconds before rinsing in deionized water for 35 seconds. The sample was then blown dry with nitrogen and examined under an optical microscope.

Electron beam deposition was then used to form the top ring electrodes (10 nm Ti/90 nm Au). Base pressures of  $\sim$ 3e-7 was achieved before the beginning of the

deposition. For titanium, a deposition rate of  $0.3 \text{ \AA/s}$  was used for the entirety of 10 nm. Immediately afterwards, gold was deposited at a rate of  $0.3 \text{ \AA/s}$  for 15 nm. The rate was slowly ramped to  $0.6 \text{ \AA/s}$  for 10 nm, and then to  $0.9 \text{ \AA/s}$  for another 10 nm. At 35 nm of total gold thickness, the rate was finally ramped to  $1.0 \text{ \AA/s}$  until the total gold thickness was 90 nm. The resist was then lifted-off using heated acetone ( $40\text{--}45 \text{ }^{\circ}\text{C}$ ) for 30 minutes. If needed, the samples were sonicated in 5 s intervals in acetone to remove the resist. The sample was then rinsed in isopropyl alcohol and blow dried with nitrogen. Images of the three samples studied in this chapter are shown in [Figure 4.2](#).

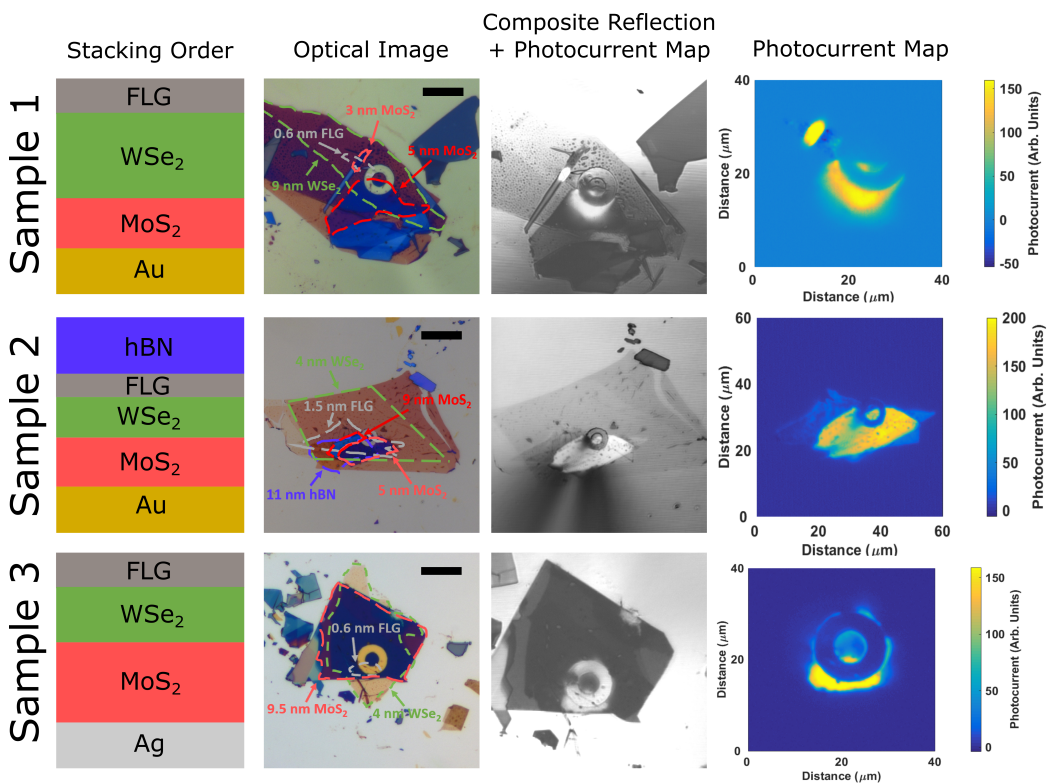


**Figure 4.2: High Photovoltaic Quantum Efficiency Sample Images.** The heterostructure designs, optical images, composite reflection & photocurrent maps, and the photocurrent maps for all the samples analyzed in this paper. The outlines in the optical images correspond to specific materials with the appropriate thickness and materials labeled (scale bar =  $20 \text{ } \mu\text{m}$ ). The composite reflection and photocurrent map is made by superimposing a reflection mode scan with a photocurrent scan ( $\lambda = 633 \text{ nm}$ ). The bright white regions in the composite image correspond to high photocurrent.

### 4.3 Spatial Photocurrent Map and IV Measurements

Samples were contacted on the top electrode and bottom metallic substrate using piezoelectric controlled probes (MiBots, Imina Technologies) with  $\sim 3 \mu\text{m}^2$  tip diameter under a confocal microscope (Axio Imager 2 LSM 710, Zeiss) with a long working distance objective (50x, NA = 0.55). Samples were first checked for photoresponse using dark IV and white light illumination. Voltage sweeps were performed using a Keithley 236 source measure unit and in-house written scripts. High resolution spatial photocurrent maps were performed using the same confocal microscope with an automated stage. The microscope was modified to measure photocurrent maps. Near-diffraction limited laser light ( $\sim 6 \mu\text{m}^2$  spot size) was coupled in and focused to perform high resolution spatial photocurrent maps ( $< 1 \mu\text{m}$  lateral resolution), and power-dependent IV measurements were performed at particular locations of the device using the spatial photocurrent maps. Illumination power was modified using neutral density filters in the microscope and the incident power was measured by a photodetector and cross-referenced with the EQE spectrum of the measured device.

### 4.4 Spectral Response Measurements

Quantitative absorbance and external quantum efficiency measurements were performed using a home-built optical set-up. A supercontinuum laser (Fianium) was coupled to a monochromator to provide monochromatic incident light. A series of apertures and mirrors were used to collimate the beam before being focused on the sample with a long working distance (NA = 0.55) 50x objective to provide a small spot size ( $\sim 1 \mu\text{m}$  lateral resolution). Importantly, the small spot sizes allow us to probe individual regions on a particular sample. In addition, the relatively angle-insensitive light trapping structure [80] used in this work along with a small NA objective allowed us assume that the collected signal is close to the normal incidence response. During all measurements, the light is first passed through a chopper ( $\sim 103 \text{ Hz}$ ) and a small fraction was split into a photodetector connected to a lock-in amplifier. The other beam-split light is used for probing the sample which is eventually sent to a photodetector (for absorbance measurements) or the sample itself is used as a photodetector (for external quantum efficiency measurements). Thus, the sample or photodetector is connected to a second lock-in amplifier for homodyne lock-in detection.

For absorption measurements, the reflected signal was collected by the same 50x objective and passed through a beam splitter before being collected by a photodetector.

The same spectral measurement was done with a calibrated silver mirror (Thorlabs) in order to obtain the absolute reflection spectrum. In the absence of transmission, the absorption is simply  $Abs(\lambda) = 1 - R(\lambda)$ . Reflection from the objective itself and other optical losses was subtracted as a background. As mentioned before, a reference spectrum was collected using a small amount of beam-split light at the same time as the sample, background, and mirror scans to account for power fluctuations in the laser beam between scans. As a second reference, the metallic back substrate was measured during all absorption scans to check if the normalization was accurate.

For external quantum efficiency measurements, the sample itself was used as a photodetector. The top ring electrode and bottom metallic substrate was probed using MiBots. Laser light was then focused on a particular spot and the current was collected by the probes and sent through a lock-in amplifier for homodyne detection, as in the reflection spectrum case. After measurement of the current signals from the sample, another spectral scan was performed with the optical system in the same configuration using a NIST calibrated photodetector (818-ST2-UV/DB, Newport). Power fluctuations between scans were again accounted for by using a small amount of beam-split light and sending it to a photodetector. The measured currents were normalized to this photodetector's current before being normalized to the calibrated photoresponse to yield the absolute EQE. Despite the various steps of calibration used for normalization, we still estimate measurement errors of  $\delta Abs/Abs \approx 0.02$  and  $\delta EQE/EQE \approx 0.05$  stemming from the assumption of normal incidence for both absorption and external quantum efficiency measurements while using a  $NA = 0.55$  objective, fluctuations in the laser power during the measurement, and sample contact stability. In addition, we have observed in our laser that there is relatively little power for  $\lambda < 450$  nm. Additionally, there is relatively high absorbance in the 50x objective for  $\lambda > 700$  nm. Combined with the fact that the simulated parasitic absorption accounts for a larger fraction of the total absorption for  $\lambda < 450$  nm and  $\lambda > 700$  nm, the significantly noisier spectra in the active layer IQE at these wavelengths can be attributed to the factors described above.

#### 4.5 Electromagnetic Simulations and Error Estimation

Calculations were performed using the transfer matrix method ([section B.3](#)) with optical constants taken from literature for each of the transition metal dichalcogenides (TMDs). [\[104\]](#) We assumed that for the TMD thicknesses analyzed in this paper, their optical response can be represented by the bulk optical permittivities. Permit-

tivities of Ag and Au were taken from McPeak [123] and Olman [141], respectively. The optical response of few-layer graphene was assumed to be like graphite, with its dielectric constant taken from Djurisic. [44] Hexagonal Boron Nitride (hBN) was assumed to be a lossless, non-dispersive dielectric in the visible with refractive index of  $n = 2.2$ . [55]

Given that there is sample-to-sample variation of the dielectric constant, it is likely that the literature values of the dielectric constant differ from the samples measured here. This difference we estimate leads to absorption simulation errors of  $\sim 5\%$ . Assuming this is true, the estimated error for the active layer IQE can be approximated as

$$\frac{\delta IQE}{IQE} \approx \sqrt{\left(\frac{\delta Abs}{Abs}\right)^2 + \left(\frac{\delta Abs_p}{Abs_p}\right)^2 + \left(\frac{\delta EQE}{EQE}\right)^2} \quad (4.1)$$

which is about 7%.

#### 4.6 Prototypical Optoelectronic Device Characterization

We analyzed the optoelectronic device characteristics of a high-performance device consisting of a vertical van der Waals heterostructure device of 0.6 nm thick few-layer graphene (FLG)/9 nm WSe<sub>2</sub>/3 nm MoS<sub>2</sub>/Au (see Figure 4.2 for optical and photocurrent images). Its optoelectronic and device characteristics are shown in Figure 4.3. First, we find that this device exhibits an EQE  $> 50\%$  (Figure 4.3a) with absorbance greater than 90% from approximately 500 nm to 600 nm. Spectral features such as the exciton resonances of MoS<sub>2</sub> and WSe<sub>2</sub> are well reproduced in the external quantum efficiency spectrum. In addition, we observe a maximum single-wavelength power conversion efficiency (PCE) of 3.4% under 740 W/cm<sup>2</sup> of 633 nm laser illumination (Figure 4.3b). Since the high-performance device is electrically in parallel with other devices, typical macroscopically large spot size ( $\sim$ cm) AM 1.5G illumination measurements would yield device characteristics substantially different from the high-performing one. Thus, we estimated the AM 1.5G performance using extracted device parameters of a diode fit under laser illumination (see section 4.10 for details). We estimate the AM 1.5G PCE of this device to be  $\sim 0.4\%$ . This value is presently too low to be useful for photovoltaics, but the high EQE values reported here indicate promise for high efficiency devices, when device engineering efforts are able to also achieve correspondingly high open circuit voltages in van der Waals based photovoltaics.

Further measurements were performed at different laser powers under 633 nm laser illumination (Figure 4.4), yielding various power-dependent characteristics. Ex-

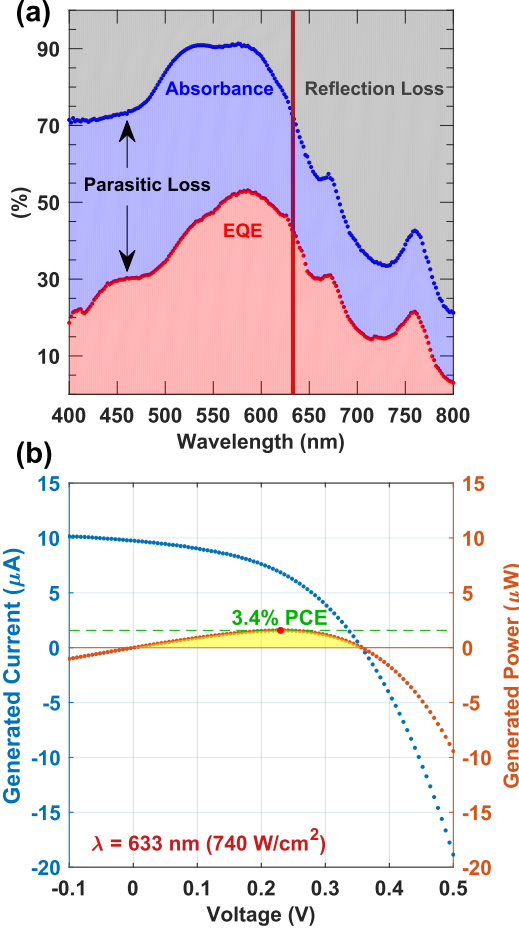


**Figure 4.3: Optoelectronic Performance Characteristics.** **a** Spectral characteristics of the experimentally measured absorbance (blue) and external quantum efficiency (red). The vertical solid line indicates the excitation wavelength (633 nm) for the measurements in **b** and Figure 3. The grey region indicates loss in photocurrent from the reflected photons. **b** I-V (light blue) and power-voltage (orange) characteristics of the device, excited at  $\lambda = 633 \text{ nm}$  with  $\sim 45 \mu\text{W}$  incident power with a spot size area of  $\sim 6 \mu\text{m}^2$ . We observe a maximum single wavelength power conversion efficiency of 3.4%. The yellow region indicates generated power from the device.

amination of the short-circuit current  $I_{sc}$  yielded nearly linear dependence on laser power, as expected in ideal photovoltaic devices Figure 4.4a. The dashed blue line represents the fit to the expression  $I_{sc} = AP^\tau$ , where  $A$  is a constant of proportionality,  $P$  is the incident power, and  $\tau$  represents the degree of nonlinearity in this device ( $\tau = 1$  is the linear case). [149] We find that  $\tau = 0.98$  in our device, indicating nearly linear behavior under short circuit conditions. In addition, in an ideal photovoltaic device, the open circuit voltage is expected to grow logarithmically with the input

power, since  $V_{oc} = (nk_bT/q) \ln(J_L/J_{dark} + 1) \approx (nk_bT)/q \ln(J_L/J_{dark})$  for large illumination current densities  $J_L$ . Here,  $J_{dark}$  is the dark current density,  $n$  is the ideality factor,  $k_b$  is the Boltzmann constant,  $T$  is the temperature of the device, and  $q$  is the fundamental unit of charge, so that  $(k_bT)/q \approx 0.0258V$  at room temperature. In [Figure 4.4b](#) we see that the experimental data match well with the diode fit (dashed black line, see [section 4.10](#) for fitting details), suggesting an ideality factor of  $n = 1.75$  and a dark current density  $J_{dark} = 0.65 \text{ mA}/(\text{cm}^2)$  assuming a  $30 \mu\text{m} \times 30 \mu\text{m}$  device area. Also, since the power conversion efficiency (PCE) is given as  $PCE = J_{sc}V_{oc}FF/P_{in}$ , where  $J_{sc}$  is the short circuit current density,  $V_{oc}$  is the open circuit voltage,  $FF$  is the fill fraction, and  $P_{in}$  in the incident power density, we would expect the power conversion efficiency to scale roughly logarithmically as well. This is true for laser powers up to  $\sim 740 \text{ W/cm}^2$  ([Figure 3 c](#)). However, for larger input power, the PCE decreases with increasing power. Such a drop in PCE can be attributed to series resistances in the device, either at the contacts or at the junction. This is corroborated by the match between the experimental data (dots) and the fitted expression (dashed line), yielding the diode fitting parameters in the lower right hand corner of the plot in [Figure 4.4c](#). The fit for the  $V_{oc}$  was simultaneously done with the PCE, therefore yielding the same set of parameters and a good match between experiment and extracted device parameters. Finally, we observed a decrease in the EQE at 633 nm with increasing power ([Figure 4.4d](#)). Using the above fitted parameters, series resistance can only be used to partially explain a decrease in the EQE at higher powers. Thus, the additional decrease in EQE at higher powers may be due to the onset of carrier density-dependent nonradiative processes such as Auger or biexcitonic recombination which are not accounted for in the diode fit used above, where the dark current is fixed for all powers.

#### 4.7 Absorption in van der Waals heterostructures

We first investigate the absorption and optical properties of van der Waals heterostructures. We formed a heterostructure composed of hexagonal boron nitride (hBN)/ FLG/WSe<sub>2</sub>/MoS<sub>2</sub>/Au. The composite heterostructure has various regions (inset of [Figure 4.5a](#)), corresponding to different vertical heterostructures. Given the sensitivity of the performance of van der Waals materials to different environmental conditions and device fabrication procedures,[[170](#)] the samples fabricated here allow us to study optical and electronic features of different heterostructures in a systematic manner by probing specific heterostructures fabricated on the same monolithic substrate. This is enabled by the small spot size of our laser, which ad-

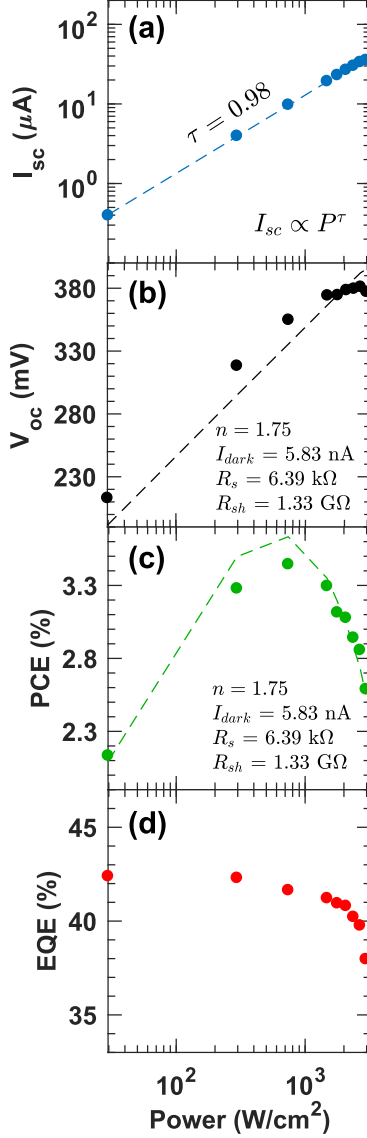


**Figure 4.4: Power dependent device characteristics.** Power dependent device characteristics at  $\lambda = 633 \text{ nm}$  excitation for the **a** short circuit current (light blue), **b** open circuit voltage (black), **c** maximum power conversion efficiency (green), and **d** external quantum efficiency (red). The dashed lines in **a**, **b**, and **c** correspond to fits. The area of the spot size of the laser in all of the above measurements is estimated to be  $\sim 6 \mu\text{m}^2$ .

ditionally allows us to properly normalize the spectral response without artificially including geometric factors (see Methods for details).

As an example, consider the optical response at the location of the blue dot in the inset of Figure 4.5a. The vertical heterostructure there is composed of 1.5 nm FLG/4 nm WSe<sub>2</sub>/5 nm MoS<sub>2</sub>/Au. This location can be probed spectrally for its

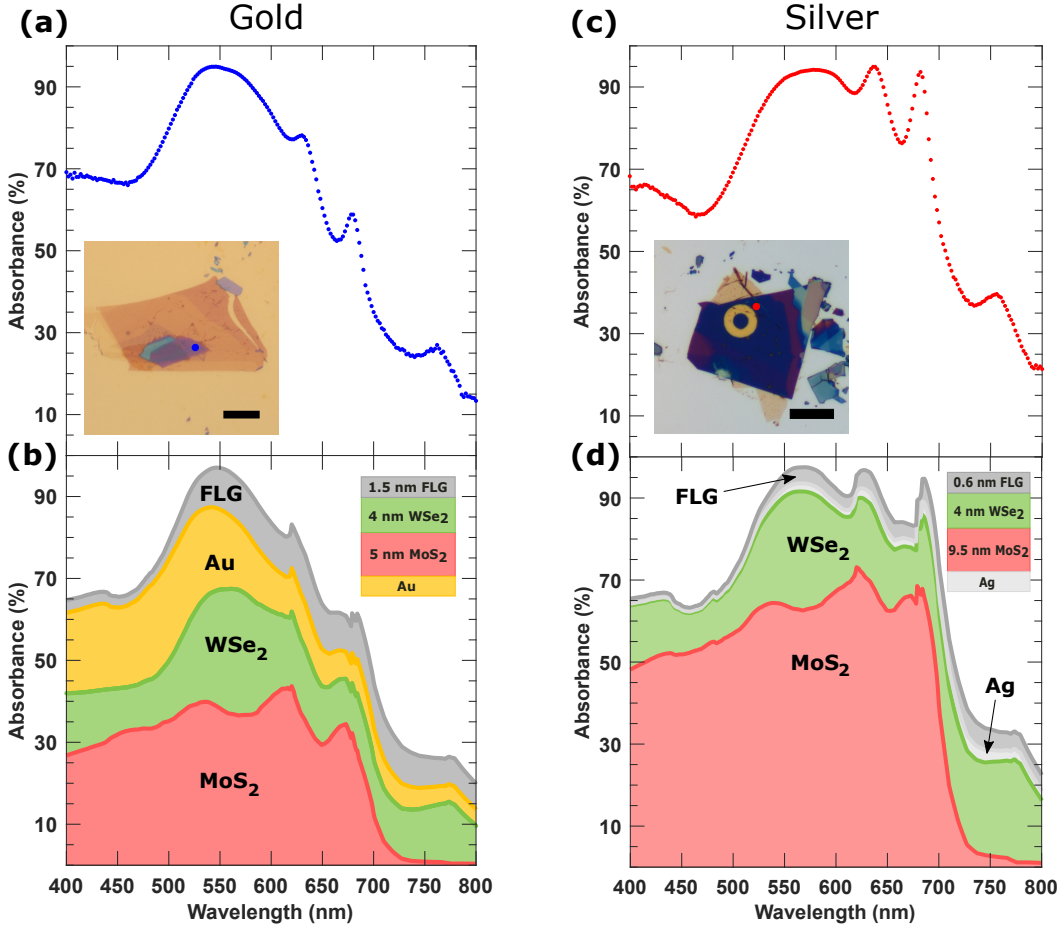


**Figure 4.5: Absorbance in van der Waals heterostructures.** **a** Experimentally measured absorbance of the 1.5 nm FLG/4 nm WSe<sub>2</sub>/5 nm MoS<sub>2</sub>/Au stack as a function of wavelength. The inset is an optical micrograph of the fabricated van der Waals heterostructure (scale bar = 20  $\mu$ m) with the blue dot corresponding to the spot of spectral measurement. **b** The simulated absorbance of the structure in **a** partitioned into the fraction of absorbance going into individual layers of the heterostructure stack. The inset is a cross-sectional schematic of the simulated and measured heterostructure. **c** Experimentally measured absorbance of the 0.6 nm FLG/4 nm WSe<sub>2</sub>/9.5 nm MoS<sub>2</sub>/Ag stack as a function of wavelength. The inset is an optical micrograph of the fabricated van der Waals heterostructure (scale bar = 20  $\mu$ m) with the red dot corresponding to the spot of spectral measurement. **d** Same as in **b** except the simulated absorbance is for the sample fabricated on silver as shown in **c**.

absorption characteristics (Figure 4.5a), revealing near-unity absorption in van der Waals heterostructures. The peaks at  $\sim$ 610,  $\sim$ 670, and  $\sim$ 770 nm correspond to the resonant excitation of the MoS<sub>2</sub> B exciton, MoS<sub>2</sub> A exciton, and WSe<sub>2</sub> A exciton, respectively.[104] On the other hand, the broad mode at  $\sim$ 550 nm corresponds to

the photonic mode that leads to near-unity absorption.[80] Measurements of the absorption can be corroborated with electromagnetic simulations, unveiling both the accuracy between simulation and experimental results as well as the fraction of photon flux absorbed into individual layers of the heterostructure stack (Figure 4.5b). Despite the near-unity absorption observed in the heterostructure stack, there is parasitic absorption in both the underlying gold substrate and in the few-layer graphene that accounts for 20% of the total absorbance. Such parasitic absorption can be reduced by using a silver back reflector, as shown in Figure 4.5c and Figure 4.5d. We find that the simulated and measured absorbance is also in good agreement for the case of a silver back reflector. Thus, the optical response of a van der Waals heterostructure can be modelled accurately using full wave electromagnetic simulations and our method of measurement yields accurate and reliable results.

To note, the subwavelength dimension of the total heterostructure thickness is critical for achieving near-unity absorption. Indeed, the entire stack can be treated as a single effective medium, where small phase shifts are present between layers and therefore the material discontinuities are effectively imperceptible to the incident light (see Supplementary Information S3 for details). Ultimately, the van der Waals heterostructure-on-metal behaves as a single absorbing material with effective medium optical properties. Therefore, as previously demonstrated, near-unity absorption at different wavelengths can be achieved for a semiconducting layer with the appropriate thickness [80, 88] ( $\sim 10 - 15$  nm total thickness for TMD heterostructures).

#### 4.8 Carrier collection efficiency in van der Waals semiconductor junctions

As discussed above, another criterion for high EQE is efficient carrier collection. Given the large exciton binding energies in TMDs ( $\sim 50 - 100$  meV in the bulk), [92, 169] the large internal electric field at the semiconductor heterojunction may play a role in exciton dissociation and subsequent carrier collection. Charge carrier separation in TMDs can be accomplished using either a pn junction or a Schottky junction, and we find that a pn heterojunction dramatically enhances the EQE when compared with a Schottky junction. The heterostructure described in Figure 4.5a and b can be probed as an optoelectronic device with the formation of a top electrode (see inset of Figure 4.6). Since the back reflector (gold) can simultaneously serve as a back contact to the entire vertical heterostructure, we can use this scheme to compare the electronic performance of various vertical heterostructures. Given the

work function between  $\text{WSe}_2$  (p-type) and Au, it is expected that a Schottky junction [130] will form between the two materials (See [Figure 4.1c](#)), whereas  $\text{WSe}_2$  (p-type) on top of  $\text{MoS}_2$  (n-type) is expected to form a pn heterojunction. [101] High spatial resolution scanning photocurrent microscopy allows us to examine the two heterostructure devices in detail ([Figure 4.6a](#)). We observe large photocurrent for the pn heterojunction geometry (yellow region) compared to the Schottky junction geometry (light blue region). The decrease of the photocurrent in the left-side of the yellow region in [Figure 4.6a](#) is due to shadowing from the electrical probes. A line cut of the spatial photocurrent map shown in [Figure 4.6b](#) provides a clearer distinction between the two junctions, demonstrating 6x more photocurrent for the pn junction relative to the Schottky junction.

The photocurrent density is directly related to the external quantum efficiency and therefore the product of the absorbance and IQE. In order to quantitatively compare the electronic differences between the two junctions, we need to normalize out the different optical absorption in the two devices, i.e. compute the IQE of each device

$$IQE_{Exp}(\lambda) = \frac{EQE(\lambda)}{Abs(\lambda)} \quad (4.2)$$

where  $EQE(\lambda)$  and  $Abs(\lambda)$  are the experimentally measured EQE and absorbance of their respective devices ([Figure 4.6c,i](#) and [Figure 4.6d,i](#)). A plot of the experimentally derived IQE (i.e.  $IQE_{Exp}$ ) is shown in purple in [Figure 4.6c,ii](#) and [Figure 4.6d,ii](#). This plot also confirms that a pn junction geometry (with  $IQE_{Exp} \sim 40\%$ ) formed of van der Waals materials is more efficient for carrier collection than a Schottky junction geometry (with  $IQE_{Exp} \sim 10\%$ ).

Embedded in the above analysis is yet another convolution of the optical and electronic properties. As per [Figure 4.5b](#), we found that absorption in FLG and Au accounted for  $\sim 20\%$  of the absorbance of the total heterostructure. Assuming very few photons absorbed in those layers ultimately are extracted as free carriers (i.e.  $IQE_{Au} \approx IQE_{FLG} \approx 0$ ), the IQE defined above convolutes the parasitic optical loss with the electronic loss in the device. [6] Thus another useful metric we shall define is  $IQE_{Active}$ , the active layer IQE:

$$IQE_{Active}(\lambda) = \frac{EQE(\lambda)}{Abs(\lambda) - Abs_P(\lambda)} \quad (4.3)$$

where the additional term  $Abs_P(\lambda)$  corresponds to the parasitic absorption in the other layers of the device that do not contribute to current (i.e., Au and FLG in this device). Thus,  $IQE_{Active}(\lambda)$  is a measure of the carrier generation and collection efficiency only in the active layer (i.e., WSe<sub>2</sub> and MoS<sub>2</sub>) of the device and is purely an electronic efficiency as defined above. We shall use this quantity to accurately compare electronic geometries. Given the good agreement between simulations and experiment shown in [Figure 4.5](#), a simple method of estimating the parasitic absorption described above is therefore through electromagnetic simulations.  $IQE_{Active}$  of the Schottky and pn heterojunction geometries calculated with [Equation 4.3](#) is shown in [Figure 4.6c,ii](#) and [Figure 4.6d,ii](#) with dotted green curves.

### Effects of a pn heterojunction

Analysis of these plots reveals several important points. First,  $IQE_{Active}$  for the pn junction geometry is 3x higher than in the Schottky junction geometry when spectrally averaged. Though yet to be fully clarified, we attribute higher IQE in pn heterojunctions to the larger electric fields in a pn heterojunction that may lead to a higher exciton dissociation efficiency and consequently IQE. Second, compared to the IQE which included the parasitic absorption (purple dots in [Figure 4.6c,ii](#) and [Figure 4.6d,ii](#)), the active layer IQE curves (green dots) are spectrally flat within measurement error and calculations ( $\delta IQE/IQE \approx 0.07$ ). Thus, the few broad peaks around the exciton energies of WSe<sub>2</sub> (~770 nm) and MoS<sub>2</sub> (~610 nm and ~670 nm) in  $IQE_{Exp}$  are not attributed to, e.g., resonant excitonic transport phenomena, but rather as a simple convolution of the optical and electronic effects when calculating the electronic IQE. In other words, consideration of parasitic absorption is critical when analyzing the electronic characteristics of thin optoelectronic devices. However,  $IQE_{Exp}$  is still a useful metric, as it effectively sets a lower bound on the true IQE. Generally, we expect  $IQE_{Exp} \leq IQE_{True} \leq IQE_{Active}$ , as electromagnetic simulations tend to slightly overestimate the absorption when compared with experimental results. Thus in this paper, we shall plot both expressions when comparing different electronic device geometries. Finally, it is important to mention that an active layer IQE of 70% is achieved in van der Waals heterostructures without complete optimization of the electronic configuration of the device, such as the band profiles and the specific choice of contacts. With careful electronic design, we suggest it may be possible to achieve active layer IQEs > 90%.

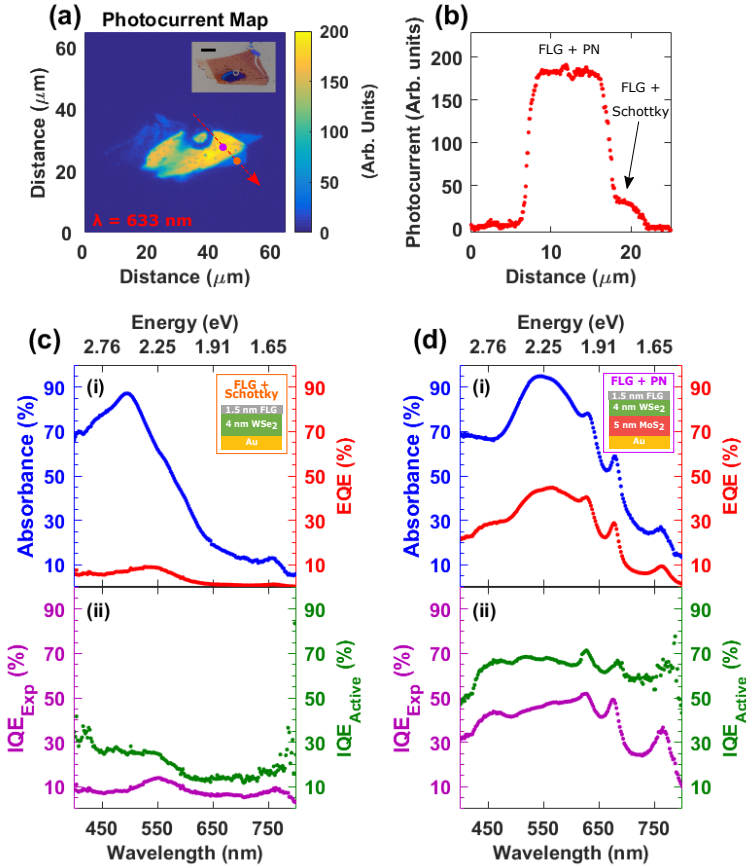


**Figure 4.6: Charge transport and collection in vertical PN and Schottky junction geometries.** **a** Spatial photocurrent map of the fabricated van der Waals heterostructure device using a 633 nm laser excitation. The inset is an optical image of the device (scale bar = 20  $\mu\text{m}$ ). **b** The line profile of the dotted red line arrow in **a**, illustrating the different photocurrent intensities depending on the device geometry (Schottky and pn junction). **c** (i) Experimentally measured spectral characteristics of the absorbance (blue) and external quantum efficiency (red) in the 1.5 nm FLG/4 nm WSe<sub>2</sub>/Au (Schottky geometry) device along with the (ii) experimentally derived internal quantum efficiency (purple) and the calculated active layer internal quantum efficiency (green). The inset is a cross-sectional schematic of the measured device, at the orange dot in **a**. **d** Same as in **c** except with a 1.5 nm FLG/4 nm WSe<sub>2</sub>/5 nm MoS<sub>2</sub>/Au (pn geometry) device. The inset is a cross-sectional schematic of the measured device, at the purple dot in **a**.

### Optically transparent contacts for carrier extraction

As another aspect of analysis, we studied the role of vertical carrier collection compared to lateral carrier collection in van der Waals heterostructures. Graphene and its few-layer counterpart can form a transparent conducting contact allowing for vertical carrier collection, in contrast to in-plane collection (see Figure 4.1d).

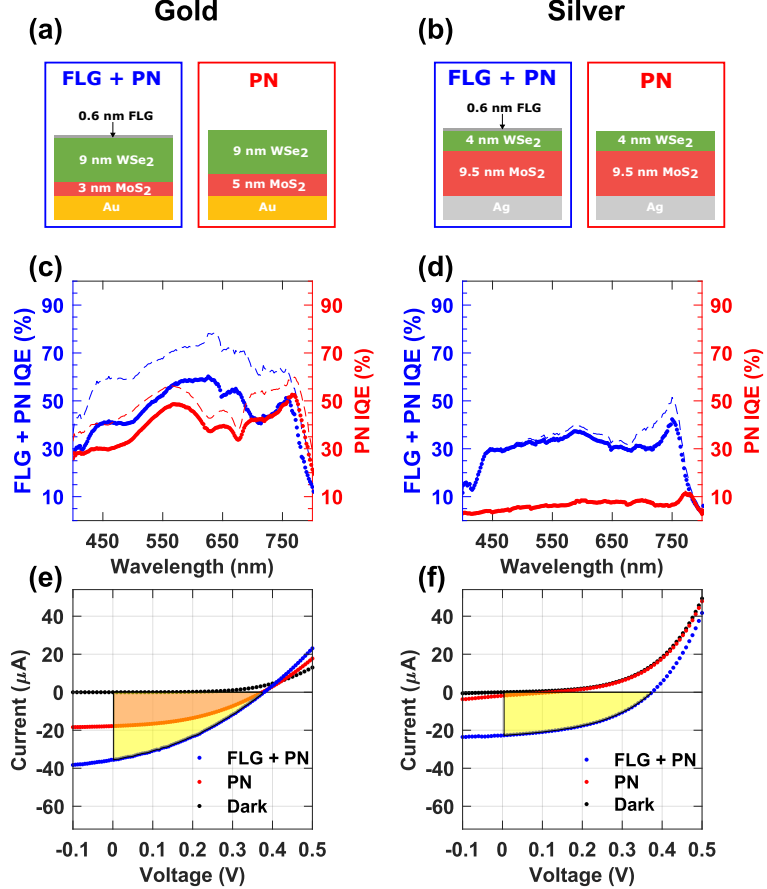


**Figure 4.7: Few-layer graphene as a transparent top contact.** **a** Cross-sectional schematic of the two structures (with and without few layer graphene) compared on gold and **b** silver back reflectors. **c** Experimentally derived internal quantum efficiency (dots) and active layer internal quantum efficiency (dashed line) for a pn junction geometry with (blue) and without (red) few layer graphene on gold. **d** is the same as **c** except on silver, corresponding to the sample shown in **b**. **e** I-V curves of a pn junction geometry with (blue) and without (red) few-layer graphene under 633 nm ( $\sim 180 \mu\text{W}$ ) laser illumination on a gold and **f** silver substrate. The shaded yellow and orange regions correspond to where there is a net generated power in the device.

The strong, in-plane covalent bonds of van der Waals materials suggest that in-plane conduction may be favorable when contrasted with the weak out-of-plane van der Waals interaction. However, the length scale for carrier transport in-plane ( $\sim \mu\text{m}$ ) is orders of magnitude larger than in the vertical direction ( $\sim \text{nm}$ ). Therefore, transport in a regime in between these two limiting cases is not surprising.

Silver exhibits lower absorption in the visible than gold, suggesting it could be

an optimal back reflector for photovoltaic devices, as seen in [Figure 4.5](#). Thus, we contrast the case of in-plane and out-of-plane conduction concurrently with the presence of two different back reflectors that simultaneously function as an electronic back contact (gold vs. silver) to a pn heterojunction, as in [Figure 4.7a and b](#). Optical and photocurrent images of the devices are shown in [Figure 4.2](#).

Our results in [Figure 4.7c](#) and d show the distinctions between the various contacting schemes. In the case of both silver and gold, a transparent top contact such as few-layer graphene seems to enhance the carrier collection efficiency. This is particularly true in the case of silver, where  $IQE_{Active}$  enhancements of  $\sim 5\times$  is apparent. In the case of gold, the IQE is enhanced by about  $\sim 1.5\times$  when parasitic absorption is taken into account. By analyzing the work functions of gold ( $\sim 4.83$  eV [\[3\]](#)) and silver ( $\sim 4.26$  eV [\[49\]](#)), along with the electron affinity of  $\text{MoS}_2$  ( $\sim 4.0$  eV [\[72\]](#)), the Schottky-Mott rule suggests in both cases that a Schottky barrier should form equal to  $\phi_B = \phi_M - \chi$ , [\[10\]](#) where  $\phi_B$  is the Schottky barrier height,  $\phi_M$  is the work function of the metal, and  $\chi$  is the electron affinity of the semiconductor. However, several reports [\[78, 79, 109\]](#) have indicated that gold appears to form an electrically Ohmic contact to  $\text{MoS}_2$ , which we observe here. Conversely, the above data suggests that silver and  $\text{MoS}_2$  follow the traditional Schottky-Mott rule, leading to the formation of a small Schottky barrier of  $\sim 0.26$  eV. Given that the energy barrier is about  $10k_bT$ , very few electrons can be extracted out of the pn heterojunction when silver is used as a back contact, leading to very low IQEs. By taking into account just the active layer (dashed lines), we see that gold is  $\sim 2\times$  better as an electronic contact than silver.

Finally, we examine the role of vertical carrier collection on the I-V characteristics of the two devices ([Figure 4.7e](#) and f). In the case of gold, we see purely an enhancement of the short circuit current with vertical carrier collection. On the other hand, vertical carrier collection for silver drastically increases both the short circuit current density and the open circuit voltage. This phenomenon is consistent with the previously described nature of gold (Ohmic) and silver (Schottky) contacts. Namely, on silver in the absence of a transparent top contact, due to both the Schottky barrier and the large in-plane propagation distance, carriers are collected with poor efficiency leading to a small  $I_{sc}$ . Consequently, a high recombination rate of the generated carriers which are inefficiently extracted leads to small  $V_{oc}$  values. On the other hand, even in the absence of a top transparent electrode, gold enables efficient extraction of electrons from the pn heterojunction as an Ohmic

contact. Thus, the short circuit current and open-circuit voltage in gold are higher compared to the silver back contact, even in the absence of a transparent electrode. When introducing few-layer graphene as a transparent top contact, the propagation distance is significantly reduced in the silver device and carriers can be extracted with much higher efficiency, leading to a large enhancement of both the current and voltage. Whereas for gold, the few-layer graphene enhances the already high carrier collection (yielding larger  $I_{sc}$ ) but only has a negligibly small enhancement effect on the open-circuit voltage. Overall, these results demonstrate that vertical carrier collection plays a crucial role in high photovoltaic device performance in van der Waals heterostructures.

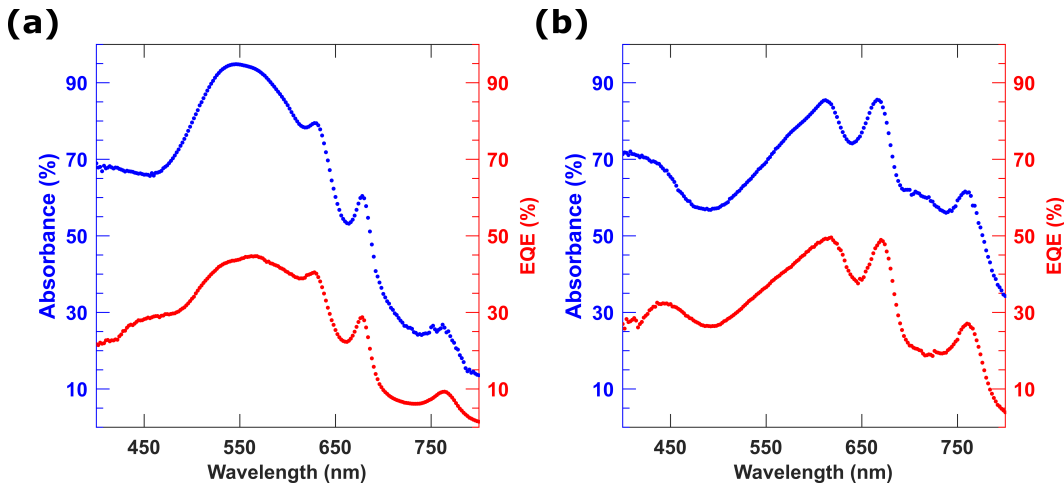


**Figure 4.8: Absorbance and EQE of thick and thin PN heterojunctions.** **a** Experimentally measured absorbance (blue) and EQE (red) of the thin pn heterojunction (1.5 nm FLG/4 nm WSe<sub>2</sub>/5 nm MoS<sub>2</sub>/Au). **b** Same as in **a** except for a thick pn heterojunction (11 nm hBN/1.5 nm FLG/4 nm WSe<sub>2</sub>/9 nm MoS<sub>2</sub>/Au).

### Thickness dependence on charge collection efficiency

As a final point of analysis, we briefly examined the effect of thickness on  $IQE_{Active}$  under vertical carrier collection. We compared the optoelectronic characteristics of a thicker pn heterojunction (11 nm hBN/1.5 nm FLG/4 nm WSe<sub>2</sub>/9 nm MoS<sub>2</sub>/Au) with a thinner pn heterojunction (1.5 nm FLG/4 nm WSe<sub>2</sub>/5 nm MoS<sub>2</sub>/Au). The experimentally measured absorbance and EQE are plotted in Figure 4.8 for reference. By normalizing out the differences in absorption between the pn junctions, we see a somewhat surprising result when we analyze the active layer IQE (dashed lines, Figure 4.9). In particular, despite the roughly 50% more length in active layer thicknesses (13 nm vs. 9 nm) and qualitatively different absorbance and EQE

spectra, the thick pn junction exhibits nearly the same active layer IQE compared to the thin pn junction. In fact, it appears to be slightly more efficient, but this is within the error bar of the measurement and simulations ( $\delta \text{IQE}/\text{IQE}_0 \approx .07$ , see [section 4.5](#) for details of errors). This observation is corroborated with the experimentally derived IQE (dotted curves, [Figure 4.9](#)), which has nearly the same spectrum between the two thicknesses, but differ in magnitude due to differences in parasitic absorption. This result suggests that in the ultrathin limit ( $\sim 10$  nm) of van der Waals heterostructures with vertical carrier collection, the IQE has a weak dependence on active layer thickness. This weak dependence may be due to a combination of increased scattering competing with charge transfer, [26, 228] tunneling, [57, 101, 218] and exciton quenching [15, 20] effects as the vdW heterostructure becomes thicker. The exact role of each of these effects, as well as possibly other effects, will require a new theoretical framework and experimental measurements to analyze their relative contributions to charge collection efficiency.

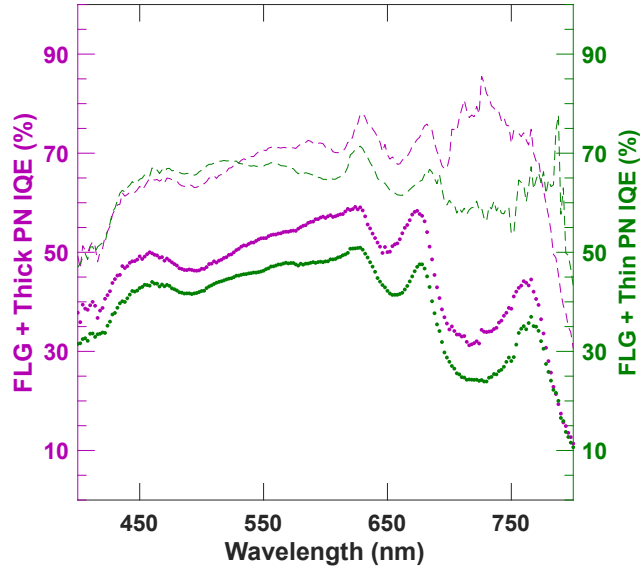


**Figure 4.9: Thickness dependence on charge collection efficiency.** The estimated active layer (dashed lines) and experimentally derived (solid dots) internal quantum efficiency of the thin pn junction device (1.5 nm FLG/4 nm WSe<sub>2</sub>/5 nm MoS<sub>2</sub>/Au, green) and the thick pn junction device (11 nm hBN/1.5 nm FLG/4 nm WSe<sub>2</sub>/9 nm MoS<sub>2</sub>/Au, purple).

#### 4.9 High Photovoltaic Quantum Efficiency Outlook

Our results suggest important challenges that must be addressed to enable high photovoltaic efficiency. For example, despite the usefulness of gold as an electrical back

contact, we found from electromagnetic simulations that it accounts for nearly 20% of the parasitic loss in the heterostructures reported here. Schemes using optically transparent carrier selective contacts could be used to avoid this parasitic optical loss. Another open question is the role and importance of exciton dissociation and transport. Indeed, the large exciton binding energies in transition metal dichalcogenides ( $\sim 50\text{--}100$  meV in the bulk) [92, 169] suggests that a significant exciton population is generated immediately after illumination. However, it is not yet clear whether such an exciton population fundamentally limits the internal quantum efficiency of the device, posing an upper limit on the maximum achievable EQE in van der Waals materials based photovoltaic devices. Finally, the problem of open-circuit voltage must also be addressed. For example, the type-II band alignment between ultrathin  $\text{MoS}_2$  and  $\text{WSe}_2$  suggests a renormalized bandgap of  $\sim 400\text{--}500$  meV, [85] given by the minimum conduction band energy and maximum valence band energy of the two materials. In accordance with the Shockley-Queisser limit, this would severely reduce the maximum power conversion efficiency attainable by a factor of  $\sim 3$ . Therefore, to achieve higher open circuit voltages, a monolithic device structure may be required to avoid low energy interlayer recombination states.

However, our results described here also suggest a different approach in addressing the optical and electronic considerations for ultrathin van der Waals heterostructures when compared with conventional photovoltaic structures. For example, our observation that ultrathin van der Waals heterostructures can be optically treated as a single effective medium is a regime of optics that is uncommon for the visible to near-infrared wavelengths analyzed in photovoltaic devices. Likewise, our observation of weak thickness dependence of the charge collection efficiency represents a realm of electronic transport that is also quite unconventional and unexplored when compared to traditional photovoltaic structures. Thus, the combination of the above observations may enable entirely different photovoltaic device physics and architectures moving forward.

To summarize, we have shown that external quantum efficiencies  $> 50\%$  and active layer internal quantum efficiencies  $> 70\%$  are possible in vertical van der Waals heterostructures. We experimentally demonstrated absorbance  $> 90\%$  in van der Waals heterostructures with good agreement to electromagnetic simulations. We further used the active layer internal quantum efficiency to quantitatively compare the electronic charge collection efficiencies of different device geometries made with van der Waals materials. By further reducing parasitic optical losses and performing

a careful study on exciton dissociation and charge transport while simultaneously engineering the band profiles and contacts, van der Waals photovoltaic devices may be able to achieve external quantum efficiencies  $> 90\%$ . Our results presented here show a promising and exciting route to designing and achieving efficient ultrathin photovoltaics composed of van der Waals heterostructures.

#### 4.10 Appendix

##### Diode Equation Fitting

A diode model is commonly used to examine the characteristics of photovoltaic devices. Here, we assume a single diode model with a series and shunt resistance as a simple model to understand the photovoltaic device characteristics

$$I(V) = I_{dark} \left( \exp \left( \frac{q(V - IR_s)}{nk_b T} \right) - 1 \right) + \frac{V - IR_s}{R_{sh}} - I_L \quad (4.4)$$

where  $I_{dark}$  is the dark current,  $q$  is the fundamental charge constant ( $1.602 \times 10^{-19}$  C),  $n$  is the ideality factor,  $k_b$  is the Boltzmann constant ( $1.38 \times 10^{-23}$  J/K),  $T$  is the thermodynamic temperature (300 K, for this case),  $R_s$  is the series resistance,  $R_{sh}$  is the shunt resistance, and  $I_L$  is the generated current from the photovoltaic effect under illumination. Here,  $V$  is the applied voltage and  $I$  is the measured current. At short circuit,  $V = 0$  and  $I = I_{sc}$ . Thus,

$$I_L = I_{dark} \left( \exp \left( \frac{-qIR_s}{nk_b T} \right) - 1 \right) - \frac{IR_s}{R_{sh}} - I_{sc} \quad (4.5)$$

For the case  $R_s = 0$ , we recover the usual expression  $I_L = -I_{sc}$ . We use the above two expressions along with the measured short circuit current  $I_{sc}$  to perform a four parameter ( $n, I_{dark}, R_s, R_{sh}$ ) fit to the open circuit voltage  $V_{oc}$  and the power conversion efficiency  $\eta = P_{device}/P_{input}$  as a function of input power. Here, we have explicitly measured the input power of the laser illumination. The fitted parameters are listed in [Figure 4.4b](#) and [Figure 4.4c](#) in the main manuscript, and are used to generate the dashed lines in those plots. Note that we use the same fitted parameters for both data sets. It is also important to note that by fitting the parameters under illumination at various powers, we expect the fitted parameters to represent primarily the device characteristics that are probed by laser illumination, and not all the other devices that are in parallel (which would be the case if we fitted to the dark IV).

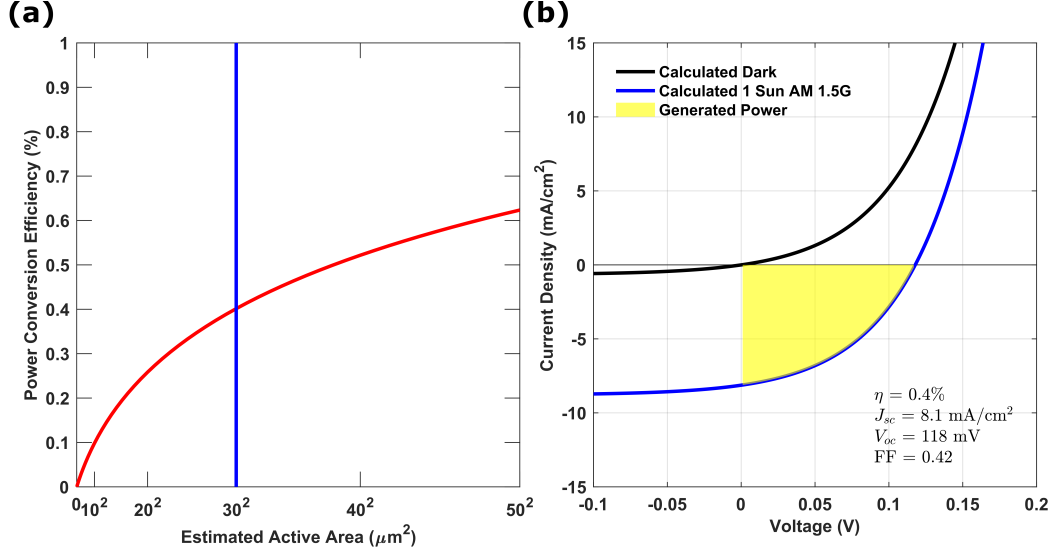


Figure 4.10: **a** Estimated 1 Sun AM 1.5G power conversion efficiency of the device measured in [Figure 4.3](#) and [Figure 4.4](#) as a function of estimated active area. The blue line corresponds to a  $30 \times 30 \mu\text{m}^2$  estimated active area used for the plot in **b**. **b** The estimated J-V curve of the device studied in [Figure 4.3](#) and [Figure 4.4](#) in the dark (black line) and under 1 Sun AM 1.5G illumination (blue) assuming a  $30 \times 30 \mu\text{m}^2$  active area. Estimated device characteristics are in the bottom right-hand corner of the plot.

### Simulated AM1.5G and Effects of Active Area on Efficiency Estimation

To estimate the power conversion efficiency under AM 1.5G illumination for the particular device, we use the expression:

$$I_{sc} = -qA \int_{400 \text{ nm}}^{800 \text{ nm}} EQE_{exp}(\lambda) S_{AM1.5G}(\lambda) d\lambda \quad (4.6)$$

where  $q$  is the fundamental charge constant ( $1.602 \times 10^{-19} \text{ C}$ ),  $A$  is the estimated active area,  $EQE_{exp}$  is the experimentally measured EQE for the device, and  $S_{AM1.5G}$  is the solar photon flux (in units of photons  $\text{m}^{-2} \text{ s}^{-1} \text{ nm}^{-1}$ ). Using the above fitted parameters and the calculated  $I_{sc}$ , we can simulate the  $I(V)$  characteristics of the device. We take  $J(V) = I(V)/A$  and calculate the power conversion efficiency  $\eta$  as

$$\eta = \frac{J_m V_m}{\int_0^{\infty} \left(\frac{hc}{\lambda}\right) S_{AM1.5G}(\lambda) d\lambda} \quad (4.7)$$

where  $J_m$ ,  $V_m$  is the current density and voltage at the maximum power point, respectively, and the denominator of the above expression represents the total incident power of solar irradiation ( $S = \int_0^{\infty} \left(\frac{hc}{\lambda}\right) S_{AM1.5G}(\lambda) d\lambda = 1000 \text{ W m}^{-2}$ ). We plot this

as a function of estimated active area  $A$  in [Figure 4.10a](#). Note that with increasing estimated active area, we observe an increase in the power conversion efficiency.

Here, the active area effectively reduces the dark current density  $J_{dark} = I_{dark}/A$  for increasing  $A$ , and therefore leads to a concentration-like effect on the power conversion efficiency. Thus, there is a logarithmic dependence of  $\eta$  on the active area  $A$  and therefore  $\eta$  varies weakly with  $A$ . Moreover, the above analysis for  $A$  also allows us to estimate the appropriate area for the simulated device performance, as this is not the area under illumination, but rather the area from which dark current, series resistance, and shunt resistance contribute to the total measured current (i.e., the total sample size). We estimate this area to be in the range of  $20^2 - 40^2 \mu\text{m}^2$  from the optical image ([Figure 4.2](#)) and plot the  $J - V$  characteristics assuming a  $30 \times 30 \mu\text{m}^2$  active area below ([Figure 4.10b](#)). Typical photovoltaic figures of merit are also shown. We achieve  $J_{sc} > 8 \text{ mA/cm}^2$  under 1 sun illumination. This value depends only on the experimentally measured EQE and does not depend on any fitting parameters, as evident in [Equation 4.6](#). However, the expected  $V_{oc}$  and  $FF$  are sub-optimal, due to the type-II band alignment and high series resistance of the device. Thus, despite having fairly large short circuit current densities, device performance is limited primarily by the open circuit voltage and fill fraction, leading to an overall predicted  $\eta_{AM1.5G} \approx 0.4\%$ .

The above analysis differs from the typical experimental scenario where we estimate the input power as  $P_{input} = SA$ , where  $S = 1000 \text{ W m}^{-2}$  and  $A$  is the illumination area. Thus, the experimental efficiency is given as  $\eta = P_{m,exp}/P_{input}$ , where  $P_{m,exp}$  is the maximum power of the experimentally measured device. In the experimental case,  $A$  is optimally the solar illumination area through some well-calibrated aperture. [\[176\]](#) In this case, the power conversion efficiency is inversely proportional to the estimated active area and therefore leads to larger  $J_{sc}$  and  $\eta$  for smaller  $A$ . This is a common source of error in estimating  $\eta$  for small devices, as  $|\delta\eta|/\eta = |\delta A|/A$ , with the error in efficiency  $\delta\eta$  depending linearly with the error in active area estimation  $\delta A$ . Particularly for micron and nano-scale devices such as in van der Waals materials, particular care must be taken to avoid errors in measuring and calculating the power conversion efficiency, as discussed by Snaith et al. in [\[176\]](#). Here, we show a distribution of efficiencies based on our active area estimation, leading to AM 1.5G power conversion efficiencies between 0.25% to 0.5%. For our above calculation methodology, we can derive the error dependence to be roughly  $|\delta\eta|/\eta \approx |\delta A|/A \left( \frac{nk_b T}{qV_{oc}} \right)$ , where the extra factor of  $nk_b T/(qV_{oc})$

comes from the dependence of  $\eta$  with an estimated  $V_{oc}$ , rather than  $J_{sc}$ . The low values of absolute efficiency and logarithmic dependence on active area using our calculation methodology imply a weak dependence of the error on estimated active area, and thus suggests our calculated performance is a reasonable estimate for an experimental AM 1.5G measurement.

## SPATIOTEMPORAL IMAGING OF THICKNESS-INDUCED BAND BENDING JUNCTIONS

*“Discovery consists in seeing what everyone else has seen and thinking what no one else has thought.”*

— Albert Szent-Györgyi

### 5.1 Introduction

Band bending in semiconductors is a fundamental consequence of incomplete screening of external fields and is critical to the operation of nearly every electronic and optoelectronic device. Its existence was theoretically proposed by the works of Mott and Schottky [128, 171] who argued that the electrostatic landscape must have electronic bands that “bend” to compensate the difference in Fermi levels at an interface to minimize the overall free energy in the system. Mott also discovered that a characteristic length scale for the band bending in semiconductors is given by

$$L_D = \sqrt{\frac{\epsilon_S \epsilon_0 k_b T}{q^2 \rho_0}} \quad (5.1)$$

which is now commonly referred to as the Debye screening length, named after Peter Debye who discovered the same length scale earlier in electrolytes. [41]  $L_D$  usually ranges from 10s of nm to a few microns, depending on the doping concentration  $\rho_0$  and static dielectric constant  $\epsilon_S$ . Here,  $\epsilon_0$  is the permittivity of free space,  $k_b T$  is the thermal energy, and  $q$  is the fundamental unit of charge. In most semiconductor systems, the region where band bending occurs is referred to as the depletion or accumulation region.

Layered van der Waals materials such as the semiconducting transition metal dichalcogenides (TMDCs) are a unique system for studying band bending physics because of their highly passivated surfaces and the ability to form a wide assortment of heterostructures, which has enabled a variety of applications including transistors, solar cells, optical modulators, metasurfaces, and lasers. [37, 79, 143, 157, 190, 207] Furthermore, these materials can be easily cleaved to yield layers over a wide range

of thicknesses, ranging from a single monolayer to 100s of nm. The heterogeneity in sample thicknesses produced during mechanical exfoliation has led to novel ‘thickness’ junctions, i.e., junctions formed from the difference in quantum confinement in few-layer thick samples. [72, 185] Apparent thickness junctions have also been formed with materials whose thicknesses are thicker than the quantum confinement regime [146, 216], however, the mechanistic explanation for charge carrier separation for this regime of thicknesses remains unclear.

Further, despite considerable research on layered materials in the atomically thin limit in recent years, there has been to our knowledge no direct observation of ‘vertical’ band bending (i.e., in the direction perpendicular to heterostructure interfaces). This is primarily due to the weak out of plane as opposed to in-plane transport in layered materials and the difficulty to probe buried interfaces. Meanwhile, direct observation of band bending can be used to estimate depletion widths, interface barrier heights, and consequently be used to deduce the electrostatic landscape and performance of the corresponding device.

In this chapter, we show evidence for the first direct measurement of vertical band bending in a MoS<sub>2</sub>-Au interface. We directly observe correlations between the thickness and surface Fermi levels in samples with identical electronic bandstructures and preparation methods and find that the MoS<sub>2</sub>-Au interface results in a strong electron transfer to the MoS<sub>2</sub> layer. The direct observation of a surface potential difference between materials with differing thicknesses suggests that a new type of homojunction, arising solely from the differences in thickness and band bending, can be used to separate charge carriers. We directly observe this charge carrier separation spatiotemporally by utilizing scanning ultrafast electron microscopy and corroborate these observations with numerical simulations. The electrostatic landscape of materials that are comparable to or thinner than their electrostatic screening length can therefore be carefully tailored by control of their thicknesses, interfaces, and local geometry.

## 5.2 Correlation between Electronic Properties and Thickness in Ultrathin Semiconductors

To examine the interplay between interfaces, thicknesses, and band bending, we first consider theoretically a semiconductor on a metallic substrate surrounded by vacuum and solve Poisson’s equation

$$\nabla^2 \phi = -\frac{\rho}{\epsilon} \quad (5.2)$$

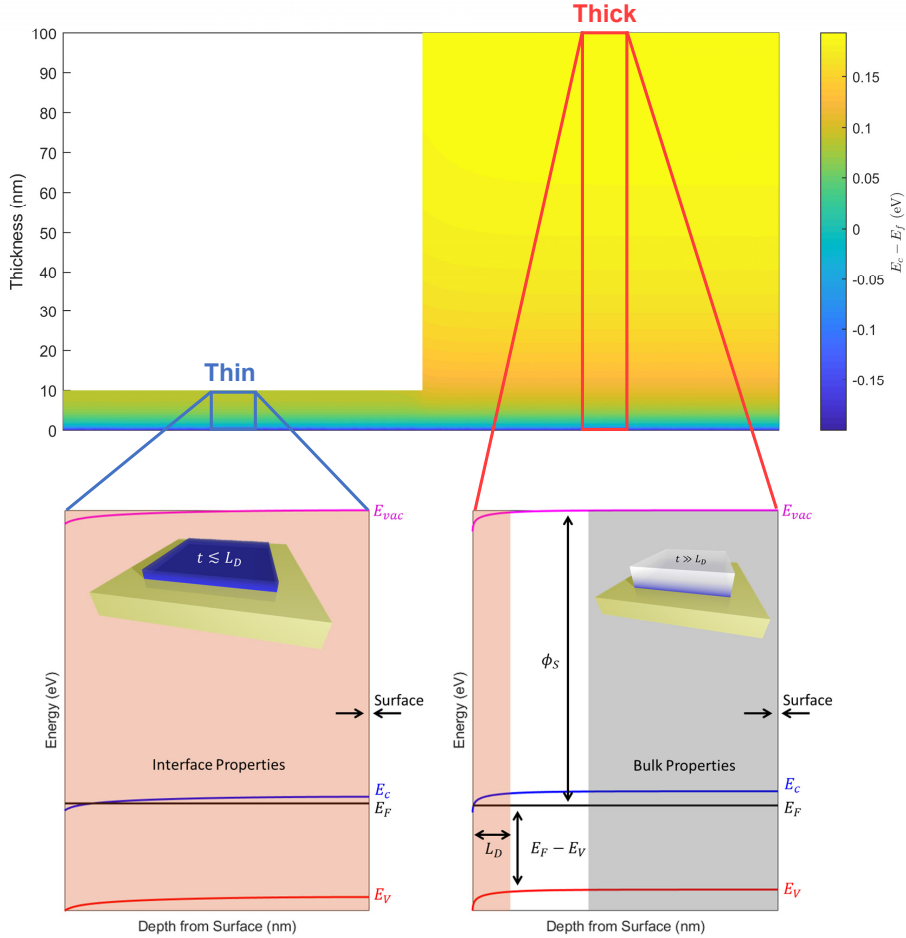


**Figure 5.1: Thickness-dependent surface potentials due to vertical band bending.** Calculated  $E_c - E_f$  band diagram for 10- and 100-nm-thick flakes of MoS<sub>2</sub> on Au assuming strong electron transfer at the MoS<sub>2</sub>/Au interface. Schematic band diagrams of a material dominated by its interface properties (bottom left) and bulk properties (bottom right), which depend on the thickness of the material relative to its electrostatic screening length ( $L_D$ ). Insets correspond to a schematic of a semiconductor (e.g., MoS<sub>2</sub>) on its substrate (e.g., Au), with the blue representing excess electron concentration relative to its bulk value. The surface of the material refers to the semiconductor-vacuum interface.

to calculate the energy band diagrams for differing thicknesses, as depicted in [Figure 5.1](#). As expected, we find the characteristic length scale to be the Debye screening length  $L_D$ , which we estimate to be approximately 40 nm for carrier concentrations corresponding to typical values for MoS<sub>2</sub>. Furthermore, our calculations suggest that layers that are thinner than their Debye screening length will have a surface potential that is directly related to its thickness. Importantly, this analysis requires

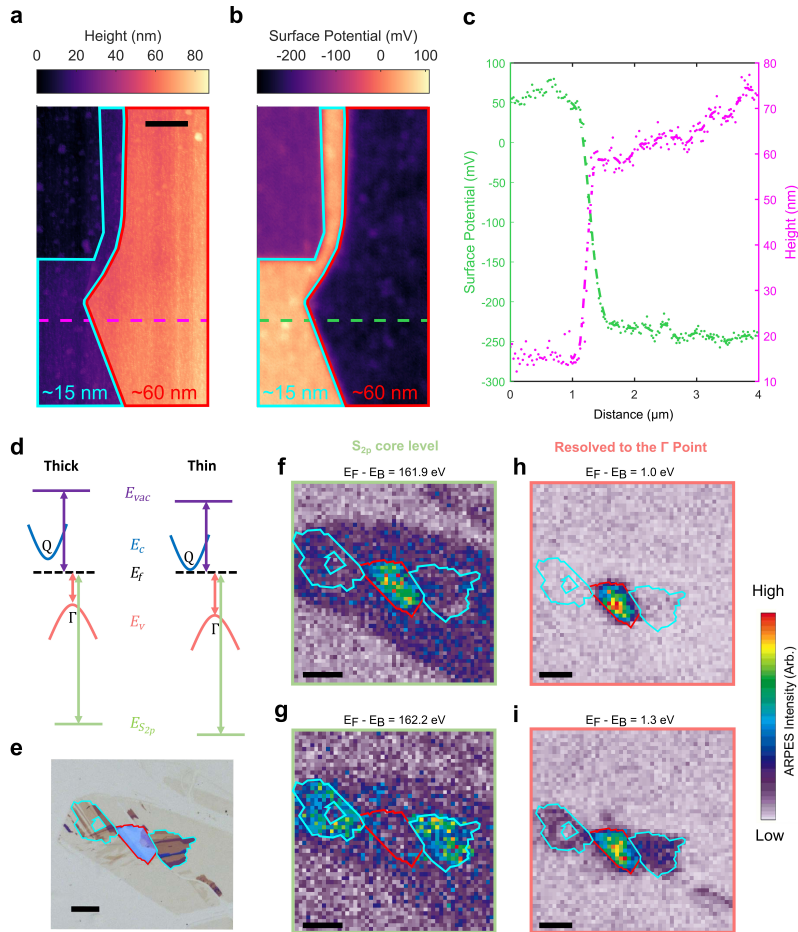


**Figure 5.2: Experimental observation of thickness-dependent surface doping in MoS<sub>2</sub>/Au.** **a** Topographic image of MoS<sub>2</sub> exfoliated onto a gold substrate with corresponding surface potential **b** mapped over the same area. The blue and red outlines correspond to a MoS<sub>2</sub> thickness of approximately 15 nm and 60 nm, respectively. The upper left region corresponds to monolayer MoS<sub>2</sub>/Au. Scale bar is 1  $\mu$ m **c** Linecut of the topography and surface potential. The dashed lines are guides for the eye. **d** Proposed energy diagram at the surface for the thin and thick MoS<sub>2</sub>. **e** Optical micrograph image of MoS<sub>2</sub> exfoliated onto a gold substrate. The thick (red outline) and thin (blue outline) regions are  $\sim$ 30 nm and  $\sim$ 5 nm thick, respectively. Intensity map of photoemitted electrons at the sulfur 2p core level for binding energies of 161.9 eV **f** and 162.2 eV **g**. Intensity map of photoemitted electrons from the valence band of MoS<sub>2</sub> resolved to its  $\Gamma$  point for binding energies of 1.0 eV **h** and 1.3 eV **i**. The thin (blue) and thick (red) flake outlines are superimposed. All scale bars in **e** – **i** are 50  $\mu$ m.

use of a material, like MoS<sub>2</sub>, with an absence of surface states and other contaminants at the top (basal-plane) semiconductor-vacuum interface that is typical in most three-dimensional materials due to the formation of dangling bonds. Van der Waals materials are therefore ideal for probing this thickness-dependent surface potential because of their naturally passivated surfaces.

To examine the effects of varying the semiconductor thickness on surface potential, we directly exfoliated MoS<sub>2</sub> on Au (see Methods for details). These exfoliated samples produce a variety of thicknesses that can be determined with atomic force microscopy (AFM) and Kelvin Probe Force Microscopy (KPFM), as shown in [Figure 5.2a](#) and [Figure 5.2b](#). These images clearly show a direct correlation between two different thicknesses of a MoS<sub>2</sub> flake (with thicknesses of about 15 nm and 60 nm), with correspondingly different surface potentials (50 mV and -230 mV), as shown in [Figure 5.2c](#). Importantly, these thicknesses are outside the realm where there are strong quantum confinement effects and therefore can be considered electronically as ‘bulk’ materials. [\[226\]](#) Since these two flakes were fabricated under the same conditions, we therefore attribute the difference in observed surface potentials to vertical band bending at the MoS<sub>2</sub>-Au interface. We further show this correlation between thickness and surface potential for a variety of thicknesses measured on other samples (See [Figure 5.3](#)).

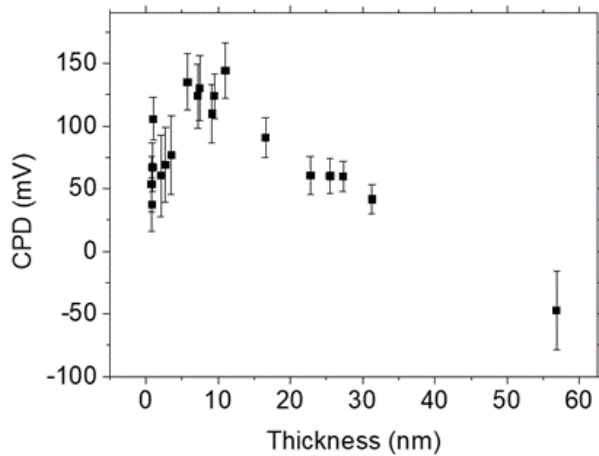


**Figure 5.3: Contact potential difference of other MoS<sub>2</sub> flakes on Au.** Measured contact potential difference of MoS<sub>2</sub> on Au for a variety of thicknesses. OmegaScope-R (AIST-NT) setup was used for KPFM with concurrent AFM measurement. Au tip was biased by 3 V and connected to a lock-in amplifier while the sample was grounded.  $R_a$  (arithmetic average) values were obtained from a standard sized region of each layer of flakes comprising  $300 \times 300$  points and the standard deviations in  $R_a$  values were plotted as error bars. The lateral areas (sizes) of the flakes ranged from  $20\text{-}50 \mu\text{m}^2$ .

The relative surface potential difference between the 15 nm and 60 nm sample is about 280 mV, suggesting strong electron transfer from the gold substrate to the ultrathin MoS<sub>2</sub> ([Figure 5.2d](#)). Strong electron transfer at the MoS<sub>2</sub>-Au interface appears contradictory to the well-known work function of Au ( $\sim 5.1$  eV), which

instead would suggest hole doping of the neighboring MoS<sub>2</sub> layer. However, recent works has shown that the MoS<sub>2</sub>-Au interface induces strong electron transfer [194, 195], particularly if the interface remains pristine during the exfoliation process, which has also enabled large area monolayer exfoliation of TMDCs and other 2D materials. [43, 76, 108, 116, 194]

To further examine this correlation between thickness and electronic properties, we perform spatially resolved angle-resolved photoemission spectroscopy (ARPES) at Beamline 7.0.2 at the Advanced Light Source (see methods) on another flake of MoS<sub>2</sub> on Au (Figure 5.2e). We find a direct correlation between the position of the sulfur 2p core levels and the thicknesses of the corresponding MoS<sub>2</sub> flakes (Figure 5.2f, g). The larger sulfur 2p binding energies for the thinner MoS<sub>2</sub> is suggestive of electron transfer at the MoS<sub>2</sub>-Au interface. Finally, we examine electron binding energies and momenta that correspond to the valence band edge, which occurs at the  $\Gamma$  point in Brillouin zone in electronically bulk samples. We find that while the thicker sample has a Fermi level of about 1 eV above the valence band edge, the Fermi level at the surface of the thinner sample is about 1.3 eV above its valence band edge (Figure 5.2h, i). Assuming an electronic bandgap of approximately 1.3 eV [117], we find direct evidence of strong electron transfer and vertical band bending at the MoS<sub>2</sub>-Au interface, which corroborates the KPFM results shown earlier. Similar results are also observed on another MoS<sub>2</sub> sample (See Figure 5.4). Given that the native doping of bulk MoS<sub>2</sub> is typically n-type, these results suggest the MoS<sub>2</sub>-Au interface would yield Ohmic n-type contacts by degenerately doping the neighboring MoS<sub>2</sub> region [78].

### 5.3 Spatiotemporal Imaging of Charge Carrier Separation due to Thickness

To investigate the effects of the different vertical band bending profiles on the charge carrier dynamics, we perform scanning ultrafast electron microscopy (SUEM) on another sample of MoS<sub>2</sub>/Au with a thin-thick junction of 10 nm and 100 nm, respectively (Figure 5.5b). Figure 5.5a shows a conceptual depiction of the SUEM measurement technique performed over this thin-thick junction. Briefly, SUEM is a pump-probe technique that uses an optical pump ( $\sim$ 514 nm) and an electron pulse ( $\sim$ 2 ps pulse width) that records the secondary electron emission with the presence of the optical pump as a function of pump-probe time delay. Contrast images can be formed at different time delays by subtracting the static SEM image (Figure 5.5c) from a similar SEM image formed with the optical pump on at a specific time delay  $\Delta t$ . The contrast in the secondary electron emission as a result of

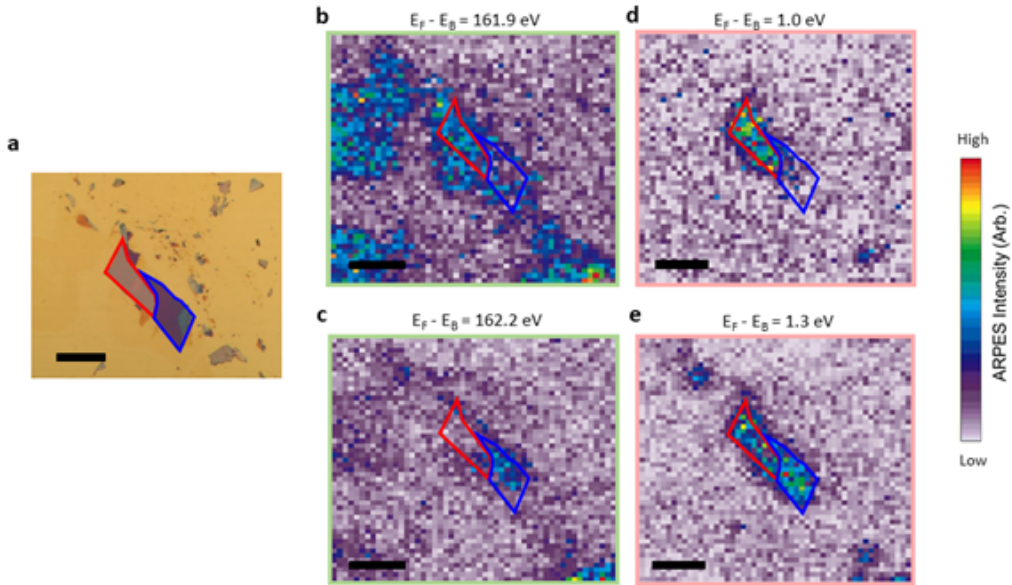


**Figure 5.4: Photoemission spectroscopy of another  $\text{MoS}_2$  flake on Au.** **a** Optical micrograph image of  $\text{MoS}_2$  exfoliated onto a gold substrate. Intensity map of photoemitted electrons at the sulfur 2p core level for binding energies of 161.9 eV **b** and 162.2 eV **c**. Intensity map of photoemitted electrons from the valence band of  $\text{MoS}_2$  resolved to its  $\Gamma$  point for binding energies of 1.0 eV **d** and 1.3 eV **e**. All scale bars are 50  $\mu\text{m}$ . Red and blue overlays correspond to thick and thin portions of the sample, respectively.

the optical pump beam has been interpreted as direct images of electron (blue) and hole (red) carrier populations under ultrafast excitation, which has been previously used to image carrier separation in pn junctions. [131] Similar methods to directly image ultrafast carrier dynamics has also been utilized in photoemission electron microscopy. [118, 206]

By examining the contrast images formed at different time delays via SUEM, we find direct evidence for carrier separation at a thin-thick junction (Figure 5.5d). First, the lack of carrier dynamics at negative time delays suggests appropriate background subtraction. At longer time delays, we initially find the appearance of excess holes (red contrast) on every thickness of  $\text{MoS}_2$  for  $\Delta t < 27$  ps. The oblong contrast profile is due to the beam shape of oblique excitation. At  $\Delta t = 33$  ps, there is a simultaneous occurrence of both excess holes and electrons on the thin (10 nm) sample, with the excess electrons located near the thin-thick junction. At slightly longer time delays ( $40 \text{ ps} < \Delta t < 60 \text{ ps}$ ), this population of excess electrons appears

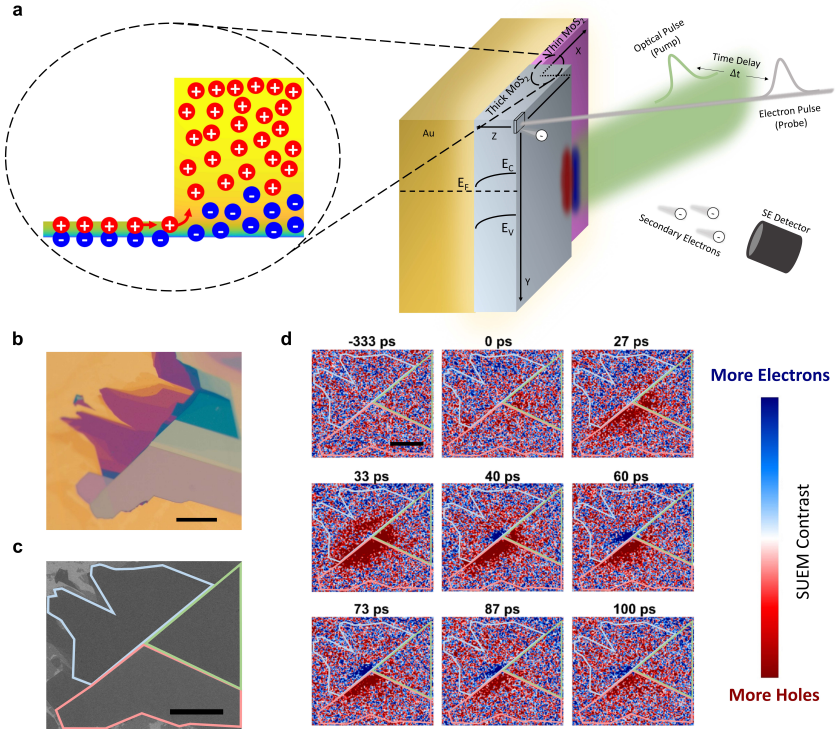


**Figure 5.5: Scanning Ultrafast Electron Microscopy Imaging of a Band Bending Junction.** **a** Conceptual depiction of the band bending junction and its measurement via scanning ultrafast electron microscopy (SUEM). In a sample with different thicknesses of MoS<sub>2</sub>, band bending induced by a gold substrate enables lateral carrier separation between electrons and holes. In SUEM, an optical pulse generates electron-hole pairs that subsequently evolve in space and time. An electron pulse is raster scanned across the surface of the sample for a given time delay  $\Delta t$  after the optical pulse. An image of the detected secondary electron (SE) intensity is formed. Contrast images are formed that correspond to the difference between the SE image at  $\Delta t$  relative to the SE image without an optical pulse. Contrast images are interpreted as images of the net charge density, i.e., increased (decreased) SE intensity corresponds to an increase in the local surface electron (hole) density. **b** Optical image of MoS<sub>2</sub> exfoliated onto a gold substrate. **c** Static scanning electron micrograph over the flake in **b**, with highlighted regions of thick (pink border,  $\sim 100$  nm), intermediate thickness (light green border,  $\sim 30$  nm) and thin (light blue border,  $\sim 10$  nm) MoS<sub>2</sub> on one sample. **d** Contrast images over the same area as **c** for different time delays, with corresponding MoS<sub>2</sub> flake outline. Blue and red contrasts are interpreted as excess electrons and holes due to photoexcitation, respectively. All scale bars are 50  $\mu$ m.

to increase and spread before monotonically decreasing with a similar time constant (single exponential fit yields  $\tau \sim 75$  ps) to that of the excess hole population on the thick MoS<sub>2</sub> ( $\Delta t > 60$  ps). Interestingly, the intermediate thickness of MoS<sub>2</sub> (light green outline, Figure 5.5d), yields little to no excess electrons, suggesting the dominant path for carrier transport is between the thin (10 nm) and thick (100 nm)

layers of MoS<sub>2</sub>. Further measurements on monolayer MoS<sub>2</sub> and bulk ( $\gg 100$  nm thick) MoS<sub>2</sub> (See [Figure 5.6](#) and [Figure 5.7](#)) yield little carrier dynamics and no appearance of excess electrons, as observed at this thin-thick junction.

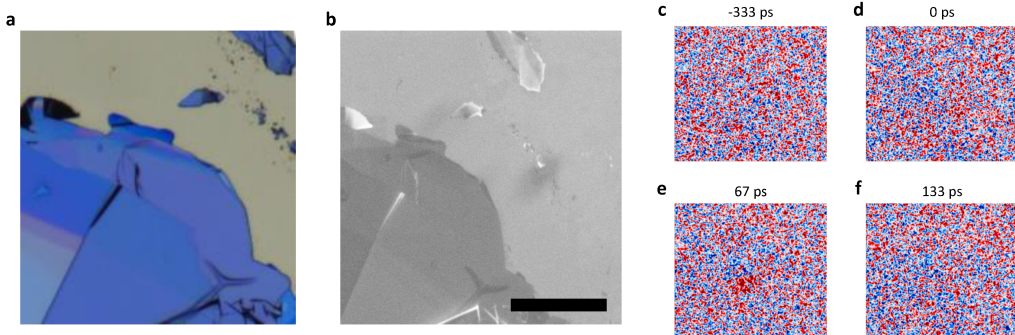


**Figure 5.6: Scanning ultrafast electron microscopy of bulk MoS<sub>2</sub> on Au.** **a** Optical micrograph image of a very thick MoS<sub>2</sub> exfoliated onto a gold substrate. **b** Static SEM image of the same flake (scale bar = 100  $\mu$ m). Contrast images formed at different pump-probe time delays of **c** -333 ps **d** 0 ps **e** 67 ps and **f** 133 ps, suggesting that vertical carrier separation in very thick MoS<sub>2</sub> on Au is unobservable through SUEM because its thickness is much larger than the band-bending Debye screening length. In the contrast images, **c – f**, the color bar is blue (red) for excess electrons (holes). Contrast images are taken over the same region as the static SEM image in **b**.

We interpret the carrier dynamics in these contrast images as direct evidence of carrier separation at a thin-thick layer interface, which we refer to hereafter as a “band bending junction”. The dynamics can be qualitatively explained as follows (See [Figure 5.8](#) for a schematic): (1) optical excitation results in generation of electron-hole pairs, which rapidly separate vertically due to vertical band bending and thicknesses in the semiconductor that are small compared to carrier diffusion lengths. The strong electron transfer at the MoS<sub>2</sub>-Au interface results in a band profile schematically depicted in [Figure 5.1](#), which causes holes (electrons) to move toward the MoS<sub>2</sub>-vacuum (MoS<sub>2</sub>-Au) interface for both thicknesses. Thus, the timescale for the initial contrast is primarily due to the vertical carrier drift velocity and thickness of the sample. (2) After the carriers are separated, both carriers can travel on average over one diffusion length within their lifetime. Therefore, if the holes on the thin side are within a diffusion length of the thin-thick junction, they can travel laterally and vertically to separate from the remaining electrons on the thin side. Electrons can also travel within their own diffusion length but will remain

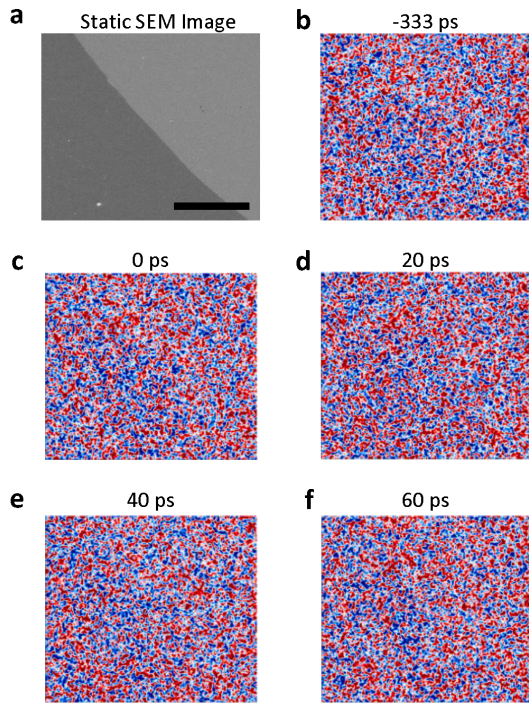


**Figure 5.7: Scanning ultrafast electron microscopy of monolayer  $\text{MoS}_2$  on Au.** **a** Static SEM image of a monolayer  $\text{MoS}_2$  on Au (scale bar =  $100 \mu\text{m}$ ). Contrast images formed at different pump-probe time delays of **b** -333 ps **c** 0 ps **d** 20 ps **e** 40 ps and **f** 60 ps, suggesting that vertical carrier separation in monolayer  $\text{MoS}_2$  on Au is unobservable through SUEM because its thickness is much smaller than the band-bending Debye screening length. In the contrast images, **b** – **f**, the color bar is blue (red) for excess electrons (holes). Contrast images are taken over the same region as the static SEM image in **a**.

near the  $\text{MoS}_2$ -Au interface due to the band profile. The lateral transport that results in carrier separation and the eventual contrast flip therefore follows the timescales of carrier diffusion. (3) Once some holes move across the thin-thick interface, remaining holes follow along due to the gradient in the quasi-Fermi level in the holes. (4) After the electrons and holes have completely separated, they recombine primarily monomolecularly through Shockley-Read-Hall recombination kinetics via trap states within the bulk of  $\text{MoS}_2$ . These trap states are naturally available due to defects in the crystalline lattice (e.g. sulfur vacancies) [1, 2].

To model the lateral carrier separation dynamics of this band bending junction, we turn to time-dependent drift-diffusion equations (see [section 5.5](#)). To simplify the numerical modelling substantially, we make the following assumptions: (1) The

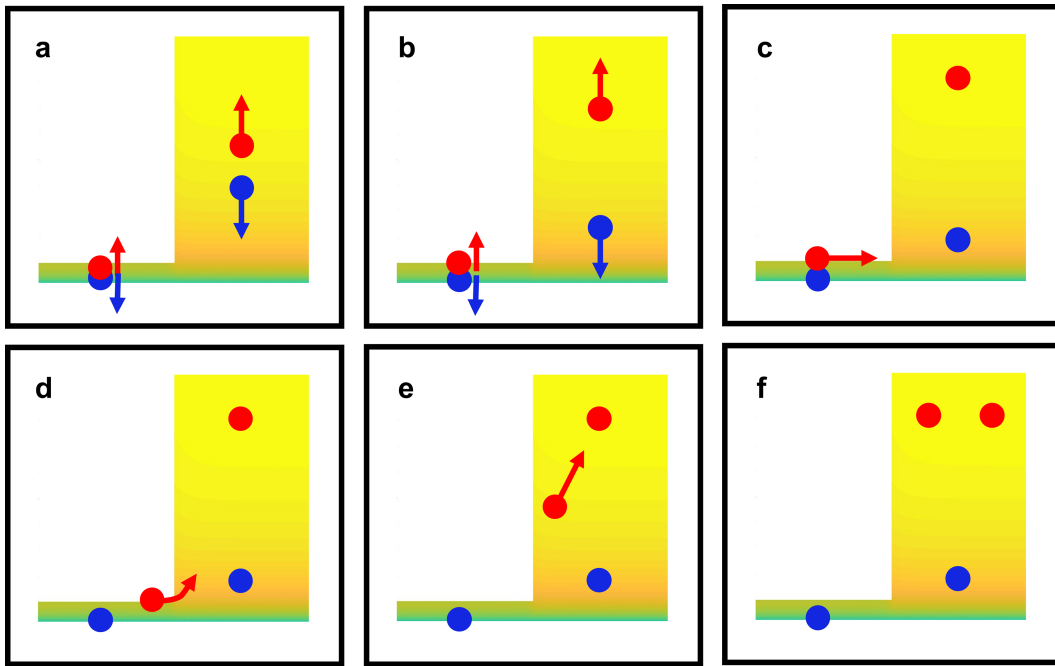


**Figure 5.8: Schematic depiction of carrier transport at a band bending junction.** In a band bending junction, carriers transport vertically before separating laterally. The population of holes (electrons) are depicted by red (blue) circles. Arrows represent the direction of the flow of carriers. Time is increasing from **a** to **f**, where **a** corresponds to when carriers are first generated and **f** corresponds to when carriers have fully separated due to this thickness junction.

MoS<sub>2</sub>-Au interface results in strong electron transfer to MoS<sub>2</sub>. (2) The dynamics can be qualitatively modelled by semiconductor drift-diffusion equations. Ab-initio calculations combined with the Boltzmann transport equations may yield more accurate results while considering the unique bandstructures of these systems. (3) the carrier dynamics can be effectively modelled in two dimensions, due to the prominent dynamics at the thin (10 nm) - thick (100 nm) interface. (4) The anisotropic mobilities in the vertical vs. horizontal directions is effectively compensated by scaling the horizontal dimension by the ratio of the square root of the mobilities. (5) While the carrier dynamics in other semiconductor materials at these time scales has been shown to exhibit super diffusion and therefore a time-dependent mobility [106, 132], we fix our mobility to a single value which represents effectively a time and spatially averaged quantity. (6) Since we are interested in primarily the lateral carrier dynamics, we assume carrier excitation occurs at 27 ps in the simulation. (7) Secondary electron contrast is primarily due to the net charge density near the surface of the MoS<sub>2</sub> layer, with the secondary electron emission decaying exponentially from

the surface of the semiconductor with a length scale  $\lambda_{SE}$ .

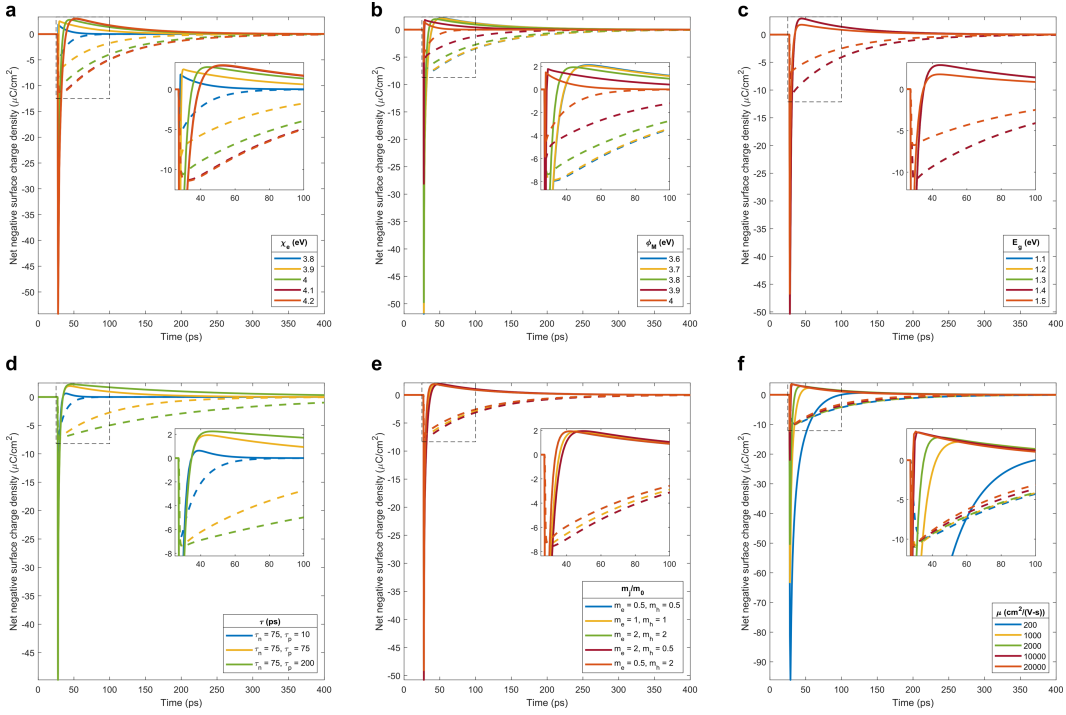


**Figure 5.9: Simulated carrier dynamics for various material parameters.** Net negative surface charge density of the thin (10 nm, solid line) and thick (100 nm, dashed line) areas of the sample for varying **a** electron affinity **b** metal workfunction **c** bandgap **d** carrier lifetime **e** effective mass **f** and carrier mobility. In all cases, the thin and thick portion of the sample exhibits rapid onset of hole surface charges. The thin portion of the sample then exhibits lateral hole transport to the thick portion of the sample, which results in electrons (holes) separated to the thin (thick) portion of the sample. Dashed lines correspond to the region of the inset. For the bandgap sweep **c**, all  $E_g < 1.4$  eV overlay with the 1.4 eV curve since the semiconductor is already degenerately doped and there is minimal change to the band profile. Similar effects occur for  $\chi_e > 4.1$  eV and  $\phi_M < 3.7$  eV. For the effective mass sweep **e**, varying the effective mass of the electron does little to the carrier dynamics because the transport is dominated by the minority carrier, i.e., the holes (see also [Figure 5.10](#)).

With these simulation assumptions in mind, we find excellent agreement between the experimental secondary electron emission contrast and the calculated time-dependent net negative surface charge density ([Figure 5.11a](#)). Snapshots of the charge density at specific times are also shown in [Figure 5.11b](#), showing lateral carrier separation at the thin-thick interface shortly after excitation. The agreement has been achieved from a variety of simplifications in the theoretical modelling, which suggests that the extracted material parameters used to achieve this matching

(specifically, the electron and hole mobility of MoS<sub>2</sub>) should not be taken to be necessarily physical. Improved modelling that explicitly includes (1) the anisotropic mobility, (2) the large aspect ratio between lateral and vertical directions, and (3) a time-dependent mobility due to hot carrier dynamics would substantially enhance the accuracy of a material parameter fit. However, we find that the qualitative picture of the band bending junction is robust (See Figure 5.9) to a variety of material constants, i.e., lateral carrier separation is achieved independent of the specific choice of material parameters, suggesting that this junction should be observable in other van der Waals materials as well. Our calculations also suggest the current density at the thin-thick interface is dominated by the hole current (See Figure 5.10), which is expected since it acts as a minority carrier in this electron-doped system. Finally, we emphasize that the carrier separation demonstrated here is in the absence of quasiparticle bandgap or exciton binding energy differences, which has previously led to novel junctions[72, 185, 189]. Here, the carrier separation is enabled by the unique interplay between thickness and band bending.

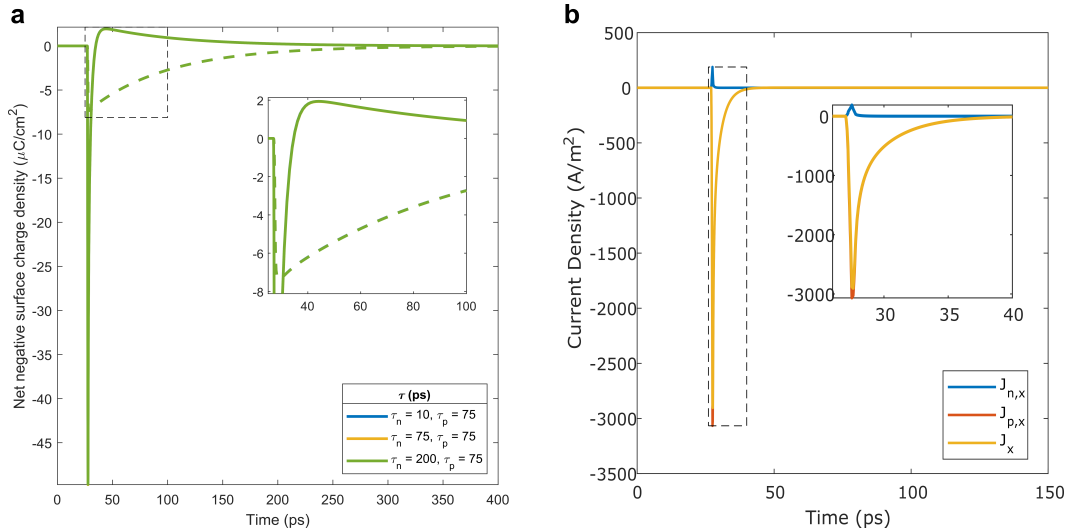
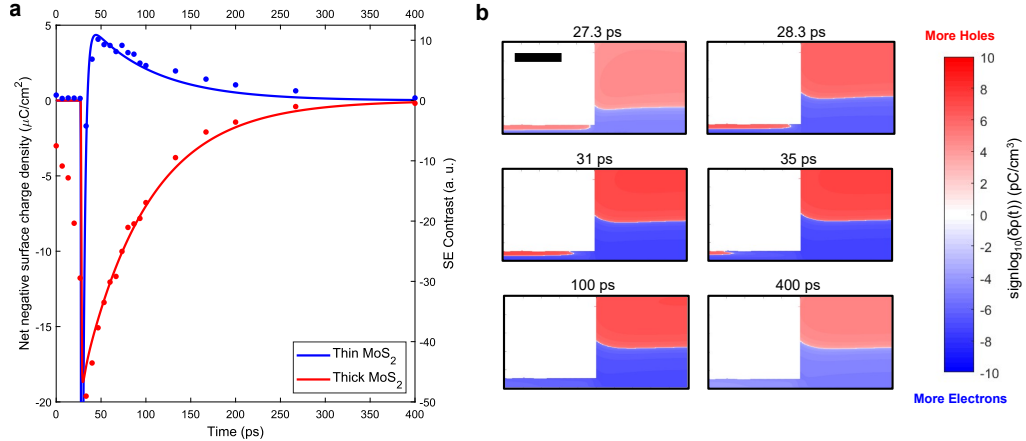


Figure 5.10: **Hole dominated charge transport.** **a** Simulated charge density plots for varying electron lifetime. All curves are overlaid on top of one another, showing that the minority carrier, i.e., the holes, dominate the carrier flow. **b** Simulated electron  $J_n$ , hole  $J_p$ , and total  $J$  current density at the thin-thick junction, showing again that the carrier transport dynamics are dominated by the holes. Current densities are resolved to the  $x$  direction, showing only the lateral transport characteristics. Dashed box refers to the inset.



**Figure 5.11: Simulation of Carrier Dynamics at a Bend Bending Junction.** **a** Experimentally measured secondary electron contrast intensity (dots, right axis) on the thin (blue) and thick (red) MoS<sub>2</sub> as a function of different pump-probe delay times, along with the simulated net negative surface charge density as a function of time (solid lines, left axis). We assume the thin and thick MoS<sub>2</sub> is 10 and 100 nm thick, respectively, for the simulation. **b** Simulated cross-sectional maps of the net charge density at different time steps, plotted with a signed log function to examine the orders of magnitude change in carrier density more easily (scale bar = 50 nm). Red corresponds to net positive charge (i.e., holes), while blue corresponds to net negative charge (i.e., electrons).

#### 5.4 Conclusions and Outlook

Our results suggest that the interplay between thickness and band bending for materials thinner than their screening length can result in the formation of a new type of homojunction, which we refer to as a band bending junction. These band bending junctions are formed by combining the highly passivated surfaces of van der Waals materials with vertical band bending in materials whose thicknesses are comparable to or below the characteristic electrostatic screening length. Thus, while these results were obtained with the MoS<sub>2</sub>/Au system, they are likely generalizable to other van der Waals heterostructures and perhaps also 3D bonded semiconductors if one can generate chemically passivated yet electronically active surfaces in the ultrathin thickness (<100 nm) limit. Furthermore, these band bending junctions may find use as new photodetector geometries or could be useful for sensing applications. From the fundamental perspective, they may enable the formation of two-dimensional electron/hole gases or enable a wide variety of surface-sensitive measurement techniques to indirectly examine vertical carrier transport in layered van der Waals materials. More generally, the observation of charge carrier transport at these band

bending junctions should be considered while modelling and interpreting ultrathin optoelectronic devices that are geometrically inhomogeneous.

## 5.5 Appendix

### Sample Preparation

Large area ultrathin flakes of MoS<sub>2</sub> were fabricated utilizing the strength of the Au-S bonds, which has been known to yield large area samples. [43, 116, 194] To summarize our procedure, we first created atomically smooth Au substrates using template stripping techniques which routinely yields  $<3$  Å RMS. [198, 207] Then, bulk crystals of MoS<sub>2</sub> (HQgraphene) were cleaved from the native crystal using thermal release tape (Semiconductor Equipment Corp., No. 3195MS) and directly pressed onto the template stripped Au substrate. With the tape and bulk MoS<sub>2</sub> directly pressed onto the Au substrate, the entire stack was then heated to  $\sim 120$  C on a hot plate for  $\sim 2$  minutes to release the bulk crystal from the tape and to promote adhesion between the MoS<sub>2</sub> and Au substrate. The MoS<sub>2</sub>/Au sample was then sonicated in Acetone for  $\sim 5$  seconds to release the bulk crystal from the ultrathin layer of MoS<sub>2</sub> that would remain adhered to the Au substrate. The sample was finally rinsed with Isopropanol and blow dried with N<sub>2</sub>. We found it was necessary to template strip the Au substrate immediately before pressing with the MoS<sub>2</sub> bulk crystal to yield large area flakes, similar to what has been observed previously. [194]

### Kelvin Probe Force Microscopy Measurements

Scanning probe microscopy was performed on OmegaScope-R SPM (AIST-NT, now-Horiba Scientific). HQ NSC-14-Cr/Au probes (Mikromasch) were used for characterization. Kelvin probe imaging was performed in frequency modulation mode which allowed improved spatial resolution of the distribution of the contact potential difference (which reflects the distribution of the surface potential on the sample). The value of the surface potential of the probes was not calibrated, so it was the contrast in the CPD images, not the absolute value of the surface potential, which bore the physical meaning in the CPD images.

### Photoemission Spectroscopy Measurements

Photoemission spectroscopy measurements were performed at Beamline 7.0.2 (MAESTRO) at the Advanced Light Source. Samples were characterized at the microARPES UHV endstation, with synchrotron beam spot sizes of approximately 10  $\mu\text{m}$ . Incident photon energies were 145 eV and 330 eV for the valence band and

core level measurements, respectively. Measurements were performed at  $\sim 72$  K and multiple frames were averaged together to achieve sufficient signal to noise ratios.

### Scanning Ultrafast Electron Microscopy Measurements

Scanning ultrafast electron microscopy is a newly developed technique that can directly image the dynamics of photoexcited carriers in both space and time with subpicosecond temporal resolution and nanometer spatial resolution. Details of the setup can be found elsewhere [126, 215] and are briefly summarized here (also illustrated in Figure 3a). Compared to optical pump-probe spectroscopy, SUEM is a photon-pump-electron-probe technique, with subpicosecond electron pulses generated by illuminating a photocathode (ZrO-coated tungsten tip) with an ultrafast ultraviolet (UV) laser beam (wavelength 257 nm, pulse duration 300 fs, repetition rate 5 MHz, fluence  $300 \mu\text{J}/\text{cm}^2$ ). A typical probing electron pulse consists of tens to hundreds of electrons, estimated by measuring the beam current through a Faraday cup, and is accelerated to 30 keV before impacting the sample. The probing electron pulses arrive at the sample after the optical pump pulses (wavelength 515 nm, fluence  $80 \mu\text{J}/\text{cm}^2$ ) by a given time controlled by a mechanical delay stage (-700 ps to 3.6 ns with 1 ps resolution). The probing electron pulses induce the emission of secondary electrons from the sample, which are subsequently collected by an Everhart-Thornley detector. To form an image, the probing electron pulses are scanned across the sample surface and the secondary electrons emitted from each location are counted. Because the yield of secondary electrons depends on the local average electron energy, more/less secondary electrons are emitted from regions of the sample surface where there is a net accumulation of electrons/holes. Typically, a reference SEM image is taken long before the pump optical pulse arrives and is then subtracted from images taken at other delay times to remove the background. In the resulting “contrast images”, blue/red contrasts are observed at places with net accumulation of electrons/holes due to higher/lower yield of secondary electrons. In this fashion, the dynamics of electrons and holes after excitation by the optical pump pulse can be monitored in real space and time.

### Electromagnetic and Transport Simulations

The coupled Drift-Diffusion and Poisson equations were solved using the CHARGE solver in Lumerical DEVICE, which uses finite-element meshing to solve the coupled differential equations iteratively. Due to the anisotropic mobility known for these materials [103, 121], solving the multi-dimensional coupled differential equa-

tions is computationally costly. Instead, we argue that since we are interested in a qualitative picture of the carrier transport and because the lateral extent of the junction is dominated by the in-plane diffusion length, a proper rescaling of the in-plane dimensions by a factor of  $L_{\parallel}/L_{\perp} = \sqrt{\mu_{\parallel}/\mu_{\perp}} \sqrt{1000}$  allows us to treat the problem with an approximate isotropic, spatially, and temporally averaged mobility ( $\mu = 2000 \text{ cm}^2/(\text{V}\cdot\text{s})$ ). Since the experimentally observed in-plane junction width is  $\sim 10 \mu\text{m}$ , the rescaled in-plane width should be about 300 nm. In our simulations our total lateral span is 500 nm. Band bending was captured assuming an Ohmic contact at the Au-MoS<sub>2</sub> interface with a metal work-function of 3.8 eV and semiconductor electron affinity of 4.0 eV. Fermi-Dirac statistics were included due to the high level of modulation doping. Furthermore, we used a bandgap value of 1.3 eV [117], hole effective mass of  $0.785m_0$  [221], an electron effective mass of  $0.686m_0$  (for the electron effective mass, we took the geometric mean of the effective masses in the transverse and longitudinal directions at the Q point [221]), dielectric constant of 7 [98], and a Shockley-Read-Hall recombination lifetime of 75 ps. Exciton dynamics were deemed not relevant, since majority of the transport should occur at the lowest energy conduction band and highest energy valence band, with exciton binding energies  $\ll k_b T$ . [25] Native doping of MoS<sub>2</sub> was assumed to be n-type with a doping level of  $10^{16} \text{ cm}^{-3}$ , similar to that quoted from the supplier. Optical generation values were calculated assuming the system is optically one-dimensional over a specific thickness (either 10 nm or 100 nm), and therefore 1D transfer matrix calculations were applicable for each region. These generation rates were then directly imported into Lumerical DEVICE. Calculated volumetric charge densities were exponentially weighted from the surface with a characteristic length scale of  $\lambda_{SE} = 4 \text{ nm}$  to yield surface charge densities. The SUEM signal is expected to be proportional to the net negative charge density  $I_{SUEM} \propto -\delta\rho = -q(\delta p - \delta n)$ , where positive/negative SUEM signal scales with the net electron/hole population.

## **Part III**

### **The Luminescence is the Voltage**

## HIGHLY STRAIN TUNABLE INTERLAYER EXCITONS IN MOS<sub>2</sub>/WSE<sub>2</sub> HETEROBILAYERS

*“Happiness only real when shared.”*

— Christopher McCandless

### 6.1 Introduction

Strain engineering of nanomaterials has received substantial interest because as the physical length scales of nanomaterials become smaller, size effects enable fewer defects, such as grain boundaries, as well as diminishing bending rigidity, resulting in a superior yield strength with a highly elastic response compared to their bulk counterparts [64, 65, 227]. Two-dimensional (2D) materials are particularly suited for strain engineering because they combine high in-plane mechanical strength and extremely small bending rigidity with substantial strain tunability of electronic band structure [42, 99, 114, 137, 147, 222]. The unique mechanical strength, flexibility, and tunability of 2D materials have therefore enabled their applications for wearable and flexible technologies [18, 86, 165], as well as fundamental studies of material properties under carefully engineered strain conditions. The semiconducting layered transition metal dichalcogenides (TMDCs) have emerged as particularly interesting candidates for strain engineering, since they have exhibited exciton funneling [53, 102, 127], strain-mediated phase transitions [177], and the ability to form site-controlled quantum emitters via localized strains [115].

Strain engineering has been explored in TMDC monolayers, multilayers, and heterostructures. Multilayer TMDCs are particularly interesting because they are known to exhibit interlayer exciton transitions, i.e., optical transitions where the electron-hole pairs are located in different constituent layers bounded by strong Coulomb interaction [164]. These interlayer excitons have been observed to be strain tunable in homobilayers of molybdenum disulfide (MoS<sub>2</sub>) [21, 138] and heterobilayers of molybdenum diselenide and tungsten diselenide (MoSe<sub>2</sub>/WSe<sub>2</sub>) [70] with deformation potentials of approximately 47 meV/% and 22 meV/%, respectively. Furthermore, other studies on multilayer structures have suggested that interlayer coupling should be an additional degree of freedom tunable via strain due

to the Poisson effect [75, 144], but these effects on interlayer exciton transitions have yet to be observed.

In this chapter, we investigate the strain characteristics of momentum-space indirect  $\Gamma - K$  interlayer exciton in wrinkled molybdenum disulfide and tungsten diselenide ( $\text{MoS}_2/\text{WSe}_2$ ) heterobilayer. We spatially probed the effects of local strain in the wrinkled heterobilayer via photoluminescence (PL) and Raman measurements, and find that the  $\Gamma - K$  momentum-space indirect transition gives rise to a larger deformation potential (107 meV%) compared to its intralayer counterpart because of the strain-sensitive orbital nature at the  $\Gamma$  point of the valence band and  $K$  point of the conduction band. Furthermore, we find that the interlayer exciton exhibits a non-monotonic dependence in PL intensity with strain, which can be explained by a competition between interlayer coupling and band structure modulation effects under strain. This hypothesis is supported by *ab initio* band structure calculations as well as Raman measurements where we can directly measure the interlayer coupling.

## 6.2 Local Strain Engineering of Intra- vs. Inter-layer excitons

For local strain engineering, we prepared wrinkled vertical heterostructures of  $\text{MoS}_2/\text{WSe}_2$  on an elastomeric substrate of polydimethylsiloxane (PDMS) by using a combination of our heat-assisted PDMS-to-PDMS (PTP) assembly method and strain-release mechanism (see [section 6.6](#) and [Figure 6.2](#) for more fabrication details). When a pre-stretched PDMS with the assembled heterobilayer of  $\text{MoS}_2/\text{WSe}_2$  via PTP method ([Figure 6.1a,c](#)) is released, the heterobilayer deforms into a periodic wrinkled structure ([Figure 6.1b](#)) with a periodicity of about 4  $\mu\text{m}$  ([Figure 6.2](#)) as shown in an optical micrograph of the fabricated crumpled structure ([Figure 6.1d](#)). The periodic wrinkled geometry induces local stretching and compression of the heterobilayer lattice at the crests and valleys, respectively, resulting in a periodic local strain profile of alternating tensile and compressive strain within the TMDC heterostructure ([Figure 6.1b](#)).

To characterize the optical properties of  $\text{MoS}_2/\text{WSe}_2$  heterobilayer, we carried out steady-state PL spectroscopy and Raman spectroscopy under 532 nm excitation at room temperature over the fabricated  $\text{MoS}_2/\text{WSe}_2$  heterobilayer and adjacent isolated constituent monolayers before the release of the pre-stretch (flat state) ([Figure 6.1e](#)). We observed the intralayer emission at the exciton energies characteristic of  $\text{MoS}_2$  ( $\sim 1.88$  eV or 680 nm) and  $\text{WSe}_2$  ( $\sim 1.65$  eV or 750 nm) in adjacent isolated monolayers. In the heterobilayer, we observed a new PL emission peak redshifted

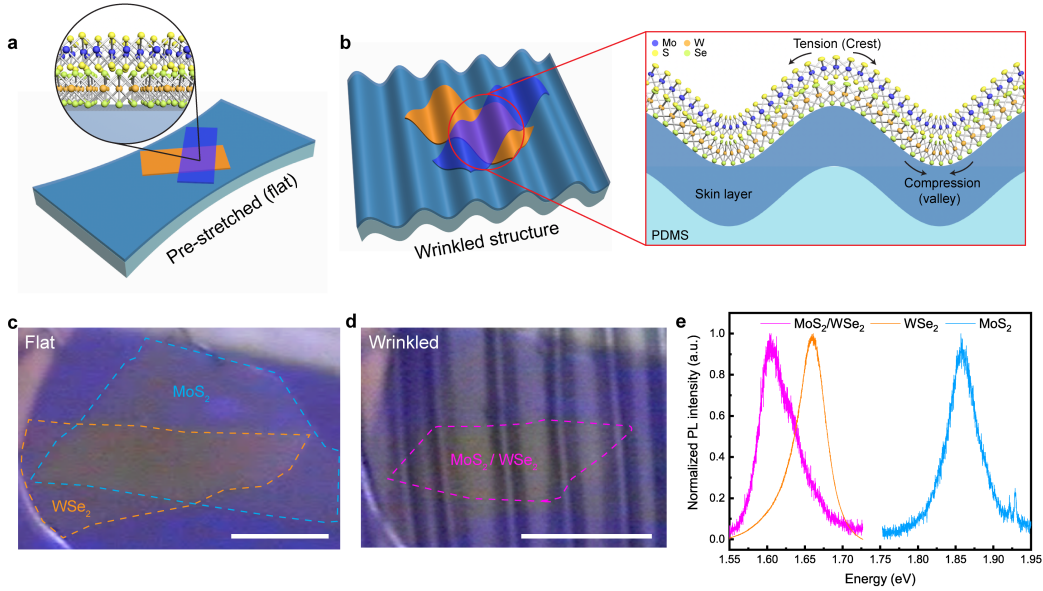


**Figure 6.1: Fabrication of wrinkled MoS<sub>2</sub>/WSe<sub>2</sub> heterobilayer.** **a** Schematic depiction of a vertical van der Waals heterobilayer on a pre-stretched elastomeric substrate. **b** After the release of the mechanically pre-stretched elastomeric substrate, a wrinkled heterostructure exhibiting heterogeneous strain profile of alternating tension (at crest) and compression (at valley) is fabricated. **c** Optical microscopy image of a flat MoS<sub>2</sub>/WSe<sub>2</sub> heterobilayer with the estimated twist angle of 50.7°. Scale bar is 10  $\mu$ m. **d** Optical microscopy image of a crumpled MoS<sub>2</sub>/WSe<sub>2</sub> heterobilayer. Scale bar is 10  $\mu$ m. **e** Photoluminescence spectra of flat monolayer MoS<sub>2</sub>, WSe<sub>2</sub>, and MoS<sub>2</sub>/WSe<sub>2</sub>.

by about 75 meV (or 30 nm) with respect to the intralayer A exciton of the WSe<sub>2</sub> monolayer, which corresponds to a  $\Gamma - K$  optical transition energy of MoS<sub>2</sub>/WSe<sub>2</sub> [95, 187]. A confocal PL map (Figure 6.2) integrated over the two characteristic intralayer exciton peaks of MoS<sub>2</sub> and WSe<sub>2</sub> showed significant PL intensity quenching over the heterobilayer area, indicative of rapid charge transfer due to the type-II nature of this interface. We further observed uniform emission of the interlayer exciton at the  $\Gamma - K$  optical transition energy of MoS<sub>2</sub>/WSe<sub>2</sub> across a relatively large area (Figure 6.3) as well as the out-of-plane Raman mode ( $A_{1g}^2$ ) of WSe<sub>2</sub> at 309 cm<sup>-1</sup> in our MoS<sub>2</sub>/WSe<sub>2</sub> heterobilayer (Figure 6.3), suggesting there is strong interlayer coupling[30] between the MoS<sub>2</sub> and WSe<sub>2</sub> layers in the heterobilayer region.

To experimentally explore the effect of local strain on the band structure and the resultant optical properties in terms of exciton emission, we first spatially resolved the PL energy shift of the intralayer and the interlayer excitons in the wrinkled monolayers and MoS<sub>2</sub>/WSe<sub>2</sub> heterobilayer (Figure 6.5 and Figure 6.4). Typical PL

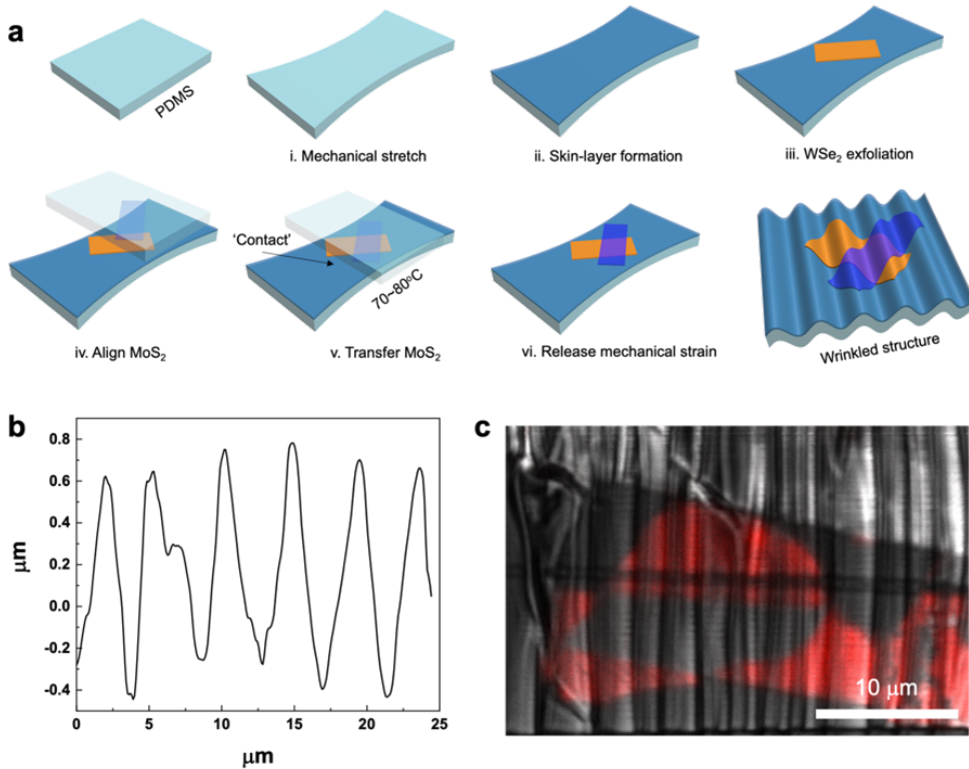


**Figure 6.2: Sample fabrication and characterization of wrinkled heterostructures.** **a**, Schematic illustrations of the sample fabrication process of wrinkled heterostructures via PDMS-to-PDMS (PTP) dry transfer method. Our PTP method involves a one-time direct stamping transfer process after the exfoliation of individual monolayers and minimizes any solvent and/or polymer residues at the van der Waals interface. **b**, A height profile of the fabricated wrinkled structure at the heterobilayer area via confocal laser scanning microscopy. **c**, A confocal photoluminescence (PL) mapping integrated over both intralayer exciton energies of  $\text{MoS}_2$  and  $\text{WSe}_2$  monolayers. The red color indicates the emission of intralayer excitons and the black color in the heterojunction indicates the PL quenching.

spectra measured at room temperature across a single wrinkle profile are shown in [Figure 6.5a](#) for the intralayer excitons of  $\text{WSe}_2$  and  $\text{MoS}_2$ , and in [Figure 6.5b](#) for the interlayer exciton of the  $\text{MoS}_2/\text{WSe}_2$  heterobilayer. In both cases, we observed a gradual shift of the emission peak energy along with the wrinkle profile and observed that the energy peak shifts within the structure can be modulated up to approximately 107 meV for the interlayer exciton, compared to approximately 54 meV for  $\text{WSe}_2$  and 55 meV for  $\text{MoS}_2$  intralayer excitons under uniaxial deformation. We observed greater tunability of the peak energy shifts in the interlayer exciton than in the intralayer excitons. We further observed the peak energies redshifted (blueshifted)

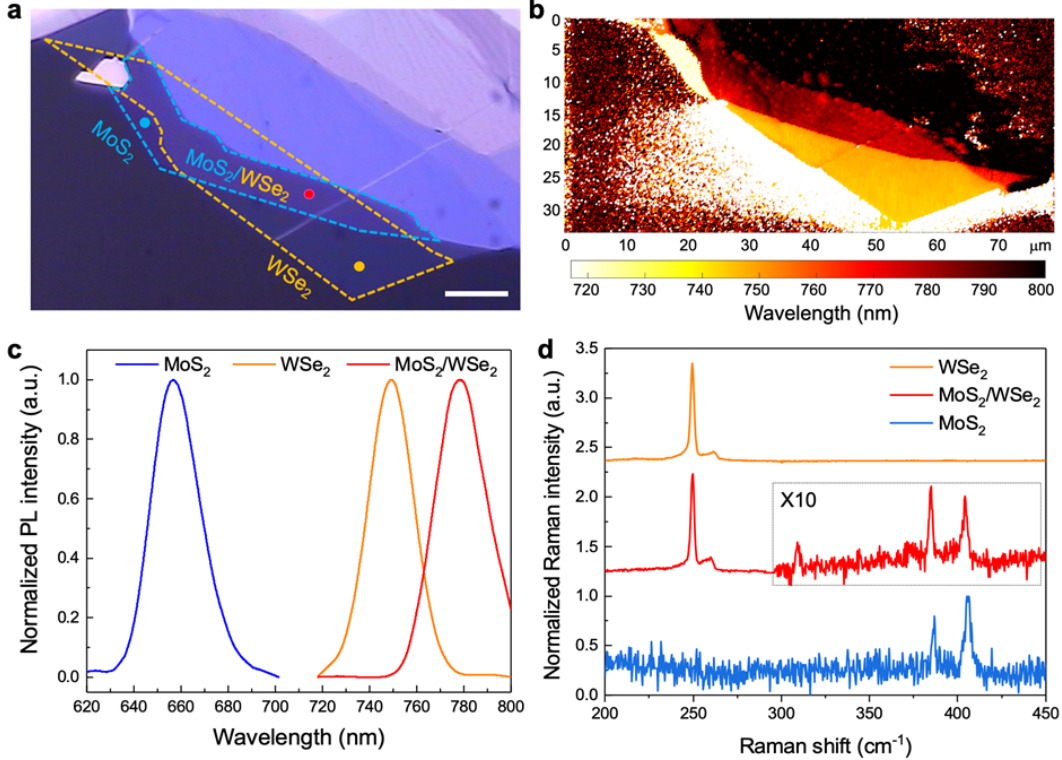


**Figure 6.3: Optical characterization of flat heterobilayers of  $\text{MoS}_2/\text{WSe}_2$  on PDMS.** **a**, An optical micrograph of the fabricated flat heterobilayer of  $\text{MoS}_2/\text{WSe}_2$  on PDMS substrate via our PTP (PDMS-to-PDMS) assembly process. A scale bar, 10  $\mu\text{m}$ . The estimated twist angle is approximately  $53^\circ$  using the sharp-edges estimation of the heterobilayer. **b**, A photoluminescence (PL) mapping of the fabricated heterobilayer. A color bar indicates corresponding emission wavelengths. The relatively uniform peak positions over the heterobilayer region indicates that there is no substantial fabrication-induced heterogeneity. **c**, Normalized PL intensity spectra of intra- and interlayer excitons. **d**, Normalized Raman intensity spectra at adjacent monolayers of  $\text{MoS}_2$  and  $\text{WSe}_2$  and at heterobilayer of  $\text{MoS}_2/\text{WSe}_2$ . A magnified (x10) inset shows the emergence of the out-of-plane vibration mode of  $\text{WSe}_2$  ( $\sim 309 \text{ cm}^{-1}$ ).

at the crest (valley) of the wrinkled structure relative to the peak energies in the flat state for both intralayer and interlayer excitons. These observations are indicative of both tensile (local stretching of atomic lattices at the crests) and compressive (at the valleys) strain applied via our fabricated wrinkled structure, which suggests band structure modulation via local strain profile [69]. The observation of luminescence peak energy shifts along the wrinkle profile allows us to correlate the spatial position with a locally applied strain.

We also observed strikingly different qualitative trends for variation of PL intensity

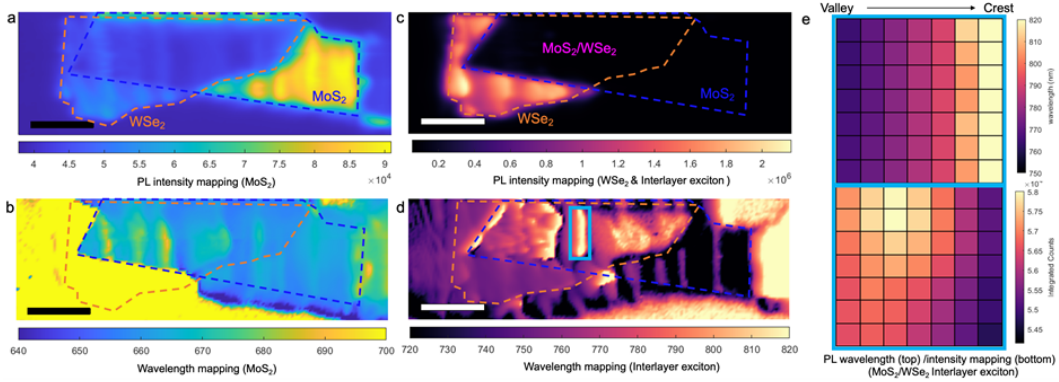


**Figure 6.4: Photoluminescent mapping of the fabricated wrinkled MoS<sub>2</sub>/WSe<sub>2</sub> heterobilayer.** **a** Photoluminescent (PL) intensity and **b** wavelength mapping over the MoS<sub>2</sub> intralayer exciton portion of the spectrum in the fabricated MoS<sub>2</sub>/WSe<sub>2</sub> heterobilayer. Dotted lines indicate boundaries of the constituent monolayers. **c** PL intensity and **d** wavelength mapping over WSe<sub>2</sub> intralayer exciton and interlayer exciton portion of the spectrum. PL intensities of intralayer excitons were substantially quenched in the heterojunction area (MoS<sub>2</sub>/WSe<sub>2</sub>). All scale bars are 5  $\mu$ m. The spatial resolution is  $\sim$ 0.4  $\mu$ m, which allows us to resolve individual spectra along the wrinkled structure. **e** PL wavelength (top) and intensity (bottom) mapping over the corresponding wrinkle from valley (left) to crest (right) indicated in blue rectangle in **d**. Pixel dimensions are 200 nm.

with strain between the intralayer and interlayer excitons for our wrinkled structure. Specifically, we observed that the PL intensity of the WSe<sub>2</sub> (MoS<sub>2</sub>) intralayer exciton was highest (lowest) at the crests and lowest (highest) at the valleys. Thus, the PL intensity of WSe<sub>2</sub> (MoS<sub>2</sub>) monotonically increases (decreases) with increasing tensile strain (Figure 6.5a). In contrast, the maximum peak intensity of the interlayer exciton in the heterobilayer region occurs at an intermediate position between the crest and valley, with a peak energy of  $\sim$ 1.6 eV. By comparing this peak energy with the flat-state peak energy, we find that the maximum peak intensity of the interlayer exciton occurs when the heterobilayer is under mild compression. Thus, by examining the relationship between the peak energy with the peak intensity, we find that the MoS<sub>2</sub>/WSe<sub>2</sub> interlayer exciton PL intensity is non-monotonic with local strain. In other words, the interlayer exciton PL intensity appears to decrease with both increasing tensile and compressive strain, which is in direct contrast to the monotonic peak intensity vs. peak energy behavior observed for intralayer monolayer emission.

To substantiate our findings, we show scatter plots between the peak intensity vs. peak energy (Figure 6.5c), where each point corresponds to an individually fitted

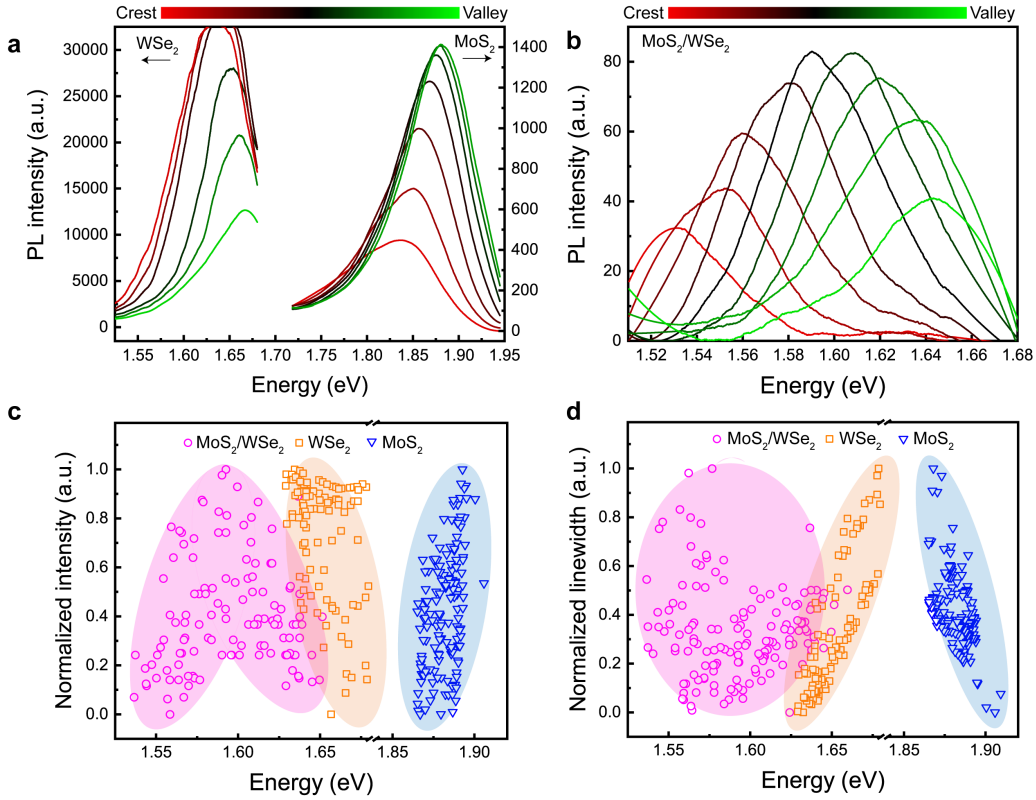


**Figure 6.5: Photoluminescence of strained heterobilayers.** Relative photoluminescence spectra (smoothed) of **a** WSe<sub>2</sub> and MoS<sub>2</sub> intralayer A excitons and **b** MoS<sub>2</sub>/WSe<sub>2</sub> interlayer exciton over a representative wrinkle (from the valley to the crest). The monolayer WSe<sub>2</sub> luminescence saturated the detector in these mapping measurements, creating a top-hat effect in the spectra. Scatter plots over multiple wrinkles that show how the **c** normalized intensity and **d** linewidth of WSe<sub>2</sub>, MoS<sub>2</sub>, and MoS<sub>2</sub>/WSe<sub>2</sub> vary with exciton energy. Each point refers to a separate spectrum measured and fitted to a Gaussian function, over the relevant region of the sample.

spectrum with the peak intensities normalized to the brightest spot within that region of the sample. We observed this non-monotonic interlayer exciton intensity trend across multiple spots throughout the entire sample. We also found that this interlayer exciton intensity trend also appears in various other samples we measured (see [Figure 6.6](#)), as well as when we account for the finite depth of focus in our measurements (see [Figure 6.7](#)). Exciton funneling effects are not a dominant effect since we did not observe highest intensity at the lowest energy of emission in our heterobilayers.

To gain additional insight on the mechanism of intensity modulation, we show similar scatter plots in [Figure 6.5d](#) between the fitted peak linewidth (full width at

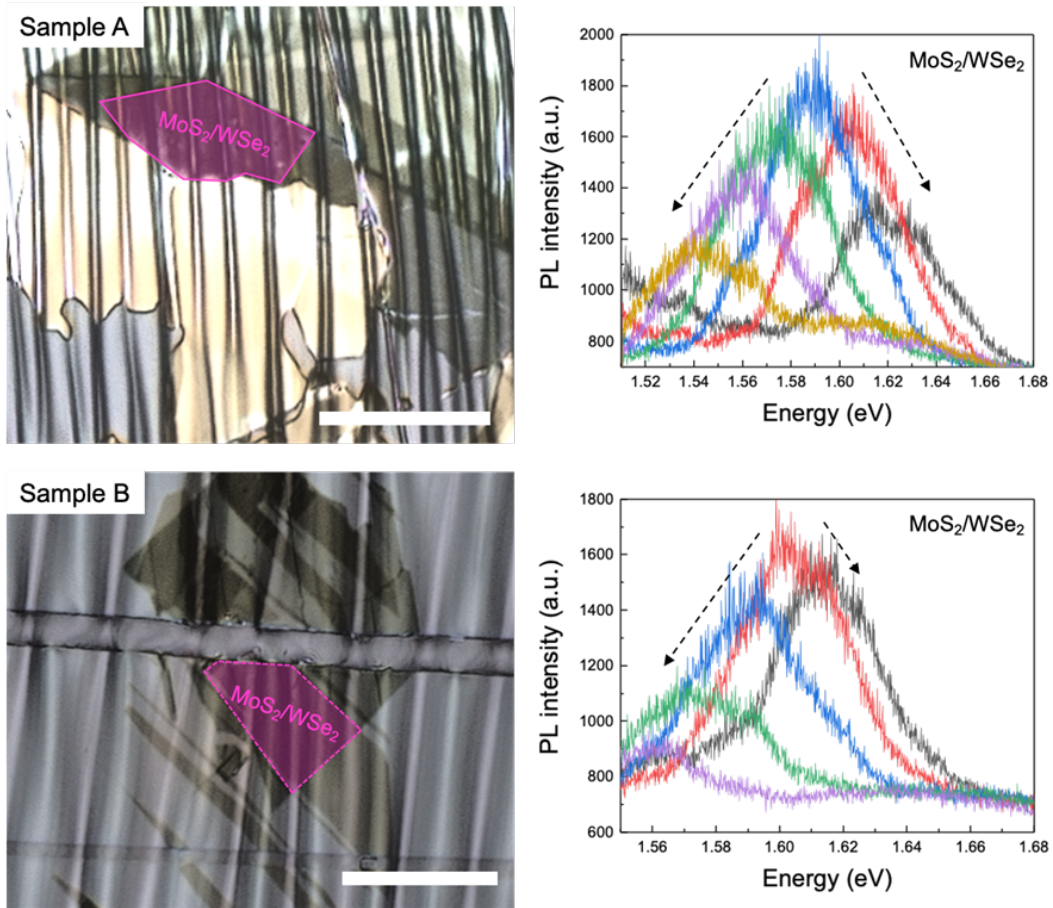


**Figure 6.6: Optical characterization of different wrinkled  $\text{MoS}_2/\text{WSe}_2$  heterobilayer samples.** Optical micrographs (left), and photoluminescence (PL) intensity of interlayer exciton measurements (right) in **a**, sample A, and **b**, sample B wrinkled  $\text{MoS}_2/\text{WSe}_2$  heterobilayers. Dotted black arrows indicate the direction of PL spectra taken towards the crest (left) and towards the valley (right) over a wrinkle in the heterobilayer samples. The estimated twist angles are  $33.5^\circ$  (sample A) and  $51.4^\circ$  (sample B).

half maximum) and peak energy. Interestingly, while the interlayer exciton shows no obvious correlation between the peak linewidth and peak energy, the  $\text{WSe}_2$  and  $\text{MoS}_2$  intralayer excitons show a clear behavior of positive and negative correlation, respectively. Moreover, these trends in linewidth contrast with the trends in intensity for the individual monolayers, i.e., peak intensity and linewidth are apparently inversely correlated, which can be observed more clearly in Figure 6.5a of the individual spectra. By correlating the peak energy shift to an applied strain, the  $\text{WSe}_2$  ( $\text{MoS}_2$ ) peak linewidth decreases (increases) with applied tensile strain. Similarly, the  $\text{WSe}_2$  ( $\text{MoS}_2$ ) peak intensity increases (decreases) with applied tensile strain.

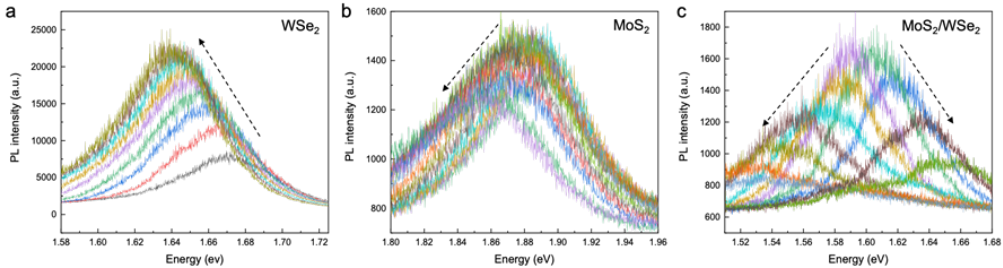


**Figure 6.7: Photoluminescence (PL) measurement on wrinkled heterobilayers of MoS<sub>2</sub>/WSe<sub>2</sub> via vertical scanning (XZ-PL scanning) accounting for the finite depth of focus.** PL spectra taken over a wrinkle (valley-to-crest) **a**, in adjacent wrinkled monolayer WSe<sub>2</sub>. PL spectra **b**, in adjacent wrinkled monolayer MoS<sub>2</sub>, **c**, in wrinkled heterobilayer of MoS<sub>2</sub>/WSe<sub>2</sub>. Dotted black arrows in **a** and **b** indicate the direction of PL spectra taken from the valley to the crest. Dotted black arrows in **c** indicate the direction of PL spectra taken towards the crest (left) and towards the valley (right) over a wrinkle in the fabricated heterobilayer sample.

These effects of strain on the PL intensity and linewidth of the individual monolayers are well [7, 36, 42, 114, 137] and can be explained by the decreased (increased) scattering to the neighboring  $Q$  ( $\Gamma$ ) valley in the WSe<sub>2</sub> (MoS<sub>2</sub>) conduction (valence) band from the  $K$  point. In other words, interband transitions in WSe<sub>2</sub> (MoS<sub>2</sub>) become effectively more direct (indirect) as tensile strain is applied. In contrast to the intralayer excitons, the lack of linewidth modulation with local strain in interlayer exciton emission suggests that there is little modulation of the non-radiative scattering channels.

### 6.3 Tuning Interlayer Coupling through Strain Engineering

To better understand the cause of the non-monotonic intensity variation for the interlayer exciton, we turn to Raman spectroscopy measurements for additional insight as to the mechanisms that may be at play, i.e., investigating the in-plane and out-of-plane strain resulting from topological deformation of the wrinkled heterobilayer (Figure 6.8a). We show that the Raman characteristics of the MoS<sub>2</sub> E<sub>2g</sub> (Figure 6.8b) and WSe<sub>2</sub> E<sub>2g</sub> (Figure 6.8c) modes [47, 105, 201] are well modulated by our wrinkled sample profile, where the peaks are redshifted (blueshifted) at the crest (valley), which corresponds well with the topographical features seen in the optical micrograph as shown in Figure 6.8a. Because the E<sub>2g</sub> mode is an in-plane vibrational mode, it is therefore sensitive to in-plane strain. We did not use the WSe<sub>2</sub> E<sub>2g</sub> mode for a quantitative measure of in-plane strain because of the degeneracy

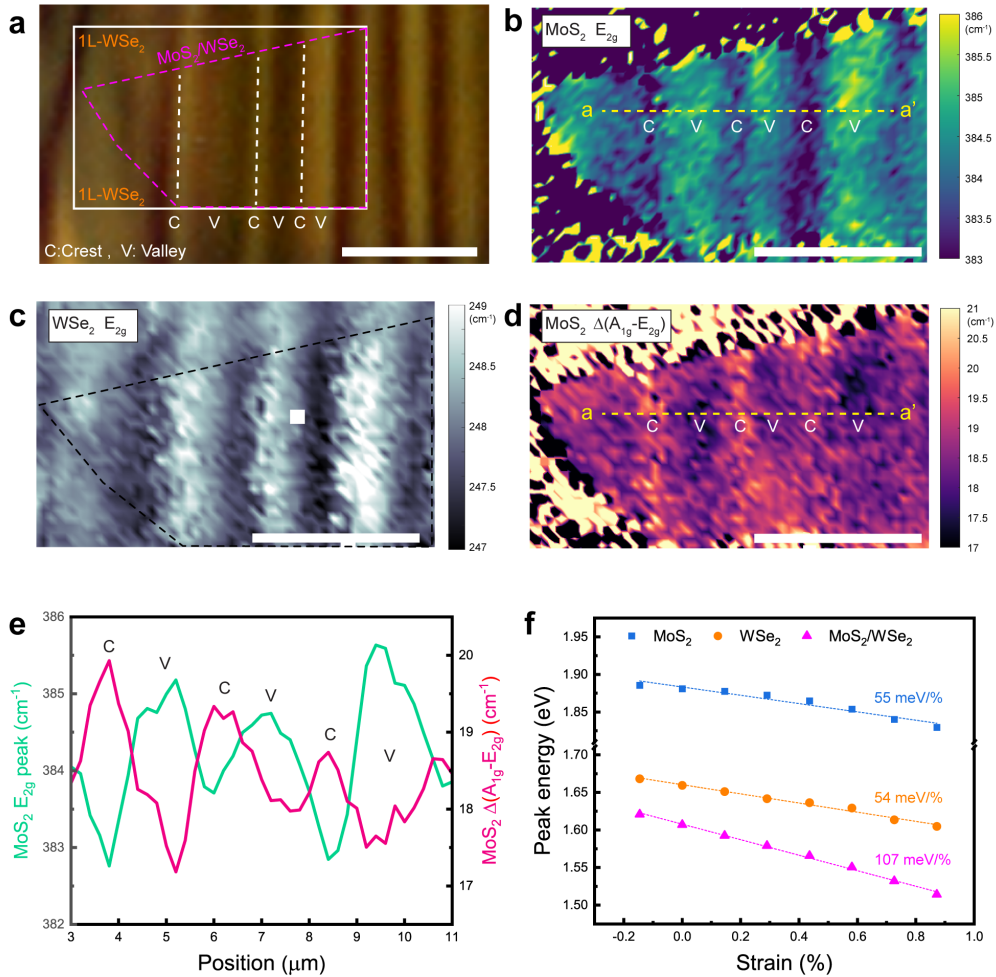


**Figure 6.8: Raman spectroscopy and deformation potentials of strained heterobilayers.** **a** An optical microscopy image of the wrinkled MoS<sub>2</sub>/WSe<sub>2</sub> heterobilayer. Vertical dotted white lines indicate crests of wrinkles. Magenta dotted lines indicate the boundary between adjacent monolayer WSe<sub>2</sub> and heterobilayer of MoS<sub>2</sub>/WSe<sub>2</sub> areas. Spatially resolved Raman mapping of **b** MoS<sub>2</sub> E<sub>2g</sub> mode and **c** WSe<sub>2</sub> E<sub>2g</sub> mode peak positions. **d** peak position separation between MoS<sub>2</sub> A<sub>1g</sub> and E<sub>2g</sub> modes (A<sub>1g</sub>-E<sub>2g</sub>). All the scale bars are 5  $\mu\text{m}$ . **e** Raman peak shifts of MoS<sub>2</sub> E<sub>2g</sub> and A<sub>1g</sub>-E<sub>2g</sub> modes as a function of position along the a-a' line indicated in **b** and **d**. C and V are the crests and valleys of the wrinkle, respectively. **f** experimentally derived deformational potentials of MoS<sub>2</sub> and WSe<sub>2</sub> intralayer excitons, and MoS<sub>2</sub>/WSe<sub>2</sub> ILE obtained from measured Raman and PL spectra. Dashed lines correspond to linear fits of the deformation potential curve.

between the WSe<sub>2</sub> E<sub>2g</sub> and A<sub>1g</sub> modes. We conclude that there is a uniform and controlled tension (compression) at the crest (valley) with our wrinkled geometry, which corroborates our observations in PL spectroscopy measurements.

To study the effects of local strain on the interlayer coupling in the heterobilayer, we examined the mode separation between the MoS<sub>2</sub> E<sub>2g</sub> (in-plane) and A<sub>1g</sub> (out-of-plane) modes. The wavenumber separation between A<sub>1g</sub> and E<sub>2g</sub> has been used as a quantitative measure of the interlayer mechanical coupling strength in artificially stacked bilayers, where larger peak separation is indicative of stronger interlayer coupling [40, 111]. The mode separation has also been used as an effective proxy for the number of layers in naturally exfoliated MoS<sub>2</sub>, i.e.,  $\sim 19$  cm<sup>-1</sup> for monolayer and  $\sim 21$  cm<sup>-1</sup> for bilayer MoS<sub>2</sub> [152, 225]. We show the map of the wavenumber separation between the MoS<sub>2</sub> A<sub>1g</sub> and E<sub>2g</sub> modes,  $\Delta(A_{1g} - E_{2g})$  in Figure 6.8d. In our strained heterobilayer, we observed the A<sub>1g</sub> and E<sub>2g</sub> mode separation changes from a value of  $\sim 20$  cm<sup>-1</sup> at the crest to  $\sim 17$  cm<sup>-1</sup> at the valley (Figure 6.8e). We also observed modulation of the integrated intensity ratio (A<sub>1g</sub>/E<sub>2g</sub>) at the crest and valley (Figure 6.9), which is comparable to the ratio observed between a naturally exfoliated bilayer and a monolayer of MoS<sub>2</sub> [100]. Therefore, we conclude that the modulation of the E<sub>2g</sub> mode together with the A<sub>1g</sub> mode along the wrinkle profile suggests the interlayer coupling in the heterobilayer is tuned between stronger interlayer coupling (larger  $\Delta$ ) and weaker interlayer coupling (smaller  $\Delta$ ) at different locations of the wrinkled heterobilayer. We therefore postulate that in our wrinkled strain profile of the heterobilayer, we are observing simultaneous modulation of the interlayer coupling between MoS<sub>2</sub> and WSe<sub>2</sub> as well as in-plane strain in the heterobilayer. Specifically, there appears to be stronger interlayer coupling at the crests, which are in tension, as compared to at the valleys, which are in compression. This trend is highlighted by the linecut in Figure 6.8e. Thus, the combination of these two effects, in-plane strain and out-of-plane interlayer coupling in our wrinkled structure, are hypothesized to result in the non-monotonic intensity profile of the interlayer exciton observed in Figure 6.5.

Together with the Grüneisen parameters of the E<sub>2g</sub> Raman modes [36, 47, 105, 201] and the PL peak shifts observed earlier, we can also extract an experimental deformation potential for our system, which yields values of approximately 55 meV/% for MoS<sub>2</sub>, 54 meV/% for WSe<sub>2</sub>, and 107 meV/% for the  $\Gamma - K$  transition interlayer exciton under uniaxial strain (Figure 6.8f). The estimated strain values from the Raman modes corroborates well with those estimated from the surface morphology (see Figure 6.10 and section 6.6). The deformation potentials of the intralayer excitons also correspond well with reported values [7, 36], and the interlayer exciton deformation potential is notably almost twice that of the intralayer excitons.

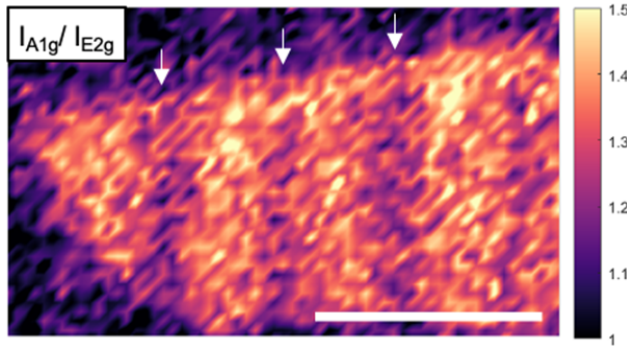


**Figure 6.9: Raman mapping of strained heterobilayers.** Spatially resolved Raman mapping of integrated intensity ratio between MoS<sub>2</sub> A<sub>1g</sub> and E<sub>2g</sub> modes ( $I_{A1g}/I_{E2g}$ ). White arrows indicate the location of the crests in the wrinkled heterobilayer. We observed decreased integrated intensity ratio at the crests, indicating stronger interlayer coupling. Scale bar indicates 5  $\mu\text{m}$ .

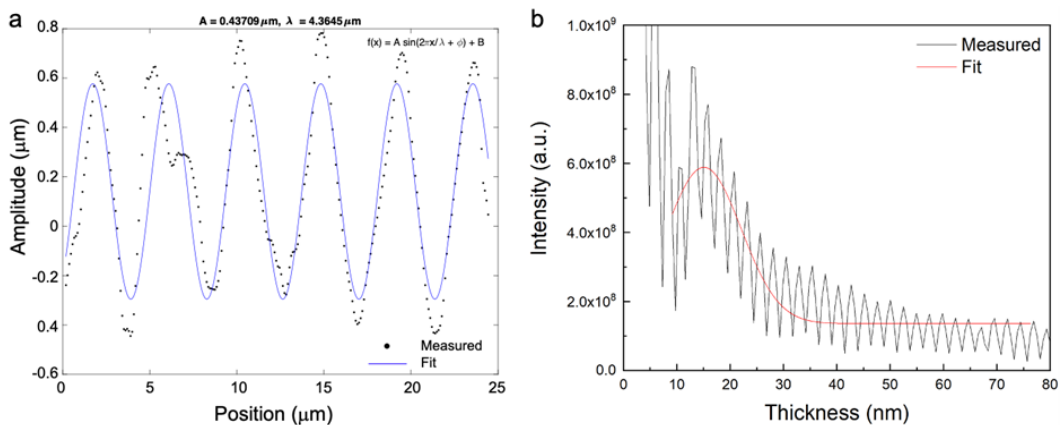


**Figure 6.10: Wrinkle geometry-driven strain analysis.** **a** Measured (black dots) and fit (blue line) data of the fabricated wrinkled geometry. The average amplitude (A) and wavelength ( $\lambda$ ) of wrinkles obtained by a sinusoidal fit to the measured wrinkle geometry profile. **b** Measured (black line) and fit (red line) data of the X-ray reflection intensity to estimate the skin layer thickness formed on the PDMS substrate.

#### 6.4 *ab initio* strain calculations of TMDC heterobilayers

To investigate whether the experimental observations described earlier are consistent with *ab initio* calculations, we examine the electronic band structure of the strained heterobilayer by performing density functional theory (DFT) calculations using the Perdew-Burke-Ernzerhof (PBE) functional [148] (see section 6.6 for more details). Although PBE functional underestimates the absolute value of the bandgap for TMDC monolayers, it has shown the ability to predict accurate deformation po-

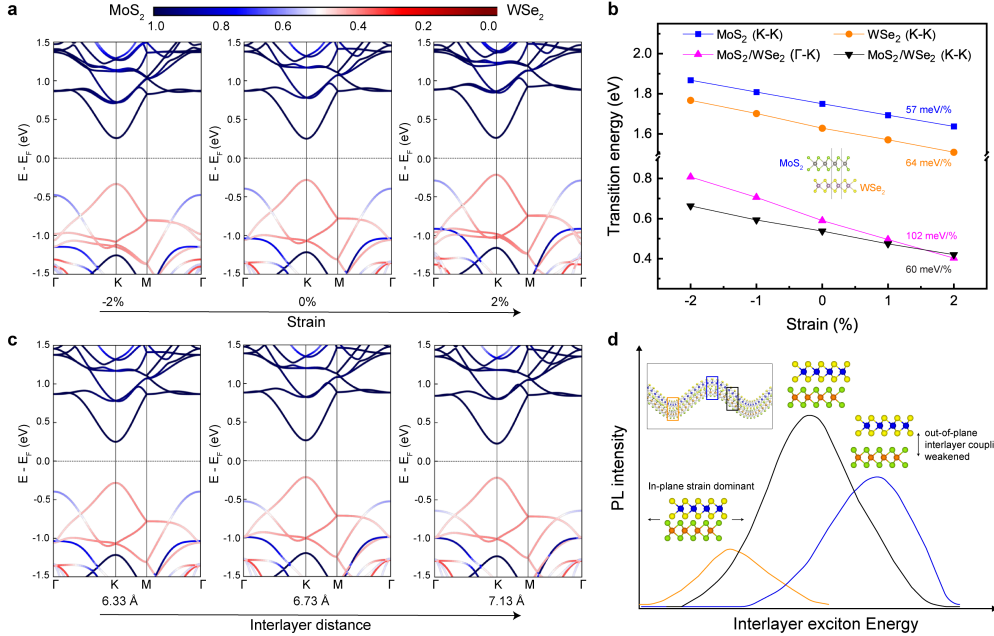


**Figure 6.11: Density functional theory calculation of strained MoS<sub>2</sub>/WSe<sub>2</sub> heterobilayers.** **a** The band structure of MoS<sub>2</sub>/WSe<sub>2</sub> heterobilayers under different in-plane strain values with AB stacking. The color scale describes the origin of the electronic states where the purely blue (red) are completely localized electronic states that come from the MoS<sub>2</sub> (WSe<sub>2</sub>) layer, and intermediate colors have electronic states which are delocalized across both layers (i.e., hybridized state that come from both MoS<sub>2</sub> and WSe<sub>2</sub> layers). **b** Electronic transition energy for K-K transitions of monolayer MoS<sub>2</sub> and monolayer WSe<sub>2</sub>,  $\Gamma$ –K transition of MoS<sub>2</sub>/WSe<sub>2</sub>, and the K-K transition of MoS<sub>2</sub>/WSe<sub>2</sub>, as a function of strain. The inset schematic depicts the AB stacking order. **c** The band structure of MoS<sub>2</sub>/WSe<sub>2</sub> heterobilayers as a function of interlayer distance. **d** Schematic depiction of the non-monotonic behavior of the interlayer exciton PL intensity due to the competition between in-plane strain and out-of-plane interlayer coupling.

tential constants that match with the experimental measurements and the high-level simulations using the coupled GW and Bethe-Salpeter equations (BSE) approach [45, 53]. We coupled PBE with D3 corrections to capture accurate van der Waals interactions in the layered materials [66, 67].

The band structure under different strain conditions is shown in Figure 6.11a for AB stacking, where we project the weighted orbital contributions onto either of the constitutive layers. As noted previously, the interlayer exciton energetic transition

we observe is presumed to be the  $\Gamma - K$  transition, because the  $\text{MoS}_2$  and  $\text{WSe}_2$  layers are not intentionally aligned to their crystallographic axes and therefore the effective oscillator strength of the  $K - K$  transition would be substantially weaker [95]. We further observe that the theoretically calculated deformation potential (Figure 6.11b) for the  $\Gamma - K$  transition provides a much closer match to the experimentally observed value (Figure 6.8f), compared to the  $K - K$  transition. The increased deformation potential constant comes from the fact that the nature of the wavefunctions at the  $\Gamma$  point (valence band) and  $K$  point (conduction band) are of similar orbital nature (specifically, the  $d_z^2$  orbital) [23] and is therefore affected in a similar way under mechanical strain. We also find that the  $\Gamma$  point is particularly sensitive to interlayer coupling and band hybridization, as observed previously [31, 203, 223] (Figure 6.12). Lastly, we remark that this  $\Gamma - K$  interlayer exciton is  $\text{MoS}_2$ -like in character and has strain characteristics akin to a natural bilayer of  $\text{MoS}_2$ , where the  $\Gamma - K$  indirect transition of a natural  $\text{MoS}_2$  bilayer was also observed to have a higher deformation potential compared to the direct  $K - K$  transition and a decreasing PL intensity under tensile strain [36].

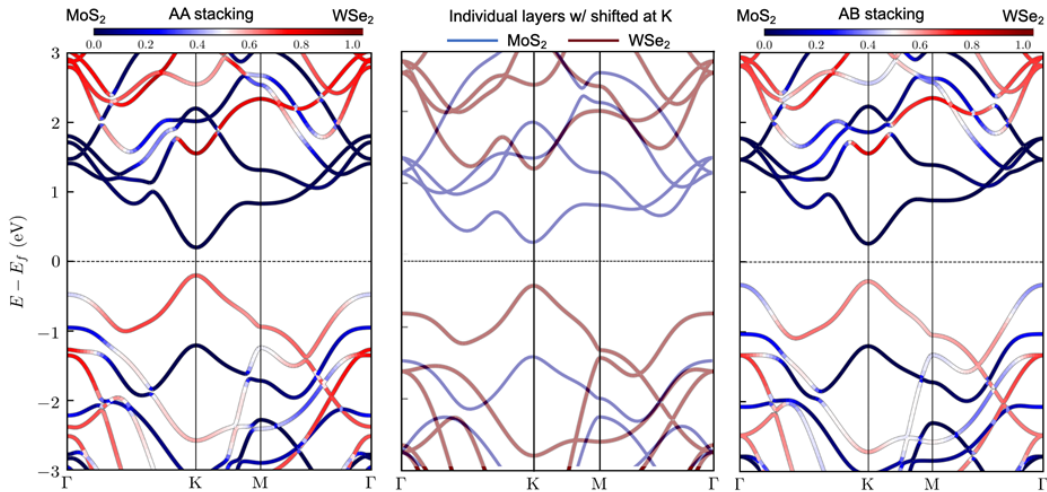
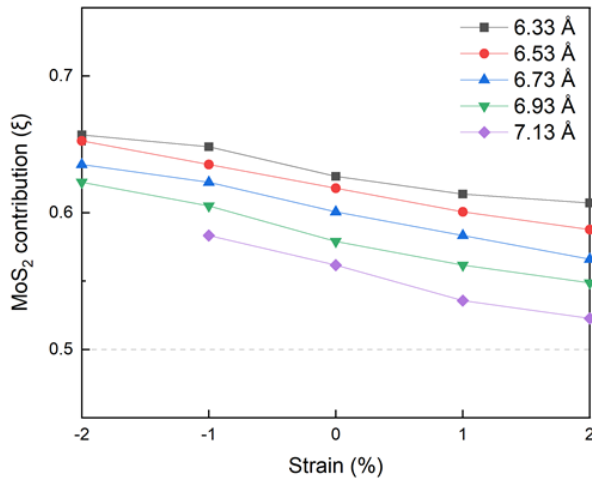


Figure 6.12: **Weighted band structures obtained using DFT calculations.** **a**, AA stacking of  $\text{MoS}_2/\text{WSe}_2$  heterobilayer, **b**, Superposition of band structures of individual monolayers of  $\text{MoS}_2$  and  $\text{WSe}_2$  energy levels aligned with respect to the vacuum level, and **c**, AB stacking of  $\text{MoS}_2/\text{WSe}_2$  heterobilayer.

The band structure calculations also enable us to understand the effects of strain on the band hybridization and therefore the PL intensity trends of the interlayer exciton observed in Figure 6.5. Specifically, we presume that the oscillator strength ( $\sigma_k$ ) of this interlayer exciton transition is proportional to the  $\text{MoS}_2$  character ( $\zeta$ ) at the

$\Gamma$  point [95], i.e.,  $\sigma_k \sim \zeta = |\langle MoS_2 | \Gamma \rangle|^2$ . Therefore, by assuming the oscillator strength scales with the MoS<sub>2</sub> character at the  $\Gamma$  point, i.e.,  $\Delta\sigma_k/\sigma_{k,0} \sim \Delta\zeta/\zeta_0$  we can calculate relative oscillator strength modulations by examining the band structure wavefunction projections (weighted orbital contributions). The calculations show an increase of band hybridization (less the MoS<sub>2</sub> contribution) with tensile strain (Figure 6.11a). The relative modulation in  $\zeta$  would be approximately -0.02/% with strain (Figure 6.13), where the negative sign signifies a decrease in  $\zeta$  with tensile strain. Similarly, we performed calculations of the band structure as a function of interlayer spacing (Figure 6.11c) and found an increase in band hybridization with increased interlayer distance. We calculate the relative modulation in  $\zeta$  to be approximately -0.13/ $\text{\AA}$  with interlayer distance (Figure 6.13). Thus, we predict that the relative oscillator strength and therefore the PL intensity would decrease with both tensile strain and increased interlayer distance.



**Figure 6.13: Band hybridization as a function of strain with different interlayer distances** Band hybridization factors are extracted from weighted projections of orbital contribution for each strain- and interlayer distance-dependent band structures.

Our theoretical calculations corroborate well with the experimental trends of PL intensity observed for the interlayer exciton if we hypothesize that, (1) as tensile strain is applied, the interlayer coupling is sufficiently strong so that the in-plane tensile strain reduces the PL intensity due to the decrease in the oscillator strength, and (2) as compressive strain is applied, the out-of-plane interlayer coupling is weakened, so that the PL intensity also decreases due to the substantially reduced interlayer coupling. Therefore, the PL intensity would likely be maximized near the zero-strain configuration, as we observed experimentally. These effects are depicted schemat-

ically in [Figure 6.11d](#) and suggest that multilayer and heterobilayers TMDCs may exhibit a positive Poisson effect where the reduced out-of-plane interlayer coupling is always accompanied by compressive in-plane strain and vice versa. The calculated effects of larger strain values, other interlayer spacings, and different stacking configurations on the electronic band structure are also shown in [Figure 6.14](#), and we find that the description given above is of general applicability for this relatively twist-angle insensitive  $\text{MoS}_2/\text{WSe}_2$  heterobilayer [95, 187].

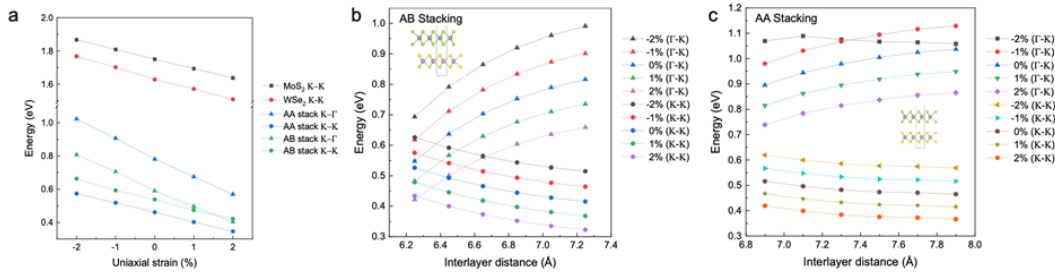


**Figure 6.14: Effects of strain, interlayer spacing, and different stacking configurations on the electronic band structure of  $\text{MoS}_2/\text{WSe}_2$  heterobilayer system obtained using DFT calculations.** **a**, Transition energies as a function of uniaxial strain for different configurations of  $\text{MoS}_2/\text{WSe}_2$  heterobilayer. **b**, Transition energies for AB-stacked heterobilayer system as a function of interlayer distance for various strains. **c**, Transition energies for AA-stacked heterobilayer system as a function of interlayer distance for various strains. The insets depict the stacking order of the heterobilayer systems considered.

## 6.5 Conclusion and Outlook

In summary, our findings suggest that interlayer excitons in transition metal dichalcogenide heterobilayers are particularly attractive for strain engineering. Specifically, we found that momentum-space indirect  $\Gamma - K$  interlayer excitons in  $\text{MoS}_2/\text{WSe}_2$  heterobilayers have a deformation potential of approximately twice that of the constituent intralayer excitons. In addition, we observed that the interlayer coupling of the heterobilayer can be directly tuned in our locally strained structures. We showed that the simultaneous modulation of the out-of-plane interlayer coupling and the in-plane strain in our wrinkled structures can explain the non-monotonic dependence of the interlayer exciton PL peak intensity with peak energy. More generally, the possibility of coupling between in-plane and out-of-plane effects in multilayered structures, akin to a Poisson effect, should be considered when strain engineering layered 2D materials. The existence of multiple knobs that strain can tune in the interlayer exciton system highlights the potential and promise for the next

generation of interlayer exciton strain-based devices.

## 6.6 Appendix

### Sample preparation via PTP assembly process

Wrinkled vdW heterostructures were fabricated via a combination of PDMS-to-PDMS (PTP) assembly process and strain-release mechanism using a stretchable substrate of PDMS. As the first step of the PTP dry assembly process, a monolayer of WSe<sub>2</sub> (HQ Graphene) is exfoliated directly on a uniaxially pre-stretched PDMS substrate (~120%) with a skin layer which was formed by O<sub>2</sub> plasma treatment (Figure 6.2). This stiff skin layer on the PDMS is used to guide conformal out-of-plane deformation (i.e., wrinkling) of the transferred vdW heterobilayer when the substrate is contracted after the release of the pre-stretched PDMS. The stiff skin layer enables an increased transfer of strain by reducing the Young's modulus mismatch between the PDMS and the TMDC heterobilayer [113]. Next, a monolayer of MoS<sub>2</sub> (HQ Graphene), is mechanically exfoliated directly on a separate PDMS substrate. Then the exfoliated monolayer MoS<sub>2</sub>/PDMS directly transfers onto the monolayer WSe<sub>2</sub>/PDMS via a gentle, heat-assisted (~70°) PTP transfer stamping (Figure 6.2), forming a vertically stacked heterostructure (Figure 6.3). Target exfoliated monolayers can be integrated into a heterostructure without contacting any other materials that are essential for avoiding lithographic or etching process-induced polymeric or solvent residues. We note that our PTP assembly process works with either commercially available PDMS slabs (e.g., Gel-Pak) or home-made PDMS (Dow Inc. Sylgard) substrates. Mechanical contraction after the release of the pre-stretched PDMS resulted in periodic wrinkled heterobilayer. We note that the assembled heterobilayer was constrained by a polymethylmethacrylate (PMMA) capping layer, which acts as a clamp to prevent slippage of the heterobilayer when it conforms to the underlying PDMS layer.

### Electronic structure calculations

We performed *ab initio* DFT calculations for the different MoS<sub>2</sub> and WSe<sub>2</sub> monolayers, and MoS<sub>2</sub>/WSe<sub>2</sub> stackings using the Vienna Ab initio simulation (VASP) package to compute the atomic electronic structures [93]. The Perdew-Burke-Ernzerhof (PBE) exchange-correlation functional was applied [148]. We used D3 corrections for van der Waals interactions [66, 67]. We considered ground-state band structure as an approximate description for the optical transitions in the MoS<sub>2</sub>/WSe<sub>2</sub> heterobilayer. The ultrasoft pseudopotentials were used with a 450-eV energy cutoff in all

simulations. The structure relaxation was performed using Gamma-point-centered k-point of  $4 \times 4 \times 1$ . All structures were fully relaxed until the force on each atom reached less than  $0.01 \text{ eV}/\text{\AA}$  and the total energy is converged within  $10^{-6} \text{ eV}$ . Each unit cell consisted of 12 atoms of  $\text{MoS}_2$  as a monolayer or 12 atoms of  $\text{WSe}_2$  as a monolayer, or both for the  $\text{MoS}_2/\text{WSe}_2$  stacking. During the relaxation of the  $\text{MoS}_2/\text{WSe}_2$  stacking structure, the volume of the unit cell is kept variable to determine the optimized lattice constant and to reduce the mismatch between the  $\text{MoS}_2$  and  $\text{WSe}_2$  allowing determination of the unstrained structure. In all simulations, the vacuum is kept at least  $15 \text{ \AA}$  to avoid spurious interactions in the aperiodic direction. Once the structures were fully relaxed and the unstrained configurations were determined, we applied strain in one of the periodic directions. After obtaining all the relaxed configurations of the unstrained and strained structures, the band structures were computed using a total of 90 K-points in the G-K-M-G path.

### Strain tuning coefficient

We also estimated maximum strain accumulated at the crest of wrinkles by using measured wrinkle geometry as shown in the wrinkle height profile (Figure 6.2b). In equilibrium wrinkles, the shear traction on the interface vanishes, and thus, in-plane membrane energy will balance the bending energy of a stiff layer, which is  $\text{MoS}_2/\text{WSe}_2/\text{skin layer}$  [74]. As a consequence, with the elastic plate theory, the maximum uniaxial tensile strain ( $\varepsilon$ ) can be estimated as  $\varepsilon \sim (\pi^2 th)/((1 - v^2)\lambda^2)$  [22, 196], where  $t$  is the thickness of the stiff layer (skin layer + flake layers),  $v$  is the effective Poisson's ratio, and  $h$  and  $\lambda$  are measured wrinkle geometry of height (crest-to-valley) and wavelength, respectively. First, we fitted our measured height profile to a sinusoidal profile to obtain the average amplitude ( $\sim 0.44 \mu\text{m}$ , and thus the height of  $\sim 0.88 \mu\text{m}$ ), and wavelength ( $\sim 4.36 \mu\text{m}$ ) of wrinkles (Figure 6.10a). The thickness of the formed silica skin layer was determined by X-ray reflection analysis, which is approximately 15 nm (Figure 6.10b). The effective Poisson's ratio is determined based on Poisson's ratios of  $\text{MoS}_2$  (0.125),  $\text{WSe}_2$  (0.19), and silica skin layer (0.17). The maximum uniaxial tensile strain is then estimated as about 0.76%. This geometry-driven estimated strain value is slightly lower than our Raman-driven estimated strain ( $\sim 0.8\%$ ), and we attributed the discrepancy to the use of averaged geometry values of wrinkles, where the actual height profile shows a smaller radius of curvature at the crest compared to the fitted curve as shown in Figure 6.10a.

## **Part IV**

### **What's next for Flatland?**

## CONCLUSIONS AND OUTLOOK

*“The first principle is that you must not fool yourself – and you are the easiest person to fool.”*

— Richard P. Feynman

In this thesis, we have demonstrated the plethora of different physics and design considerations for photovoltaic systems with atomically thin active layers. Specifically, we have demonstrated the following:

1. In [Chapter 2](#), we laid out the theoretical framework that shows the impact of band-edge abruptness on the efficiency potential of a photovoltaic active layer. This analysis is applicable to all photovoltaic systems that obey the optoelectronic reciprocity relations, which includes both atomically-thin and conventional systems. We further discussed the role of the indirect and direct band-edge in electronically bulk transition metal dichalcogenides, and showed that materials that minimized this energetic difference had a substantially higher efficiency potential (i.e., is much closer to its detailed balance limit).
2. In [Chapter 3](#), we laid out the theoretical framework and experimentally achieved near-unity absorbance in both ultrathin ( $\sim 10$  nm) and atomically-thin ( $\sim 7$  Å) transition metal dichalcogenides at room temperature. In the case of the ultrathin active layers, this unity absorbance was achieved by using loss as a critical component of the design space. In the case of the atomically-thin active layers, we required an impedance matching of the surface conductivity to free space, which ultimately related the radiative and non-radiative rates of the excitonic system. Finally, with these demonstrations of unity absorbance, we considered theoretically the possibility of creating multijunction excitonic absorbers with efficiency potentials that far surpass the single-junction limit, which takes advantage of the van der Waals coupling in these layered materials. In a van der Waals heterostructure, the solar absorbance can further be distributed amongst many different layers.
3. In [Chapter 4](#), we used the optical architecture demonstrated in the previous chapter for ultrathin unity absorbers and combined it with an electronic geom-

try suitable for high exciton dissociation efficiency and subsequent carrier collection efficiency. Specifically, we demonstrated that a combination of a  $\text{MoS}_2$ - $\text{WSe}_2$  pn heterojunction with a transparent top graphene contact would enable both internal quantum efficiencies above 70% and external quantum efficiencies above 50%. These values remain the highest values for this thickness regime of active layers (subsequent work led by Cora Went demonstrated internal quantum efficiencies above 90% [204]).

4. In [Chapter 5](#), we theoretically and experimentally demonstrated the concept of a ‘band bending junction’, a junction that separates charge carriers due to the extent of vertical band bending. The difference in the vertical band bending, in this case, was due to a difference in thicknesses in the active layer. Therefore, materials that are effectively the same, i.e., with the same quasi-particle bandgap, can separate carriers at the thickness step due to the local symmetry breaking of the band profile.
5. In [Chapter 6](#), we theoretically and experimentally demonstrated the strain tuning of *interlayer* excitons in a  $\text{MoS}_2$ - $\text{WSe}_2$  heterobilayer. We demonstrated a deformation potential of approximately 100 meV/%, which is roughly twice that of the conventional intralayer excitons of the constituent materials. Furthermore, we postulated that an additional effect strain may have on van der Waals heterostructures is there interlayer coupling. Therefore, van der Waals heterostructures may have significant potential for strain engineering applications.

Combined, these results demonstrate the exciting possibilities, physics, and different engineering challenges that atomically-thin materials face as active layers in photovoltaic systems. We briefly surmise possible future directions and give an outlook on each of the main results demonstrated in this thesis:

### 7.1 Outlook from Semiconductor Band Tails Work

In the analysis related to the semiconductor band tails, there are a few interesting research directions to pursue. One aspect is to quantitatively constrain the efficiency potential of the different TMDC systems by accurately and systematically measuring their low-energy absorption coefficients and radiative efficiencies. Specifically, we have found that the absorption coefficient at the indirect band-edge to be quite critical to the specific efficiency penalty, and so the indirect band-edge of materials like  $\text{WSe}_2$ ,  $\text{MoSe}_2$ , and  $\text{MoTe}_2$  should be carefully measured. To perform

these measurements, it is possible to do them directly through a highly sensitive absorbance measurement, such as photothermal deflection spectroscopy, fourier transform photocurrent spectroscopy, or just typical photocurrent spectroscopy with lock-in detection. However, a potentially critical component is that *the specific indirect band-edge absorption coefficient will likely depend on thickness*. This can be intuited from examining the effects of thickness on the bandstructure. While this is readily evident in the one-to-seven layer regime, it likely extends for 10s of nm, since typically quantum-well physics takes over in that regime of thickness. Therefore, it may be important to devise an experimental method of extracting the indirect band-edge *as a function of thickness*. One method to do so is purely from photoluminescence measurements. As we know from [Chapter 2](#), the luminescence is a direct read-out on the absorption profile near the band-edge. Therefore, with some careful quantitative measurements and analysis, it should be possible to use thickness-dependent photoluminescence data to extract out the thickness-dependent absorption coefficient of the different TMDCs.

Another research direction to pursue in regards to semiconductor band tails is examining the role of band tails in excitonic spectra and understanding their microscopic origin. Specifically, while the Lorentzian oscillator model seems to suggest that nearly all resonances should ‘look’ like a Lorentzian, it is well documented that there are significant differences both on the low and high energy side of the resonance. On the high energy side of an excitonic resonance, at room temperature, the spectrum should have a Boltzmann tail, which describes the occupation factor and thermalization of excitons as they scatter with each and off the crystalline lattice. On the low energy side, the dynamics of the tail are related to the excitonic dissociation and dephasing process. Specifically, it can be shown that under the application of an electric field, excitonic absorption resonances also exhibit a band tail that is due to the tunneling of an electron out of its Coulomb potential with the hole. This tunneling is exponentially suppressed, which results in an exponential tail near the band-edge [48]. This physics is similar to that of the band tail in the Franz-Keldysh effect, but is modified in the presence of excitons. Disorder in the energetic landscape furthers increases this band-tailing, and gives ample opportunity for the excitons to dissociate and dephase. A highly sensitive spectroscopic technique near the excitonic absorption edge, as a function of external parameters such as the electric field and/or temperature, may provide a lucid description of the internal physics.

Finally, we postulate a completely different application of semiconductor band tails, which is to achieve low-threshold (solar-driven) lasing. In particular, it is well known that the condition for lasing is some form of population inversion. In the case of semiconductors, this is sometimes referred to as the Bernard-Duraffourg condition:

$$\Delta\mu = E_{f_n} - E_{f_p} > E_g \quad (7.1)$$

In conventional solar systems, this condition is never reached since the solar fluence is substantially lower than the injection densities required. Even in the radiative limit, i.e., no non-radiative recombination, we have  $\Delta\mu = qV_{oc} < E_g$ , and is usually several hundred millivolts away. However, we also found in [Chapter 2](#) that this condition is routinely satisfied at 1-sun conditions when we have semiconductor band tails (in the radiative limit). The simple intuitive explanation for this is that the system is akin to that of a 4-level system, which is well-studied in laser systems and substantially relaxes the condition for population inversion by providing (1) a large source of carriers at the high energy state (2) rapid transfer of carriers to the low energy states (3) sufficiently long lifetimes at the low energy state. An analogous system would be a semiconductor with a large Stokes shift between the absorption and emission edges with near-unity radiative efficiency. This is certainly uncommon experimentally given the typical nature of band tails and the coupling of that internal physics to that of radiative efficiency. However, recent work in the quantum dots literature suggests that they can act as both near-unity radiative emitters with a sizable Stokes shift. In this case, the unity radiative efficiency is achieved by careful surface passivation and epitaxy of the nanocrystal core-shell-ligand structure, and the Stokes shift stems not from defective energy states, but from a type-I band alignment between the core and the shell.

## 7.2 Outlook on Unity Absorbance and Cavity Coupling to Excitonic Absorbers

The work in [Chapter 3](#) describes the methods of achieving *critical* coupling to active layers of TMDCs, which results in unity absorbance. This condition can also be intuited as a matching of radiative and non-radiative rates of the system. However, of substantial interest is the prospect of *strong coupling* to the excitonic systems. This occurs when  $\kappa > \gamma_1, \gamma_2$ , where  $\kappa$  describes the coupling rate constant and  $\gamma_{1,2}$  describe the internal loss constant of each individual system (in this case, the two systems are that of the exciton and of the optical cavity). When the exchange in energy between the systems is faster than their individual decay rates, the individual

modes *hybridize* and form new eigenstates of the system. While strong coupling typically does not result in unity absorbance (as we are moving away from the critical coupling regime), it is of considerable interest to understand whether the presence of exciton-polariton states affect the transport or recombination dynamics. Some of this work has begun in the organic photovoltaics literature [139, 200], where improved energy harvesting and modified recombination dynamics have been achieved. In the case of layered TMDCs, the excitons are more akin to that of a Mott-Wannier type, and therefore it'd be of interest to explore the differences and consequences of ‘strongly coupled’ photovoltaics.

Another research direction of interest is the consequences of the unity absorbance in the monolayer excitonic absorber. Specifically, let us consider the situation where we excite the exciton *on resonance* with a coherent source, e.g., a laser. In this case, the excitons that are generated must obey momentum conservation (this is generally true) and therefore must be generated at the intercept between the light cone and the excitonic bandstructure in the dispersion relations. If the excitons do not scatter strongly with phonons or other quasiparticles, they will remain precisely where they were generated, and if they were to emit (which they would be able to do so efficiently, by reciprocity), their angular emission profile would be exactly the same as the angular profile of the excitation source. In other words, there is a conservation of *etendue* due to the momentum conservation of the excitons, and this would yield several hundred millivolts in the open-circuit voltage. In other words, the momentum conservation would enable natural angle restriction. This physics requires weak interaction of the exciton with other quasiparticles (such as phonons). Equivalently, a strong light-matter interaction (i.e., large optical absorption/emission rates) would also significantly enhance these effects. The effects of the cavity enhances this physics, and the main experimental difficulty would be to discriminate between the excitation source (i.e., the laser) and emission (luminescence from the exciton), since the energies would be quite similar near resonance. One way to do this is to do polarization-resolved measurements, or examining the side bands of the absorption/emission profiles and using sufficiently sharp energy filters. Another possibility is to couple and examine the light sufficiently off-incidence.

Finally, we discuss the prospects and microscopic origin of near-unity absorbance, reflectance, and quantum yield in monolayer TMDCs. The analysis described in [Chapter 3](#) show a direct relationship between the absorbance (and equivalently, reflectance, since  $A = 1 - R$ ) between the radiative and non-radiative rates of the

exciton. It is also understood that the quantum yield of an emitter is generally given as

$$QY = \frac{\gamma_r}{\gamma_r + \gamma_{nr}} \quad (7.2)$$

Thus, we consider a few different regimes of non-radiative rates. For very low non-radiative rates, the sheet conductivity model predicts a large increase in reflectance due to the admittance approaching zero. In the limit of no non-radiative recombination,  $\tilde{r} \rightarrow -1$ , which is the same reflectance amplitude of a perfect mirror. This can also be observed by analyzing the expression for reflectivity of a suspended excitonic system, where

$$R(\omega = \omega_{exc}) = \frac{\gamma_r^2}{(\gamma_r + \gamma_{nr})^2} = QY^2 \quad (7.3)$$

In other words, the reflectance from a suspended exciton can be used to infer the quantum yield of the system. Similarly, we understand from [Chapter 3](#) that near-unity absorbance occurs when  $\gamma_r \approx \gamma_{nr}$  (i.e.,  $QY \approx 50\%$ ). Finally, we should note that the total linewidth is typically given as  $\gamma_T = \gamma_r + \gamma_{nr}$ . Therefore, one would expect that as the non-radiative rates decreases, the quantum yield increases and the reflectance increases. This can be observed even in the dielectric lorentzian oscillator model ([Equation 3.1](#)), where the decreased non-radiative rate would reduce the scattering rate  $\gamma_k$ . These observations also correspond quite well with recent experiments where excitons are strain tuned [\[7\]](#) to reduce their non-radiative scattering rates. However, while near-unity reflectance and absorbance has recently been demonstrated by our group and others [\[51, 173, 208\]](#) (where the total linewidth corresponds quite well to specific reflectance/absorbance measured), the Javey group has demonstrated near-unity quantum yield at room temperature with no apparent change in the linear dielectric function [\[2\]](#). This peculiar observation suggests that the internal physics of the unity quantum yield observed by the Javey group is likely quite different than that due to the pure radiative and non-radiative broadening of an excitonic transition. Recent analysis from the Tisdale group has also suggested that the unity radiative efficiency is likely not a consequence of the intrinsic properties of the exciton, but rather a consequence of highly radiative, long lifetime trap states that effectively protect the exciton from non-radiative recombination by capturing them into this defect state and subsequently thermalizing the excitons back to the band-edge [\[61\]](#).  $WS_2$  may serve as a highly interesting candidate since unity absorbance and quantum yield has been demonstrated at room temperature. Therefore, by further varying the material's properties with electrical gating, temperature, strain, and

cavity coupling, it may be possible to discriminate the origin of the near-unity quantum yield. If these two effects are decoupled, it may also pave way for a material that can exhibit near-unity absorbance and quantum yield *simultaneously*, which would be an ideal optoelectronic material for many applications, including photovoltaics.

### 7.3 Outlook on Achieving High-Efficiency, TMDC-based Photovoltaic Devices

In [Chapter 3](#) and [Chapter 4](#), we demonstrated that ultrathin TMDC active layers can achieve both near-unity absorption and carrier collection efficiency. Therefore, the main challenge that remains is addressing the open-circuit voltage. Aside from circuit-level degradation of photovoltaic behavior (e.g. see [section 1.1](#)), what else could degrade the open-circuit voltage? Furthermore, despite the low relatively low radiative efficiency of electronically bulk TMDCs, their radiative efficiencies still have been characterized as being approximately  $10^{-4}$ . In other words, using the well-known voltage penalty due to a non-radiative component (c.f. [Chapter 2](#)), we would expect a  $q\Delta V_{oc} = k_b T \ln(ERE) \approx -240$  meV voltage penalty. For a bandgap of  $E_g \approx 1.3$  eV, the radiative limit  $V_{oc}$  is roughly  $V_{oc,rad} = 1.0$  V. Therefore, even accounting for the non-unity radiative efficiency, we would expect an open-circuit voltage limit that approaches 700 mV. However, in the cells described in [Chapter 4](#), we have drastically lower open circuit voltages, and more generally, low open circuit voltages has been observed throughout the literature [81]. What causes such a discrepancy?

The main difference between the case where the radiative efficiency is approximately  $10^{-4}$  and that of the device architecture is *the electronic materials that surround the active layer*. More specifically, the insulating substrates like PDMS or  $\text{SiO}_2$  that is typically used to characterize the optical properties of TMDCs do not drastically modify the surface recombination. However, near a metal (like that in a device), carriers are rapidly quenched and additional surface recombination occurs at these interface. Therefore, the open circuit voltage potential is substantially reduced compared to the previous situation, and there is an effective decrease in the external radiative efficiency even further. To mitigate this issue, we explored ‘carrier selective contacts’, i.e., large bandgap materials that are predominantly conducting for a single carrier type (i.e., either electrons or holes). These types of contacts ‘repel’ the presence of the other charge carrier, and therefore, by reducing the overall overlap between the electron and hole, we can significantly reduce the presence of additional surface recombination. The situation with a dielectric like  $\text{SiO}_2$  is one where we effectively repel carriers of both types, and so that the internal

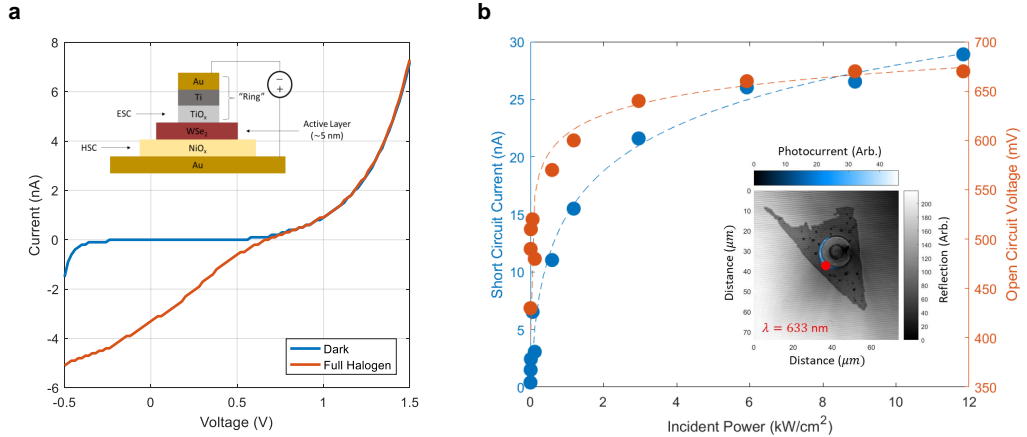
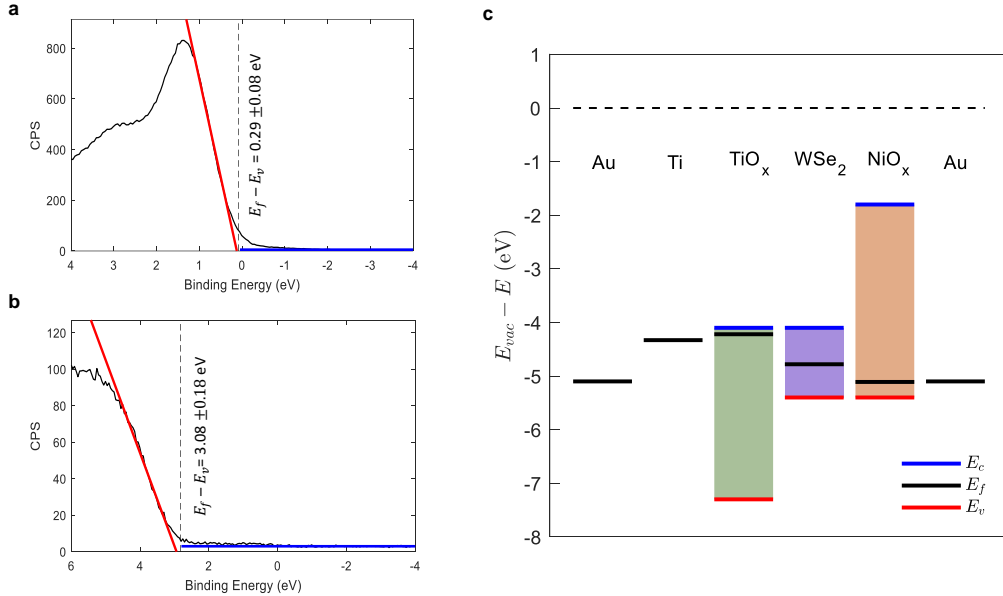


Figure 7.1: **I-V performance of a carrier selective contact device.** **a**  $I - V$  curves in the dark and under illumination for a Au/Ti/TiO<sub>x</sub>/WSe<sub>2</sub>/NiO<sub>x</sub>/Au device. Inset is a cross-sectional schematic of the device under study. **b** Laser power-dependent properties of the short-circuit current (blue, left) and of the open-circuit voltage (orange, right) of the device under study. The inset is an image where the photocurrent image (blue-white scale) and reflection image are superimposed (grey scale), showing the region where the device was illuminated (red dot,  $\lambda = 633$  nm)

luminescence is maintained but because of the lack of conductivity, no photocurrent could be extracted in a hypothetical device with SiO<sub>2</sub>. Therefore, carrier selective contacts require *both* passivation and conductivity (which would result in carrier selectivity [142]). An examination of these carrier selective contacts is shown in Figure 7.1, where we demonstrate open circuit voltages that approach 700 mV. In this geometry, we utilize TiO<sub>x</sub> and NiO<sub>x</sub> as selective contact materials, whose band diagrams are shown in Figure 7.2. This electrical geometry is optimal for blocking carriers of the ‘wrong’ type, since the bandgap of the contact materials are so large that the effective conductivity of the other material type approaches zero [211]. However, the overall conductivity of the contacts could be substantially improved, as evidenced by the low short-circuit current.

The low short-circuit current observed in Figure 7.1 suggests that carefully controlling the doping of these selective contacts will be important. Exploring other materials as selective contacts may be of great interest too, borrowing specifically from the existing literature of perovskites and organic photovoltaics [205]. It may be of interest to use other 2D materials, such as large bandgap materials like GaS, to create atomically-pristine van der Waals interfaces. The main challenge in every case will be to achieve both high passivation and high carrier conductivity. How-



**Figure 7.2: X-ray photoemission spectroscopy of  $\text{TiO}_x$  and  $\text{NiO}_x$ .** Photoemission spectrum near the valence band-edge of **a**  $\text{NiO}_x$  and **b**  $\text{TiO}_x$ . Also shown is a linear fit to the background (blue line) and the valence band (red line). The intercept can be used to quantify the valence band edge relative to the Fermi level. Binding energies are referenced to the Au 4f core level. **c** Drawn band diagram using literature values of the work-function, electron affinity, and bandgap.  $E_f - E_v$  is taken from the values in **a** and **b**.

ever, it is important to note that this scheme of carrier selective contacts has been an extremely effective method of achieving near the maximum power conversion efficiency potential of a given material (limited by the material's optical properties, c.f. [Chapter 2](#)) in other photovoltaic active layers, and could be applied to both ultrathin and atomically-thin TMDC materials if successful.

## Bibliography

- [1] Rafik Addou, Luigi Colombo, and Robert M Wallace. Surface defects on natural mos2. *ACS applied materials & interfaces*, 7(22):11921–11929, 2015.
- [2] Matin Amani, Peyman Taheri, Rafik Addou, Geun Ho Ahn, Daisuke Kiriya, Der Hsien Lien, Joel W. Ager, Robert M. Wallace, and Ali Javey. Recombination kinetics and effects of superacid treatment in sulfur- and selenium-based transition metal dichalcogenides. *Nano Letters*, 16(4):2786–2791, 2016. ISSN 15306992. doi:[10.1021/acs.nanolett.6b00536](https://doi.org/10.1021/acs.nanolett.6b00536).
- [3] Paul A. Anderson. Work function of gold. *Physical Review*, 115(3):553–554, 1959. ISSN 0031899X. doi:[10.1103/PhysRev.115.553](https://doi.org/10.1103/PhysRev.115.553).
- [4] Nicklas Anttu. Shockley-queisser detailed balance efficiency limit for nanowire solar cells. *ACS Photonics*, 2(3):446–453, 2015. ISSN 23304022. doi:[10.1021/ph5004835](https://doi.org/10.1021/ph5004835).
- [5] Gerardo L. Araújo and Antonio Martí. Absolute limiting efficiencies for photovoltaic energy conversion. *Solar Energy Materials and Solar Cells*, 33 (2):213–240, 1994. ISSN 09270248. doi:[10.1016/0927-0248\(94\)90209-7](https://doi.org/10.1016/0927-0248(94)90209-7).
- [6] Ardalan Armin, Marappan Velusamy, Pascal Wolfer, Yuliang Zhang, Paul L Burn, and Paul Meredith. Quantum efficiency of organic solar cells Electro-optical cavity considerations. *ACS Photonics*, 1:173–181, 2014.
- [7] Ozgur Burak Aslan, Minda Deng, and Tony F. Heinz. Strain tuning of excitons in monolayer wse<sub>2</sub>. *Physical Review B*, 98(11):115308, 2018. ISSN 24699969. doi:[10.1103/PhysRevB.98.115308](https://doi.org/10.1103/PhysRevB.98.115308).
- [8] Harry A Atwater and Albert Polman. Plasmonics for improved photovoltaic devices. *Nat. Mater.*, 9(10):205–213, 2010. ISSN 1476-1122. doi:[10.1038/nmat2866](https://doi.org/10.1038/nmat2866).
- [9] D. Baran, T. Kirchartz, S. Wheeler, S. Dimitrov, M. Abdelsamie, J. Gorman, R. S. Ashraf, S. Holliday, A. Wadsworth, N. Gasparini, P. Kaienburg, H. Yan, A. Amassian, C. J. Brabec, J. R. Durrant, and I. McCulloch. Reduced voltage losses yield 10solar cells with >1 v open circuit voltages. *Energy and Environmental Science*, 9(12):3783–3793, 2016. ISSN 17545706. doi:[10.1039/c6ee02598f](https://doi.org/10.1039/c6ee02598f).
- [10] John Bardeen. Surface states and rectification at a metal semi-conductor contact. *Physical Review*, 71(10):717–727, 1947. ISSN 0031899X. doi:[10.1103/PhysRev.71.717](https://doi.org/10.1103/PhysRev.71.717).
- [11] Britton W H Baugher, Hugh O H Churchill, Yafang Yang, and Pablo Jarillo-Herrero. Optoelectronic devices based on electrically tunable p-n diodes in a

monolayer dichalcogenide. *Nature nanotechnology*, 9(4):262–7, 2014. ISSN 1748-3395. doi:[10.1038/nnano.2014.25](https://doi.org/10.1038/nnano.2014.25).

[12] M. Beaudoin, A. J.G. DeVries, S. R. Johnson, H. Laman, and T. Tiedje. Optical absorption edge of semi-insulating gaas and inp at high temperatures. *Applied Physics Letters*, 70(26):3540–3542, 1997. ISSN 00036951. doi:[10.1063/1.119226](https://doi.org/10.1063/1.119226).

[13] Timothy C. Berkelbach, Mark S. Hybertsen, and David R. Reichman. Theory of neutral and charged excitons in monolayer transition metal dichalcogenides. *Phys. Rev. B*, 88:045318, Jul 2013. doi:[10.1103/PhysRevB.88.045318](https://doi.org/10.1103/PhysRevB.88.045318).

[14] Marco Bernardi, Maurizia Palummo, and Jeffrey C. Grossman. Extraordinary sunlight absorption and one nanometer thick photovoltaics using two-dimensional monolayer materials. *Nano Letters*, 13(8):3664–3670, 2013. ISSN 15306984. doi:[10.1021/nl401544y](https://doi.org/10.1021/nl401544y).

[15] Udai Bhanu, Muhammad R. Islam, Laurene Tetard, and Saiful I. Khondaker. Photoluminescence quenching in gold - mos2 hybrid nanoflakes. *Scientific Reports*, 4(1):5575, 2015. ISSN 2045-2322. doi:[10.1038/srep05575](https://doi.org/10.1038/srep05575).

[16] Rupak Bhattacharya, Bipul Pal, and Bhavtosh Bansal. On conversion of luminescence into absorption and the van roosbroeck-shockley relation. *Applied Physics Letters*, 100(22):1–4, 2012. ISSN 00036951. doi:[10.1063/1.4721495](https://doi.org/10.1063/1.4721495).

[17] Beatrix Blank, Thomas Kirchartz, Stephan Lany, and Uwe Rau. Selection metric for photovoltaic materials screening based on detailed-balance analysis. *Physical Review Applied*, 8(2), 2017. ISSN 23317019. doi:[10.1103/PhysRevApplied.8.024032](https://doi.org/10.1103/PhysRevApplied.8.024032).

[18] Melina K. Blees, Arthur W. Barnard, Peter A. Rose, Samantha P. Roberts, Kathryn L. McGill, Pinshane Y. Huang, Alexander R. Ruyack, Joshua W. Kevek, Bryce Kobrin, David A. Muller, and Paul L. McEuen. Graphene kirigami. *Nature*, 524(7564):204–207, 2015. ISSN 14764687. doi:[10.1038/nature14588](https://doi.org/10.1038/nature14588).

[19] L Britnell, R M Ribeiro, A Eckmann, R Jalil, B D Belle, A Mishchenko, Y-J Kim, V R Gorbachev, T Georgiou, V S Morozov, A N Grigorenko, A K Geim, C Casiraghi, A H Castro Neto, and K S Novoselov. Strong light-matter interactions in heterostructures of atomically thin films. *Science*, 340: 1311–1314, 2013. ISSN 1095-9203. doi:[10.1126/science.1235547](https://doi.org/10.1126/science.1235547).

[20] Michele Buscema, Gary A. Steele, Herre S J van der Zant, and Andres Castellanos-Gomez. The effect of the substrate on the raman and photoluminescence emission of single-layer mos2. *Nano Research*, 7(4):1–11, 2014. ISSN 19980000. doi:[10.1007/s12274-014-0424-0](https://doi.org/10.1007/s12274-014-0424-0).

- [21] Felix Carrascoso, Der Yuh Lin, Riccardo Frisenda, and Andres Castellanos-Gomez. Biaxial strain tuning of interlayer excitons in bilayer mos<sub>2</sub>. *Journal of Physical Materials*, 3, 2020. doi:<https://doi.org/10.1088/2515-7639/ab4432>.
- [22] Andres Castellanos-Gomez, Michele Buscema, Rianda Molenaar, Vibhor Singh, Laurens Janssen, Herre S J van der Zant, and Gary A Steele. Deterministic transfer of two-dimensional materials by all-dry viscoelastic stamping. *2D Materials*, 1(1):011002, 2014. ISSN 2053-1583. doi:<10.1088/2053-1583/1/1/011002>.
- [23] Chung Huai Chang, Xiaofeng Fan, Shi Hsin Lin, and Jer Lai Kuo. Orbital analysis of electronic structure and phonon dispersion in mos<sub>2</sub>, mose<sub>2</sub>, ws<sub>2</sub>, and wse<sub>2</sub> monolayers under strain. *Physical Review B - Condensed Matter and Materials Physics*, 88(19):1–9, 2013. ISSN 10980121. doi:<10.1103/PhysRevB.88.195420>.
- [24] A J Chaves, R M Ribeiro, T Frederico, and N M R Peres. Excitonic effects in the optical properties of 2d materials:an equation of motion approach. *2D Materials*, 4(2):025086, apr 2017. doi:<10.1088/2053-1583/aa6b72>.
- [25] Tawinan Cheiwhanchamnangij and Walter R.L. Lambrecht. Quasiparticle band structure calculation of monolayer, bilayer, and bulk mos<sub>2</sub>. *Physical Review B - Condensed Matter and Materials Physics*, 85(20):1–4, 2012. ISSN 10980121. doi:<10.1103/PhysRevB.85.205302>.
- [26] Hailong Chen, Xiewen Wen, Jing Zhang, Tianmin Wu, Yongji Gong, Xiang Zhang, Jiangtan Yuan, Chongyue Yi, Jun Lou, Pulickel M. Ajayan, Wei Zhuang, Guangyu Zhang, and Junrong Zheng. Ultrafast formation of interlayer hot excitons in atomically thin mos<sub>2</sub>/ws<sub>2</sub> heterostructures. *Nature Communications*, 7:12512, 2016. ISSN 2041-1723. doi:<10.1038/ncomms12512>.
- [27] Cheng-Wei Cheng, Kuen-Ting Shiu, Ning Li, Shu-Jen Han, Leathen Shi, and Devendra K Sadana. Epitaxial lift-off process for gallium arsenide substrate reuse and flexible electronics. *Nature Communications*, 4:1577, 2013. ISSN 2041-1723. doi:<10.1038/ncomms2583>.
- [28] Rui Cheng, Dehui Li, Hailong Zhou, Chen Wang, Anxiang Yin, Shan Jiang, Yuan Liu, Yu Chen, Yu Huang, and Xiangfeng Duan. Electroluminescence and photocurrent generation from atomically sharp wse<sub>2</sub>/mos<sub>2</sub> heterojunction p–n diodes. *Nano letters*, 14(10):5590–5597, 2014.
- [29] Alexey Chernikov, Timothy C. Berkelbach, Heather M. Hill, Albert Rigosi, Yilei Li, Ozgur Burak Aslan, David R. Reichman, Mark S. Hybertsen, and Tony F. Heinz. Exciton binding energy and nonhydrogenic rydberg series in monolayer ws<sub>2</sub>. *Phys. Rev. Lett.*, 113:076802, Aug 2014. doi:<10.1103/PhysRevLett.113.076802>.

- [30] Ming Hui Chiu, Ming Yang Li, Wengjing Zhang, Wei Ting Hsu, Wen Hao Chang, Mauricio Terrones, Humberto Terrones, and Lain Jong Li. Spectroscopic signatures for interlayer coupling in  $\text{mos}_2$ - $\text{wse}_2$  van der waals stacking. *ACS Nano*, 8(9):9649–9656, 2014. ISSN 1936086X. doi:[10.1021/nn504229z](https://doi.org/10.1021/nn504229z).
- [31] Ming-hui Chiu, Chendong Zhang, Hung-wei Shiu, Chih-piao Chuu, Chang-hsiao Chen, Chih-yuan S Chang, Chia-hao Chen, Mei-ying Chou, Chih-kang Shih, and Lain-jong Li. Determination of band alignment in the single-layer  $\text{mos}_2$ / $\text{wse}_2$  heterojunction. *Nature Communications*, 6:1–6, 2015. doi:[10.1038/ncomms8666](https://doi.org/10.1038/ncomms8666).
- [32] Chia Hao Marcus Chuang, Andrea Maurano, Riley E. Brandt, Gyu Weon Hwang, Joel Jean, Tonio Buonassisi, Vladimir Bulović, and Mounig G. Bawendi. Open-circuit voltage deficit, radiative sub-bandgap states, and prospects in quantum dot solar cells. *Nano Letters*, 15(5):3286–3294, 2015. ISSN 15306992. doi:[10.1021/acs.nanolett.5b00513](https://doi.org/10.1021/acs.nanolett.5b00513).
- [33] G. D. Cody. *The Optical Absorption Edge of a-Si: H*, volume 21. Academic Press, Inc., 1984. ISBN 0127521488. doi:[10.1016/S0080-8784\(08\)62910-5](https://doi.org/10.1016/S0080-8784(08)62910-5).
- [34] G. D. Cody. Urbach edge of crystalline and amorphous silicon: a personal review. *Journal of Non-Crystalline Solids*, 141(C):3–15, 1992. ISSN 00223093. doi:[10.1016/S0022-3093\(05\)80513-7](https://doi.org/10.1016/S0022-3093(05)80513-7).
- [35] George D. Cody, Tom Tiedje, Benjamin Abeles, Bonnie Brookes, and Yehuda Goldstein. Disorder and the optical-absorption edge of hydrogenated amorphous silicon. *Physical Review Letters*, 47(20):1480–1483, 1981. doi:<https://doi.org/10.1103/PhysRevLett.47.1480>.
- [36] Hiram J. Conley, Bin Wang, Jed I. Ziegler, Richard F. Haglund, Sokrates T. Pantelides, and Kirill I. Bolotin. Bandgap engineering of strained monolayer and bilayer  $\text{mos}_2$ . *Nano Letters*, 13(8):3626–3630, 2013. ISSN 15306984. doi:[10.1021/nl4014748](https://doi.org/10.1021/nl4014748).
- [37] Ipsita Datta, Sang Hoon Chae, Gaurang R. Bhatt, Mohammad Amin Tadayon, Baichang Li, Yiling Yu, Chibeom Park, Jiwoong Park, Linyou Cao, D. N. Basov, James Hone, and Michal Lipson. Low-loss composite photonic platform based on 2d semiconductor monolayers. *Nature Photonics*, 14(4):256–262, 2020. ISSN 17494893. doi:[10.1038/s41566-020-0590-4](https://doi.org/10.1038/s41566-020-0590-4).
- [38] Alexis De Vos and Herman Pauwels. On the thermodynamics limit of photovoltaic energy conversion. *Applied Physics*, 25(2):119–125, 1981.
- [39] Stefaan De Wolf, Jakub Holovsky, Soo-Jin Moon, Philipp Loper, Bjoern Niesen, Martin Ledinsky, Franz-Josef Haug, Jun-Ho Yum, and Christophe Ballif. Organometallic halide perovskites: Sharp optical absorption edge and its relation to photovoltaic performance. *Journal of Physical Chemistry Letters*, 5:1035–1039, 2014. doi:[10.1021/jz500279b](https://doi.org/10.1021/jz500279b).

[40] Rahul Debnath, Indrajit Maity, Rabindra Biswas, Varun Raghunathan, Manish Jain, and Arindam Ghosh. Evolution of high-frequency raman modes and their doping dependence in twisted bilayer mos<sub>2</sub>. *Nanoscale*, 12(33):17272–17280, 2020. ISSN 20403372. doi:[10.1039/c9nr09897f](https://doi.org/10.1039/c9nr09897f).

[41] P Debye and E. Hückel. Zur theorie der elektrolyte. i. gefrierpunktsniedrigung und verwandte erscheinungen. *Physikalische Zeitschrift*, 24(9):185–206, 1923. doi:[10.1007/bfb0111753](https://doi.org/10.1007/bfb0111753).

[42] Sujay B. Desai, Gyungseon Seol, Jeong Seuk Kang, Hui Fang, Corsin Battaglia, Rehan Kapadia, Joel W. Ager, Jing Guo, and Ali Javey. Strain-induced indirect to direct bandgap transition in multilayer wse<sub>2</sub>. *Nano Letters*, 14(8):4592–4597, 2014. ISSN 15306992. doi:[10.1021/nl501638a](https://doi.org/10.1021/nl501638a).

[43] Sujay B. Desai, Surabhi R. Madhvapathy, Matin Amani, Daisuke Kiriya, Mark Hettick, Mahmut Tosun, Yuzhi Zhou, Madan Dubey, Joel W. Ager, Daryl Chrzan, and Ali Javey. Gold-mediated exfoliation of ultralarge optoelectronically-perfect monolayers. *Advanced Materials*, 28(21):4053–4058, 2016. ISSN 09359648. doi:[10.1002/adma.201506171](https://doi.org/10.1002/adma.201506171).

[44] Aleksandra Djurisic and E. Herbert Li. Optical properties of graphite. *Journal of Applied Physics*, 85(10):7404–7410, 1999.

[45] Liang Dong, Raju R. Namburu, Terrance P. O'Regan, Madan Dubey, and Avinash M. Dongare. Theoretical study on strain-induced variations in electronic properties of monolayer mos<sub>2</sub>. *Journal of Materials Science*, 49(19):6762–6771, 2014. ISSN 15734803. doi:[10.1007/s10853-014-8370-5](https://doi.org/10.1007/s10853-014-8370-5).

[46] C. Donolato. A reciprocity theorem for charge collection. *Applied Physics Letters*, 46(3):270–272, 1985. ISSN 00036951. doi:[10.1063/1.95654](https://doi.org/10.1063/1.95654).

[47] Danna Doratotaj, Jeffrey R. Simpson, and Jia An Yan. Probing the uniaxial strains in mos<sub>2</sub> using polarized raman spectroscopy: A first-principles study. *Physical Review B*, 93(7):075401, 2016. ISSN 24699969. doi:[10.1103/PhysRevB.93.075401](https://doi.org/10.1103/PhysRevB.93.075401).

[48] John D. Dow and David Redfield. Electroabsorption in semiconductors: The excitonic absorption edge. *Phys. Rev. B*, 1:3358–3371, Apr 1970. doi:[10.1103/PhysRevB.1.3358](https://doi.org/10.1103/PhysRevB.1.3358). URL <https://link.aps.org/doi/10.1103/PhysRevB.1.3358>.

[49] A. W. Dwyerdari and C. H. B. Mee. Work function measurements on (100) and (110) surfaces of silver. *Physica Status Solidi (A) Applications and Materials Science*, 27:223–230, 1975.

[50] Goki Eda and Stefan A. Maier. Two-dimensional crystals: Managing light for optoelectronics. *ACS Nano*, 7(7):5660–5665, 2013. ISSN 19360851. doi:[10.1021/nn403159y](https://doi.org/10.1021/nn403159y).

[51] Itai Epstein, Bernat Terrés, André J. Chaves, Varun-Varma Pusapati, Daniel A. Rhodes, Bettina Frank, Valentin Zimmermann, Ying Qin, Kenji Watanabe, Takashi Taniguchi, Harald Giessen, Sefaattin Tongay, James C. Hone, Nuno M. R. Peres, and Frank H. L. Koppens. Near-unity light absorption in a monolayer ws<sub>2</sub> van der waals heterostructure cavity. *Nano Letters*, 20(5):3545–3552, 2020. doi:[10.1021/acs.nanolett.0c00492](https://doi.org/10.1021/acs.nanolett.0c00492). URL <https://doi.org/10.1021/acs.nanolett.0c00492>. PMID: 32283034.

[52] B. L. Evans, J. Bordas, R. Zallen, D. F. Blossey, P. M. Williams, R. C. Fivaz, Ph. E. Schmid, D. J. Huntley, R. F. Frindt, and J. M. Vandenberg-Voorhoeve. *Optical and Electrical Properties*, volume 4. D. Reidel Publishing Company, 1976. ISBN 978-94-010-1478-6. doi:[10.1007/978-94-010-1478-6](https://doi.org/10.1007/978-94-010-1478-6).

[53] Ji Feng, Xiaofeng Qian, Cheng Wei Huang, and Ju Li. Strain-engineered artificial atom as a broad-spectrum solar energy funnel. *Nature Photonics*, 6(12):866–872, 2012. ISSN 17494885. doi:[10.1038/nphoton.2012.285](https://doi.org/10.1038/nphoton.2012.285).

[54] Marco M Furchi, Andreas Pospischil, Florian Libisch, Joachim Burgdo, and Thomas Mueller. Photovoltaic effect in an electrically tunable van der waals heterojunction. *Nano Letters*, 14:4785–4791, 2014.

[55] R. Geick, C. Perry, and G. Rupprecht. Normal modes in hexagonal boron nitride. *Physical Review*, 146(2):543–547, 1966. ISSN 0031-899X. doi:[10.1103/PhysRev.146.543](https://doi.org/10.1103/PhysRev.146.543).

[56] Andre K Geim and Irina V Grigorieva. Van der waals heterostructures. *Nature*, 499(7459):419–425, 2013.

[57] Thanasis Georgiou, Rashid Jalil, Branson D Belle, Liam Britnell, V Roman Gorbachev, V Sergey Morozov, Yong-Jin Kim, Ali Ghosh, Sarah J Haigh, Oleg Makarovsky, Laurence Eaves, Leonid a Ponomarenko, Andre K Geim, Kostya S Novoselov, and Artem Mishchenko. Vertical field-effect transistor based on graphene-ws<sub>2</sub> heterostructures for flexible and transparent electronics. *Nature nanotechnology*, 8(2):100–3, 2013. ISSN 1748-3395. doi:[10.1038/nnano.2012.224](https://doi.org/10.1038/nnano.2012.224).

[58] François Gibelli, Laurent Lombez, and Jean François Guillemoles. Accurate radiation temperature and chemical potential from quantitative photoluminescence analysis of hot carrier populations. *Journal of Physics Condensed Matter*, 29(6):0–6, 2017. ISSN 1361648X. doi:[10.1088/1361-648X/29/6/06LT02](https://doi.org/10.1088/1361-648X/29/6/06LT02).

[59] Peter E Glaser. Power from the sun: Its future. *Science*, 162(3856):857–861, 1968.

[60] Tayfun Gokmen, Oki Gunawan, Teodor K. Todorov, and David B. Mitzi. Band tailing and efficiency limitation in kesterite solar cells. *Applied Physics Letters*, 103(10), 2013. ISSN 00036951. doi:[10.1063/1.4820250](https://doi.org/10.1063/1.4820250).

- [61] A. J. Goodman, A. P. Willard, and W. A. Tisdale. Exciton trapping is responsible for the long apparent lifetime in acid-treated mos<sub>2</sub>. *Phys. Rev. B*, 96:121404, Sep 2017. doi:[10.1103/PhysRevB.96.121404](https://doi.org/10.1103/PhysRevB.96.121404). URL <https://link.aps.org/doi/10.1103/PhysRevB.96.121404>.
- [62] Tamihiro Gotoh, Shuichi Nonomura, Satoshi Hirata, and Shoji Nitta. Photothermal bending spectroscopy and photothermal deflection spectroscopy of c 60 thin films. *Applied Surface Science*, 113-114:278–281, 1997. ISSN 01694332. doi:[10.1016/S0169-4332\(96\)00776-3](https://doi.org/10.1016/S0169-4332(96)00776-3).
- [63] Martin A. Green. Self-consistent optical parameters of intrinsic silicon at 300 k including temperature coefficients. *Solar Energy Materials and Solar Cells*, 92(11):1305–1310, 2008. ISSN 09270248. doi:[10.1016/j.solmat.2008.06.009](https://doi.org/10.1016/j.solmat.2008.06.009).
- [64] Julia R. Greer and William D. Nix. Nanoscale gold pillars strengthened through dislocation starvation. *Physical Review B*, 73(24):1–6, 2006. ISSN 10980121. doi:[10.1103/PhysRevB.73.245410](https://doi.org/10.1103/PhysRevB.73.245410).
- [65] A. A. Griffith. The phenomena of rupture and flow in solids. *Philos. Trans. R. Soc. London Ser. A*, 221, 1921. ISSN 00254576. doi:[10.1098/rsta.1921.0006](https://doi.org/10.1098/rsta.1921.0006).
- [66] Stefan Grimme, Jens Antony, Stephan Ehrlich, and Helge Krieg. A consistent and accurate ab initio parametrization of density functional dispersion correction (dft-d) for the 94 elements h-pu. *Journal of Chemical Physics*, 132(15), 2010. ISSN 00219606. doi:[10.1063/1.3382344](https://doi.org/10.1063/1.3382344).
- [67] Stefan Grimme, Stephan Ehrlich, and Lars Goerigk. Effect of the damping function in dispersion corrected density functional theory. *Journal of computational chemistry*, 32:1456–1465, 2011. ISSN 1096-987X. doi:[10.1002/jcc](https://doi.org/10.1002/jcc).
- [68] M. C. Hanna and A. J. Nozik. Solar conversion efficiency of photovoltaic and photoelectrolysis cells with carrier multiplication absorbers. *Journal of Applied Physics*, 100(7), 2006. ISSN 00218979. doi:[10.1063/1.2356795](https://doi.org/10.1063/1.2356795).
- [69] Keliang He, Charles Poole, Kin Fai Mak, and Jie Shan. Experimental demonstration of continuous electronic structure tuning via strain in atomically thin mos<sub>2</sub>. *Nano Letters*, 13(6):2931–2936, 2013. ISSN 15306984. doi:[10.1021/nl4013166](https://doi.org/10.1021/nl4013166).
- [70] Yongmin He, Yang Yang, Zhuhua Zhang, Yongji Gong, Wu Zhou, Zhili Hu, Gonglan Ye, Xiang Zhang, Elisabeth Bianco, Sidong Lei, Zehua Jin, Xiaolong Zou, Yingchao Yang, Yuan Zhang, Erqing Xie, Jun Lou, Boris Yakobson, Robert Vajtai, Bo Li, and Pulickel Ajayan. Strain-induced electronic structure changes in stacked van der waals heterostructures. *Nano Letters*, 16(5):3314–3320, 2016. ISSN 15306992. doi:[10.1021/acs.nanolett.6b00932](https://doi.org/10.1021/acs.nanolett.6b00932).

[71] J. T. Heath, J. D. Cohen, W. N. Shafarman, D. X. Liao, and A. A. Rockett. Effect of ga content on defect states in cuin1-xga xse2 photovoltaic devices. *Applied Physics Letters*, 80(24):4540–4542, 2002. ISSN 00036951. doi:[10.1063/1.1485301](https://doi.org/10.1063/1.1485301).

[72] Sarah L. Howell, Deep Jariwala, Chung Chiang Wu, Kan Sheng Chen, Vinod K. Sangwan, Junmo Kang, Tobin J. Marks, Mark C. Hersam, and Lincoln J. Lauhon. Investigation of band-offsets at monolayer-multilayer mos<sub>2</sub> junctions by scanning photocurrent microscopy. *Nano Letters*, 15(4):2278–2284, 2015. ISSN 15306992. doi:[10.1021/nl504311p](https://doi.org/10.1021/nl504311p).

[73] Lujun Huang, Guoqing Li, Alper Gurarslan, Yiling Yu, Ronny Kirste, Wei Guo, Junjie Zhao, Ramon Collazo, Zlatko Sitar, Gregory N. Parsons, Michael Kudenov, and Linyou Cao. Atomically thin mos<sub>2</sub> narrowband and broadband light superabsorbers. *ACS Nano*, 10(8):7493–7499, 2016. ISSN 1936086X. doi:[10.1021/acsnano.6b02195](https://doi.org/10.1021/acsnano.6b02195).

[74] R Huang, H Yin, J Liang, JC Sturm, KD Hobart, and Z Suo. Mechanics of relaxing sige islands on a viscous glass. *Acta Mechanica Sinica*, 18(5):441–456, 2002.

[75] Shenyang Huang, Guowei Zhang, Fengren Fan, Chaoyu Song, Fanjie Wang, Qiaoxia Xing, Chong Wang, Hua Wu, and Hugen Yan. Strain-tunable van der waals interactions in few-layer black phosphorus. *Nature Communications*, 10(1):1–7, 2019. ISSN 20411723. doi:[10.1038/s41467-019-10483-8](https://doi.org/10.1038/s41467-019-10483-8).

[76] Yuan Huang, Yu Hao Pan, Rong Yang, Li Hong Bao, Lei Meng, Hai Lan Luo, Yong Qing Cai, Guo Dong Liu, Wen Juan Zhao, Zhang Zhou, Liang Mei Wu, Zhi Li Zhu, Ming Huang, Li Wei Liu, Lei Liu, Peng Cheng, Ke Hui Wu, Shi Bing Tian, Chang Zhi Gu, You Guo Shi, Yan Feng Guo, Zhi Gang Cheng, Jiang Ping Hu, Lin Zhao, Guan Hua Yang, Eli Sutter, Peter Sutter, Ye Liang Wang, Wei Ji, Xing Jiang Zhou, and Hong Jun Gao. Universal mechanical exfoliation of large-area 2d crystals. *Nature Communications*, 11(1), 2020. ISSN 20411723. doi:[10.1038/s41467-020-16266-w](https://doi.org/10.1038/s41467-020-16266-w).

[77] Muhammad Monirul Islam, Mohammad Abdul Halim, Takeaki Sakurai, Noriyuki Sakai, Takuya Kato, Hiroki Sugimoto, Hitoshi Tampo, Hajime Shibata, Shigeru Niki, and Katsuhiro Akimoto. Determination of deep-level defects in cu2znsn(s,se)4 thin-films using photocapacitance method. *Applied Physics Letters*, 106(24), 2015. ISSN 00036951. doi:[10.1063/1.4922810](https://doi.org/10.1063/1.4922810).

[78] Deep Jariwala, Vinod K. Sangwan, Dattatray J. Late, James E. Johns, Vinayak P. Dravid, Tobin J. Marks, Lincoln J. Lauhon, and Mark C. Hersam. Band-like transport in high mobility unencapsulated single-layer mos<sub>2</sub> transistors. *Applied Physics Letters*, 102(17):173107, 2013. ISSN 00036951. doi:[10.1063/1.4803920](https://doi.org/10.1063/1.4803920).

- [79] Deep Jariwala, Vinod K Sangwan, Lincoln J Lauhon, Tobin J Marks, and Mark C Hersam. Emerging device applications for semiconducting two-dimensional transition metal dichalcogenides. *ACS nano*, 8(2):1102–1120, 2014. ISSN 1936-086X. doi:[10.1021/nn500064s](https://doi.org/10.1021/nn500064s).
- [80] Deep Jariwala, Artur R. Davoyan, Giulia Tagliabue, Michelle C. Sherrott, Joeson Wong, and Harry A. Atwater. Near-unity absorption in van der waals semiconductors for ultrathin optoelectronics. *Nano Letters*, 16(9):5482–5487, 2016. ISSN 15306992. doi:[10.1021/acs.nanolett.6b01914](https://doi.org/10.1021/acs.nanolett.6b01914).
- [81] Deep Jariwala, Artur R. Davoyan, Joeson Wong, and Harry A. Atwater. Van der waals materials for atomically-thin photovoltaics: Promise and outlook. *ACS Photonics*, 11 2017. doi:[10.1021/acsphtnics.7b01103](https://doi.org/10.1021/acsphtnics.7b01103).
- [82] Joel Jean, Thomas S. Mahony, Deniz Bozyigit, Melany Sponseller, Jakub Holovský, Moungi G. Bawendi, and Vladimir Bulović. Radiative efficiency limit with band tailing exceeds 30dot solar cells. *ACS Energy Letters*, 2(11):2616–2624, 2017. ISSN 23808195. doi:[10.1021/acsenergylett.7b00923](https://doi.org/10.1021/acsenergylett.7b00923).
- [83] Sajeev John, Costas Soukoulis, Morrel H. Cohen, and E. N. Economou. Theory of electron band tails and the urbach optical-absorption edge. *Physical Review Letters*, 57(14):1777–1780, 1986. ISSN 00319007. doi:[10.1103/PhysRevLett.57.1777](https://doi.org/10.1103/PhysRevLett.57.1777).
- [84] S. R. Johnson and T. Tiedje. Temperature dependence of the urbach edge in gaas. *Journal of Applied Physics*, 78(9):5609–5613, 1995. ISSN 00218979. doi:[10.1063/1.359683](https://doi.org/10.1063/1.359683).
- [85] Jun Kang, Sefaattin Tongay, Jian Zhou, Jingbo Li, and Junqiao Wu. Band offsets and heterostructures of two-dimensional semiconductors. *Applied Physics Letters*, 102(1):012111, 2013. ISSN 00036951. doi:[10.1063/1.4774090](https://doi.org/10.1063/1.4774090).
- [86] Pilgyu Kang, Michael Cai Wang, Peter M. Knapp, and Sung Woo Nam. Crumpled graphene photodetector with enhanced, strain-tunable, and wavelength-selective photoresponsivity. *Advanced Materials*, 28(23):4639–4645, 2016. ISSN 15214095. doi:[10.1002/adma.201600482](https://doi.org/10.1002/adma.201600482).
- [87] John K. Katahara and Hugh W. Hillhouse. Quasi-fermi level splitting and sub-bandgap absorptivity from semiconductor photoluminescence. *Journal of Applied Physics*, 116(17), 2014. ISSN 10897550. doi:[10.1063/1.4898346](https://doi.org/10.1063/1.4898346).
- [88] Mikhail A. Kats, Romain Blanchard, Patrice Genevet, and Federico Capasso. Nanometre optical coatings based on strong interference effects in highly absorbing media. *Nature Materials*, 12(1):20–24, 2012. ISSN 1476-1122. doi:[10.1038/nmat3443](https://doi.org/10.1038/nmat3443).

[89] Mark J. Keevers and Martin A. Green. Absorption edge of silicon from solar cell spectral response measurements. *Applied Physics Letters*, 66(2):174–176, 1995. doi:[10.1063/1.113125](https://doi.org/10.1063/1.113125).

[90] Gustav Kirchhoff. Ueber das verhältniss zwischen dem emissionsvermögen und dem absorptionsvermögen der körper für wärme und licht. *Annalen der Physik*, 185(2):275–301, 1860. doi:<https://doi.org/10.1002/andp.18601850205>.

[91] Victor I. Klimov. Detailed-balance power conversion limits of nanocrystal-quantum-dot solar cells in the presence of carrier multiplication. *Applied Physics Letters*, 89(12):87–90, 2006. ISSN 00036951. doi:[10.1063/1.2356314](https://doi.org/10.1063/1.2356314).

[92] Hannu Pekka Komsa and V. Arkady Krasheninnikov. Effects of confinement and environment on the electronic structure and exciton binding energy of  $\text{mos}_2$  from first principles. *Physical Review B - Condensed Matter and Materials Physics*, 86(24):241201, 2012. ISSN 10980121. doi:[10.1103/PhysRevB.86.241201](https://doi.org/10.1103/PhysRevB.86.241201).

[93] G. Kresse and J. Hafner. Ab initio molecular dynamics for liquid metals. *Physical Review B*, 47(1):558–561, 1993. ISSN 01631829. doi:[10.1103/PhysRevB.47.558](https://doi.org/10.1103/PhysRevB.47.558).

[94] Auke J. Kronemeijer, Vincenzo Pecunia, Deepak Venkateshvaran, Mark Nikolka, Aditya Sadhanala, John Moriarty, Monika Szumilo, and Henning Sirringhaus. Two-dimensional carrier distribution in top-gate polymer field-effect transistors: Correlation between width of density of localized states and urbach energy. *Advanced Materials*, 26:728–733, 2014.

[95] Jens Kunstmüller, Fabian Mooshammer, Philipp Nagler, Andrey Chaves, Frederick Stein, Nicola Paradiso, Gerd Plechinger, Christoph Strunk, Christian Schüller, Gotthard Seifert, David R. Reichman, and Tobias Korn. Momentum-space indirect interlayer excitons in transition-metal dichalcogenide van der waals heterostructures. *Nature Physics*, 14(8):801–805, 2018. ISSN 17452481. doi:[10.1038/s41567-018-0123-y](https://doi.org/10.1038/s41567-018-0123-y).

[96] V. Michail Kurik. Urbach rule. *Physica Status Solidi (A) Applications and Materials Science*, 8(1), 1971. doi:<https://doi.org/10.1002/pssa.2210080102>.

[97] Gordon Lasher and Frank Stern. Effect in soli ds e )—. *Physical Review*, 1963, 1964.

[98] Akash Laturia, Maarten L. Van de Put, and William G. Vandenberghe. Dielectric properties of hexagonal boron nitride and transition metal dichalcogenides: from monolayer to bulk. *npj 2D Materials and Applications*, 2(6), 2018. ISSN 23977132. doi:[10.1038/s41699-018-0050-x](https://doi.org/10.1038/s41699-018-0050-x).

- [99] Changgu Lee, Xiaoding Wei, Jeffrey W Kysar, and James Hone. Measurement of the elastic properties and intrinsic strength of monolayer graphene. *Science*, 321:385–388, 2008.
- [100] Changgu Lee, Hugen Yan, Louis E. Brus, Tony F. Heinz, James Hone, and Sunmin Ryu. Anomalous lattice vibrations of single- and few-layer mos<sub>2</sub>. *ACS Nano*, 4(5):2695–2700, 2010. ISSN 19360851. doi:[10.1021/nn1003937](https://doi.org/10.1021/nn1003937).
- [101] Chul-Ho Lee, Gwan-hyoung Lee, Arend M. van der Zande, Wenchao Chen, Yilei Li, Minyong Han, Xu Cui, Ghidewon Arefe, Colin Nuckolls, Tony F Heinz, Jing Guo, James Hone, and Philip Kim. Atomically thin p–n junctions with van der waals heterointerfaces. *Nature Nanotechnology*, 9(9):676–681, 2014. ISSN 1748-3387. doi:[10.1038/nnano.2014.150](https://doi.org/10.1038/nnano.2014.150).
- [102] Jubok Lee, Seok Joon Yun, Changwon Seo, Kiwon Cho, Tae Soo Kim, Gwang Hwi An, Kibum Kang, Hyun Seok Lee, and Jeongyong Kim. Switchable, tunable, and directable exciton funneling in periodically wrinkled ws<sub>2</sub>. *Nano Letters*, 2020. ISSN 15306992. doi:[10.1021/acs.nanolett.0c02619](https://doi.org/10.1021/acs.nanolett.0c02619).
- [103] Dehui Li, Rui Cheng, Hailong Zhou, Chen Wang, Anxiang Yin, Yu Chen, Nathan O. Weiss, Yu Huang, and Xiangfeng Duan. Electric-field-induced strong enhancement of electroluminescence in multilayer molybdenum disulfide. *Nature Communications*, 6(May), 2015. ISSN 20411723. doi:[10.1038/ncomms8509](https://doi.org/10.1038/ncomms8509).
- [104] Yilei Li, Alexey Chernikov, Xian Zhang, Albert Rigosi, Heather M. Hill, Arend M. van der Zande, Daniel A. Chenet, En-Min Shih, James Hone, and Tony F. Heinz. Measurement of the optical dielectric function of monolayer transition-metal dichalcogenides: Mos<sub>2</sub>, mose<sub>2</sub>, ws<sub>2</sub>, and wse<sub>2</sub>. *Physical Review B*, 90(20):205422, 2014. ISSN 1098-0121. doi:[10.1103/PhysRevB.90.205422](https://doi.org/10.1103/PhysRevB.90.205422).
- [105] Fang Liang, Hejun Xu, Xing Wu, Chaolun Wang, Chen Luo, and Jian Zhang. Raman spectroscopy characterization of two-dimensional materials. *Chinese Physics B*, 27(3):037802, 2018. ISSN 20583834. doi:[10.1088/1674-1056/27/3/037802](https://doi.org/10.1088/1674-1056/27/3/037802).
- [106] Bolin Liao, Huan Zhao, Ebrahim Najafi, Xiaodong Yan, He Tian, Jesse Tice, Austin J. Minnich, Han Wang, and Ahmed H. Zewail. Spatial-temporal imaging of anisotropic photocarrier dynamics in black phosphorus. *Nano Letters*, 17(6):3675–3680, 2017. ISSN 15306992. doi:[10.1021/acs.nanolett.7b00897](https://doi.org/10.1021/acs.nanolett.7b00897).
- [107] Darren J. Lipomi and Zhenan Bao. Stretchable, elastic materials and devices for solar energy conversion. *Energy & Environmental Science*, 4(9):3314, 2011. ISSN 1754-5692. doi:[10.1039/c1ee01881g](https://doi.org/10.1039/c1ee01881g).
- [108] Fang Liu, Wenjing Wu, Yusong Bai, Sang Hoon Chae, Qiuyang Li, Jue Wang, James Hone, and X. Y. Zhu. Disassembling 2d van der waals crystals into

macroscopic monolayers and reassembling into artificial lattices. *Science*, 367(6480):903–906, 2020. ISSN 10959203. doi:[10.1126/science.aba1416](https://doi.org/10.1126/science.aba1416).

[109] Han Liu, Adam T Neal, and Peide D Ye. Channel length scaling of mos<sub>2</sub> mosfets. *ACS nano*, 6(10):8563–9, 2012. ISSN 1936-086X. doi:[10.1021/nn303513c](https://doi.org/10.1021/nn303513c).

[110] Jing Liu, Shangshang Chen, Deping Qian, Bhoj Gautam, Guofang Yang, Jingbo Zhao, Jonas Bergqvist, Fengling Zhang, Wei Ma, Harald Ade, Olle Inganäs, Kenan Gundogdu, Feng Gao, and He Yan. Fast charge separation in a non-fullerene organic solar cell with a small driving force. *Nature Energy*, 1(7):1–7, 2016. ISSN 20587546. doi:[10.1038/nenergy.2016.89](https://doi.org/10.1038/nenergy.2016.89).

[111] Kaihui Liu, Liming Zhang, Ting Cao, Chenhao Jin, Diana Qiu, Qin Zhou, Alex Zettl, Peidong Yang, Steve G. Louie, and Feng Wang. Evolution of interlayer coupling in twisted molybdenum disulfide bilayers. *Nature Communications*, 5:1–6, 2014. ISSN 20411723. doi:[10.1038/ncomms5966](https://doi.org/10.1038/ncomms5966).

[112] Sha Liu, Jun Yuan, Wanyuan Deng, Mei Luo, Yuan Xie, Quanbin Liang, Yingping Zou, Zhicai He, Hongbin Wu, and Yong Cao. High-efficiency organic solar cells with low non-radiative recombination loss and low energetic disorder. *Nature Photonics*, 14(May), 2020. ISSN 17494893. doi:[10.1038/s41566-019-0573-5](https://doi.org/10.1038/s41566-019-0573-5).

[113] Zheng Liu, Matin Amani, Sina Najmaei, Quan Xu, Xiaolong Zou, Wu Zhou, Ting Yu, Caiyu Qiu, A. Glen Birdwell, Frank J. Crowne, Robert Vajtai, Boris I. Yakobson, Zhenhai Xia, Madan Dubey, Pulickel M. Ajayan, and Jun Lou. Strain and structure heterogeneity in mos<sub>2</sub> atomic layers grown by chemical vapour deposition. *Nature Communications*, 5, 2014. ISSN 20411723. doi:[10.1038/ncomms6246](https://doi.org/10.1038/ncomms6246).

[114] David Lloyd, Xinghui Liu, Jason W. Christopher, Lauren Cantley, Anubhav Wadehra, Brian L. Kim, Bennett B. Goldberg, Anna K. Swan, and J. Scott Bunch. Band gap engineering with ultralarge biaxial strains in suspended monolayer mos<sub>2</sub>. *Nano Letters*, 16(9):5836–5841, 2016. ISSN 15306992. doi:[10.1021/acs.nanolett.6b02615](https://doi.org/10.1021/acs.nanolett.6b02615).

[115] Yue Luo, Gabriella D. Shepard, V. Jenny Ardelean, Daniel A. Rhodes, Bumho Kim, Katayun Barmak, James C. Hone, and Stefan Strauf. Deterministic coupling of site-controlled quantum emitters in monolayer wse<sub>2</sub> to plasmonic nanocavities. *Nature Nanotechnology*, 13(12):1137–1142, 2018. ISSN 17483395. doi:[10.1038/s41565-018-0275-z](https://doi.org/10.1038/s41565-018-0275-z).

[116] Gábor Zsolt Magda, János Pető, Gergely Dobrik, Chanyong Hwang, László P. Biró, and Levente Tapasztó. Exfoliation of large-area transition metal chalcogenide single layers. *Scientific Reports*, 5:14714, 2015. ISSN 2045-2322. doi:[10.1038/srep14714](https://doi.org/10.1038/srep14714).

- [117] Kin Fai Mak, Changgu Lee, James Hone, Jie Shan, and Tony F. Heinz. Atomically thin  $\text{mos}_2$ : A new direct-gap semiconductor. *Physical Review Letters*, 105(13):2–5, 2010. ISSN 00319007. doi:[10.1103/PhysRevLett.105.136805](https://doi.org/10.1103/PhysRevLett.105.136805).
- [118] Michael K.L. Man, Athanasios Margiolakis, Skylar Deckoff-Jones, Takaaki Harada, E. Laine Wong, M. Bala Murali Krishna, Julien Madéo, Andrew Winchester, Sidong Lei, Robert Vajtai, Pulickel M. Ajayan, and Keshav M. Dani. Imaging the motion of electrons across semiconductor heterojunctions. *Nature Nanotechnology*, 12(1):36–40, 2017. ISSN 17483395. doi:[10.1038/nnano.2016.183](https://doi.org/10.1038/nnano.2016.183).
- [119] D. T.F. Marple. Optical absorption edge in  $\text{cdte}$ : Experimental. *Physical Review*, 150(2):728–734, 1966. ISSN 0031899X. doi:[10.1103/PhysRev.150.728](https://doi.org/10.1103/PhysRev.150.728).
- [120] Antonio Martí and Gerardo L. Araújo. Limiting efficiencies for photovoltaic energy conversion in multigap systems. *Solar Energy Materials and Solar Cells*, 43(2):203–222, 1996. doi:[https://doi.org/10.1016/0927-0248\(96\)00015-3](https://doi.org/10.1016/0927-0248(96)00015-3).
- [121] M. Massicotte, P. Schmidt, F. Vialla, K. G. Schädler, A. Reserbat-Plantey, K. Watanabe, T. Taniguchi, K. J. Tielrooij, and F. H.L. Koppens. Picosecond photoresponse in van der waals heterostructures. *Nature Nanotechnology*, 11(1):42–46, 2016. ISSN 17483395. doi:[10.1038/nnano.2015.227](https://doi.org/10.1038/nnano.2015.227).
- [122] Julian J. McMorrow, Amanda R. Walker, Vinod K. Sangwan, Deep Jariwala, Emily Hoffman, Ken Everaerts, Antonio Facchetti, Mark C. Hersam, and Tobin J. Marks. Solution-processed self-assembled nanodielectrics on template-stripped metal substrates. *ACS Applied Materials and Interfaces*, 7(48):26360–26366, 2015. ISSN 19448252. doi:[10.1021/acsami.5b07744](https://doi.org/10.1021/acsami.5b07744).
- [123] Kevin M Mcpeak, V Sriharsha Jayanti, Stephan J P Kress, Stefan Meyer, Stelio Iotti, Aurelio Rossinelli, and David J Norris. Plasmonic films can easily be better: Rules and recipes. *ACS Photonics*, 2:326–333, 2015. doi:[10.1021/ph5004237](https://doi.org/10.1021/ph5004237).
- [124] A. Meeder, D. Fuertes Marrón, A. Rumberg, M. Ch Lux-Steiner, V. Chu, and J. P. Conde. Direct measurement of urbach tail and gap state absorption in cugase 2 thin films by photothermal deflection spectroscopy and the constant photocurrent method. *Journal of Applied Physics*, 92(6):3016–3020, 2002. ISSN 00218979. doi:[10.1063/1.1501745](https://doi.org/10.1063/1.1501745).
- [125] Owen D Miller, Eli Yablonovitch, and Sarah R Kurtz. Strong internal and external luminescence as solar cells approach the shockley-queisser limit. *Photovoltaics, IEEE Journal of*, 2(3):303–311, 2012. ISSN 2156-3381. doi:[10.1109/JPHOTOV.2012.2198434](https://doi.org/10.1109/JPHOTOV.2012.2198434).

- [126] Omar F. Mohammed, Ding Shyue Yang, Samir Kumar Pal, and Ahmed H. Zewail. 4d scanning ultrafast electron microscopy: visualization of materials surface dynamics. *Journal of the American Chemical Society*, 133(20):7708–7711, 2011. ISSN 00027863. doi:[10.1021/ja2031322](https://doi.org/10.1021/ja2031322).
- [127] Hyowon Moon, Gabriele Grossi, Chitraleema Chakraborty, Cheng Peng, Takashi Taniguchi, Kenji Watanabe, and Dirk Englund. Dynamic exciton funneling by local strain control in a monolayer semiconductor. *Nano Letters*, 20(9):6791–6797, 2020. ISSN 15306992. doi:[10.1021/acs.nanolett.0c02757](https://doi.org/10.1021/acs.nanolett.0c02757).
- [128] N F Mott. Note on the contact between a metal and an insulator or semiconductor. *Proceedings of Cambridge Philosophical Society*, 34(October):568–572, 1938.
- [129] J. T. Mullins, J. Carles, and A. W. Brinkman. High temperature optical properties of cadmium telluride. *Journal of Applied Physics*, 81(9):6374–6379, 1997. ISSN 00218979. doi:[10.1063/1.364371](https://doi.org/10.1063/1.364371).
- [130] Winfried Mönch. Valence-band offsets and schottky barrier heights of layered semiconductors explained by interface-induced gap states. *Applied Physics Letters*, 72(15):1899–1901, 1998. ISSN 00036951. doi:[10.1063/1.121220](https://doi.org/10.1063/1.121220).
- [131] Ebrahim Najafi, Timothy D. Scarborough, Jau Tang, and Ahmed Zewail. Four-dimensional imaging of carrier interface dynamics in p-n junctions. *Science*, 347(6218):164–167, 2015. ISSN 10959203. doi:[10.1126/science.aaa0217](https://doi.org/10.1126/science.aaa0217).
- [132] Ebrahim Najafi, Vsevolod Ivanov, Ahmed Zewail, and Marco Bernardi. Super-diffusion of excited carriers in semiconductors. *Nature Communications*, 8(May):1–7, 2017. ISSN 20411723. doi:[10.1038/ncomms15177](https://doi.org/10.1038/ncomms15177).
- [133] Pabitra K. Nayak, Suhas Mahesh, Henry J. Snaith, and David Cahen. Photovoltaic solar cell technologies: analysing the state of the art. *Nature Reviews Materials*, 4(4):269–285, 2019. ISSN 20588437. doi:[10.1038/s41578-019-0097-0](https://doi.org/10.1038/s41578-019-0097-0).
- [134] RA Neville and BL Evans. The band edge excitons in 2h-mos2. *physica status solidi (b)*, 73(2):597–606, 1976.
- [135] Tat Ming Ng, Mark T. Weller, Gabriela P. Kissling, Laurence M. Peter, Phillip Dale, Finn Babbe, Jessica De Wild, Bernard Wenger, Henry J. Snaith, and David Lane. Optoelectronic and spectroscopic characterization of vapour-transport grown cu<sub>2</sub>znsns<sub>4</sub> single crystals. *Journal of Materials Chemistry A*, 5(3):1192–1200, 2017. ISSN 20507496. doi:[10.1039/c6ta09817g](https://doi.org/10.1039/c6ta09817g).
- [136] Dac Trung Nguyen, Laurent Lombez, François Gibelli, Soline Boyer-Richard, Alain Le Corre, Olivier Durand, and Jean François Guillemoles. Quantitative experimental assessment of hot carrier-enhanced solar cells at

room temperature. *Nature Energy*, 3(3):236–242, 2018. ISSN 20587546. doi:[10.1038/s41560-018-0106-3](https://doi.org/10.1038/s41560-018-0106-3).

[137] Iris Niehues, Robert Schmidt, Matthias Drüppel, Philipp Marauhn, Dominik Christiansen, Malte Selig, Gunnar Berghäuser, Daniel Wigger, Robert Schneider, Lisa Braasch, Rouven Koch, Andres Castellanos-Gomez, Tilmann Kuhn, Andreas Knorr, Ermin Malic, Michael Rohlfing, Steffen Michaelis De Vasconcellos, and Rudolf Bratschitsch. Strain control of exciton-phonon coupling in atomically thin semiconductors. *Nano Letters*, 18(3):1751–1757, 2018. ISSN 15306992. doi:[10.1021/acs.nanolett.7b04868](https://doi.org/10.1021/acs.nanolett.7b04868).

[138] Iris Niehues, Anna Blob, Torsten Stiehm, Steffen Michaelis De Vasconcellos, and Rudolf Bratschitsch. Interlayer excitons in bilayer  $\text{mos}_2$  under uniaxial tensile strain. *Nanoscale*, 11(27):12788–12792, 2019. ISSN 20403372. doi:[10.1039/c9nr03332g](https://doi.org/10.1039/c9nr03332g).

[139] Vasileios C Nikolis, Andreas Mischok, Bernhard Siegmund, Jonas Kublitski, Xiangkun Jia, Johannes Benduhn, Ulrich Hörmann, Dieter Neher, Malte C Gather, Donato Spoltore, et al. Strong light-matter coupling for reduced photon energy losses in organic photovoltaics. *Nature communications*, 10(1):1–8, 2019.

[140] K. S. Novoselov, A. K. Geim, S. V. Morozov, D. Jiang, Y. Zhang, S. V. Dubonos, I. V. Grigorieva, and A. A. Firsov. Electric field effect in atomically thin carbon films. *Science*, 306(5696):666–669, 2004. doi:[10.1126/science.1102896](https://doi.org/10.1126/science.1102896).

[141] Robert L. Olmon, Brian Slovick, Timothy W. Johnson, David Shelton, Sang Hyun Oh, Glenn D. Boreman, and Markus B. Raschke. Optical dielectric function of gold. *Physical Review B - Condensed Matter and Materials Physics*, 86(23):235147, 2012. ISSN 10980121. doi:[10.1103/PhysRevB.86.235147](https://doi.org/10.1103/PhysRevB.86.235147).

[142] Arthur Onno, Christopher Chen, Priyaranga Koswatta, Mathieu Boccard, and Zachary C Holman. Passivation, conductivity, and selectivity in solar cell contacts: Concepts and simulations based on a unified partial-resistances framework. *Journal of Applied Physics*, 126(18):183103, 2019.

[143] Eunice Y. Paik, Long Zhang, G. William Burg, Rahul Gogna, Emanuel Tutuc, and Hui Deng. Interlayer exciton laser of extended spatial coherence in atomically thin heterostructures. *Nature*, 576(7785):80–84, 2019. ISSN 14764687. doi:[10.1038/s41586-019-1779-x](https://doi.org/10.1038/s41586-019-1779-x).

[144] Sangyeon Pak, Juwon Lee, Young Woo Lee, A. Rang Jang, Seongjoon Ahn, Kyung Yeol Ma, Yuljae Cho, John Hong, Sanghyo Lee, Hu Young Jeong, Hyunsik Im, Hyeon Suk Shin, Stephen M. Morris, Seungnam Cha, Jung Inn Sohn, and Jong Min Kim. Strain-mediated interlayer coupling effects on the excitonic behaviors in an epitaxially grown  $\text{mos}_2/\text{ws}_2$  van der

waals heterobilayer. *Nano Letters*, 17(9):5634–5640, 2017. ISSN 15306992. doi:[10.1021/acs.nanolett.7b02513](https://doi.org/10.1021/acs.nanolett.7b02513).

[145] John E. Parrott. Self-consistent detailed balance treatment of the solar cell. *IEE Proceedings*, 133(5):314–318, 1986.

[146] Tien Hsin Peng, Chung Hung Hong, Ming Ru Tang, and Si Chen Lee. Photoresponse of homostructure wse<sub>2</sub> rectifying diode. *AIP Advances*, 9(7), 2019. ISSN 21583226. doi:[10.1063/1.5115423](https://doi.org/10.1063/1.5115423).

[147] Zhiwei Peng, Xiaolin Chen, Yulong Fan, David J. Srolovitz, and Dangyuan Lei. Strain engineering of 2d semiconductors and graphene: from strain fields to band-structure tuning and photonic applications. *Light: Science and Applications*, 9(1), 2020. ISSN 20477538. doi:[10.1038/s41377-020-00421-5](https://doi.org/10.1038/s41377-020-00421-5).

[148] John P. Perdew, Kieron Burke, and Matthias Ernzerhof. Generalized gradient approximation made simple. *Physical Review Letters*, 77(18):3865–3868, 1996. ISSN 10797114. doi:[10.1103/PhysRevLett.77.3865](https://doi.org/10.1103/PhysRevLett.77.3865).

[149] Leif A A Pettersson, Lucimara S Roman, and Olle Inganäs. Modeling photocurrent action spectra of photovoltaic devices based on organic thin films. *Journal of Applied Physics*, 86(1):487–496, 1999. doi:[10.1063/1.370757](https://doi.org/10.1063/1.370757).

[150] Jessica R. Piper and Shanhui Fan. Total absorption in a graphene monolayer in the optical regime by critical coupling with a photonic crystal guided resonance. *ACS Photonics*, 1(4):347–353, 2014. doi:[10.1021/ph400090p](https://doi.org/10.1021/ph400090p).

[151] Jessica R. Piper and Shanhui Fan. Broadband absorption enhancement in solar cells with an atomically thin active layer. *ACS Photonics*, 3(4):571–577, 2016. ISSN 23304022. doi:[10.1021/acsphotonics.5b00510](https://doi.org/10.1021/acsphotonics.5b00510).

[152] Marcel Placidi, Mirjana Dimitrievska, Victor Izquierdo-Roca, Xavier Fontané, Andres Castellanos-Gomez, Amador Pérez-Tomás, Narcis Mestres, Moises Espindola-Rodriguez, Simon López-Marino, Markus Neuschitzer, Veronica Bermudez, Anatoliy Yaremko, and Alejandro Pérez-Rodríguez. Multiwavelength excitation raman scattering analysis of bulk and two-dimensional mos<sub>2</sub>: Vibrational properties of atomically thin mos<sub>2</sub> layers. *2D Materials*, 2(3), 2015. ISSN 20531583. doi:[10.1088/2053-1583/2/3/035006](https://doi.org/10.1088/2053-1583/2/3/035006).

[153] Max Planck. *Vorlesungen über die Theorie der Wärmestrahlung*. Verlag Von Johann Ambrosius-Barth, Leipzig, 1906.

[154] Albert Polman, Mark Knight, Erik C Garnett, Bruno Ehrler, and Wim C Sinke. Photovoltaic materials – present efficiencies and future challenges. *Science*, 352(6283):307, 2016. ISSN 0036-8075. doi:[10.1126/science.aad4424](https://doi.org/10.1126/science.aad4424).

[155] Andreas Pospischil, Marco M Furchi, and Thomas Mueller. Solar-energy conversion and light emission in an atomic monolayer p-n diode. *Nature nanotechnology*, 9(4):257–61, 2014. ISSN 1748-3395. doi:[10.1038/nnano.2014.14](https://doi.org/10.1038/nnano.2014.14).

[156] Deping Qian, Zilong Zheng, Huifeng Yao, Wolfgang Tress, Thomas R. Hopper, Shula Chen, Sunsun Li, Jing Liu, Shangshang Chen, Jiangbin Zhang, Xiao Ke Liu, Bowei Gao, Liangqi Ouyang, Yingzhi Jin, Galia Pozina, Irina A. Buyanova, Weimin M. Chen, Olle Inganäs, Veaceslav Coropceanu, Jean Luc Bredas, He Yan, Jianhui Hou, Fengling Zhang, Artem A. Bakulin, and Feng Gao. Design rules for minimizing voltage losses in high-efficiency organic solar cells. *Nature Materials*, 17(8):703–709, 2018. ISSN 14764660. doi:[10.1038/s41563-018-0128-z](https://doi.org/10.1038/s41563-018-0128-z).

[157] B. Radisavljevic, A. Radenovic, J. Brivio, V. Giacometti, and A. Kis. Single-layer  $\text{mos}_2$  transistors. *Nature nanotechnology*, 6(3):147–50, 2011. ISSN 1748-3387. doi:[10.1038/nnano.2010.279](https://doi.org/10.1038/nnano.2010.279).

[158] A. E. Rakhshani. Heterojunction properties of electrodeposited cdte/cds solar cells. *Journal of Applied Physics*, 90(8):4265–4271, 2001. ISSN 00218979. doi:[10.1063/1.1397279](https://doi.org/10.1063/1.1397279).

[159] Niva A. Ran, John A. Love, Christopher J. Takacs, Aditya Sadhanala, Justin K. Beavers, Samuel D. Collins, Ye Huang, Ming Wang, Richard H. Friend, Guillermo C. Bazan, and Thuc Quyen Nguyen. Harvesting the full potential of photons with organic solar cells. *Advanced Materials*, 28(7):1482–1488, 2016. ISSN 15214095. doi:[10.1002/adma.201504417](https://doi.org/10.1002/adma.201504417).

[160] Uwe Rau. Reciprocity relation between photovoltaic quantum efficiency and electroluminescent emission of solar cells. *Physical Review B - Condensed Matter and Materials Physics*, 76(8):1–8, 2007. ISSN 10980121. doi:[10.1103/PhysRevB.76.085303](https://doi.org/10.1103/PhysRevB.76.085303).

[161] Uwe Rau and Jürgen H. Werner. Radiative efficiency limits of solar cells with lateral band-gap fluctuations. *Applied Physics Letters*, 84(19):3735 –3737, 2004. doi:[10.1063/1.1737071](https://doi.org/10.1063/1.1737071).

[162] Uwe Rau, Ulrich W. Paetzold, and Thomas Kirchartz. Thermodynamics of light management in photovoltaic devices. *Phys. Rev. B*, 90:035211, Jul 2014. doi:[10.1103/PhysRevB.90.035211](https://doi.org/10.1103/PhysRevB.90.035211). URL <https://link.aps.org/doi/10.1103/PhysRevB.90.035211>.

[163] Uwe Rau, Beatrix Blank, Thomas C.M. Müller, and Thomas Kirchartz. Efficiency potential of photovoltaic materials and devices unveiled by detailed-balance analysis. *Physical Review Applied*, 7(4):1–9, 2017. ISSN 23317019. doi:[10.1103/PhysRevApplied.7.044016](https://doi.org/10.1103/PhysRevApplied.7.044016).

- [164] Pasqual Rivera, Hongyi Yu, Kyle L. Seyler, Nathan P. Wilson, Wang Yao, and Xiaodong Xu. Interlayer valley excitons in heterobilayers of transition metal dichalcogenides. *Nature Nanotechnology*, 13(11):1004–1015, 2018. ISSN 17483395. doi:[10.1038/s41565-018-0193-0](https://doi.org/10.1038/s41565-018-0193-0).
- [165] John A. Rogers, Takao Someya, and Yonggang Huang. Materials and mechanics for stretchable electronics. *Science*, 327:1603–1607, 2010. ISSN 00368075. doi:[10.1126/science.1182383](https://doi.org/10.1126/science.1182383).
- [166] Jason S Ross, Philip Klement, Aaron M Jones, Nirmal J Ghimire, Jiaqiang Yan, DG Mandrus, Takashi Taniguchi, Kenji Watanabe, Kenji Kitamura, Wang Yao, et al. Electrically tunable excitonic light-emitting diodes based on monolayer wse<sub>2</sub> p–n junctions. *Nature nanotechnology*, 9(4):268–272, 2014.
- [167] Robert T. Ross and Arthur J. Nozik. Efficiency of hot-carrier solar energy converters. *Journal of Applied Physics*, 53(5):3813–3818, 1982. ISSN 00218979. doi:[10.1063/1.331124](https://doi.org/10.1063/1.331124).
- [168] Aditya Sadhanala, Felix Deschler, Tudor H. Thomas, Siân E. Dutton, Karl C. Goedel, Fabian C. Hanusch, May L. Lai, Ullrich Steiner, Thomas Bein, Pablo Docampo, David Cahen, and Richard H. Friend. Preparation of single-phase films of ch3nh3pb(i 1- xbrx)3 with sharp optical band edges. *Journal of Physical Chemistry Letters*, 5(15):2501–2505, 2014. ISSN 19487185. doi:[10.1021/jz501332v](https://doi.org/10.1021/jz501332v).
- [169] Nihit Saigal, Vasam Sugunakar, and Sandip Ghosh. Exciton binding energy in bulk mos<sub>2</sub>: A reassessment. *Applied Physics Letters*, 108(13):132105, 2016. ISSN 00036951. doi:[10.1063/1.4945047](https://doi.org/10.1063/1.4945047).
- [170] Vinod K. Sangwan, Heather N. Arnold, Deep Jariwala, Tobin J. Marks, Lincoln J. Lauhon, and Mark C. Hersam. Low-frequency electronic noise in single-layer mos<sub>2</sub> transistors. *Nano Letters*, 13(9):4351–4355, 2013. ISSN 15306984. doi:[10.1021/nl402150r](https://doi.org/10.1021/nl402150r).
- [171] Walter Schottky. Zur halbleitertheorie der sperrsicht- und spitzengleichrichter. *Zeitschrift für Physik volume*, 113:367–414, 1939.
- [172] J. L. Sculfort, R. Triboulet, and P. Lemasson. The semiconductor-electrolyte interface: Photocurrent and related parameters in cadmium telluride. *Journal of The Electrochemical Society*, 131(1):209–213, 1984. ISSN 0013-4651. doi:[10.1149/1.2115529](https://doi.org/10.1149/1.2115529).
- [173] Giovanni Scuri, You Zhou, Alexander A. High, Dominik S. Wild, Chi Shu, Kristiaan De Greve, Luis A. Jauregui, Takashi Taniguchi, Kenji Watanabe, Philip Kim, Mikhail D. Lukin, and Hongkun Park. Large excitonic reflectivity of monolayer mose<sub>2</sub> encapsulated in hexagonal boron nitride. *Phys. Rev. Lett.*, 120:037402, Jan 2018. doi:[10.1103/PhysRevLett.120.037402](https://doi.org/10.1103/PhysRevLett.120.037402).

- [174] T. Shioda, S. Chichibu, T. Irie, H. Nakanishi, and T. Kariya. Influence of nonstoichiometry on the urbach's tails of absorption spectra for cuinse<sub>2</sub> single crystals. *Journal of Applied Physics*, 80(2):1106–1111, 1996.
- [175] William Shockley and Hans J. Queisser. Detailed balance limit of efficiency of p-n junction solar cells. *Journal of Applied Physics*, 32(3):510–519, 1961. ISSN 00218979. doi:[10.1063/1.1736034](https://doi.org/10.1063/1.1736034).
- [176] Henry J. Snaith. The perils of solar cell efficiency measurements. *Nature Photonics*, 6(6):337–340, 2012. ISSN 1749-4885. doi:[10.1038/nphoton.2012.119](https://doi.org/10.1038/nphoton.2012.119).
- [177] Seunghyun Song, Dong Hoon Keum, Suyeon Cho, David Perello, Yunseok Kim, and Young Hee Lee. Room temperature semiconductor-metal transition of mott<sub>2</sub> thin films engineered by strain. *Nano Letters*, 16(1):188–193, 2016. ISSN 15306992. doi:[10.1021/acs.nanolett.5b03481](https://doi.org/10.1021/acs.nanolett.5b03481).
- [178] Andrea Splendiani, Liang Sun, Yuanbo Zhang, Tianshu Li, Jonghwan Kim, Chi-Yung Chim, Giulia Galli, and Feng Wang. Emerging photoluminescence in monolayer mos<sub>2</sub>. *Nano Letters*, 10(4):1271–1275, 2010. doi:[10.1021/nl903868w](https://doi.org/10.1021/nl903868w).
- [179] A. B. Sproul. Dimensionless solution of the equation describing the effect of surface recombination on carrier decay in semiconductors. *Journal of Applied Physics*, 76(5):2851–2854, 1994. doi:[10.1063/1.357521](https://doi.org/10.1063/1.357521).
- [180] W. Sritrakoo, V. Sa-yakanit, and H. R. Glyde. Band tails in disordered systems. *Physical Review B*, 33(2):1199–1202, 1986.
- [181] M. D. Sturge. Optical absorption of gallium arsenide between 0.6 and 2.75 ev. *Physical Review*, 127(3):768–773, 1962. ISSN 0031899X. doi:[10.1103/PhysRev.127.768](https://doi.org/10.1103/PhysRev.127.768).
- [182] V. Arsen Subashiev, Oleg Semyonov, Zhichao Chen, and Serge Luryi. Urbach tail studies by luminescence filtering in moderately doped bulk inp. *Applied Physics Letters*, 97(18):12–15, 2010. ISSN 00036951. doi:[10.1063/1.3510470](https://doi.org/10.1063/1.3510470).
- [183] T. Tiedje, Cebulka J. M., Morel D. L., and Abeles B. Evidence for exponential band tails in amorphous silicon hydride. *Physical Review Letters*, 46(21): 1425–1428, 1981.
- [184] T. Tiedje, B. Abeles, and Cebulka J. M. Urbach edge and the density of states in hydrogenated amorphous silicon. *Solid State Communications*, 47 (6):493–496, 1983.
- [185] Mahmut Tosun, Deyi Fu, Sujay B. Desai, Changhyun Ko, Jeong Seuk Kang, Der Hsien Lien, Mohammad Najmzadeh, Sefaattin Tongay, Junqiao Wu, and

Ali Javey. *Mos<sub>2</sub>* heterojunctions by thickness modulation. *Scientific Reports*, 5:1–8, 2015. ISSN 20452322. doi:[10.1038/srep10990](https://doi.org/10.1038/srep10990).

[186] M. Troviano and K. Taretto. Analysis of internal quantum efficiency in double-graded bandgap solar cells including sub-bandgap absorption. *Solar Energy Materials and Solar Cells*, 95(3):821–828, 2011. ISSN 09270248. doi:[10.1016/j.solmat.2010.10.028](https://doi.org/10.1016/j.solmat.2010.10.028).

[187] Dmitrii Unuchek, Alberto Ciarrocchi, Ahmet Avsar, Kenji Watanabe, Takashi Taniguchi, and Andras Kis. Room-temperature electrical control of exciton flux in a van der waals heterostructure. *Nature*, 560(7718):340–344, 2018. ISSN 14764687. doi:[10.1038/s41586-018-0357-y](https://doi.org/10.1038/s41586-018-0357-y).

[188] Franz Urbach. The long-wavelength edge of photographic sensitivity and of the electronic absorption of solids. *Physical Review*, 92(5):1324–1324, 1953. ISSN 13464558. doi:[10.1103/PhysRev.92.1324](https://doi.org/10.1103/PhysRev.92.1324).

[189] M Iqbal Bakti Utama, Hans Kleemann, Wenyu Zhao, Chin Shen Ong, H Felipe, Diana Y Qiu, Hui Cai, Han Li, Rai Kou, Sihan Zhao, et al. A dielectric-defined lateral heterojunction in a monolayer semiconductor. *Nature Electronics*, 2(2):60–65, 2019.

[190] Jorik van de Groep, Jung Hwan Song, Umberto Celano, Qitong Li, Pieter G. Kik, and Mark L. Brongersma. Exciton resonance tuning of an atomically thin lens. *Nature Photonics*, 14(7):426–430, 2020. ISSN 17494893. doi:[10.1038/s41566-020-0624-y](https://doi.org/10.1038/s41566-020-0624-y).

[191] W. Van Roosbroeck and W. Shockley. Photon-radiative recombination of electrons and holes in germanium. *Physical Review*, 94(6):1558–1560, 1954. ISSN 0031899X. doi:[10.1103/PhysRev.94.1558](https://doi.org/10.1103/PhysRev.94.1558).

[192] M. K. Van Veen and R. E.I. Schropp. Beneficial effect of a low deposition temperature of hot-wire deposited intrinsic amorphous silicon for solar cells. *Journal of Applied Physics*, 93(1):121–125, 2003. ISSN 00218979. doi:[10.1063/1.1527208](https://doi.org/10.1063/1.1527208).

[193] Koen Vandewal, Steve Albrecht, Eric T. Hoke, Kenneth R. Graham, Johannes Widmer, Jessica D. Douglas, Marcel Schubert, William R. Mateker, Jason T. Bloking, George F. Burkhard, Alan Sellinger, Jean M.J. Fréchet, Aram Amassian, Moritz K. Riede, Michael D. McGehee, Dieter Neher, and Alberto Salleo. Efficient charge generation by relaxed charge-transfer states at organic interfaces. *Nature Materials*, 13(1):63–68, 2014. ISSN 14761122. doi:[10.1038/nmat3807](https://doi.org/10.1038/nmat3807).

[194] Mat Velický, Gavin E Donnelly, William Robert Hendren, Stephen Mcfarland, Declan Scullion, J I Debenedetti, Gabriela Calinao Correa, Yimo Han, Andrew John Wain, Melissa A Hines, A David, Kostya S Novoselov, Héctor D Abruña, Robert M Bowman, Elton J G Santos, and Fumin

Huang. Mechanism of gold-assisted exfoliation of centimeter-sized transition metal dichalcogenide monolayers. *ACS Nano*, 12:10463–10472, 2018. doi:[10.1021/acsnano.8b06101](https://doi.org/10.1021/acsnano.8b06101).

[195] Matěj Velický, Alvaro Rodriguez, Milan Bouša, V. Andrey Krayev, Martin Vondráček, Jan Honolka, Mahdi Ahmadi, Gavin E. Donnelly, Fumin Huang, Héctor D. Abruña, Kostya S. Novoselov, and Otakar Frank. Strain and charge doping fingerprints of the strong interaction between monolayer mos<sub>2</sub> and gold. *The Journal of Physical Chemistry Letters*, 11(15):6112–6118, 2020. ISSN 1948-7185. doi:[10.1021/acs.jpclett.0c01287](https://doi.org/10.1021/acs.jpclett.0c01287).

[196] Dominic Vella, José Bico, Arezki Boudaoud, Benoit Roman, and Pedro M Reis. The macroscopic delamination of thin films from elastic substrates. *Proceedings of the National Academy of Sciences*, 106(27):10901–10906, 2009.

[197] Ruggero Verre, Denis G. Baranov, Battulga Munkhbat, Jorge Cuadra, Mikael Käll, and Timur Shegai. Transition metal dichalcogenide nanodisks as high-index dielectric mie nanoresonators. *Nature Nanotechnology*, 14(7):679–683, Jul 2019. ISSN 1748-3395. doi:[10.1038/s41565-019-0442-x](https://doi.org/10.1038/s41565-019-0442-x).

[198] Nicolas Vogel, Julius Zieleniecki, and Ingo Köper. As flat as it gets: ultra-smooth surfaces from template-stripping procedures. *Nanoscale*, 4(13):3820, 2012. ISSN 2040-3372. doi:[10.1039/c2nr30434a](https://doi.org/10.1039/c2nr30434a).

[199] Gang Wang, Alexey Chernikov, Mikhail M. Glazov, Tony F. Heinz, Xavier Marie, Thierry Amand, and Bernhard Urbaszek. Colloquium: Excitons in atomically thin transition metal dichalcogenides. *Rev. Mod. Phys.*, 90: 021001, Apr 2018. doi:[10.1103/RevModPhys.90.021001](https://doi.org/10.1103/RevModPhys.90.021001). URL <https://link.aps.org/doi/10.1103/RevModPhys.90.021001>.

[200] Mao Wang, Manuel Hertzog, and Karl Börjesson. Polariton-assisted excitation energy channeling in organic heterojunctions. *Nature communications*, 12(1):1–10, 2021.

[201] Yanlong Wang, Chunxiao Cong, Caiyu Qiu, and Ting Yu. Raman spectroscopy study of lattice vibration and crystallographic orientation of monolayer mos<sub>2</sub> under uniaxial strain. *Small*, 9(17):2857–2861, 2013. ISSN 16136810. doi:[10.1002/smll.201202876](https://doi.org/10.1002/smll.201202876).

[202] Zhong Lin Wang and Wenzhuo Wu. Nanotechnology-enabled energy harvesting for self-powered micro-/nanosystems. *Angewandte Chemie - International Edition*, 51(47):11700–11721, 2012. ISSN 14337851. doi:[10.1002/anie.201201656](https://doi.org/10.1002/anie.201201656).

[203] Dacen Waters, Yifan Nie, Yifan Nie, Felix Lüpke, Yi Pan, Yi Pan, Stefan Fölsch, Yu Chuan Lin, Bhakti Jariwala, Kehao Zhang, Chong Wang, Hongyan Lv, Hongyan Lv, Kyeongjae Cho, Di Xiao, Joshua A. Robinson,

and Randall M. Feenstra. Flat bands and mechanical deformation effects in the moiré superlattice of  $\text{mos}_2\text{-wse}_2$  heterobilayers. *ACS Nano*, 14(6): 7564–7573, 2020. ISSN 1936086X. doi:[10.1021/acsnano.0c03414](https://doi.org/10.1021/acsnano.0c03414).

[204] Cora M. Went, Joeson Wong, Phillip R. Jahelka, Michael Kelzenberg, Souvik Biswas, Matthew S. Hunt, Abigail Carbone, and Harry A. Atwater. A new metal transfer process for van der waals contacts to vertical schottky-junction transition metal dichalcogenide photovoltaics. *Science Advances*, 5 (12), 2019. doi:[10.1126/sciadv.aax6061](https://doi.org/10.1126/sciadv.aax6061).

[205] Cora M. Went, Joeson Wong, Phil Jahelka, Morgaine Mandigo-Stoba, and Harry Atwater. Applying perovskite carrier selective contacts to transition metal dichalcogenide solar cells. *In Preparation*, 2022.

[206] E. Laine Wong, Andrew J. Winchester, Vivek Pareek, Julien Madéo, Michael K.L. Man, and Keshav M. Dani. Pulling apart photoexcited electrons by photoinducing an in-plane surface electric field. *Science Advances*, 4(9), 2018. ISSN 23752548. doi:[10.1126/sciadv.aat9722](https://doi.org/10.1126/sciadv.aat9722).

[207] J. Wong, D. Jariwala, G. Tagliabue, K. Tat, A.R. Davoyan, M.C. Sherrrott, and H.A. Atwater. High photovoltaic quantum efficiency in ultrathin van der waals heterostructures. *ACS Nano*, 11(7), 2017. ISSN 1936086X. doi:[10.1021/acsnano.7b03148](https://doi.org/10.1021/acsnano.7b03148).

[208] Joeson Wong, Tyler Colenbrander, Cora Went, Susana Torres-Londono, Rachel Tham, and Harry A. Atwater. Perfect absorption in monolayer  $\text{ws}_2$ . *In Preparation*, 2022.

[209] P Wurfel. The chemical potential of radiation. *Journal of Physics C: Solid State Physics*, 15(18):3967–3985, 1982. ISSN 0022-3719. doi:[10.1088/0022-3719/15/18/012](https://doi.org/10.1088/0022-3719/15/18/012).

[210] Peter Würfel. Solar energy conversion with hot electrons from impact ionisation. *Solar Energy Materials and Solar Cells*, 46(1):43–52, 1997. ISSN 0927-0248. doi:[10.1016/S0927-0248\(96\)00092-X](https://doi.org/10.1016/S0927-0248(96)00092-X).

[211] Uli Würfel, Andres Cuevas, and Peter Würfel. Charge carrier separation in solar cells. *IEEE Journal of Photovoltaics*, 5(1):461–469, 2015. doi:[10.1109/JPHOTOV.2014.2363550](https://doi.org/10.1109/JPHOTOV.2014.2363550).

[212] Yunlu Xu, Tao Gong, and Jeremy N. Munday. The generalized shockley-queisser limit for nanostructured solar cells. *Scientific Reports*, 5:13536, 2015. ISSN 2045-2322. doi:[10.1038/srep13536](https://doi.org/10.1038/srep13536).

[213] E. Yablonovitch and G.D. Cody. Intensity enhancement in textured optical sheets for solar cells. *IEEE Transactions on Electron Devices*, 29(2):300–305, 1982. doi:[10.1109/T-ED.1982.20700](https://doi.org/10.1109/T-ED.1982.20700).

- [214] Chang Yan, Kaiwen Sun, Jialiang Huang, Steve Johnston, Fangyang Liu, Binesh Puthen Veettil, Kaile Sun, Aobo Pu, Fangzhou Zhou, John A. Stride, Martin A. Green, and Xiaojing Hao. Beyond 11Effects of cadmium alloying. *ACS Energy Letters*, 2(4):930–936, 2017. ISSN 23808195. doi:[10.1021/acsenergylett.7b00129](https://doi.org/10.1021/acsenergylett.7b00129).
- [215] Ding Shyue Yang, Omar F. Mohammed, and Ahmed H. Zewail. Scanning ultrafast electron microscopy. *Proceedings of the National Academy of Sciences of the United States of America*, 107(34):14993–14998, 2010. ISSN 00278424. doi:[10.1073/pnas.1009321107](https://doi.org/10.1073/pnas.1009321107).
- [216] Yujue Yang, Nengjie Huo, and Jingbo Li. Gate tunable photovoltaic effect in a mose<sub>2</sub> homojunction enabled with different thicknesses. *Journal of Materials Chemistry C*, 5(28):7051–7056, 2017. ISSN 20507526. doi:[10.1039/c7tc01806a](https://doi.org/10.1039/c7tc01806a).
- [217] Zu-Po Yang, Lijie Ci, James A. Bur, Shawn-Yu Lin, and Pulickel M. Ajayan. Experimental observation of an extremely dark material made by a low-density nanotube array. *Nano Letters*, 8(2):446–451, 2008. doi:[10.1021/nl072369t](https://doi.org/10.1021/nl072369t).
- [218] Woo Jong Yu, Zheng Li, Hailong Zhou, Yu Chen, Yang Wang, Yu Huang, and Xiangfeng Duan. Vertically stacked multi-heterostructures of layered materials for logic transistors and complementary inverters. *Nature Materials*, 12(3):246–252, 2012. ISSN 1476-1122. doi:[10.1038/nmat3518](https://doi.org/10.1038/nmat3518).
- [219] Woo Jong Yu, Yuan Liu, Hailong Zhou, Anxiang Yin, Zheng Li, Yu Huang, and Xiangfeng Duan. Highly efficient gate-tunable photocurrent generation in vertical heterostructures of layered materials. *Nature Nanotechnology*, 8 (October):952–958, 2013. doi:[10.1038/nnano.2013.219](https://doi.org/10.1038/nnano.2013.219).
- [220] Zongfu Yu, Aaswath Raman, and Shanhui Fan. Thermodynamic upper bound on broadband light coupling with photonic structures. *Phys. Rev. Lett.*, 109: 173901, Oct 2012. doi:[10.1103/PhysRevLett.109.173901](https://doi.org/10.1103/PhysRevLett.109.173901). URL <https://link.aps.org/doi/10.1103/PhysRevLett.109.173901>.
- [221] Ferdows Zahid, Lei Liu, Yu Zhu, Jian Wang, and Hong Guo. A generic tight-binding model for monolayer, bilayer and bulk mos<sub>2</sub>. *AIP Advances*, 3 (5), 2013. ISSN 21583226. doi:[10.1063/1.4804936](https://doi.org/10.1063/1.4804936).
- [222] Hao Zhan, Dan Guo, and Guo Xin Xie. Two-dimensional layered materials: From mechanical and coupling properties towards applications in electronics. *Nanoscale*, 11(28):13181–13212, 2019. ISSN 20403372. doi:[10.1039/c9nr03611c](https://doi.org/10.1039/c9nr03611c).
- [223] Chendong Zhang, Chih Piao Chuu, Xibiao Ren, Ming Yang Li, Lain Jong Li, Chuanhong Jin, Mei Yin Chou, and Chih Kang Shih. Interlayer couplings, moiré patterns, and 2d electronic superlattices in mos<sub>2</sub>/wse<sub>2</sub>

hetero-bilayers. *Science Advances*, 3(1):1–8, 2017. ISSN 23752548. doi:[10.1126/sciadv.1601459](https://doi.org/10.1126/sciadv.1601459).

[224] Wei Zhang, Michael Saliba, David T. Moore, Sandeep K. Pathak, Maximilian T. Hörantner, Thomas Stergiopoulos, Samuel D. Stranks, Giles E. Eperon, Jack A. Alexander-Webber, Antonio Abate, Aditya Sadhanala, Shuhua Yao, Yulin Chen, Richard H. Friend, Lara A. Estroff, Ulrich Wiesner, and Henry J. Snaith. Ultrasmooth organic-inorganic perovskite thin-film formation and crystallization for efficient planar heterojunction solar cells. *Nature Communications*, 6, 2015. ISSN 20411723. doi:[10.1038/ncomms7142](https://doi.org/10.1038/ncomms7142).

[225] Xin Zhang, Xiao Fen Qiao, Wei Shi, Bin Jiang Wu, De Sheng Jiang, and Ping Heng Tan. Phonon and raman scattering of two-dimensional transition metal dichalcogenides from monolayer, multilayer to bulk material. *Chemical Society Reviews*, 44(9):2757–2785, 2015. ISSN 14604744. doi:[10.1039/c4cs00282b](https://doi.org/10.1039/c4cs00282b).

[226] Weijie Zhao, R. M. Ribeiro, Minglin Toh, Alexandra Carvalho, Christian Kloc, A. H. Castro Neto, and Goki Eda. Origin of indirect optical transitions in few-layer  $\text{mos}_2$ ,  $\text{ws}_2$ , and  $\text{wse}_2$ . *Nano Letters*, 13(11):5627–5634, 2013. ISSN 1530-6984. doi:[10.1021/nl403270k](https://doi.org/10.1021/nl403270k).

[227] Ting Zhu and Ju Li. Ultra-strength materials. *Progress in Materials Science*, 55(7):710–757, 2010. ISSN 00796425. doi:[10.1016/j.pmatsci.2010.04.001](https://doi.org/10.1016/j.pmatsci.2010.04.001).

[228] Xiaoyang Zhu, Nicholas R. Monahan, Zizhou Gong, Haiming Zhu, Christopher W. Williams, and Cory A. Nelson. Charge transfer excitons at van der waals interfaces. *Journal of the American Chemical Society*, 137(26):8313–8320, 2015. ISSN 15205126. doi:[10.1021/jacs.5b03141](https://doi.org/10.1021/jacs.5b03141).

# **Appendices**

## MICROSCOPIC PHYSICS OF EXCITONIC SYSTEMS

### A.1 Formation and Dissociation of Excitons

#### Introduction to the 3D Hydrogenic Model for the Exciton

An exciton is a quasiparticle in condensed matter systems that was first theorized when sharp resonances in *absorption* appeared below the quasiparticle bandgap. These sharp resonances were attributed to electron-hole interactions, i.e. electron-hole pairs were correlated with Coulomb interactions. There correlations describes the motion and dynamics of a new quasiparticle, called an exciton. The simplest model for an exciton is analogous to a Hydrogen atom (more precisely, positronium), where the appropriate Hamiltonian to describe this system is given simply by

$$\left(-\frac{\hbar^2}{2\mu}\nabla^2 - \frac{1}{4\pi\epsilon_0\epsilon_s}\frac{e^2}{r}\right)\psi = E\psi \quad (\text{A.1})$$

where note the difference between the Hydrogen atom and the exciton in this simple model is primarily the reduced effective mass

$$\frac{1}{\mu} = \frac{1}{m_e^*} + \frac{1}{m_h^*} \quad (\text{A.2})$$

and the static dielectric screening  $\epsilon_s$ . We are also at the present, not interested in the center of mass momentum  $K$ , as the solutions are merely a plane-wave  $\exp(iK \cdot r)/\sqrt{V}$  with energies  $\hbar^2 K^2 / 2\mu$  and do not contribute to the main physics. In practice, we must also consider that the static dielectric screening must be spatiotemporally dependent, i.e.

$$\epsilon_s = \epsilon_s(\omega, k) \quad (\text{A.3})$$

to my knowledge, it is not particularly clear what the exact dependence is for this relation, but a rough physical picture suggests that the frequencies to consider are  $2\pi/\tau \lesssim \omega \lesssim E_b/\hbar$  i.e. the frequencies of the dielectric should be faster than the exciton lifetime  $\tau$ , or else the interactions are too slow to be of interest to renormalize the electron-hole interaction. The highest frequency will be given by the energy of the exciton itself, i.e. its binding energy  $E_b$ . In terms of its spatial dependence, we suspect the maximum extent will be governed by the wavefunction of the exciton, whose natural length scale will be its Bohr radius  $a_0$ . In other words, we would expect the interactions to be interesting only for  $r \lesssim a_0$  i.e.  $k \gtrsim 2\pi/a_0$ . Despite not

knowing the exact functional dependence of  $\varepsilon_s$ , we shall solve for the eigenenergies anyway assuming a constant value (or an averaged value). To do so, we note that we can define the renormalized Rydberg energies and Bohr radius as

$$\text{Ry} \equiv \frac{1}{2} \frac{e^4 \mu}{(4\pi\varepsilon_s\varepsilon_0)^2 \hbar^2} = \frac{1}{2} \frac{e^2}{(4\pi\varepsilon_s\varepsilon_0)a_0}, \quad a_0 \equiv \frac{4\pi\varepsilon_s\varepsilon_0 \hbar^2}{e^2 \mu} \quad (\text{A.4})$$

and in these new energy and spatial units, i.e.  $E = \epsilon \text{Ry}$  and  $x = Xa_0$ ,  $y = Ya_0$ ,  $z = Za_0$ ,  $r = Ra_0$ , we can divide (A.1) by the Rydberg energy to yield

$$\left( -a_0^2 \nabla^2 - 2 \frac{a_0}{r} \right) \psi = \epsilon \psi \quad (\text{A.5})$$

which is conveniently compatible with the dimensionless units of the Bohr radius, i.e.,

$$\left( -\nabla^2 - \frac{2}{R} \right) \psi = \epsilon \psi \quad (\text{A.6})$$

The solutions for the differential equation can now be solved in various ways, e.g. rewriting the Laplacian into spherical coordinates, using separation of variables and expanding in terms of spherical harmonics, Legendre polynomials, and solving the resultant differential equation in terms of  $R$ . This mathematical analysis is not particularly interesting, and is repeated in many textbooks - what is found is that discrete bound states indeed exist, with energies given by the relation

$$\epsilon_n = -\frac{1}{n^2}, \quad n = 1, 2, 3, \dots \quad (\text{A.7})$$

i.e., the solutions are exactly the same as the Hydrogen atom, with a new Rydberg energy. Notice these energies are *negative*, in other words, if a free electron-hole pair can be generated at the quasiparticle gap  $E_g$ , then the excitonic absorption occurs at  $\hbar\omega = E_g - \text{Ry}/n^2$ .

### Field Dissociation of a 3D Exciton

We are now interested in the question of whether it is possible to dissociate an exciton with an electric field  $F$ . We shall assume this field  $F$  is uniform throughout the exciton, and is akin to the situation of a field throughout the bulk of a material. However, this analysis represents a qualitative picture of the effects e.g. of fields at an interface (e.g. a built-in field in a semiconductor junction). The analysis begins similar to what is described above, in analogy to field dissociation in a Hydrogen atom. The field modifies the Hamiltonian with an extra term

$$\left( -\frac{\hbar^2}{2\mu} \nabla^2 - \frac{1}{4\pi\varepsilon_0\varepsilon_s} \frac{e^2}{r} - eF_z z \right) \psi = E\psi \quad (\text{A.8})$$

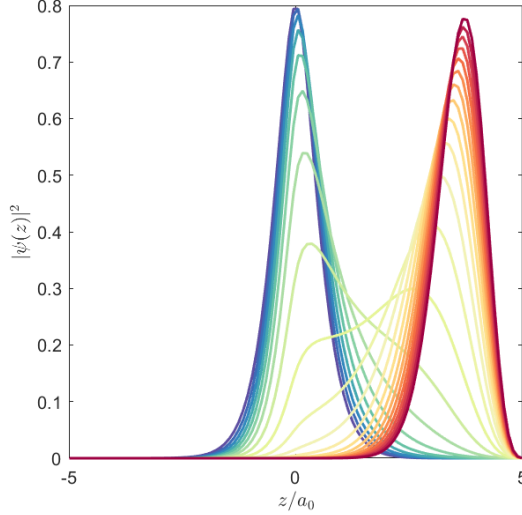


**Figure A.1: Exciton Wavefunction under an Electric Field.** Wavefunction of an exciton in an electric field for different electric field values (see [Figure A.2](#)) for the corresponding electric field strength for a given color.

where we rotate the system such that the field occurs in the  $z$  direction and  $F_z$  describes the magnitude of that field. The subsequent analysis proceeds similarly to before, where we conveniently can rewrite the Hamiltonian into excitonic units to get

$$\left(-\nabla^2 - \frac{2}{R} - \mathcal{F}Z\right)\psi = \epsilon\psi \quad (\text{A.9})$$

where we have defined the electric field in atomic units to be  $\mathcal{F} = eF_z a_0 / E_{b,0}$ . Here, notice that we have used the previous notion that the binding energy of the exciton is given by the largest energy in the Rydberg series ( $n = 1$ ), i.e.  $E_{b,0} = \text{Ry}$ . This equation, to the author's knowledge, cannot be solved analytically. A numerical solution can be found, however. Below, we plot in [Figure A.1](#) the normalized wavefunction integrated over the two other spatial dimensions  $|\psi(z, F_z)|^2 = \int \int |\psi(X, Y, Z)|^2 dX dY$  to analyze the effects of field on the wavefunction properties. We consider a finite difference grid with dimensions given by  $[-5, 5] \times [-5, 5] \times [-5, 5]$  all in excitonic radii units. Interestingly, we find that as the field increases, the electron partially escapes the Coulombic attraction with the hole, i.e. the exciton dissociates. To analyze this dissociation effect, we note that if  $R \approx Z$ , the potential for  $Z > 0$  is maximized at  $Z = Z_{max} = \sqrt{2/\mathcal{F}}$ . We consider any part of the wavefunction that is past this maximum potential effectively ionized, giving the dissociation efficiency to be  $\eta_{diss} = \int_{Z_{max}}^{\infty} |\psi(Z)|^2 dZ$ . We plot this efficiency for different field strengths in

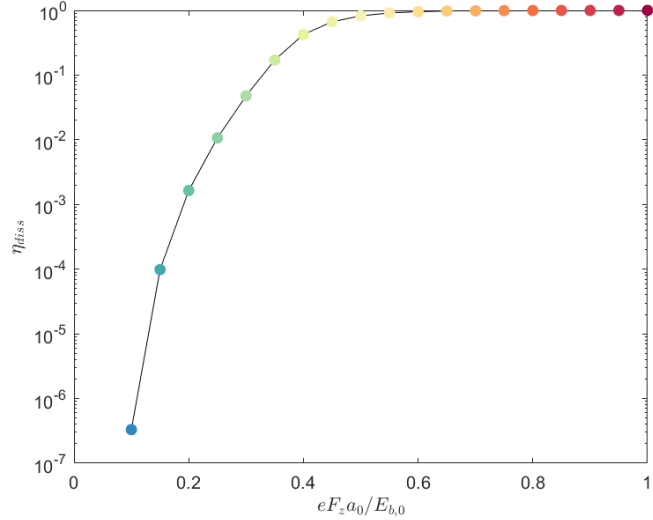


**Figure A.2: Exciton Dissociation Efficiency under an Electric Field.** Dissociation efficiency of an exciton, calculated via a tunneling probability, of an exciton in an electric field.

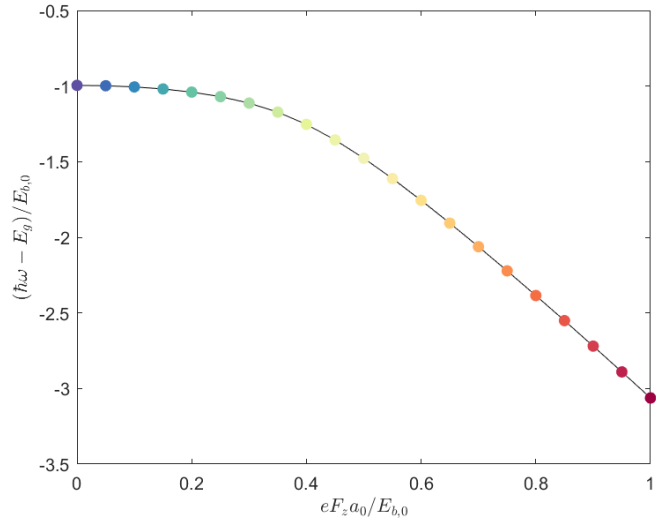


**Figure A.3: Exciton Binding Energy under an Electric Field.** Quadratic Stark shift of the 1s exciton in an electric field.

**Figure A.2.** Lastly, we analyze the consequences of the electric field on the binding energy  $E_b$ . We first note that for a 1s exciton that obeys spherical symmetry, there is no preferred orientation. Therefore, to first order, we expect no field dependence. To second order, we expect there to be a field dependence given as  $\Delta E_b \approx -\beta F_z^2$ . We can solve for this dependence numerically, which is plotted below in [Figure A.3](#).

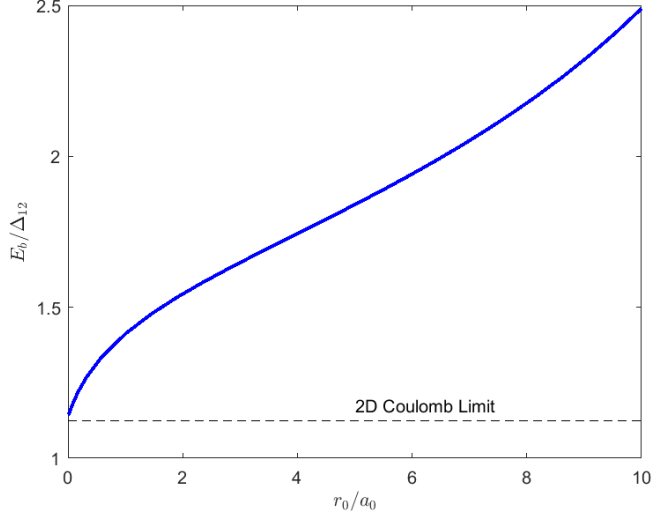


**Figure A.4: Exciton Binding Energy vs. Screening Length.** Binding energy of the exciton  $E_b$  relative to the energy difference of the first and second excited state  $\Delta_{12}$  for a given screening length  $r_0$  in units of the Bohr radius  $a_0$ . For a 2D Hydrogenic exciton, the first excited exciton has a binding energy of 4Ry and second excited exciton has a binding energy of  $(4/9)$ Ry. Thus, the difference in transition energies is  $\Delta_{12} = (32/9)$ Ry and  $E_b/\Delta_{12} = 9/8$ , which is referred to as the "2D Coulomb Limit" in this plot. For a given screening length  $r_0/a_0$ , it is possible to use an experimentally measured  $\Delta_{12}$  to deduce the binding energy of the exciton  $E_b$ .

## 2D Keldysh Problem

Recall the Hamiltonian for a 2D Coulomb Problem, given as

$$\left( -\frac{\hbar^2}{2\mu} \nabla^2 - \frac{e^2}{4\pi\epsilon_s\epsilon_0 r} \right) \psi = E\psi \quad (\text{A.10})$$

Recall that there are two important definitions in this problem, given by the Rydberg energy and Bohr radius:

$$\text{Ry} \equiv \frac{1}{2} \frac{e^4 \mu}{(4\pi\epsilon_s\epsilon_0)^2 \hbar^2} = \frac{1}{2} \frac{e^2}{(4\pi\epsilon_s\epsilon_0) a_0}, \quad a_0 \equiv \frac{4\pi\epsilon_s\epsilon_0 \hbar^2}{e^2 \mu} \quad (\text{A.11})$$

We can define dimensionless units  $x = a_0 X$ ,  $y = a_0 Y$ ,  $r = a_0 \rho$  and  $E = \epsilon \text{Ry}$  and divide the time-independent Schrodinger equation by the Rydberg energy to get

$$\left( -\frac{\hbar^4 (4\pi\epsilon_s\epsilon_0)^2}{e^4 \mu^2} \nabla^2 - \frac{2(4\pi\epsilon_s\epsilon_0) \hbar^2}{e^2 \mu} \frac{1}{r} \right) \psi = \epsilon \psi \quad (\text{A.12})$$

notice that the terms neatly reorganize into the bohr radius, i.e.,

$$\left( -a_0^2 \nabla^2 - 2 \frac{a_0}{r} \right) \psi = \epsilon \psi \quad (\text{A.13})$$

Rewriting the length units in terms of the bohr radius gives

$$\left(-\nabla_\rho^2 - \frac{2}{\rho}\right)\psi = \epsilon\psi \quad (\text{A.14})$$

which is the Coulomb problem in excitonic units. Note that we use  $\rho$  to denote the 2D nature of the expression, as opposed to when we used  $R$  for the 3D Hydrogenic model. Let's now see if we can do the same with the Keldysh potential, given as

$$V_{eh}(r) = -\frac{\pi e^2}{4\pi\epsilon_S\epsilon_0(\epsilon_1 + \epsilon_2)r_0} \left[ H_0\left(\frac{r}{r_0}\right) - Y_0\left(\frac{r}{r_0}\right) \right] \quad (\text{A.15})$$

which is an effective electrostatic interaction for two charges within a thin 2D dielectric continuum [13, 29]. The screening length  $r_0$  gives a crossover length scale between a  $1/r$  Coulomb interaction at large separation and a weaker  $\log(r)$  interaction at small separation. To solve the binding energy problem for these 2D excitons, we use similar analysis to above, where we can again divide by the Rydberg energy to get

$$\nu_{eh}(r) = -\frac{2\pi a_0}{(\epsilon_1 + \epsilon_2)r_0} \left[ H_0\left(\frac{r}{r_0}\right) - Y_0\left(\frac{r}{r_0}\right) \right] \quad (\text{A.16})$$

rewriting in terms of dimensionless units, where  $r = a_0\rho$ , we have

$$\left(-\nabla_\rho^2 - \frac{2\pi a_0}{(\epsilon_1 + \epsilon_2)r_0} \left[ H_0\left(\frac{a_0\rho}{r_0}\right) - Y_0\left(\frac{a_0\rho}{r_0}\right) \right]\right)\psi = \epsilon\psi \quad (\text{A.17})$$

which can be solved numerically by discretizing the differential equation, as before. The solutions can be used to infer the exciton binding energy for an observed value of  $\Delta_{12}$ , as seen in [Figure A.4](#). Here,  $\Delta_{12} = |E_1 - E_2|$  is the energetic differences between the first two excitons in a hydrogen-like series. Also depicted in [Figure A.5](#) are the excitonic wavefunction solutions of the 2D Keldysh potential.

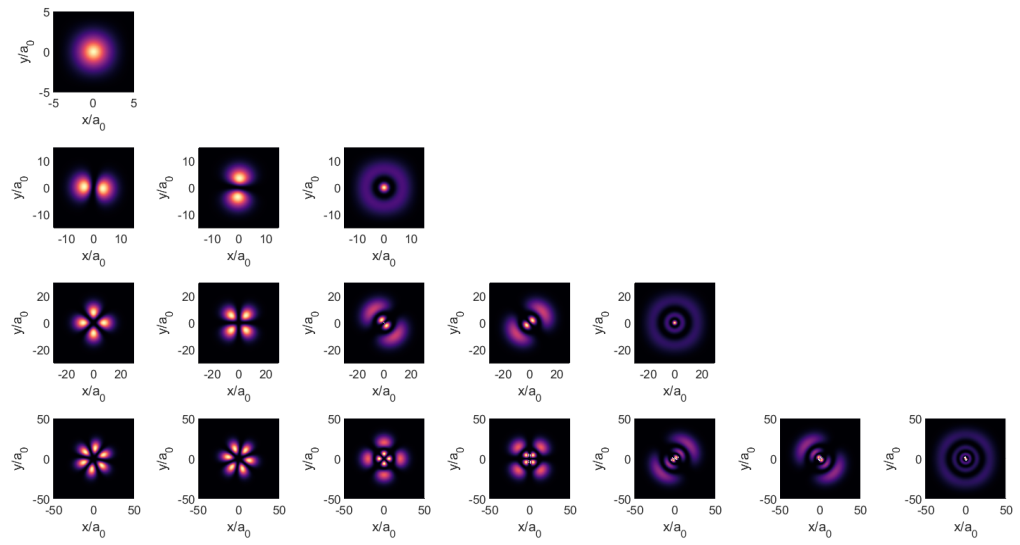


Figure A.5: Wavefunctions of the excitons in the 2D Keldysh potential, for  $n = 1, 2, 3, 4$  for each row, i.e.  $s, p, d, f$ -like wavefunctions. Wavefunctions are similar to the hydrogenic model.

## Appendix B

## MACROSCOPIC OPTICAL PROPERTIES OF LAYERED STRUCTURES

### B.1 Boundary conditions on Electromagnetic Fields

Let us do a brief introduction and primer on Maxwell's equations before we go into the scattering matrix method. The method is generically simple and only requires us to recall Maxwell's equations and its boundary conditions. Let's state Maxwell's equations in differential form:

$$\begin{aligned}
 \nabla \cdot \mathbf{E} &= \frac{\rho}{\epsilon_0} \\
 \nabla \cdot \mathbf{B} &= 0 \\
 \nabla \times \mathbf{E} &= -\frac{\partial \mathbf{B}}{\partial t} \\
 \nabla \times \mathbf{B} &= \mu_0 \mathbf{J} + \mu_0 \epsilon_0 \frac{\partial \mathbf{E}}{\partial t}
 \end{aligned} \tag{B.1}$$

which is what we normally see in introductory electromagnetism courses. Of course, we can also state how they change in matter by using the constitutive relations

$$\begin{aligned}
 \mathbf{D} &= \epsilon \mathbf{E} \\
 \mathbf{B} &= \mu \mathbf{H}
 \end{aligned} \tag{B.2}$$

where  $\epsilon$  and  $\mu$  are the dielectric permitivity and magnetic permeability respectively. Then, we can reformulate Maxwell's equations in a particularly simple form. Moreover, let's take there to be no free electrical charges or source of currents, which is usually the case when we're considering the type of optical experiments we're interested in. So, Maxwell's equations become

$$\begin{aligned}
 \nabla \cdot \mathbf{D} &= 0 \\
 \nabla \cdot \mathbf{B} &= 0 \\
 \nabla \times \mathbf{E} &= -\frac{\partial \mathbf{B}}{\partial t} \\
 \nabla \times \mathbf{H} &= \frac{\partial \mathbf{D}}{\partial t}
 \end{aligned} \tag{B.3}$$

which looks particularly simple and free of phenomenological parameters! (Of course, this is an illusion, as they're embedded in the  $\mathbf{D}$  and  $\mathbf{H}$  fields.) Then, let's

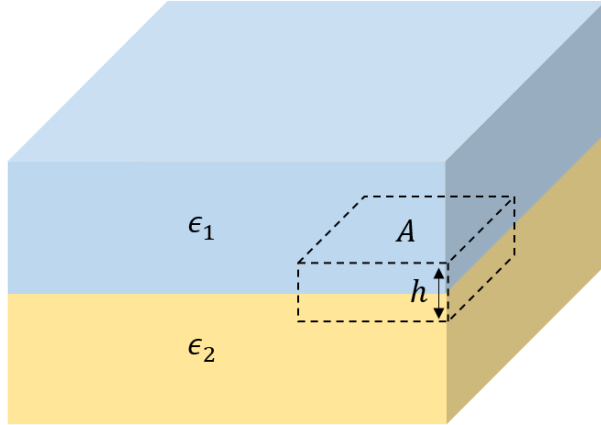


Figure B.1: A schematic of a Gaussian pillbox (dotted box) with height  $h$  and area  $A$  sandwiched between two materials with dielectric constant  $\epsilon_1$  and  $\epsilon_2$ .

derive the boundary conditions from using Stokes' and Gauss's theorem:

$$\begin{aligned} \iint_S (\nabla \times \mathbf{F}) \cdot d\mathbf{A} &= \oint_{\partial S} \mathbf{F} \cdot d\mathbf{r} & \text{(Stokes)} \\ \iiint_E (\nabla \cdot \mathbf{F}) dV &= \iint_{\partial E} \mathbf{F} \cdot d\mathbf{A} & \text{(Gauss)} \end{aligned} \quad (\text{B.4})$$

for which we shall apply to Maxwell's equations.

### Perpendicular Components

Let's look at the first two Maxwell's equations in (B.3), which essentially look the same except for what we call  $\mathbf{D}$  and  $\mathbf{B}$  (incidentally, because of the symmetry of the two fields, textbooks typically stick to a basis of using either  $\mathbf{D}$  and  $\mathbf{B}$  or  $\mathbf{E}$  and  $\mathbf{H}$ . Personally, I've found using  $\mathbf{E}$  and  $\mathbf{H}$  rather convenient and pretty). Then, suppose we draw a Gaussian pillbox (which we shall abbreviate as G.P.) as we do in Figure B.1 which we can use as our volume in Gauss's theorem. Then

$$\iiint_{\text{Vol(G.P.)}} (\nabla \cdot \mathbf{D}) dV = \iint_{\text{Surf(G.P.)}} \mathbf{D} \cdot d\mathbf{A} = 0 \quad (\text{B.5})$$

In the limit as the thickness  $h$  goes to 0, there must not be any contribution from the sidewalls of the pillbox, for the flux is proportional to the area of the sidewall, which is going to 0 as  $h \rightarrow 0$ . Thus, the only contribution can come from the top and bottom areas, each with area  $A$ . If we call the direction perpendicular to the top

and bottom surface  $\hat{n}_{\text{top}}$  and  $\hat{n}_{\text{bottom}}$ , then we have

$$\mathbf{D}_1 \cdot \hat{n}_{\text{top}} = -\mathbf{D}_2 \cdot \hat{n}_{\text{bottom}} \quad (\text{B.6})$$

where  $\mathbf{D}_{1,2}$  is the displacement field in the layer with dielectric constant  $\epsilon_{1,2}$ , respectively, and we have used the fact that the surfaces have equal areas and divided them out. However, notice that actually  $\hat{n}_{\text{top}} = -\hat{n}_{\text{bottom}}$  because the outward pointing normals for the top and bottom surfaces are in opposite directions, so let's just call one of them  $\hat{n}$  (it doesn't matter which one, as long as we stay consistent). Moreover, notice that in the limit of looking at one point, there is only one normal vector at that point and the surface looks *flat* in that limit. Then, the above boundary condition holds point-by-point for all points between the two surfaces. Lastly, as we said before, the first two Maxwell's equations are exactly the same under interchange of  $\mathbf{D}$  and  $\mathbf{B}$ . So, we have

$$\begin{aligned} \mathbf{D}_1 \cdot \hat{n} &= \mathbf{D}_2 \cdot \hat{n} \\ \mathbf{B}_1 \cdot \hat{n} &= \mathbf{B}_2 \cdot \hat{n} \end{aligned} \quad (\text{B.7})$$

which are our first two boundary conditions that relate the components perpendicular to the boundary.

### Parallel Components

In a very analogous way, we can derive the boundary conditions on the components of the fields parallel to the interface. If we examine the third and fourth of Maxwell's equations in (B.3), we see that they are essentially equivalent up to a redefinition:  $\mathbf{E} \leftrightarrow \mathbf{H}$  and  $\mathbf{B} \leftrightarrow -\mathbf{D}$ . So, let us just derive the boundary conditions on, say, the third equation. Let us draw a rectangular loop as in Figure B.2 with length  $l$  and height  $h$ . We shall integrate over this loop and use Stokes' equation:

$$\begin{aligned} \oint_{\text{Loop}} \mathbf{E} \cdot d\mathbf{r} &= \iint_{\text{Surf(Loop)}} (\nabla \times \mathbf{E}) \cdot d\mathbf{A} \\ &= \iint_{\text{Surf(Loop)}} -\frac{\partial \mathbf{B}}{\partial t} \cdot d\mathbf{A} \\ &= -\frac{\partial \phi_B}{\partial t} \end{aligned} \quad (\text{B.8})$$

where we have interchanged the time derivative and the surface integral and defined the magnetic flux as  $\phi_B = \iint \mathbf{B} \cdot d\mathbf{A}$ . Then, notice what happens when we take  $h \rightarrow 0$ . It necessarily takes  $\phi_B \rightarrow 0$  since the magnetic flux is proportional to the

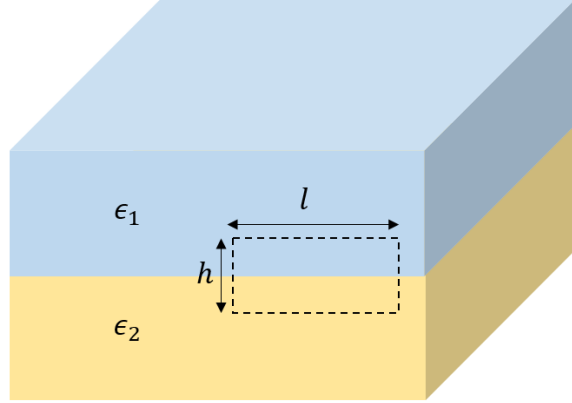


Figure B.2: A schematic of a Gaussian loop (dotted rectangle) with height  $h$  and length  $l$  drawn between two materials with dielectric constant  $\epsilon_1$  and  $\epsilon_2$ .

area it threads. Moreover, the contribution of the line integral across the interfaces (i.e., the sides of the rectangular loop with width  $h$ ) also goes to 0. Then, in this limit, we have

$$\mathbf{E}_1 \cdot \hat{p}_{\text{top}} = -\mathbf{E}_2 \cdot \hat{p}_{\text{bottom}} \quad (\text{B.9})$$

where we have divided out the factor of  $l$  associated with the length of the loop. Again, notice that in fact  $\hat{p}_{\text{top}} = -\hat{p}_{\text{bottom}}$ , in the limit that we also take  $l \rightarrow 0$ , so that all wiggles of the loop are smoothed out. Thus, these parallel vectors are actually point by point constraints on the fields, and we shall arbitrarily denote the top surface  $\hat{p}_{\text{top}} = \hat{p}$ . As before, we can equivalently do the same with the  $\mathbf{H}$  field, so that the boundary conditions on the parallel components are

$$\begin{aligned} \mathbf{E}_1 \cdot \hat{p} &= \mathbf{E}_2 \cdot \hat{p} \\ \mathbf{H}_1 \cdot \hat{p} &= \mathbf{H}_2 \cdot \hat{p} \end{aligned} \quad (\text{B.10})$$

Using  $\mathbf{E}$  and  $\mathbf{H}$  as our basis fields, we shall then summarize the boundary conditions using the constitutive relations in (B.2) and write things in a more succinct form:

$$\begin{aligned} (\epsilon_1 \mathbf{E}_1 - \epsilon_2 \mathbf{E}_2) \cdot \hat{n} &= 0 \\ (\mathbf{E}_1 - \mathbf{E}_2) \times \hat{n} &= 0 \\ (\mu_1 \mathbf{H}_1 - \mu_2 \mathbf{H}_2) \cdot \hat{n} &= 0 \\ (\mathbf{H}_1 - \mathbf{H}_2) \times \hat{n} &= 0 \end{aligned} \quad (\text{B.11})$$

which are boundary conditions on the  $\mathbf{E}$  and  $\mathbf{H}$  fields! As a reminder,  $\hat{n}$  is a unit vector normal to the interface between  $\epsilon_1$  and  $\epsilon_2$ .

## B.2 Optical Waves in Homogenous Media

The motion of the wave must come from some wave equation, which we shall derive now. Let's begin with Maxwell's equations, which governs any classical electro-magnetic interaction:

$$\begin{aligned}\nabla \cdot \mathbf{D} &= \rho_f \\ \nabla \cdot \mathbf{B} &= 0 \\ \nabla \times \mathbf{E} &= -\frac{\partial \mathbf{B}}{\partial t} \\ \nabla \times \mathbf{H} &= \mathbf{J}_f + \frac{\partial \mathbf{D}}{\partial t}\end{aligned}\tag{B.12}$$

where we shall use the bold-face of letters to refer to things that act like vectors (e.g.  $\mathbf{D}, \mathbf{B}$ ) and non bold-faced things act like scalars (e.g.  $\rho_f$ ). At the moment we are interested in getting a wave equation for the electric and magnetic field. Our previous math courses have taught us that the generic wave equation looks like

$$\frac{\partial^2 f}{\partial x^2} = \frac{1}{v^2} \frac{\partial^2 f}{\partial t^2}\tag{B.13}$$

because *any* function of the form  $f(x \pm vt)$  solves the PDE (partial differential equation). You can check this by inserting this back above, but more specifically, "waving" functions like  $\sin(x \pm vt)$ ,  $\cos(x \pm vt)$ , and  $\exp(i(x \pm vt))$  also satisfy the wave equation, as you can easily see. With this in mind, let's find the wave equation for electromagnetic waves. Let's focus first on the electric field (we shall show that this is generally much stronger than the magnetic field in a moment):

$$\begin{aligned}\nabla \times (\nabla \times \mathbf{E}) &= -\nabla \times \frac{\partial \mathbf{B}}{\partial t} \\ &= -\frac{\partial}{\partial t}(\nabla \times \mathbf{B}) \\ &= -\mu_0 \frac{\partial}{\partial t} \left( \mathbf{J}_f + \frac{\partial \mathbf{D}}{\partial t} \right) \quad (\text{assuming non-magnetic materials, i.e., } \mathbf{B} = \mu_0 \mathbf{H})\end{aligned}\tag{B.14}$$

where in the last line, we use the constitutive relation between  $\mathbf{B}$  and  $\mathbf{H}$ , i.e.  $\mathbf{B} = \mu_0 \mathbf{H} + \mathbf{M}$ , where the magnetization  $\mathbf{M} \rightarrow 0$  for non-magnetic materials. We shall also assume that some Ohm's law holds, that is, the current is proportional to the electric field applied (i.e.,  $\mathbf{J}_f = \sigma \mathbf{E}$ ). Electrical engineers usually write this as  $V = IR$ , but this expression says the same thing. We may also use the constitutive relation for the  $\mathbf{D}$ -field, i.e.,  $\mathbf{D} = \epsilon_0 \mathbf{E} + \mathbf{P}$ . Here,  $\mathbf{P}$  plays the role of polarizability, i.e., the amount of polarization that is induced from some external electric field (could

be static or an AC-field). We shall not assume any form for  $\mathbf{P}$  for now. Inserting these expressions into above, we finally arrive at

$$\nabla \times \nabla \times \mathbf{E} = -\mu_0 \sigma \frac{\partial \mathbf{E}}{\partial t} - \frac{1}{c^2} \frac{\partial^2 \mathbf{E}}{\partial t^2} - \mu_0 \frac{\partial^2 \mathbf{P}}{\partial t^2} \quad (\text{B.15})$$

where we have also used the fact that  $\mu_0 \epsilon_0 = 1/c^2$ , with  $c$  being the speed of light. This is the equation we've been seeking! While being admittedly complex looking, equation (B.15) simplifies to the wave-equation (B.13) referred to above in 1D, and if we take  $\sigma \rightarrow 0$ , and  $\mathbf{P} \rightarrow 0$ . In fact the curls are a more general expression for the wave equation, if we do some further manipulation of the curls and use the first Maxwell as well, but we will ignore this for now. What we *do know* is that the presence of pure material properties (i.e.,  $\sigma$  and  $\mathbf{P}$ ) modify the wave equation to be something slightly different. So the waves could move differently in matter, compared to vacuum. Let's figure this out. In the wave equation above, we have yet to specify how  $\mathbf{P}$  relates to  $\mathbf{E}$ . We shall focus our attention to a class of materials that are specified as *linear* materials. That is, they obey

$$\mathbf{P} = \epsilon_0 \chi \mathbf{E} \quad (\text{B.16})$$

and as you can see, they are referred to as linear because they are linear with  $\mathbf{E}$ . There are non-linear materials that obey  $P \sim \chi^{(2)} E^2$ , but those are challenging equations to deal with and linear optics describes most of the world around us. So, (B.15) is now completely in terms of  $\mathbf{E}$ , which is still unknown.  $\chi$  is sometimes referred to as the electric susceptibility.

Like every differential equation, they can more or less only be solved if you know the solution already (or re-write the problem into something you know how to solve). So, let's assume we know the solution is actually a plane wave:

$$\mathbf{E} = \mathbf{E}_0 \exp(i(\mathbf{k} \cdot \mathbf{r} - \omega t)) \quad (\text{B.17})$$

This expression is referred to a plane-wave because for a given time  $t'$ ,  $\mathbf{k} \cdot \mathbf{r}$  defines a plane with normal vector  $\mathbf{k}$ . Exponentials also turn out to be a great function, because from Fourier math we know that this is a good basis function that can be expanded into any other wave-form (i.e., exponentials form a complete basis set). Thus, our results can be applied to *any* wave, and not just this simple plane-wave. Let's see what we find if we insert this plane-wave into our wave-equation. We get

$$-\mathbf{k} \times \mathbf{k} \times \mathbf{E}_0 = -\mu_0 \sigma (-i\omega) \mathbf{E}_0 - \frac{(-i\omega)^2}{c^2} \epsilon_r \mathbf{E}_0 \quad (\text{B.18})$$

where we have divided out the exponential factor because that can never be 0, and we have defined  $\epsilon_r = 1 + \chi$ . Let's further simplify this expression by using the well-known "back of the cab" rule ( $\mathbf{A} \times \mathbf{B} \times \mathbf{C} = \mathbf{B} \cdot (\mathbf{A} \cdot \mathbf{C}) - \mathbf{C} \cdot (\mathbf{A} \cdot \mathbf{B})$ ). This gives

$$k^2 = i\sigma\mu_0\omega + \epsilon_r \frac{\omega^2}{c^2} \quad (\text{B.19})$$

where we have used the fact that  $\mathbf{k} \cdot \mathbf{E}_0 = 0$  for a plane-wave and that  $|\mathbf{k}| \equiv k$ . This expression describes the relationship between  $k$  and  $\omega$ , for a given set of material parameters. We can redefine another parameter that encapsulates all the other parameters as

$$k^2 = \epsilon_{\text{complex}} \frac{\omega^2}{c^2} \quad (\text{B.20})$$

where

$$\epsilon_{\text{complex}} = \epsilon_r + \frac{i\sigma}{\epsilon_0\omega} \equiv \epsilon_1 + i\epsilon_2 \quad (\text{B.21})$$

This equation describes the complex dielectric constant (which we will, from this point forward, refer to as  $\epsilon \equiv \epsilon_{\text{complex}}$  for brevity) as some component that has some real response  $\epsilon_r$  but that  $\sigma$  is related to the imaginary part of this dielectric constant (which we shall soon find out is related to loss). Let us further define a constant that is useful to us, i.e.,

$$n \equiv \sqrt{\epsilon} \quad (\text{B.22})$$

so that  $k = \omega n/c$  and that  $n \equiv \eta + i\kappa$ . This constant  $n$  will be referred to as the complex refractive index, and either this quantity or the complex dielectric constant is enough to describe the optical response of almost every material. These two quantities can be related to each other with the following:

$$\begin{aligned} \epsilon_1 &= \eta^2 - \kappa^2, & \eta &= \sqrt{\frac{|\epsilon| + \epsilon_1}{2}} \\ \epsilon_2 &= 2\eta\kappa, & \kappa &= \sqrt{\frac{|\epsilon| - \epsilon_1}{2}} \end{aligned} \quad (\text{B.23})$$

where  $|\epsilon| = \sqrt{\epsilon_1^2 + \epsilon_2^2}$ .

Let's briefly examine how the real and imaginary parts of  $n$  relate to the plane wave expression that we used earlier to arrive at these properties. In other words, let's insert the  $k$  into the plane-wave expression:

$$\begin{aligned} \mathbf{E} &= \mathbf{E}_0 \exp\left(i \left(\frac{\omega}{c}(\eta + i\kappa)x - \omega t\right)\right) \\ &= \underbrace{\mathbf{E}_0}_{\text{initial amplitude}} \underbrace{\exp\left(i \frac{\omega\eta}{c} \left(x - \frac{c}{\eta}t\right)\right)}_{\text{travelling wave}} \underbrace{\exp\left(-\frac{\omega\kappa}{c}x\right)}_{\text{decaying amplitude}} \end{aligned} \quad (\text{B.24})$$

and notice that there are three components. The first term  $\mathbf{E}_0$  is just the initial amplitude of the wave, whereas the second term describes a traveling wave moving at velocity  $c/\eta$ . The last term describes a decaying amplitude term that has a  $1/e$  distance of  $c/(\omega\kappa)$ . Since we are typically interested in intensities (which go as the field squared), a common definition for the decay rate is

$$\alpha = \frac{2\omega\kappa}{c} \quad (\text{B.25})$$

where the factor of 2 comes from squaring, and  $\alpha$  refers to the *absorption coefficient* of a material, in units of 1/length. We finally have arrived at the two contributions of the complex refractive index, i.e.  $n$  modifies the speed of the wave, whereas  $\kappa$  describes the decay of the wave.

In summary,  $n$  or equivalently,  $\epsilon$  completely describes the linear optical response of any material. In general,  $\kappa$  and  $\epsilon_2$  both describe loss/absorption within a material, whereas  $\eta$  describes the speed and refractive properties of the wave.

### B.3 Transfer Matrix Method for Layered Media

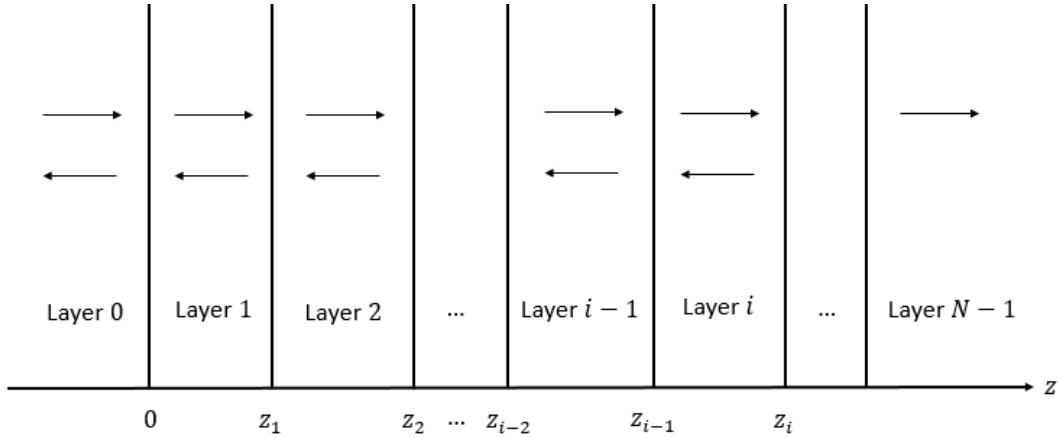


Figure B.3: Schematic of a one-dimensional stack consisting of  $N$  layers. The arrows represent the reflected and transmitted electromagnetic waves in each layer.

We assume a problem definition similar to what's shown in [Figure B.3](#). That is, we have an electromagnetic plane wave propagating in the  $z$  direction towards a one-dimensional stack of  $N$  layers. We shall assume the materials are isotropic, nonmagnetic, and linear. The electric field in the  $j$ th layer is then given by

$$E_j(z) = A_j e^{i q_j z} + B_j e^{-i q_j z} \quad (\text{B.26})$$

where  $q_j$  is the wavevector in the  $j$ th layer and is given by  $q_j = 2\pi n_j / \lambda = 2\pi(\eta_j + i\kappa_j) / \lambda$ . Thus, the optical response of the materials in encapsulated in the wavevector of the field.  $A_j$  and  $B_j$  are the field amplitudes of the forward and backward propagating waves, respectively. By Fourier's theorem, we can simply assume a monochromatic wave is incident on the stack i.e.  $E(z, t) = E(z)e^{-i\omega t}$  and assume the same for the  $\mathbf{H}$  field. Faraday's law in Maxwell's equations then gives

$$H(z) = \frac{q_j}{\omega \mu_0} (A_j e^{i q_j z} - B_j e^{-i q_j z}) \quad (\text{B.27})$$

where we have assumed the material stack is composed of non-magnetic materials (i.e.  $\mu_r = 1$ ). Since the electric and magnetic fields are in a plane perpendicular to the direction of propagation, the relevant boundary conditions are the ones parallel to an interface. Maxwell's curl equations are

$$\begin{aligned} \nabla \times \mathbf{E} &= -\frac{\partial \mathbf{B}}{\partial t} \\ \nabla \times \mathbf{H} &= \mathbf{J}_f + \frac{\partial \mathbf{D}}{\partial t} \end{aligned} \quad (\text{B.28})$$

and in the absence of a sheet current we must then have that the parallel components of  $\mathbf{E}$  and  $\mathbf{H}$  fields are continuous at the boundary. Between the  $j$ th and  $j+1$ th layer (i.e. at  $z_j$  in [Figure B.3](#)), this implies a condition on the field amplitudes:

$$\begin{aligned} A_j e^{iq_j z_i} + B_j e^{-iq_j z_j} &= A_{j+1} e^{iq_{j+1} z_j} + B_{j+1} e^{-iq_{j+1} z_j} \\ q_j (A_j e^{iq_j z_j} - B_j e^{-iq_j z_j}) &= q_{j+1} (A_{j+1} e^{iq_{j+1} z_j} - B_{j+1} e^{-iq_{j+1} z_j}) \end{aligned} \quad (\text{B.29})$$

which allows us to form matrices

$$\begin{pmatrix} e^{iq_j z_j} & e^{-iq_j z_j} \\ q_j e^{iq_j z_j} & -q_j e^{-iq_j z_j} \end{pmatrix} \begin{pmatrix} A_j \\ B_j \end{pmatrix} = \begin{pmatrix} e^{iq_{j+1} z_i} & e^{-iq_{j+1} z_j} \\ q_{j+1} e^{iq_{j+1} z_j} & -q_{j+1} e^{-iq_{j+1} z_j} \end{pmatrix} \begin{pmatrix} A_{j+1} \\ B_{j+1} \end{pmatrix} \quad (\text{B.30})$$

Note that in [\(B.30\)](#) we can rewrite it as

$$\underbrace{\begin{pmatrix} 1 & 1 \\ q_j & -q_j \end{pmatrix}}_{M_j} \underbrace{\begin{pmatrix} e^{iq_j z_j} & 0 \\ 0 & e^{-iq_j z_j} \end{pmatrix}}_{P_{j,j}} \begin{pmatrix} A_j \\ B_j \end{pmatrix} = \underbrace{\begin{pmatrix} 1 & 1 \\ q_{j+1} & -q_{j+1} \end{pmatrix}}_{M_{j+1}} \underbrace{\begin{pmatrix} e^{iq_{j+1} z_j} & 0 \\ 0 & e^{-iq_{j+1} z_j} \end{pmatrix}}_{P_{j+1,j}} \begin{pmatrix} A_{j+1} \\ B_{j+1} \end{pmatrix} \quad (\text{B.31})$$

so if we now take  $M_j^{-1} M_{j+1}$ , we have

$$\begin{pmatrix} A_j \\ B_j \end{pmatrix} = P_{j,j}^{-1} M_j^{-1} M_{j+1} P_{j+1,j} \begin{pmatrix} A_{j+1} \\ B_{j+1} \end{pmatrix} \quad (\text{B.32})$$

Now, let us define an interface matrix  $J_{j,j+1} = M_j^{-1} M_{j+1}$  which, calculating explicitly, gives us

$$\begin{aligned} J_{j,j+1} &= M_j^{-1} M_{j+1} = \frac{1}{-2q_j} \begin{pmatrix} -q_j & -1 \\ -q_j & 1 \end{pmatrix} \begin{pmatrix} 1 & 1 \\ q_{j+1} & -q_{j+1} \end{pmatrix} \\ &= \frac{1}{2q_j} \begin{pmatrix} q_j + q_{j+1} & q_j - q_{j+1} \\ q_j - q_{j+1} & q_j + q_{j+1} \end{pmatrix} \\ &= \frac{1}{t_{j,j+1}} \begin{pmatrix} 1 & r_{j,j+1} \\ r_{j,j+1} & 1 \end{pmatrix} \end{aligned} \quad (\text{B.33})$$

where, in the last step, we have factored out a  $q_j + q_{j+1}$  from the entire matrix and have defined

$$t_{j,j+1} \equiv \frac{2q_j}{q_j + q_{j+1}}, \quad r_{j,j+1} \equiv \frac{q_j - q_{j+1}}{q_j + q_{j+1}} \quad (\text{B.34})$$

Therefore, in total we have

$$\begin{pmatrix} A_j \\ B_j \end{pmatrix} = P_{j,j}^{-1} J_{j,j+1} P_{j+1,j} \begin{pmatrix} A_{j+1} \\ B_{j+1} \end{pmatrix} \quad (\text{B.35})$$

Acting recursively, we have

$$\begin{pmatrix} A_{j+1} \\ B_{j+1} \end{pmatrix} = P_{j+1,j+1}^{-1} J_{j+1,j+2} P_{j+2,j+1} \begin{pmatrix} A_{j+2} \\ B_{j+2} \end{pmatrix} \quad (\text{B.36})$$

so that

$$\begin{pmatrix} A_j \\ B_j \end{pmatrix} = P_{j,j}^{-1} J_{j,j+1} P_{j+1,j} P_{j+1,j+1}^{-1} J_{j+1,j+2} P_{j+2,j+1} \begin{pmatrix} A_{j+2} \\ B_{j+2} \end{pmatrix} \quad (\text{B.37})$$

Now notice what  $P_{j+1,j} P_{j+1,j+1}^{-1}$  gives you, i.e.,

$$P_{j+1,j} P_{j+1,j+1}^{-1} = \begin{pmatrix} e^{iq_{j+1}z_j} & 0 \\ 0 & e^{-iq_{j+1}z_j} \end{pmatrix} \begin{pmatrix} e^{-iq_{j+1}z_{j+1}} & 0 \\ 0 & e^{iq_{j+1}z_{j+1}} \end{pmatrix} = \begin{pmatrix} e^{-iq_{j+1}(z_{j+1}-z_j)} & 0 \\ 0 & e^{iq_{j+1}(z_{j+1}-z_j)} \end{pmatrix} \quad (\text{B.38})$$

Note that  $z_j$  refer to the actual coordinates. We can define the  $j$ th layer as having some thickness  $t_{j+1} \equiv z_{j+1} - z_j$ . Thus,

$$L_{j+1} \equiv P_{j+1,j} P_{j+1,j+1}^{-1} = \begin{pmatrix} e^{-iq_{j+1}t_{j+1}} & 0 \\ 0 & e^{iq_{j+1}t_{j+1}} \end{pmatrix} \quad (\text{B.39})$$

In total then we have

$$\begin{pmatrix} A_j \\ B_j \end{pmatrix} = P_{j,j}^{-1} J_{j,j+1} L_{j+1} J_{j+1,j+2} P_{j+2,j+1} \begin{pmatrix} A_{j+2} \\ B_{j+2} \end{pmatrix} \quad (\text{B.40})$$

If we do this now  $N$  times and begin at 0, it's clear we have

$$\underbrace{P_{0,0} \begin{pmatrix} A_0 \\ B_0 \end{pmatrix}}_{E_0} = \underbrace{J_{0,1} L_1 J_{1,2} L_2 J_{2,3} \cdots L_{N-1} J_{N-1,N}}_S \underbrace{P_{N,N-1} \begin{pmatrix} A_N \\ B_N \end{pmatrix}}_{E_N} \quad (\text{B.41})$$

where we define  $E_j^+$  as the right moving wave and  $E_j^-$  as the left moving wave, in the total  $E$  field,  $E_j = E_j^+ + E_j^-$ . Thus,

$$\begin{pmatrix} E_0^+ \\ E_0^- \end{pmatrix} = S \begin{pmatrix} E_N^+ \\ E_N^- \end{pmatrix} \quad (\text{B.42})$$

where

$$S = \left( \prod_{j=1}^{N-1} J_{j-1,j} L_j \right) J_{N-1,N} \quad (\text{B.43})$$

where successive terms are multiplied to the *right* of the previous terms. We can now easily define other terms that are interesting by looking at the elements of  $S$ . That is,

$$\begin{aligned} E_0^+ &= S_{11}E_N^+ + S_{12}E_N^- \\ E_0^- &= S_{21}E_N^+ + S_{22}E_N^- \end{aligned} \quad (\text{B.44})$$

and enforce that  $E_N^- = 0$ , since there is no left-propagating wave at the end of the stack. In this scenario, we can calculate the reflection and transmission amplitudes as

$$r = \frac{E_0^-}{E_0^+} = \frac{S_{21}}{S_{11}}, \quad t = \frac{E_N^+}{E_0^+} = \frac{1}{S_{11}} \quad (\text{B.45})$$

which can be simply found by examining at the elements of  $S$ .

### Accounting for Sheet Conductors at the Interface

We consider an infinitesimally thin sheet conductor at the  $j$ th interface, e.g. in the case of a 2D material. The conductivity induces a current with an electric field given by Ohm's law  $\mathbf{J} = \sigma \mathbf{E} \delta(z - z_j)$ . By inserting this current in (B.28), we have a new boundary condition for the  $H$ -field at the interface:

$$H_j(z_j) = H_{j+1}(z_j) + \sigma E(z_j) \quad (\text{B.46})$$

which gives a new set of conditions when including the electric field continuity:

$$\begin{aligned} A_j e^{iq_j z_j} + B_j e^{-iq_j z_j} &= A_{j+1} e^{iq_{j+1} z_j} + B_{j+1} e^{-iq_{j+1} z_j} \\ q_j (A_j e^{iq_j z_j} - B_j e^{-iq_j z_j}) &= q_{j+1} (A_{j+1} e^{iq_{j+1} z_j} - B_{j+1} e^{-iq_{j+1} z_j}) \\ &\quad + \omega \mu_0 \sigma (A_{j+1} e^{iq_{j+1} z_j} + B_{j+1} e^{-iq_{j+1} z_j}) \end{aligned} \quad (\text{B.47})$$

where note that the additional  $E(z_j)$  term in the  $H$ -field boundary condition can be evaluated in either material, because of the continuity of the electric field. The  $j$ th transfer matrix with a sheet conductor at  $z_j$  is then renormalized to

$$\begin{aligned} &\underbrace{\begin{pmatrix} 1 & 1 \\ q_j & -q_j \end{pmatrix}}_{M_j} \underbrace{\begin{pmatrix} e^{iq_j z_j} & 0 \\ 0 & e^{-iq_j z_j} \end{pmatrix}}_{P_{j,j}} \begin{pmatrix} A_j \\ B_j \end{pmatrix} \\ &= \underbrace{\begin{pmatrix} 1 & 1 \\ q_{j+1} + \omega \mu_0 \sigma & -q_{j+1} + \omega \mu_0 \sigma \end{pmatrix}}_{M_{j+1}} \underbrace{\begin{pmatrix} e^{iq_{j+1} z_j} & 0 \\ 0 & e^{-iq_{j+1} z_j} \end{pmatrix}}_{P_{j+1,j}} \begin{pmatrix} A_{j+1} \\ B_{j+1} \end{pmatrix} \end{aligned} \quad (\text{B.48})$$

and the interface matrix  $J_{j,j+1}$  becomes modified to

$$J_{j,j+1}^\sigma = \frac{1}{t_{j,j+1}} \begin{pmatrix} 1 + (Z_0\sigma)/(n_j + n_{j+1}) & r_{j,j+1} + (Z_0\sigma)/(n_j + n_{j+1}) \\ r_{j,j+1} - (Z_0\sigma)/(n_j + n_{j+1}) & 1 - (Z_0\sigma)/(n_j + n_{j+1}) \end{pmatrix} \quad (\text{B.49})$$

where

$$t_{j,j+1} \equiv \frac{2q_j}{q_j + q_{j+1}}, \quad r_{j,j+1} \equiv \frac{q_j - q_{j+1}}{q_j + q_{j+1}} \quad (\text{B.50})$$

as usual,  $Z_0$  is the impedance of free space, and  $n_j = \eta_j + i\kappa_j$  is the refractive index in the  $j$ th layer. The procedure for calculating reflection and transmittance of a one-dimensional stack is then the same as above, except replacing  $J_{j,j+1}$  with  $J_{j,j+1}^\sigma$  whenever there is sheet conductor at the  $j$ th interface.

### Absorption within a Layer

To examine the optical losses and therefore optoelectronic losses in a given system, one would like to decompose the fraction of absorption going into various layers in a given stack. To do so, recall that the time-averaged power density absorbed by a lossy non-magnetic medium is given by

$$\langle Q \rangle = \frac{1}{2}\omega\epsilon''|\mathbf{E}(z)|^2 \quad (\text{B.51})$$

where the factor of 1/2 comes from time averaging the power in a harmonic and we have explicitly assumed one-dimensionality, so  $\mathbf{E}$  is only a function of  $z$ . The incident power flux is given by the usual equation

$$I = \frac{1}{2}c\eta_0\epsilon_0|\mathbf{E}_0|^2 \quad (\text{B.52})$$

so that the fraction of absorption going into an individual layer is given by

$$\text{Abs}_j = \frac{\int_{z_{j-1}}^{z_j} \langle Q \rangle dz}{I} = \frac{\eta_j\alpha_j}{\eta_0} \int_{z_{j-1}}^{z_j} |A_j|^2 e^{-\alpha_j z} + |B_j|^2 e^{+\alpha_j z} + 2 \text{Re} \left\{ A_j B_j^* e^{i\frac{4\pi\eta_j}{\lambda} z} \right\} dz \quad (\text{B.53})$$

where  $\eta_j$  is the real part of the refractive index in the  $j$ th layer and  $\alpha_j \equiv 4\pi\kappa_j/\lambda$  is the absorption coefficient of the  $j$ th material. Here, the field amplitudes  $A_j$  and  $B_j$  are the normalized field amplitudes, which can be calculated explicitly by taking

$$\begin{pmatrix} A_0 \\ B_0 \end{pmatrix} = \begin{pmatrix} 1 \\ r \end{pmatrix} \quad (\text{B.54})$$

and calculating the  $n$ th amplitudes by using

$$\begin{pmatrix} A_n \\ B_n \end{pmatrix} = J_{n-1} J_{n-2} \cdots J_0 \begin{pmatrix} 1 \\ r \end{pmatrix} \quad (\text{B.55})$$

Note that  $r$  is explicitly found by using the full transfer matrix. To summarize, one can calculate the reflection amplitude  $r$  by calculating  $J_{\text{total}}$ . After finding this value, the same set of transfer matrices  $J_i$  can be used to find the field amplitudes in the  $i$ th material. Explicitly evaluating the expression in (B.53) gives the fraction of absorption in the  $i$ th layer.

Similarly, for calculating the absorption going into a sheet conductor (e.g. a monolayer of graphene), we use the power flux dissipated by a conductor  $\int \text{Re}(\mathbf{E}^* \cdot \mathbf{J}) dz$  and using the form for the current density in an infinitesimally thin material ( $\mathbf{J} = \frac{1}{2}\sigma\mathbf{E}\delta(z - z_i)$ ), we have

$$\begin{aligned} \text{Abs}_\sigma &= \frac{\int \text{Re}(\mathbf{E}^* \cdot \sigma\mathbf{E}\delta(z - z_i)) dz}{I} \\ &= \frac{\text{Re}(\sigma)}{c\eta_0\epsilon_0} \left[ |A_i|^2 e^{-\alpha_i z_i} + |B_i|^2 e^{+\alpha_i z_i} + 2 \text{Re} \left\{ A_i B_i^* e^{i \frac{4\pi\eta_i}{\lambda} z_i} \right\} \right] \end{aligned} \quad (\text{B.56})$$

where note that, again, we can use the electric field of the  $i$ th or  $i + 1$ th material for which the sheet conductor is sandwiched between, as the electric field is continuous across the boundary and therefore the values are equivalent.

### B.4 Lorentz Oscillator Model

Let's consider a damped harmonic oscillator as a canonical example for the motion of a bound electron-hole pair in a semiconductor (i.e., an exciton). The equation of motion for this system is given from Newton's equations as

$$m\ddot{x} + 2m\gamma\dot{x} + m\omega_0^2x = e\mathcal{E} \quad (\text{B.57})$$

where  $\dot{x}$  is the first time derivative of the position  $x$ ,  $\omega_0$  is the characteristic frequency of oscillation, and  $\gamma$  describes the damping of the oscillation in terms of Ohmic losses. We'll see the factor of 2 here as simplifying our definitions later on.  $\mathcal{E}$  is the electric field driving our electron-hole pair. Often we are dealing with harmonic signals, i.e.,

$$\mathcal{E}(t) = \mathcal{E}(\omega) \exp(-i\omega t) \quad (\text{B.58})$$

and we can take as an ansatz that the motion also follows the same harmonic motion

$$x(t) = x(\omega) \exp(-i\omega t) \quad (\text{B.59})$$

so that the above equation of motion becomes

$$-m\omega^2x(\omega) + 2m\gamma(-i\omega x(\omega)) + m\omega_0^2x(\omega) = e\mathcal{E}(\omega) \quad (\text{B.60})$$

where we have divided out the time dependence,  $\exp(-i\omega t)$ . Solving for  $x(\omega)/\mathcal{E}(\omega)$  yields

$$\frac{x(\omega)}{\mathcal{E}(\omega)} = \frac{-e}{m(\omega^2 - \omega_0^2 + i2\gamma\omega)} \quad (\text{B.61})$$

and if we recall the linear polarization response is given as

$$P = \epsilon_0\chi\mathcal{E} \quad (\text{B.62})$$

with the polarization being the average dipole moment per unit volume, i.e.  $P = \mu n = exn$ , where  $\mu$  defines the average dipole moment per unit volume,  $n$  is the density of electrons, and  $x$  is the displacement of the electrons. Clearly, we can solve for  $\chi$  as

$$\chi = \frac{P}{\epsilon_0\mathcal{E}} = \frac{ne}{\epsilon_0}\frac{x}{\mathcal{E}} = -\frac{ne^2}{m\epsilon_0}\frac{1}{\omega^2 - \omega_0^2 + i2\gamma\omega} \quad (\text{B.63})$$

Let us define  $\omega_{osc}^2 \equiv ne^2/(m\epsilon_0)$  as being some measure of the natural strength of  $\chi(\omega)$ , which has units of frequency. Thus, we have

$$\chi(\omega) = \frac{\omega_{osc}^2}{\omega_0^2 - \omega^2 - i2\gamma\omega} \quad (\text{B.64})$$

which is the Lorentzian oscillator model (occasionally, oscillator strength is written as the parameter  $f_{osc} = \omega_{osc}^2$ ,  $2\gamma \rightarrow \gamma$ , and  $\omega_0$  is the characteristic oscillator frequency. It is important to note that this model obeys Kramer-Kronig consistency, i.e., obeys causality, which comes from the physical nature of the model we are solving.

Note also that we can rewrite the denominator by expanding as

$$\omega^2 - \omega_0^2 + i2\gamma\omega = \omega^2 - \omega_0^2 + i2\gamma\omega + \gamma^2 - \gamma^2 = (\omega + i\gamma)^2 - (\omega_0^2 - \gamma^2) \quad (\text{B.65})$$

which, if we define a new frequency  $\omega'_0 = \omega_0^2 - \gamma^2$ , then the expression is of the form  $a^2 - b^2$ , where  $a = \omega + i\gamma$  and  $b = \omega'_0$ . Recall furthermore we can perform a partial fraction decomposition,

$$\frac{1}{a^2 - b^2} = \frac{1}{2b} \left( \frac{1}{a - b} - \frac{1}{a + b} \right) \quad (\text{B.66})$$

which allows us to rewrite our expression for  $\chi$  finally as

$$\chi(\omega) = -\frac{\omega_{osc}^2}{2\omega'_0} \left( \frac{1}{\omega - \omega'_0 + i\gamma} - \frac{1}{\omega + \omega'_0 + i\gamma} \right) \quad (\text{B.67})$$

which is optical susceptibility of a damped harmonic oscillator in separated partial fractions. In order to further simplify this expression, we will consider the fairly realistic scenario where  $\omega_0 \gg \gamma$  and that we are mostly interested in the contribution from the resonant contribution, i.e.,  $\omega \sim \omega_0$ . In this case, the susceptibility simplifies as

$$\chi(\omega) = -\frac{\omega_{osc}^2}{2\omega_0} \frac{1}{\omega - \omega_0 + i\gamma} \equiv \chi_R(\omega) + i\chi_I(\omega) \quad (\text{B.68})$$

which is the equation of a Lorentzian. Let us look more specifically at the real and imaginary parts, given as

$$\chi_R(\omega) = -\frac{\omega_{osc}^2}{2\omega_0} \frac{\omega - \omega_0}{(\omega - \omega_0)^2 + \gamma^2}, \quad \chi_I(\omega) = \frac{\omega_{osc}^2}{2\omega_0} \frac{\gamma}{(\omega - \omega_0)^2 + \gamma^2} \quad (\text{B.69})$$

We are now interested in looking at the susceptibility of an 2D exciton. We shall assume that it can be well modeled as a Lorentzian oscillator, giving a similar form to the one above. Here, however, we shall use the fact that  $\omega_{osc}^2/2 \rightarrow c\gamma_r/(d)$ , where  $\gamma_r$  describes the radiative rate of the exciton decay, which is a measure of its oscillator strength,  $c$  is the speed of light, and  $d$  is the thickness of the material. Furthermore, we shall take  $\gamma \rightarrow \gamma_{nr}/2$  as the damping coefficient, to finally yield

$$\chi(\omega) = -\frac{c}{\omega_0 d} \frac{\gamma_r}{\omega - \omega_0 + i\gamma_{nr}/2} \quad (\text{B.70})$$

which is the susceptibility of an excitonic material, parametrized as a Lorentzian<sup>1</sup>. Note here that  $\omega_0$  here refers to the exciton energy. Furthermore, we have derived an expression where

$$\epsilon_{complex} = \epsilon_r + \frac{i\sigma}{\epsilon_0\omega} \quad (B.71)$$

where for a 2D excitonic material, we have  $\sigma = \sigma_{2D}/d$  and assuming a single resonance in the entire dielectric spectrum, we have  $\epsilon_r = \epsilon_\infty \rightarrow 1$ . Thus,

$$\sigma_{2D}(\omega) = -i\epsilon_0\omega d\chi(\omega) \quad (B.72)$$

where, defining  $Z_0 = 1/(c\epsilon_0) = c\mu_0 = \sqrt{\mu_0/\epsilon_0} = 4\alpha/G_0$ , where  $\alpha = e^2Z_0/(2h)$  is the fine structure constant and  $G_0 = 2e^2/h$  is the conductance quantum.  $Z_0$  is the impedance of free space. Thus, we finally have

$$\sigma_{2D}(\omega) = \frac{1}{Z_0} \frac{\omega}{\omega_0} \frac{i\gamma_r}{\omega - \omega_0 + i\gamma_{nr}/2} \quad (B.73)$$

On resonance, note that

$$\mathcal{R}[\sigma_{2D}(\omega)] = \frac{2}{Z_0} \frac{\gamma_r}{\gamma_{nr}}, \quad \mathcal{I}[\sigma_{2D}(\omega)] = 0 \quad (B.74)$$

### B.5 Reflection, Transmission, and Absorption of a 2D exciton

Let us consider a 2D excitonic system that is parametrized as a sheet conductor with an optical conductivity given as

$$\sigma_{2D}(\omega) = \frac{1}{Z_0} \frac{\omega}{\omega_0} \frac{i\gamma_r}{\omega - \omega_0 + i\gamma_{nr}/2} \quad (B.75)$$

notice that this sheet conductivity expression describes the optical response of the exciton, and has terms that are directly dependent on  $\gamma_r$  and  $\gamma_{nr}$ . Thus, in terms of the optical response of the 2D exciton, we would certainly expect it to depend on  $\gamma_r$  and  $\gamma_{nr}$ . We shall find that for the absorbance of a 2D exciton, optimizing the relative ratio of the radiative and non-radiative decay rate can be used to maximize the absorption in a given geometry.

### Suspended 2D Exciton

We are now interested in analyzing what is the reflection, transmission, and absorption of the 2D exciton suspended in vacuum. In an earlier section we derived the

---

<sup>1</sup>A much more thorough derivation is shown in [24, 173] for the form of the above expression. Here, we simply motivate the form of the expression by showing the Lorentzian oscillator model.

scattering and transfer matrices when we have a sheet conductor between interface  $j$  and  $j + 1$ . The interface matrix is given as

$$J_{j,j+1}^\sigma = \frac{1}{t_{j,j+1}} \begin{pmatrix} 1 + (Z_0\sigma)/(n_j + n_{j+1}) & r_{j,j+1} + (Z_0\sigma)/(n_j + n_{j+1}) \\ r_{j,j+1} - (Z_0\sigma)/(n_j + n_{j+1}) & 1 - (Z_0\sigma)/(n_j + n_{j+1}) \end{pmatrix} \quad (\text{B.76})$$

where  $r_{j,j+1}$  and  $t_{j,j+1}$  are the Fresnel coefficients for the interface. Since we are considering a sheet conductor suspended in air, we have that  $n_1 = n_2 = 1$  and  $S = J_{1,2}$ , so that  $r_{1,2} = 0$  and  $t_{1,2} = 1$ . This drastically simplifies our expressions, and inserting in the 2D sheet conductivity from above, we have for the scattering matrix:

$$S_{2D\text{ Exciton}} = \begin{pmatrix} 1 + Z_0\sigma_{2D}/2 & Z_0\sigma_{2D}/2 \\ -Z_0\sigma_{2D}/2 & 1 - Z_0\sigma_{2D}/2 \end{pmatrix} \quad (\text{B.77})$$

from which we can readily read off the reflectance and transmittance as

$$R = |r|^2 = \left| \frac{S_{21}}{S_{11}} \right|^2 = \left| -\frac{Z_0\sigma_{2D}}{2 + Z_0\sigma_{2D}} \right|^2, \quad T = |t|^2 = \left| \frac{1}{S_{11}} \right|^2 = \left| \frac{2}{2 + Z_0\sigma_{2D}} \right|^2 \quad (\text{B.78})$$

Note that we are interested in how these expressions look as  $\omega \rightarrow \omega_0$ , i.e. we are operating near resonance. The sheet conductivity then approaches  $\sigma_{2D} \rightarrow 2\gamma_r/(Z_0\gamma_{nr})$ , resulting in the reflection and transmission coefficients:

$$R(\omega_0) = \frac{\gamma_r^2}{(\gamma_{nr} + \gamma_r)^2}, \quad T(\omega_0) = \frac{\gamma_{nr}^2}{(\gamma_{nr} + \gamma_r)^2} \quad (\text{B.79})$$

as well as the absorbance

$$A(\omega_0) = 1 - T(\omega_0) - R(\omega_0) = \frac{2\gamma_r\gamma_{nr}}{(\gamma_{nr} + \gamma_r)^2} \quad (\text{B.80})$$

Examining this expression for absorbance, we examine what occurs for a fixed  $\gamma_r$ . As  $\gamma_{nr} \rightarrow 0$ , the absorbance goes to 0. In the other limit, as  $\gamma_{nr} \rightarrow \infty$ , we also have absorbance going to 0. Therefore, if a value of  $\gamma_{nr}$  maximizes the absorption, it must be some value in between. A simple derivative test shows that this maximum occurs when  $\gamma_r = \gamma_{nr}$ , yielding an absorbance of 50%. In some ways this maximum absorption value is intuitively obvious: a suspended exciton is a symmetric two port system where only one of the ports is utilized. Thus, illumination from one side of this two port system will only ever reach 50% absorption at its maximum [150].

The absorbance spectrum of this free-standing system can be calculated explicitly. Consider the scenario where  $\omega \approx \omega_0 \gg \gamma_r, \gamma_{nr}$ . In this case, the sheet conductivity is given by

$$\sigma_{2D}(\omega) = \frac{1}{Z_0} \frac{i\gamma_r}{\omega - \omega_0 + i\gamma_{nr}/2} \quad (\text{B.81})$$

and the corresponding reflectance given as

$$r = -\frac{i\gamma_r}{2(\omega - \omega_0 + i\gamma_{nr}/2) + i\gamma_r} \implies R = \frac{\gamma_r^2}{4(\omega - \omega_0)^2 + (\gamma_r + \gamma_{nr})^2} \quad (\text{B.82})$$

with transmittance given by

$$t = \frac{2(\omega - \omega_0 + i\gamma_{nr}/2)}{2(\omega - \omega_0 + i\gamma_{nr}/2) + i\gamma_r} \implies T = \frac{4(\omega - \omega_0)^2 + \gamma_{nr}^2}{4(\omega - \omega_0)^2 + (\gamma_r + \gamma_{nr})^2} \quad (\text{B.83})$$

so that the absorbance is given as

$$A = \frac{2\gamma_r\gamma_{nr}}{4(\omega - \omega_0)^2 + (\gamma_r + \gamma_{nr})^2} \quad (\text{B.84})$$

## 2D Exciton with a single mirror

It is clear that from the above analysis, the simplest method of reaching near-unity absorbance is to remove the additional port for which no light is being coupled through. This can be done with a mirror. Consider now the situation where we have an ideal 2D exciton with a single mirror a certain distance  $d$  away from the exciton. This mirror will be parametrized by an interface reflection  $r_{23}$  and transmission amplitude  $t_{23}$ . The analysis continues similar to the above case, except now we have a more complicated scattering matrix in this air/exciton/air/mirror system:

$$S = J_{1,2}^\sigma L_2 J_{2,3} \quad (\text{B.85})$$

where

$$\begin{aligned} J_{1,2}^\sigma &= \begin{pmatrix} 1 + Z_0\sigma/2 & Z_0\sigma/2 \\ -Z_0\sigma/2 & 1 - Z_0\sigma/2 \end{pmatrix} \\ L_2 &= \begin{pmatrix} \exp(-iqd) & 0 \\ 0 & \exp(iqd) \end{pmatrix} \\ J_{2,3} &= \frac{1}{t_{23}} \begin{pmatrix} 1 & r_{23} \\ r_{23} & 1 \end{pmatrix} \end{aligned} \quad (\text{B.86})$$

where we have implicitly taken  $n_1 = n_2 = 1$ , so that  $r_{12} = 0$  and  $t_{12} = 1$ . We have not specified  $r_{23}$  or  $t_{23}$  yet, but we will soon.  $q = 2\pi/\lambda$  and  $d$  is the spacing from the exciton and the back mirror. Multiplying the matrices together and examining the reflection amplitude gives us the expression:

$$r = \frac{-\frac{Z_0\sigma}{2} [r_{23} \exp(2iqd) + 1] + r_{23} \exp(2iqd)}{\frac{Z_0\sigma}{2} [r_{23} \exp(2iqd) + 1] + 1} \quad (\text{B.87})$$

Note that if we now consider a perfect mirror on the back, we would expect  $r_{23} = -1$ . This is because a perfect mirror would cause a null in the electric field at the surface of the mirror, and the reflected wave would be opposite in sign. Moreover, if the exciton was placed exactly at  $d = \lambda/4$ , our reflectivity would be modified to:

$$r = \frac{1 - Z_0\sigma}{1 + Z_0\sigma} \quad (\text{B.88})$$

where the absorbance,  $A = 1 - |r|^2$  (note that  $T = 0$  since a perfect metal forces  $t_{23} = 0$ ) is therefore maximized when  $Z_0\sigma = 1$ . This occurs for example, when  $\omega = \omega_0$  and therefore  $\sigma(\omega_0)Z_0 = 2\gamma_r/\gamma_{nr}$ . Thus, perfect absorption in this case requires  $2\gamma_r = \gamma_{nr}$ . Notice for a fixed  $\gamma_r$ , the mirror has now reduced the required  $\gamma_{nr}$  to achieve this critical coupling by now a factor of two! Moreover, the absorbance can now reach a value of 100%, and this is from removing the superfluous port with the back mirror.

## 2D Exciton in an arbitrary photonic structure

We consider now a slightly different problem of a 2D excitonic absorber in an arbitrary photonic environment. We know from Maxwell's equations that the absorbance within the layer is still given by

$$A_{2D\ Exciton} = \frac{\text{Re}(\sigma)}{c\eta_0\epsilon_0} \frac{|E(x_0, y_0, z_0)|^2}{|E_0|^2} \quad (\text{B.89})$$

where, considering the incident medium to be vacuum or air,  $\eta_0 \rightarrow 1$  and  $c\epsilon_0 = 1/Z_0$  is the impedance of free space. Therefore,

$$A_{2D\ Exciton} = Z_0 \text{Re}(\sigma) \frac{|E(x_0, y_0, z_0)|^2}{|E_0|^2} = \frac{\omega}{2\omega_0} \frac{\gamma_r\gamma_{nr}}{(\omega - \omega_0)^2 + (\gamma_{nr}/2)^2} \frac{|E(x_0, y_0, z_0)|^2}{|E_0|^2} \quad (\text{B.90})$$

Considering now the situation where  $\omega \rightarrow \omega_0$ , i.e., we operate at the excitonic resonance, we have:

$$A(\omega_0) = \frac{2\gamma_r}{\gamma_{nr}} \frac{|E(\omega_0, x_0, y_0, z_0)|^2}{|E_0|^2} \quad (\text{B.91})$$

We now make the ansatz that we can engineer the electric field intensities to be sufficiently high such that the absorption reaches its maximum value, i.e.,  $A(\omega_0) = A_0$  (in many cases,  $A_0$  can approach 1). In this case, this optimum is therefore reached when

$$\gamma_{nr} = 2 \frac{|E(\omega_0, x_0, y_0, z_0)|^2}{|E_0|^2} \gamma_r \quad (\text{B.92})$$

where the electric field intensity enhancement is proportional to the LDOS and therefore the Purcell factor. Thus, this physics is akin to one where we increase the radiative rate of emitters by placing them in a photonic structure. Here, it is clear that a similar enhancement in LDOS would also “effectively increase” the radiative rate, although there are slightly different multiplicative factors that differentiate the two factors. Nonetheless, we can define  $\gamma_{nr} = F_{p,abs}\gamma_r$ , where  $F_{p,abs}$  is a constant that determines the relative  $\gamma_{nr}$  and  $\gamma_r$  to achieve perfect absorption. Notice that the  $\gamma_r$  defined so far is that of an exciton suspended in vacuum. Thus, it is possible to interpret a new radiative rate  $\gamma'_r = F_{p,abs}\gamma_r$  as the radiative rate of the exciton within a photonic medium that is *modified* compared to its native counterpart.

## Appendix C

## THERMODYNAMICS CONSIDERATIONS OF PHOTOVOLTAIC SYSTEMS

### C.1 Derivation of Blackbody Radiation

The well-known and universal blackbody radiation expression is given by the expression

$$S_{BB}(E)dE = \frac{2\pi}{h^3c^2} \frac{E^2}{\exp(E/kT) - 1} dE \quad (\text{C.1})$$

where  $S_{BB}(E)dE$  describes the spectral flux of photons emitted by a blackbody in a given spectral window  $dE$ . Let us derive this expression from first principles. First, let us consider the occupation factor of a photon, given by

$$f_{BE}(E) = \frac{1}{\exp(E/kT) - 1} \quad (\text{C.2})$$

This expression says that if a photon has some energy  $E$ , the probability of it being occupied is given by  $f_{BE}(E)$ . Interestingly, this probability appears to tend towards infinity at low energies, which represents the fact that when many particles interact with one another, they prefer to occupy the lowest energy available state. Moreover, bosons are particles with symmetric wavefunctions, i.e., their wavefunctions can be arbitrarily exchanged with one another with no penalty. This allows them to occupy the same states as one another.

To understand where this factor comes from, consider we have some small system  $A$  nearby some thermal reservoir  $A'$ , where  $A \ll A'$ . We are now interested in understanding the probability  $P_r$  of finding the system in a particular microstate  $r$  of energy  $E_r$ . Assuming the system  $A$  interacts weakly with the thermal reservoir  $A'$ , it is possible to consider their energies as separate and additive. Therefore, by conservation of energy, we have:

$$E_r + E' = E_0 \quad (\text{C.3})$$

where  $E_0$  is some fixed constant. Thus, if  $A$  has some energy  $E_r$ , it must be the case that the reservoir  $A'$  has energy  $E_0 - E_r$ . Therefore, if  $A$  is in *one* definite microstate  $r$ , then the total number of possible states of the combined system is  $\Omega'(E' = E_0 - E_r)$ . Here,  $\Omega'$  is a function for system  $A'$  that describes the number of

states are available for a given energy  $E'$ . According to the fundamental statistical postulate, the probability of occurrence for system  $A$  in state  $r$  is proportional to the total number of possible configurations where  $A$  can be in state  $r$ , which is given by

$$P_r = C' \Omega'(E_0 - E_r) \quad (\text{C.4})$$

here,  $C'$  is just a proportional constant that can be calculated by normalizing  $P_r$ , i.e.  $\sum_r P_r = 1$ . Let us now use the assumption that  $A$  is much smaller than  $A'$ . Therefore, the energies of a particular microstate of  $A$ , i.e.  $r$ , would have energies  $E_r \ll E_0$ . It is therefore possible to expand the function  $\ln(\Omega')$ , which varies slowly as a function of  $E'$ . That is,

$$\ln(\Omega'(E_0 - E_r)) \approx \ln(\Omega'(E_0)) - \frac{\partial \ln(\Omega')}{\partial E'} \bigg|_{E'=E_0} E_r \quad (\text{C.5})$$

Note that

$$\frac{\partial \ln(\Omega')}{\partial E'} \bigg|_{E'=E_0} = \beta \quad (\text{C.6})$$

where  $\beta$  is a constant independent of the system energy  $E_r$ . This constant turns out to be exactly the inverse of the thermal energy. It is straightforward to see this by considering the definition of entropy  $S$ , given by

$$S = k \ln(\Omega) \quad (\text{C.7})$$

where  $\Omega$  is the number of microstates and  $k$  is the Boltzmann constant. Recall the thermodynamic definition of temperature is given by

$$\frac{1}{T} = \frac{\partial S}{\partial E} \quad (\text{C.8})$$

Thus, it follows that

$$\frac{\partial \ln(\Omega')}{\partial E'} \bigg|_{E'=E_0} = \beta = \frac{1}{kT} \quad (\text{C.9})$$

Inserting this into (C.5) and solving for  $\Omega'$ , we have

$$\Omega'(E_0 - E_r) = \Omega'(E_0) \exp(-\beta E_r) \quad (\text{C.10})$$

where  $\Omega'(E_0)$  is a constant independent of the microstate  $r$ . Thus,

$$P_r = C \exp(-\beta E_r) \quad (\text{C.11})$$

where  $C$  is again a normalization constant given by  $C = 1/(\sum_r \exp(-\beta E_r))$ . This derivation is quite general and applies to all systems that are small compared to a

thermal reservoir  $A'$ . Knowing this fundamental probability relation with this exponential dependence, it is possible to calculate many macroscopic thermodynamic quantities of a given system. For example, the average energy of a system  $\bar{E}$  would be given as

$$\bar{E} = \frac{\sum_r E_r \exp(-\beta E_r)}{\sum_r \exp(-\beta E_r)} \quad (\text{C.12})$$

where it is useful to define a function called the partition function

$$Z = \sum_r \exp(-\beta E_r) \quad (\text{C.13})$$

because thermodynamic quantities like the average energy can be calculated from this partition function as

$$\bar{E} = -\frac{1}{Z} \frac{\partial Z}{\partial \beta} = -\frac{\partial \ln(Z)}{\partial \beta} \quad (\text{C.14})$$

We are now interested in calculating the occupation factor for a photon. To do so, let us assume we have a gas of photons that can be treated as identical particles in equilibrium at the temperature  $T$ . We shall also assume they are weakly interacting, so that the if each energetic photon state  $\epsilon_r$  is occupied by  $n_r$  number of photons, then the total energy for a given configuration  $R$  is given as

$$E_R = \sum_r n_r \epsilon_r \quad (\text{C.15})$$

Therefore, suppose we are interested in the average number of photons  $n_s$  that occupy some energetic state  $\epsilon_s$ . This number is given by

$$\bar{n}_s = \frac{\sum_R n_s P_R}{\sum_R P_R} \quad (\text{C.16})$$

where  $P_R = \exp(-\beta E_R)$  describes the probability of the entire system of gas photons to be in some specific state  $R$ . To perform this calculation, we notice that we can separate the terms out in the exponential, i.e.,

$$\bar{n}_s = \frac{[\sum_{n_s} n_s \exp(-\beta n_s \epsilon_s)] [\sum_{n_1, n_2, \dots} \exp(-\beta(n_1 \epsilon_1 + n_2 \epsilon_2 + \dots))]}{[\sum_{n_s} \exp(-\beta n_s \epsilon_s)] [\sum_{n_1, n_2, \dots} \exp(-\beta(n_1 \epsilon_1 + n_2 \epsilon_2 + \dots))]} \quad (\text{C.17})$$

where the second exponential on the right is a sum over all  $n_r$  except  $n_s$ , which has been factored out. Note that these sums are identical on the top and bottom, because  $n_r$  can assume any non-negative integer value  $n_r = 0, 1, 2, 3$  for each  $r$ . Therefore, we have

$$\bar{n}_s = \frac{\sum_{n_s} n_s \exp(-\beta n_s \epsilon_s)}{\sum_{n_s} \exp(-\beta n_s \epsilon_s)} \quad (\text{C.18})$$

This calculation can be easily done by noting that

$$\bar{n}_s = -\frac{1}{\beta} \frac{\partial}{\partial \epsilon_s} \ln \left( \sum_{n_s} \exp(-\beta n_s \epsilon_s) \right) = -\frac{1}{\beta} \frac{\partial}{\partial \epsilon_s} \ln \left( \frac{1}{1 - \exp(-\beta \epsilon_s)} \right) \quad (\text{C.19})$$

where the sum was computed using the geometric series,  $\sum_n x^n = 1/(1-x)$ , which is true as long as  $x = \exp(-\beta n_s \epsilon_s) < 1$ , i.e., the energies are positive. Since this is true, we finally have for the average photon occupation factor:

$$\bar{n}_s = -\frac{1}{\beta} (1 - \exp(-\beta \epsilon_s)) \left[ -\frac{\beta \exp(-\beta \epsilon_s)}{(1 - \exp(-\beta \epsilon_s))^2} \right] = \frac{\exp(-\beta \epsilon_s)}{1 - \exp(-\beta \epsilon_s)} \quad (\text{C.20})$$

therefore, finally, we have for the occupation factor of a given energy state  $\epsilon_s$ :

$$\bar{n}_s = \frac{1}{\exp(\beta \epsilon_s) - 1} \quad (\text{C.21})$$

the subscript  $s$  can be dropped since our analysis applies to any energetic state  $\epsilon_s$ . Thus, the occupation factor is

$$f_{BE}(E) = \frac{1}{\exp(E/kT) - 1} \quad (\text{C.22})$$

where  $f_{BE}(E)$  is a renaming of the average number of photons  $\bar{n}_s$ , i.e., the Bose-Einstein occupation factor, and describes the average number of bosons (in this case, photons), that occupy a state with energy  $E$ .

To finally derive the blackbody distribution, we realize that if we have a perfectly black absorber/emitter, the photons should be able to couple to every available mode of free space  $\rho_v(E)$ , with an occupation factor given by  $f_{BE}(E)$ . The photons have a velocity given by the speed of light  $c$ , and the hypothetical spectrum can be considered in the limit of having perfect mirrors that surround the blackbody emitter, so that thermal equilibrium is achieved. If we were able to peak through the perfect mirrors with an infinitesimally small hole, the blackbody radiation through that surface would be given as

$$S_{BB}(E)dE = \frac{1}{4} c \rho_v(E) f_{BE}(E) dE \quad (\text{C.23})$$

where  $\rho_v(E)dE$  is the density of photonic states in vacuum for an energy bandwidth  $dE$  when surrounded by these perfect mirrors, and the factor of 4 comes from examining the relative amount of volumetric flux assuming a Lambertian surface, i.e.,

$$\frac{\int_0^{\pi/2} \cos(\theta) \sin(\theta) d\theta \int_0^{2\pi} d\phi}{\int_0^{\pi} \sin(\theta) d\theta \int_0^{2\pi} d\phi} = \frac{1}{4} \quad (\text{C.24})$$

This expression is analogous to the current density of electrons, i.e.,  $J = qnv$ , if we take the density of photons  $n_\gamma = \int \rho_v(E) f_{BE}(E) dE$ . In the current density expression,  $q$  is the fundamental unit of charge,  $n$  is the density of electrons, and  $v$  is the velocity of charge carriers. To calculate this density of photonic states, assume we are in an isotropic environment (specifically, vacuum) with perfect mirrors that surround a 3D box of length  $L$  and therefore a volume of  $V = L^3$ . The size of the box will turn out to not be important when we normalize and take  $L$  to be large. A parallelepiped analysis will not change the results, since the volumes will be normalized away anyway. The perfect mirrors, as mentioned before, are necessary for the blackbody emitter to reach thermal equilibrium, otherwise, electromagnetic radiation would actually cool the emitter. In this case, waves will propagate to the edges of the box and can be approximated as plane waves, which has wavevectors of

$$k_{i,n} = \frac{n\pi}{L} \quad (C.25)$$

where  $n$  is an integer, as enforced by the boundary conditions of the system, and  $i = x, y, z$ . Therefore, the spacing in  $k$ -space for this isotropic system would be given as

$$\Delta k_i = \frac{\pi}{L} \quad (C.26)$$

Now consider the situation where we are interested in the number of possible states with a given  $k = \sqrt{k_x^2 + k_y^2 + k_z^2}$ , where  $k$  is the magnitude of the wavevector. What is the density of available states in  $k$ -space for a given  $k$ ? What is  $\rho_v(k)dk$ ? To answer this question, let us first try to calculate the *total* number of states  $k' < k$ . This is given as

$$N(k' < k) = \frac{\text{Volume with radius } k}{\text{Volumetric spacing for each } k \text{ point}} = 2 \times \frac{4}{3}\pi k^3 \times \frac{L^3}{(2\pi)^3} = \frac{1}{3\pi^2} k^3 V \quad (C.27)$$

This total number of states has a factor of 2 because each  $k$  point can actually have two states, given by the two polarizations of light. Thus, we can calculate the *density* of states  $\rho_v(k)$  (states per unit volume per unit  $k$ ) can be simply calculated as

$$\rho_v(k) = \frac{1}{V} \frac{dN}{dk} = \frac{k^2}{\pi^2} \quad (C.28)$$

Finally, to convert this expression to a density of electronic states, i.e.  $\rho_v(E)$ , we simply have to use the dispersion relation of the photon in this environment, i.e., as

$$E = \hbar\omega = \hbar ck \quad (C.29)$$

Thus,

$$\rho_v(k)dk = \rho_v(E)dE = \frac{1}{\pi^2} \frac{E^2}{(\hbar c)^3} dE \quad (C.30)$$

Using finally the fact that  $\hbar = h/(2\pi)$ , we have

$$S_{BB}(E)dE = \frac{1}{4}c\rho_v(E)f_{BE}(E)dE = \frac{2\pi}{h^3 c^2} \frac{E^2}{\exp(E/kT) - 1} dE \quad (C.31)$$

This expression is the well-known blackbody radiation, which was derived in the limit of considering only far-field radiation with a uniform density of states (i.e., in vacuum). The derivation of the photon gas also requires that a single temperature  $T$  characterizes the entire system of photons, and that this system is in thermal equilibrium. This characterizes the emission from a *surface*.

Consider there is a probability of emission given by  $e(E)$  and a probability of absorption  $a(E)$  that characterizes the emission and absorption of a photon of energy  $E$  for a given surface. It is clear that under thermal equilibrium, the net flux through the surface must be exactly equal, i.e.,

$$\int [a(E) - e(E)] S_{BB}(E)dE = 0 \quad (C.32)$$

Since it is possible to construe a system with a wavelength selective mirror, this balance must actually occur at each wavelength to achieve thermal equilibrium. Thus, we must have

$$a(E) = e(E) \quad (C.33)$$

## C.2 The Chemical Potential of a Photon

We are now interested in considering the spontaneous emission rate of a semiconductor, which is seemingly a different phenomena compared to thermal radiation. While thermal radiation is known to give broad and dim spectra and is known to be due to the thermal shaking of atoms, the spontaneous emission from a semiconductor is relatively bright, narrow in bandwidth, and is due to electronic interband transitions. What separates the two phenomena and can they be related?

Let us first consider a similar situation to what we considered in a blackbody emitter, where a homogeneous semiconductor is surrounded by a perfectly reflecting wall. The total number of occupied electrons in the conduction band is given by the usual expression

$$n(E) = g(E)f(E) = g_c(E)f_e(E) = g_c(E) \frac{1}{\exp((E - E_{f,n})/kT) + 1} \quad (C.34)$$

where  $g_c(E)$  is the density of electronic states at the conduction band and  $f(E)$  is the Fermi-Dirac occupation factor. A similar expression is true for occupied holes in the valence band, i.e.,

$$p(E) = g(E)(1 - f(E)) = g_v(E)f_h(E) = g_v(E) \frac{1}{\exp(-(E - E_{f,p})/kT) + 1} \quad (C.35)$$

Note that  $E_{f,n}$  and  $E_{f,p}$  are referred to as the electron and hole quasi-Fermi levels. In assigning a single chemical potential and temperature  $T$  to all the electrons/holes, we take into account the rapid chemical equilibrium achieved between carrier-carrier interaction within a given conduction/valence band, as well as the thermal equilibrium between the carriers and the lattice which acts as a thermal reservoir. This analysis is similar to derivation above for the Boltzmann factor  $P_r = \exp(-\beta E_r)$ .

Notice also that generation and recombination results in a pair-wise formation of electrons and holes, and the flux of absorption and emission processes must be balanced in the perfect cavity to achieve thermal equilibrium. The absorption rate per unit volume per photon energy interval  $r_a(E)$  can be written as

$$r_a(\hbar\omega) = n_\gamma(\hbar\omega) \times \int_0^\infty M(E_e, E_h, \hbar\omega) g_c(E_e)(1-f_e(E_e)) g_v(E_h)(1-f_h(E_h)) \delta(\hbar\omega - (E_e - E_h)) dE_e dE_h \quad (C.36)$$

where  $M(E_e, E_h, \hbar\omega)$  is the transition matrix element and describes the relative rate of an electron with energy  $E_e$  and hole with energy  $E_h$  to couple with a photon with energy  $\hbar\omega$ . The density of photons is given as  $n_\gamma(\hbar\omega)$ . The delta function  $\delta(\hbar\omega - (E_e - E_h))$  conserves the energy of the transition, which can be integrated to give the condition  $\hbar\omega = E_e - E_h$ . The expressions  $1 - f_j(E_j)$  describes the fact that absorption of photons requires unoccupied states. Thus, integrating the delta function gives

$$r_a(\hbar\omega) = n_\gamma(\hbar\omega) \int_0^\infty M(E_h, \hbar\omega) g_c(E_h + \hbar\omega) g_v(E_h) (1 - f_e(E_h + \hbar\omega)) (1 - f_h(E_h)) dE_h \quad (C.37)$$

We can drop the subscript  $h$ , since it is just an integration variable. Therefore,

$$r_a(\hbar\omega) = n_\gamma(\hbar\omega) \int_0^\infty M(E, \hbar\omega) g_c(E + \hbar\omega) g_v(E) (1 - f_e(E + \hbar\omega)) (1 - f_h(E)) dE \quad (C.38)$$

We can derive a similar expression for a stimulated emission process, where an electron transitions from an excited state  $E_e$  to a lower energy state  $E_h$ . This process

is *stimulated* by the density of photons  $n_\gamma(\hbar\omega)$ , and is therefore a time-reversal process to absorption. It requires an occupied electron and hole in the conduction and valence band. In other words,

$$r_{st}(\hbar\omega) = n_\gamma(\hbar\omega) \int_0^\infty M(E, \hbar\omega) g_c(E + \hbar\omega) g_v(E) f_e(E + \hbar\omega) f_h(E) dE \quad (\text{C.39})$$

Finally, we have the spontaneous emission rate  $r_{sp}(\hbar\omega)$ , which does not depend on the density of photons in the cavity, but by the density of available photonic states in the semiconductor  $\rho_s(\hbar\omega)$ . It has a similar form to the stimulated emission otherwise:

$$r_{sp}(\hbar\omega) = \rho_s(\hbar\omega) \int_0^\infty M(E, \hbar\omega) g_c(E + \hbar\omega) g_v(E) f_e(E + \hbar\omega) f_h(E) dE \quad (\text{C.40})$$

where we have already derived from above that

$$\rho_v(\hbar\omega) d(\hbar\omega) = \frac{(\hbar\omega)^2}{\pi^2(\hbar c)^3} d(\hbar\omega) \quad (\text{C.41})$$

Note in our derivation that we made use that the speed of light was  $c$ . In a semiconductor with refractive index  $n_r$ , the speed of light would decrease to  $c/n_r$ . Therefore, the density of photonic states in a semiconductor is given by

$$\rho_s(\hbar\omega) d(\hbar\omega) = \frac{n_r^3(\hbar\omega)^2}{\pi^2(\hbar c)^3} d(\hbar\omega) \quad (\text{C.42})$$

We now know that these rates must balance in steady state, so that

$$r_a - r_{st} - r_{sp} = 0 \quad (\text{C.43})$$

It is therefore possible to solve for the photon density within this perfect cavity, given by  $n_\gamma(\hbar\omega)$ . Solving for it gives

$$\begin{aligned} n_\gamma(\hbar\omega) = \rho_s(\hbar\omega) \times \\ \frac{\int_0^\infty M(E, \hbar\omega) g_c(E + \hbar\omega) g_v(E) f_e(E + \hbar\omega) f_h(E) dE}{\int_0^\infty M(E, \hbar\omega) g_c(E + \hbar\omega) g_v(E) f_e(E + \hbar\omega) f_h(E) \left[ \frac{(1 - f_e(E + \hbar\omega))(1 - f_h(E))}{f_e(E + \hbar\omega) f_h(E)} - 1 \right] dE} \end{aligned} \quad (\text{C.44})$$

The term in the brackets can be dramatically simplified if written out, it is given as

$$\left[ \frac{(1 - f_e(E + \hbar\omega))(1 - f_h(E))}{f_e(E + \hbar\omega) f_h(E)} - 1 \right] = \left[ \frac{(1 - f_e(E + \hbar\omega))(1 - f_h(E)) - f_e(E + \hbar\omega) f_h(E)}{f_e(E + \hbar\omega) f_h(E)} \right] \quad (\text{C.45})$$

which can be simplified further as

$$\begin{aligned}
\left[ \frac{(1 - f_e(E + \hbar\omega))(1 - f_h(E)) - f_e(E + \hbar\omega)f_h(E)}{f_e(E + \hbar\omega)f_h(E)} \right] &= \frac{1 - f_e(E + \hbar\omega) - f_h(E)}{f_e(E + \hbar\omega)f_h(E)} \\
&= \frac{1 - f_e(E + \hbar\omega)}{f_e(E + \hbar\omega)f_h(E)} - \frac{1}{f_e(E + \hbar\omega)} \\
&= \frac{1}{f_e(E + \hbar\omega)} \left[ \frac{1 - f_e(E + \hbar\omega)}{f_h(E)} - 1 \right]
\end{aligned} \tag{C.46}$$

where we can further simplify the term within the brackets as

$$\begin{aligned}
\left[ \frac{1 - f_e(E + \hbar\omega)}{f_h(E)} - 1 \right] &= \frac{\exp(-(E - E_{f,p})/kT) + 1}{\exp(-(E + \hbar\omega - E_{f,n})/kT) + 1} - 1 \\
&= \frac{\exp(-(E - E_{f,p})/kT) - \exp(-(E + \hbar\omega - E_{f,n})/kT)}{\exp(-(E + \hbar\omega - E_{f,n})/kT) + 1} \\
&= \frac{\exp((\hbar\omega - E_{f,n} + E_{f,p})/kT) - 1}{1 + \exp((E + \hbar\omega - E_{f,n})/kT)} \\
&= \left[ f_e(E + \hbar\omega) \right] \left[ \exp((\hbar\omega - (E_{f,n} - E_{f,p}))/kT) - 1 \right]
\end{aligned} \tag{C.47}$$

therefore combining the terms and referring to equation (C.45), we have

$$\left[ \frac{(1 - f_e(E + \hbar\omega))(1 - f_h(E))}{f_e(E + \hbar\omega)f_h(E)} - 1 \right] = \left[ \exp((\hbar\omega - \Delta\mu)/kT) - 1 \right] \tag{C.48}$$

where we define  $\Delta\mu = E_{f,n} - E_{f,p}$  as the quasi-Fermi level splitting. Interestingly, this simplified term of (C.45) results in a term that is *independent of E*, which allows equation (C.44) to be dramatically simplified by taking the *E*-independent term outside of the integral:

$$n_\gamma(\hbar\omega) = \frac{\rho_s(\hbar\omega)}{\exp((\hbar\omega - \Delta\mu)/kT) - 1} \tag{C.49}$$

where this term is independent of the properties of the semiconductor, except through the quasi-Fermi level splitting. Therefore, since the electron-hole generation and recombination reach an equilibrium with the population of photons, it is appropriate to define a *chemical potential* for the photons,  $\mu_\gamma = \Delta\mu = E_{f,n} - E_{f,p}$ , so that the density of photons can be written as

$$n_\gamma(\hbar\omega, \mu_\gamma) = \frac{\rho_s(\hbar\omega)}{\exp((\hbar\omega - \mu_\gamma)/kT) - 1} \tag{C.50}$$

This expression is of general validity, since the details of the system, such as the transition matrix elements, drop out in the derivation.

Knowing this density of photons  $n_\gamma$ , it is possible to define an absorption coefficient  $\alpha(\hbar\omega)$  given by

$$r_a - r_{st} = \alpha(\hbar\omega)j_\gamma = \alpha(\hbar\omega)n_\gamma \frac{c}{n_r} \quad (\text{C.51})$$

where  $c/n_r$  is the velocity of light within a semiconductor with index  $n_r$ , which results in a photon flux of  $j_\gamma$ . By examining the earlier definitions for  $r_a$  and  $r_{st}$ , we arrive at

$$\alpha(\hbar\omega) = \frac{n_r}{c} \left[ \int_0^\infty M(E, \hbar\omega) g_c(E + \hbar\omega) g_v(E) [1 - f_e(E + \hbar\omega) - f_h(E)] dE \right] \quad (\text{C.52})$$

Furthermore equation (C.51) relates the absorption coefficient to the spontaneous emission rate because, in equilibrium, we have  $r_a - r_{st} = r_{sp}$ , which we used earlier. Therefore,

$$r_{sp}(\hbar\omega) = \frac{n_r^2}{\pi^2 \hbar^3 c^2} \frac{(\hbar\omega)^2 \alpha(\hbar\omega)}{\exp((\hbar\omega - \mu_\gamma)/kT) - 1} \quad (\text{C.53})$$

Using again the fact that  $\hbar = h/(2\pi)$ , we can rewrite this expression as

$$r_{sp}(\hbar\omega) = \left(4n_r^2\right) \frac{2\pi}{h^3 c^2} \frac{(\hbar\omega)^2 \alpha(\hbar\omega)}{\exp((\hbar\omega - \mu_\gamma)/kT) - 1} \quad (\text{C.54})$$

which is the blackbody spectrum modified by a factor of  $4n_r^2\alpha(\hbar\omega)$  because we are looking at the *internal* volumetric emission rate inside a semiconductor, and the chemical potential of the photon  $\mu_\gamma = E_{f,n} - E_{f,p}$  is used here to describe the non-equilibrium (but steady-state) nature of the process.

### C.3 The Validity of a Thermalized Population as the Major Contribution to Photoluminescence Under Steady State Excitation

There is a general picture in semiconductor optoelectronics that quasi-fermi levels can form given enough carrier thermalization and electron-electron interactions. Let's be a bit more rigorous and see when this is true, and how much of luminescence may occur from non-thermalized carriers. Let's consider a coupled set of equations governed by different rates:

$$\begin{aligned} \frac{\partial n}{\partial t} &= G - \frac{n}{\tau_{ee}} - \frac{n}{\tau_{rad,n}} \\ \frac{\partial n_{ee}}{\partial t} &= \frac{n}{\tau_{ee}} - \frac{n_{ee}}{\tau_{ep}} - \frac{n_{ee}}{\tau_{rad,ee}} \\ \frac{\partial n_{ep}}{\partial t} &= \frac{n_{ee}}{\tau_{ep}} - \frac{n_{ep}}{\tau_{rad,ep}} \end{aligned} \quad (\text{C.55})$$

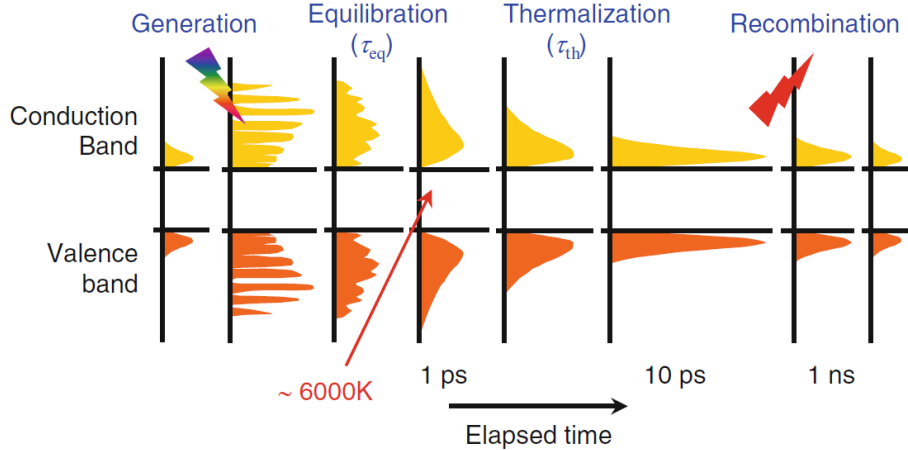


Figure C.1: Schematic depiction of the relative timescales relevant to electron-electron scattering (equilibration), electron-phonon coupling (thermalization), and electron-hole recombination. Adapted from Y. Takeda et al., 2014

where  $n$  corresponds to the electron population that follows the same spectral dependence as the excitation,  $n_{ee}$  is the population of carriers that have undergone electron-electron interactions, i.e. follows a Fermi-Dirac distribution, and  $n_{ep}$  is the population of electrons that have undergone both electron-electron interactions and subsequently thermalized with the lattice through electron-phonon interactions. The coupled equations can be solved algebraically under steady state conditions, where  $\partial_t = 0$ . Thus, the first expression is simply:

$$n = G\tau_{eff,1}, \quad \text{where} \quad \frac{1}{\tau_{eff,1}} = \frac{1}{\tau_{ee}} + \frac{1}{\tau_{rad,n}}. \quad (\text{C.56})$$

This allows solutions to the second expression rather simply, yielding

$$n_{ee} = \frac{G\tau_{eff,1}}{\tau_{ee}}\tau_{eff,2}, \quad \text{where} \quad \frac{1}{\tau_{eff,2}} = \frac{1}{\tau_{ep}} + \frac{1}{\tau_{rad,ee}} \quad (\text{C.57})$$

and finally, the last population can be solved as

$$n_{ep} = \tau_{rad,ep} \frac{G\tau_{eff,1}\tau_{eff,2}}{\tau_{ee}\tau_{ep}} \quad (\text{C.58})$$

Each population can contribute to the average photoluminescence rate with the population density scaled by their respective radiative rates, i.e.

$$r_{sp} = \frac{n}{\tau_{rad,n}} + \frac{n_{ee}}{\tau_{rad,ee}} + \frac{n_{ep}}{\tau_{rad,ep}} \quad (\text{C.59})$$

To understand the fraction of luminescence from the different electron populations, all we have to do is examine the relative rates. To see if the majority of the

luminescence comes from electrons that have gone through both electron-electron and electron-phonon coupling, we can analyze their relative luminescence rates. Comparing for the completely uncoupled population:

$$\frac{r_{sp,ep}}{r_{sp,n}} = \frac{n_{ep}}{n} \frac{\tau_{rad,n}}{\tau_{rad,ep}} = \frac{\tau_{rad,n}}{\tau_{rad,ep}} \frac{\tau_{rad,ep} \tau_{eff,2}}{\tau_{ee} \tau_{ep}} = \frac{\tau_{rad,n} \tau_{eff,2}}{\tau_{ee} \tau_{ep}} \quad (C.60)$$

Note that if  $\tau_{ep} \ll \tau_{rad,ee}$ ,  $\tau_{eff,2} \approx \tau_{ep}$ , and thus the ratio becomes  $\tau_{rad,n}/\tau_{ee}$ . Clearly, if we assume that  $\tau_{ee} \ll \tau_{rad,n}$ ,  $r_{sp,ep}/r_{sp,n} \gg 1$ . Comparing the populations for those that have and have not gone through electron-phonon coupling, we arrive at a somewhat similar expression:

$$\frac{r_{sp,ep}}{r_{sp,ee}} = \frac{n_{ep}}{n_{ee}} \frac{\tau_{rad,ee}}{\tau_{rad,ep}} = \frac{\tau_{rad,ep}}{\tau_{ep}} \frac{\tau_{rad,ee}}{\tau_{rad,ep}} \gg 1 \quad (C.61)$$

where the last equality comes from the fact that we have already assumed that  $\tau_{ep} \ll \tau_{rad,ee}$ . In conclusion, it is clear that the majority of the luminescence comes from carriers that completely thermalized to their respective band-edges. For somewhat realistic values of for example,  $\tau_{rad} \sim ns$  (we have assumed all the radiative lifetimes from the different subpopulations to be the same, for simplicity) and for  $\tau_{ee} \sim fs$  and  $\tau_{ep} \sim ps$ , we have the ratios:

$$\frac{r_{sp,ep}}{r_{sp,n}} \sim 10^6, \quad \frac{r_{sp,ep}}{r_{sp,ee}} \sim 10^3 \quad (C.62)$$

With more realistic numbers, it is clear that the other populations contribute very little to the observed steady state luminescence. However, in some nanostructured and exotic systems, we have  $\tau_{rad} \sim \tau_{ep} \sim ps$ . In this case, non-thermalized ("hot") carriers can play a large role to the luminescence observed, while still obeying Fermi-Dirac statistics.

#### C.4 The Validity of A Single Quasi-Fermi Level to Describe Carriers Occupying Multiple Energy Levels

The analysis above suggests that given sufficient electron-electron coupling and the relative types of electron populations, the majority of the observed photoluminescence should occur from the thermalized carriers in steady state. However, our analysis *a priori* does not suggest that a single quasi Fermi level is sufficient to describe all the electrons in the band. To do so, we develop a three-level system model which has energies  $E_1, E_2, E_3$  and  $n_1, n_2, n_3$  number of electrons occupying each level, respectively. The total number of available states per level will be denoted as  $N_1, N_2, N_3$ . Consider the situation where there are a total of  $n = n_1 + n_2 + n_3$ .

Assuming these are all the states that are involved, we shall make the reasonable assumption that turning on the light does not change the total number of electrons  $n$ , i.e.,

$$\frac{dn}{dt} = 0 \quad (\text{C.63})$$

We shall also assume that photogeneration only couples to one of the states, e.g.  $E_1$ . Thus, the coupled rate equations in this scenario become

$$\begin{aligned} \frac{dn_1}{dt} &= -k_{13}n_1(N_3 - n_3) + k_{31}(N_1 - n_1)n_3 - k_{12}n_1(N_2 - n_2) + k_{21}(N_1 - n_1)n_2 + K(N_1 - n_1)n_3 \\ \frac{dn_2}{dt} &= -k_{23}n_2(N_3 - n_3) + k_{32}(N_2 - n_2)n_3 + k_{12}n_1(N_2 - n_2) - k_{21}(N_1 - n_1)n_2 \\ \frac{dn_3}{dt} &= -\left(\frac{dn_1}{dt} + \frac{dn_2}{dt}\right) \end{aligned} \quad (\text{C.64})$$

note that the expressions are in a bi-linear form, i.e., they depend on *both* the occupation of filled states  $n_i$  transitioning to unoccupied states  $N_j - n_j$  with some rate constant  $k_{ij}$  that describes the relative coupling. These forms are bi-linear due to the fact that we assume they obey Fermi-Dirac statistics, thus, in equilibrium, we have  $n_i = n_i^0$  and that

$$n_i^0 = N_i f_i^0 \quad (\text{C.65})$$

where  $i = 1, 2, 3$  and

$$f_i^0 = \frac{1}{1 + \exp\left(\frac{E_i - E_F}{kT}\right)} \quad (\text{C.66})$$

note that in equilibrium, a single  $E_F$  is sufficient to describe the equilibrium population distribution. We also note that in equilibrium, *all reactions must have zero net rate* i.e. there is no net flow of carriers from one state  $E_i$  to another  $E_j$ . That is, we have

$$k_{ij}n_i^0(N_j - n_j^0) = k_{ji}n_j^0(N_i - n_i^0) \quad (\text{C.67})$$

Thus, there is an intimate relationship between  $k_{ij}$  and  $k_{ji}$ . To see this relationship, we use our above definitions for the equilibrium carrier populations, so that

$$k_{ji} = k_{ij} \left( \frac{f_i^0}{1 - f_i^0} \right) \left( \frac{1 - f_j^0}{f_j^0} \right) \quad (\text{C.68})$$

and since

$$\frac{f_i^0}{1 - f_i^0} = \exp\left(-\frac{E_i - E_F}{kT}\right) \quad (\text{C.69})$$

we have that

$$\left( \frac{f_i^0}{1 - f_i^0} \right) \left( \frac{1 - f_j^0}{f_j^0} \right) = \exp \left( -\frac{E_i - E_j}{kT} \right) \quad (\text{C.70})$$

For compactness, let us define  $A_{ij} \equiv \exp(-(E_i - E_j)/kT)$  so that  $k_{ji} = k_{ij}A_{ij}$ . Let us now consider the possibility that we may be out of equilibrium. We first assume that the carriers continue to have Fermi-Dirac statistics in this situation, where

$$n_i = N_i f_i \quad (\text{C.71})$$

but now each energy level may have its own Fermi level, which we define as a *quasi-Fermi level*. That is,

$$f_i \equiv \frac{1}{1 + \exp \left( \frac{E_i - E_{f_i}}{kT} \right)} \quad (\text{C.72})$$

so that the coupled rate equation can be written as

$$\begin{aligned} \frac{dn_1}{dt} &= -k_{13}N_1N_3 [f_1(1 - f_3) - A_{13}f_3(1 - f_1)] \\ &\quad - k_{12}N_1N_2 [f_1(1 - f_2) - A_{12}f_2(1 - f_1)] \\ &\quad + KN_1N_3f_3(1 - f_1) \\ \frac{dn_2}{dt} &= -k_{23}N_2N_3 [f_2(1 - f_3) - A_{23}f_3(1 - f_2)] \\ &\quad + k_{12}N_1N_2 [f_1(1 - f_2) - A_{12}f_2(1 - f_1)] \\ \frac{dn_3}{dt} &= - \left( \frac{dn_1}{dt} + \frac{dn_2}{dt} \right) \end{aligned} \quad (\text{C.73})$$

and we now consider the situation where *steady state* (i.e. not equilibrium) can occur, where

$$\frac{dn_1}{dt} = \frac{dn_2}{dt} = \frac{dn_3}{dt} = 0 \quad (\text{C.74})$$

Consider now the population of carriers in  $E_2$  in steady state ( $dn_2/dt = 0$ ), where

$$\frac{f_1(1 - f_2) - A_{12}f_2(1 - f_1)}{f_2(1 - f_3) - A_{23}f_3(1 - f_2)} = \frac{k_{23}N_3}{k_{12}N_1} \quad (\text{C.75})$$

We now consider some relative values for the scales of the interactions. First, the denominator of the left hand side is at most 1, since  $f_i(1 - f_j) \leq 1$  and  $A_{23} < 1$  if  $E_2 > E_3$ . Let us now consider the right-hand side where  $k_{12} \gg k_{23}$ , i.e. the coupling between states  $E_1$  and  $E_2$  is much higher than that between  $E_2$  and  $E_3$ . This, for example, would be the scenario in most semiconductors where  $k_{12}$  corresponds to *intraband* interactions whereas  $k_{23}$  would correspond to *interband* interactions. In

this scenario,  $k_{12} \gg k_{23}$  and therefore the right-hand side is much less than 1 if  $N_1 \approx N_3$  (which we shall assume). Thus, the numerator of the left-hand side must be close to vanishing, and if it were to completely vanish, we would have:

$$\left( \frac{f_1}{1 - f_1} \right) = A_{12} \left( \frac{f_2}{1 - f_2} \right) \quad (\text{C.76})$$

Notice that if we insert our definitions for the quasi-Fermi levels, as defined above, we would then have

$$\exp\left(-\frac{E_1 - E_{f_1}}{kT}\right) = \exp\left(-\frac{E_1 - E_2}{kT}\right) \exp\left(-\frac{E_2 - E_{f_2}}{kT}\right) \implies E_{f_1} = E_{f_2} \quad (\text{C.77})$$

This important result says that if the rate of scattering between levels is *much greater* than the transition rate between either level to a third level, then the two levels will have almost the same fractional occupancy, or alternatively, the same quasi-Fermi level. Now, let's see how different the quasi-Fermi levels can be if it were not vanishing:

$$f_1(1 - f_2) - A_{12}f_2(1 - f_1) = \left( \frac{k_{23}N_3}{k_{12}N_1} \right) [f_2(1 - f_3) - A_{23}f_3(1 - f_2)] \quad (\text{C.78})$$

and then dividing by  $(1 - f_1)(1 - f_2)$ , we have

$$\left( \frac{f_1}{1 - f_1} \right) - A_{12} \left( \frac{f_2}{1 - f_2} \right) = \left( \frac{k_{23}N_3}{k_{12}N_1} \right) \left[ \left( \frac{f_2}{1 - f_2} \right) \left( \frac{1 - f_3}{1 - f_1} \right) - A_{23} \left( \frac{f_3}{1 - f_1} \right) \right] \quad (\text{C.79})$$

and further simplifying gives us

$$\frac{1}{A_{12}} \left( \frac{1 - f_2}{f_2} \right) \left( \frac{f_1}{1 - f_1} \right) - 1 = \left( \frac{k_{23}N_3}{k_{12}N_1} \right) \left[ \frac{1}{A_{12}} \left( \frac{1 - f_3}{1 - f_1} \right) - \frac{A_{23}}{A_{12}} \left( \frac{1 - f_2}{f_2} \right) \left( \frac{f_3}{1 - f_1} \right) \right] \quad (\text{C.80})$$

note that the left-hand side simplifies to  $\exp((E_{f_1} - E_{f_2})/kT) - 1$ . Thus,

$$E_{f_1} - E_{f_2} = kT \ln \left( 1 + \left( \frac{k_{23}N_3}{k_{12}N_1} \right) \left[ \frac{1}{A_{12}} \left( \frac{1 - f_3}{1 - f_1} \right) - \frac{A_{23}}{A_{12}} \left( \frac{1 - f_2}{f_2} \right) \left( \frac{f_3}{1 - f_1} \right) \right] \right) \quad (\text{C.81})$$

Using the same assumptions as before, we something of the form  $\ln(1 + x)$  for small  $x$ , thus, if  $x \ll 1$ ,  $E_{f_1} - E_{f_2} \ll kT$ . For other situations where this assumption of  $k_{12}$  and  $k_{23}$  is not true, we can explicitly calculate the difference between the two energies. Note also that  $A_{12}$  also shows up as a common multiplicative factor, as well as occupation factors like  $1 - f_1$ . Thus, it is important to remember that resonant excitation into a specific energy or sufficiently large enough energy separations (e.g. if  $E_1 - E_2 \gtrsim kT$ ), we may also have substantially different quasi-Fermi levels.

## Appendix D

## COMPUTER CODE

Listing D.1: Modified Detailed Balance Code for Band Tails

```

1  function SubGap_ReciprocityDetailedBalance_v8
2  % Detailed balance analysis of band-edge sharpness ,
3  % parametrized by a general band-edge sharpness parameter (gam) in the
4  % absorption
5  % coefficient , with an exponential fall-off raised to some power (theta) ,
6  % with band filling parametrized simply by tanh((E-qV)/(4*kbT))
7  %
8  % Written by Joeson Wong
9  % Last updated on October 17, 2019.
10 %
11 % Written for MATLAB 2018A. Requires Curve Fitting Toolbox and Panel
12 % function
13 % (https://www.mathworks.com/matlabcentral/fileexchange/20003-panel)
14
15 clear all; close all; clc;
16
17 % check if modified absorption table matrix is available
18 if fopen('Gtable.mat') == -1 % filename is not available
19     disp('file named "Gtable.mat" not found. Press any key to begin
20         calculation of Gtable');
21     pause;
22     disp('Calculating Gtable...');

23 % Generate Gvals for table look up, only need to do this once
24 thetalabels = [1, 5/4, 3/2, 2]; % typical thetas of interest , can change
25 % this for other theta
26 xlabel = -5000:0.01:5000;
27 Gvals = zeros(length(thetalabels), length(xlabel));
28 tic;
29 for i = 1:length(thetalabels)
30     for j = 1:length(xlabel)
31         Gvals(i,j) = G(xlabel(j), thetalabels(i));
32     end
33 end
34 toc; % display total time it took to calculate
35
36 figure; % display Gvals , make sure it has enough numerical accuracy (esp.
37 % small values)
38 semilogy(xlabel, Gvals(1,:), xlabel, Gvals(2,:), xlabel, Gvals(3,:),
39 xlabel, Gvals(4,:));
40 save('Gtable.mat', 'Gvals', 'xlabel', 'thetalabels');
41
42 % make a structure labelled a similar to if I had just opened the file ,
43 % for running rest of code
44 a.Gvals = Gvals;
45 a.xlabel = xlabel;

```

```

42     a.thetalabels = thetalabels;
43     disp('Gtable calculated, press any key to start subgap analysis');
44     pause;
45 else % open data file for G, if it exists
46     a = open('Gtable.mat');
47     disp('Possible Gtable found, press any key to start subgap analysis');
48     pause;
49 end
50 disp('Starting subgap analysis ...');

51
52 %% Definitions

53
54 % define physical constants
55 e = 1.6021766208e-19; % [C], fundamental charge
56 Fsun = 2.16e-5*pi; % hemispherical angular range, sun (1/46000 factor for
57 % concentration)
58 Fcell = pi; % emission geometrical factor, cell
59 h = 6.62607004e-34/e; % [eV-s], Planck's constant
60 c = 299792458; % [m/s], speed of light
61 k = 1.38064852e-23/e; % [eV/K], Boltzmann's constant
62 Tsun = 5760; % [Kelvin], Temperature of Sun, for full black-body expression
63 Tcell = 300; % [Kelvin], Temperature of Cell
64 E2lam_factor = 1.23984193*1e-6; % conversion factor between energy [eV] to
65 % wavelengths [m], E [eV] = E2lam_factor./lambda[m]
66 numTol = 1e-1;
67 relVal = 1;

68 % Load Solar Spectrum, use for calculating SQ limit
69 ASTMG173_filename = 'ASTMG173.xlsx';
70 sheet = 'SMARTS2';
71 xlRange = ['A', '3', ':', 'D', '2004'];
72 outdoor_data = xlsread(ASTMG173_filename, sheet, xlRange, 'basic');
73 lambda_outdoor = outdoor_data(:,1)*1e-9; % [m]
74 AM0 = outdoor_data(:,2)/1e-9; % [W/m^3]
75 AM15G = outdoor_data(:,3)/1e-9; % [W/m^3]
76 AM15D = outdoor_data(:,4)/1e-9; % [W/m^3]

77 % Define energy/wavelength ranges of interest
78 E_range = 0.001:0.001:5; % [eV] range of energies of interest. Avoid singular
79 % point (E = 0)
80 lambda_range = E2lam_factor./E_range; % [m], range of wavelengths

81 % define new ranges based on spectral data & target spectral range
82 newAM0 = interp1(lambda_outdoor, AM0, lambda_range, 'linear', 0);
83 newAM15G = interp1(lambda_outdoor, AM15G, lambda_range, 'linear', 0);
84 newAM15D = interp1(lambda_outdoor, AM15D, lambda_range, 'linear', 0);

85
86
87 %% Simulation Parameters
88 % plotting data
89 plotMainFigs = true; % decide whether to plot main figures
90 plotneffFig = false; % decide whether to plot/calculate neff figure
91 plotSIfigs = false; % decide whether to plot SI figures
92 plotGaussFig = false;
93

```

```

94 % light source
95 isBB = false; % use 5760 K blackbody as illumination light source if true,
96     otherwise use specified irrad
97 flux = newAM15G./E_range.^3/e*h*c; % flux of interest, if not blackbody (e.g.
98     AM 15G). Extra conversion factor to use energy integral
99
100 % auxillary parameters for simulation, not main focus
101 ERE = 1; % external radiative efficiency
102 IQE_AG = 1; % internal quantum efficiency, above gap
103 compRatio = 2; % for compressing G, which makes things run faster (and
104     dependent on (E-Eg)/gam, may not actually make things less accurate)
105
106 % materials parameters
107 Eg_spacing = 0.5; % spacing of bandgaps to calculate. 0.02 for "good"
108     resolution
109 Eg = 0.5:Eg_spacing:2.5; % [eV], bandgap of material
110 L = 1e-3; % thickness of material [cm]
111 alpha0 = 1e3; % [1/cm], absorption of direct gap material, alpha0L is what
112     matters, set alpha0L = 10
113 isPB = true; % include pauli-blocking/band filling effects
114
115 % Subgap parameters
116 gam_spacing = 0.05; % 0.02 for "good" resolution
117 gam = 10.^[-3:gam_spacing:0.0]; % Bandege sharpness parameter [eV],
118 theta = 1; % "order" of the exponential, 1 is urbach, 2 is Gaussian, etc.
119 IQE SG = 1; % internal quantum efficiency, sub gap
120 isIQE SG_Urbach = 0; % decide whether we need to calculate a subgap IQE that
121     drops off like Urbach
122
123 % code is faster if we figure out the right theta first, compress Gx,
124 % and then use as table look-up data set. Otherwise, passing around too
125 % much data/matrices.
126 Gx_comp = a.Gvals(a.thetalabels==theta, :);
127 Gx_comp = Gx_comp(1:compRatio:end);
128 x_comp = a.xlabels(1:compRatio:end);
129
130 % calculate input power
131 if isBB
132     Pin = abs(trapz(E_range, e*E_range.*bb(E_range, Fsun, Tsun, 0))); % input
133         power, W/m^2
134 else
135     Pin = abs(trapz(E_range, e*E_range.*flux));
136 end
137
138 %% Calculation for main Figures
139
140 if plotMainFigs
141
142     out = SQ_FOM(isBB, flux, Gx_comp, x_comp, gam, Eg, alpha0*L, isPB, IQE SG,
143         IQE AG, isIQE SG_Urbach); % does all the FOM calculations
144
145     Voc_vals1 = reshape(out.Voc, length(Eg), length(gam))'; % output, data, shape
146         it for data plots
147     Jsc_vals1 = reshape(out.Jsc, length(Eg), length(gam))';
148     PCE_vals1 = reshape(out.PCE, length(Eg), length(gam))';

```

```

140
141
142 %% -----Plot Figures-----
143
144 %% Fig 2, main result , EQE + SQ Limit
145 Fig2 = figure;
146 set(Fig2, 'Position', [60,80,800,400]);
147 gamWhich = [0.1, 0.5, 1, 2, 3]*k*Tcell; % which gamma for EQE, PCE
148 EgWhich = 1.5; % which Eg for EQE
149
150 % plot EQE
151 EQEcolorPlots = get(gca, 'colororder');
152 subplot(1,2,1);
153 hold on;
154 leg_str = ['S-Q'];
155 plot(E_range, E_range>=EgWhich, 'k--');
156 for i = 1:length(gamWhich)
157     plot(E_range, EQE_vals(E_range, 0, EgWhich, gamWhich(i), alpha0, isPB,
158         Gx_comp, x_comp, L, IQE_SG, IQE_AG, isIQE_SG_Urbach), 'Color',
159         EQEcolorPlots(i,:), 'LineWidth', 1.5);
160     leg_str = [leg_str, string(num2str(gamWhich(i)./k./Tcell))];
161 end
162 hold off;
163 hleg = legend(leg_str, 'Location', 'SouthEast');
164 title(hleg, '\gamma (kT)', 'FontWeight', 'Normal');
165 xlabel('Energy (eV)'); xlim([min(Eg), max(Eg)]);
166 ylabel('Absorbance');
167 axis square; box on;
168
169 % PCE at different gamma
170 subplot(1,2,2);
171 hold on;
172 for i = 1:length(gamWhich)
173     plot(Eg, interp2(Eg, gam, PCE_vals1*100, Eg, gamWhich(i)), 'Color',
174         EQEcolorPlots(i,:), 'LineWidth', 1.5);
175 end
176
177 % calculate SQ limit
178 PCE_SQ = zeros(1,length(Eg));
179 Voc_SQ = zeros(1,length(Eg));
180 Jsc_SQ = zeros(1,length(Eg));
181 for i = 1:length(Eg)
182     EQE_SQ = E_range>=Eg(i);
183     Vmax_SQ = fminbnd(@(V) V.*JV_noBF(V, E_range, EQE_SQ, isBB, flux), 0, Eg(i));
184     PCE_SQ(i) = -Vmax_SQ.*JV_noBF(Vmax_SQ, E_range, EQE_SQ, isBB, flux)./Pin;
185     Jsc_SQ(i) = -JV_noBF(0, E_range, EQE_SQ, isBB, flux);
186     Voc_SQ(i) = fzero(@(V) JV_noBF(V, E_range, EQE_SQ, isBB, flux), Eg(i));
187 end
188 plot(Eg, PCE_SQ*100, 'k--')
189
190 hold off;
191 xlabel('Band gap (eV)'); ylabel('Efficiency (%)');
192 axis square; box on;

```

```

191
192 %%% Fig 3, PL at Voc & fraction of subgap PL/Stokes Shift
193 Fig3 = figure;
194 set( Fig3 , 'Position' , [60,80,400,500]);
195 gamWhich = [0.2:0.4:2.6]*k*Tcell; % which gamma for PL + EQE
196 EgWhich = 1.5; % which Eg for EQE
197 offset = 1:1.35:15; % offset for plotting PL
198 PLcolorPlots = get(gca , 'colororder');
199 hold on;
200 h1 = plot(E_range , -1*ones(1,length(E_range)) , 'k--' , 'LineWidth' , 1.5);
201 h2 = plot(E_range , -1*ones(1,length(E_range)) , 'k-' , 'LineWidth' , 1.5);
202 h3 = plot(E_range , -1*ones(1,length(E_range)) , 'k:' , 'LineWidth' , 1.5);
203 % assume that the system, under illumination & no contacts, reaches its
204 % Voc. Thus, PL is the PL at Voc.
205 for i = 1:length(gamWhich)
206 Voc_gam = interp2(Eg , gam , Voc_vals1 , EgWhich , gamWhich(i));
207 PL_spect = J_spect(E_range , Voc_gam , EgWhich , gamWhich(i) , alpha0 , isPB ,
208 Gx_comp , x_comp , L , IQE_SG , IQE_AG , isIQE_SG_Urbach);
209 PLplot = plot(E_range , PL_spect./max(PL_spect)+offset(i) , '--' , 'Color' ,
210 PLcolorPlots(i,:) , 'LineWidth' , 1.5);
211
212 EQE_spect = EQE_vals(E_range , Voc_gam , EgWhich , gamWhich(i) , alpha0 , isPB ,
213 Gx_comp , x_comp , L , IQE_SG , IQE_AG , isIQE_SG_Urbach);
214 plot(E_range , EQE_spect./max(EQE_spect) + offset(i) , 'Color' , PLplot.
215 Color , 'LineWidth' , 1.5)
216
217 PEg = EQE_spect(3:end) - EQE_spect(1:end-2); %bandgap distribution ,
218 % central difference
219 plot(E_range(2:end-1) , PEg./max(PEg) + offset(i) , ':' , 'Color' , PLplot.
220 Color , 'LineWidth' , 1.5);
221
222 if gamWhich(i) == k*Tcell
223 text(1.65 , offset(i)+0.5 , [ '\gamma = kT' ] , 'FontSize' , 10 , 'Color' ,
224 PLplot.Color);
225 else
226 text(1.65 , offset(i)+0.5 , [ '\gamma = ' , num2str(gamWhich(i)/(k*Tcell)) ,
227 'kT' ] , 'FontSize' , 10 , 'Color' , PLplot.Color);
228 end
229 end
230 hold off;
231 xlabel('Energy (eV)'); xlim([0.0 , 2.1]); ylim([0.5 , 11.5]);
232 yticks ([]);
233 legend([h1 , h2 , h3] , { 'PL' , 'Abs' , 'P(E_g)' } , 'Location' , 'North' ,
234 'Orientation' , 'horizontal');
235 legend('boxoff');
236 box on;
237
238 figure;
239 J_subgap_Ratio = zeros(size(gam)); % fraction of recombination that is below
240 % the bandgap
241 PL_peaksUrbach = zeros(size(gam)); % find out peak PL position for each gam,
242 % for Stokes shift calculation
243 for i = 1:length(gam)
244 Voc_gam = interp2(Eg , gam , Voc_vals1 , EgWhich , gam(i));

```

```

234 PL_spect = J_spect(E_range, Voc_gam, EgWhich, gam(i), alpha0, isPB,
235 Gx_comp, x_comp, L, IQE_SG, IQE_AG, isIQE_SG_Urbach);
236 [~,pk_indx] = max(PL_spect); % find E_range indx for PL peak
237 PL_peaksUrbach(i) = E_range(pk_indx);
238 J_subgap_Ratio(i) = trapz(E_range(E_range < EgWhich), PL_spect(E_range <
239 EgWhich)) ./ trapz(E_range, PL_spect);
240
241 yaxis left;
242 semilogx(gam*1e3, J_subgap_Ratio, 'LineWidth', 1.5); hold on;
243 plot(ones(1,100)*k*Tcell*1e3, linspace(0,1,100), 'k--', 'LineWidth', 1.5);
244 text(k*Tcell*1e3*0.7, 0.23, '\gamma = kT', 'Color', 'black', 'Rotation', 90, 'FontSize', 12);
245 xlabel('gamma (meV)'); ylabel('Fraction of PL below band gap');
246 box on;
247 ylim([0, 1]);
248
249 yaxis right;
250 semilogx(gam*1e3, EgWhich - PL_peaksUrbach, 'LineWidth', 1.5);
251 ylabel('Stokes Shift (eV)');
252 ylim([min(EgWhich - PL_peaksUrbach), max(EgWhich - PL_peaksUrbach)]);
253
254 end
255
256 if plotneffFig
257 %% Figure S4, IV curve + n_eff Analysis
258 FigS4 = figure;
259 set(FigS4, 'Position', [60,40,700,600]);
260
261 numV_vals = 100;
262 EgWhich = [0.8, 1.34, 2.0]; % bandgap of linecuts
263 neff_gam_Eg = zeros(length(Eg), length(gam));
264 deltan_gam_Eg = zeros(length(Eg), length(gam), 2);
265 colorPlots = zeros(length(EgWhich), 3);
266
267 %% panel parameters
268 p = panel();
269 p.pack('h', 2);
270 p(1).pack('v', [0.06, 0.47, 0.47]);
271 p(2).pack('v', 3);
272
273 p.de.margin = 0;
274 p(1).de.margin = 2;
275 p(2).de.margin = 2;
276 p(1,1).margintop = 40;
277 p(1).marginright = 20;
278 p(2).marginleft = 20;
279
280 %% plot n_eff contour
281 h1 = p(1,2).select();
282 for i = 1:length(Eg)
283 V = linspace(3*k*Tcell, Eg(i)-3*k*Tcell, numV_vals);
284 for j = 1:length(gam)
285 JV_dark = zeros(size(V));

```

```

286     for m = 1:length(V)
287         EQEV_gam_Eg = EQE_vals(E_range, V(m), Eg(i), gam(j), alpha0, isPB,
288             Gx_comp, x_comp, L, IQE_SG, IQE_AG, isIQE_SG_Urbach);
289         JV_dark(m) = JV_Full(V(m), E_range, EQEV_gam_Eg, 0, 0);
290     end
291     fitresult = fit(V', log(JV_dark)', 'poly1'); % log(J) = log(J0) + qV/(
292         nkT), i.e. y = p(1)*x + p(2)
293     pvals = coeffvalues(fitresult); % get values of p
294     ci = confint(fitresult, 0.95); % find range of p, 95% confidence. size
295         (2xn), where n in number of coefficients
296     neff_gam_Eg(i,j) = 1/(k*Tcell*pvals(1)); % 1/(nkT/q) = p(1)
297     deltan_gam_Eg(i,j,[1,2]) = abs(1. / (k*Tcell*ci([2,1],1)) - neff_gam_Eg(
298         i,j));
299     end
300 end
301 surf(gam, Eg, neff_gam_Eg);
302 axis([min(gam), max(gam), min(Eg), max(Eg)]); colormap('hot');
303 view([0 90]);
304 shading interp;
305 set(gca, 'xscale', 'log');
306 ylabel('Band gap (eV)');
307 box on; hold on;
308 xticklabels([]);
309 for i = 1:length(EgWhich)
310     EgPlot = plot3(logspace(-3,0, 100), EgWhich(i)*ones(1,100), 1000*ones
311         (1,100), '--', 'LineWidth', 1.5);
312     colorPlots(i,:) = EgPlot.Color;
313 end
314
315 % Colorbars for respective contours
316 cbh = colorbar(h1, 'Location', 'NorthOutside'); colormap(cbh, hot);
317 p(1,1).select(cbh); cbh.Limits = [0.9, 7.1]; cbh.Ticks = 1:7;
318 xlabel(cbh, 'n_{eff}');
319
320 % plot the n_eff linecuts
321 h2 = p(1,3).select();
322 h2.XScale='log';
323 hold all
324 gam_mev = gam*1e3;
325 leg_str = [];
326 haveleg = [];
327 for i = 1:length(EgWhich)
328     n_vals = interp2(Eg, gam, neff_gam_Eg', EgWhich(i), gam);
329     deltan1 = interp2(Eg, gam, reshape(deltan_gam_Eg(:, :, 1), length(Eg), length(
330         gam))', EgWhich(i), gam);
331     deltan2 = interp2(Eg, gam, reshape(deltan_gam_Eg(:, :, 2), length(Eg), length(
332         gam))', EgWhich(i), gam);
333
334     plot_leg = plot(gam_mev, n_vals, '--', 'LineWidth', 1.5, 'Color',
335         colorPlots(i,:)); hold on;
336     plot(gam_mev, n_vals-deltan1, '—', 'LineWidth', 1.5, 'Color', colorPlots(i,
337         :));
338     plot(gam_mev, n_vals+deltan2, '—', 'LineWidth', 1.5, 'Color', colorPlots(i
339         :));
340     x2 = [gam_mev, fliplr(gam_mev)];

```

```

331 inBetween = [ transpose(n_vals-deltan1), fliplr(transpose(n_vals+deltan2)) ];
332 fillPlot = fill(x2, inBetween, colorPlots(i,:));
333 set(fillPlot, 'facealpha', 0.25);
334 set(fillPlot, 'edgealpha', 0.25);
335 leg_str = [leg_str, string(num2str(EgWhich(i)))];
336 haveleg = [haveleg, plot_leg];
337
338 xlabel('\gamma (meV)'); ylabel('n_{eff}');
339 box on;
340 plot(ones(1,100)*k*Tcell*1e3, linspace(0,10,100), 'k--', 'LineWidth', 1.5);
341 text(k*Tcell*1e3*0.7, 2.5, '\gamma = kT', 'Color', 'black', 'Rotation', 90, 'FontSize', 12);
342 ylim([0.6, 7.4]); yticks(1:1:7);
343 hleg = legend(haveleg, leg_str, 'Location', 'NorthWest');
344 title(hleg, 'E_g (eV)', 'FontWeight', 'normal');
345 set(gca, 'LineWidth', 1.25);
346
347 % plot IVs
348 gamWhich = [0.1, 0.5, 1, 2, 3]*k*Tcell; % which gamma for IV
349 JVcolorPlots = get(gca, 'colororder');
350 for i = 1:length(EgWhich)
351     hi = p(2,i).select();
352     V = logspace(-7, log10(EgWhich(i)), numV_vals); % voltage points
353     V = [-max(V), V];
354
355     % Generate Dark JV curve for a given gamma
356
357     % plot SQ limit JV
358     JV_SQ = zeros(1,length(V));
359     for m = 1:length(V)
360         JV_SQ(m) = JV_noBF(V(m), E_range, E_range >= EgWhich(i), 0, 0);
361     end
362     semilogy(V./(k*Tcell), abs(JV_SQ/JV_SQ(1)), 'k--'); hold on;
363
364     % plot JV
365     JV_gamma = zeros(length(gamWhich), length(V));
366     leg_str = [];
367     for j = 1:length(gamWhich)
368         for m = 1:length(V)
369             EQEV_gam = EQE_vals(E_range, V(m), EgWhich(i), gamWhich(j), alpha0
370                 , isPB, Gx_comp, x_comp, L, IQE_SG, IQE_AG, isIQE_SG_Urbach);
371             JV_gamma(j,m) = JV_Full(V(m), E_range, EQEV_gam, 0, 0);
372         end
373         semilogy(V./(k*Tcell), abs(JV_gamma(j,:)./JV_gamma(j,1)), 'Color',
374             JVcolorPlots(j,:), 'LineWidth', 1.5);
375         leg_str = [leg_str, string(num2str(gamWhich(j)./k./Tcell))];
376     end
377     hold off;
378     xlim([0, min(EgWhich)/(k*Tcell)]);
379     xticklabels([]);
380     xlabel('J/J_0(\gamma)');
381     box on;
382     set(gca, 'XColor', colorPlots(i,:)); set(gca, 'YColor', colorPlots(i,:));
383     set(gca, 'LineWidth', 1.25);

```

```

382         ylim([1e-1, 1e7]);
383
384 end
385 xticklabels(0:5:30);
386 xlabel('qV/{kT}');
387 p(2,1).select();
388 hleg = legend(['S-Q', leg_str], 'Location', 'SouthEast', 'fontsize', 8);
389 title(hleg, '\gamma (kT)', 'FontWeight', 'normal');
390
391
392
393 disp('Now plotting SI figures. Press any key to continue');
394 pause;
395
396 %% Fig S1, different gamma and Eg, FOM contours/linecuts
397 FigS1 = figure;
398 set( FigS1, 'Position', [70,40,900,600]);
399
400 %% panel parameters
401 p = panel();
402 p.pack('h', [0.47, 0.06, 0.47]);
403 p(1).pack('v', 4);
404 p(2).pack('v', 4);
405 p(3).pack('v', 4);
406
407 p.de.margin = 0;
408 p(1).de.margin = 2;
409 p(2).de.margin = 2;
410 p(1).marginright = 2;
411 p(2).marginright = 40;
412 p(3).marginleft = 40;
413
414 EgWhich = [0.8, 1.34, 2.0]; % which Eg for FOM linecuts
415 FF_vals1 = PCE_vals1.*Pin./(Voc_vals1.*Jsc_vals1); % calculate Fill factors
416
417 %% PCE contour
418 h1 = p(1,1).select();
419 surf(gam, Eg, PCE_vals1'*100); colormap(hot);
420 axis([min(gam), max(gam), min(Eg), max(Eg)]);
421 view([0 90]);
422 shading interp;
423 set(gca, 'xscale', 'log');
424 xticklabels([]);
425 ylabel('Band gap (eV)');
426 yticks(0.7:0.5:2.7);
427 box on; hold on;
428 for i = 1:length(EgWhich)
429     plot3(logspace(-3,0, 100), EgWhich(i)*ones(1,100), 1000*ones(1,100), '--',
430           'LineWidth', 1.5);
431 end
432
433 %% Voc contour
434 h2 = p(1,2).select();
435 surf(gam, Eg, Voc_vals1');

```

```

436 axis([ min(gam) , max(gam) , min(Eg) , max(Eg) ]);  

437 view([0 90]);  

438 shading interp;  

439 set(gca , 'xscale' , 'log');  

440 xticklabels([]);  

441 yticks(0.7:0.5:2.7);  

442 ylabel('Band gap (eV)');  

443 box on; hold on;  

444 for i = 1:length(EgWhich)  

445 plot3(logspace(-3,0, 100) , EgWhich(i)*ones(1,100) , 1000*ones(1,100) , '---',  

446 'LineWidth' , 1.5);  

447 end  

448  

449 % Jsc contour  

450 h3 = p(1,3).select();  

451 surf(gam, Eg, Jsc_vals1 '*1e-1');  

452 axis([ min(gam) , max(gam) , min(Eg) , max(Eg) ]);  

453 view([0 90]);  

454 shading interp;  

455 set(gca , 'xscale' , 'log');  

456 xticklabels([]); yticks(0.7:0.5:2.7);  

457 ylabel('Band gap (eV)');  

458 box on; hold on;  

459 for i = 1:length(EgWhich)  

460 plot3(logspace(-3,0, 100) , EgWhich(i)*ones(1,100) , 1000*ones(1,100) , '---',  

461 'LineWidth' , 1.5);  

462 end  

463  

464 % Fill Factor contour  

465 h4 = p(1,4).select();  

466 surf(gam, Eg, FF_vals1 );  

467 axis([ min(gam) , max(gam) , min(Eg) , max(Eg) ]);  

468 view([0 90]);  

469 shading interp;  

470 set(gca , 'xscale' , 'log');  

471 yticks(0.7:0.5:2.7);  

472 ylabel('Band gap (eV)');  

473 box on; hold on;  

474 for i = 1:length(EgWhich)  

475 plot3(logspace(-3,0, 100) , EgWhich(i)*ones(1,100) , 1000*ones(1,100) , '---',  

476 'LineWidth' , 1.5);  

477 end  

478 xticklabels({'10^0' , '10^1' , '10^2' , '10^3'});  

479 xlabel('gamma (meV)');  

480  

481 % Colorbars for respsective contours  

482 cbh = colorbar(h1, 'Location' , 'EastOutside');  

483 p(2,1).select(cbh);  

484 colormap(cbh, hot);  

485 xlabel(cbh, 'Efficiency (%)');  

486  

487 cbh = colorbar(h2, 'Location' , 'EastOutside'); colormap(cbh, hot);

```

```

488 p(2,2).select(cbh);
489 xlabel(cbh, 'V_{oc} (V)');
490
491 cbh = colorbar(h3, 'Location', 'EastOutside'); colormap(cbh, hot);
492 p(2,3).select(cbh);
493 xlabel(cbh, 'J_{sc} (mA cm^{-2})');
494
495 cbh = colorbar(h4, 'Location', 'EastOutside'); colormap(cbh, hot);
496 p(2,4).select(cbh);
497 xlabel(cbh, 'Fill Factor');
498
499 % Plot Linecuts
500 p(3,1).select(); % eta
501 leg_str = [];
502 for i = 1:length(EgWhich)
503     semilogx(gam, interp2(Eg, gam, PCE_vals1*100, EgWhich(i), gam), 'LineWidth
504         ', 1.5); hold on;
505     leg_str = [leg_str, string(EgWhich(i))];
506 end
507 xticklabels([]); yticks(10:10:30);
508 ylim([0,35]); ylabel('Efficiency (%)');
509 hleg = legend(leg_str, 'Location', 'NorthEast', 'FontSize', 8); title(hleg, '
510     Band gap (eV)', 'FontWeight', 'Normal');
511 box on;
512
513 p(3,2).select(); % Voc
514 for i = 1:length(EgWhich)
515     semilogx(gam, interp2(Eg, gam, Voc_vals1, EgWhich(i), gam), 'LineWidth', 1.5)
516         ; hold on;
517 end
518 xticklabels([]); yticks(0.4:0.4:1.6); ylabel('V_{oc} (V)');
519 box on;
520
521 p(3,3).select(); % Jsc
522 for i = 1:length(EgWhich)
523     semilogx(gam, interp2(Eg, gam, Jsc_vals1*1e-1, EgWhich(i), gam), 'LineWidth',
524         1.5); hold on;
525 end
526 yticks(10:20:70); ylabel('J_{sc} (mA cm^{-2})');
527 xticklabels([]);
528 box on;
529
530 p(3,4).select(); % Fill Factor
531 for i = 1:length(EgWhich)
532     semilogx(gam, interp2(Eg, gam, FF_vals1, EgWhich(i), gam), 'LineWidth', 1.5);
533         hold on;
534 end
535 yticks(0.1:0.2:0.9); ylabel('Fill Factor');
536 box on;
537 xticklabels({'10^0', '10^1', '10^2', '10^3'});
538 xlabel('gamma (meV)');
539
540 if plotSIfigs
541 disp('Now calculating effects of alpha0L. Press any key to continue');

```

```

538 % pause;
539
540 %%% Fig S2, EQE & FOM linecuts for different gamma, alpha0L (thickness)
541
542 FigS2 = figure;
543 set( FigS2, 'Position', [60,20,750,600] );
544
545 % materials parameters
546 EgWhich = 1.5; % [eV], bandgap of material
547 L = 1; % thickness of material, just set to 1 so that alpha0 is in units of 1/L
548
549 alpha0 = [0.01, 0.1, 0.3, 1, 10]; % absorption of direct gap material,
550 % alpha0L is what matters
551 % Subgap parameters
552 gam = 10.^[-3:gam_spacing:0]; % Bandedge sharpness parameter [eV],
553
554 % panel parameters
555 p = panel();
556 p.pack('h', [1/2, 1/2]);
557 p(1).pack('v', 2);
558 p(2).pack('v', 4);
559
560 p.de.margin = 0;
561
562 p(1).marginright = 20;
563 p(2).marginleft = 20;
564 p(1,1).marginbottom = 2;
565
566 % first gamma to plot
567 gam1 = 0.5*k*Tcell;
568 p(1,1).select();
569 hold on;
570 leg_str = [];
571 % text(0.7, 0.1, [ '\gamma = ', num2str(gam1./k./Tcell), 'kT'], 'FontWeight', 'Bold', 'Color', 'Red');
572 for i = 1:length(alpha0)
573 plot(E_range, EQE_vals(E_range, 0, EgWhich, gam1, alpha0(i), isPB, Gx_comp
574 , x_comp, L, IQE_SG, IQE_AG, isIQE_SG_Urbach), 'LineWidth', 1.5);
575 leg_str = [leg_str, string(num2str(alpha0(i)))];
```

576 end

577 hold off;

578 hleg = legend(leg\_str, 'Location', 'NorthWest', 'fontsize', 10);

579 title(hleg, '\alpha\_0L', 'FontWeight', 'normal');

580 xlim([0.5, 2.5]); xticklabels([]);

581 yticks(0.1:0.2:0.9);

582 ylabel('Absorbance');

583 box on;

584

585 % second gamma to plot

586 gam2 = 2\*k\*Tcell;

587 p(1,2).select();

588 hold on;

589 % text(0.7, 0.1, [ '\gamma = ', num2str(gam2./k./Tcell), 'kT'], 'FontWeight', 'Bold', 'Color', 'Red');

590 for i = 1:length(alpha0)

```

588 plot(E_range, EQE_vals(E_range, 0, EgWhich, gam2, alpha0(i), isPB, Gx_comp
589 , x_comp, L, IQE_SG, IQE_AG, isIQE_SG_Urbach), 'LineWidth', 1.5);
590 end
591 hold off;
592 xlabel('Energy (eV)'); xlim([0.5, 2.5]);
593 yticks(0.1:0.2:0.9);
594 ylabel('Absorbance');
595 box on;
596
597 % Calculate FOM for varying alpha0L and gamma, for fixed Eg and IQE
598 out = SQ_FOM(isBB, flux, Gx_comp, x_comp, gam, EgWhich, alpha0*L, isPB, IQE_SG
599 , IQE_AG, isIQE_SG_Urbach); % does all the FOM calculations
600
601 Voc_vals2 = reshape(out.Voc, length(alpha0), length(gam))'; % output, data,
602 shape it for data plots
603 Jsc_vals2 = reshape(out.Jsc, length(alpha0), length(gam))';
604 PCE_vals2 = reshape(out.PCE, length(alpha0), length(gam))';
605 FF_vals2 = PCE_vals2*Pin./(Voc_vals2.*Jsc_vals2);
606
607 p(2,1).select(); % eta
608 for i = 1:length(alpha0)
609     semilogx(gam, interp2(alpha0, gam, PCE_vals2*100, alpha0(i), gam), '
610     'LineWidth', 1.5);
611     hold on;
612 end
613 hold off; box on; yticks(10:10:30);
614 ylim([0,35]);
615 xticklabels([]);
616 ylabel('Efficiency (%)');
617
618 % just mention which Eg in SI
619 % title(['E_g = ', num2str(EgWhich), ' eV'], 'FontWeight', 'normal');
620
621 p(2,2).select(); % Voc
622 for i=1:length(alpha0)
623     semilogx(gam, interp2(alpha0, gam, Voc_vals2, alpha0(i), gam), 'LineWidth'
624     , 1.5);
625     hold on;
626 end
627 hold off;
628 ylabel('V_{oc} (V)'); xticklabels([]); yticks(0.4:0.4:1.6);
629 box on;
630
631 p(2,3).select(); % Jsc
632 for i = 1:length(alpha0)
633     semilogx(gam, interp2(alpha0, gam, Jsc_vals2*1e-1, alpha0(i), gam), '
634     'LineWidth', 1.5);
635     hold on;
636 end
637 xticklabels([]); ylabel('J_{sc} (mA cm^{-2})'); yticks(10:20:70);
638 box on;

```

```

637
638 p(2,4).select(); % FF
639 for i = 1:length(alpha0)
640     semilogx(gam, interp2(alpha0, gam, FF_vals2, alpha0(i), gam), 'LineWidth',
641                 1.5);
642     hold on;
643 end
644 ylabel('Fill Factor'); yticks(0.1:0.2:0.9);
645 box on;
646 xticklabels({'10^0', '10^1', '10^2', '10^3'});
647 xlabel('\gamma (meV)');
648
649
650 %% Fig S3, effect of including Pauli-blocking to FOM
651 FigS3 = figure; %
652 set( FigS3, 'Position', [60,40,700,500]);
653
654 %% panel parameters
655 p = panel();
656 p.pack('h', [1/2, 1/2]);
657 p(1).pack('v', 1);
658 p(2).pack('v', 4);
659
660 p.de.margin = 0;
661
662 p(1).marginright = 20;
663 p(2).marginleft = 20;
664
665 %% materials parameters
666 EgWhich = 1.5; % [eV], bandgap of material
667 L = 1e-3; % thickness of material, units of 1/alpha0
668 alpha0 = 1e3; % [1/cm], absorption of direct gap material, alpha0L is what
669     matters
670 isPB = false; % include pauli-blocking/band filling effects
671
672 %% Subgap parameters
673 gam = 10.^[-3:gam_spacing:0]; % Bandge sharpness parameter [eV],
674 IQE_SG = 1; % internal quantum efficiency, sub gap
675
676 %% PL parameters
677 gamWhich = [0.2:0.4:2.6]*k*Tcell; % which gamma for EQE, PCE
678 offset = 1:1.35:15;
679
680 p(1,1).select();
681 hold on;
682 % assume that the system, under illumination & no contacts, reaches its
683 % Voc. Thus, PL is the PL at Voc.
684 h1 = plot(E_range, -1*ones(1,length(E_range)), 'k--', 'LineWidth', 1.5);
685 h2 = plot(E_range, -1*ones(1,length(E_range)), 'k-', 'LineWidth', 1.5);
686 h3 = plot(E_range, -1*ones(1,length(E_range)), 'k:', 'LineWidth', 1.5);
687
688 for i = 1:length(gamWhich)
689     PL_spect = J_spect(E_range, 0, EgWhich, gamWhich(i), alpha0, isPB, Gx_comp
690                         , x_comp, L, IQE_SG, IQE_AG, isIQE_SG_Urbach);

```

```

689 PLplot = plot(E_range, PL_spect./max(PL_spect)+offset(i), '--', 'Color',
690 PLcolorPlots(i,:), 'LineWidth', 1.5);
691
692 EQE_spect = EQE_vals(E_range, 0, EgWhich, gamWhich(i), alpha0, isPB,
693 Gx_comp, x_comp, L, IQE_SG, IQE_AG, isIQE_SG_Urbach);
694 plot(E_range, EQE_spect./max(EQE_spect) + offset(i), 'Color', PLplot.
695 Color, 'LineWidth', 1.5)
696
697 PEg = EQE_spect(3:end) - EQE_spect(1:end-2); % smooth out EQE first?
698 plot(E_range(2:end-1), PEg./max(PEg) + offset(i), ':', 'Color', PLplot.
699 Color, 'LineWidth', 1.5);
700
701 if gamWhich(i) == k*Tcell
702     text(1.65, offset(i)+0.5, ['\gamma = kT'], 'FontSize', 10, 'Color',
703 PLplot.Color);
704 else
705     text(1.65, offset(i)+0.5, ['\gamma = ', num2str(gamWhich(i)/(k*Tcell))
706 , 'kT'], 'FontSize', 10, 'Color', PLplot.Color);
707 end
708
709 hold off;
710 xlabel('Energy (eV)'); xlim([0.0, 2.1]); ylim([0.5, 11.5]);
711 yticks([]);
712 legend([h1, h2, h3], {'PL', 'Abs', 'P(E_g)'}, 'Location', 'North',
713 'Orientation', 'horizontal');
714 legend('boxoff');
715 box on;
716
717 % Calculate FOM for no band-filling
718
719 Voc_vals_noBF = zeros(1, length(gam));
720 PCE_vals_noBF = Voc_vals_noBF;
721 Jsc_vals_noBF = Voc_vals_noBF;
722 FF_vals_noBF = Voc_vals_noBF;
723
724 for i = 1:length(gam)
725     EQE_noBF = EQE_vals(E_range, 0, EgWhich, gam(i), alpha0, isPB, Gx_comp,
726     x_comp, L, IQE_SG, IQE_AG, isIQE_SG_Urbach);
727     Voc_vals_noBF(i) = Voc_noBF(E_range, EQE_noBF, isBB, flux);
728     Jsc_vals_noBF(i) = Jsc_noBF(E_range, EQE_noBF, isBB, flux);
729     VmaxnoBF = fminbnd(@(V) V.*JV_noBF(V, E_range, EQE_noBF, isBB, flux), 0,
730     EgWhich);
731     PCE_vals_noBF(i) = -VmaxnoBF.*JV_noBF(VmaxnoBF, E_range, EQE_noBF, isBB,
732     flux)./Pin;
733     FF_vals_noBF(i) = PCE_vals_noBF(i)*Pin./(Voc_vals_noBF(i).*Jsc_vals_noBF(i));
734 end
735
736 p(2,1).select(); % eta
737 semilogx(gam, PCE_vals_noBF*100, gam, interp2(Eg, gam, PCE_vals1*100, EgWhich,
738 gam), 'LineWidth', 1.5)
739 box on; yticks(10:10:30); ylim([0,35]);
740 xticklabels([]);
741 ylabel('Efficiency (%)');

```

```

732 legend({'No Band-Filling', 'Band-Filling'}, 'Location', 'SouthWest', 'fontsize
733 ', 10);
734
735 p(2,2).select(); % Voc
736 semilogx(gam, Voc_vals_noBF, gam, interp2(Eg, gam, Voc_vals1, EgWhich, gam), '%
737 LineWidth', 1.5);
738 xlabel('V_{oc} (V)'); xticklabels([]); yticks(0.4:0.4:1.6);
739 box on;
740 xlabel('V_{oc} (V)'); xticklabels([]); yticks(0.4:0.4:1.6);
741
742 p(2,3).select(); % Jsc
743 semilogx(gam, Jsc_vals_noBF*1e-1, gam, interp2(Eg, gam, Jsc_vals1*1e-1,
744 EgWhich, gam), 'LineWidth', 1.5);
745 xticklabels([]); xlabel('J_{sc} (mA cm^{-2})'); yticks(10:20:70);
746 box on;
747
748 p(2,4).select(); % FF
749 semilogx(gam, FF_vals_noBF, gam, interp2(Eg, gam, FF_vals1, EgWhich, gam), '%
750 LineWidth', 1.5);
751 xlabel('Fill Factor'); yticks(0.1:0.2:0.9);
752 box on;
753
754 xlabel('gamma (meV)');
755
756 disp('Now calculating effects of different subgap IQE. Press any key to
757 continue');
758 pause;
759
760 %%% Fig S8, IQE Subgap dependence with gamma, FOM
761
762 FigS4 = figure;
763 set( FigS4, 'Position', [60,30,450,600]);
764
765 % materials parameters
766 EgWhich = 1.5; % [eV], bandgap of material
767 L = 1e-3; % thickness of material, units of 1/alpha0
768 alpha0 = 1e3; % absorption of direct gap material, alpha0L is what matters
769 isPB = true; % include pauli-blocking/band filling effects
770
771 % panel parameters
772 p = panel();
773 p.pack('h', 1);
774 p(1).pack('v', {0.1, 0.225, 0.225, 0.225, 0.225});
775
776 p.de.margin = 0;
777
778 % Subgap parameters
779 gam = 10.^[-3:gam_spacing:0]; % Bandge sharpness parameter [eV],
780 IQE_SG = 10.^[-6:2:0]; % internal quantum efficiency, sub gap
781
782 out = SQ_FOM(isBB, flux, Gx_comp, x_comp, gam, EgWhich, alpha0*L, isPB, IQE_SG
783 , IQE_AG, isIQE_SG_Urbach); % does all the FOM calculations
784
785
786
787
788
789
790
791
792
793
794
795
796
797
798
799
800

```

```

781 Voc_vals3 = reshape(out.Voc, length(IQE_SG), length(gam))'; % output, data,
782 % shape it for data plots
783 Jsc_vals3 = reshape(out.Jsc, length(IQE_SG), length(gam))';
784 PCE_vals3 = reshape(out.PCE, length(IQE_SG), length(gam))';
785 FF_vals3 = Pin*PCE_vals3./(Jsc_vals3.*Voc_vals3);
786
787 % calculate urbach IQE, need to set IQE_SG to single number to have the
788 % right size output
789 out = SQ_FOM(isBB, flux, Gx_comp, x_comp, gam, EgWhich, alpha0*L, isPB, 1,
790 IQE_AG, 1); % does all the FOM calculations
791
792 Voc_vals4 = reshape(out.Voc, [1, length(gam)]);
793 Jsc_vals4 = reshape(out.Jsc, [1, length(gam)]);
794 PCE_vals4 = reshape(out.PCE, [1, length(gam)]);
795 FF_vals4 = Pin.*PCE_vals4./(Jsc_vals4.*Voc_vals4);
796
797 p(1,2).select(); % eta
798 leg_str = [];
799 for i = 1:length(IQE_SG)
800     semilogx(gam, interp2(IQE_SG, gam, PCE_vals3*100, IQE_SG(i), gam),
801               'LineWidth', 1.5);
802     hold on;
803     leg_str = [leg_str, string(['10^{', num2str(log10(IQE_SG(i))), '}'])];
804 end
805 semilogx(gam, PCE_vals4*100, 'k--'); leg_str = [leg_str, 'Urbach'];
806 hold off;
807 ylim([0 35]);
808 xticklabels([]); yticks(10:10:30);
809 hleg = legend(leg_str, 'Location', 'NorthOutside', 'Orientation', 'Horizontal',
810                 'FontSize', 8);
811 hleg.Position(2) = hleg.Position(2) + 0.075;
812 title(hleg, 'IQE_{SG}', 'FontWeight', 'Normal');
813 ylabel('Efficiency (%)');
814 box on;
815
816 p(1,3).select(); % Voc
817 for i=1:length(IQE_SG)
818     semilogx(gam, interp2(IQE_SG, gam, Voc_vals3, IQE_SG(i), gam), 'LineWidth'
819               , 1.5);
820     hold on;
821 end
822 semilogx(gam, Voc_vals4, 'k--'); yticks(0.4:0.4:1.6);
823 hold off;
824 xticklabels([]);
825 ylabel('V_{oc} (V)');
826 box on;
827
828 p(1,4).select(); % Jsc
829 for i = 1:length(IQE_SG)
830     semilogx(gam, interp2(IQE_SG, gam, Jsc_vals3*1e-1, IQE_SG(i), gam),
831               'LineWidth', 1.5);
832     hold on;
833 end
834 semilogx(gam, Jsc_vals4*1e-1, 'k--');
835 hold off;

```

```

830 xticklabels([]); yticks(10:20:70);
831 ylabel('J_{sc} (mA cm^{-2})');
832 box on;
833
834 p(1,5).select(); % Fill Factor
835 for i = 1:length(IQE_SG)
836     semilogx(gam, interp2(IQE_SG, gam, FF_vals3, IQE_SG(i), gam), 'LineWidth',
837                 1.5);
838     hold on;
839 end
840 semilogx(gam, FF_vals4, 'k--'); yticks(0.1:0.2:0.9);
841 box on; hold off;
842 xticklabels({'10^0', '10^1', '10^2', '10^3'});
843 xlabel('\gamma (meV)'); ylabel('Fill Factor');
844
845 disp('Now calculating effects of a Gaussian Tail. Press any key to continue');
846 pause;
847 if plotGaussFig
848 %% Fig S7, theta = 2 (Gaussian Tail);
849
850 % gam, Eg, FOM contours
851 FigS7 = figure; %
852 set( FigS7, 'Position', [60,40,750,600]);
853
854 % panel parameters
855 p = panel();
856 p.pack('h', [0.47, 0.47]);
857 p(1).pack('v', 1);
858 p(2).pack('v', 2);
859
860 p.de.margin = 0;
861
862 p(1).marginright = 20;
863 p(2).marginleft = 20;
864 p(2,1).marginbottom = 20;
865
866
867
868 %% Gaussian Simulation Parameters
869
870 % materials parameters
871 Eg = 0.5:Eg_spacing:2.5; % [eV], bandgap of material
872 L = 1e-3; % thickness of material [cm]
873 alpha0 = 1e3; % [1/cm], absorption of direct gap material, alpha0L is what
874 % matters
875 isPB = true; % include pauli-blocking/band filling effects
876 isIQE_SG_Urbach = false;
877
878 % Subgap parameters
879 gam = 10.^[-3:gam_spacing:log10(0.55)]; % Bandege sharpness parameter [eV],
880 IQE_SG = 1; % internal quantum efficiency, sub gap
881
882 % code is faster if we figure out the right theta first, compress Gx,
883 % and then use as table look-up data set. Otherwise, passing around too

```

```

883 % much data.
884 theta = 2; % "order" of the exponential, 1 is urbach, 2 is Gaussian, etc.
885 Gx_comp = a.Gvals(a.thetalabels==theta, :);
886 Gx_comp = Gx_comp(1:compRatio:end);
887 x_comp = a.xlabels(1:compRatio:end);
888
889 % calculate SQ limit
890 PCE_SQ = zeros(1,length(Eg));
891 for i = 1:length(Eg)
892     EQE_SQ = E_range >= Eg(i);
893     Vmax_SQ = fminbnd(@(V) V.*JV_noBF(V, E_range, EQE_SQ, isBB, flux), 0, Eg(i));
894     PCE_SQ(i) = -Vmax_SQ.*JV_noBF(Vmax_SQ, E_range, EQE_SQ, isBB, flux)./Pin;
895 end
896
897 out = SQ_FOM(isBB, flux, Gx_comp, x_comp, gam, Eg, alpha0*L, isPB, IQE_SG,
898 IQE_AG, isIQE_SG_Urbach); % does all the FOM calculations
899
900 Voc_vals_theta2 = reshape(out.Voc, length(Eg), length(gam))'; % output, data,
901 % shape it for data plots
902 Jsc_vals_theta2 = reshape(out.Jsc, length(Eg), length(gam))';
903 PCE_vals_theta2 = reshape(out.PCE, length(Eg), length(gam))';
904
905 % Spectral Plots, PL, EQE, P(Eg)
906 p(1,1).select();
907 gamWhich = [0.5:1:6.5]*k*Tcell; % which gamma for EQE, PCE
908 EgWhich = 1.5; % which Eg for EQE
909 offset = 1:1.35:15;
910 PLcolorPlots = get(gca, 'colororder');
911
912 hold on;
913 % assume that the system, under illumination & no contacts, reaches its
914 % Voc. Thus, PL is the PL at Voc.
915 h1 = plot(E_range, -1*ones(1,length(E_range)), 'k--', 'LineWidth', 1.5);
916 h2 = plot(E_range, -1*ones(1,length(E_range)), 'k-', 'LineWidth', 1.5);
917 h3 = plot(E_range, -1*ones(1,length(E_range)), 'k:', 'LineWidth', 1.5);
918
919 for i = 1:length(gamWhich)
920     Voc_gam = interp2(Eg, gam, Voc_vals_theta2, EgWhich, gamWhich(i));
921     PL_spect = J_spect(E_range, Voc_gam, EgWhich, gamWhich(i), alpha0, isPB,
922     Gx_comp, x_comp, L, IQE_SG, IQE_AG, isIQE_SG_Urbach);
923     PLplot = plot(E_range, PL_spect./max(PL_spect)+offset(i), '--', 'Color',
924     PLcolorPlots(i,:), 'LineWidth', 1.5);
925     EQE_spect = EQE_vals(E_range, 0, EgWhich, gamWhich(i), alpha0, isPB,
926     Gx_comp, x_comp, L, IQE_SG, IQE_AG, isIQE_SG_Urbach);
927     plot(E_range, EQE_spect./max(EQE_spect) + offset(i), '-', 'Color', PLplot.
928     .Color, 'LineWidth', 1.5)
929
930 PEg = EQE_spect(3:end) - EQE_spect(1:end-2);
931 plot(E_range(2:end-1), PEg./max(PEg) + offset(i), ':', 'Color', PLplot.
932     Color, 'LineWidth', 1.5);
933 if gamWhich(i) == k*Tcell
934     text(1.65, offset(i)+0.5, ['\gamma = kT'], 'FontSize', 10, 'Color',
935     PLcolorPlots(i,:));

```

```

929     else
930         text(1.65, offset(i)+0.5, ['\gamma = ', num2str(gamWhich(i)/(k*Tcell))
931             , 'kT'], 'FontSize', 10, 'Color', PLcolorPlots(i,:));
932     end
933 end
934 hold off;
935 xlabel('Energy (eV)'); xlim([0.3, 2.1]); ylim([0.5, 11.5]);
936 yticks([]);
937 legend([h1, h2, h3], {'PL', 'Abs', 'P(Eg)'}, 'Location', 'North', ...
938     'Orientation', 'horizontal');
939 legend('boxoff');
940 box on;
941 p(2,1).select();
942 J_subgap_Ratio = zeros(size(gam)); % fraction of recombination that is below
943     the bandgap
944 PL_peaksGaussian = zeros(size(gam));
945 EgPV = zeros(size(gam));
946
947 for i = 1:length(gam)
948     Voc_gam = interp2(Eg, gam, Voc_vals_theta2, EgWhich, gam(i));
949     PL_spect = J_spect(E_range, Voc_gam, EgWhich, gam(i), alpha0, isPB,
950         Gx_comp, x_comp, L, IQE_SG, IQE_AG, isIQE_SG_Urbach);
951
952     EQE_spect = EQE_vals(E_range, 0, EgWhich, gam(i), alpha0, isPB, Gx_comp,
953         x_comp, L, IQE_SG, IQE_AG, isIQE_SG_Urbach);
954     PEg = EQE_spect(3:end) - EQE_spect(1:end-2);
955     [~, pk_idx] = max(PEg);
956     EgPV(i) = E_range(pk_idx);
957     J_subgap_Ratio(i) = trapz(E_range(E_range < EgPV(i)), PL_spect(E_range < EgPV(
958         i)))./ trapz(E_range, PL_spect);
959 %     [~, pk_idx] = max(PL_spect); % find E_range indx for PL peak
960     PL_peaksGaussian(i) = findEgPL(E_range, PL_spect, relVal, numTol); %
961         E_range(pk_idx);
962 end
963
964 yyaxis left;
965 semilogx(gam*1e3, J_subgap_Ratio, 'LineWidth', 1.5); hold on;
966 xlabel('\gamma (meV)'); ylabel('Fraction of PL below E_{g, Abs}');
967 box on;
968 ylim([0, 1]);
969
970 yyaxis right;
971 semilogx(gam*1e3, EgPV - PL_peaksGaussian, 'LineWidth', 1.5);
972 ylabel('Delta Eg (eV)');
973 ylim([min(EgPV - PL_peaksGaussian), max(EgPV - PL_peaksGaussian)]);
974 xlim([min(gam), max(gam)]*1e3);
975
976 % Plot new SQ limit for Gaussian Tails
977 p(2,2).select();
978 leg_str = ['S-Q'];
979 hold on;
980 plot(Eg, PCE_SQ*100, 'k--');

```



```

1026     Voc_guess = Voc(i1,i2,i3,i4,i5); % use last Voc point for
1027     % next optimization
1028
1029     Jsc(i1,i2,i3,i4,i5) = -JV_Full(0, E_range, EQEV(0), isBB,
1030     % flux);
1031     Vmax = fminbnd(@(V) V.*JV_Full(V, E_range, EQEV(V), isBB,
1032     % flux), 0, Voc_guess);
1033
1034     PCE(i1,i2,i3,i4,i5) = -Vmax.*JV_Full(Vmax, E_range, EQEV(
1035     % Vmax), isBB, flux)./Pin;
1036
1037     end
1038
1039     end
1040
1041     end
1042
1043
1044     % save data as output struct, resize matrix in main function
1045     out.Voc = Voc;
1046     out.Jsc = Jsc;
1047     out.PCE = PCE;
1048
1049
1050
1051
1052
1053
1054
1055
1056
1057
1058
1059
1060
1061
1062
1063
1064
1065
1066
1067
1068
1069
1070
function out = G(x,theta) % calculations "unitless" absorption coefficient
f = @(xp) exp(-abs(xp).^theta).*sqrt(x-xp); % complex numbers take up
precision!
if x < 50 % somewhat arbitrary division, but makes the integrals converge
properly and run in timely manner
out = 1./(2*gamma(1 + 1/theta))*integral(f,-inf,x, 'AbsTol', 1e-12, '
RelTol', 1e-12);
else
out = real(1./(2*gamma(1 + 1/theta))*integral(f,-inf,inf));
end
end
function out = alpha(E, V, Eg, gam, alpha0, isPB, Gx, xlabel)
xq = (E-Eg)./gam; % calculate dimensionless x
GE = interp1(xlabel, Gx, xq); % table look up
out = alpha0*sqrt(gam/(k*Tcell))*GE;
if isPB % include pauli-blocking effect
occFactor = tanh((E-V)/(4*k*Tcell));
out = out.*occFactor;
end
end
% spectral current, i.e. J_rad(E)
function out = J_spect(E_range, V, Eg, gam, alpha0, isPB, Gx, xlabel, L,
IQE_SG, IQE_AG, isIQE_SG_Urbach)
temp = EQE_vals(E_range, V, Eg, gam, alpha0, isPB, Gx, xlabel, L, IQE_SG,
IQE_AG, isIQE_SG_Urbach).*bb(E_range, Fcell, Tcell, V);
singularIndex = find(E_range == V);
temp(singularIndex) = (temp(singularIndex+1) + temp(singularIndex-1))/2; % linear interpolation to get rid of singularity at E = qV

```

```

1071         out = temp;
1072     end
1073
1074     % EQE
1075     function out = EQE_vals(E_range, V, Eg, gam, alpha0, isPB, Gx, xlabel, L,
1076         IQE_SG, IQE_AG, isIQE_SG_Urbach)
1077         % simple parametrization with an IQE that falls off like the Urbach
1078         % parameter
1079         if isIQE_SG_Urbach
1080             IQE_SG = zeros(1,length(E_range)); % do this in two steps so that we
1081             % don't get weird NaN errors from 0*exp(large number)
1082             IQE_SG(E_range <= Eg) = IQE_AG.*exp((E_range(E_range <= Eg)-Eg)/gam);
1083         end
1084         out = dubpass(alpha(E_range, V, Eg, gam, alpha0, isPB, Gx, xlabel), L).*((E_range <= Eg).*IQE_SG + (E_range > Eg).*IQE_AG);
1085     end
1086
1087     function Eg = findEgPL(E_range, spec, relVal, numTol)
1088         cumRat1 = fliplr(cumtrapz(E_range, fliplr(spec)))./trapz(E_range, spec);
1089         Eg = max(E_range(abs(cumRat1-relVal)<numTol));
1090     end
1091
1092     % Full JV, including band-filling effects
1093     function out = JV_Full(V, E_range, EQE, isBB, flux)
1094         % either assume blackbody illumination, or some spectrum given by
1095         % flux. Must be same size as E_range and EQE
1096         if isBB
1097             Jsc = -e*abs(trapz(E_range, EQE.*bb(E_range, Fsun, Tsun, 0)+bb(
1098                 E_range, Fcell, Tcell, 0)));
1099         else
1100             Jsc = -e*abs(trapz(E_range, EQE.*(flux+bb(E_range, Fcell, Tcell, 0))));
1101             ;
1102         end
1103
1104         % correct for singularity by interpolation
1105         Jspec = EQE.*bb(E_range, Fcell, Tcell, V);
1106         singularIndex = find(E_range == V);
1107         Jspec(singularIndex) = (Jspec(singularIndex+1) + Jspec(singularIndex-1))
1108             /2; % linear interpolation to get rid of apparent singularity at E =
1109             qV
1110         Jrad = -e*abs(trapz(E_range, Jspec));
1111
1112         out = Jsc - Jrad;
1113     end
1114
1115     % Bose-Einstein black-body spectrum with some chemical potential, no approx
1116     function spectrum = bb(E_range, F, T, V)
1117         spectrum = 2*F./(h^3*c^2).*...
1118             E_range.^2 ./ (exp( (E_range-V)/(k*T) ) - 1); % blackbody photon
1119             flux [Photons/(sec*m^2*wavelength)]
1120     end
1121
1122     % Voc of cell assuming no band-filling, using "diode" approximation
1123     function out = Voc_noBF(E_range, EQE, isBB, flux)

```

```

1118 Jrad = e*abs(trapz(E_range, EQE.*bb(E_range, Fcell, Tcell,0)));
1119 Jsc = Jsc_noBF(E_range, EQE, isBB, flux);
1120 out = k*Tcell*log(1 + Jsc/Jrad);
1121 end
1122
1123 function out = Jsc_noBF(E_range, EQE, isBB, flux)
1124 if isBB
1125     out = e*abs(trapz(E_range, EQE.*bb(E_range, Fsun, Tsun, 0)));
1126 else
1127     out = e*abs(trapz(E_range, EQE.*flux));
1128 end
1129
1130 end
1131
1132 function out = JV_noBF(V, E_range, EQE, isBB, flux)
1133 Jsc = -Jsc_noBF(E_range, EQE, isBB, flux);
1134 Jrad = -e*abs(trapz(E_range, EQE.*bb(E_range, Fcell, Tcell,0)))*(exp(V./(k
1135 *Tcell))-1);
1136 out = Jsc - Jrad;
1137 end
1138
1139 % Beer-Lambert absorption law, does not include interference effects or
1140 % backward propagating waves
1141 function out = dubpass(alpha,L)
1142     out = -expml(-2*alpha*L); %absorbance, unitless. expml for high precision
1143     of small alpha
1144 end
1145
1146 end

```

## Listing D.2: Modified Detailed Balance Code for Excitonic Multijunctions

```

1
2 function ExcitonicTandem_DetailedBalance_Sweep_v2
3 % Requires:
4 % MATLAB 2020a, Global Optimization Toolbox, Parallel Computing Toolbox
5 %
6 % Description:
7 % This function calculates the detailed balance efficiency of an optimized
8 % multijunction excitonic solar cell from 1 to numExc number of absorbers
9 % and plots their optimized EQE spectra and JV curves.
10 %
11 % Assumptions and Details:
12 % 1. Abs = EQE and is described by a Gaussian with an absorption maximum,
13 % peak position, and linewidth
14 % 2. Detailed balance relations holds, ERE = 1, and no optical coupling
15 % exists between subcells
16 % 3. Incident spectrum is the solar AM1.5G
17 % 4. Spectral windowing from top absorbers modelled by subtracting the
18 % EQE response of the top absorbers from the incident spectrum, which is
19 % effectively a ray optics approximation
20 % 5. Enforces current matching at the maximum power point
21 % (i.e.  $J(V_{max})_i = J(V_{max})_j$ ) in the optimization process
22 % 6. Optimization performed by a Global Optimization Routine (surrogateopt)
23 % in MATLAB's Global Optimization Toolbox
24 % 7. All data is saved in a new directory labelled by the date and time of
25 % when this script is ran.
26 %
27 % Written by Joeson Wong
28 % Last Updated on April 12, 2020
29
30 % clear files, figures, and make directory
31 clear all; close all; clc;
32 time = clock;
33 time = fix(time);
34 dir_name = [];
35 for i_time = 1:length(time)-1 % no need to add seconds marker on there...
36     dir_name = [dir_name, num2str(time(i_time)), '_'];
37 end
38 dir_name(end) = [];
39 mkdir(dir_name);
40 %& Definitions
41
42 % define physical constants
43 e = 1.6021766208e-19; % [C], fundamental charge
44 Fsun = 2.16e-5*pi; % hemispherical angular range, sun (1/46000 factor for
45 % concentration)
46 Fcell = pi; % emission geometrical factor, cell
47 h = 6.62607004e-34/e; % [eV-s], Planck's constant
48 c = 299792458; % [m/s], speed of light
49 k = 1.38064852e-23/e; % [eV/K], Boltzmann's constant
50 Tsun = 5760; % [Kelvin], Temperature of Sun, for full black-body expression
51 Tcell = 300; % [Kelvin], Temperature of Cell
52 E2lam_factor = 1.23984193*1e-6; % conversion factor between energy [eV] to
53 % wavelengths [m],  $E$  [eV] =  $E2lam\_factor ./ lambda[m]$ 

```



```

102 % initialize starting point for optimization
103 Apeak0 = 0.5*ones(1, idx); % peak value of absorbance
104 E_exco = linspace(0.7, 3.2, idx); % exciton excitation energy
105 Exc_LW0 = 80e-3*ones(1, idx); % Linewidth of exciton
106 x0 = [Apeak0, E_exco, Exc_LW0];
107
108 if idx == 1
109     oldPCE_uncon = 0;
110     oldPCE_con = 0;
111 else
112     oldPCE_uncon = maxPCE_exc_uncon(idx-1);
113     oldPCE_con = maxPCE_exc_con(idx-1);
114 end
115
116 % Perform Optimization
117 [maxPCE, x] = optimExciton(flux, idx, 0, x0, oldPCE_uncon);
118 maxPCE_exc_uncon(idx) = -maxPCE;
119 x_exc_uncon(idx, 1:3*idx) = x;
120
121 if doSeriesCon
122 % use results from unconstrained as initial starting point for
123 % constrained. Also force the constrained PCEs to increase with
124 % number of excitonic absorbers.
125 [maxPCE, x] = optimExciton(flux, idx, 1, x, oldPCE_con);
126 maxPCE_exc_con(idx) = -maxPCE;
127 x_exc_con(idx, 1:3*idx) = x;
128 end
129
130
131 figure;
132 SQ1JPCE = 33.7; % single junction SQ limit
133 plot(1:numExc, maxPCE_exc_uncon*100, '-o', 'MarkerFaceColor', 'b', 'MarkerSize', 10); hold on;
134 if doSeriesCon
135     plot(1:numExc, maxPCE_exc_con*100, '-o', 'MarkerFaceColor', 'r', 'MarkerSize', 10);
136     plot(1:numExc, SQ1JPCE*ones(1, numExc), 'k--', 'LineWidth', 1.5);
137     legend({'Unconstrained', 'Series Constrained', 'SQ Limit'}, 'Location', 'NorthWest');
138 else
139     plot(1:numExc, SQ1JPCE*ones(1, numExc), 'k--', 'LineWidth', 1.5);
140     legend({'Unconstrained', 'SQ Limit'}, 'Location', 'NorthWest');
141 end
142 xlabel('Number of Excitonic Absorbers'); ylabel('Maximum PCE (%)');
143 xticks(1:numExc);
144 savefig([dir_name, '/maxPCE_vs_numExc.fig']);
145
146 %% Plot Spectral Data of Optimized Excitonic Absorbers
147
148 if plotSpec
149 % Use a different color for a different number of excitonic absorbers
150 colorLines = [
151     0     0.4470    0.7410
152     0.8500   0.3250    0.0980
153     0.9290   0.6940    0.1250

```

```

154    0.4940    0.1840    0.5560
155    0.4660    0.6740    0.1880
156    0.3010    0.7450    0.9330
157    0.6350    0.0780    0.1840
158      0    0.7500    0.7500
159    0.2500    0.2500    0.2500
160    0.7500        0    0.7500
161    0.7500    0.7500        0
162    0.0000    0.0000    1.0000
163    0.0000    0.5000    0.0000
164    1.0000    0.0000    0.0000
165    0.5000    0.5000    0.7500
166    0.8000    0.1050    0.5000
167    0.5000    0.8000    0.1050
168    0.1050    0.5000    0.8000
169    0.7500    0.5000    0.0000
170    0.0000    0.7500    0.0000
171    0.0000    0.0000    0.7500];
172
173
174 figure;
175 hold on;
176 set(gcf, 'Position', [300, 75, 300, 500]);
177 AbsSpectra_uncon = zeros(numExc, numExc, length(E_range));
178 for i1 = 1:numExc
179     for i2 = 1:i1
180         spec = excGauss(E_range, x_exc_uncon(i1, i2), ...
181                         x_exc_uncon(i1, i1+i2), x_exc_uncon(i1, 2*i1+i2));
182         AbsSpectra_uncon(i1, i2, :) = spec;
183         plot(E_range, (i1-1)*ones(1, length(E_range)) + spec, ...
184               '-', 'Color', colorLines(i1,:), 'LineWidth', 1.5);
185     end
186 end
187 hold off;
188 xlim([0.5, 3.5]); box on;
189 xlabel('Energy (eV)'); ylabel('Excitonic Absorption Spectra');
190 savefig([dir_name, '/AbsSpectra_optim_uncon.fig']);
191
192 if doSeriesCon
193     figure;
194     hold on;
195     set(gcf, 'Position', [300, 75, 300, 500]);
196     AbsSpectra_con = zeros(numExc, numExc, length(E_range));
197     for i1 = 1:numExc
198         for i2 = 1:i1
199             spec = excGauss(E_range, x_exc_con(i1, i2), ...
200                             x_exc_con(i1, i1+i2), x_exc_con(i1, 2*i1+i2));
201             AbsSpectra_con(i1, i2, :) = spec;
202             plot(E_range, (i1-1)*ones(1, length(E_range)) + spec, ...
203                   '-', 'Color', colorLines(i1,:), 'LineWidth', 1.5);
204         end
205     end
206     hold off;
207     xlim([0.5, 3.5]); box on;
208     xlabel('Energy (eV)'); ylabel('Excitonic Absorption Spectra');

```

```

209 savefig([dir_name, '/AbsSpectra_optim_con.fig']);
210 end
211
212
213 %% Perform Analysis to Plot J-V Characteristics of Optimized Excitonic
214 Absorbers
215 if plotIV
216
217 % Initialize Device Output storage
218 Voc_uncon = zeros(numExc, numExc);
219 Jsc_uncon = Voc_uncon;
220 PCE_uncon = Voc_uncon;
221
222 % Do unconstrained IV
223 for i1 = 1:numExc
224     EQE_vals = [zeros(1, length(E_range));
225                  IQE_exc*reshape(AbsSpectra_uncon(i1,1:i1,:), [i1, length(
226                  E_range)])];
227     TransWindow_vals = 1-cumsum(EQE_vals,1); % for calculating the flux
228     % the lower layer sees
229     TransWindow_vals(TransWindow_vals<0) = 0;
230
231     figure;
232     for i2 = 1:i1
233         influx = TransWindow_vals(i2,:).*flux;
234         Jsc_uncon(i1,i2) = -JV_boltz(0, E_range, EQE_vals(i2+1,:), isBB,
235             influx);
236         Voc_uncon(i1,i2) = fzero(@(V) JV_boltz(V, E_range, EQE_vals(i2
237             +1,:), isBB, influx), 0.8*x_exc_uncon(i1, i1+i2));
238         Vmax = fminbnd(@(V) V.*JV_boltz(V, E_range, EQE_vals(i2+1,:), isBB
239             , influx), 0, Voc_uncon(i1,i2));
240         PCE_uncon(i1,i2) = -Vmax.*JV_boltz(Vmax, E_range, EQE_vals(i2+1,:)
241             , isBB, influx)./Pin;
242
243         V_vals = linspace(0, Voc_uncon(i1,i2), 100);
244         J_vals = JV_boltz(V_vals, E_range, EQE_vals(i2+1,:), isBB, influx)
245             ;
246         plot(V_vals, -J_vals*1e-1, 'LineWidth', 1.5, 'Color', colorLines(
247             i1,:)); hold on;
248         text(Vmax-0.1, Jsc_uncon(i1,i2)*1e-1+0.3, ['\eta = ', num2str(
249             round(PCE_uncon(i1,i2),3)*1e2), '%'], 'Color', colorLines(i1
250             ,:));
251     end
252     xlabel('Voltage (V)'); ylabel('Current Density (mA/cm^2)');
253     ylim([0, 1.1*max(Jsc_uncon(i1,:))*1e-1]);
254     savefig([dir_name, '/JV_optim_uncon_numExc=', num2str(i1), '.fig']);
255 end
256
257 if doSeriesCon
258 % Do constrained IV
259 Voc_con = zeros(numExc, numExc);
260 Jsc_con = Voc_con;
261 PCE_con = Voc_con;
262 for i1 = 1:numExc
263     EQE_vals = [zeros(1, length(E_range))];

```

```

253     IQE_exc*reshape(AbsSpectra_con(i1,1:i1,:), [i1, length(
254         E_range)]]);
255     TransWindow_vals = 1-cumsum(EQE_vals,1); % for calculating the flux
256         the lower layer sees
257     TransWindow_vals(TransWindow_vals<0) = 0;
258
259     figure;
260     for i2 = 1:i1
261         influx = TransWindow_vals(i2,:).*flux;
262         Jsc_con(i1,i2) = -JV_boltz(0, E_range, EQE_vals(i2+1,:), isBB,
263             influx);
264         Voc_con(i1,i2) = fzero(@(V) JV_boltz(V, E_range, EQE_vals(i2+1,:),
265             isBB, influx), 0.8*x_exc_con(i1, i1+i2));
266         Vmax = fminbnd(@(V) V.*JV_boltz(V, E_range, EQE_vals(i2+1,:), isBB,
267             influx), 0, Voc_con(i1,i2));
268         PCE_con(i1,i2) = -Vmax.*JV_boltz(Vmax, E_range, EQE_vals(i2+1,:),
269             isBB, influx)./Pin;
270
271         V_vals = linspace(0, Voc_con(i1,i2), 100);
272         J_vals = JV_boltz(V_vals, E_range, EQE_vals(i2+1,:), isBB, influx)
273             ;
274         plot(V_vals, -J_vals*1e-1, 'LineWidth', 1.5, 'Color', colorLines(
275             i1,:)); hold on;
276         text(Vmax-0.1, Jsc_con(i1,i2)*1e-1+0.3, ['\eta = ', num2str(round(
277             PCE_con(i1,i2),3)*1e2), '%'], 'Color', colorLines(i1,:));
278     end
279     xlabel('Voltage (V)'); ylabel('Current Density (mA/cm^2)');
280     ylim([0, 1.1*max(Jsc_con(i1,:))*1e-1]);
281     savefig([dir_name, '/JV_optim_con_numExc=', num2str(i1), '.fig']);
282
283 end
284
285
286 % save all variables in this sweep
287 close all;
288 filename = [dir_name, '/ExcitonicTandem_VariableData.mat'];
289 save(filename);
290
291 %%%%%% Sub Functions %%%%%%
292
293 function [maxPCE,x] = optimExciton(flux, numExc, isSeries, x0, oldPCE)
294
295     % length of x is numExc*3
296
297     % Set-up Optimization Parameters
298     maxExc_LW = 150e-3;
299     maxEg = 5;
300     maxA = 0.5;
301     lb = zeros(1, 3*numExc);
302     ub = [maxA*ones(1,numExc), maxEg*ones(1,numExc), maxExc_LW*ones(1,numExc)
303         ];
304     objconstr = @(x) conopt(x, flux, numExc, oldPCE, isSeries); % rewrite
305         optimization for surrogateopt

```

```

297 options = optimoptions('surrogateopt', 'InitialPoints', x0, ...
298 'UseParallel', true, 'MaxFunctionEvaluations', max(500,200*numExc), ...
299 'PlotFcn','surrogateoptplot');
300
301 % Perform Optimization
302 rng default;
303 [x, maxPCE] = surrogateopt(objconstr, lb, ub, options);
304
305 end
306
307 % Subfunction that calculates PCE and Jmax as the objective function
308 % and nonlinear constraint for surrogateopt. Includes spectral
309 % windowing effects. Enforces larger PCE values as a constraint as well
310 function f = conopt(x, flux, numExc, oldPCE, isSeries)
311
312 AbsSpectra = zeros(numExc, length(E_range));
313 for i = 1:numExc
314 AbsSpectra(i,:) = excGauss(E_range, x(i), x(numExc+i), x(2*numExc+i));
315 end
316
317 EQE = [zeros(1, length(E_range));
318 IQE_exc*AbsSpectra];
319 TransWindow = 1-cumsum(EQE,1); % for calculating the flux the lower layer
320 % sees
321 TransWindow(TransWindow<0) = 0;
322
323 Jmax_vals = zeros(numExc, 1);
324 newPCE = 0;
325 for i = 1:numExc
326 inputflux = TransWindow(i,:).*flux;
327 [Vmax_val, Pout] = fminbnd(@(V) V.*JV_boltz(V, E_range, EQE(i+1,:),
328 isBB, inputflux), 0, x(numExc+i));
329 Jmax_vals(i) = JV_boltz(Vmax_val, E_range, EQE(i+1,:), isBB, inputflux
330 );
331 newPCE = newPCE - Pout./Pin;
332 end
333
334 f.Fval = -newPCE;
335 minIneq = realmin; % log(minIneq) is the lowest value we can reach in the
336 % constraint, so there are no infinities for log(0). Use floating point
337 % precision
338 if isSeries
339 % Perform current matching using nonlinear inequalities (Ineq
340 % <= 0) by rewriting equality constraint with a log function
341 f.Ineq = [oldPCE - newPCE; log(minIneq+abs((Jmax_vals - Jmax_vals(1))
342 ./Jmax_vals(1))*CurTol)];
343 else
344 f.Ineq = oldPCE - newPCE;
345 end
346 end
347
348 % Gaussian spectra for excitons
349 function out = excGauss(E_range, Apeak, E_exc, Exc_LW)
350 out = Apeak*exp(-0.5*((E_range - E_exc)./Exc_LW).^2);
351 end

```

```

346
347 % Bose-Einstein black-body spectrum with some electrochemical potential
348 function spectrum = bb(E_range, F, T, V)
349 spectrum = 2*F./(h^3*c^2) .* ...
350 E_range.^2 ./ (exp( (E_range-V)/(k*T) ) - 1); % blackbody photon
351 flux [Photons/(sec*m^2*wavelength)]
352 end
353
354 % Calculate JV characteristics under Boltzmann approximation
355 function out = JV_boltz(V, E_range, EQE, isBB, flux)
356 if isBB
357 Jphoton = -e*abs(trapz(E_range, EQE.*bb(E_range, Fsun, Tsun, 0)));
358 else
359 Jphoton = -e*abs(trapz(E_range, EQE.*flux));
360 end
361 Jrad = -e*abs(trapz(E_range, EQE.*bb(E_range, Fcell, Tcell, 0)))*(exp(V./(k
362 *Tcell))-1);
363 out = Jphoton - Jrad;
364 end
365 end

```

## Listing D.3: Transfer Matrix Code for Monolayer Excitonic Absorbers

```

1 % 1D, Normal Incidence, Transfer Matrix Method
2 % Accounting for TMDC as a sheet conductivity parametrized by a Lorentzian
3 % Also account for absorption in individual layers
4 %
5 % Assumed structure is GaS/Mica/TMDC/Mica/Ag. Performs the following sweeps:
6 %
7 % - Sweeps thickness of GaS and Mica
8 % - Sweeps radiative and non-radiative rates of Exciton
9 % - Examines the absorption spectra at either the optimum thickness or the
10 % specified thickness (if thickness sweep not ran)
11 % - Examines the Electric Field Profile at either the optimum thickness or
12 % the specified thickness (if thickness sweep not ran). Requires running
13 % absorption spectra calculation.
14 % - Performs a Lorentzian total linewidth fit as the non-radiative rate is
15 % varied.
16 %
17 % Joeson Wong
18 % Last Updated: 11/14/2021
19
20 %& Load in Data and Initialize Variables
21
22 % load material data
23 clear all;
24 close all;
25 a = load('Au_nk.mat');
26 b = load('Ag_nk.mat');
27
28 % wavelengths of interest
29 lambda = 550e-9:1e-9:700e-9; % Wavelengths of interest (units of m^-1)
30 Ag_interp_ntilde = interp1(b.lambda, b.Ag_interp_ntilde, lambda);
31
32 % physical constants
33 c = 299792458; % [m/s], speed of light
34 ce = 1.60217656535e-19; % charge of electron, [C or J/eV]
35 hbar = 1.054571817e-34; % reduced Planck's constant, [J-s]
36 mu0 = 4*pi*1e-7; % [Henry/meter], permeability of free space
37 eps0 = 8.854187821e-12; % [Farads/meter], permittivity of free space
38 G0 = 2*ce^2/(2*pi*hbar); % 1/Ohms
39 n_GaS = 2.7;
40 n_Mica = 1.55;
41 n_SiO2 = 1.49;
42
43 % load and define TMDC (WS2)/hBN data
44 gamma_r_default = 4.11e-3;
45 gamma_nr_default = 38.6e-3;
46 omega_exc_default = 2.01; % [eV]
47 omega_peak = omega_exc_default*ce./hbar; % frequency, in units of rad/s
48 lambda_peak = 2*pi*c./omega_peak; % wavelength
49 k_peak = find(abs(lambda-lambda_peak)*1e9<mean(abs(diff(lambda))*1e9)/2); % wavelength index of peak
50 omega_energy = 2*pi*hbar*c./lambda./ce; % frequency, in units of energy
51 sigma_s = fun_exc_sigma(gamma_r_default, gamma_nr_default, omega_energy,
                           omega_exc_default); % conductivity of TMDC, in [1/Ohms]

```

```

52
53 % define thicknesses
54 d1 = 58e-9; % top GaS
55 d2 = 99e-9; % top Mica
56 d3 = 77e-9; % bottom Mica
57 d4 = 0e-9; % bottom SiO2, if any
58 thicknesses = [d1, d2, d3, d4]; %thickness of each layer
59 z = cumsum([0,thicknesses]); % units of [m], z position of layers. Start at z = 0.
60
61 % define what to calculate
62 doThickSweep = false;
63 doGamSweep = false;
64 doSpectraCalc = true;
65 doFieldPlot = true;
66 doGamNR_FWHM = true;
67
68 % definition of layers, each layer is a separate column
69 ntilde = [ones(length(lambda), 1), ... %first layer, which is air usual
70 n_GaS*ones(length(lambda), 1), ...
71 n_Mica*ones(length(lambda), 1), ...
72 n_Mica*ones(length(lambda), 1), ...
73 n_SiO2*ones(length(lambda), 1), ...
74 reshape(Ag_interp_ntilde, [length(lambda), 1])...
75 ]; % last layer is substrate/air, should have length(t)+2 number of layers
76
77 % Stack ordering is: [ntilde(1), hasTMDC, ntilde(2), hasTMDC, ...]
78 % ntilde(1) usually air. hasTMDC(1) is a layer of TMDC between air and
79 % first layer of dielectric if hasTMDC(1) = 1. Otherwise, nothing at
80 % interface.
81 hasTMDC = [0,0,1,0,0,0]; % 1 if interface has graphene, 0 if no graphene. There are
82 % length(z) number of interfaces.
83 ParIndex = [1,2,4,5,6];
84 ActIndex = 3;
85
86 % Define normalized E-Field intensity for plane waves
87 ElectricIntensity = @(z, An, Bn, qp) abs(An)^2*exp(1i*z*(qp - conj(qp))) + ...
88 abs(Bn)^2*exp(-1i*z*(qp - conj(qp))) + ...
89 2*real(An*conj(Bn)*exp(1i*z*(qp + conj(qp))));
```

90 % Some simple error Checking

91 if length(hasTMDC) ~= length(z)

92 error('Make sure the number of TMDC locations matches number of interfaces');

93 elseif length(thicknesses)+2 ~= size(ntilde,2)

94 error('Make sure you have specified a thickness for each layer');

95 end

96

97 if doFieldPlot

98 if ~doSpectraCalc

99 error('Make sure to perform spectrum calculation before field calculation');

100 end

101 end

102

103 %% Sweep top Metal and hBN Thicknesses

```

104
105 if doThickSweep
106 d1 = 0e-9:1e-9:120e-9;
107 d2 = 40e-9:1e-9:140e-9;
108 d3 = 30e-9:1e-9:130e-9;
109 TotalAbs = zeros(length(d1), length(d2), length(d3));
110 AbsTMDC = TotalAbs;
111 sigma_exc = fun_excsigma(gamma_r_default, gamma_nr_default, 0,
112     omega_exc_default, omega_exc_default); % conductivity of TMDC, in [1/Ohms]
113 maxAbsTMDC = 0; % for finding max active layer absorption
114 d1_max = 0;
115 d2_max = 0;
116 d3_max = 0;
117 for idx_d1 = 1:length(d1)
118     for idx_d2 = 1:length(d2)
119         for idx_d3 = 1:length(d3)
120             thicknesses = [d1(idx_d1), d2(idx_d2), d3(idx_d3), d4]; %
121             thickness of each layer
122             z = cumsum([0,thicknesses]); % units of [m], z position of
123             layers. Start at z = 0.
124
125             % first layer is air, coordinates are such that the air-
126             % dielectric
127             % stack starts at z = 0
128             for j = 1:length(z)
129                 q = 2*pi*ntilde(k_peak,j)/lambda_peak;
130                 qp = 2*pi*ntilde(k_peak,j+1)/lambda_peak;
131                 J = 1/2*[exp(1i*(q - qp)*z(j)) * (1+(q-omega_peak*mu0*
132                     sigma_exc*hasTMDC(j))/qp) , exp(-1i*(q + qp)*z(j)) *
133                     (1-(q+omega_peak*mu0*sigma_exc*hasTMDC(j))/qp); ...
134                     exp(1i*(q + qp)*z(j)) * (1-(q-omega_peak*mu0*sigma_exc*
135                         hasTMDC(j))/qp) , exp(-1i*(q - qp)*z(j)) * (1+(q+
136                         omega_peak*mu0*sigma_exc*hasTMDC(j))/qp)*J];
137             end
138             r = -J(2,1)/J(2,2); % reflection amplitude
139             TotalAbs(idx_d1, idx_d2, idx_d3) = 1-abs(r).^2;
140
141             % Calculate absorption and E-field in individual layers, go
142             % through
143             % layers again using the fact that we start with [1;r] for the
144             % field amplitude
145
146             % Coefficients of E-field in first layer, e.g. air
147             A(1:2,1) = [1;r];
148             for j = 1:length(z)
149                 q = 2*pi*ntilde(k_peak,j)/lambda_peak;
150                 qp = 2*pi*ntilde(k_peak,j+1)/lambda_peak;
151                 Jn = 1/2*[exp(1i*(q - qp)*z(j)) * (1+(q-omega_peak*mu0*
152                     sigma_exc*hasTMDC(j))/qp) , exp(-1i*(q + qp)*z(j)) *
153                     (1-(q+omega_peak*mu0*sigma_exc*hasTMDC(j))/qp); ...
154                     exp(1i*(q + qp)*z(j)) * (1-(q-omega_peak*mu0*sigma_exc*
155                         hasTMDC(j))/qp) , exp(-1i*(q - qp)*z(j)) * (1+(q+
156                         omega_peak*mu0*sigma_exc*hasTMDC(j))/qp)*J];
157             end

```

```

147          omega_peak*mu0*sigma_exc*hasTMDC(j))/qp)];
148
149          A(1:2, j+1) = Jn*A(1:2, j); % update E-field coefficients
150
151          % Absorption in TMDC
152          if hasTMDC(j)
153              AbstMDC(idx_d1, idx_d2, idx_d3) = real(sigma_exc)/(c*
154                  ntilde(k_peak,1)*eps0)*ElectricIntensity(z(j),A(1,
155                  j+1), A(2, j+1), qp);
156          end
157
158          if AbsTMDC(idx_d1, idx_d2, idx_d3) > maxAbsTMDC
159              d1_max = d1(idx_d1);
160              d2_max = d2(idx_d2);
161              d3_max = d3(idx_d3);
162              maxAbsTMDC = AbsTMDC(idx_d1, idx_d2, idx_d3);
163          end
164
165          FigSpecX = figure;
166          surf(d1*1e9, d2*1e9, transpose(squeeze(AbsTMDC(:, :, abs(d3-d3_max)<mean(abs(
167              diff(d3))/2))));;
168          view([0, 90]);
169          shading interp; axis tight;
170          daspect([1, 1, 1]);
171          xlabel('Top GaS Thickness (nm)');
172          ylabel('Top Mica Thickness (nm)');
173          axis square; box on;
174          hc = colorbar; xlabel(hc, 'Peak TMDC Absorption');
175          colormap('parula'); caxis([0, 1]);
176
177          FigSpecY = figure;
178          surf(d2*1e9, d3*1e9, transpose(squeeze(AbsTMDC(abs(d1-d1_max)<mean(abs(diff(d1
179              ))/2,:,:))));;
180          view([0, 90]);
181          shading interp; axis tight;
182          daspect([1, 1, 1]);
183          xlabel('Top Mica Thickness (nm)');
184          ylabel('Bottom Mica Thickness (nm)');
185          axis square; box on;
186          hc = colorbar; xlabel(hc, 'Peak TMDC Absorption');
187          colormap('parula'); caxis([0, 1]);
188
189          FigSpecZ = figure;
190          surf(d1*1e9, d3*1e9, transpose(squeeze(AbsTMDC(:, abs(d2-d2_max)<mean(abs(diff(
191              d2))/2,:))));;
192          view([0, 90]);
193          shading interp; axis tight;
194          daspect([1, 1, 1]);
195          xlabel('Top GaS Thickness (nm)');
196          ylabel('Bottom Mica Thickness (nm)');
197          axis square; box on;
198          hc = colorbar; xlabel(hc, 'Peak TMDC Absorption');

```

```

196 colormap('parula'); caxis([0, 1]);
197
198
199 figure;
200 plot(d1*1e9, squeeze(AbsTMDC(:, abs(d2-d2_max)<mean(abs(diff(d2)))/2, abs(d3-
201 d3_max)<mean(abs(diff(d3))/2)), 'LineWidth', 1.5);
202 axis tight;
203 xlabel('Top GaS Thickness (nm)');
204 ylabel('Excitonic Absorbance');
205 axis square; box on;
206
207 figure;
208 plot(d2*1e9, squeeze(AbsTMDC(abs(d1-d1_max)<mean(abs(diff(d1)))/2, :, abs(d3-
209 d3_max)<mean(abs(diff(d3))/2)), 'LineWidth', 1.5);
210 axis tight;
211 xlabel('Top Mica Thickness (nm)');
212 ylabel('Excitonic Absorbance');
213 axis square; box on;
214
215 figure;
216 plot(d3*1e9, squeeze(AbsTMDC(abs(d1-d1_max)<mean(abs(diff(d1)))/2, abs(d2-
217 d2_max)<mean(abs(diff(d2))/2, :)), 'LineWidth', 1.5);
218 axis tight;
219 xlabel('Bottom Mica Thickness (nm)');
220 ylabel('Excitonic Absorbance');
221 axis square; box on;
222
223 % if ran, set d1,d2,d3 to optimal values
224 d1 = d1_max;
225 d2 = d2_max;
226 d3 = d3_max;
227 thicknesses = [d1,d2,d3,d4]; %thickness of each layer
228 z = cumsum([0,thicknesses]); % units of [m], z position of layers. Start at z
229 = 0.
230
231 end
232
233 %& Peak Absorption for varying gamma_nr, gamma_r
234 if doGamSweep
235 gamma_r = [1e-3, 3e-3, 5e-3];
236 gamma_nr = 0.2e-3:0.2e-3:50e-3;
237 omega_peak = omega_exc_default*ce./hbar; % frequency, in units of rad/s
238 lambda_peak = 2*pi*c./omega_peak; % wavelength
239 k_peak = find(abs(lambda-lambda_peak)<mean(abs(diff(lambda))/2));
240 TotalAbs = zeros(length(gamma_r), length(gamma_nr));
241 AbsTMDC = TotalAbs;
242 FigSpec2 = figure; hold on;
243 legH = zeros(length(gamma_r), 1);
244 for idx_gam_r = 1:length(gamma_r)
    for idx_gam_nr = 1:length(gamma_nr)
        sigma_exc = fun_excsigma(gamma_r(idx_gam_r), gamma_nr(idx_gam_nr), 0,
        omega_exc_default, omega_exc_default); % conductivity of TMDC, in
        [1/Ohms]
    end
end

```

```

245 J = [1, 0 ;
246     0, 1]; % initialize J as identity matrix
247
248 % first layer is air, coordinates are such that the air-dielectric
249 % stack starts at z = 0
250 for j = 1:length(z)
251     q = 2*pi*ntilde(k_peak,j)/lambda_peak;
252     qp = 2*pi*ntilde(k_peak,j+1)/lambda_peak;
253     J = 1/2*[exp(1i*(q - qp)*z(j)) * (1+(q-omega_peak*mu0*sigma_exc*
254         hasTMDC(j))/qp) , exp(-1i*(q + qp)*z(j)) * (1-(q+omega_peak*
255         mu0*sigma_exc*hasTMDC(j))/qp); ...
256         exp(1i*(q + qp)*z(j)) * (1-(q-omega_peak*mu0*sigma_exc*hasTMDC(j))
257             /qp) , exp(-1i*(q - qp)*z(j)) * (1+(q+omega_peak*mu0*
258             sigma_exc*hasTMDC(j))/qp)]*J;
259 end
260
261 % reflection amplitude & transmission
262 r = -J(2,1)/J(2,2);
263 TotalAbs(idx_gam_r, idx_gam_nr) = 1 - abs(r).^2 ; % assuming T = 0
264
265 % Calculate absorption and E-field in individual layers, go through
266 % layers again using the fact that we start with [1;r] for the
267 % field amplitude
268
269 % Coefficients of E-field in first layer, e.g. air
270 A(1:2,1) = [1;r];
271 for j = 1:length(z)
272     q = 2*pi*ntilde(k_peak,j)/lambda_peak;
273     qp = 2*pi*ntilde(k_peak,j+1)/lambda_peak;
274     Jn = 1/2*[exp(1i*(q - qp)*z(j)) * (1+(q-omega_peak*mu0*sigma_exc*
275         hasTMDC(j))/qp) , exp(-1i*(q + qp)*z(j)) * (1-(q+omega_peak*
276         mu0*sigma_exc*hasTMDC(j))/qp); ...
277         exp(1i*(q + qp)*z(j)) * (1-(q-omega_peak*mu0*sigma_exc*hasTMDC(j)
278             /qp) , exp(-1i*(q - qp)*z(j)) * (1+(q+omega_peak*mu0*
279             sigma_exc*hasTMDC(j))/qp)];
280     A(1:2, j+1) = Jn*A(1:2, j); % update E-field coefficients
281     % Absorption in TMDC
282     if hasTMDC(j)
283         AbsTMDC(idx_gam_r, idx_gam_nr) = real(sigma_exc)/(c*ntilde(
284             k_peak,1)*eps0)*ElectricIntensity(z(j),A(1,j+1), A(2, j+1)
285             , qp);
286     end
287 end
288
289 end
290
291 a = plot(gamma_nr*1e3, TotalAbs(idx_gam_r,:), 'LineWidth', 1.5);
292 plot(gamma_nr*1e3, AbsTMDC(idx_gam_r,:), '--', 'LineWidth', 1.5, 'Color',
293 a.Color);
294 legH(idx_gam_r) = a;
295
296 end
297 box on;
298 xlabel('$\gamma_{nr}$ (meV)', 'interpreter', 'latex'); ylabel('Absorbance');
299 hleg = legend(legH, string(gamma_r*1e3), 'location', 'southeast');
300 title(hleg, '$\gamma_r$ (meV)', 'interpreter', 'latex');
301
302 end

```

```

289
290 if doSpectraCalc
291 % Initialization of matrices
292 TotalAbs = zeros(length(lambda), 1); % total absorption
293
294 % absorption in individual layers, add in additional layers for graphene,
295 % ignore air
296 AbsLayer = zeros(length(lambda), min(size(ntilde))+sum(hasTMDC)-1);
297 A = zeros(2*length(lambda), min(size(ntilde))); % E-field coefficients, odd
298 % coefficients are Ai, even coefficients are Bi
299
300 % Calculate spectrally, monochromatic wave assumption
301 for k = 1: length(lambda)
302
303     J = [1, 0 ;
304           0, 1]; % initialize J as identity matrix
305
306     omega = 2*pi*c./lambda(k); % frequency, useful for not repeating
307     % calculations.
308
309     % first layer is air, coordinates are such that the air-dielectric
310     % stack starts at z = 0
311     for j = 1:length(z)
312         q = 2*pi*ntilde(k,j)/lambda(k);
313         qp = 2*pi*ntilde(k,j+1)/lambda(k);
314         J = 1/2*[exp(1i*(q - qp)*z(j)) * (1+(q-omega*mu0*sigma_s(k)*
315             hasTMDC(j))/qp) , exp(-1i*(q + qp)*z(j)) * (1-(q+omega*mu0*
316             sigma_s(k)*hasTMDC(j))/qp); ...
317             exp(1i*(q + qp)*z(j)) * (1-(q-omega*mu0*sigma_s(k)*hasTMDC(j))/qp)
318             , exp(-1i*(q - qp)*z(j)) * (1+(q+omega*mu0*sigma_s(k)*
319             hasTMDC(j))/qp)]; J;
320     end
321
322     % reflection amplitude & transmission
323     r = -J(2,1)/J(2,2);
324     TotalAbs(k) = 1 - abs(r).^2 ; % assuming T = 0
325
326     % Calculate absorption and E-field in individual layers, go through
327     % layers again using the fact that we start with [1;r] for the
328     % field amplitude
329
330     % Coefficients of E-field in first layer, e.g. air
331     A(2*k-1:2*k,1) = [1;r];
332
333     for j = 1:length(z)
334         q = 2*pi*ntilde(k,j)/lambda(k);
335         qp = 2*pi*ntilde(k,j+1)/lambda(k);
336         Jn = 1/2*[exp(1i*(q - qp)*z(j)) * (1+(q-omega*mu0*sigma_s(k)*
337             hasTMDC(j))/qp) , exp(-1i*(q + qp)*z(j)) * (1-(q+omega*mu0*
338             sigma_s(k)*hasTMDC(j))/qp); ...
339             exp(1i*(q + qp)*z(j)) * (1-(q-omega*mu0*sigma_s(k)*hasTMDC(j))/qp)
340             , exp(-1i*(q - qp)*z(j)) * (1+(q+omega*mu0*sigma_s(k)*
341             hasTMDC(j))/qp)];
342
343         A(2*k-1:2*k, j+1) = Jn*A(2*k-1:2*k, j); % update E-field

```



```

372
373 % Generate Appropriats Points for sampling , numlinspacepts per layer
374 zPoints = [];
375 for i = 1:numLayers
376     % add extra point , to remove later
377     zLayer = linspace(LayerCoordinates(i), LayerCoordinates(i+1),
378                         numlinspacePts+1);
379     zLayer(end) = []; % remove end pt, to avoid repeat values
380     zPoints = [zPoints , zLayer];
381 end
382
383 for lam_idx = 1:length(lambda)
384     for i = 1:numLayers
385         EFieldDist(lam_idx , (numlinspacePts*(i-1)+1:numlinspacePts*i)) = ...
386             ElectricIntensity (zPoints (numlinspacePts*(i-1)+1:numlinspacePts*i) , ...
387             A(2*lam_idx-1, i+1) , A(2*lam_idx , i+1) , 2*pi*ntilde(lam_idx , i+1)/
388             lambda(lam_idx));
389     end
390 end
391
392 % Efield contour Plot
393 figure;
394 surf(lambda*1e9 , zPoints*1e9 , EFieldDist ');
395 xlabel('Wavelength (nm)');
396 ylabel('Distance from surface of heterostructure (nm)');
397 view([0 , 90]);
398 axis tight; shading interp;
399 hc = colorbar; xlabel(hc, '$|E|^2/|E_0|^2$' , 'interpreter' , 'latex');
400 colormap(parula);
401
402 % Efield at the exciton peak position
403 figure; hold on;
404 plot(zPoints*1e9 , EFieldDist(k_peak , :) , 'k-' , 'LineWidth' , 1.5);
405 ylimsplot = ylim;
406 xlimsplot = xlim;
407 yvals = [ylimsplot(1) , ylimsplot(1) , ylimsplot(2) , ylimsplot(2)];
408 MetalColor = [0.2 , 0.2 , 0.2];
409 GaSColor = [0.2 , 0.7 , 0.7];
410 TMDCColor = [1 , 0.3 , 0.1];
411 MicaColor = [0.1 , 0.9 , 0.2];
412 SiO2Color = [0.7 , 0.7 , 0.7];
413 FaceColors = [GaSColor; MicaColor; TMDCColor; MicaColor; SiO2Color; MetalColor
414     ];
415 FaceAlpha = 0.5;
416 TMDC_thick = 0.7e-9;
417
418 for i = 1:numLayers
419     if hasTMDC(i)
420         xvals = [LayerCoordinates(i)-TMDC_thick/2 , LayerCoordinates(i)+
421             TMDC_thick/2 , LayerCoordinates(i)+TMDC_thick/2 , LayerCoordinates(i)
422             -TMDC_thick/2];
423         patch(xvals*1e9 , yvals , FaceColors(i+sum(hasTMDC(1:i))-1,:) , 'EdgeColor
424             ' , 'none');
425         xvals = [LayerCoordinates(i) , LayerCoordinates(i+1) , LayerCoordinates(i
426             +1) , LayerCoordinates(i)];

```

```

420     patch(xvals*1e9, yvals, FaceColors(i+sum(hasTMDC(1:i)),:), 'FaceAlpha',
421           FaceAlpha, 'EdgeColor', 'none');
422     else
423         xvals = [LayerCoordinates(i), LayerCoordinates(i+1), LayerCoordinates(i
424             +1), LayerCoordinates(i)];
425         patch(xvals*1e9, yvals, FaceColors(i+sum(hasTMDC(1:i)),:), 'FaceAlpha',
426               FaceAlpha, 'EdgeColor', 'none');
427     end
428     xlim([0, LayerCoordinates(end)*1e9]); box on;
429     xlabel('Distance from surface of heterostructure (nm)');
430     ylabel('$|E|^2/|E_0|^2$', 'interpreter', 'latex');
431
432 end
433
434 if doGamNR_FWHM
435     gamma_nr = 5e-3:1e-3:50e-3;
436
437     f_lorentz = @(x, xdata) x(1).*(x(3).^2./((x(2)-xdata).^2 + x(3).^2)) + x(4);
438     LB = [0, omega_exc_default.*0.95, 0, 0];
439     UB = [1, omega_exc_default.*1.05, 0.1, 1];
440     lsqOpts = optimoptions('lsqcurvefit', 'StepTolerance', 1e-18, '
441                           'FunctionTolerance', 1e-18, 'OptimalityTolerance', 1e-18, '
442                           'MaxFunctionEvaluations', 300);
443     ms_lsqOpts = optimoptions('lsqcurvefit', 'StepTolerance', 1e-6, '
444                               'FunctionTolerance', 1e-6, 'OptimalityTolerance', 1e-6, '
445                               'MaxFunctionEvaluations', 10);
446     num_MS_startpts = 500;
447     do_MS = false;
448
449     % Initialization of matrices
450     FWHM = zeros(1, length(gamma_nr)); % total absorption
451     AbsExc = zeros(length(lambda), length(gamma_nr));
452     TotalAbs = AbsExc;
453
454     fig_gamnr = figure;
455     for idx_gam_nr = 1:length(gamma_nr)
456         sigma_gam_nr = fun_excsigma(gamma_r_default, gamma_nr(idx_gam_nr), 0,
457             omega_energy, omega_exc_default); % conductivity of TMDC, in [1/Ohms]
458
459         % Calculate spectrally, monochromatic wave assumption
460         for k = 1: length(lambda)
461             J = [1, 0 ;
462                  0, 1]; % initialize J as identity matrix
463
464             omega = 2*pi*c./lambda(k); % frequency, useful for not repeating
465             % calculations.
466
467             % first layer is air, coordinates are such that the air-dielectric
468             % stack starts at z = 0
469             for j = 1:length(z)
470                 q = 2*pi*ntilde(k, j)/lambda(k);
471                 qp = 2*pi*ntilde(k, j+1)/lambda(k);

```

```

466      J = 1/2*[ exp(1i*(q - qp)*z(j)) * (1+(q-omega*mu0*sigma_gam_nr(
467          k)*hasTMDC(j))/qp) , exp(-1i*(q + qp)*z(j)) * (1-(q+
468          omega*mu0*sigma_gam_nr(k)*hasTMDC(j))/qp); ...
469          exp(1i*(q + qp)*z(j)) * (1-(q-omega*mu0*
470          sigma_gam_nr(k)*hasTMDC(j))/qp) , exp(-1i*(
471          q - qp)*z(j)) * (1+(q+omega*mu0*sigma_gam_nr(
472          k)*hasTMDC(j))/qp)]*J;
473      end
474
475      % reflection amplitude & transmission
476      r = -J(2,1)/J(2,2);
477      TotalAbs(k, idx_gam_nr) = 1 - abs(r).^2 ; % assuming T = 0
478
479      % Coefficients of E-field in first layer, e.g. air
480      A_gam_nr = [1; r];
481
482      for j = 1:length(z)
483          q = 2*pi*ntilde(k,j)/lambda(k);
484          qp = 2*pi*ntilde(k,j+1)/lambda(k);
485          Jn = 1/2*[ exp(1i*(q - qp)*z(j)) * (1+(q-omega*mu0*sigma_gam_nr(
486              k)*hasTMDC(j))/qp) , exp(-1i*(q + qp)*z(j)) * (1-(q+
487              omega*mu0*sigma_gam_nr(k)*hasTMDC(j))/qp); ...
488              exp(1i*(q + qp)*z(j)) * (1-(q-omega*mu0*
489              sigma_gam_nr(k)*hasTMDC(j))/qp) , exp(-1i*(
490              q - qp)*z(j)) * (1+(q+omega*mu0*sigma_gam_nr(
491              k)*hasTMDC(j))/qp)];
492
493          A_gam_nr = Jn*A_gam_nr; % update E-field coefficients
494
495          % Absorption in TMDC
496          if hasTMDC(j)
497              AbsExc(k, idx_gam_nr) = real(sigma_gam_nr(k))/(c*ntilde(k
498                  ,1)*eps0)*ElectricIntensity(z(j),A_gam_nr(1), A_gam_nr
499                  (2), qp);
500          end
501      end
502
503      xdata = 1239.84./(lambda*1e9);
504      ydata = reshape(TotalAbs(:, idx_gam_nr), size(xdata));
505
506      if idx_gam_nr == 1
507          x0 = [max(ydata), omega_exc_default, (gamma_r_default + gamma_nr(
508              idx_gam_nr))/2, min(ydata)];
509      end
510
511      if do_MS
512          stpts = [(UB(1)-LB(1))*rand(num_MS_startpts, 1) + LB(1), ...
513                  (UB(2)-LB(2))*rand(num_MS_startpts, 1) + LB(2), ...
514                  (UB(3)-LB(3))*rand(num_MS_startpts, 1) + LB(3), ...
515                  (UB(4)-LB(4))*rand(num_MS_startpts, 1) + LB(4)];
516
517          startpts = CustomStartPointSet(stpts);
518          problem = createOptimProblem('lsqcurvefit', 'objective', f_lorentz, '
519              x0', x0, ...

```

```

507     'xdata', xdata, 'ydata', ydata, 'lb', LB, 'ub', UB, 'options',
508     ms_lsqOpts);
509     ms = MultiStart;
510     x0 = run(ms, problem, startpts);
511 end
512
513 x_fit = lsqcurvefit(f_lorentz, x0, xdata, ydata, LB, UB, lsqOpts);
514 FWHM(idx_gam_nr) = 2*x_fit(3);
515 x0 = x_fit;
516
517 figure(fig_gamnr);
518 plot(xdata, ydata, 'k.', xdata, f_lorentz(x_fit, xdata), 'b--');
519 axis_gamnr = gca;
520 xlabel(axis_gamnr, 'Energy (eV)');
521 ylabel(axis_gamnr, 'Absorbance');
522 legend(axis_gamnr, {'Simulation', 'Fit'}, 'Location', 'NorthWest');
523 title(axis_gamnr, [ '\gamma_{nr}: ', num2str(round(gamma_nr(idx_gam_nr)*1e3
524     )), ' meV', ' ... ...
525     'Fitted \gamma_T: ', num2str(round(FWHM(idx_gam_nr)*1e3)), ' meV']);
526 drawnow;
527
528 end
529
530 figure;
531 plot(gamma_nr*1e3, FWHM*1e3, gamma_nr*1e3, (FWHM - gamma_nr)*1e3, 'LineWidth',
532     1.5);
533 axis square; box on;
534 xlabel(' \gamma_{nr} (meV)');
535 hleg = legend({' \gamma_T ', ' \gamma_T - \gamma_{nr} '}, 'Location',
536     'NorthWest');
537 ylabel(' \gamma (meV)');
538
539 % Make some spectral absorption plots
540 figure;
541 omega_peak = omega_exc_default*ce./hbar; % frequency, in units of rad/s
542 lambda_peak = 2*pi*c./omega_peak; % wavelength
543 k_peak = find(abs(lambda-lambda_peak)<mean(abs(diff(lambda)))/2);
544
545 plot(FWHM*1e3, TotalAbs(k_peak,:), 'k-', 'LineWidth', 1.5); hold on;
546 plot(FWHM*1e3, AbsExc(k_peak, :), 'k--', 'LineWidth', 1.5);
547 axis square; box on;
548 xlabel(' \gamma_T (meV)');
549 ylabel('Absorbance');
550
551 end
552
553 function exc_sigma = fun_exc_sigma(gamma_r, gamma_nr, omega, omega_exc)
554 % all omegas and gammas are with the same units, either in rad/s or energy.
555 % which only has a different of hbar, which is cancelled everywhere of
556 % relevance
557
558 ce = 1.60217656535e-19; % charge of electron, [C]
559 hbar = 1.054571817e-34; % reduced Planck's constant, [J-s]
560 sigma_0 = ce^2/(4*hbar); % conductance quantum, [1/Ohm]

```

```

558 alpha = 0.0072973525693; % fine structure constant, [unitless]
559 p0 = gamma_r./(4*pi*omega_exc*alpha); % oscillator strength, [unitless]
560
561 sigma_lorentz = 4*sigma_0*p0.*omega*1i./(omega - omega_exc + 1i*gamma_nr/2);
562
563 exc_sigma = sigma_lorentz;
564 end
565
566 function eps = GaS_epsilon(E)
567 default_fk = 94.0;
568 default_Ek = 4.86;
569 default_gammak = 0.0498;
570 default_eps_bg = 2.187;
571 eps = epsilon(default_fk, default_Ek, default_gammak, E, length(default_fk),
572 default_eps_bg);
573 end
574
575 function eps = epsilon(fk, Ek, gammak, E, N, eps_bg)
576 eps = eps_bg*ones(size(E));
577 for idx = 1:N
578     eps = eps + fk(idx)./(Ek(idx)^2-E.^2-1i*E*gammak(idx));
579 end
579 end

```

Listing D.4: PDE Solver and Fitting for Excitons coupled to Heat

```

1
2     function fit_and_solve_ExcitonSeebeck_v6
3
4     clear;
5     close all;
6     rng('default');
7
8     %% Load stroboSCAT Data
9     sample_data = load('stroboSCAT_encaps_data.mat');
10
11    %% Guesses for Parameters (x0)
12    muX0 = 0; % [cm^2/(V-s), exciton mobility]
13    S0 = 0; % [uV/K, Seebeck coefficient for excitons]
14    tauT0 = 10; % [ns], heat decay time
15    tauX0 = 10; % [ns], exciton lifetime
16    RA0 = 0; % [cm^2/s], Auger coefficient/Biexciton recombination rate
17    Pavg0 = 0.48; % [uW], time-averaged pump power, 480 nW for 1.85e13 generation
18
19    alpha0 = 1; % fitting parameter that scales the 520 and 705 data...
20
21    justplotx0 = true; % if true, only calculate using the x0 specified above
22
23    %% MultiStart Parameters
24    doMS = true; % perform multistart optimization if true
25    plotMSLive = true; % plot the "best" value and "live" value of optimization
26    num_MS_startpts = 1000; % number of multistart points
27
28    maxfunceval = 50;
29    OptimTol = 1e-6;
30    StepTol = 1e-6;
31    maxIter = 5e1;
32    FuncTol = 1e-6;
33    ms_lsqOpts = optimoptions('lsqcurvefit', 'MaxFunctionEvaluations', maxfunceval
34        , ...
35        'OptimalityTolerance', OptimTol, 'StepTolerance', StepTol, ...
36        'MaxIterations', maxIter, 'FunctionTolerance', FuncTol);
37
38    %% lsqcurvefit Parameters
39    maxfunceval = 1000;
40    OptimTol = 1e-18;
41    StepTol = 1e-15;
42    maxIter = 1e4;
43    FuncTol = 1e-12;
44    lsqOpts = optimoptions('lsqcurvefit', 'MaxFunctionEvaluations', maxfunceval, ...
45        'OptimalityTolerance', OptimTol, 'StepTolerance', StepTol, ...
46        'MaxIterations', maxIter, 'FunctionTolerance', FuncTol);
47
48    %% Fitting Bounds and Parameter Definitions
49    rphys_end = 3e-4; % [cm]
50    tphys_end = 10e-9; % [s]
51    xdata = sample_data.position_705;
52    ydata = [sample_data.stroboSCAT_520(:); sample_data.stroboSCAT_705(:)];
53    fun = @(x, xdata) fitfunc(x, xdata(:), ydata(:), sample_data.timepts, rphys_end,

```

```

      tphys_end);

53  LB = [1, 0, 0.01, 0.01, 0, 0, 0];
54  UB = [100, 1e3, 5, 5, 5, 50, 10];
55  x0 = [muX0, S0, tauT0, tauX0, RA0, Pavg0, alpha0];
56

57  %% Start the optimization and plotting
58  tic;
59  if justplotx0
60      xopt = x0;
61  else
62      if doMS % write custom MS
63
64          % initialize
65          if plotMSLive
66              fig_ms = figure;
67          end
68
69          best_resnorm = inf;
70          xbest = x0;
71          x_ms = zeros(num_MS_startpts, length(x0));
72          resnorm_ms = zeros(num_MS_startpts, 1);
73
74          % starting points are random points within the length(LB)-dimensional
75          % space, bounded by LB,UB
76          stpts = zeros(num_MS_startpts, length(x0));
77          for idx = 1:length(x0)
78              stpts(:, idx) = (UB(idx) - LB(idx)) * rand(num_MS_startpts, 1) + LB(idx)
79              ;
80          end
81
82          for idx = 1:num_MS_startpts
83              % try running a local optimizer for each point
84              try
85                  [x_ms(idx, :) , resnorm_ms(idx)] = lsqcurvefit(fun, stpts(idx, :),
86                      xdata, ydata, LB, UB, ms_lsqOpts);
87              catch
88                  resnorm_ms(idx) = inf;
89              end
90
91              % if a new best value is found, plot and save it.
92              if resnorm_ms(idx) < best_resnorm
93                  xbest = x_ms(idx, :);
94                  best_resnorm = resnorm_ms(idx);
95                  plotnewbest = true;
96              else
97                  plotnewbest = false;
98              end
99
100             if plotMSLive
101                 figure(fig_ms);
102                 semilogy(idx, resnorm_ms(idx), 'o', 'MarkerEdgeColor', 'b', 'MarkerFaceColor', 'b');
103                 hold on;
104                 semilogy(idx, best_resnorm, 'o', 'MarkerEdgeColor', 'r', 'MarkerFaceColor', 'r');
105                 xlabel('Fitting Iteration');

```

```

102     ylabel('Normalized Residual');
103     legend('Live', 'Best');
104     box on;
105     axis tight;
106     drawnow;
107
108     if plotnewbest
109         plotFittedData(xbest, xdata, ydata, sample_data.timepts, 1);
110         % plots the data, saves it, and closes it
111     end
112
113     % save parameters of optimization for each run
114     save(strcat(extractAfter(mfilename, 'Seebeck_'), '_MSfit_vals.mat')
115         , 'idx', 'num_MS_startpts', 'ms_lsqOpts', 'lsqOpts', 'rphys_end'
116         , 'tphys_end', ...
117         'LB', 'UB', 'xdata', 'ydata', 'best_resnorm', 'xbest', 'resnorm_ms', 'x_ms', 'stpts');
118
119     end
120     % run final optimization for "fine" tuning
121     xopt = lsqcurvefit(fun, xbest, xdata, ydata, LB, UB, lsqOpts);
122
123 else
124     % run only one optimization
125     xopt = lsqcurvefit(fun, x0, xdata, ydata, LB, UB, lsqOpts);
126 end
127
128 disp(['Total time for optimization is: ', num2str(toc), ' seconds']);
129
130
131
132
133
134
135
136
137
138
139
140
141
142
143
144
145
146
147
148
149
150
151

```

function plotFittedData(xopt, xdata, ydata, timepts, closefigs)

%&% Draw the plots on top of data

yfit = fitfunc(xopt, xdata, ydata, timepts, rphys\_end, tphys\_end);

str = {[ '\mu\_X: ', num2str(round(xopt(1),3)), ' cm^2/(V-s)' ]
 [ 'S: ', num2str(round(xopt(2),3)), ' \muV/K' ]
 [ '\tau\_T: ', num2str(round(xopt(3),3)), ' ns' ]
 [ '\tau\_X: ', num2str(round(xopt(4),3)), ' ns' ]
 [ 'R\_A: ', num2str(round(xopt(5),3)), ' cm^2/s' ]
 [ 'P\_{avg}: ', num2str(round(xopt(6),3)), ' \muW' ]
 [ '\alpha: ', num2str(round(xopt(7),3))]};

line\_colors = linspecer(length(timepts));

fig520 = figure;

fig520.Position = [200, 50, 600, 500];

for idx2 = 1:length(timepts)

yline\_data = ydata((idx2-1)\*length(xdata)+1:idx2\*length(xdata));

yline\_fit = yfit((idx2-1)\*length(xdata)+1:idx2\*length(xdata));

h = subplot(4,3,idx2);
 plot(xdata, yline\_data, 'o', 'Color', line\_colors(idx2,:)); hold on;

```

152 plot(xdata, yline_fit, ' -', 'Color', line_colors(idx2,:));
153 title(h,[num2str(timepts(idx2)), ' ns']);
154 pos = get(h, 'Position');
155 set(h, 'Position', [pos(1) + 0.06, pos(2) - 0.05, pos(3:end)]);
156 end
157 dim = [0, 0, 0.5, 1];
158 annotation('textbox', dim, 'FontSize', 7, 'String', str, 'interpreter', 'tex', 'LineStyle', 'none');
159 sgttitle('520 nm Probe');
160 try
161     saveas(gcf, strcat(extractAfter(mfilename, 'Seebeck_'), '_520_fit'), 'png');
162 catch
163     disp(['File ', strcat(extractAfter(mfilename, 'Seebeck_'), '_520_fit.'), ' did not save']);
164 end
165
166 fig705 = figure;
167 fig705.Position = [200, 50, 600, 500];
168 for idx2 = length(timepts)+1:2:length(timepts)
169     yline_data = ydata((idx2-1)*length(xdata)+1:idx2*length(xdata));
170     yline_fit = yfit((idx2-1)*length(xdata)+1:idx2*length(xdata));
171
172     h = subplot(4,3,idx2 - length(timepts));
173     plot(xdata, yline_data, 'o', 'Color', line_colors(idx2-length(timepts),:));
174     hold on;
175     plot(xdata, yline_fit, ' -', 'Color', line_colors(idx2-length(timepts),:));
176     title(h, [num2str(timepts(idx2 - length(timepts))), ' ns']);
177     pos = get(h, 'Position');
178     set(h, 'Position', [pos(1) + 0.06, pos(2) - 0.05, pos(3:end)]);
179 end
180 dim = [0, 0, 0.5, 1];
181 annotation('textbox', dim, 'FontSize', 7, 'String', str, 'interpreter', 'tex', 'LineStyle', 'none');
182 sgttitle('705 nm Probe');
183 try
184     saveas(gcf, strcat(extractAfter(mfilename, 'Seebeck_'), '_705_fit'), 'png');
185 catch
186     disp(['File ', strcat(extractAfter(mfilename, 'Seebeck_'), '_705_fit.'), ' did not save']);
187 end
188
189 %&% Examine "Real" Populations from calculations
190 [Nout, Tout, rout, tout, t0_idx, t0_sim, ~, ~] = solveExcitonSeebeck(
191     rphys_end, tphys_end, xopt);
192 Nout = Nout(t0_idx:end,:);
193 Tout = Tout(t0_idx:end,:);
194 tout = tout(t0_idx:end) - t0_sim*1e9; % [ns]
195
196 excpop = figure;
197 for idx2 = 1:length(timepts)
198     N_phys_slice = interp2(rout, tout, Nout, xdata, timepts(idx2));

```

```

198     h = subplot(4,3,idx2);
199     plot(xdata, N_phys_slice, ' - ', 'Color', line_colors(idx2,:), ' '
200             LineWidth', 2);
201     title(h,[ num2str(timepts(idx2)), ' ns']);
202 end
203 sgtitle('Exciton Population (1/cm^{2})');
204 try
205     saveas(excpop, strcat(extractAfter(mfilename, 'Seebeck_'), ' '
206                             '_fitted_exc'), 'png');
207 catch
208     disp(['File ', strcat(extractAfter(mfilename, 'Seebeck_'), ' '
209             '_fitted_exc.png'), ' did not save']);
210 end
211
212 temppop = figure;
213 for idx2 = 1:length(timepts)
214     T_phys_slice = interp2(rout, tout, Tout, xdata, timepts(idx2));
215     h = subplot(4,3,idx2);
216     plot(xdata, T_phys_slice, ' - ', 'Color', line_colors(idx2,:), ' '
217             LineWidth', 2);
218     title(h,[ num2str(timepts(idx2)), ' ns']);
219     ytickformat('%.1f');
220 end
221 sgtitle('Temperature (K)');
222 try
223     saveas(temppop, strcat(extractAfter(mfilename, 'Seebeck_'), ' '
224                             '_fitted_temp'), 'png');
225 catch
226     disp(['File ', strcat(extractAfter(mfilename, 'Seebeck_'), ' '
227             '_fitted_temp.png'), ' did not save']);
228 end
229
230 if closefigs
231     close(fig520);
232     close(fig705);
233     close(excpop);
234     close(temppop);
235 end
236
237
238 function y = fitfunc(x, xdata, ydata, tpts, rphys_end, tphys_end)
239
240     alpha = x(end-1); % used for fitting
241
242     [Nphys, Tphys,rphys,tphys,zero_idx,t0, N0, T0] = solveExcitonSeebeck(
243         rphys_end, tphys_end, x);
244
245     tphys_new = tphys(zero_idx:end) - t0*1e9; % [ns]
246
247     % 520 nm Calculation
248     space_convo_520 = 0.45*0.52/1.4; % (0.45)*wavelength./NA
249     time_convo_520 = 0.108./2.355; % [ns], FWHM = 108 ps
250

```

```

246 % Time Convolution
247 Tconv520 = gauss_time_convolution(tphys, rphys, Tphys/T0-1, time_convolution_520);
248
249 % Redefine t = 0 to be at t0 after time convolution
250 Tconv520 = Tconv520(zero_idx:end,:);
251
252 % Space convolution
253 Tconv520 = gauss_space_convolution(tphys_new, rphys, Tconv520, space_convolution_520
254 );
255
256 % Sampling to be the same as the dataset
257 [xmesh, tmesh] = meshgrid(xdata, tpts);
258 Tt_520 = interp2(rphys, tphys_new, Tconv520, xmesh, tmesh);
259 Tt_520 = Tt_520';
260 Tt_520 = Tt_520(:);
261
262
263 beta = -trapz(xdata, ydata(1:length(xdata)))/trapz(xdata, Tt_520(1:length(
264 xdata))); % Assume beta to be the first equal to the point at first
265 time point/space point
266 I520 = -beta*Tt_520;
267
268 %&% 705 nm Calculation
269 space_convolution_705 = 0.45*0.705/1.4; % (0.45)*wavelength./NA
270 time_convolution_705 = 0.60./2.355; % [ns], FWHM = 60 ps
271
272 % Time Convolution
273 Tconv705 = gauss_time_convolution(tphys, rphys, Tphys/T0-1, time_convolution_705);
274 Nconv705 = gauss_time_convolution(tphys, rphys, Nphys/N0, time_convolution_705); %
275 % need to make sure tphys and probe_pulse_time_width have same units
276
277 % Redefine t = 0 to be at t0 after time convolution
278 Nconv705 = Nconv705(zero_idx:end,:);
279 Tconv705 = Tconv705(zero_idx:end,:);
280
281 % Space convolution
282 Nconv705 = gauss_space_convolution(tphys_new, rphys, Nconv705, space_convolution_705
283 );
284 Tconv705 = gauss_space_convolution(tphys_new, rphys, Tconv705, space_convolution_705
285 );
286
287 % Sampling to be the same as the dataset
288 Nt_705 = interp2(rphys, tphys_new, Nconv705, xmesh, tmesh);
289 Tt_705 = interp2(rphys, tphys_new, Tconv705, xmesh, tmesh);
290
291 % turn into column vector with the time traces stacked vertically
292 Nt_705 = Nt_705';
293 Nt_705 = Nt_705(:);
294 Tt_705 = Tt_705';
295 Tt_705 = Tt_705(:);
296 numDatapts = length(xdata)*length(tpts)+1;
297
298 % gamma = trapz(xdata, ydata(numDatapts:numDatapts+length(xdata)))/
299 % trapz(xdata, Nt_705(1:length(xdata)) - alpha*beta*Tt_705(1:length(xdata)));

```

```

294 % I705 = gamma*(Nt_705 - alpha*beta*Tt_705); % gamma here is like the
295 % alpha parameter from Hannah
296
297 gamma = trapz(xdata, ydata(numDatapts:numDatapts-1+length(xdata)) + alpha*
298 % beta*Tt_705(1:length(xdata)))./trapz(xdata, Nt_705(1:length(xdata)));
299 I705 = gamma*Nt_705 - alpha*beta*Tt_705; % gamma here is like the alpha
300 % parameter from Hannah
301
302 y = [I520; I705]; % 520 data, followed by 705 data, all time data points
303
304
305 function [Nphys, Tphys, rphys, tphys, zero_idx, t0, N0, T0] =
306 % solveExcitonSeebeck(rphys_end, tphys_end, x)
307
308 % Rewrite so that most numbers are of order 1...
309 muX = x(1); % [cm^2/(V-s)], exciton mobility
310 S = x(2)*1e-6; % [V/K], Seebeck coefficient for excitons
311 tauT = x(3)*1e-9; % [s], heat decay time
312 tauX = x(4)*1e-9; % [s], exciton lifetime
313 RA = x(5); % [cm^2/s], Auger-Meitner/Biexciton Rate
314 Pavg = x(6)*1e-6; % [W], Time-averaged pump power
315
316 %%% Fundamental Constants
317 kb = 1.38e-23; % [J/K, Boltzmann Constant]
318 q = 1.6e-19; % [C, Fundamental unit of Charge]
319
320 %%% Assumed Fixed Parameters
321 DT = 0.15; % [cm^2/s], heat diffusivity
322 heat_cap = 0.54e-6; % [J/(cm^2-K)] [mass heat cap*density*thickness]
323 Ephot = 1239.8/440*q; % 440 nm Exc, [J]
324 T0 = 300; % [K, equilibrium temperature]
325 Eg = 1.38; % [eV]
326 Abs = 0.35; % unitless absorbance, at laser wavelength
327 frep = 16e6; % 16 MHz, [Hz or 1/s]
328
329 LT = sqrt(DT*tauT); % [cm], thermal diffusion length
330 lambda_exc = 440e-7; % [cm]
331 NA = 1.4;
332 pump_pulse_phys_width = 0.45*lambda_exc/NA; % [cm], laser pulse width
333 sigpr = pump_pulse_phys_width/LT; % [unitless, but factors of sqrt(DT*tauT)
334 % equivalent to spot size]
335 sigpt = 72e-12./2.355; % [s], pump pulse width, in time, FWHM = 72 ps
336
337 %%% Derived Parameters
338 % N0 = 1.85e13; % Pavg*Abs/(Ephot*frep)/(2*pi*pump_pulse_phys_width^2);
339 % [1/cm^2, integrated carrier density excited by laser]
340 N0 = Pavg*Abs/(Ephot*frep)/(2*pi*pump_pulse_phys_width^2); % [1/cm^2,
341 % integrated carrier density excited by laser]
342 xi = muX*kb*T0/(q*DT); % [unitless], ratio of exciton/heat diffusivity
343 chi = tauT/tauX; % [unitless], ratio of lifetimes
344 psi = RA*N0*tauT; % [unitless], fraction of carriers loss via Auger during
345 % heat lifetime

```

```

341 zeta = q*Eg*N0/(heat_cap*T0); % [unitless], average heat generation
342 relative to T0
343 zeta2 = (Ephoton - q*Eg)*N0/(heat_cap*T0); % [unitless], direct generation
344 of heat due to thermalization
345 s = q*S/kb; % [= q^2*S/kb], i.e., is unitless. Reduced Seebeck coeff]
346
347 %% Simulation Parameters/Range
348 tot_t_pts = 1001;
349 tot_r_pts = 51;
350
351 rsol = linspace(0,rphys_end/LT,tot_r_pts); % [unitless, in units of LT]
352 t0 = 1000e-12; % [s], center of pulse in time
353 t_end = (tphys_end + t0)/tauT; % [unitless, in units of tauT]
354
355 numt1pts = round(t0/tauT/t_end*(tot_t_pts -1))+1;
356 numt2pts = round((t_end - t0/tauT)/t_end*(tot_t_pts -1))+1;
357 t1 = linspace(0, t0/tauT, numt1pts); % [unitless, in units of tauT]
358 t2 = linspace(t0/tauT, t_end, numt2pts);
359 tsol = [t1, t2(2:end)];
360 m = 1; % cylindrical symmetry
361
362 %& Solve PDE in two parts, for the pulse rise and fall.
363 pdeoptions = odeset('RelTol', 2.222e-14, 'AbsTol', 2.222e-14);
364 sol1 = pdepe(m, @(r,t,u,dudx) seebeckpde(r,t,u,dudx, tauT, t0, sigpr,
365 sigpt, xi, chi, psi, zeta, zeta2, s), ...
366 @(seebeckic, @seebeckbc, rsol,t1, pdeoptions); % pde solver
367 sol2 = pdepe(m, @(r,t,u,dudx) seebeckpde(r,t,u,dudx, tauT, t0, sigpr,
368 sigpt, xi, chi, psi, zeta, zeta2, s), ...
369 @(r) seebeckic2(r, sol1, rsol), @seebeckbc, rsol,t2, pdeoptions); %%
370 pde solver
371
372 %& Convert Solution to Physical Units
373 u1 = [sol1(:,:,1); sol2(2:end,:,:)];
374 u2 = [sol1(:,:,2); sol2(2:end,:,:)];
375
376 rphys = rsol*LT*1e4; % [um]
377 tphys = tsol*tauT*1e9; % [ns]
378 Nphys = u1*N0; % [1/cm^2]
379 Tphys = u2*T0; % [K]
380 zero_idx = numt1pts;
381
382 end
383
384
385 function [C,F,S] = seebeckpde(r,t,u,dudx, tauT, t0, sigpr, sigpt, xi, chi, psi
386 , zeta, zeta2, s)
387 tp = t.*tauT; % [s], real time
388 Gen = (1./sqrt(2.*pi.*sigpt^2)).*exp(-r.^2/(2.*sigpr^2)).*exp(-(tp-t0)
389 .^2./(2.*sigpt^2)); % [1/s]
390
391 C = [1; 1];
392 F = [xi.*u(2).*dudx(1) + s.*xi.*u(1).*dudx(2);
393 dudx(2)];
394 S = [-(1+s).*xi.*dudx(1).*dudx(2) + Gen.*tauT - chi.*u(1) - psi.*u(1).^2;
395 zeta.*chi.*u(1) + zeta.*psi.*u(1).^2 - (u(2)-1) + zeta2.*Gen.*tauT];
396
397 % pump pulse width can be the t0 ...

```

```

389 end
390
391 function u0 = seebeckic(r)
392     u0 = [0; 1];
393 end
394
395 function u0 = seebeckic2(r, sol, rsol)
396     u0 = [interp1(rsol, sol(end,:,:,1), r); interp1(rsol, sol(end,:,:,2), r)];
397 end
398
399 function [pl, ql, pr, qr] = seebeckbc(r1, ul, rr, ur, t)
400     pl = [0; 0]; % ignored since m = 1;
401     ql = [0; 0]; % ignored since m = 1;
402     pr = [0; 0];
403     qr = [1; 1];
404 end
405
406 function out = gauss_time_convolution(tpts, rpts, n, sigma_convolution)
407     n = reshape(n, length(tpts), length(rpts));
408     out = zeros(size(n));
409     t0_ctr = mean(tpts); % added so the gaussian is normalized when integrated
410     % over t
411     kernel = 1/sqrt(2*pi*sigma_convolution.^2).*exp(-(tpts-t0_ctr).^2./(2*
412         sigma_convolution.^2));
413     DelT = mean(diff(tpts));
414     for i = 1:length(rpts)
415         out(:,i) = conv(kernel, n(:,i), 'same').*DelT;
416     end
417 end
418
419 function out = gauss_space_convolution(tpts, rpts, n, sigma_convolution)
420     n = reshape(n, length(tpts), length(rpts));
421     r0_ctr = mean(rpts);
422     kernel = 1./sqrt(2*pi*sigma_convolution.^2).*exp(-(rpts-r0_ctr).^2./(2*
423         sigma_convolution.^2));
424     DelR = mean(diff(rpts));
425     nconv = zeros(length(tpts), 2*length(rpts)-1);
426     for i = 1:length(tpts)
427         nconv(i,:) = conv(kernel, n(i,:), 'full').*DelR;
428     end
429     [~,max_idx] = max(max(nconv));
430     out = nconv(:,max_idx:max_idx + length(rpts)-1);
431 end
432
433 end

```

**Listing D.5: Sample Code for Controlling Leica Microscope to Perform Reflection Contrast Measurements and Subsequent Fitting**

```

1  % This program uses micromanager to control the ASI stage, Leica microscope,
2  % and Cobolt laser, and uses lightfield to take a spectra. If a reference
3  % measurement or datafile is given, then the plotted reflectivity spectrum
4  % is appropriately normalized, but the data that is saved is the raw spectrum.
5  % Other properties related to the measurement are also saved whenever possible.
6  %
7  % Written by Joeson Wong
8  % Last Updated October 6, 2021
9  %-----
10 close all;
11
12 %-----Measurement parameters-----
13 exposure_time = 350; % exposure time in ms
14 num_frames = 20; % number of measurement frames
15 Refl_filter_cube_pos = 0; % 0 is BF (top of Leica Buttons), and goes down
    incrementally until 5 (empty).
16 If_experiment_name = 'PL_PIXIS(VIS)_300gpmm_BL500_JWong_Reflection.lfe';
17
18 % ref10 (either take a ref10 first or use a specified ref10 datafile)
19 meas_ref10 = 1; % either 0 for no ref10 measurement, 1 to record ref10, 2 to use a
    specific ref10 file/directory
20 ref10_directory = 'C:\Users\Ateam\Desktop\Users\Joeson\10-21-2020\For_Pickup'; %
    only used when meas_bg = 2
21 ref10_filename =
    'Ag_refl_25umExc_105umColl_50xLWD_no425nmLP_70msExp_1frame_run3_2020_10_21_20_16
    .csv'; % only used when meas_bg = 2
22 ref10_waves_idx = 3;
23 ref10_counts_idx = 6;
24
25 meas_bg = 2; % either 0 for no bg measurement, 1 to record bg, 2 to use a specific
    bg file/directory
26 bg_directory = 'C:\Users\Ateam\Desktop\Users\Joeson\01-17-2021\old_GaS_PDMS'; %
    only used when meas_bg = 2
27 bg_filename = 'bg_1.csv'; % only used when meas_bg = 2
28 bg_waves_idx = 3;
29 bg_counts_idx = 6;
30 num_bg_frames = 20;
31
32 wave_fit_min = 400; % [nm]
33 wave_fit_max = 800; % [nm]
34 numCameraXPixels = 1340;
35
36 % Jogging Parameters
37 Xjogstep = 5; % [um]
38 Yjogstep = 5; % [um]
39 Zjogstep = 1; % [um]
40 StageSpeed = 100e-3; % [mm/s]
41
42 % Fitting Parameters
43 t_thinFilm_min = 0; % [nm]
44 t_thinFilm_max = 5; % [nm]
45

```

```

46 t_overlayer_min = 270;
47 t_overlayer_max = 300;
48
49 num_MS_startpts = 500; % number of points for multistart optimization
50 % t_overlayer = 285; % [nm]
51
52
53 %-----
54
55 %& Initialize Micromanager and Lightfield
56 if ~exist('mmc', 'var')
57     disp('Initializing Equipment Connections ...');
58     micromanager_path = 'C:\Program Files\Micro-Manager-2.0gamma';
59     defaultStageSpeed = 0.005; % [mm/s]
60     defaultStageBacklash = 0; % [mm]
61
62     addpath(micromanager_path);
63     import mmcorej.*;
64     mmc = CMMCore;
65
66 %& Set-up Stage
67 mmc.loadDevice("P2", "SerialManager", "COM2"); % setup serial port
68 mmc.loadDevice("XYStage", "ASISStage", "XYStage"); % setup stage
69 mmc.setProperty("XYStage", "Port", "P2"); % connect port to stage
70
71 %& Set-up Leica Microscope
72 mmc.loadDevice("P12", "SerialManager", "COM12");
73 mmc.loadDevice("Scope", "LeicaDMI", "Scope");
74 mmc.loadDevice("IL-Turret", "LeicaDMI", "IL-Turret");
75 mmc.loadDevice("ObjectiveTurret", "LeicaDMI", "ObjectiveTurret");
76 mmc.loadDevice("FocusDrive", "LeicaDMI", "FocusDrive");
77 mmc.loadDevice("SidePort", "LeicaDMI", "SidePort");
78 mmc.loadDevice("IL-Shutter", "LeicaDMI", "IL-Shutter");
79 mmc.loadDevice("TL-Shutter", "LeicaDMI", "TL-Shutter");
80 mmc.loadDevice("Transmitted Light", "LeicaDMI", "Transmitted Light");
81 mmc.setProperty("P12", "AnswerTimeout", 500);
82 mmc.setProperty("P12", "BaudRate", 19200);
83 mmc.setProperty("P12", "DTR", "Disable");
84 mmc.setProperty("P12", "Fast USB to Serial", "Disable");
85 mmc.setProperty("P12", "StopBits", 1);
86 mmc.setProperty("P12", "Parity", "None");
87 mmc.setProperty("P12", "DataBits", 8);
88 mmc.setProperty("P12", "DelayBetweenCharsMs", 0)
89
90 mmc.setProperty("Scope", "AnswerTimeOut", 250);
91 mmc.setProperty("Scope", "Port", "P12");
92 mmc.setParentLabel("IL-Turret", "Scope");
93 mmc.setParentLabel("ObjectiveTurret", "Scope");
94 mmc.setParentLabel("FocusDrive", "Scope");
95 mmc.setParentLabel("SidePort", "Scope");
96
97 %& Set-up XCite
98 mmc.loadDevice("P11", "SerialManager", "COM11");
99 mmc.loadDevice("X-Cite", "XCiteXT600", "Turbo/XT600 Controller");
100 mmc.loadDevice("LED1", "XCiteXT600", "LED1 Device");

```

```

101 mmc.setProperty("P11", "AnswerTimeout", 500);
102 mmc.setProperty("P11", "BaudRate", 19200);
103 mmc.setProperty("P11", "DTR", "Disable");
104 mmc.setProperty("P11", "Fast USB to Serial", "Disable");
105 mmc.setProperty("P11", "StopBits", 1);
106 mmc.setProperty("P11", "Parity", "None");
107 mmc.setProperty("P11", "DataBits", 8);
108 mmc.setProperty("P11", "DelayBetweenCharsMs", 0)
109 mmc.setProperty("X-Cite", "Port", "P11");
110
111 mmc.initializeAllDevices();
112
113
114 mmc.setXYStageDevice("XYStage"); % choose correct xy stage
115 mmc.setProperty("XYStage", "Speed-S", defaultStageSpeed); % set speed of
116     translation stage
117 mmc.setProperty("XYStage", "Backlash-B", defaultStageBacklash); % amount of
118     backlash while moving
119
120 %%% Set-up Labels for Microscope
121 mmc.setFocusDevice("FocusDrive");
122 mmc.setFocusDirection("FocusDrive", 0);
123
124 mmc.defineStateLabel("IL-Turret", 0, "1-BF");
125 mmc.defineStateLabel("IL-Turret", 1, "2-405/414 nm PL");
126 mmc.defineStateLabel("IL-Turret", 2, "3-532 nm PL");
127 mmc.defineStateLabel("IL-Turret", 3, "4-Empty");
128 mmc.defineStateLabel("IL-Turret", 4, "5-Empty");
129 mmc.defineStateLabel("IL-Turret", 5, "6-Empty");
130
131 mmc.defineStateLabel("ObjectiveTurret", 0, "1-5x 0.15na");
132 mmc.defineStateLabel("ObjectiveTurret", 1, "2-10x 0.3na");
133 mmc.defineStateLabel("ObjectiveTurret", 2, "3-20x 0.5na");
134 mmc.defineStateLabel("ObjectiveTurret", 3, "4-50x 0.55na");
135 mmc.defineStateLabel("ObjectiveTurret", 4, "5-50x 0.8na");
136 mmc.defineStateLabel("ObjectiveTurret", 5, "6-100x 0.9na");
137
138 mmc.defineStateLabel("SidePort", 0, "Camera");
139 mmc.defineStateLabel("SidePort", 1, "Left (Spectrometer)");
140 mmc.defineStateLabel("SidePort", 2, "Right (Empty)");
141
142 % Initialize for X-Cite
143 mmc.setProperty("LED1", "L.14 On/Off State (1=On 0=Off)", 0);
144 mmc.setProperty("LED1", "L.15 Intensity (0.0 or 5.0 - 100.0)", 5);
145
146 end
147 mmc.setProperty("XYStage", "Speed-S", StageSpeed); % set speed of translation
148     stage
149
150 %initialize Light Field
151 if ~exist('instance', 'var')
152     run Setup_LightField_Environment.m;
153     instance=lfm(true);
154     instance.load_experiment(lf_experiment_name);
155     % Startup delay when loading experiment/setting up spectrometer

```



```

198 disp('Please type "start" to start measurement, adjust focus with "r" and
199      "f"');
200 str = [];
201 while ~strcmp(str, "start")
202
203     str = input(' ', 's');
204
205     if strcmp(str, "a")      % jog left
206         mmc.setRelativeXYPosition(-Xjogstep, 0);
207     elseif strcmp(str, "d") % jog right
208         mmc.setRelativeXYPosition(Xjogstep, 0);
209     elseif strcmp(str, "w") % jog up
210         mmc.setRelativeXYPosition(0, Yjogstep);
211     elseif strcmp(str, "s") % jog down
212         mmc.setRelativeXYPosition(0, -Yjogstep);
213     elseif strcmp(str, "r") % jog up in z
214         mmc.setRelativePosition("FocusDrive", Zjogstep);
215     elseif strcmp(str, "f") % jog down in z
216         mmc.setRelativePosition("FocusDrive", -Zjogstep);
217     elseif strcmp(str, "double") % doubles size and speed of jog
218         disp('Doubling Step Size');
219         Xjogstep = 2*Xjogstep;
220         Yjogstep = 2*Yjogstep;
221         Zjogstep = 2*Zjogstep;
222         StageSpeed = 2*StageSpeed;
223         mmc.setProperty("XYStage", "Speed-S", StageSpeed);
224     elseif strcmp(str, "half") % halves size and speed of jog
225         disp('Halving Step Size');
226         Xjogstep = Xjogstep/2;
227         Yjogstep = Yjogstep/2;
228         Zjogstep = Zjogstep/2;
229         StageSpeed = StageSpeed/2;
230         mmc.setProperty("XYStage", "Speed-S", StageSpeed);
231     elseif strcmp(str, "start")
232         break;
233     else
234         disp('Not a valid key. Use "a, d, w, s" to move left, right, up,
235              down');
236     end
237 end
238
239 x0_bg_meas = mmc.getXPosition(); % [mm], center of map, where we began
240     measurements
241 y0_bg_meas = mmc.getYPosition(); % [mm], center of map, where we began
242     measurements
243 z0_bg_meas = mmc.getPosition("FocusDrive"); % [mm], center of map, where
244     we began measurements
245
246 mmc.setProperty("LED1", "L.14 On/Off State (1=On 0=Off)", 0);
247
248 disp(['Performing background measurement at x: ', num2str(x0_bg_meas), 'um
249       , y: ', num2str(y0_bg_meas), 'um, z: ', num2str(z0_bg_meas), 'um']);
250 disp(['Exposure Time for background: ', num2str(exposure_time), ' ms']);
251 disp(['Number of Frames: ', num2str(num_frames)]);

```

```

247 mmc.setState("IL-Turret", Refl_filter_cube_pos); % change to appropriate
248   filter cube
249 mmc.setState("SidePort", 1); % Use left sideport with spectrometer
250 mmc.waitForSystem();
251
252 % sets the filename and directory in lightfield
253 meas_bg_filename = strcat('bg_for_', lf_data_name);
254 instance.set(PrincetonInstruments.LightField.AddIns.ExperimentSettings.
255   FileNameGenerationDirectory, data_directory);
256 instance.set(PrincetonInstruments.LightField.AddIns.ExperimentSettings.
257   FileNameGenerationBaseFileName, meas_bg_filename);
258
259 instance.set_exposure(exposure_time);
260 instance.set_frames(num_frames);
261 [spectrum, bg_waves]=acquire(instance);
262
263 raw_bg_spectrum = squeeze(spectrum);
264
265 if length(size(spectrum))>2
266   bg_counts = mean(squeeze(spectrum),2);
267 else
268   bg_counts = squeeze(spectrum);
269 end
270 disp('Background measurement complete!');
271 mmc.setState("SidePort", 0); % Go back to camera
272
273 case 2
274   try
275     bg_data = csvread(strcat(bg_directory, '/', bg_filename), 0, 0);
276   catch
277     bg_data = csvread(strcat(bg_directory, '/', bg_filename), 1, 0);
278   end
279   bg_waves = bg_data(:,bg_waves_idx); % [nm]
280   bg_counts = bg_data(:,bg_counts_idx); % counts
281
282   if num_bg_frames>1
283     bg_counts = mean(reshape(bg_counts, [numCameraXPixels, num_bg_frames])
284     , 2);
285   end
286
287   x0_bg_meas = nan;
288   y0_bg_meas = nan;
289   z0_bg_meas = nan;
290   raw_bg_spectrum = nan;
291
292 otherwise
293   error('Use 0 for no bg subtraction/measurement, 1 for bg meas, 2 for bg
294         datafile');
295
296 end
297
298 switch meas_refl0
299   case 0
300     refl0_waves = nan;
301     refl0_counts = 0;
302     x0_refl0_meas = nan;
303     y0_refl0_meas = nan;

```

```

297 z0_refl0_meas = nan;
298 raw_refl0_spectrum = nan;
299 case 1
300
301 disp('Move to desired reference position. Press "a,d,w,s" to move left,
302 right, up, down, respectively.');
303 mmc.setState("SidePort", 0); % Use camera
304 mmc.setProperty("LED1", "L.14 On/Off State (1=On 0=Off)", 1);
305 mmc.setProperty("LED1", "L.15 Intensity (0.0 or 5.0 - 100.0)", 5);
306
307 disp('Please type "start" to start measurement, adjust focus with "r" and
308 "f"');
309 str = [];
310 while ~strcmp(str, "start")
311
312 str = input(' ', 's');
313
314 if strcmp(str, "a") % jog left
315 mmc.setRelativeXYPosition(-Xjogstep, 0);
316 elseif strcmp(str, "d") % jog right
317 mmc.setRelativeXYPosition(Xjogstep, 0);
318 elseif strcmp(str, "w") % jog up
319 mmc.setRelativeXYPosition(0, Yjogstep);
320 elseif strcmp(str, "s") % jog down
321 mmc.setRelativeXYPosition(0, -Yjogstep);
322 elseif strcmp(str, "r") % jog up in z
323 mmc.setRelativePosition("FocusDrive", Zjogstep);
324 elseif strcmp(str, "f") % jog down in z
325 mmc.setRelativePosition("FocusDrive", -Zjogstep);
326 elseif strcmp(str, "double") % doubles size and speed of jog
327 disp('Doubling Step Size');
328 Xjogstep = 2*Xjogstep;
329 Yjogstep = 2*Yjogstep;
330 Zjogstep = 2*Zjogstep;
331 StageSpeed = 2*StageSpeed;
332 mmc.setProperty("XYStage", "Speed-S", StageSpeed);
333 elseif strcmp(str, "half") % halves size and speed of jog
334 disp('Halving Step Size');
335 Xjogstep = Xjogstep/2;
336 Yjogstep = Yjogstep/2;
337 Zjogstep = Zjogstep/2;
338 StageSpeed = StageSpeed/2;
339 mmc.setProperty("XYStage", "Speed-S", StageSpeed);
340 elseif strcmp(str, "start")
341 break;
342 else
343 disp('Not a valid key. Use "a, d, w, s" to move left, right, up,
344 down');
345 end
346
347 x0_refl0_meas = mmc.getXPosition(); % [mm], center of map, where we began
348 measurements
349 y0_refl0_meas = mmc.getYPosition(); % [mm], center of map, where we began
350 measurements

```

```

347 z0_ref10_meas = mmc.getPosition("FocusDrive"); % [mm], center of map,
348 % where we began measurements
349
350 mmc.setProperty("LED1", "L.14 On/Off State (1=On 0=Off)", 0);
351
352 disp(['Performing reference measurement at x: ', num2str(x0_ref10_meas), ' '
353 'um, y: ', num2str(y0_ref10_meas), 'um, z: ', num2str(z0_ref10_meas), ' '
354 'um']);
355 disp(['Exposure Time for Reference: ', num2str(exposure_time), ' ms']);
356 disp(['Number of Frames: ', num2str(num_frames)]);
357
358 mmc.setState("IL-Turret", Refl_filter_cube_pos); % change to appropriate
359 % filter cube
360 mmc.setState("SidePort", 1); % Use left sideport with spectrometer
361 mmc.waitForSystem();
362
363 % sets the filename and directory in lightfield
364 meas_ref10_filename = strcat('ref10_for_', lf_data_name);
365 instance.set(PrincetonInstruments.LightField.AddIns.ExperimentSettings.
366 FileNameGenerationDirectory, data_directory);
367 instance.set(PrincetonInstruments.LightField.AddIns.ExperimentSettings.
368 FileNameGenerationBaseFileName, meas_ref10_filename);
369
370 instance.set_exposure(exposure_time);
371 instance.set_frames(num_frames); % always use 1 frame for bg
372 [spectrum, ref10_waves]=acquire(instance);
373
374 raw_ref10_spectrum = squeeze(spectrum);
375
376 if length(size(spectrum))>2
377     ref10_counts = mean(squeeze(spectrum),2);
378 else
379     ref10_counts = squeeze(spectrum);
380 end
381 disp('Reference measurement complete!');
382 mmc.setState("SidePort", 0); % Go back to camera
383
384 case 2
385 try
386     ref10_data = csvread(strcat(ref10_directory, '/', ref10_filename), 0,
387     0);
388 catch
389     ref10_data = csvread(strcat(ref10_directory, '/', ref10_filename), 1,
390     0);
391 end
392 ref10_waves = ref10_data(:,ref10_waves_idx); % [nm]
393 ref10_counts = ref10_data(:,ref10_counts_idx);
394 x0_ref10_meas = nan;
395 y0_ref10_meas = nan;
396 z0_ref10_meas = nan;
397 raw_ref10_spectrum = nan;
398
399 otherwise
400     error('Use 0 for no ref10 normalization/measurement, 1 for ref10 meas, 2
401         for ref10 datafile');
402 end

```

```

393
394 if meas_bg && meas_ref0
395   bg_counts = reshape(bg_counts, size(ref0_counts));
396 end
397
398 %& Prepare for Reflection measurement
399 disp('Move to desired position for reflectance measurements. Press "a,d,w,s" to
       move left, right, up, down, respectively.');
400 mmc.setProperty("LED1", "L.14 On/Off State (1=On 0=Off)", 1);
401 mmc.setProperty("LED1", "L.15 Intensity (0.0 or 5.0 - 100.0)%", 5);
402 mmc.setState("SidePort", 0); % Use camera
403
404 disp('Please type "start" to start measurement, adjust focus with "r" and "f"');
405 str = [];
406 while ~strcmp(str, "start")
407
408   str = input(' ', 's');
409
410   if strcmp(str, "a") % jog left
411     mmc.setRelativeXYPosition(-Xjogstep, 0);
412   elseif strcmp(str, "d") % jog right
413     mmc.setRelativeXYPosition(Xjogstep, 0);
414   elseif strcmp(str, "w") % jog up
415     mmc.setRelativeXYPosition(0, Yjogstep);
416   elseif strcmp(str, "s") % jog down
417     mmc.setRelativeXYPosition(0, -Yjogstep);
418   elseif strcmp(str, "r") % jog up in z
419     mmc.setRelativePosition("FocusDrive", Zjogstep);
420   elseif strcmp(str, "f") % jog down in z
421     mmc.setRelativePosition("FocusDrive", -Zjogstep);
422   elseif strcmp(str, "double") % doubles size and speed of jog
423     disp('Doubling Step Size');
424     Xjogstep = 2*Xjogstep;
425     Yjogstep = 2*Yjogstep;
426     Zjogstep = 2*Zjogstep;
427     StageSpeed = 2*StageSpeed;
428     mmc.setProperty("XYStage", "Speed-S", StageSpeed);
429   elseif strcmp(str, "half") % halves size and speed of jog
430     disp('Halving Step Size');
431     Xjogstep = Xjogstep/2;
432     Yjogstep = Yjogstep/2;
433     Zjogstep = Zjogstep/2;
434     StageSpeed = StageSpeed/2;
435     mmc.setProperty("XYStage", "Speed-S", StageSpeed);
436   elseif strcmp(str, "start")
437     break;
438   else
439     disp('Not a valid key. Use "a, d, w, s" to move left, right, up, down');
440   end
441 end
442
443 mmc.setProperty("LED1", "L.14 On/Off State (1=On 0=Off)", 0);
444 x0_meas = mmc.getXPosition(); % [mm], where we began measurements
445 y0_meas = mmc.getYPosition(); % [mm], where we began measurements
446 z0_meas = mmc.getPosition("FocusDrive");

```

```

447
448 disp(['Performing reflectance measurement at x: ', num2str(x0_meas), 'um, y: ',
449     num2str(y0_meas), ' um, z: ', num2str(z0_meas), ' um']);
450 disp(['Exposure Time for Spectrum: ', num2str(exposure_time), ' ms']);
451 disp(['Number of Frames: ', num2str(num_frames)]);
452
453 mmc.setState("IL-Turret", Refl_filter_cube_pos); % change to appropriate filter
454     cube
455 mmc.setState("SidePort", 1); % Use left sideport with spectrometer
456 objective_in_use = mmc.getStateLabel("ObjectiveTurret");
457 % add in some code to turn off the X-cite light when we figure out how to
458 % control it again
459 mmc.waitForSystem();
460
461 % Sets the filename and directory in lightfield, and takes a spectrum
462 instance.set(PrincetonInstruments.LightField.AddIns.ExperimentSettings.
463     FileNameGenerationDirectory, data_directory);
464 instance.set(PrincetonInstruments.LightField.AddIns.ExperimentSettings.
465     FileNameGenerationBaseFileName, lf_data_name);
466 instance.set_exposure(exposure_time);
467 instance.set_frames(num_frames);
468 [spectrum, waves] = acquire(instance);
469
470 raw_spectrum = squeeze(spectrum);
471
472 if length(size(spectrum)) > 2
473     refl_counts = reshape(mean(squeeze(spectrum), 2), size(refl0_counts));
474 else
475     refl_counts = reshape(squeeze(spectrum), size(refl0_counts));
476 end
477
478 if meas_refl0 && meas_bg
479     spectrum_w_norm = (refl_counts - bg_counts) ./ (refl0_counts - bg_counts);
480 elseif meas_refl0 && ~meas_bg
481     spectrum_w_norm = (refl_counts) ./ (refl0_counts);
482 elseif ~meas_refl0 && meas_bg
483     spectrum_w_norm = refl_counts - bg_counts;
484 else
485     spectrum_w_norm = refl_counts;
486 end
487
488 %< Generate Reflectivity Contrast Plot
489 % Wavelength
490 specFig = figure;
491 set(specFig, 'Position', [200, 400, 500, 500]);
492 box on;
493 xlabel('Wavelength (nm)'); ylabel('R/R_0');
494 xlim([min(waves), max(waves)]);
495 axis tight; hold on;
496 pspec = plot(waves, spectrum_w_norm);
497 saveas(specFig, fig_data_name);
498
499 % Energy
500 specFig2 = figure;

```

```

498 set(specFig2, 'Position', [600, 400, 500, 500]);
499 box on;
500 energy = 1239.8./waves;
501 xlabel('Energy (eV)'); ylabel('R/R_0');
502 xlim([min(energy), max(energy)]);
503 axis tight; hold on;
504 pspec = plot(energy, spectrum_w_norm);
505
506 filter_in_use = mmc.getStateLabel("IL-Turret");
507 grating_center_wavelength = instance.get(PrincetonInstruments.LightField.AddIns.
508     SpectrometerSettings.GratingCenterWavelength);
509 grating_selected = string(instance.get(PrincetonInstruments.LightField.AddIns.
509     SpectrometerSettings.GratingSelected));
510 disp('Acquisition Complete!');
511 mmc.setState("IL-Turret", 0); % change back to BF filter cube
512 mmc.setState("SidePort", 0); % Go back to camera
513 mmc.setProperty("LED1", "L.14 On/Off State (1=On 0=Off)", 1);
514 mmc.setProperty("LED1", "L.15 Intensity (0.0 or 5.0 - 100.0)", 5);
515
516 %& Perform Fitting using "simple" ellipsometry
517 disp('Starting Fitting ...');
518 wave_bool = waves>wave_fit_min & waves<wave_fit_max;
519 wave_fit = waves(wave_bool);
520 energy_fit = 1239.84./wave_fit;
521
522 ntilde_thinFilm = sqrt(MoS2_epsilon(energy_fit));
523
524 n_Si = load('ntilde_Si.mat');
525 ntilde_sub = interp1(n_Si.lambda_Si, n_Si.ntilde_Si, wave_fit);
526 lambda_SiO2 = 0.2:0.001:3;
527 n_SiO2 = sqrt(1+0.6961663./(1-(0.0684043./lambda_SiO2).^2)
528     +0.4079426./(1-(0.1162414./lambda_SiO2).^2)+0.8974794./(1-(9.896161./
529     lambda_SiO2).^2));
530 ntilde_overlayer = interp1(lambda_SiO2*1e3, n_SiO2, wave_fit);
531
532 %& MultiStart Parameters
533 maxfuncEval = 1e2;
534 OptimTol = 1e-9;
535 StepTol = 1e-9;
536 maxIter = 1e2;
537 FuncTol = 1e-9;
538 ms_lsqOpts = optimoptions('lsqcurvefit', 'MaxFunctionEvaluations', maxfuncEval, ...
539     'OptimalityTolerance', OptimTol, 'StepTolerance', StepTol, ...
540     'MaxIterations', maxIter, 'FunctionTolerance', FuncTol);
541
542 %& lsqcurvefit Parameters
543 maxfuncEval = 1e3;
544 OptimTol = 1e-15;
545 StepTol = 1e-15;
546 maxIter = 1e3;
547 FuncTol = 1e-15;
548 lsqOpts = optimoptions('lsqcurvefit', 'MaxFunctionEvaluations', maxfuncEval, ...
549     'OptimalityTolerance', OptimTol, 'StepTolerance', StepTol, ...

```

```

549 %MaxIterations', maxIter, 'FunctionTolerance', FuncTol);

551

552 x0 = [(t_thinFilm_min + t_thinFilm_max)/2, (t_overlayer_min + t_overlayer_max)/2];
553 fun = @(x, xdata) fitfunc(x, xdata, ntilde_thinFilm, ntilde_overlayer, ntilde_sub);
554 xdata = wave_fit();
555 ydata = spectrum_w_norm(wave_bool);
556 ydata = ydata(:);
557 lb = [t_thinFilm_min, t_overlayer_min];
558 ub = [t_thinFilm_max, t_overlayer_max];
559

560 stpts = [(t_thinFilm_max - t_thinFilm_min)*rand(num_MS_startpts,1) +
561 t_thinFilm_min, ...
562 (t_overlayer_max - t_overlayer_min)*rand(num_MS_startpts,1) +
563 t_overlayer_min];

564 startpts = CustomStartPointSet(stpts);
565 problem = createOptimProblem('lsqcurvefit', 'objective', fun, 'x0', x0, ...
566 'xdata', xdata, 'ydata', ydata, 'lb', lb, 'ub', ub, 'options', ms_lsqOpts);
567 ;
568 ms = MultiStart;
569 tic;
570 x_ms = run(ms, problem, startpts);
571 [x_lsq, resnorm] = lsqcurvefit(fun, x_ms, xdata, ydata, t_thinFilm_min,
572 t_thinFilm_max, lsqOpts);
573 fitted_thickness = x_lsq(1);
574 oxide_thickness = x_lsq(2);
575 disp(['Total time for fit: ', num2str(round(toc,1)), ' seconds']);

576 % Wavelength
577 specFigFit = figure;
578 set(specFigFit, 'Position', [200, 400, 500, 500]);
579 box on;
580 xlabel('Wavelength (nm)'); ylabel('R/R_0');
581 xlim([min(wave_fit), max(wave_fit)]);
582 axis tight; hold on;
583 pspec1 = plot(xdata, ydata, 'k.');
584 pspec2 = plot(xdata, fun(x_lsq, xdata), 'b-');
585 title(['Film Thickness: ', num2str(round(fitted_thickness,1)), ' nm, Oxide
586 Thickness: ', num2str(round(oxide_thickness,1)), ' nm, Fitting Residual: ',
587 num2str(round(resnorm,1))]);
588 legend([pspec1, pspec2], {'Experiment', 'Fit'}, 'Orientation', 'Horizontal', 'Location', 'NorthOutside');
589 saveas(specFigFit, fit_fig_name);

590

591 % save all relevant data in a .mat file
592 save(mat_data_name, 'lf_experiment_name', 'exposure_time', 'num_frames', ...
593 'objective_in_use', 'filter_in_use', 'Refl_filter_cube_pos', ...
594 'grating_center_wavelength', 'grating_selected',...
595 'x0_meas', 'y0_meas', 'z0_meas', 'waves', 'raw_spectrum', ...
596 'spectrum_w_norm', ...
597 'bg_directory', 'bg_filename', 'bg_waves_idx', 'bg_counts_idx', ...
598 'meas_bg', 'bg_waves', 'bg_counts', ...
599 'x0_bg_meas', 'y0_bg_meas', 'z0_bg_meas', 'raw_bg_spectrum', ...
600 'bg_waves_idx', 'bg_counts_idx');

```

```

595 'refl0_directory', 'refl0_filename', 'refl0_waves_idx', 'refl0_counts_idx'
596     ,
597     ...
598 'meas_refl0', 'refl0_waves', 'refl0_counts', ...
599 'x0_refl0_meas', 'y0_refl0_meas', 'z0_refl0_meas', 'raw_refl0_spectrum', ...
600 'fitted_thickness', 'oxide_thickness', 'ntilde_thinFilm', 'ntilde_sub', ' '
601     ntilde_overlayer', 't_overlayer', 'wave_fit_min', 'wave_fit_max', ...
602 'numCameraXPixels', 'num_bg_frames', 'Xjogstep', 'Yjogstep', 'Zjogstep', ' '
603     StageSpeed');
604
605 function y = fitfunc(x,xdata, ntilde_thinFilm, ntilde_overlayer, ntilde_sub)
606     R = FourLayer_thinFilmFast(ntilde_thinFilm, x(1), ntilde_overlayer, x(2),
607         ntilde_sub, xdata);
608     R0 = FourLayer_thinFilmFast(ntilde_thinFilm, 0, ntilde_overlayer, x(2),
609         ntilde_sub, xdata);
610     y = R(:)./R0(:);
611 end
612
613
614 function R = thinFilmSub(ntilde_thinFilm, t_thinFilm, ntilde_sub, lambda)
615 % ntilde_thinFilm has size size(ntilde_sub)
616 %
617 % t_thinFilm is a single scalar [same units as lambda]
618 %
619 % ntilde_sub has dimensions of usually length(lambda) x 1 or 1 x
620 % length(lambda)
621 %
622 % lambda is a vector and has units of t_thinFilm
623 %
624 % Output R is a vector with the same dimensions as lambda, i.e. R =
625 % R(lambda)
626 %
627 % Reshape matrices to the right size
628 n_air = ones(size(ntilde_sub));
629 ntilde_thinFilm = reshape(ntilde_thinFilm, size(ntilde_sub));
630 lambda = reshape(lambda, size(ntilde_sub));
631
632 r12 = (n_air-ntilde_thinFilm)./(n_air+ntilde_thinFilm);
633 r23 = (ntilde_thinFilm - ntilde_sub)./(ntilde_thinFilm + ntilde_sub);
634 beta = (2*pi.*ntilde_thinFilm.*t_thinFilm)./lambda;
635
636 r = (r12+r23.*exp(2i*beta))./(1+r12.*r23.*exp(2i*beta)); % simple 3-layer
637     interference model
638 R = abs(r).^2;
639 end
640
641
642 function R = FourLayer_thinFilmFast(ntilde_thinFilm, t_thinFilm, ntilde_overlayer,
643     t_overlayer, ntilde_sub, lambda)
644 %
645 % Reshape matrices to the right size
646 n_air = ones(size(ntilde_sub));
647 ntilde_thinFilm = reshape(ntilde_thinFilm, size(ntilde_sub));
648 ntilde_overlayer = reshape(ntilde_overlayer, size(ntilde_sub));
649 lambda = reshape(lambda, size(ntilde_sub));
650
651 r01 = (n_air - ntilde_thinFilm)./(n_air + ntilde_thinFilm);
652 r12 = (ntilde_thinFilm - ntilde_overlayer)./(ntilde_thinFilm +

```

```

        ntilde_overlayer);
643 r23 = (ntilde_overlayer - ntilde_sub)./(ntilde_overlayer + ntilde_sub);
644 beta1 = (2*pi.*ntilde_thinFilm.*t_thinFilm)./lambda;
645 beta2 = (2*pi.*ntilde_overlayer*t_overlayer)./lambda;
646
647 % J01 = [1, r01; r01, 1];
648 % L1 = [exp(-1i*beta1), 0; 0, exp(1i*beta1)];
649 % J12 = [1, r12; r12, 1];
650 % L2 = [exp(-1i*beta2), 0; 0, exp(1i*beta2)];
651 % J23 = [1, r23; r23, 1];
652 %
653 % S = J01*L1*J12*L2*J23;
654 % r = S(2,1)./S(1,1);
655
656 num = (r01 + r12.*exp(2i*beta1)) + exp(2i*beta2).*r23.*(r01.*r12 + exp(2i*
657     beta1));
658 denom = (1 + exp(2i*beta1).*r01.*r12) + exp(2i*beta2).*r23.*(r12 + exp(2i*
659     beta1).*r01);
660 R = abs(num./denom).^2;
661
662 end
663
664 function R = FourLayer_thinFilm(ntilde_thinFilm, t_thinFilm, ntilde_overlayer,
665 t_overlayer, ntilde_sub, lambda)
666
667 % definition of layers, each layer is a separate column vector. Total
668 % matrix of ntilde is m x n, where m is the number of wavelengths and n is
669 % the number of layers of material
670 ntilde = [ones(length(lambda), 1), ... %first layer, which is air usual
671     reshape(ntilde_thinFilm, [length(lambda), 1]), ...
672     reshape(ntilde_overlayer, [length(lambda), 1]), ...
673     reshape(ntilde_sub, [length(lambda), 1]), ...
674     ]; % last layer is substrate/air, should have length(t)+2 number of layers
675
676 z = cumsum([0, t_thinFilm, t_overlayer]); % units of [m], actual z position of
677 % layers. Start at z = 0.
678
679 R = zeros(length(lambda), 1);
680
681 % Calculate spectrally, monochromatic wave assumption
682 for k = 1: length(lambda)
683
684     J = [1, 0 ;
685         0, 1]; % initialize J as identity matrix
686
687     % first layer is air, coordinates are such that the air-dielectric
688     % stack starts at z = 0
689     for j = 1:length(z)
690         q = 2*pi*ntilde(k,j)/lambda(k);
691         qp = 2*pi*ntilde(k,j+1)/lambda(k);
692         J = 1/2*[exp(1i*(q - qp)*z(j)) * (1+q/qp) , exp(-1i*(q + qp)*z(j)
693             ) * (1-q/qp); ...
694             exp(1i*(q + qp)*z(j)) * (1-q/qp) , exp(-1i*(q - qp)
695                 *z(j)) * (1+q/qp)]*J;
696     end
697 end

```

```

690     end
691
692     % reflection amplitude
693     r = -J(2,1)/J(2,2);
694
695     % Reflection coefficient from J
696     R(k) = abs(r).^2;
697
698 end
699
700 end
701
702 function eps = GaS_epsilon(E)
703     default_fk = [0.0081, 70.2622];
704     default_Ek = [2.8236, 4.6093];
705     default_gammak = [0.1, 0.0352];
706     default_eps_bg = 2.8912;
707 %     default_fk = 30; % default
708 %     default_Ek = 4.7163;
709 %     default_gammak = 3.8859e-14;
710 %     default_eps_bg = 6.0430;
711     eps = epsilon(default_fk, default_Ek, default_gammak, E, length(default_fk),
712                   default_eps_bg);
713 end
714
715 function eps = MoS2_epsilon(E)
716     default_fk = [0.9824, 3.3385, 9.5771, 30, 30];
717     default_Ek = [1.866, 2.010, 2.489, 2.8596, 3.185];
718     default_gammak = [0.05811, 0.1545, 0.6605, 0.36189, 0.4481];
719     default_eps_bg = 7.523;
720     eps = epsilon(default_fk, default_Ek, default_gammak, E, length(default_fk),
721                   default_eps_bg);
722 end
723
724 function eps = MoSe2_epsilon(E)
725     default_fk = [0.7770, 1.5210, 2.4830, 10.1110, 26.3230, 13.5090,
726                 14.2800, 18.6230];
727     default_Ek = [1.5470, 1.7490, 1.9890, 2.3500, 2.6250, 3.0280,
728                 3.3930, 3.6610];
729     default_gammak = [0.0500, 0.1120, 0.3890, 0.5480, 0.4730,
730                 0.6250, 0.2170, 0.1400];
731     default_eps_bg = 2.753;
732
733     eps = epsilon(default_fk, default_Ek, default_gammak, E, length(default_fk),
734                   default_eps_bg);
735 end
736
737 function eps = WSe2_epsilon(E)
738     default_fk = [0.6776, 1.9509, 8.1767, 28.0458, 27.7930];
739     default_Ek = [1.652, 2.079, 2.431, 2.927, 3.507];
740     default_gammak = [0.0462, 0.1856, 0.3297, 0.4950, 0.0607];
741     default_eps_bg = 5.68552;
742     eps = epsilon(default_fk, default_Ek, default_gammak, E, length(default_fk),
743                   default_eps_bg);

```

```
738 end
739
740 function eps = WS2_epsilon(E)
741     default_fk = [1.963, 3.505, 20.212, 30.000]; % default
742     default_Ek = [2.012, 2.403, 2.862, 3.219];
743     default_gammak = [0.0356, 0.1892, 0.3568, 0.3585];
744     default_eps_bg = 6.9233;
745     eps = epsilon(default_fk, default_Ek, default_gammak, E, length(default_fk),
746                   default_eps_bg);
746 end
747
748 function eps = epsilon(fk, Ek, gammak, E, N, eps_bg)
749     eps = eps_bg*ones(size(E));
750     for idx = 1:N
751         eps = eps + fk(idx)./(Ek(idx)^2-E.^2-1i*E*gammak(idx));
752     end
753 end
```

## Listing D.6: Excitons dissociating in an Electric Field Code

```

1 numPts = 100; % use g = 40 for reasonable speed and accuracy. 200 is "high
2   resolution"
3 p = linspace(-5, 5, numPts); % 1D mesh
4 h = p(2) - p(1); % spacing
5
6 [Xmesh, Ymesh, Zmesh] = meshgrid(p,p,p); % 3D Mesh
7 X = Xmesh(:); Y = Ymesh(:); Z = Zmesh(:); % all elements as a single
8   column
9 R = sqrt(X.^2 + Y.^2 + Z.^2); % distance from the center
10 e = ones(numPts,1);
11 L = spdiags([e -2*e e], -1:1, numPts, numPts) / h^2; % 1D finite
12   difference Laplacian
13 I = speye(numPts);
14 L3 = kron(kron(L,I), I) + kron(kron(I, L), I) + kron(kron(I, I), L); % extend
15   Laplacian to 3 D
16
17 F_vals = linspace(0,1,21); % Field values, in excitonic units
18 EvsF = zeros(size(F_vals)); % 1s eigenenergies vs. field
19 PsivsF = zeros(g3, length(F_vals)); % wavefunctions vs. field
20 TunnelProb = zeros(size(F_vals)); % tunneling probability = dissociation
21   efficiency
22 fig = figure;
23 colorLines = linspecer(length(F_vals)); % create colors for pretty lines
24
25 for F_idx = 1:length(F_vals)
26   Vext = -2./R - F_vals(F_idx).*Z; % potential energy
27   H = -L3 + spdiags(Vext, 0, numPts^3, numPts^3); % Hamiltonian of exciton
28   [PSI,E] = eigs(H, 1, 'smallestreal'); % Smallest eigenvalue of exciton
29
30   EvsF(F_idx) = E; % 1s energies vs. field, units of Rydberg
31   PsivsF(:,F_idx) = PSI; % wavefunctions in column format, vs field
32
33   PSI_3 = reshape(PSI, [numPts, numPts, numPts]); % shape properly to
34   integrate
35   PSI_zInt = squeeze(trapz(p, trapz(p, abs(PSI_3).^2))); % integrate over
36   all x,y
37   PSI_zInt = PSI_zInt ./ sqrt(trapz(p, abs(PSI_zInt).^2)); % normalize
38   plot(p, abs(PSI_zInt).^2, 'k-', 'Color', colorLines(F_idx,:), 'LineWidth',
39   1.5); hold on; % plot wavefns
40
41   z0 = sqrt(2/F_vals(F_idx)); % maximum value of potential for z > 0
42   TunnelProb(F_idx) = trapz(p(p>z0), abs(PSI_zInt(p>z0)).^2); % treat any
43   part of the wfcn that is past this point as being ionized

```

```
44      ,:), 'MarkerEdgeColor', colorLines(F_idx,:)); hold on;
45  end
46 xlabel('$eF_z a_0/E_b$', 'interpreter', 'latex');
47 ylabel('${(\hbar\omega-E_g)/E_{b,0}}$', 'interpreter', 'latex');
48
49 % Create another figure for how dissociation efficiency changes with field
50 figure;
51 semilogy(F_vals, TunnelProb, 'k-', 'LineWidth', 0.5); hold on;
52 for F_idx = 1:length(F_vals)
53     semilogy(F_vals(F_idx), TunnelProb(F_idx), 'o', 'MarkerFaceColor',
54               colorLines(F_idx, :), 'MarkerEdgeColor', colorLines(F_idx,:)); hold on
55     ;
56 end
57 xlabel('$eF_z a_0/E_b$', 'interpreter', 'latex');
58 ylabel('${\eta_{diss}}$', 'interpreter', 'latex');
```

Listing D.7: Solutions to the 2D Keldysh Potential Code

```

1  clear;
2  close all;
3
4  numpt_vals = [100, 100];
5  rvals = [5, 15];
6
7  eps1 = 1;
8  eps2 = 1;
9
10 a0 = 1;
11 r0_vals = [logspace(-5, 0, 21), linspace(1,10,21)];
12 EN = zeros(2, length(r0_vals)); % a
13
14 for rho_idx = 1:length(r0_vals)
15   for idx = 1:2
16     numpts = numpt_vals(idx);
17     rmax = rvals(idx);
18     linmesh = linspace(-rmax, rmax, numpts); % one dimension space
19     lattice
20     [X, Y] = meshgrid(linmesh, linmesh); % two dimension space
21     delta = linmesh(2) - linmesh(1); % spacing
22     X = X(:); Y = Y(:); % all elements of array as a single column
23     R = sqrt(X.^2 + Y.^2); % distance from the center
24     % Vext = -2 ./ R; % potential energy
25     Vext = -2*pi*a0 ./((eps1+eps2)*r0_vals(rho_idx))*StruveH0Y0(R*a0 ./ r0_vals(
26       rho_idx));
27     e = ones(numpts,1);
28     L = spdiags([e -2*e e], -1:1, numpts, numpts) / delta.^2; % 1D finite
29     difference Laplacian
30     I = speye(numpts);
31     L2 = kron(L,I) + kron(I, L); % extend Laplacian to 2 D
32     H = -L2 + spdiags(Vext, 0, numpts.^2, numpts.^2); % Hamiltonian of H atom
33     [PSI, E] = eigs(H, idx.^2, 'smallestreal'); % Smallest eigenvalue
34     of H
35     E = diag(E);
36
37     EN(idx, rho_idx) = mean(E( (idx-1)*(idx-1) + 1 : idx*idx)); % average the
38     energies
39   end
40 end
41
42 Delta12 = abs(EN(1,:)-EN(2,:));
43 Eb = abs(EN(1,:));
44 CoulombVal = 9/8; % From 2D Coulomb
45
46 figure;
47 plot(r0_vals./a0, Eb./Delta12, 'b-', 'LineWidth', 2); hold on;
48 plot(linspace(0, max(r0_vals)./a0), CoulombVal.*ones(1, 100), 'k--');
49 xlabel('$r_0/a_0$', 'interpreter', 'latex');
50 ylabel('$E_b/\Delta_{12}$', 'interpreter', 'latex');
51 text(5, 1.175, '2D Coulomb Limit');

```